Laboratoire de Constructions Hydrauliques
Ecole Polytechnique Fédérale de Lausanne

Communication 13

Transient water pressures in joints and formation of rock scour due to high-velocity jet impact

Erik Bollaert

Editeur : Prof. Dr A. Schleiss

Lausanne, 2002

Communications du Laboratoire de constructions hydrauliques
Ecole Polytechnique Fédérale de Lausanne
Editeur: Prof. R. Sinniger

N° 1 1986 W. H. Hager
Discharge measurement structures

N° 2 1988 N. V. Bretz
Ressaut hydraulique forcé par seuil

N° 3 1990 R. Bremen
Expanding stilling basin

N° 4 1996 Dr R. Bremen
Ressaut hydraulique et bassins amortisseurs, aspects hydrauliques particuliers

N° 5 1997 Compte-rendu du séminaire à l'EPFL
Recherche dans le domaine des barrages, crues extrêmes

Communications du Laboratoire de constructions hydrauliques
Ecole Polytechnique Fédérale de Lausanne
Editeur: Prof. Dr A. Schleiss

N° 6 1998 N. Beyer Portner
Erosion des bassins versants alpins suisse par ruissellement de surface

N° 7 1998 G. De Cesare
Alluvionnement des retenues par courants de turbidité

N° 8 1998 J. Dubois
Comportement hydraulique et modélisation des écoulements de surface

N° 9 2000 J. Dubois, J.-L. Boillat
Routing System - Modélisation du routage de crues dans des systèmes hydrauliques à surface libre

N° 10 2002 J. Dubois, M. Pirotton
Génération et transfert des crues extrêmes - Le logiciel Faitou

N° 11 2002 A. Lavelli, G. De Cesare, J.-L. Boillat
Modélisation des courants de turbidité dans le bassin Nord du Lac de Lugano

N° 12 2002 P. de Almeida Manso
Stability of linings by concrete elements for surface protection of overflow earthfill dams

N° 13 2002 Erik Bollaert
Transient water pressures in joints and formation of rock scour due to high-velocity jet impact

Laboratoire de Constructions Hydrauliques
Ecole Polytechnique Fédérale de Lausanne

Communication 13

Transient water pressures in joints and formation of rock scour due to high-velocity jet impact

Erik Bollaert

Editeur : Prof. Dr A. Schleiss

Lausanne, 2002

PREFACE

The safety of hydraulic structures in general and dams in particular is very often endangered by the formation of scour near the foundation as a result of high-velocity jets leaving from appurtenant structures as spillways and plunging into the tailwater. Scouring is a very complex physical process, which is assessed normally in practice by analytical-empirical methods combining laboratory and field observations with some physics. Full physical understanding of the water-air-rock interaction in the scouring process is still lacking.

With the research described in the present communication, Dr. Erik Bollaert filled up a considerable gap towards a better scientific understanding of the scouring process. For the first time the transient pressures in rock joints due to high-velocity jet impact could be measured and reproduced in a numerical model. New phenomena could be observed and explained, such as the reflection and superposition of pressure waves, resonance pressures and quasi-instantaneous air release and re-solution due to pressure drops in the joints. With these observations the physical key for scour formation could be clearly identified. If the corresponding stresses due to the hydrodynamic pressures at the tip of the joint exceed the fracture toughness of the rock, depending on its tensile strength and initial compressive stresses, the rock will crack and the joint can grow further. In the case of open-end rock joints in fully jointed rock, the pressure waves inside the joints create a significant dynamic uplift force on the rock blocks. This dynamic uplift force will break up the remaining rock bridges in the joints by fatigue and, if high enough, eject the so formed rock blocks from the rock mass into the macroturbulent plunge pool flow.

Based on the experimental results and numerical simulations as well as on an extensive physical analysis, Dr. Erik Bollaert derived a new scour model, which includes all relevant processes starting from the free falling jet to the fissured rock mass. This new model is a significant step in research towards a better assessment of the scour process. The application for the well-known case of rock scour at the Cahora Bassa Dam in Mozambique confirms the promising nature of the new scour model.

We would like to thank Prof. Dr. Michel Pirotton and Sébastien Erpicum from the Université de Liège for their contributions in the field of numerical modelling. Furthermore Prof. Dr. Henk Falvey, from Colorado State University, and Dr. George Annandale, from Engineering & Hydrosystems Inc., gave significant support and guidance during their stay as academic guest at LCH-EPFL. Furthermore we would like to thank Prof. Dr. Alan Ervine for his useful advice on turbulence and aeration of jets and plunge pools. Finally we thank the Swiss Committee on Dams (SwissCOD), Stucky Consulting Engineers Ltd. and the Commission on Technology and Innovation (CTI) for their financial support to the project.

Prof. Dr Anton J. Schleiss

PREFACE

La sécurité des constructions hydrauliques en général et des barrages en particulier est souvent mise en danger par l'affouillement des fondations du à des jets d'eau à haute vitesse qui proviennent des évacuateurs de crue et qui impactent sur le rocher en aval. L'érosion par affouillement est un processus physique très complexe, qui est normalement appréhendé en pratique par des méthodes analytique-empirique, com-binant des observations en laboratoire ou in situ avec quelques bases physiques. Une compréhension physique complète de l'interaction eau-rocher fait actuellement défaut.

Par la recherche décrite dans la présente communication, le Dr Erik Bollaert a comblé une lacune importante, permettant de mieux comprendre scientifiquement le processus d'affouillement. Pour la première fois, les pressions transitoires dans des fissures du rocher, dues à l'impact de jets d'eau à haute vitesse, ont été mesurées sur modèle physique et reproduites dans un modèle numérique. De nouveaux phénomènes ont été observés et appréhendés, tels que la réflexion et la superposition des ondes de pression, la résonance des pressions et finalement le gazage et le dégazage quasi-instantanés de bulles d'air dû à des chutes de pression dans les fissures.

Ces observations ont permis d'identifier les bases physiques de la formation des fosses d'érosion. Si la contrainte due aux pressions hydrodynamiques à la pointe de la fissure dépasse la résistance à la fracturation, la fissure se propagera. La résistance à la fracturation dépend notamment des contraintes initiales dans le massif rocheux et du type de rocher. Dans le cas d'une fissuration complète du massif rocheux, les ondes de pression dans les fissures créent une force de soulèvement dynamique qui est considérable. Cette force de soulèvement enlève les points de contact restants entre les différents blocs de rocher et peut, le cas échéant, éjecter les blocs. Basé sur les résultats expérimentaux et les simulations numériques, ainsi que sur une analyse extensive, le Dr Erik Bollaert a développé un nouveau modèle d'évaluation de l'érosion, incluant tous les processus relevants depuis le jet à sa sortie de l'évacuateur de crue jusqu'à la formation de la fosse d'affouillement dans le massif rocheux. Ce modèle est une contribution considérable dans la recherche d'une appréhension de l'érosion. L'application à la fosse d'affouillement du barrage de Cahora Bassa en Mozambique confirme le caractère prometteur de cette nouvelle méthode de calcul.

Nous aimerions remercier le Prof. Dr Michel Pirotton et M. Sébastien Erpicum de l'Université de Liège pour leurs contributions significatives dans le domaine de la modélisation numérique. Ensuite, le Prof. Dr Hank Falvey du Colorado State University et le Dr George Annandale de Engineering & Hydrosystems Inc. ont donné un support considérable en tant qu'hôtes académiques au LCH-EPFL. Le Prof. Dr Alan Ervine a donné des renseignements précieux sur la turbulence et l'aération des jets et des fosses d'affouillement. Finalement, nous aimerions remercier le Comité Suisse des Barrages (CSB), ainsi que le bureau d'ingénieurs Stucky Ingénieurs-Conseil et la Commission pour l'Innovation et la Technologie (CTI) pour le support financier au projet.

Prof. Dr Anton J. Schleiss

Mais avant d'aller plus loin, je ferai d'abord quelques expériences, car mon intention est de présenter d'abord l'expérience, puis de démontrer par la raison pourquoi cette expérience doit obligatoirement se dérouler de cette façon. Et c'est ici la véritable règle que doivent observer ceux qui réfléchissent aux phénomènes naturels: bien que la nature commence par la raison et termine par l'expérience, nous, nous devons suivre l'ordre contraire, c'est-à-dire commencer, comme je l'ai dit, par l'expérience, et à partir de là explorer la raison.

Léonardo da Vinci (1452 – 1519)

A Marianne et ma famille

TABLE OF CONTENTS

Summary

High-velocity plunging water jets, appearing at the downstream end of dam weirs and spillways, can create scour of the rock. The prediction of this scour is necessary to ensure the safety of the toe of the dam as well as the stability of its abutments. Scour is often predicted by empirical or semi-empirical formulae, developed from physical models or prototype observations. These formulae are not fully representative because they cannot describe all of the physical effects involved. Above all, the characteristics of pressure wave propagation in the fissures of the jointed rock mass are unknown.

The main purpose of the research is to close up this gap by investigating transient water pressures in rock joints due to high-velocity jet impact. Based on a theoretical analysis of the physical parameters, an experimental facility was built at prototype scale. This allowed generating correct frequency spectra and aeration of the turbulent shear layer of a jet impacting at a plunge pool bottom. The turbulence of the jet at its outlet corresponds to real turbulent jets. The turbulent pressure fluctuations of the shear layer of the jet at the water-rock interface have been measured at different locations. This allowed quantifying the excitation capacity of the impacting jet.

The water pressures inside the rock joints were governed by the propagation, superposition and reflection of pressure waves induced at the entrance. These waves revealed a transient and cyclic behavior, which is defined by the presence of free air. Two physical laws describe this: the ideal gas law and Henry's law. The former expresses the change in volume of a free air bubble as a function of pressure. The latter describes the quantity of air that is released from the liquid or dissolved in the liquid due to a change in pressure. These two laws result in "wave celerity-pressure" relationships that express the non-linear transient characteristics of the system.

The water pressures have been measured inside four closed-end joints and one open-end joint. The transient pressures in an I-shaped rock joint are characterized by a continuous change between peak pressures and periods of low, near-atmospheric pressure. The frequency of these changes is governed by the amount of free air. Peak pressures up to several times the kinetic energy head of the impacting jet (= $V^2/2g$) have been measured, indicating the formation of standing waves and resonance conditions. Free air contents were between 0.5 and 10 %, corresponding to wave celerities ranging from only 50 to 250 m/s. Similar effects were obtained for an L-shaped closed-end joint, although the amount of free air was significantly higher due to the accumulation of an air cushion in the horizontal part of the joint (downstream of the 90° bend). Hence, it can be concluded that changes in orientation of the joint pattern are of secondary importance. The values of the peak pressures were found to decrease at air concentrations higher than 10 %. This is due to the dampening effect of the air. Air bubbles dissipate a large amount of energy (heat) by subsequent compression and expansion. This was confirmed by pressure measurements inside a two-dimensional closed-end joint. Both the amount of free air and two-dimensional diffusion effects excluded the appearance of peak pressures. Finally, an open-end rock joint has been investigated. For such a joint, the jet impact pressures enter the joint at its two ends simultaneously. Net uplift pressures of 0.8 to 1.6 times the incoming kinetic energy have been measured. This is significantly higher than any previous assumptions in literature and clearly demonstrates that transient effects have to be accounted for when investigating rock block uplift.

The above findings have also been analysed numerically. A one-dimensional two-phase numerical modelling has been performed of the transient pressures that were measured at the end of the I-shaped closed-end joint. The calculated pressures are in good agreement with the measured ones. The numerical adjustment was based on the optimisation of celerity-pressure relationships.

The cyclic behaviour of the pressures made it interesting to apply the hydrodynamic loading to tensile failure criteria of rock, such as the linear elastic fracture mechanics approach. In practice, three parameters are of interest: the maximum pressure at the joint end and the amplitude and the frequency of the cycling loading. With these, both instantaneous and time-dependent cracking of closed-end rock joints can be assessed.

Fracture mechanics states that a crack will propagate if the stress intensity at the tip exceeds a critical value, called the fracture toughness. The stress intensity is defined by the water pressures inside the joint and by the geometry of the joint and its surroundings. The fracture toughness of the rock mass is

a material property, but also depends on the in-situ stresses. It can be derived from the tensile strength or the unconfined compressive strength. Two types of failure are distinguished: brittle and subcritical. The former happens when the stress intensity exceeds the fracture toughness. The latter occurs when the stress intensity is less than the fracture toughness. The cyclic behavior of the hydrodynamic loading is convenient for this type of crack growth. Theoretical fatigue laws have been derived from literature data for different types of rock. As such, a time evolution is added to the scour phenomenon. Brittle and subcritical break-up are described in a Comprehensive Fracture Mechanics (CFM) model.

For completely jointed rock, failure is obtained by dynamic uplift of a representative rock block. This block is subjected to pressure forces that change with time. The most relevant forces are the immerged weight of the block, the pressure forces over and under the block and the shear forces between the block and its surroundings. The net impulse, defined as the integral over a certain time period of the net forces, accelerates the mass of the block up to a certain velocity. Conversion into potential energy determines the uplift displacement of the block. This process is defined in a Dynamic Impulsion (DI) model. Ejection of the block theoretically needs a displacement of minimum the height of the block. However, the critical displacement depends on the degree of interlocking of the blocks. As such, a very tightly jointed rock needs a displacement equal to or higher than the height of the block itself. For less tightly jointed rock masses, the critical uplift height is probably somewhat lower. The critical height is a parameter that needs to be calibrated through model and/or prototype data.

A new model for ultimate scour depth evaluation is proposed. The model represents a comprehensive assessment of two physical processes: hydrodynamic fracturing of closed-end rock joints and dynamic uplift of rock blocks. The model consists of three modules: 1) module for the falling jet, 2) module for the plunge pool, 3) module for the rock mass. The physical parameters are defined such that a practicing engineer can easily handle them. This guarantees the comprehensive character of the model, without neglecting basic physics behind it.

The model has been firstly applied to a fictitious rock mass. This highlights the methodology and the major parameters of interest. Secondly, the scour model is compared with the Erodibility Index (EI) method of Annandale (1995). This comparison allows to determine the sensibility of the scour model as a function of the main parameters. Finally, the well-known case of rock scour at the Cabora-Bassa dam in Mozambique is used as a first calibration of some of the model parameters.

Version abrégée

Les jets d'eau à haute vitesse, apparaissant par exemple à l'aval d'évacuateurs de crue des barrages, sont capables de générer un affouillement local du massif rocheux. La prédiction de cet affouillement est nécessaire pour garantir la sécurité du pied de l'ouvrage ainsi que la stabilité de ses fondations. Les fosses d'affouillements sont souvent décrites par des formules empiriques ou semi-empiriques, développées à partir d'essais sur modèle physique ou d'observations sur prototype. Ces formules ne tiennent pas compte de tous les phénomènes physiques concernés et, de ce fait, ne sont pas entièrement représentatives. Surtout les caractéristiques des ondes de pression apparaissant dans le médium discontinu sont inconnues.

L'objectif principal de la recherche est de combler cette lacune par une investigation des pressions transitoires dans les fissures du rocher, sous l'impact de jets à haute vitesse. Une analyse théorique des paramètres en question a permis de construire une installation expérimentale à échelle prototype. Les vitesses du jet varient ainsi entre 5 et 40 m/s et la géométrie des fissures du rocher est bien réelle. Ceci a permis de générer une densité spectrale et une aération de la zone turbulente du jet dans la fosse d'eau qui sont correctes. La turbulence initiale du jet a été mesurée et s'est révélée caractéristique pour des jets réels. Les fluctuations de pression dans la zone d'impact du jet à l'interface eau-rocher ont été quantifiées à différents endroits. Ceci a permis de décrire la capacité d'excitation du jet.

Les pressions d'eau dans les fissures du rocher sont caractérisées par la propagation, la superposition et la réflexion d'ondes de pression induites à l'entrée de la fissure. Ces ondes de pression se sont révélées de caractère transitoire et cyclique, et sont gérées par la présence de bulles d'air. Ceci peut être décrit par deux lois physiques : la loi des gaz idéaux et la loi d'Henry. La première loi décrit le rapport entre le volume d'une bulle d'air et la pression. La deuxième loi exprime la quantité d'air qui peut être dégagée du liquide suite à une chute de pression de ce dernier. Les deux lois conduisent à des relations entre la célérité et la pression des ondes. Il est évident que la présence de bulles d'air augmente fortement la non-linéarité des caractéristiques transitoires du système.

Les pressions transitoires ont été mesurées dans quatre fissures à extrémité fermée et une fissure à extrémité ouverte. Les pressions dans la fissure en forme de I sont caractérisées par une alternance de pics et de creux de pression. La fréquence de cette alternance est dictée par la quantité d'air. Des pics de pression jusqu'à plusieurs fois l'énergie cinétique du jet à l'impact ($= V^2/2g$) ont ainsi été mesurés. Ceci révèle la présence de phénomènes oscillatoires et à caractère de résonance. Des quantités d'air entre 0.5 et 10 % ont conduit à des célérités d'onde entre 50 et 250 m/s. Des phénomènes similaires ont été constatés dans une fissure en forme de L, bien que la quantité d'air libre soit plus élevée à cause d'une accumulation de bulles d'air dans la partie horizontale aval du coude à 90°. Il en résulte que des changements brusques de la géométrie des fissures n'ont que peu d'influence sur les pressions. Les pics de pression diminuent à partir de concentrations d'air supérieur à 10 %, due à un effet d'amortisseur de l'air. Les bulles d'air dissipent une quantité importante d'énergie sous forme de chaleur par les phénomènes de compression et d'expansion.

Ceci a été confirmé par des mesures de pression dans une fissure bidimensionnelle à extrémité fermée. La quantité d'air importante, ainsi que les effets de diffusion bidimensionnelle, évitent la formation des pics de pression. Finalement, une fissure à extrémité ouverte, en forme de D, est alimentée par le jet des deux extrémités simultanément. Une telle fissure représente un bloc de rocher en deux dimensions. Des pressions de soulèvement de 0.8 à 1.6 fois l'énergie cinétique d'impact ont été mesurées. Celles-ci sont passablement supérieures à toutes les valeurs généralement admises dans la littérature et font la preuve que les pressions transitoires ont leur importance dans le soulèvement dynamique des blocs de rocher.

Ces résultats expérimentaux ont également été étudiés numériquement. Un modèle numérique bi-phasique et unidimensionnel a ainsi été développé. Ce modèle décrit les pressions transitoires à l'extrémité aval de la fissure en forme de I. Les pressions calculées sont en bonne concordance avec celles mesurées. L'ajustement numérique est basé sur une optimisation des relations célérité-pression.

Le caractère cyclique des pressions conduit à une application de la sollicitation hydrodynamique à des critères de rupture par traction du rocher, comme par exemple l'approche de la mécanique de la

fracturation élastique linéaire. Pour la pratique, trois paramètres sont importants: la pression maximum à l'extrémité fermée de la fissure et l'amplitude et la fréquence des cycles de pression. Ainsi, les propagations instantanée et progressive des fissures peuvent être entièrement décrites.

La mécanique des fractures postule qu'une fissure se propage quand l'intensité des contraintes à son extrémité fermée dépasse une valeur critique, appelée la résistance à la fracturation. L'intensité des contraintes est définie par les pressions dans la fissure et par la géométrie de la fissure et de ses environs. La résistance à la fracturation est une propriété intrinsèque du rocher qui dépend néanmoins des contraintes in-situ du massif rocheux. Elle est déterminée à partir de la résistance à la traction ou à la compression du rocher.

Deux types de rupture peuvent être distingués : la rupture instantanée et la rupture progressive. Le premier se fait quand l'intensité des contraintes est supérieure ou égale à la résistance à la traction. Le deuxième correspond à une intensité des contraintes inférieure à cette même résistance et est assimilé au caractère cyclique de la sollicitation hydrodynamique. Ainsi, des lois théoriques de fatigue ont été développées à partir de données dans la littérature, pour différents types de rocher. Ceci permet d'exprimer le développement de l'affouillement en fonction du temps. Les ruptures instantanée et progressive sont décrites dans un modèle de Fracturation Mécanique Compréhensive (FMC).

Pour un massif rocheux complètement fissuré, la rupture s'exprime par l'éjection dynamique d'un bloc de rocher qui est représentatif pour le massif. A part du poids immergé du bloc, le bloc est soumis à des forces qui dépendent du temps et de l'espace, telles que les forces de pression hydrodynamique au-dessus et au-dessous du bloc et les forces de frottement entre le bloc et ses environs. L'impulsion nette, définie comme l'intégration dans le temps des forces nettes sur le bloc, accélère le bloc et lui donne une certaine vitesse. La conversion de cette vitesse en énergie potentielle détermine la hauteur de soulèvement du bloc. Ce processus est décrit dans le modèle d'Impulsion Dynamique (ID). L'éjection d'un bloc nécessite une hauteur de soulèvement qui est minimum égale à la hauteur du bloc. Néanmoins, la hauteur critique de soulèvement dépend aussi du degré de connexion entre les blocs. Ainsi, pour des blocs qui ne sont pas étroitement liés entre eux, la hauteur critique de soulèvement pourraient être légèrement inférieure. Ce paramètre doit faire l'objet d'un calibrage basé sur des données in-situ.

Finalement, un nouveau modèle pour l'évaluation de la profondeur ultime d'affouillement du rocher est proposé. Le modèle représente de manière compréhensive les processus suivants : la fracturation hydrodynamique de fissures à extrémité aval fermée et l'éjection dynamique de blocs de rocher. Il consiste notamment en les modules suivants : 1) le jet plongeant ; 2) la fosse; 3) le massif rocheux. Les paramètres physiques ont été décrits tels qu'un ingénieur de la pratique peut facilement les manipuler. Ceci garantit le caractère compréhensif du modèle, sans perdre les bases physiques.

Le modèle a premièrement été appliqué à un massif rocheux fictif. Cela a permis de définir la méthodologie et de dégager les paramètres d'importance. Deuxièmement, le modèle a été comparé avec le « Erodibility Index Method » de Annandale (1995). Cette comparaison détermine la sensibilité des différents paramètres du modèle. Finalement, le cas bien connu de la fosse d'affouillement du barrage de Cabora-Bassa a été utilisé comme premier calibrage des paramètres.

Chapter I. Introduction

1. Background

The twentieth century has been characterized by a huge evolution of high-head dams. The end of World War II saw the beginning of economical development and, at the same time, the start of perhaps the most intense and productive period of hydraulic constructions. In Switzerland alone, about 100 large dams (height of more than 15 m) were constructed during the 1950's and the 1960's.

The growth of electrical consumption called for hydropower as source of energy. Combined with the technological evolution, the development of large dams increased. The highest dams in the world have reached 300 m. The created dam reservoirs store water for energy production, industrial and agricultural use. Almost 90% of Switzerland's large dams were constructed for hydroelectric purposes.

As modeling and prediction of extreme floods improved, mainly due to the increasing amount of data on extreme events, another aspect of dams became important in the last decades: downstream flood protection. All high dams are equipped with hydraulic structures, which allow the transfer of reservoir water downstream. These structures were designed for extreme floods based on estimates at time of dam construction, often nearly half a century ago. The trend towards larger flood discharges and durations modifies the operation period of these structures.

Hydraulic structures, such as crest weirs, spillway gates and bottom or intermediate outlets, transfer water from the reservoir level to the tailwater level downstream. This creates high-velocity and highly aerated flows. The transfer calls for massive energy dissipation downstream the dam. This can be performed by means of hydraulic jump stilling basins, by aeration and/or by jet diffusion in natural or constructed plunge pools (Photo 1).

Since the beginning of the 20^{th} century, the dissipation process has been investigated by hydraulic model tests. In the 1950's, it became obvious that this massive energy dissipation had been largely underestimated in many cases, resulting in the phenomenon of scour or erosion of the downstream rock mass. The parameters of interest are the ultimate depth the scour can attain as well as the maximum possible extension of the eroded zone. One example is the Malpaso dam (Mexico), equipped with a wide-shaped weir and related stilling basin, designed for 11'000 m^3/s. The spillway worked from 1967 to 1969 without problems. In 1970, due to a 3'000 m^3/s discharge during two weeks, severe damage was observed on the concrete slabs of the stilling basin, as well as on the underlying rock foundation (Bribiesca & Viscaino, 1973). Other examples are Kariba Dam in

Zimbabwe (Ramos, 1982) or Cabora Bassa Dam in Mozambique (Quintela & Da Cruz, 1982). The former case is presented in Fig. I-1 (Whittaker & Schleiss, 1984).

Since then, many empirical and semi-empirical expressions have been developed, based on physical model tests, in order to evaluate the ultimate scour depth. Nevertheless, these equations are only applicable to the specific case for which they were developed. With improving physical understanding of energy dissipation processes, mainly governed by aeration and flow turbulence, the complexity of the phenomenon became highlighted. The investigation of flow turbulence characteristics was difficult due to their random nature. However, technological progress since the 1960's resulted in appropriate measurement techniques and statistical analyses for this kind of flows.

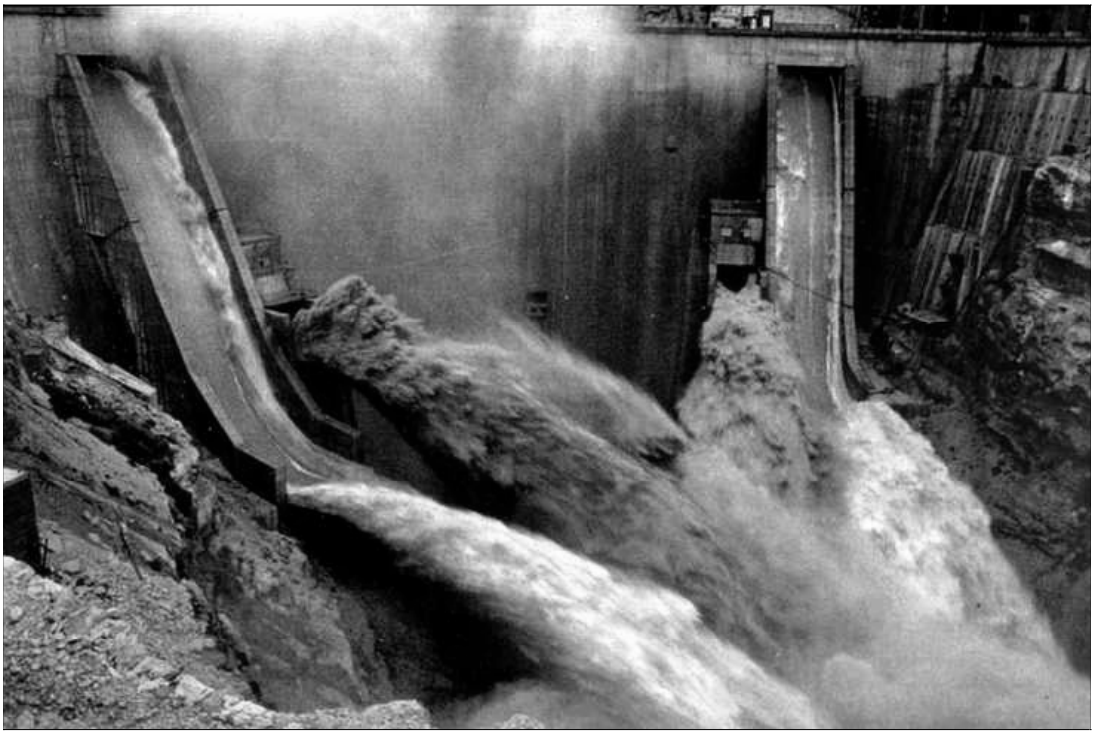

Photo 1 A 5'000 m^3/s flood discharge at Jiroft dam (Iran): combination of highly sediment-laden flow, issuing from intermediate outlet works, with clear water coming from the ski-jump overflow structure (Photo B. Hagin, Stucky Ing. Conseils).

This was also the beginning of research of turbulent flows. These flows appear for example in stilling basins or plunge pools, and result in dynamic water pressures in the joints of concrete bottom linings or rocky foundations. A lot of scour damage could be explained by applying maximum pool bottom pressures underneath the concrete slabs of the bottom linings, or underneath the rock blocks, and a minimum pressure at the surface of these elements. Net uplift pressures are so generated. This method, however, neglects any time correlation between surface and underpressures.

In the 1990's, several studies have been conducted on the theory of instantaneous pressure differences. According to this theory, surface pressures enter into a joint and, by means of pressure wave propagation, act on the whole surface underneath the rock block or the concrete slab. The instantaneous character of this propagation creates a time lag with the surface pressures and results in a net uplift force. The major difference with the previous technique is that the over-and underpressures are analyzed at the same time interval.

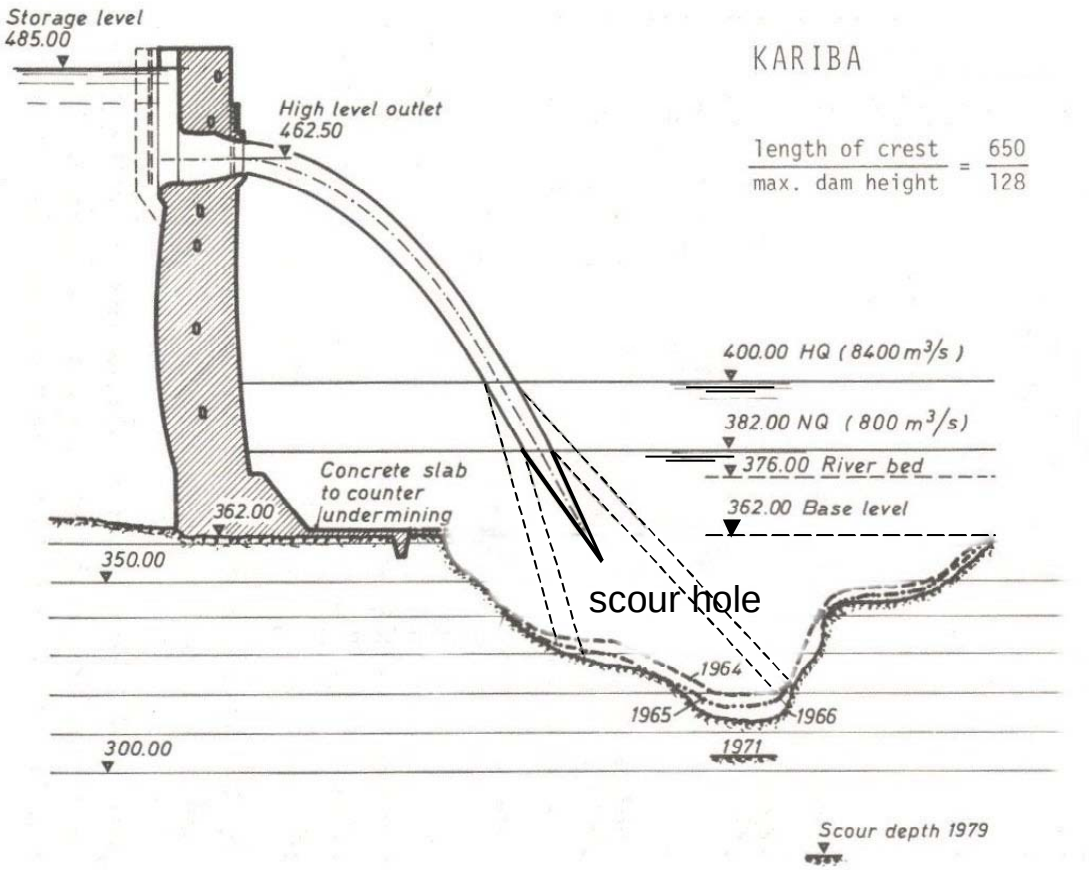

Fig. I-1 The high level outlet spillway structure of Kariba Dam (Zimbabwe). The evolution of the scour hole as a function of time indicates a maximum scour depth in 1979 of about 85 m.

This theory does not consider transient flow conditions generated by the boundary conditions at the joint ends. They cause reflection of pressure waves at the open or closed-end of the joint and superposition with the initial wave. This can result in amplified transient phenomena, such as oscillatory flow and resonance conditions. This unsteady character influences two physical processes: the hydraulic jacking phase, causing a break-up of the rock mass by progressive growing of the joints, and the hydrodynamic uplift phase, ejecting a so formed rock block out of its mass.

These transient phenomena have never been considered in any experimental or numerical model. The classical assumptions of very high wave celerities (1'400 m/s) and small slab or block lengths (1-10 m) make it impossible for macroturbulent pressure fluctuations to generate severe transient effects and to stimulate a rock joint to resonance conditions. The impacting pressures of the modeled jets simply do not contain the appropriate frequency range.

The present work reveals that high-velocity jets generate pressures at impact with a frequency range that is capable to stimulate underlying joints. Two statements are at the base of this assumption. First of all, high-velocity jets have a spectral content that is still significant at high frequencies. Physical model studies have always been performed at low jet velocities. For such velocities, the higher frequencies cannot be simulated. Appropriate modeling needs near-prototype or prototype velocities. Secondly, it will be pointed out that the pressure wave celerities in rock joints can be much lower than 1'400 m/s. This is due to the presence of free air in the water. Free air lowers down the wave celerities and, thus, also the resonance frequencies of the joints.

2. Research project objectives

2.1. General

High-velocity plunging water jets, which occur for example downstream of dam weirs and spillways, can erode the rock bed. The prediction of this scour is necessary to ensure the stability of the dam foundation as well as its abutments. Scour has often been predicted on the basis of empirical or semi-empirical formulae developed from physical models or prototype observations. These formulae are not fully representative because they do not take into account all of the physical effects involved. The knowledge of the development of scour and the interaction of the various agents of this process is needed. A generally applicable theoretical solution to the problem is actually missing. Above all, the characteristics of the transient pressure wave propagation in the fissures of the jointed media are unknown.

The main purpose is to close up this gap by investigating transient pressures in artificially simulated joints due to high-velocity aerated jet impact. The following topics are dealt with:

- Theoretical analysis of the physical parameters involved in the occurrence of dynamic pressures in joints and in the scouring process. The parameters comprise falling jet characteristics, plunge pool aeration, plunge pool turbulence and geometric as well as geo-mechanical characteristics of the jointed medium.
- Experimental investigation of transient pressures in different rock joint configurations. These pressures are generated by the impact of high-velocity jets at the joint entrance. The experiments consider jet, joint and plunge pool characteristics and are performed at near-prototype jet velocities (max. 40 m/s). The rock joint geometry is at prototype scale, whereas the plunge pool and jet geometries are at model scale (1/10 to 1/20).
- Determination of a relationship between jet characteristics and dynamic pressures in joints, based on the results of the experimental modelling and on existing theoretical approaches.
- Application of these dynamic pressures to intermittently jointed rock. This results in a progressive break-up of the joints and in the formation of single rock blocks.
- Application of these dynamic pressures to completely jointed rock (= single blocks). This conducts to net dynamic uplift pressures and ejection of the rock blocks out of their mass.
- Numerical simulation of the experimentally measured transient pressures in rock joints.
- Formulation of a physically-based evaluation method for the development of ultimate scour depth.

2.2. Physical-mechanical processes of the scour phenomenon

Scouring is a complex three-phase (gas-liquid-solid) interactive problem, governed by a multitude of hydraulic, hydrodynamic and geomechanical phenomena that are strongly dependent on both time and space. A first assessment shows that scour can be described by a series of physical-mechanical processes (Fig. I-2): aerated jet impingement, plunge pool turbulent flow, pressure fluctuations at the water-rock interface, hydrodynamic fracturing of closed-end rock joints by pressure propagation, hydrodynamic uplift of the so formed rock blocks and finally downstream displacement of the blocks (Bollaert & Schleiss, 2001e).

Every process is characterized by several parameters and their particular nature (stochastic or deterministic). Aerated jet impingement is depending on the jet velocity at impact, the initial turbulence intensity of the jet, and the degree of aeration. The initial turbulence intensity of the jet defines the spread of the jet and the jet break-up length. For laboratory model studies, it is crucial to correctly simulate the velocity of the jet. At near-prototype velocities, representative turbulence intensity and aeration rates can be ensured.

The flow conditions in plunge pools can be divided into a high-velocity, two-phase turbulent shear layer flow and a macroturbulent flow outside of this zone. The shear layer produces severe pressure fluctuations at the water-rock interface and is highly influenced by aeration. Existing theories on two-dimensional vertical jet diffusion in a semi-infinite or bounded medium define the outer limits of the zone at the water-rock interface that is directly subjected to these pressures. Knowledge has also been acquired by physical modeling of hydraulic jumps and plunging jets. This allowed the description of statistical characteristics and of the spatial distribution of the pressure fluctuations.

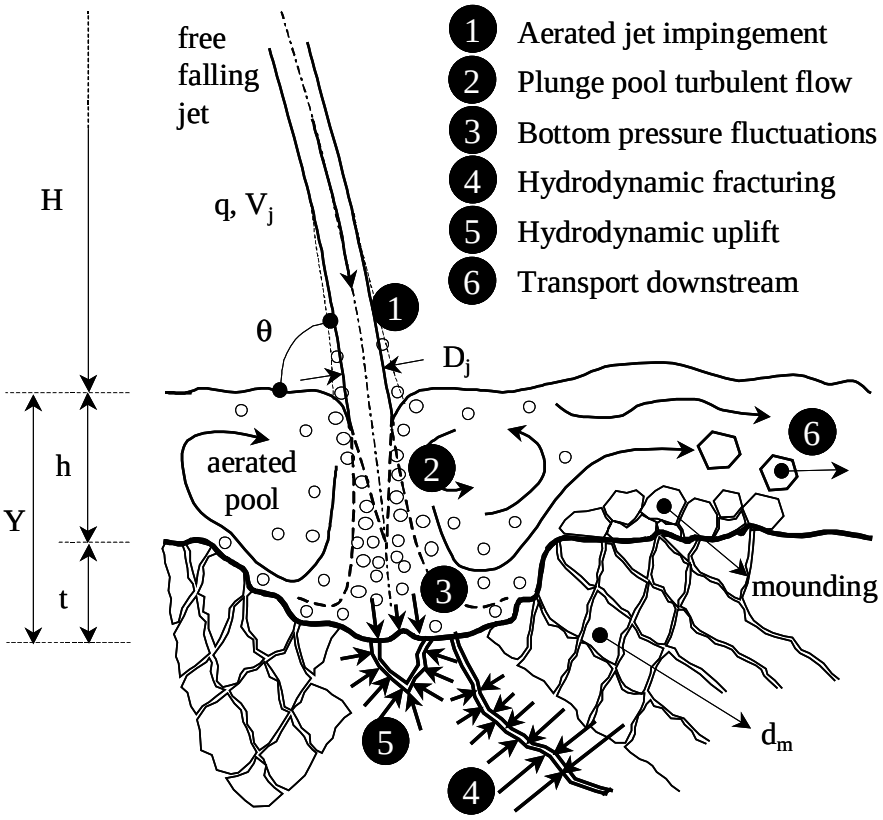

Fig. I-2 Physical-mechanical processes involved in the scouring phenomenon. The present research project focuses on the processes of hydrodynamic fracturing and hydrodynamic uplift, by considering transient pressure wave propagation in the joints of the rock mass (Bollaert & Schleiss, 2001e).

The transfer of pool bottom pressures into rock joints results in transient flow that is governed by the propagation of pressure waves. For closed-end rock joints, as encountered in intermittently jointed rock, the reflection and superposition of the pressure waves generate a hydrodynamic loading at the tip of the joint that progressively breaks up the joint. Hence, failure criteria are governed by the tensile strength of the rock. For open-end rock joints, as encountered in fully jointed rock, the pressure waves inside the joints create a significant uplift force on the rock blocks. This force can be sufficiently high to eject the block from the rock mass. Once the rock block ejected from its surrounding mass, it can be taken up by the macroturbulent eddies. Two possibilities exist: 1) the block is too big to be transported by the flow and will further break-up into smaller pieces (ball milling); 2) the block is displaced downstream of the plunge pool, where it deposits or is taken away by the river stream.

3. Research methodology

The research methodology and the different chapters are visualized in Fig. I-3. These chapters have either geomechanic or hydrodynamic bases, and are theoretical, experimental or numerical oriented.

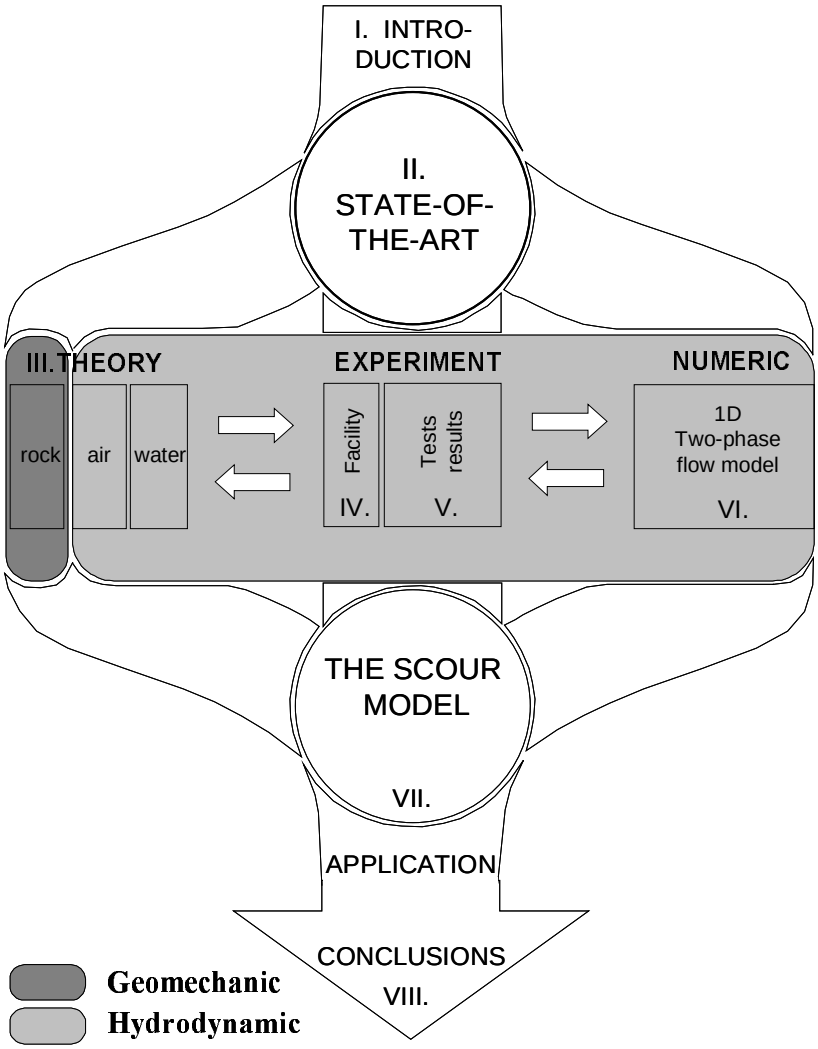

Fig. I-3 Schematic visualization of the methodology of the project. Theoretical, experimental and numerical interaction results in a physically based, transient two-phase approach for assessment of rock scour.

An introduction explains the general background and the methodology of the research project. Chapter II deals with the state-of-the-art in the field of rock scour evaluation methods. Emphasis is given on empirical and semi-empirical formulas, extreme pool bottom pressures and instantaneous or average pressure differences over and under the rock blocks. This state-of-the-art underlines the need for assessment of transient water pressures in rock joints. A three-dimensional visualization is provided that compares the state-of-the-art and future research as a function of the three phases that are involved: the liquid phase (water), the gas phase (air) and the solid phase (rock mass).

The theoretical bases are explained in Chapter III for each of these phases separately. Where possible, interaction between the phases is also dealt with. The liquid phase is governed by turbulent shear layer flow in the plunge pool and transient pressurized flow in the rock joints. The gas phase deals with falling jet aeration, plunge pool aeration and rock joint aeration. The latter phenomenon is novel to the author's knowledge. The solid phase defines the geometrical and geo-mechanical rock mass characteristics. Furthermore, failure criteria of intermittently (fracture mechanics) or completely (uplift) jointed rock are presented.

Chapter IV describes the experimental facility and the measurement equipment, as well as a detailed test program. The facility is at near-prototype scale and is conceived such that any form of artificial rock joint can be tested. The test equipment consists of two data acquisition cards with a series of 8 micro-pressure sensors that have been used to measure the initial jet turbulence intensity, the pool bottom pressure fluctuations and the resulting pressures inside rock joints.

The experimentally measured pressures are analyzed in Chapter V. A first section is devoted on the initial turbulence intensity of the generated jets. Two types of jet outlet have been used: a cylindrical form and a convergent form. The former generates jets with both a low-frequency component and a high turbulence intensity. The latter created a compact jet with a low turbulence intensity. A second section deals with dynamic pressure fluctuations measured at the plunge pool bottom. Distinction is made between pressures measured under the jet's centerline and pressures measured at radial outwards locations. As such, the spatial distribution of the surface pressure field of a plunge pool has been defined. This pressure field entirely determines the excitation capacity of a jet impacting onto a rock joint.

The third section presents the pressures measured inside different rock joint configurations. Both one- and two-dimensional rock joints have been tested. Their ends can be open or closed. Special attention was paid to air bubbles that are present inside the joints, because they influence the transient characteristics of the system.

It forms the input for application of rock mass failure criteria. Chapters III, IV and V have been set up in a parallel manner. Theory about air and water flow inside rock joints has been outlined based on performed pressure measurements and, vice versa, the highly transient 2-phase character of the measurements could be analyzed by means of theoretical considerations.

The complementary aspects of theory and experiments conducted to a synergy that allowed a detailed numerical simulation of the hydrodynamic pressures in Chapter VI. The numerical simulation is although restricted to closed-end rock joints.

Chapter VII proposes a new, physically-based model for evaluation of the development of ultimate scour in partially or fully jointed rock. The model relates measured water pressures in rock joints to tensile failure criteria of jointed rock and to hydrodynamic uplift of rock blocks. An application example is provided, as well as a comparison with the Erodibility Index method (Annandale, 1995). This method is a semi-empirical method in which the erosive power of the jet, as well as the resistance of the jointed rock against erosion, are expressed by means of an index. It constitutes one of the most pertinent and reliable method of scour evaluation that is actually available. More details of this method are also provided in Chapter II.

The last chapter summarizes the research project and the major conclusions that can be drawn

.

Chapter II. State-of-the-art on scour evaluation methods

The present state-of-the-art on rock scour due to high-velocity jet impact does not intend to analyse every existing experimental, statistical or analytical evaluation technique. It rather presents a global overview of these approaches. As such, a first section summarizes some well-known empirical expressions for the ultimate scour depth. These expressions have been obtained through physical model studies and are simple and useful tools to get a first idea of the ultimate scour depth and to identify scour tendencies. However, they incorporate significant scaling effects and should only be applied within their application range. Secondly, expressions obtained through clearly outlined analytical developments, and most often calibrated by the use of available experimental data, are labeled as "semi-empirical" relationships. Distinction is made between the application of shear-stress based "initiation of motion" theories, the use of conservation equations and the incorporation of geomechanical characteristics. Many of these expressions are based on the theory of a two-dimensional jet diffusing through a water cushion and impinging on a flat boundary.

A third widely used technique to estimate the ultimate scour depth is the determination of extreme dynamic pressures at the plunge pool bottom. The following parameters are of significance: mean value, root-mean-square (RMS) value, extreme positive and negative values and power spectral content of the fluctuating part of the dynamic pressures. These parameters characterize the extreme loading conditions on rock blocks or concrete slabs by applying a maximum pressure underneath and a minimum pressure on the upper side of the block or the slab. In this way, the maximum possible net uplift pressure can be determined. Ultimate scour depth is reached when this net uplift pressure is not capable anymore to eject the block or the slab.

Finally, time-averaged and instantaneous pressure differences over and under rock blocks can be quantified by appropriate physical model studies. These studies account for the instantaneous spatial structure of the pressures at the pool bottom, but the pressures under the blocks are dealt with in a steady-state manner and thus assumed constant. No transient effects are considered inside the joints.

Hence, the framework for a fully transient, three-phase assessment of dynamic pressures is outlined. It is believed that transient pressure wave propagation inside rock joints and underneath concrete slabs constitutes a key element for a deeper insight into the physics of the rock scour phenomenon. The need for a more physically based approach is visualized by means of a three-phase cubic representation of the current state-of-the-art as well as of the research objectives (Bollaert & Schleiss, 2001e).

1. Empirical expressions

1.1. General

Since the pioneering work of Schoklitsch (1932) on overflow jets, many researchers experimentally investigated the relation between the hydraulic characteristics of a falling jet and the formation of plunge pool scour. A lot of scaled physical model studies have been made, resulting in a significant amount of empirical expressions. However, the application limits of these expressions are generally very restricted. Hence, an evaluation of summaries is more valuable than an examination of every equation on its own. The present section focuses on referential summaries of previous research and on scaling effects that are frequently encountered during physical model tests.

Empirical relationships are one of the most popular tools for establishing hydraulic design criteria, because of their relative simplicity and feasibility. Model and prototype tests results can be related to the main parameters in a straightforward manner. This is obtained through general mathematical techniques, such as dimensional analysis (Reeve, 1932; Doddiah et al., 1953; Rajaratnam, 1981), direct correlations between predominant variables, trial and error adjustments, etc. These techniques furthermore permit a global evaluation of the physical problem and general tendencies often can be outlined. One example is the work published by Doddiah et al. (1953). They found that scouring firstly increases with increasing pool depth up to a critical value, and that further increase of the pool depth rapidly diminishes. This phenomenon was attributed to the appearance and strength of recirculating pool currents and has been confirmed later on by measurements of turbulent flow characteristics.

However, the correct physical background of test results remains unknown and so care has to be taken when applying such formulas for other cases than the one for which they were designed. This was clearly outlined by Mason & Arumugam (1985) who analyzed the most important empirical formulas and divided them into different groups, as a function of the parameters considered. They evaluated the accuracy of these groups of formulas by generating sets of scour data from prototypes and their relevant models. The results showed an important difference in applicability of all formulas between model and prototype test conditions. In other words, expressions that were developed under model conditions should not be used in prototype applications and vice versa. Several authors investigated this important aspect of empirical expressions and contributed in that way to a better assessment of some major scaling effects, such as rock mass scaling, aeration scaling and time scaling.

1.2. Rock mass scaling effects

Whittaker & Schleiss (1984) established a state-of-the-art for scour related to high head structures. A first difficulty often encountered during physical model tests is the simulation of the foundation by a material that adequately represents the dynamic behavior of partially or totally fractured rock. For this reason, most model tests assume that the disintegration process of the rock mass has already taken place and consider the rock as a piecewise broken up medium. As a result, only the entrainment and transport of rock blocks is modelled. This is done by use of cohesionless granular material.

Reeve (1932) established scaled model tests to design erosion protection works downstream of the Conowingo ski-jump spillway dam. The 1/30 scaled model simulated the fractured rocky river bottom by crushed rock in pieces large enough to correspond to the natural large blocks of granite. Test runs were conducted and after several years of operation, the plunge pool developed the predicted erosion pattern. Later on, Cunha & Lencastre (1966) established three-dimensional model tests of the Picote Dam. The rocky river bed was modeled by means of cohesionless granular material (d_m = 20 mm), because their tests with slightly cemented concrete failed. The steep riverbanks were simulated with a homogenous material. During the experiments, a large downstream mound of entrained granular material formed. This accumulation was largely superior to the corresponding prototype deposit. Therefore, two types of test runs were executed: one with a systematic, periodic leveling of the formed artificial mound, and one without modifying this process. As such, an intermediate solution was

derived that seemed to correspond to prototype measurements. The model adjustment was used afterwards to predict further scour hole development in case of extreme floods.

Yuditskii (1971) and Ramos (1982) also pointed out that model tests tend to exaggerate the deposition of material at the downstream end of a plunge pool, which inhibits the formation of the total scour depth. This significant scaling effect resulted in a "dynamic scour limit", valid when no material is removed from the mound, and a "static scour limit", reached by progressive removal of the deposition.

Martins (1973) developed another three-dimensional model case. He used a riverbed made of equally sized cubic blocks, systematically arranged and without any cohesive effects between them. Mason and Arumugam (1985) found the proposed expression works poorly for prototype values, but agrees fairly well for model tests. This again indicates the risk of using model data obtained with cohesionless material.

In general, only poorly to moderately reasonable results are obtained in terms of total scour depth, and the extension of the scour hole remains overestimated in scaled model tests, due to the impossibility of simulating steep channel slopes. Wisner et al. (1967) pointed out the limitations of the use of cohesionless material for simulation of rocky river beds and proposed comparable tests with cohesive bottoms. They investigated the use of sand and plaster which gave a higher scour depth in the latter case. Secondly, a comparison was made of the scour hole shape obtained for successive layers of cubic concrete blocks on one hand, and for rough sand on the other one. The scour hole with the concrete blocks was much more localized and shallower, indicating a totally different mechanism of erosion. The author already mentioned the existence of pressure fluctuations in the joints between the cubes, attaining 40% of the incident velocity head and generating significant instantaneous underpressures.

Other investigators (Johnson, 1977; Gerodetti, 1982; Quintela and Da Cruz, 1982) also made use of slightly cohesive material (such as cement, clay, caulk, paraffin wax etc.). However, these model tests were mostly performed after dam construction using available prototype data for calibration.

Furthermore, some investigators (Veronese, 1937; Mirtskhulava et al., 1967; Machado, 1982) accounted for grain size limitation problems. They found out that, for grain sizes smaller than 2 to 5 mm, the ultimate scour depth becomes constant. Breusers (1963) found a grain size independent scour depth for a grain size range of 0.1 to 0.5 mm. He related this phenomenon to a constant critical entrainment velocity, making it of absolute rather than relative nature. Finally, Mason and Arumugam (1985) stated that use of the mean particle size d_m is in general more appropriate than the d_{90} size.

As a conclusion, the application of model test results to prototype situations often fails because the physical process of progressive break-up of the partially fractured rock mass cannot be simulated.

1.3. Aeration scaling effects

A second significant scaling effect is introduced by the aeration of the jet and the plunge pool. Aeration is governed by the initial jet turbulence intensity (Tu) and is Froude, Reynolds and Weber number dependent. Hence, it cannot be appropriately represented by Froude-based scaling laws.

Johnson (1967) compared the scour depth for aerated jets with that for non-aerated conditions but didn't develop a relevant formula. The former case resulted in lower scour depths. Based on a study by Rubinstein (1963), Martins (1973) took into account a reduction of 25% of the calculated scour depth in case of high air entrainment, and 10% for intermediate air entrainment. Mason (1989) developed an empirical expression incorporating the volumetric air-to-water ratio β [–]. He stated that this ratio allows replacing the drop height H from classical formulas, based on a direct relation between β and H developed by Ervine (1976). His formula is very accurate for model data and gives a reasonable upper bound of scour depth for prototype conditions. A plausible physical explanation for this phenomenon, however, is lacking.

The assessment of aeration effects is one of the major challenges in a correct evaluation of the ultimate scour depth. Air entrainment cannot be scaled appropriately and has a highly random character. Moreover, the phenomenon is present in every physical process of the scour development: in the plunging water jet, through the water cushion, and even inside the discontinuities of the fractured rock mass. This is discussed in Chapters III and V more in detail.

1.4. Time scaling effects

Scouring is highly dynamic and thus characterized by time scaling effects. These effects appear at two completely different time scales. The first time scale is a macro-time scale and deals with the duration and the frequency of occurrence of water transfer downstream of the dam. Due to a lack of prototype data, this scaling effect has been poorly studied up to now. Some attempts have been made to incorporate it in general formulas, mainly based on a logarithmic time dependence.

Rouse (1940) was the first to state that scouring never ends with time. He also found that the jet impingement height represents the characteristic length for the scour hole profile and established a correlation between two non-dimensional parameters: the ratio of scour depth to jet impingement height and the ratio of jet velocity to particle fall velocity.

Doddiah (1949) summarized some important theoretical considerations on vertical circular jet impact into alluvial bed material, for a varying pool depth. By use of dimensional analysis and curve fitting, he developed erosion depth equations as a function of time. His most important conclusions are comparable to the ones made by Rouse (1940).

Doddiah et al. (1953) conducted a similar analysis for the case of free (plane) overfall jets and compared their results with Schoklitsch' (1932) expression. The data agreed well with Schoklitsch' equation for small scour depths. However, for greater depths, Schoklitsch' scour prediction is only half as large as the one that occurred during the experiments, showing the time influence on the phenomenon.

Breusers (1967) developed an empirical-analytical equation as a function of time. Kobus et al. (1979) also pointed out that the scour volume is proportional to the logarithm of time, and found different relationships for steady and pulsating jets.

The second time scale is a micro-time scale. Transient hydrodynamic water pressures acting inside the discontinuities of a fractured rock mass constitute a micro-time scale effect and cannot be taken into account by steady-based formulas. It requires the analysis of turbulence and pressure waves inside rock joints, as discussed in Chapter III.

As a summary, it is assumed that the major part of the ultimate scour depth (up to 90%) is reached within the first few days or weeks of discharge. Further deepening of the scour hole requires much more time to develop. No reliable development exist to express this time dependence.

1.5. Standard scouring expression

In general, empirical formulae expressing an equilibrium scour depth have the following form (based on Mason et al., 1985, see Fig. I-2 for definition of parameters):

$$Y = t + h = K \frac{H^y \cdot q^x \cdot h^w}{g^v \cdot d_m^z} \tag{2.1}$$

$Y = t + h$ = depth of scour below tailwater [m]
x, y,.. = exponential coefficients [-]
t = effective scour depth [m]
h = tailwater depth [m]

H = head difference up to downstream [m]
q = specific discharge [m^2/s]
g = gravitational acceleration [m/s^2]
d_m = mean sediment size, rock cube [m]
K = $(6.42 – 3.10H^{0.10})$ [-]
v = 0.30 [-]
w = 0.15 [-]
x = (0.60 – H/300) [-]
y = (0.15 – H/200) [-]
z = 0.10 [-]

As investigated by Mason & Arumugam (1985), a comparative analysis of all such formula results in a variation of 25% for model conditions and 30% for prototype conditions. The applicability for head drops "H" lies between 0.325 and 2.15 m for models, and 15.82 and 109 m for prototypes. At the same time, the formula covers cohesive and non-cohesive granular models, with mean particle sizes between 0.001 and 0.028 m. For prototype rock, a mean block size of 0.25 m is assumed.

Since the 1970's, authors also began to incorporate the jet impact angle, adding one more parameter to the above formula. Examples can be found in Chee & Kung (1971), Chee et al. (1972), Martins (1973), Mason (1983), Yuen (1984) and Bormann (1988). Preliminary studies assumed a jet impact angle between 60° and 90°, neglecting so its importance on the ultimate scour depth.

Accurate expressions for the extension of the scour hole are hardly possible, due to the aforementioned rock mass scaling problems. One of the most pertinent studies has been made by Rajaratnam (1981). Using dimensional analysis, he obtained an expression for the ultimate scour depth as a function of a densimetric Froude number, and established similarity profiles for the eroded bed form.

Hoffmans (1994a & 1994b) made an overview of empirical expressions for plunging and submerged jets and compared their relative accuracy by use of an extensive database.

A general report of all possible scouring forms, such as scour around bridge piers, scour by high velocity jets, scour in river bends, etc., was given by Breusers & Raudkivi (1991).

1.6. Conclusions on empirical expressions

Empirical expressions represent a simple but comprehensive tool that allows a global evaluation of the ultimate scour depth. Due to their specific straightforward nature, care has to be taken, even when applied for the cases for which they were designed. Their major limits are the lack of theoretical background, the appearance of significant scaling effects and the absence of dynamic aspects. This makes it hardly possible to obtain a detailed and physically correct description of the phenomenon.

Nevertheless, empirical expressions can be useful to get an "on-the-shelf" first idea and to identify general scouring tendencies. Furthermore, the variety of available formulas makes it possible to compare between them.

2. Semi-empirical expressions

The lack of accuracy of empirical formulas stimulated many researchers to obtain more theoretically correct formulas. Mathematical expressions obtained through clearly outlined analytical developments and calibrated by use of available experimental data are referred to as semi-empirical relationships. Distinction is made between shear-stress based initiation of motion theories, use of conservation equations and incorporation of geomechanical characteristics. Moreover, lots of these expressions use the steady-state two-dimensional jet diffusion theory as hydrodynamic basis. Hence, this section starts with an overview of this theory. At the end, some aeration effects are discussed.

2.1. Two-dimensional jet diffusion

The diffusion of a two-dimensional jet through a medium at rest was firstly solved following basic equations of fluid mechanics. These equations assume a hydrostatic pressure distribution, infinitesimal plunge pool thickness, shear forces expressed by Prandtl's formula (Tollmien, 1926) or a Gaussian velocity distribution (Reichardt, 1941; Albertson et al., 1950) and finally dynamic similarity conditions. Many textbooks describe these mathematical developments in detail (Abramovich, 1963; Rajaratnam, 1976).

The fundamental concept of a jet of uniform velocity field penetrating into a medium at rest is based on the progressive growing thickness of the related boundary layer by exchange of momentum. This boundary layer consists of particles of the jet itself as well as of particles of the surrounding medium. It is characterized by two major effects: an increase of the total cross section of the jet and a corresponding convergence of the wedge-like region between the boundary layers. This non-viscous region is called the **jet core** and its disappearance gives rise to the fully **developed flow** region.

The hydrostatic pressure assumption leads to a constant velocity in the core of the jet. Many researchers have investigated experimentally or theoretically the extension of this very important region. A summary is presented at Table II-1 and in Fig. II-1, where the core length is presented as K times the jet diameter "d" (for circular jets) or the jet width "b" (for rectangular jets).

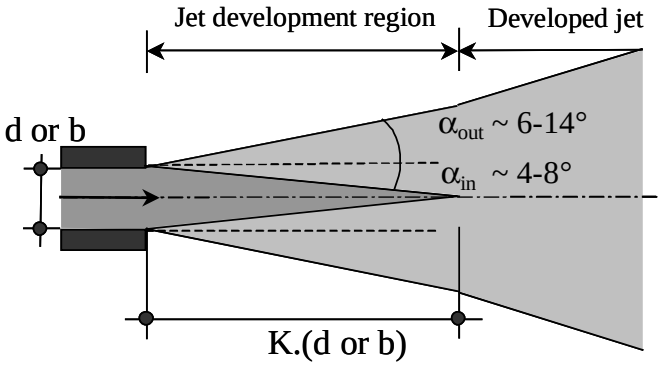

Fig. II-1 Two-dimensional jet diffusion: the jet development region, containing the core, and the developed jet region. The core length is expressed as K times the jet diameter "d" or the jet width "b".

The core length clearly depends on the inner angle of diffusion α_{in}, about 4-5° for submerged jets and 8° for highly turbulent jets (McKeogh, 1978). Furthermore, along the jet's centreline in the developed region, the velocity profiles are of self-preserving shape when plotted against an appropriate length

scale (for example the width corresponding to half of the maximum velocity). This important characteristic has been largely used for predicting mean velocity and mean pressure fields.

Author	Year	K	Jet type	Analysis
Albertson et al.	1950	5.2	rectangular	2D jet diffusion + experimentally
Albertson et al.	1950	6.2	circular	2D jet diffusion + experimentally
Homma	1953	4.8	circular	experimentally
Cola	1965	7.2	rect/submerged	conserv. equations + experimentally
Poreh & Hefez	1967	9.0	circular	2D jet diffusion
Hartung & Häusler	1973	5.0	circ/impinging	estimation of diffusion angle
Hartung & Häusler	1973	5.0	rect/impinging	estimation of diffusion angle
Beltaos & Rajaratnam	1973	8.3	rectangular	momentum flux of the jet
Beltaos & Rajaratnam	1974	5.8-7.4	circular	momentum flux of the jet
Franzetti & Tanda	1984	4.7	circ/impinging	2D jet diffusion + experimentally
Franzetti & Tanda	1984	6.0	circ/submerged	2D jet diffusion + experimentally
Chee & Yuen	1985	3.3	circ/impinging	dimensional anal. of momentum
Tao	1985	6.4	rect/impinging	based on Aki (1969)
Ervine & Falvey	1987	4	circ/impinging	momentum jet + experimentally
Ervine & Falvey	1987	6.2	circ/submerged	experimentally
Bormann & Julien	1991	3.2	rect/impinging	jet diffusion coefficient C_d
Ervine et al.	1997	4	circ/impinging	experimentally

Table II-1 Summary of studies on the coefficient K of jet core length. The jets are circular or rectangular in shape, for impinging (with air) or submerged (without air) impact conditions.

However, this fundamental diffusion concept didn't take into account the existence of flow boundaries, largely modifying the hydrostatic pressure distribution and making the problem gravitational dependent. Cola (1965) experimentally found that the boundary influences the uniform velocity field in a region of up to 12.9 times the jet thickness from the bottom.

Hartung & Häusler (1973) summarized some interesting descriptions of the velocity and pressure fields. They pointed out the significant influence of dynamic water pressures inside rock joints and reproduced this destructive process under laboratory conditions. The impact of a high-velocity vertical jet on a squared concrete plate was conveyed inside an inner flaw of the plate by means of a small hole. This caused complete destruction of the plate. The authors stated that realistic tailwater cushions almost never provide a reliable scour protection.

The first complete empirical-analytical study of plane and circular jet impingement on a flat and smooth surface has been established by Beltaos & Rajaratnam (1973, 1974, 1976). Their analysis was based on experimental calibration of theoretical expressions as obtained by dimensional analysis, conservation equations and two-dimensional jet diffusion theory.

They distinguished three main jet regions: the free jet region, the impingement region and the wall jet region (Fig. II-2a). The impingement region represents thereby the region where the bottom influences the uniform flow field of the incoming jet. It is estimated at roughly 30 % of the total water depth. They extended existing knowledge on the free jet and the wall jet region up to the less known impingement region. The time-averaged velocity, pressure and wall shear stress fields were described in the three regions for a plane jet, and in the jet impingement region for a circular jet.

All these developments produce valuable information about the mean velocity and pressure fields of jets impinging on plunge pool bottoms. However, they do not allow the quantification of the fluctuating part of the flow field, such as root-mean-square values and corresponding power spectral densities. Hence, they can be considered as a "static version" of the later developed turbulence theories. When incorporated in semi-empirical expressions, their steady-state nature is although

appropriate. Therefore, many authors combined the two-dimensional jet diffusion theory with the initiation of motion concept or with a rock erodibility index method.

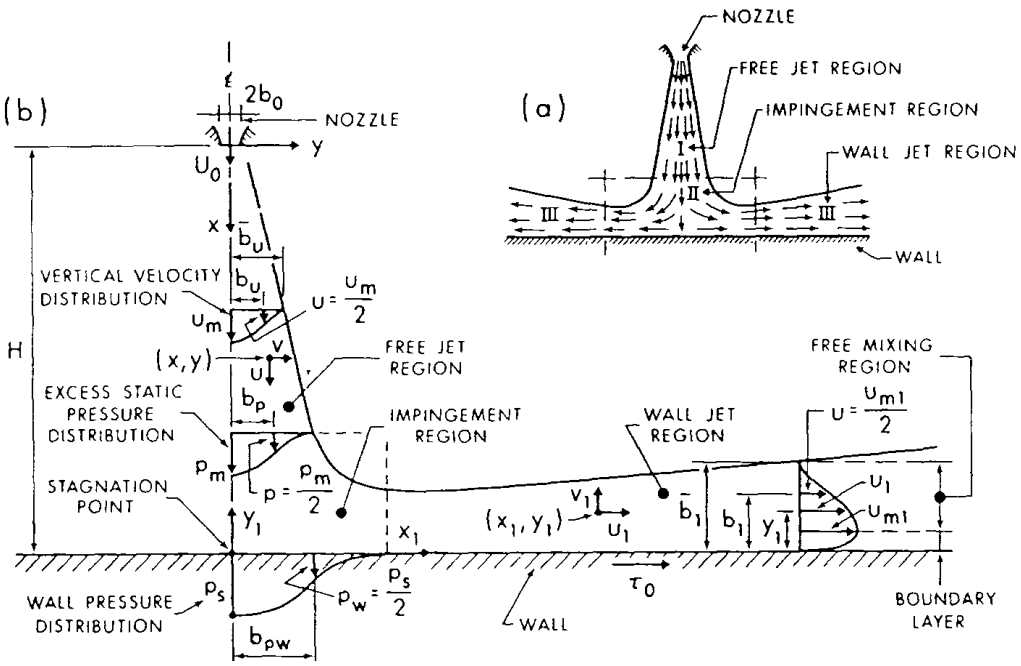

Fig. II-2 Two-dimensional jet diffusion and impingement on a flat smooth surface: a) main jet regions; b) velocity and pressure distributions in each region (Beltaos & Rajaratnam, 1973).

2.2. Initiation of motion concept

The shear-stress based concept of initiation of motion has been largely applied to cohesionless granular material. Referential theoretical work on this subject has been established by Simons & Stevens (1971), who performed a complete three-dimensional analysis of the hydrodynamic forces and moments on a solid particle. Their results constitute a theoretical framework for many authors.

A method for determination of initial sediment motion in case of rough boundaries was developed by Poreh & Hefez (1967). Based on Shields' experimental evaluation of critical shear stress in open channel flows, they proposed a modified formula taking into account specific characteristics of radial wall jet flow. These are for example a higher turbulence intensity and smaller thickness of the laminar sub-layer near the boundary. The following expression is proposed by the authors (Fig. 3):

$$\frac{\tau_c}{\gamma_s d} = 0{,}79 \cdot S\left(1{,}46 \cdot V_c^* \cdot \frac{d}{\upsilon}\right) \tag{2.2}$$

τ_c = critical shear stress [N/m^2]
γ_s = submerged specific weight of sediment on bottom [N/m^3]
d = sediment particle diameter [mm]
S = experimental function [-]
V_c^* = $\sqrt{\tau_c/\rho}$ critical shear velocity [m/s]

Moreover, the authors proposed an expression for the shear stress distribution in the case of rough boundaries as:

$$\frac{\tau \cdot b^2}{\rho \cdot M} = C \cdot \left(\frac{r}{b}\right)^{-2,3} \tag{2.3}$$

in which:

b = height of impingement of the jet [m]
M = kinematic momentum flux of the jet [m^4/s^2]
r = radial distance from jet axis [m]
C = constant independent of Reynolds number and equal to ~ 0,012 [-]

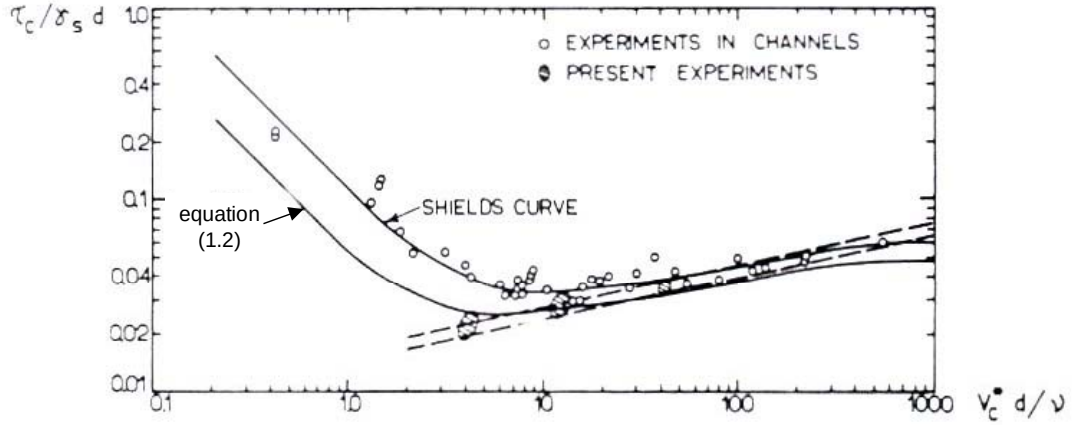

Fig. II-3 Initiation of sediment motion for rough boundaries. Modified Shields criterion applied to radial wall jet flow (Poreh & Hefez, 1967).

An approximation of the "S" function in equation (2.2), combined with equation (2.3), permits a prediction of the region of sediment entrainment. Experimental data obtained by use of air jets impinging on partially cemented sand beds confirmed this modified Shields' equation. However, this approach is not applicable in the zone of transition between the impingement jet and the wall jet, because its turbulent character cannot be expressed by the mean local shear stress. As such, the Shields' critical shear stress isn't representative.

Similar experiments have been established by Kobus, Leister & Westrich (1979). They aimed at the flow field and the erosion pattern of continuous and pulsating jets on a horizontal sand bed of uniform grain size. Their systematic investigations focused on pressure, shear stress and maximum velocity. These parameters were estimated along rough walls, taking into account the permeability of the bottom. Flow field data were gathered by means of an air model with a rough and unerodible bed, while a corresponding water model aimed the quantification of erosion processes. Main jet regions are according Fig. II-2a. Some notations used by the authors are:

d_0 = jet diameter [m]
d_s = mean particle diameter [mm]
u_0 = jet outlet velocity [m/s]
w = particle fall velocity [m/s]
f = pulsation frequency [Hz]
α = pulsation amplitude [m]

k_s = equivalent sand roughness by Nikuradse [mm]
l_0 = jet impingement height [m]
r = radial coordinate [-]
Re_0 = jet Reynolds number (= $u_0 \cdot d_0/\nu$) [-]
Re_s = particle Reynolds number (= $w \cdot d_s/\nu$) [-]
S_r = Strouhal number = $f \cdot d_0/u_0$ [-]

The pressure distribution is not influenced by the roughness as long as the roughness height is small compared to the size of the impingement region. The distribution can be described in a dimensionless manner by an experimental constant A:

$$\frac{p_w}{\rho \cdot \frac{\overline{u_0^2}}{2} \cdot (l_0/d_0)^2} = A \cdot e^{\left[-2A\left(r/l_0\right)^2\right]}; A = 57 \qquad (2.4)$$

The wall shear stress increases linearly with radial distance in the impingement region to decrease exponentially in the wall jet region. In both cases, the shear stress values increase with growing wall roughness, and the maximum value shifts slightly towards the jet axis. For rough walls, velocities decay more rapidly with distance from the stagnation point, together with an increase of the boundary-layer thickness. Turbulence intensity is only increased in the boundary layer, not in the above shear-free zone. The measurements of turbulence intensity for $k_s = 0$ showed good agreements with the tests made by Poreh & Hefez (1967) for smooth walls.

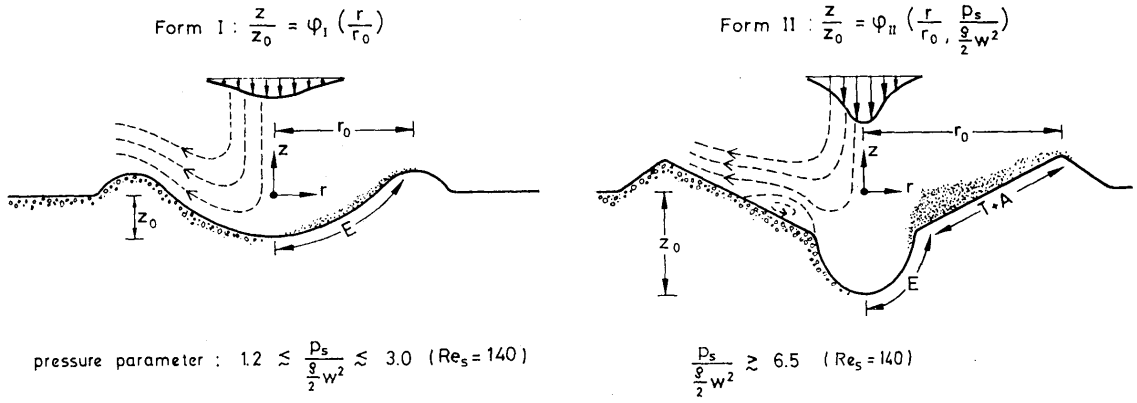

Fig. II-4 Similarity profiles of the scour hole as a function of the pressure parameter k_0 (Kobus et al., 1979)

Erosion processes were first of all investigated for steady impinging jets. Beside the time development of the scour formation, assumed to be logarithmic, the permeability and erodibility of the wall were taken into account. The stagnation pressure p_s, radial velocity and shear stress decrease with increasing permeability. Defining a dimensionless pressure coefficient k_o as $[p_s/(\rho/2)w^2]$, the following scour forms were generated (Fig. II-4):

- $1{,}2 < k_0 < 3$ scour form I, corresponding to a shallow profile, with attachment of the jet up to the edge of the scour hole. Erosion is established mainly by bedload transport.

- $6{,}5 < k_0 < 140$ scour form II, with a very pronounced central deformation of the bed and straight slopes in the outer region, combined with suspension transport and partial deposition.
- $140 << k_0$ injection flow, where form II is transformed into an extremely deep centre hole.

The erosive capacity of the jet is strongly related to the impingement height, with maximum erosion occurring at large heights. A decrease in height results in a stronger jet deflection and, thus, a larger energy dissipation into seepage flow. Furthermore, the higher the jet velocity, the higher the erosion rate, except in the transition zone between form I and II, where a very pronounced bed deformation causes high energy dissipation.

An attempt to quantify the dynamic action of a water jet has been made by superimposing velocity pulsations on the mean jet outlet velocity. The influence of these pulsations on the flow field has been evaluated based on the momentum flux at the outlet and can be summarised as follows: above a certain Strouhal number S_r, the stagnation pressure diminishes and the pressure field becomes comparatively wider for increasing frequencies. The amplitude of the pulsations is of no importance.

The dimensionless pressure distribution is expressed as:

$$\frac{\bar{p}_{wpulsating}}{p_{wsteady}} = 1 - 60 \cdot S_r^{1,5} \cdot e^{\left[-0{,}0017 \cdot Sr \left(r/l_0\right)^2\right]} \tag{2.5}$$

Above a certain Strouhal number, the wall shear stresses decrease in the impingement region and in the first part of the wall region. At large distances, no influence has been noticed. The amplitude also is of secondary importance. Velocity profiles in the wall jet region are quite similar. Turbulence structures however are completely different. For a steady jet, instantaneous fluctuations in the radial outward direction are not correlated. On the other hand, pulsating jets showed well-correlated fluctuations. Moreover, it was found that the turbulence structure in the boundary layer is not influenced by the pulsations, while in the free-shear layer zone, the velocity pulsations interfere with the eddies of same frequency and transfer energy into the latter. Turbulence intensity measurements confirmed an increased total fluctuation in the free-shear layer zone. The erosive capacity of a pulsating jet is influenced in two manners. First of all, the mean flow field is characterised by a diminished velocity on the jet axis and, thus, a wider pressure field and wider deflection zone. Together with a decrease in seepage velocity, this leads to an increased erosion action. Secondly, the strong radial correlation of the turbulent fluctuations enhances less random and more radial directed forces on the sediment particles. This results in increased erosion and transport outside the scour hole.

As a summary, the periodic pulsation of a jet can cause a significant increase in erosion capacity. This capacity increases with the pulsating frequency and the amplitude.

Rajaratnam (1981) used dimensional analysis to investigate characteristic features of sand bed scour in the asymptotic state (= ultimate scour depth), due to impingement of plane turbulent jets formed by water and air. He summarised the main studies established in the field of erosion of beds of uniform, cohesionless material due to turbulent jet impact. The maximum depth of erosion in the asymptotic state $\varepsilon_{m\infty}$ is expressed as a function of the jet momentum flux M_0 at the nozzle, the jet impingement height H, the median particle diameter d_m, the density of the fluid ρ and finally the difference in densities between bed particles and fluid $\Delta\rho$:

$$\varepsilon_{m\infty} = f\ (M_0, \rho, H, g\Delta\rho, d_m)$$

Using the PI-theorem and neglecting the H/d_m parameter, because non important unless it gets very small, leads to:

$$\frac{\varepsilon_{m\infty}}{H} = f\left[\frac{F_0}{\sqrt{H/2b_0}}\right] \tag{2.6}$$

$$F_0 = \frac{U_0}{\sqrt{g\frac{\Delta\rho}{\rho}D}} \quad = \text{ the densimetric Froude number} \tag{2.7}$$

in which U_0 stands for the velocity of the jet and D for the grain diameter. From the experiments, this functional relationship was found to be different for air-sand and water-sand systems, due to the difference in mode of transport of the eroded bed material out of the scour hole. Indeed, in the case of water jets, an important portion of eroded material is kept in suspension and settles back once the jet is stopped. Other functions, such as the height of the outside ridge and its distance from the jet axis, have also been found to vary with $F_0 / (\sqrt{H/2b_0})$. The bed profile in the scour hole was found similar for air and water and could be expressed as follows (Fig. II-5):

$$\left[\frac{\varepsilon}{\varepsilon_m}\right]_\infty = e^{-0{,}693\cdot(x/b)^2} \tag{2.8}$$

in which:

ε	=	depth of erosion [m]
x	=	longitudinal distance from jet outlet [m]
b	=	value of x where $(\varepsilon/\varepsilon_m)_\infty$ = 0,5 [m]

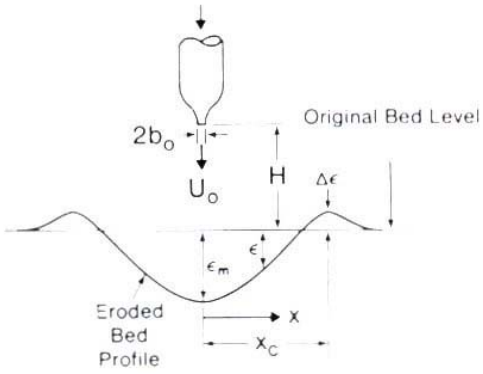

Fig. II-5 Parameter definition sketch. (Rajaratnam, 1981)).

Mih & Kabir (1983) performed an analysis of a submerged jet impinging on non-uniform granular beds, through the use of a dimensionless impingement number, and taking into account the jet obliqueness effect. They searched ideal jet conditions for the flushing out of fine silt from gravel in natural riverbeds, in order to increase the survival rate of salmon eggs. They stated that for large impingement heights, defined as more than 8.3 times the jet outlet diameter, the height itself plays the role of characteristic length for scour holes. For impingement heights less than 5.5 times the jet outlet diameter, the jet diameter becomes the characteristic length.

Their development considered two important forces acting on an individual solid particle moved away by impinging jet flow: the drag force F_d in the direction of flow, and the net downward force F_g, resulting from gravity and buoyancy effects. By defining friction forces as a friction coefficient times F_g, it gets obvious that the ratio F_d/F_g signifies a very important parameter in predicting particle motion:

$$\frac{F_d}{F_g} = \frac{3C_d}{4}\cdot\frac{V^2}{gd_s\left(\frac{\Delta\rho}{\rho}\right)} \tag{2.9}$$

in which :

C_d	=	drag coefficient [-]
d_s	=	diameter of a solid sphere [m]
$\Delta\rho$	=	difference between gravel density and water density [kg/m^3]

The drag coefficient C_d is a function of the Reynolds number and of the particle shape. Furthermore, the second part of the right hand side of the expression corresponds to the square of the densimetric Froude number, as defined by Rajaratnam (1981), and based on the PI-theorem. Interesting also is the agreement with the ratio of jet velocity to fall velocity as introduced by Rouse (1940) and Doddiah et al. (1953). This underlines the relevance of the initiation of motion concept as a sort of preliminary "static version" of the later developed dynamic uplift methods, just like the two-dimensional jet diffusion constitutes the "static version" of later developed fluctuating turbulence characteristics. For two distinct flow zones, the core region (less than 6.2 jet diameters) and the region of established flow (more than 6.2 jet diameters), (Albertson et al., 1950), the experimental results allowed the scour depths to be determined as a function of the impingement number and of the jet diameter at the bottom of the scour hole.

Chee & Yuen (1985) combined dimensional analysis, two-dimensional jet diffusion theory and initiation of motion to derive a relationship for scour of granular beds that takes into account the obliqueness of the impinging water jet. The parameters that determine the threshold condition for particle motion are the critical bed shear stress τ_c, the width of the scour hole B_s, the depth of flow at the deepest point of scour $H_s.\sin\beta$ (with β the jet impact angle), the effective size of bed material d_s, the mass densities of water and sediment particles ρ and ρ_s, the gravitational acceleration g and finally the cinematic viscosity of the water ν. A dimensional analysis combined with the Brahms' formula (1753), as described in Lelliavsky (1955), stating that τ_c is proportional to u^2_{ms} (with u_{ms} the velocity near the bed at the deepest part of the scour hole), gives the following equation:

$$\frac{u_{ms}^2}{g\cdot(S_s-1)\cdot d_s} = f\left(\frac{d_s\cdot u_{*c}}{\upsilon}\right) \tag{2.10}$$

in which:

S_s = specific gravity of the bed particle [-]

u_{*c} = $\sqrt{\tau_c/\rho}$, the shear velocity at threshold condition [m/s]

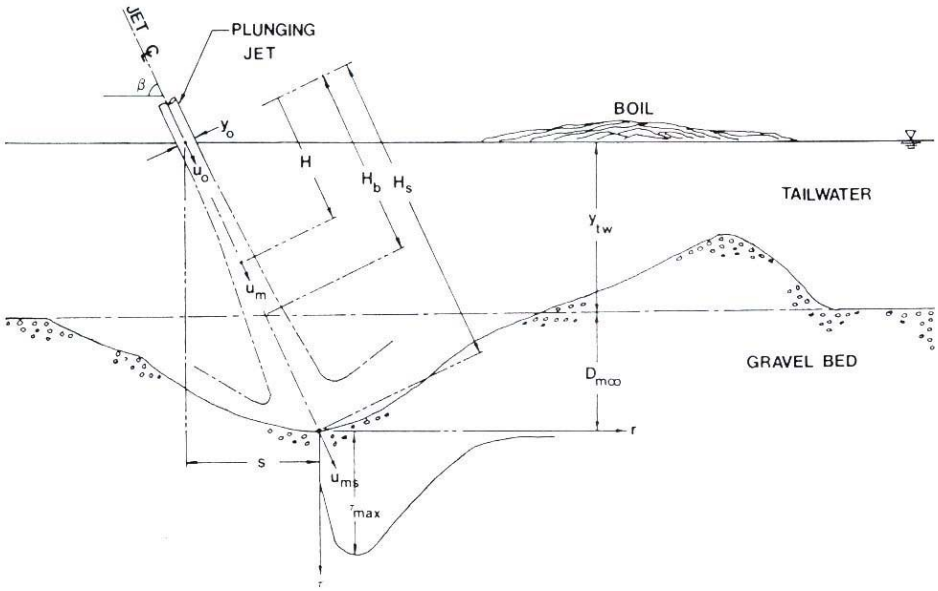

Fig. II-6 Scour of granular beds due to obliqueness jet impingement. Definition sketch of parameters (Chee & Yuen, 1985).

The bed-velocity u_{ms} was determined by dimensional analysis, based on a jet centreline velocity decay rate as expressed by Beltaos & Rajaratnam (1974), and based on a regression analysis of the experimental results:

$$\frac{u_{ms}}{u_0} = 0{,}508 \cdot \left(\frac{y_0}{H_s} \right)^{\frac{1}{2}} \tag{2.11}$$

Where the stagnation effect of a solid plate influences the centre velocity just at about 30 % of the impingement height (Beltaos & Rajaratnam, 1973), the corresponding region in case of a pervious gravel bed only extents up to 21 %. The threshold shear velocity reflects the intensity of turbulent fluctuations near the bottom and can be calculated based on the maximum wall shear stress in the impingement region as defined by Beltaos (1976), with a coefficient η accounting for the bottom surface roughness, justified by Kobus et al. (1979). A generalisation for all cross sections, with J_a the total jet area, is expressed below:

$$u_{*c} = \left(\sqrt{\eta} \right) \cdot \sqrt{0{,}166 \cdot \left(u_0 / H_s \right)^2 \cdot \left(4J_a / \pi \right)} \tag{2.12}$$

The final scour depth relationship then becomes, after multiplication by the relative roughness (d_s/H_s) in order to obtain an excellent agreement with the test results (Fig. II-6):

$$\frac{u_{ms}^2}{g \cdot \left(S_s - 1 \right) \cdot H_s} = 0{,}00429 \cdot \left[\frac{d_s \cdot \sqrt{0{,}166 \cdot \left(u_0 / H_s \right)^2 \cdot \left(4J_a / \pi \right)}}{\upsilon} \right]^{0{,}182} \tag{2.13}$$

$$H_s = \left(D_{m\infty} + y_{tw} \right) / \sin \beta \tag{2.14}$$

in which:

H_s = distance along the jet centreline between the tailwater level and max. scour bed [m]
$D_{m\infty}$ = max. scour below original bed level [m]
d_s = sediment particle size [mm]
y_{tw} = tailwater depth [m]
u_{ms} = near bed velocity [m/s]
S_s = specific gravity of the bed particle [-]
u_0 = jet impact velocity [m/s]
J_a = total jet cross-sectional area [m^2]
β = jet impact angle [°]

The formula accounts for grain size effects and underlines the importance of bed shear velocity as a measure of the intensity of turbulent fluctuations at the bottom. Comparison of measured and calculated locations of maximum scour depth confirmed that the jet follows a straight-line path down to the pool bottom.

Bormann & Julien (1991) also established an equation based on the two-dimensional jet diffusion (Beltaos & Rajaratnam, 1973) and on non-cohesive particle stability in scour holes as a function of Shields' critical bed shear stress. The authors made use of a diffused jet velocity in the scour hole, as well as of a diffused jet thickness, both based on Beltaos & Rajaratnam (1973). Moreover, the stability analysis of noncohesive particles is expressed as a function of a critical bed shear stress. This shear stress is dependent on a local friction coefficient, incorporating the critical Shields number θ_{cr}, the sediment particle size, a parameter constant B and an exponent x. Based on Simons & Stevens (1971), the critical shear stress τ_b required to move upslope at an angle α in the downstream direction is

expressed as a function of the value τ_{cr} for a flat bed (ϕ = submerged angle of repose of the granular material):

$$\frac{\tau_b}{\tau_{cr}} = \frac{\sin(\phi + \alpha)}{\sin\phi} \tag{2.15}$$

Equilibrium conditions conducted to the following expression for the total scour depth beneath a grade-control structure (Fig. II-7):

$$h + D_p = K \cdot q^{0,6} \cdot \frac{U_0}{g^{0,8} \cdot d_s^{0,4}} \cdot \sin\alpha \tag{2.16}$$

$$K = C_d^2 \left[\gamma \cdot \sin\phi / \sin(\phi + \alpha) \cdot B \cdot (\gamma_s - \gamma)\right]^{0,8} \tag{2.17}$$

in which:

h	=	equilibrium scour depth [m]
D_p	=	drop height of grade-control structure [m]
α	=	jet angle of impact [°]
ϕ	=	angle of repose = 25 [°]
q	=	specific water discharge [m^2/s]
d_s	=	sediment particle size = d_{90} [mm]
U_0	=	jet velocity entering tailwater [m/s]
B	=	2 (coefficient of friction) [-]
C_d	=	1.8 (jet diffusion coefficient) [-]
γ_s/γ	=	2.7 (specific weight ratio) [-]

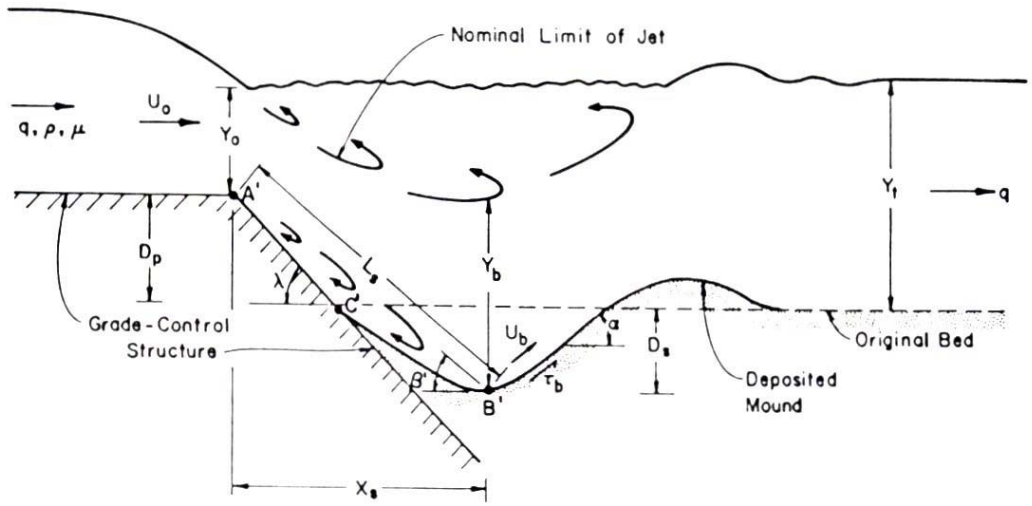

Fig. II-7 Ultimate scour depth downstream of grade-control structures. Definition sketch of parameters (Bormann & Julien, 1991).

By comparison with the experimental formulas discussed by Mason & Arumugam (1985), it was found that the exponents of equation (2.1) agree very well with the here proposed expression. Large-scale experiments (up to 1.4 m of scour depth) allowed calibration of this expression and largely extended the range of conditions for which previous scour data were available. Direct application of this formula to plunging jets is possible by neglecting D_p and results in an equation comparable to the

standard empirical form presented in § 1.5 (equation (2.1)). Hoffmans & Verheij (1997) tested the above formula with a large data set and found acceptable accuracy and wide-range applicability.

2.3. Conservation equations

Approaches based on the continuity, momentum or energy equations are of interest because they express the main physical processes in a global but exact manner. Despite the fact that several of the aforementioned analytical methods make partially use of some conservation equation, the studies presented herein merit particular attention.

One of the first analyses was developed by Altinbilek & Okyay (1973), based on the continuity principle. They assumed that the pressure and velocity distribution in the scour hole are functions of the geometry of the latter. The continuity equation for the scour hole volume is expressed as follows:

$$t = \int_0^S \frac{dV}{Q_{s0}} \tag{2.18}$$

in which:
V = scour hole volume [m^3]
t = time [s]
Q_{s0} = rate of sediment transport [m^3/s]
S = depth of scour [m]

Scour depth versus time functions are obtained through integration of equation (2.18). Q_{s0} and dV were determined based on experimental results and dimensional analysis. General non-dimensional functions can be obtained by repeated numerical integration. However, these curves have to be established separately for each sediment size and jet thickness. The experiments resulted in the following conclusions:

- the geometry of the scour hole remains similar during the scouring,
- the scour depth attains a limiting value. This value depends on the jet Froude number Fr, the mean grain diameter D_g, the jet thickness b, the jet velocity U and the particle fall velocity w in the following manner:

$$\frac{S_T}{b} = \frac{30{,}5 \cdot \left(\frac{U}{w}\right)^2 \cdot \left(\frac{D_g}{b}\right)}{Fr \cdot \left(\frac{H}{b}\right)^{0{,}5}} \tag{2.19}$$

- at higher flow depths, the scour hole becomes irregular due to irregular jet diffusion.

Fahlbusch (1994) derived a basic relationship by application of the momentum principle. He reasoned that, in spite of the complexity of the phenomenon, in the final equilibrium state, all the forces acting on a certain control volume must obey the momentum principle. An estimation of the forces imparted by the scour walls on the control volume by assuming a linear pressure distribution still depends on the unknown rock strength and is quite delicate. However, by ignoring the water pressure in the jet, the following dimensional homogenous expression that groups the most important parameters is written:

$$D = \sqrt{\frac{2(1-\varepsilon)}{\beta}} \cdot \sqrt{\frac{qv \sin\alpha}{g}} \tag{2.20}$$

in which:

D	=	scour depth + tailwater depth [m]
q	=	discharge per unit width [m^2/s]
v	=	jet velocity [m/s]
ε	=	average volumetric air concentration [%]
α	=	angle of impact [°]
β	=	correction factor [-]

A comparison with 104 model and prototype data showed good agreement. The first part of the right hand side of the formula had an upper limit of 3.92 and an average value of 2.79, which was almost identical to the value of 2.83 found by Veronese in 1937. However, a potential under- or overestimation of the real scour depth by 40 % was still observed.

Hoffmans (1998) also calculated the equilibrium scour depth by application of Newton's second law of motion on a mass of fluid particles. He assumed that the horizontal component of the external force acting on the body of fluid is equal to the horizontal component of the drag force that is acting upon bed particles by flowing fluid. This drag force can be related to the near bed velocity and, thus, indirectly to the mean jet impact velocity. Furthermore, in the equilibrium phase, the upstream scour angle corresponds to the natural angle of repose of the bed material. In that way, application of the PI-theorem and calibration by experimental data results in an expression similar to that of Fahlbusch (1994). Analogous to the Schoklitsch' (1932) formula, the scouring factor λ depends on d_{90} and is presented in Fig. II-8.

$$D = c_{2v} \cdot \sqrt{\frac{qv \sin\theta}{g}} \qquad \text{with} \qquad c_{2v} = \sqrt{\lambda' \cdot c_b^2 \cdot \tan\delta - \tan\theta} \tag{2.21}$$

in which:

λ'	=	friction coefficient [-]
δ	=	angle of the resultant force of the jet on the scour hole [°]
θ	=	angle of jet impingement [°]

This dimensionally homogenous relation, however, cannot be used to predict equilibrium scour depths because of the multitude of physical factors that influence the bed particle resistance to motion. These are for example particle diameter, particle size distribution, particle shape, density, cohesion, near bed turbulence level, etc. By application of the PI-theorem, the c_{2v} coefficient can be expressed in the following manner:

$$c_{2v} = f\left(D^*, \Delta, \frac{d_{90}}{d_{50}}, \frac{k_b}{u_b^2}\right) = 20/\lambda \tag{2.22}$$

D*	=	sediment diameter [m]
Δ	=	relative density [-]
k_b	=	turbulent kinetic energy near the bottom [m^2/s^2]
u_b	=	near bed velocity [m/s]

Based on experimental data, c_{2v} could be related to D* and d_{90}. This was tested by the author and resulted in a reasonable prediction of the ultimate scour depth.

The ratio of computed scour depth to measured scour depth has been analysed for the Schoklitsch (1932) empirical expression, the Hoffmans' equation and two semi-analytical formulas (the one by Bormann & Julien (1991) and the one by Fahlbusch (1994)), based on 450 experiments collected from

literature. Schoklitsch' formula gave excellent results only for flume experiments. Hoffmans' equation provided reasonable scour prediction for both model and prototype conditions: more than 80 % of the computed scour depths were located in the range of 0.5 to 2 times the measured depths.

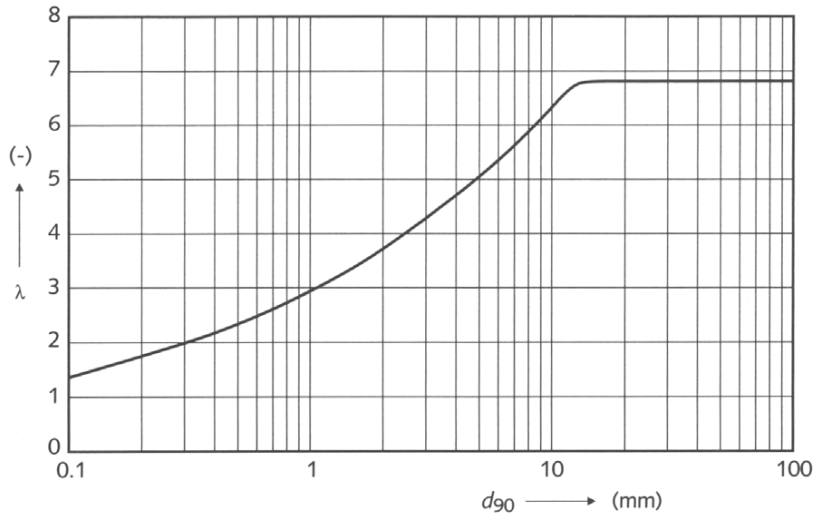

Fig. II-8 Non-dimensional scouring factor λ for determination of c_{2v} (Hoffmans & Verheij, 1997)

2.4. Geomechanical characteristics

The first studies that attempted to incorporate geomechanical characteristics have been conducted by Yuditskii (1963, 1971) and Taraimovich (1980). These authors performed model studies on scaled rectangular rock blocks. The dynamic pressure measurements in rock joints made by Yuditskii (1963) are described more in detail in § 4 of this chapter.

Further pioneering work on plunge pool geology was conducted by Spurr (1985). He proposed a procedure that compares the hydraulic energy with the erosion resistance of the rock mass. This procedure also accounts for the time duration of spillage. Scour occurs when the jet energy available at the bedrock is greater than the sum of the rock's capacity of energy absorption (or reflection) and the energy deflected towards the pool boundaries. As such, two physical situations can be distinguished:

- Initial state ($t = t_0$): the unscoured bedrock acts as a flat plate deflecting the jet. By the total absence of turbulent diffusion, the scour potential is at its maximum and the deflected jet energy is large.
- Equilibrium state ($t = t_e$): the available jet energy is reduced to the rock's threshold level, signifying the end of the scour process.

The energy absorbed between these two stages corresponds to the turbulent energy plus the deflected energy, the latter being negligibly small at the equilibrium state. Moreover, the time t_e largely depends on the resistance of the rock mass against erosion. The characteristics of the free falling jet are steady-state, i.e. self-preserving velocity profiles are assumed, according to the two-dimensional jet diffusion theory. The mean bottom velocity varies inversely with the plunge pool depth to the power of x, whereas x is generally close to 1 for high head dams (= circular jet case).

The rock mass resistance is composed of the resistance to hydrofracturing and the resistance to shear forces. The former is governed by tensile properties and natural faults, while the latter can be expressed by cohesive strength. These parameters can be defined by the effective uniaxial compressive strength σ'_c, which depends on the Rock Quality Designate (RQD). They are related to the intact uniaxial compressive stress σ_c by means of the Bieniawski's Rock Mass Range (RMR).

The proposed procedure uses a reference plunge pool for calibration of an existing empirical formula for the ultimate scour depth. Transformation of this formula to the study site is then performed by means of an energy scour index (ESI). This index is defined as the ratio of the energy lost by the jet in the measured (referenced) case to the corresponding energy loss in the studied case. It accounts for hydraulic and geomechanic differences between the two sites. These differences are quantifiable through established tables summarizing the geological characteristics of the plunge pool bottom. The adapted scour depth is than equal to the reference depth times a factor $(1/ESI)^x$, in which x is depending on the plunge pool velocity decay rate.

Spurr validated his procedure by applying it to a prototype site and by using Mason's empirical formula (equation (2.1)). This, however, constitutes the only application example. The practical significance of the present method has not yet been clearly outlined.

A similar concept has been developed between 1992 and 1998 at the Colorado State University, in collaboration with the US Bureau of Reclamation (Annandale, 1995; Annandale et al., 1998). This study was called the Dam Foundation Erosion Study and is based on the geomechanical properties of the rock mass combined with the rate of energy dissipation of the jet. Graphical expression of prototype observations of the relationship between a geomechanical index of the rock bed and the erosive power of water determines a rock erosion threshold (Annandale, 1995). The erosive power of water is determined by the degree of jet energy dissipation through the plunge pool depth, which is expressed by the rate of velocity decay at the centreline of the jet. The geomechanical index defines the resistance of the rock mass against erosion.

In a first stage of this extensive study, experiments were conducted aiming the prediction of jet impact velocities in plunge pools. The impact velocities were determined for both compact and totally broken up jets (Lewis, 1996). For broken up jets, a modification of the Ervine & Falvey (1987) relationship was performed by incorporation of aerodynamic drag (Fig. II-9).

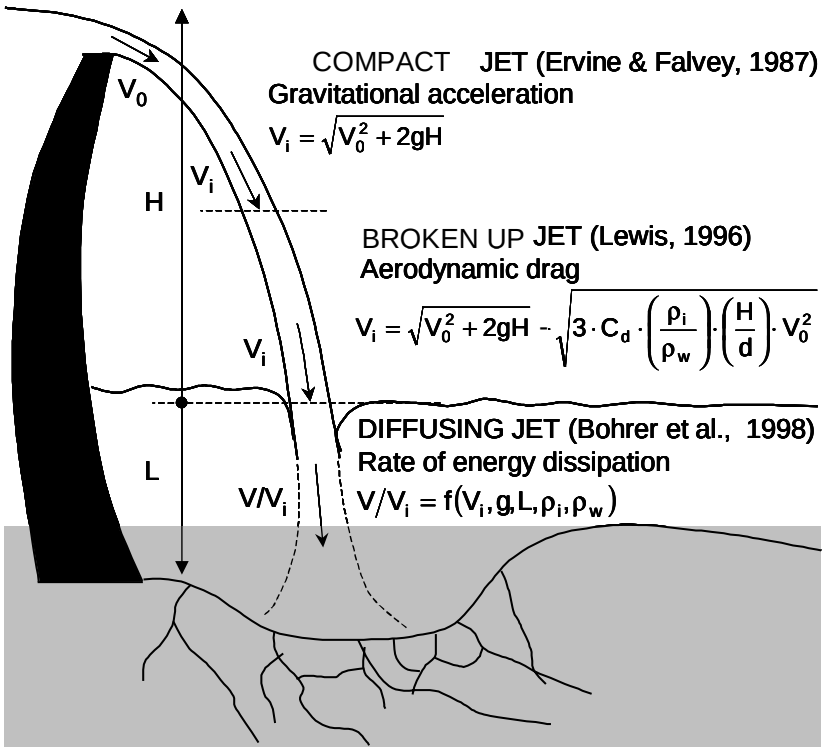

Fig. II-9 Jet velocity acceleration and decay from the point of issuance down to the plunge pool bottom. The velocity decay V/V_i defines the rate of energy dissipation and, thus, the scour potential of the diffusing jet.

Secondly, the decay of the jet velocity through the plunge pool depth has been related (Bohrer, 1996) to the jet impact velocity and impact angle, the air concentration at impact and gravitation. For totally broken-up jets, the following expression has been proposed (Fig. II-9):

$$-\ln\left(\frac{V}{V_i}\right) = -0.638 \cdot \ln\left[\left(\frac{\rho_i}{\rho_w}\right)\cdot\left(\frac{V_i^2}{gL}\right)\right] + 1.848 \tag{2.23}$$

The velocity decay for compact jets holds an analogous relation:

$$\frac{V}{V_i} = 0.0675 \cdot \left[\left(\frac{\rho_i}{\rho_w}\right)\cdot\left(\frac{V_i^2}{gL}\right)\right] + 0.1903 \tag{2.24}$$

in which:

L = $(z_j - z_{j+1})/\cos\alpha$ [m]
V = velocity at a distance L beneath water surface (along centreline) [m/s]
V_i = velocity at jet impact [m/s]
ρ_i = average mass density of aerated jet at impact [kg/m^3]
ρ_w = mass density of water [kg/m^3]

The rate of energy dissipation, or the stream power, is then expressed as a function of this velocity decay and can finally be compared with the stream power required to erode the rock (Fig. II-10b). The elevation where the available and required stream powers are equal is being considered as the ultimate scour depth.

The rate of energy dissipation is a discretized function of the total head at various distances along the jet centreline. The change in energy ΔE_j between two points j and j+1, as well as the corresponding available power p_{Aj} [kW/m^2], can be written:

$$\Delta E_j = \frac{v_j^2 - v_{j+1}^2}{2g} + \frac{P_j - P_{j+1}}{\gamma} + z_j - z_{j+1} \tag{2.25}$$

$$p_{Aj} = \frac{\gamma \cdot v_{j_j} \cdot \Delta E}{1000 \cdot (z_j - z_{j+1})} \tag{2.26}$$

The rock erosion resistance is expressed by the **erodibility index K_h**. This index is based on Kirsten's ripability index, established in the 1980's in the field of excavation equipment. It takes into account the major mechanical characteristics of the rock mass, such as the unconfined compressive strength, the relative density, the block size, the discontinuity bond shear strength, the shape of rock entities, and the orientation of the discontinuities relative to the flow. The erodibility index is the scalar product of the indices of the constituent parameters, and is written as follows:

$$K_h = M_s \cdot K_b \cdot K_d \cdot J_s \tag{2.27}$$

in which:

M_s = mass strength number
K_b = particle or block size number
K_d = discontinuity or inter-particle bond shear strength number
J_s = relative ground structure number

The mass strength number M_s represents the material strength of an intact representative sample without regard to geologic heterogeneity within the mass. The particle or block size number K_b refers to the mean grain size for granular material and the mean size of blocks of intact rock material (the cube root of the volume) as determined by joint spacing within the rock mass. The discontinuity or inter-particle bond shear strength number K_d represents the strength of joint interfaces in rock masses, or the inter-particle friction and cohesion of gouge (infilling) between such units. The relative ground structure number J_s accounts for the structure of the ground with respect to the direction of the stream flow. It is a complex function expressed in terms of the orientation and shape of individual blocks determined by joint set spacings, dip angles and dip directions.

These properties can be measured in the field at low cost and are quantifiable through tables that can be found in Annandale (1995).

A log-log relationship between calculated rates of energy dissipation and the corresponding calculated erodibility index is presented at Fig. II-10a. The calculations are based on 150 field observations of scour and on published data on initiation of sediment motion. The correlation allows the prediction of a critical erosion threshold for any given set of hydraulic conditions and for any type of foundation material (granular soils, rock, etc.).

Recently, Annandale et al. (1998) have conducted an erosion experiment on near-prototype scale by means of a rectangular jet impinging on an artificially created fractured rock. The rock was simulated by two consecutive dipped layers of lightweight concrete blocks. The blocks were of rectangular shape and very flat. The obtained result confirmed the theoretically derived scour threshold.

The structure of this erosion study combines jet velocity decay both in the air and trough the plunge pool (empirically), jet and plunge pool aeration (empirically) and geomechanical characteristics of the rock mass (analytically). It perhaps actually constitutes the most pertinent and directly applicable evaluation method for the ultimate scour depth. However, despite its recent experimental validation, no direct dynamic parameters are incorporated and no physical background of rock break-up is evident in the model.

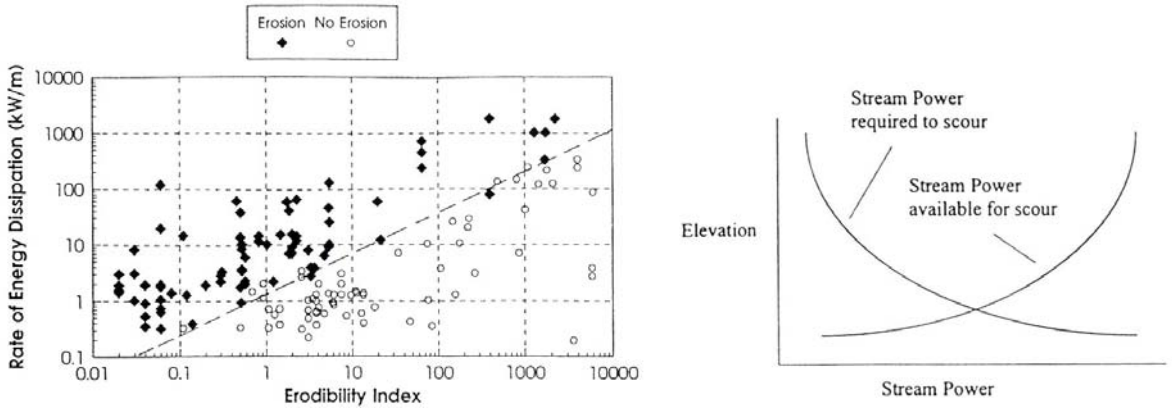

Fig. II-10 a) Rate of energy dissipation as a function of the erodibility index K_h (Annandale, 1995); b) Comparison of available and required stream power as a function of the location in the plunge pool.

2.5. Conclusions on semi-empirical expressions

Semi-empirical expressions differ from empirical expressions in that they are partially based on analytical descriptions of basic physical background. As such, the hydrodynamic aspects of scour are often derived from the two-dimensional jet diffusion theory. The geomechanical aspects, on the other hand, can be obtained by applying the shear-stress based initiation of motion concept, mainly useful for non-cohesive granular soils, or by use of an index that defines the resistance of the rock mass against erosion.

Combination of an analytical description of both hydrodynamic and geomechanic characteristics results in several different scour evaluation methods. Examples are Bormann & Julien's (1991) expression for cohesionless granular soils, Spurr's (1985) and Annandale's (1995) erodibility index methods for rocks, and momentum conservation equations for cohesionless material, established by Fahlbusch (1994) and Hoffmans (1998).

Despite a reasonable accuracy and degree of applicability of most of these methods, still a significant lack of physical insight and background remains. Furthermore, for the case of high-head dams, very little case studies of these techniques are available. Hence, their relevance to prototype cases is not easy to point out.

Other methods have been developed, mainly due to an increased assessment of scour following damage on stilling basins by dynamic uplift of their concrete slabs. These methods go back to the direct cause of scour of concrete slabs of stilling basins or of fractured rock, i.e. the appearance of dynamic pressures inside the joints. However, just like for empirical expressions, they consider the rock mass as already broken-up. They are discussed in the next section.

3. Extreme pool bottom pressures

Failure by dynamic uplift of concrete slabs of several stilling basins (Malpaso Dam, Cabora Bassa Dam, Tarbela Dam) pointed out the importance of dynamic pressure fluctuations on the stability of concrete linings or rock blocks. Technological progress in measurement techniques since the 1960's has made it possible to assess turbulent pressure fluctuations. These have been studied both in hydraulic jump stilling basins and at plunge pool bottoms.

The following parameters are of significance: the mean pressure value, the root-mean-square pressure value, the extreme positive and negative pressure values and the power spectral content of the fluctuating part of the pressures. These parameters characterize extreme loading conditions on concrete slabs or rock blocks by applying a maximum pressure underneath the slab or the block and a minimum pressure on the upper side of the slab or the block (Fig. II-11).

The ultimate scour depth is reached when the net pressure difference Δp on the block or the slab is not capable anymore to eject it. It has to be underlined that the maximum and the minimum pressure values are not measured simultaneously. They correspond to the extreme values that were measured at some moment during a long enough test run. Moreover, no measurements are made inside joints or underneath simulated slabs or blocks. It is assumed that the maximum pressure measured at the surface is automatically transferred through the joints underneath the slab or the block. If only one measurement position is used, the centreline of the slab or the block is most appropriate. If more than one measurement position is available, spatial averages of the extreme pressures should be determined.

The so-defined net uplift pressure constitutes a physical upper limit of dynamic loading conditions. As such, the method of extreme pressures often results in conservative design.

Dynamic pressures at the water-rock interface can be generated by direct impact of the jet core, appearing for small plunge pool depths, or by turbulent shear flow impact, appearing for ratios of pool depth to jet thickness Y/D_j higher than 4 to 6, according to the two-dimensional jet diffusion theory (Table II-1). The corresponding pressure patterns of these two types of jet impact are completely different. Core jet impact generates a constant and high mean pressure with low fluctuations. Turbulent shear flow, on the other hand, can be described as an ensemble of recirculating eddies of different size. These eddies produce large, fluctuating pressures with low mean values.

Since pioneering work on macroturbulent dynamic pressures has mainly concentrated on hydraulic jump stilling basins, this will be briefly dealt with in a first stage.

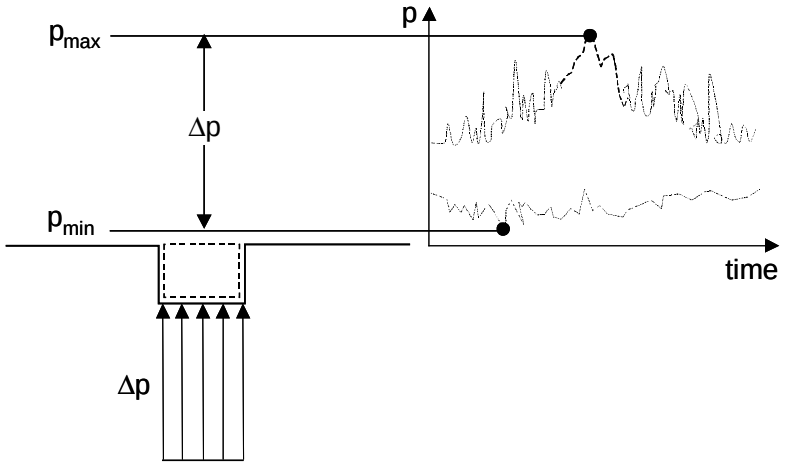

Fig. II-11 Definition sketch of extreme dynamic pressures at the plunge pool bottom. The maximum and minimum pressures are defined at the centre of the slab and for a long enough time interval.

3.1. Hydraulic jump pressure fluctuations

Macroturbulence associated with hydraulic jumps was studied by Rouse & Nagaratnam (1959), Elder (1961), Levy (1961), Gunko (1967), Resch & Leutheusser (1971) and Ribeiro (1975). The pressure fluctuations that result from this macroturbulence have been analysed for appropriate design of bottom linings of stilling basins. These concrete linings present a risk of uplift due to dynamic pressure propagation along their joints. Due to the random nature of the process, an analytical description of the pressures is impossible. Hence, statistical techniques have been widely applied.

A first series of studies focused on the determination of probability density functions of the pressures and their deviation from a Gaussian distribution. Vasiliev & Bukreyev (1967) found that the probability of large pressure variations exceeds that of a normal distribution. The density function thus is positively skewed. They stated that the largest eddies appear in the lateral flow direction. Bowers & Tsai (1969) found pressure fluctuations in the order of 40 % of the incident velocity head.

In 1973, Viscaino & Bribiesca pointed out the uplift phenomenon and proposed a simple design procedure, based on test results with cement slabs on a 1/100 scale. Later on, Lopardo & Henning (1985) examined the influence of inflow conditions on the dynamic pressure field and found local negative skewness values, indicating the presence of flow separation zones. Fiorotto & Rinaldo (1988) made a very complete statistical analysis of bottom pressure fluctuations to define a practical design criterion for concrete slabs under hydraulic jumps. This criterion makes use of uplift pressures and is discussed in § 4. They were the first to examine in a general and systematic manner spatial longitudinal and transversal correlations for a whole range of Froude numbers of the incoming flow field. Farhoudi & Narayanan (1991) studied direct force measurements on concrete slabs, focussing on the spatial structure of the force field rather than the maximum intensity. Force fluctuations indicated that the transverse spatial correlation is considerably higher than the longitudinal one, a phenomenon already pointed out by other authors. Skewness was found to be negative in the upstream part of the jump and to become progressively positive towards the downstream part.

Research also focused on extreme values, with an emphasis on maximum loading conditions on bottom linings or maximum uplift forces on slabs. Toso & Bowers (1988) studied the magnitude and spatial extension of extreme pressure fluctuations. They also found that extreme data are not described by a Gaussian distribution, and alternative (positively skewed) distributions were proposed by the authors. A practical limit of 80-100% of the incident velocity head is proposed for the maximum instantaneous pressure values, based on long-time test runs (24 hours). Farhoudi & Narayanan (1991) found peak values up to 3,5 times the root-mean-square values.

Lopardo (1988) made an interesting model-prototype comparison that showed the limits of Froude scale models. Skewness and extreme values were overestimated by a 1/50 scale model, due to the absence of aeration. Other influences of Froude similarity scaling on dynamic pressure statistics has been treated by Elder (1961), King (1967), Toso & Bowers (1988), Ervine & Falvey (1987) and Ervine et al. (1997). They all stated that Froude law scaling is only correct in case of low frequency pressure fluctuations (large-scale eddies), because these are determined by gravity and inertia forces. However, high-frequency fluctuations governed by viscous forces do not scale accurately. They need appropriate Reynolds numbers and, thus, near-prototype flow velocities.

3.2. Plunge pool bottom pressure fluctuations

The hydrodynamic variables that are dealt with are the mean value, the root-mean-square value, the maximum and minimum values and the power spectral densities. Ervine et al. (1997) presented an overview in the framework of their experimental study of circular jet impingement on plunge pool bottoms.

The first important topic, already investigated by many authors studying two-dimensional jet diffusion, is the mean dynamic pressure under the jet's centreline. Fig. II-12 gives an overview of 11

independent studies and represents the C_p-value, defined as the mean pressure head divided by the total incoming kinetic energy, as a function of the pool depth to jet diameter ratio Y/D_j (Bollaert & Schleiss, 2001e).

Distinction is made between plunging and submerged jets, for both circular and rectangular outlets. The region of jet core impact, according to two-dimensional jet diffusion theory, is up to 5 times the jet diameter for plunging jets and up to 7 times the jet diameter for submerged jets.

It is interesting to observe that circular jets have a more pronounced decrease of C_p with Y/D_j than rectangular ones. This may be due to the definition of the impingement width B_j or to the radial degree of freedom for turbulent diffusion with circular jets. Secondly, due to jet spreading and aeration effects, the maximum C_p value for plunging jets is 0.8-0.9 instead of 1.

The second relevant topic is the root-mean-square (RMS) value of the fluctuations. Fig. II-13 summarizes results obtained by several authors and expressed by the C'_p coefficient (= ratio of RMS value over incoming kinetic energy of the jet). In general, three effects strongly influence the RMS values: the initial jet turbulence intensity Tu, the degree of break-up of the jet and finally aeration effects. The degree of break-up of the jet is defined as the ratio of jet fall length to the jet break-up length.

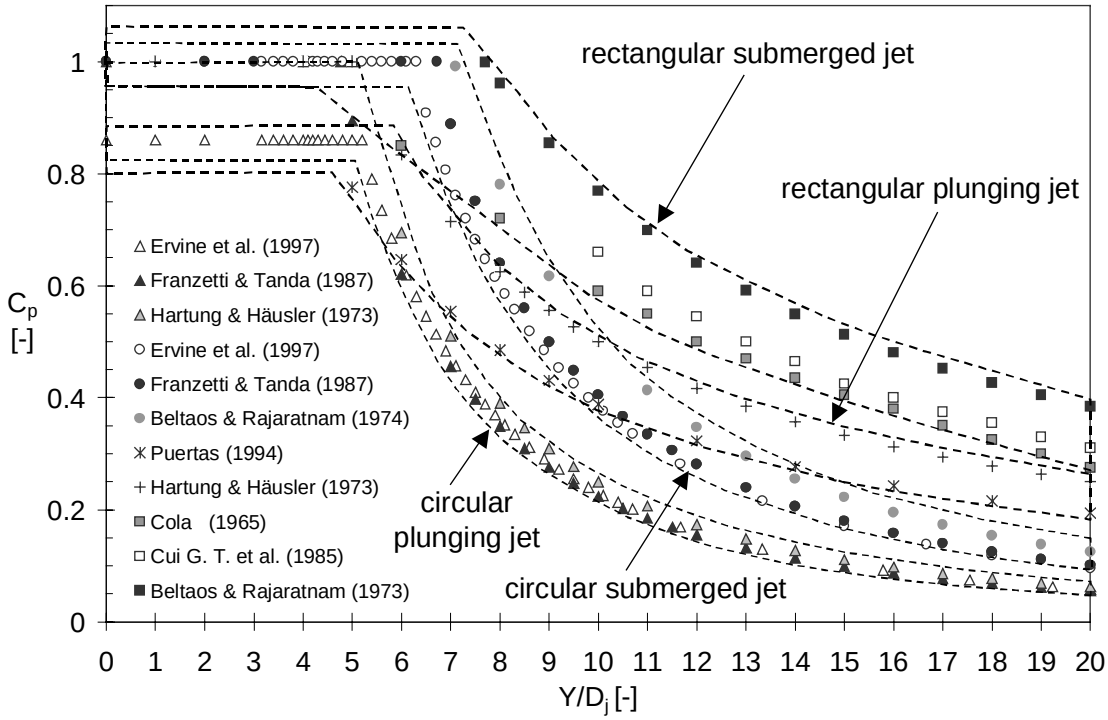

Fig. II-12 Summary of studies on the non-dimensional mean dynamic pressure coefficient C_p as a function of Y/D_j. Distinction is made between circular and rectangular jets, and between impinging and submerged jets (Bollaert & Schleiss, 2001e).

Most of the turbulent fluctuations attain a maximum value between 4 and 12 times the plunge pool depth over jet diameter ratio Y/D_j, except the data for highly oblique (angle 40-50° with the horizontal) impinging circular jets (Xu –Duo-Ming, 1983). This is probably due to the definition of the jet width B_j. All other authors report an increase of turbulence followed by an almost linear decrease. This phenomenon was already noticed by Doddiah (1949), who found a maximum at 10 times the characteristic length. A minimum depth is required to develop large energy containing eddies; with further increase of the water depth diffusion effects become predominant.

A best-fit of available expressions for circular jets has been proposed by Jia et al. (2001). Their curve shows a maximum at a Y/D_j of about 7 and closely follows the curve for circular plunging jet impact found by Ervine et al. (1997). Xu-Duo-Ming (1983) and Franzetti & Tanda (1984) also presented non-dimensional results for the radial distributions of RMS values. They found that fluctuations could persist far away from the impact point, even when mean dynamic pressures fall to zero.

A third important dynamic quantity is the extreme instantaneous pressure value: most authors found values of up to 2 to 4 times the corresponding RMS value (Bollaert & Schleiss, 2001e). Ervine et al. (1997) obtained extreme values up to 4 times the RMS values for positive values and 3 times the RMS values for negative ones, in accordance with the positive skewness generally found in hydraulic jumps. The corresponding maxima occurred at pool depth to jet diameter ratios of 10 respectively 5. Franzetti & Tanda (1984) found that the ratio of extreme pressure value to RMS value increases with increasing Y/D_j ratio and obtained values up to 8 for Y/D_j = 25-30. Thus, in accordance with the findings of May & Willoughby (1991), extreme values do not necessarily appear at the centreline of the jet. This aspect can be important when considering net uplift pressures at locations away from the point of impact of the jet. The latter ones also found higher positive as negative extremes, appearing at about the same Y/D_j ratios than Ervine et al. (1997). They also pointed out higher extremes for plunging than for submerged jets.

However, these extremes are obtained for relatively short run times, and care has to be taken. Toso & Bowers (1988) found, in a hydraulic jump, extreme values during 24 hour tests that were twice as large as the ones for 10-minute observations.

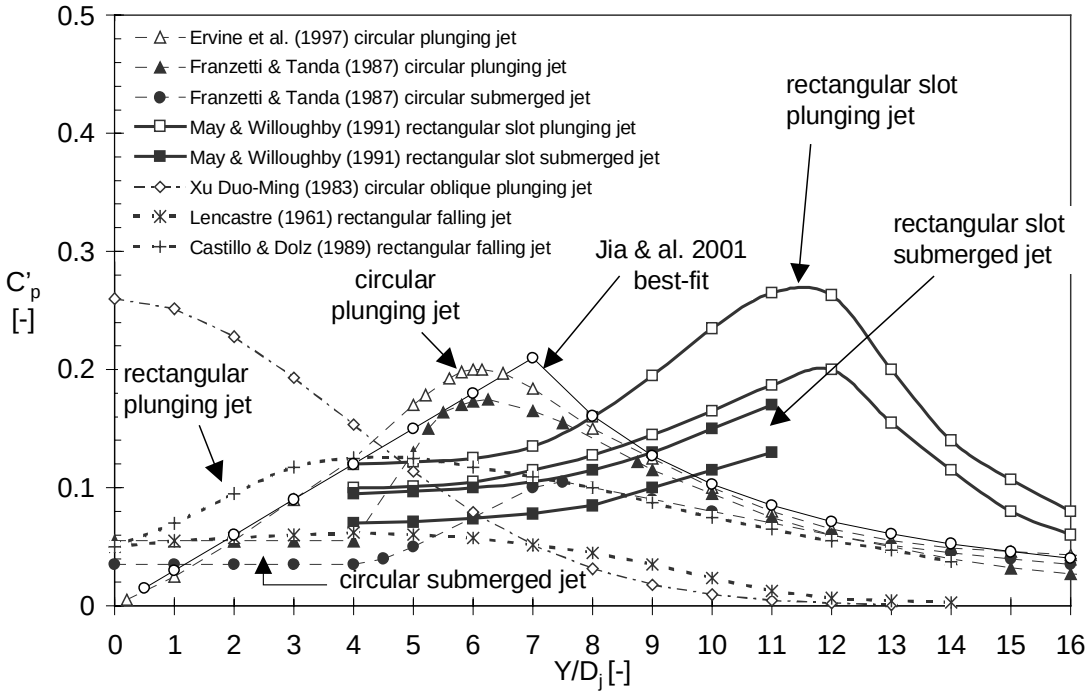

Fig. II-13 Summary of studies on the non-dimensional fluctuating dynamic pressure coefficient C'_p as a function of Y/D_j. Distinction is made between circular and rectangular jets, and between impinging and submerged jets (Bollaert & Schleiss, 2001e).

The last relevant dynamic aspect is the power spectral content $S_{xx}(f)$, which provides important information concerning the cyclic nature and the energy content of the pressure fluctuations. S_{xx} is thereby defined as a decomposition of the variance (σ^2) of the pressure fluctuations as a function of frequency. A summary of power spectral densities is presented at Fig. II-14 (Bollaert, 2001; Bollaert

& Schleiss, 2001e). A log-log scale was used. Both dimensional and non-dimensional results are presented. The spectral content is made non-dimensional by dividing it by the variance σ^2.

Lencastre (1961) found significant spectral energy at frequencies between 1 and 4 Hz and stated that plunge pool flow is described by large-scale vortices. Ervine et al. (1997) focused on dominant frequencies and found two dominant Strouhal numbers S_h (= $f \cdot Y/V_j$), i.e. 0.01, for large scale eddies, and 0.25, for shear layer eddies. May & Willoughby (1991) tested rectangular slot jets and found the major turbulent energy between 0 and 3 Hz. Nevertheless, they noticed significant energy up to 15-20 Hz, for both submerged and plunging jets. Ramos (1979) also found dominant frequencies between 0 and 3 Hz, while Xu-Duo-Ming (1983) showed that spectral energy is strongly decreasing beyond 5-10 Hz. He outlined that, as a function of the plunge pool depth, turbulent energy is still present for much higher frequencies. Tao et al. (1985) obtained maximum spectral content at frequencies between 10 and 20 Hz. Puertas & Dolz (1994) indicated a frequency range of 0-2 Hz and stated that this range corresponds to the extreme values that were measured.

As a summary, most plunge pool and hydraulic jump studies ignored frequencies higher than the ones typical for macroturbulent eddies (25 Hz). Hence, very little information is available for higher frequencies in plunge pools. However, research on turbulent flow around bluff bodies or against flat surfaces (Bearman, 1972; Huot et al., 1986; Ballio et al., 1992), performed for the study of vertical take-off of aircrafts and rockets, outlined that the low frequency zone, with almost constant spectral energy, can extend up to several tens of Hz.

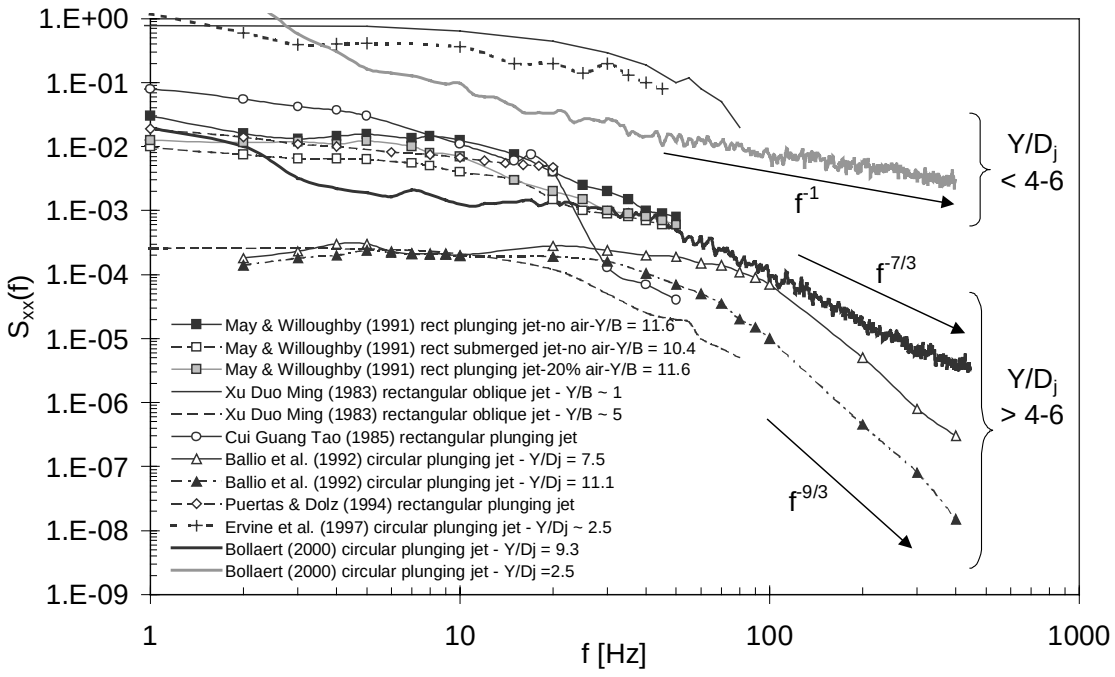

Fig. II-14 Summary of studies on the power spectral density S_{xx} as a function of frequency f. Both dimensional and non-dimensional spectral contents are presented. Distinction is made between core jets, for Y/D_j < 4-6, and developed jets, for Y/D_j > 4-6 (Bollaert & Schleiss, 2001e).

Ballio et al. (1992) measured the spectral content of impinging circular jets for frequencies up to 500 Hz. Two main zones characterize these spectra: the first one in the low frequency part, with relatively constant values, and the second zone at higher frequencies (several hundreds of Hz), showing a quasi-rectilinear decay. The separation between the two zones depends on the jet velocity and the ratio of Y/D_j. They obtained spectral decay slopes independent of this ratio.

As will be outlined more in detail in Chapter V, the present study generated similar spectral contents (Figure II-14). Core jet impact generates quasi-linear decaying spectra, even at very high frequencies. The rate of energy decrease follows f^{-1} (Bollaert & Schleiss, 2001e). Developed jet impact shows two spectral ranges: a first one in the low frequency part (up to max. 100 Hz) where a considerable amount of energy exists, and a second one at higher frequencies (> 100 Hz), with a rate of energy decay according $f^{-7/3}$, corresponding to values available in literature. The exact frequency of separation between these two ranges depends on the flow conditions. These spectra are mainly governed by shear layer eddies of different sizes and importance (Bollaert, 2001).

3.3. Aeration effects

Aeration strongly influences the hydrodynamic variables. This happens at three different stages: aeration of falling jets, plunge pool aeration by jet impact and finally aeration of rock fissures.

The first stage can be expressed by the jet break-up length, depending on the initial jet turbulence intensity T_u. Expressions can be found in Baron (1949), Horeni (1956), McKeogh (1978, 1980) and Withers (1991).

The second stage concerns a relationship between pool aeration and related bottom pressure fluctuations and has been poorly investigated. May & Willoughby (1991) studied the effect of 10% and 20% air ratios on mean and fluctuating pressures for rectangular slot jets and found relatively little influence by changes in air concentration.

Finally, the third stage concerns air entrainment in rock fissures and will be discussed in the next chapter on pressure wave propagation.

3.4. Scaling effects

Ervine & Falvey (1987) showed that turbulence spectra, and thus pressure fluctuations, don't scale between model and prototype and proposed careful choice of the model size and interpretation of the results. Some important processes in free jets, as for example jet aeration and jet spreading, largely depend on Weber (Pinto & Neidert, 1982) and Reynolds (Pan & Shao, 1984) numbers and are consequently difficult to reproduce accurately in Froude scale models. Prototype jets diffuse more than model jets and have greater air concentrations that produce lower mean dynamic pressure values.

Prototype experiments of pressure fluctuations were conducted by De Vries & Volkart (1988) and Volkart & Speerli (1994), on high head bottom outlet structures. Their measurements were made in the hydraulic structure itself.

3.5. Conclusions on extreme pool bottom pressures

Studies on pressure fluctuations in plunge pools have mainly been conducted by Ervine et al. (1997), Xu-Duo-Ming (1983) and Franzetti & Tanda (1984, 1987) for circular jet impingement, and by Tao et al. (1985), Lopardo (1988), Armengou (1991), May & Willoughby (1991) and Puertas & Dolz (1994) on rectangular jets.

These studies deliver useful information on bottom pressure fluctuations, but don't deal with their propagation inside the joints of the underlying rock mass.

As a conclusion, the simultaneous application of extreme positive and negative bottom pressures over and under rock blocks or concrete slabs can result in a net pressure difference of up to 7 times the root-mean-square value, or up to 1.5-1.75 times the incoming kinetic energy of the jet. This seems to provide a conservative design criterion. However, it doesn't consider violent transient phenomena that could occur inside the rock joints or under the concrete slabs.

4. Extreme pressure difference techniques

4.1. General

The present section deals with pressure differences over and under concrete slabs or rock blocks. The major difference with the previous method, based on extreme pool bottom pressures, is that the here considered pressures are measured both at the surface and underneath the slab or the block. This means that the test results account for eventual correlation between the surface and the underside of the slab or the block.

Distinction is made between time-averaged pressure differences and time-instantaneous pressure differences. The former correspond to the difference of the time-mean values of the pressures over and under the block, measured during a certain time interval. The latter defines the maximum instantaneous pressure differences that can occur at any time instant between the underside and the surface of the block. For this case, the correlation between the surface pressures and the underpressures can become significant.

Pressure difference techniques assume a quasi-instantaneous propagation of pressure waves through the joints between the slabs or the rock blocks. Viscous damping of these pressures is often neglected. The surface pressures are governed by turbulent shear-layer flow. The corresponding low-frequency vortices move at a speed that is defined by the velocity and the characteristic water depth of the incoming jet flow. Pressure waves travel at a much higher speed, up to 1'400 m/s. As such, the pressurized flow inside the joints can be considered as instantaneous compared to the turbulent surface flow. This time lag effect is responsible for the building up of net pressure differences.

However, no fully transient flow conditions are considered. The pressures underneath the block are determined by the pressure pulses at the joint entrances of the block, but the pressure distribution is considered as steady-state (= already stabilized), i.e. initial transient wave phenomena due to the sudden change in flow and pressure conditions at the entrance are assumed to be damped out. Thus, eventual standing or resonance waves between two pressure pulses entering a joint underneath a rock block are completely discarded from the analysis. Before steady-state conditions are attained these transient conditions, however, can subsist during a significant time interval. As pointed out by Kirschke (1974), several tens to hundreds of resonance cycles may occur, depending on the damping ratio of the system.

In fact, when assuming pressure pulses at the joint entrance that have a frequency that is close to the resonance frequency of the pressure waves inside the joints, steady-state conditions may probably never exist in practice. This is because the transient system will never have the time to be equilibrated before a new pulse is coming in. The relevance of these statements increases with increasing frequency of the impacting flow and with decreasing wave celerity of the pressure waves underneath the blocks. This is pointed out in the next section.

A direct result of pressure differences is the net uplift force exerted on slabs or blocks. Two experimental methods are available for evaluation of this force: direct measurement, by force transducers, and indirect calculus by use of simultaneous measurements of pressure fluctuations over and underneath the structure (Ramos, 1979; Fiorotto & Rinaldo, 1992a).

4.2. Time-averaged pressure differences

Yuditskii (1963) (reported by Gunko et al., 1965) at first stated that time-averaged and pulsating pressures are responsible for rock block uplift. He made model tests with a ski-jump spillway impinging on a single rock block and presented the pressures in non-dimensional graphs as a function of the length of the block and of the depth of the pool. He pointed out the importance of instantaneous pulsating pressures that enter the joints and disintegrate the rock. Dynamic uplift of the block, however, is only attributed to the time-averaged part of the joint pressures.

The experimental set-up is presented in Fig. II-15a. The forces on the modelled rock block are transferred to a force transducer by a mechanical system of steel bars. As such, it is obvious that this system is poorly suited for the measurement of dynamic effects on the blocks. Yuditskii (1963) found that two jet locations produced maximum uplift forces. These are presented in Fig. II-15b and logically correspond to the impinging of the jet on either of the joints.

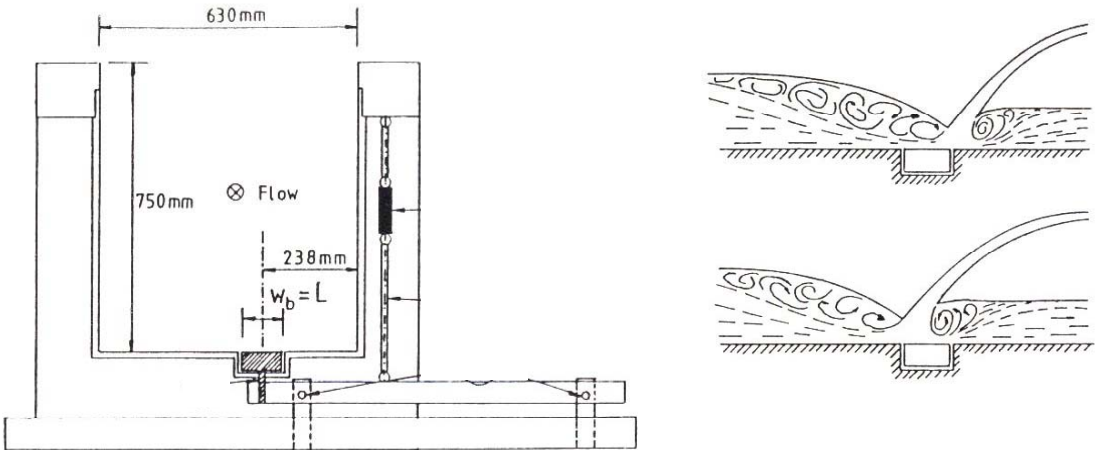

a) b)

Fig. II-15 Test facility of Yuditskii with ski-jump impinging jet and single rock block on a flat pool bottom: a) Geometrical configuration of the pool bottom and the rock block, as well as of the force transfer system; b) Jet locations for maximum uplift forces on the rock block (Yuditskii, 1963).

Reinius (1986), based on a study by Montgomery (1984), investigated the time-averaged pressures on a rock block subjected to water flowing parallel to its surface. The obtained time-averaged uplift pressures attained up to 67 % of the incoming kinetic energy, sufficiently high to cause uplift of the block (Fig. II-16).

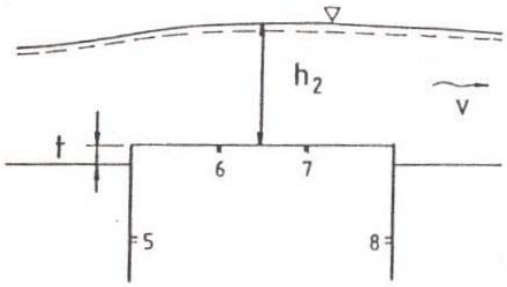

Fig. II-16 Mean dynamic pressures over and under a rock block due to oblique parallel jet impingement: a) sketch of the parameters; b) pressure field over and under the rock block (Otto, 1989).

Otto (1989) furthermore underlined the expansion of rock joints by the dynamic action of the jet. He quantified time-averaged uplift pressures on a rock block for plane jets impinging obliquely. Depending on the relative protrusion of the block and on the point of jet impact, important surface suction effects occurred, leading to mean uplift pressures of almost the total incoming kinetic energy. Without accounting for suction, the maximum underpressures were of half of the incoming kinetic energy. Fig. II-17b shows the pressure fields over and under the rock block. It has to be noted that the

underpressure field assumes a linear relation between the surface pressures at the two joints. As outlined before, this means that no transient effects are considered.

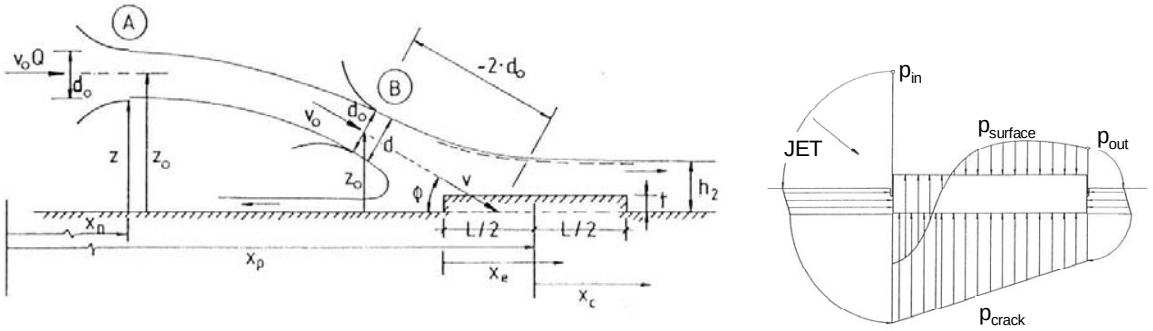

Fig. II-17 Mean dynamic pressures over and under a rock block due to oblique parallel jet impingement: a) sketch of the parameters; b) pressure field over and under the rock block (Otto, 1989).

All these studies illustrate the significance of time-averaged dynamic pressures in joints, but don't explain the exact mechanism of rock destruction (Vischer & Hager, 1995). To assess the dynamic character of the uplift forces, several laboratory studies have been conducted focusing on the conveyance of instantaneous surface pressures to the underside of rock blocks or concrete slabs.

4.3. Instantaneous pressure differences

Hartung & Häusler (1973) described the destructive effects of dynamic pressures entering tiny rock joints and building up tremendous forces inside the rock mass. They reproduced the phenomenon by impact of a vertical jet on a square concrete plate, linked to an underlying corrugated cardboard via a 1mm diameter tube. Once the tube opened, the dynamic pressures developed inside over the total area of the cardboard and quickly destroyed the entire concrete plate.

Kirschke (1974) at first performed an analytical and numerical analysis of pressure wave propagation in rock joints. He used one-dimensional fine discontinuities of rigid, elastic or plastic rock, and applied a constant pressure at the joint entry. As such, following an incoming pressure pulse, he formulated the time interval necessary to obtain steady-state flow conditions inside the system. This pointed out that, in practice, several tens to hundreds of wave cycles are necessary. The static character of the excitation pressure did not allow, however, the simulation of fully transient conditions.

In case of rigid boundaries, no interaction between water and rock is taken into account. The pressure and velocity propagation are expressed as a function of viscous damping effects with laminar flow. For elastic boundaries, it was found that the modulus of elasticity and the mass of the boundary are important, as well as shear forces between elementary boundary parts. An irregular thickness of the discontinuity seemed to be not significant. Contact points between the boundaries had an important effect on their deformations due to dynamic pressures. The application of a constant pressure at the entrance of a rigid discontinuity has been investigated and described as a function of the end boundary (open or closed) and the joint geometry (thickness, entrance section, longitudinal profile, etc.). Finally, a qualitative explanation of the influence of plastic rock behaviour on dynamic pressure propagation is given.

This work provides a valuable theoretical and numerical description of joint pressures, but does not consider real pressure values.

Fiorotto & Rinaldo (1992a) were the first to measure instantaneous pressure differences, based on transient flow assumptions. They experimentally investigated the statistical structure of surface pressure fluctuations at the bottom of hydraulic jumps, aiming the prediction of net uplift forces on concrete slabs of stilling basins. Their theory is based on instantaneous pressure transients in a layer of arbitrary thickness between the soil and the underside of the slabs, using water as propagator (Fig. II-18). The momentum and continuity equations of one-dimensional transient flow are written:

$$\begin{aligned} &\frac{\partial V}{\partial t} + V \cdot \frac{\partial V}{\partial x} + g \cdot \frac{\partial p'}{\partial x} + \lambda(V) \cdot V = 0 \\ &\frac{\partial p'}{\partial t} + V \cdot \frac{\partial p'}{\partial x} + \frac{a^2}{g} \cdot \frac{\partial V}{\partial x} = 0 \end{aligned} \qquad (2.31)$$

in which:

$V(x,t)$ = velocity averaged along the layer thickness δ [m/s]
a = celerity of pressure wave [m/s]
$\lambda(V)$ = parameter of friction effects [-]
p' = piezometric head = $p(x,t)/\gamma$ [m]

However, the authors did not investigate the effects of the boundaries on wave reflections and wave superpositions. Hence, they do not consider fully transient flow. The reason for this lies in their assumption of very high wave celerities, in the order of 10^2–10^3 m/s, combined with very low frequencies of the main pressure pulses, i.e. maximum 2 Hz. The discrepancy between the high resonance frequency of the joint and the low frequencies of the excitation results in unrealistic resonance lengths of joints, i.e. several hundreds of metres.

Hence, the uplift forces under the slab or the block are completely determined by the pressure values at the joints entrances, and the following design criterion was established:

$$s > \Omega \left(\frac{l_x}{y_1}, \frac{l_x}{I_x}, \frac{l_y}{I_y} \right) \cdot C_p \cdot \frac{V_1^2}{2g} \cdot \frac{\gamma}{\gamma_c - \gamma} \qquad (2.32)$$

in which:

s = equivalent thickness of the slab or the block necessary to avoid uplift [m]
Ω = dimensionless reduction factor [-]
l_x, l_y = longitudinal and transversal slab or block length [m]
I_x, I_y = longitudinal and transversal integral scale of turbulent pressure fluctuations [m]
V_1 = incoming flow velocity [m/s]
C_p = $\Delta p_{max} / (\gamma \cdot V_1^2/2g)$ (pressure coefficient) [-]
Δp_{max} = maximum pressure difference [N/m^2]
γ, γ_c = specific weights of water and concrete [N/m^3]

The reduction coefficient Ω expresses the influence of the surface pressure field on the net uplift force. The combination of a maximum underpressure and no overpressure leads to a value of 1. In practice, however, this is hardly possible. Even for a maximum pressure under the slab, a certain surface over the slab will exhibit a significant counter pressure from the eddy that caused the maximum underpressure. For a maximum counter pressure that covers the whole surface of the slab, Ω becomes equal to 0. A real situation lies somewhere in between these two extremes. As such, the reduction coefficient Ω defines the discrepancy between the maximum possible pressure difference, as discussed in § 3 on extreme pool bottom pressures, and the real pressure difference.

Scale model experiments were conducted simulating concrete slabs with different geometries and bottom roughness. They confirmed the above theories. Underpressures were measured at the

extremities and in the middle of the joints. No frictional effects were observed. However, the scale of the model tests, as well as the data acquisition rate (up to 50 Hz), didn't allow measuring any oscillatory or resonance effects.

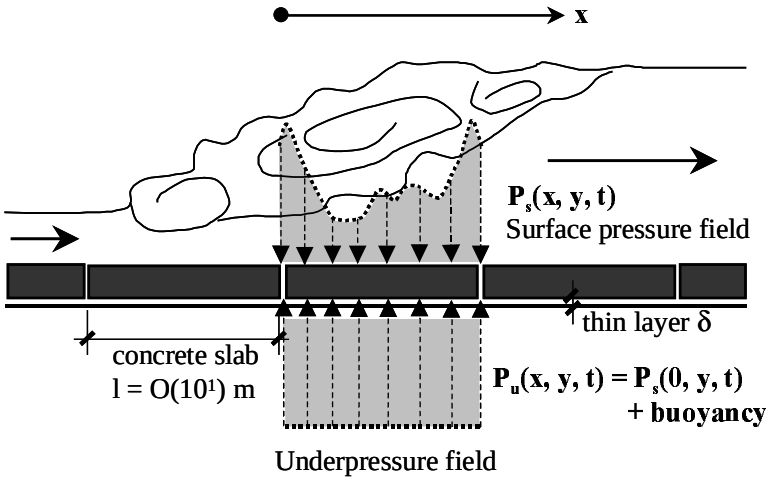

Fig. II-18 Instantaneous surface pressures and underpressures causing uplift forces on concrete slabs of hydraulic jump stilling basins (Fiorotto & Rinaldo, 1992a).

In order to verify this design criterion, Bellin & Fiorotto (1995) performed simultaneous force and pressure measurements on simulated concrete slabs of hydraulic jump stilling basins. The measured net uplift forces were related to the corresponding pressure fluctuation measurements. The aim was to provide a direct evaluation of the uplift coefficient Ω. Values for Ω of 0.10 to 0.25 have been obtained, as a function of the shape of the slabs and the Froude number of the incoming flow field. For practical design purposes, C_p in equation (2.32) can safely be assumed equal to 2. This corresponds to a maximum uplift pressure of 0.5 times the incoming kinetic energy. Bellin & Fiorotto (1995) furthermore concluded that the most appropriate shape of the slabs is rectangular, with the largest dimension in longitudinal direction and the transversal length maintained to a minimum.

Fiorotto & Salandin (2000) extended the above design criterion to a dynamic calculus of anchored slabs, accounting for the persistence time of the surface pressures that enter underneath the slabs. The governing dynamic equation is shown hereunder and assumes a constant underpressure pulse during the time interval τ, neglecting any oscillatory or resonance characteristics.

$$\rho_c \cdot 2p_s' \cdot \frac{\Omega}{(\gamma_c - \gamma)} = -\frac{E_a \cdot A_a}{L} \cdot z(t) + 2\Omega \cdot \left[p'(t) - p_s'\right] \tag{2.33}$$

in which:

ρ_c = concrete density [kg/m^3]
z(t) = steel elongation in function of L [m]
A_a = steel area per unit slab surface [m^2]
E_a = steel elastic modulus [N/mm^2]
p'_s = defined pressure level [mce]
p'(t) = $p(t) - \bar{p}$ = pressure peak [mce]

The persistence time τ of pressure pulses has been determined both analytically and experimentally, based on a Gaussian surface pressure distribution assumption.

Annandale et al. (1998) simulated the erosion of fractured rock by use of lightweight concrete blocks. The blocks were placed in a series of two layers on a 45° dip angle. Jet impingement allowed confirming their theory that the erosion threshold criterion for rock and earth material can be defined by means of a geomechanical index. As such, the erosive power of water can be related to the relative ability of material to resist erosion.

Liu et al. (1998) performed an experimental and numerical study focusing on fluctuating net uplift forces on simulated rock blocks and leading to a design criterion for rock block uplift. They considered superposition of pressure waves underneath the rock block, but combined with a constant pressure field over the block. No resonance effects were considered. As such, the net pressure difference for uplift is maximum equal to twice the incoming pressure of the waves (by superposition) minus one time the same incoming pressure at the surface, i.e. one time the incoming surface pressure. Maximum measured net uplift pressures fluctuated between 2.2 and 4.2 times the root-mean-square value of the surface pressure fluctuations, for frequencies up to 12 Hz. Stating that extreme pool bottom pressures are about 4 times the root-mean-square value of the fluctuations (Ervine et al., 1997), this would result in an uplift pressure equal to 0.5 to 1 time the incoming kinetic energy. The scale of the rock blocks, in the order of 10^{-1} m, and the low data acquisition rates (< 200 Hz), did not allow measurement of transient effects. Furthermore, the experimental investigations were performed by means of a force transducer linked to different types of Perspex blocks. Statistical analysis confirmed the theoretical predictions.

Liu (1999) also discussed a two-dimensional analysis of the aforementioned transient flow model. This resulted in a slab stability condition that is based on random vibration.

Jia et al. (2001) presented a numerical model that calculates the uplift forces on loose-bed material due to plane impinging jets. The mechanism of uplift, however, was empirically introduced and calibrated based on Hoffmans‘ modification of equation (1.6). The obtained relation between the surface pressure fluctuations and the fluctuating uplift is in agreement with the findings of Liu et al. (1998). They pointed out the need for further research in order to improve the understanding of the exact physical mechanism of uplift.

4.4. Concluding remarks on extreme pressure difference techniques

The mentioned and discussed studies on concrete slabs and rock blocks deal with net uplift pressures and forces in a steady-state differential manner: where the surface pressure field is well described as a function of space and time, the underpressure field is assumed constant all over the underlying surface and equal to the pressure injected at the entrance. Hence, fully transient flow conditions, such as pressure wave reflections and superpositions, are discarded from the analysis. This is only justified when assuming high wave celerities (1’400 m/s) of the pressure waves inside the joints combined with very low excitation frequencies at the joint entrance (maximum several Hz).

The studies on hydraulic jump impact result in a maximum net uplift pressure of 0.5 times the incoming kinetic energy head. The corresponding studies on jet impingement conduct to safe values for practice of 0.5 to 1 times the incoming kinetic energy head, depending on the relative protrusion of the block and the location of impingement of the jet. The physical assumption of a constant pressure pattern inside the joints results in a net uplift pressure of one time the kinetic energy. This means that the jet’s stagnation pressure is present all under the block, together with a total lack of pressure over the block. This is clearly incompatible with realistic flow conditions. Referring to the study made by Otto (1989), it is not excluded that suction effects at the surface of the slabs or blocks play an important role when performing physical model studies.

5. Summary of evaluation methods: the knowledge cube

Table II-2 presents a summary of the existing evaluation methods for the ultimate scour depth. In accordance with the previous sections, four groups of methods can be distinguished: empirical expressions, semi-empirical expressions, expressions for extreme pool bottom pressures and finally expressions for instantaneous or time-averaged pressure differences over and under rock blocks or concrete slabs (Bollaert & Schleiss, 2001e).

The parameters of these groups are classified into four types: time parameter, hydraulic parameters, aeration parameters and geomechanical parameters. No method actually presents a complete description. Three methods incorporate the three phases (water, air and rock), but without time evolution: the erodibility index method (Annandale, 1995) and two methods based on the momentum equation (Fahlbusch, 1994; Hoffmans, 1998). It is interesting to notice that these three methods belong to the group of semi-empirical expressions. Some empirical formulas also try to combine the three phases, but in a very simplified manner. They consider the rock mass as already broken up. Furthermore, expressions for extreme pool bottom pressures account for hydraulic and aeration characteristics in a quite detailed and straightforward manner, but unfortunately neglect geomechanical aspects. Pressure difference methods provide a good description of hydraulic and geomechanical characteristics, but without valid assumptions regarding the air content. Kirschke (1974) performed a numerical study of water hammer in fissures, but only for constant pressures at the fissure entry and without aeration.

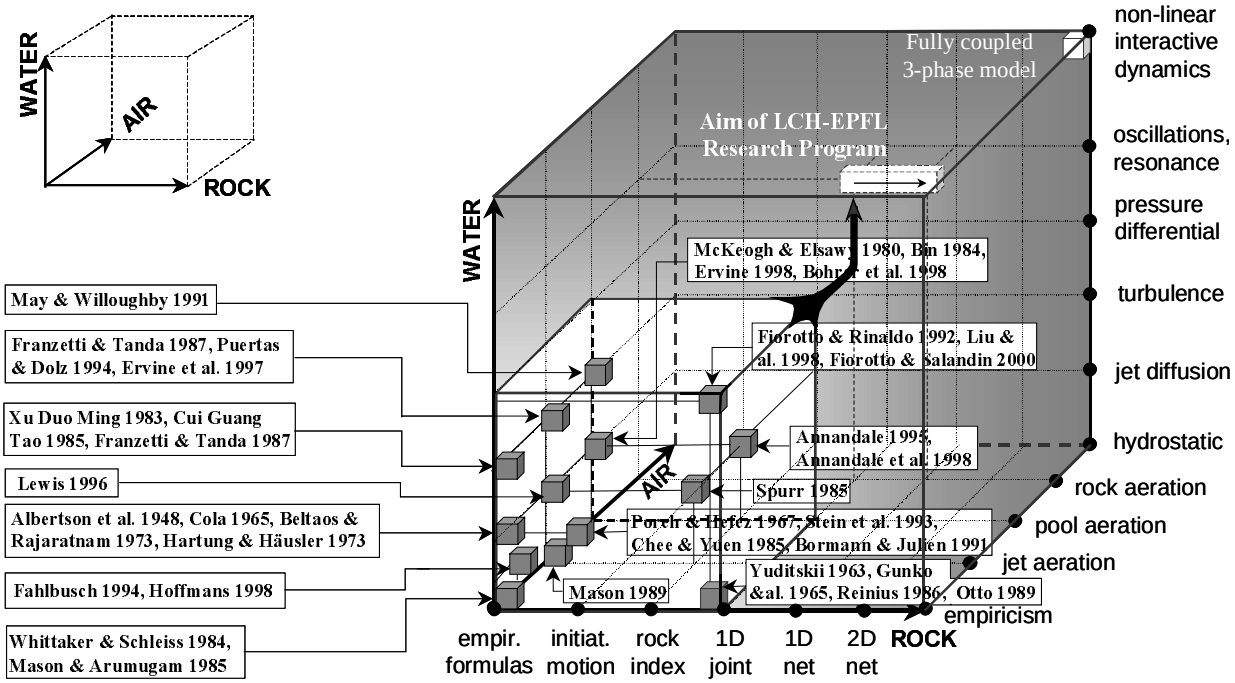

Fig. II-19 Three-dimensional representation of the actual state-of-the-art on scour evaluation methods. The three main axes represent the water, rock and air characteristics (Bollaert & Schleiss, 2001e).

The same information is presented in Fig. II-19. The different methods of representation of the three phases are developed along the three axes of a cubic volume, called the **knowledge cube**. As such, a three-dimensional insight is obtained. The precision and accuracy of the methods grows with increasing value on each of the axes. For the rock axis, the following methods can be distinguished:

simple empirical formulas, initiation of motion theories, rock mass representation by an erodibility index, use of one-dimensional rock joint, use of one-dimensional network of rock joints and finally a more complicated two-dimensional rock joint network. Actual knowledge along this axis is restricted to a one-dimensional rock joint description. Analogously, the axis that summarizes the hydrodynamic methods incorporates empirical methods, two-dimensional jet diffusion theory, turbulence measurements, time-averaged and instantaneous pressure differences, fully transient flow (oscillations…) and finally non-linear flow dynamics that take into account the interaction with the rock mass. Actually, the most valuable developments are situated in the field of instantaneous pressure differences. Finally, the aeration axis shows empirical (mean pressure reduction) coefficients, falling jet aeration, plunge pool aeration and rock joint air content. To the author's knowledge, no method ever considered the latter.

Type	Year	Author(s)	Applicability	Time	Hydraulic characteristics										Geomechanical characteristics										Aeration characteristics			
					hydrostatic							hydrodynamic			gran. soil			jointed rock mass										
				T	q	h	H	g	V_j	θ	RMS	Sxx(f)	trans		d_m	w_s	ρ_s	σ_c,σ_t	RQD	N_j	z	α	ϕ_j	C	β	Tu	L_b
				[-]	[m^2/s]	[m]	[m]	[m/s^2]	[m/s]	[°]	[-]	[m^2]	[-]		[mm]	[m/s]	[kg/m^3]	[N/m^2]	[%]	[-]	[-]	[°]	[°]	[-]	[-]	[%]	[m]
empirical	1932	Schoklitsch	plunging jet	-	■	-	■	-	-	-	-	-	-		■	-	-	-	-	-	-	-	-	-	-	-	-	
	1937	Veronese A	horiz. & plunging jet	-	■	-	■	-	-	-	-	-	-		■	-	-	-	-	-	-	-	-	-	-	-	-	
	1937	Veronese B	as A, but d_m < 0.005m	-	■	-	■	-	-	-	-	-	-		-	-	-	-	-	-	-	-	-	-	-	-	-	
	1939	Jaeger	plunging jet	-	■	■	■	-	-	-	-	-	-		■	-	-	-	-	-	-	-	-	-	-	-	-	
	1953	Doddiah et al.	plunging jet	■	■	-	■	-	-	-	-	-	-		■	■	-	-	-	-	-	-	-	-	-	-	-	
	1957	Hartung	plunging jet	-	■	-	■	■	-	-	-	-	-		■	-	-	-	-	-	-	-	-	-	-	-	-	
	1963	Rubinstein	ski-jump, rock cubes	-	-	■	■	■	■	■	-	-	-		-	-	-	-	-	-	■	-	-	■	-	-	-	
	1966	Damle et al.*	ski-jump	-	■	-	■	-	-	-	-	-	-		-	-	-	-	-	-	-	-	-	-	-	-	-	
	1967	Kotoulas	plunging jet	-	■	-	■	-	-	-	-	-	-		■	-	-	-	-	-	-	-	-	-	-	-	-	
	1969	Chee & Padiyar	flip bucket	-	■	-	■	-	-	-	-	-	-		■	-	-	-	-	-	-	-	-	-	-	-	-	
	1974	Chee & Kung	plunging jet	-	■	-	■	■	-	■	-	-	-		■	-	-	-	-	-	-	-	-	-	-	-	-	
	1973	Martins A	plunging jet, rock cubes	-	■	■	■	-	-	■	-	-	-		-	-	-	-	-	-	■	-	-	-	-	-	-	
	1975	Martins B	ski-jump	-	■	-	■	-	-	-	-	-	-		-	-	-	-	-	-	-	-	-	-	-	-	-	
	1978	Taraimovich	ski-jump	-	-	-	■	-	■	■	-	-	-		-	■	-	-	-	-	-	-	-	-	-	-	-	
	1981	INCYTH	plunging jet	-	■	-	■	-	-	-	-	-	-		-	-	-	-	-	-	-	-	-	-	-	-	-	
	1982	Machado A	plunging jet, rocky bed	-	■	-	■	■	-	-	-	-	-		■	-	-	-	-	-	-	-	-	■	-	-	-	
	1982	Machado B	plunging jet, rocky bed	-	■		■	■	-	-	-	-	-		-	-	-	-	-	-	-	-	-	■	-	-	-	
	1985	Mason & Arumugam*	plunging jet	-	■	■	■	■	-	-	-	-	-		■	-	-	-	-	-	-	-	-	-	-	-	-	
	1989	Mason	plunging jet	-	■	■	■	■	-	-	-	-	-		■	-	-	-	-	-	-	-	-	-	■	-	-	
semi-empirical	1960	Mikhalev	plunging jet	-	■	■	■	■	-	■	-	-	-		■	-	-	-	-	-	-	-	-	-	-	-	-	
	1967	Mirtskhulava et al.*	plunging jet, rocky bed	-	■	■	■	■	■	■	-	-	-		-	■	■	■	-	-	■	-	-	■	-	-	-	
	1967	Poreh & Hefez	circ. submerged imp. jet	-	■	-	■	-	■	-	-	-	-		■	-	■	-	-	-	-	-	-	-	-	-	-	
	1975	Zvorykin	ski-jump	-	-	■	-	-	■	■	-	-	-		-	-	-	-	-	-	-	-	-	-	-	-	-	
	1983	Mih & Kabir	circ. submerged imp. jet	-	-	■	-	■	■	■	-	-	-		■	-	■	-	-	-	-	-	-	-	-	-	-	
	1985	Chee & Yuen	plunging jet	-	-	■	-	■	■	■	-	-	-		■	-	■	-	-	-	-	-	-	-	-	-	-	
	1985	Spurr*	plunging jet	■	■	■	■	■	■	■	-	-	-		■	-	-	■	■	■	■	■	-	-	-	-	-	
	1991	Bormann & Julien*	grade-control, plung. jet	-	■	-	-	■	■	■	-	-	-		■	-	■	-	-	-	-	-	-	-	-	-	-	
	1993	Stein et al.	plunging jet	■	-	-	-	■	■	■	-	-	-		■	-	-	-	-	-	-	-	-	-	-	-	-	
	1994	Fahlbusch	general	-	■	■	-	■	■	■	-	-	-		■	-	-	■	-	-	-	-	-	-	■	-	-	
	1998	Annandale & al.*	general	-	■	■	■	■	■	■	-	-	-		■	-	■	■	■	■	■	■	■	-	■	-	-	
	1998	Hoffmans	general	-	■	■	-	■	■	■	-	-	-		■	-	■	-	-	-	-	-	-	-	■	-	-	
plunge pool pressure fluctuations	1983	Xu Duo Ming	rectang. impinging jet	-	■	■	■	■	■	■	■	■	-		-	-	-	-	-	-	-	-	-	-	-	-	-	
	1985	Cui Guang Tao	rectang. impinging jet	-	■	■	■	■	■	■	■	■	-		-	-	-	-	-	-	-	-	-	-	-	-	-	
	1987	Franzetti & Tanda	circular impinging jet	-	■	■	■	■	■	-	■	-	-		-	-	-	-	-	-	-	-	-	-	-	-	-	
	1991	Armengou	rectang. falling nappe	-	■	■	■	■	■	-	■	■	-		-	-	-	-	-	-	-	-	-	-	-	-	-	
	1991	May & Willoughby	rectangular slot jet	-	■	■	■	■	■	-	■	■	-		-	-	-	-	-	-	-	-	-	-	■	■	■	
	1994	Puertas & Dolz	rectang. falling nappe	-	■	■	■	■	■	-	■	■	-		-	-	-	-	-	-	-	-	-	-	-	-	-	
	1997	Ervine & al.	circular impinging jet	-	■	■	■	■	■	-	■	■	-		-	-	-	-	-	-	-	-	-	-	■	■	■	
pressure difference techniques	1963	Yuditskii	oblique imp. rect. jet	-	■	-	-	■	-	■	-	-	-		-	-	■	-	-	-	■	-	-	-	-	-	-	
	1986	Reinius	parallel flow impact	-	-	■	-	■	■	-	-	-	-		-	-	■	-	-	-	-	■	-	-	-	-	-	
	1989	Otto	oblique imp. rect. jet	-	-	-	-	■	■	■	-	-	-		-	-	■	-	-	-	■	-	■	-	-	-	-	
	1992	Fiorotto & Rinaldo	concrete slab uplift	-	■	■	■	■	■	-	■	-	-		-	-	■	-	-	-	■	-	-	-	-	-	-	
	1998	Liu & al.	rock block uplift	-	■	■	■	■	■	■	■	■	-		-	-	■	-	-	-	■	-	-	-	-	-	-	
	1999	Liu & al.	vibration. slab uplift	-	■	■	■	■	■	■	■	■	-		-	-	■	-	-	-	■	-	-	-	-	-	-	
	2000	Fiorotto & Salandin	anchored slab uplift	-	■	■	■	■	■	-	■	■	-		-	-	■	-	-	-	■	-	-	-	-	-	-	
EPFL Project	2002	2-phase transient jacking/uplift		■	■	■	■	■	■	■	■	■	■		-	-	■	■	■	■	■	■	■	■	■	■	■	

Table II-2 Summary of existing scour evaluation methods, showing the four different groups of parameters: time, hydraulics, geomechanics and aeration (Bollaert & Schleiss, 2001e).

The methods presented at Table II-2 are enclosed by the white cubic volume that is situated inside the main cube in Fig. II-19. This shows the actual limits of scour description and asks for a physically

more refined approach. The ultimate description that could be attained is situated in the upper right corner of the main cube and represents a fully interactive, 3-phase transient model. The present project tries to approach this ultimate state of physical representation. Existing methods consider the jointed rock mass as a sort of “black box”. Something is happening inside the joints, but it is unclear what exactly. This macroscopic approach has to be discarded and a totally new way of thinking should be applied. This physical reassessment of the situation should analyse the jointed rock mass and the water pressures in a **microscopic** manner.

For this, the current project focuses on the following topics: incorporation of air content and of fully transient flow conditions, as a function of the degree of jointing of the rock mass and of the geometrical configuration of the joints.

It is obvious that this microscopic approach generates lots of questions: a detailed and sophisticated approach always asks for a detailed and sophisticated list of characteristics. This means that, parallel to this new way of thinking, further research is needed on every distinct topic. This also implies that still a long way has to be travelled before acquaintance of the final, ultimate state of description of the problem. This is clearly not the aim of the project. The project just wants to point out a new direction and tries to set up some basic improvements pertaining to the actual state-of-the-art.

Lots of parameters that influence the macroturbulent flow in a plunge pool are still partly or completely mystery, mainly due to scaling problems. Examples are the influence of the air content of falling jets on the zone of jet impingement, the effect of the pool bottom geometry on the direction of circulation of the macroturbulent flow and thus on the turbulent fluctuations at the water-rock interface, the time evolution of the plunge pool bottom geometry, etc.

Chapter III. Theoretical framework

1. Introduction

The previous chapter demonstrated that scouring due to high-velocity jet impact is governed by an interaction between three phases: the liquid phase (water jet), the gas phase (air bubbles) and the solid phase (rock mass). In the present chapter, a theoretical background is presented for each of the phases. Moreover, whenever possible, the interaction between the phases is dealt with.

The first section presents a short review of some basic fluid mechanics principles. These principles are relevant to the two flow conditions that are encountered: 1) turbulent shear layer flow in a plunge pool, 2) pressurized flow inside rock joints. Turbulent flow conditions in plunge pools have mostly been studied based on two-dimensional diffusion of a jet impinging on a medium at rest. Emphasis is given here on the pressure fluctuations acting at the underlying water-rock interface. Pressurized flow conditions in rock joints, on the contrary, have rarely been investigated. Hence, no basic theoretical developments exist. Therefore, the theory used herein is based on transient pressurized flow as encountered in hydraulic systems, such as for example pipelines and water-cooling systems.

The second section considers the air that is entrained: 1) in the falling jet, 2) in the plunge pool, 3) inside rock joints. Where the former two points are known rather well, the latter is unusual in the field of dam hydraulics. As for the liquid phase, basic theory is taken from air-water studies on hydraulic systems.

Finally, an accurate description of jointed rock is given. This description is based on parameters that can be found in any textbook on rock mechanics (e.g. Jaeger & Cook, 1979; Goodman, 1980). The resistance of rock against scour can be expressed by appropriate failure criteria. For intact or intermittently jointed rock, these criteria are based on the tensile strength of the rock mass and involve a strength-of-material or a fracture mechanics approach. For completely broken-up rock, failure criteria are based on a dynamic equilibrium of the forces (pressures) acting on a single rock block.

The present chapter aims at providing a basic theoretical framework for a better assessment of the physical processes that govern scour of rock. This theoretical framework is based on existing knowledge and will be used to analyse the experimental results that are described in Chapter V. Furthermore, it defines the new methodology for the ultimate scour depth as outlined in Chapter VII.

2. Theory of fluid dynamics

2.1. Turbulent flow conditions in a plunge pool

2.1.1. Comparison of ideal two-dimensional jet diffusion with jets as encountered in practice

The impact of a water jet into a plunge pool is governed by the diffusion of a jet through a medium at rest. This particular process has been described in many textbooks on jets (e.g. Hinze, 1959; Abramovich, 1963; Rajaratnam, 1976), and is based on a theoretically ideal impact, i.e. on a "free-turbulent" jet case. Free turbulent jets have been of great interest in the past because they are the simplest case of turbulent flow, least dependent on viscosity effects. As a result, their study may be considered as a preliminary stage of turbulent flow assessment. The most known theories of free turbulence are:

1) Prandtl's first mixing-length theory (1925), based on momentum transfer (Tollmien, 1926),
2) Taylor's vorticity theory (1932), based on vorticity transfer,
3) Prandtl's second mixing-length theory (1942), based on a Newtonian law of viscous friction,
4) Reichardt's inductive theory (1941), based on momentum transfer.

For ideal jet impact conditions, the exchange of the jet's momentum with the surrounding pool creates a progressively growing (or mixing) shear layer. This shear layer consists of a mixture of particles of the surrounding medium, carried along with the jet, and of particles of the jet itself, that are slowed down. Such a momentum exchange is characterized by linearly diverging boundaries. This causes an increase of the jet's total cross section and a convergence of the non-viscous core region with a constant velocity profile (Fig.III-1). The fundamental properties of such an ideal jet diffusion can be summarized as follows:

1) hydrostatic pressure distribution throughout the flow depth,
2) constant velocity profile inside the core of the jet,
3) constant longitudinal non-dimensional velocity profiles,
4) negligible transverse velocity profiles.

Two main regions are distinguished: the **core jet** region (or jet development region) and the **developed jet** region. In the following, emphasis is given on the aspects of jet impact that are relevant to engineering practice.

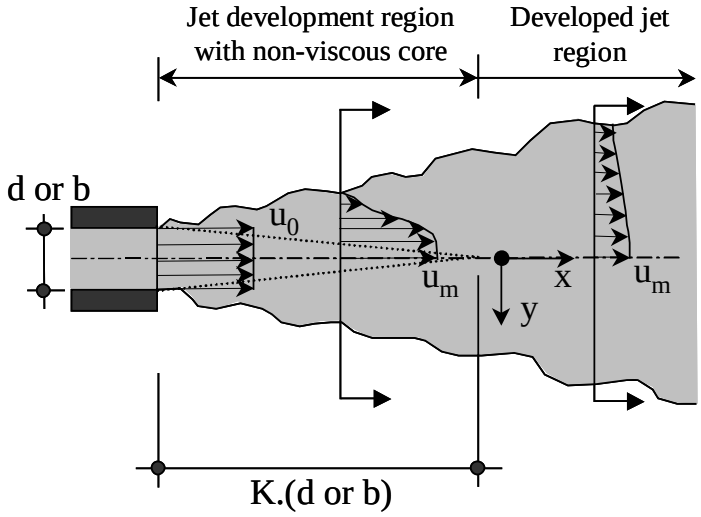

Fig. III-1 Free turbulence jet issuance, showing different jet regions, longitudinal velocity profiles and the extension of the non-viscous core of the jet = K· (d or b)

Jets as observed in practical engineering can be quite different from the abovementioned ideal flow conditions. A first difference is the high **air entrainment** of real jets. At impact into the pool, a large amount of air bubbles enter the diffusing mixing layer. This modifies the theoretical velocity and pressure profiles. The difference between impinging (= aerated) and submerged (= non-aerated) jets is clearly outlined when considering the length of the core of the jet. As presented at Table II-1, impinging jets have core lengths of typically 4 to 6 times the jet diameter or jet width at impact in the pool. Submerged jets, however, attain values up to 8-9. Their core region is thus more established.

A second influence is the presence of a **downstream solid boundary**. The boundary deflects the flow field laterally and, as a result, significant pressure fluctuations build up at the interface. Beltaos & Rajaratnam (1973, 1974) performed an extensive experimental and analytical research of plane and circular, oblique and vertical jets that impinge on a flat and smooth boundary. As already pointed out in Chapter II, they recognized three distinct flow regions: 1) the free jet region, where the flow characteristics approach that of a free turbulent jet, 2) the impingement region, where the jet undergoes a considerable deflection and a change in velocity and pressure, due to the presence of the solid boundary, and 3) the wall jet region, where the jet becomes parallel to the solid boundary. A general conclusion from these studies on time-averaged jet characteristics is that the most severe hydrodynamic action of the jet on the solid boundary occurs in the impingement region, where both the wall shear stress and the pressure gradients are very important. Therefore, in the following, only the impingement region will be considered.

Finally, the **low-frequency turbulence** of a falling jet is of significance to the flow conditions in the plunge pool. These turbulences are mainly caused by the jet conditions at issuance from the dam. During the fall of the jet, they can be further accentuated. As such, upon impact into the plunge pool, they can significantly affect the turbulent pressure fluctuations at the pool bottom. This aspect is dealt with in Chapter VII.

2.1.2. Turbulent flow conditions

The theory of two-dimensional jet diffusion through a medium at rest defines the time-averaged flow structure in a plunge pool. It distinguishes between the following elements: the jet core, the jet turbulent shear layer, the surrounding impingement region, the wall jet region and finally the outer region that is subjected to macroturbulent eddy recirculation. Although the time-averaged flow structure is essential, exact quantification of the hydrodynamic action on the water-rock interface requires assessment of the instantaneous turbulent pressure fluctuations. Catastrophic failure of concrete slabs of stilling basins by dynamic uplift demonstrated the need for a non-stationary approach and turbulent fluctuations have been investigated and quantified both experimentally and theoretically. These studies provided considerable insight into the damage capabilities of dynamic pressures and resulted in similar studies at plunge pool bottoms downstream of high head dams (Chapter II, § 3.1).

Turbulence is described here in a very basic manner. It just focuses on an understanding of the nature and extent of turbulent pressure fluctuations at the water-rock interface. For a deeper insight into these aspects, the reader is referred to classical textbooks (e.g. Hinze, 1959; Rotta, 1972; Tennekes & Lumley, 1973; Reynolds, 1974).

The dynamic action of a jet impinging in a pool generates a highly turbulent shear layer flow. This flow can be described as a superposition of circular motions of different sizes. The largest possible motions are of a size equal to the lateral extent of the shear layer. These large-scale circulations govern the exchange of energy between the jet and the pool. Following Taylor's theory, they transmit their turbulent energy to smaller motions. This transfer goes on, down to the smallest possible (viscous) scales, where the energy finally gets dissipated mainly by heat. It is much like a cascade of energy from energy-extracting scales up to energy dissipating scales, with a range of intermediate scales. These motions that comprise turbulence are frequently referred to as **eddies** of various sizes. Eddies represent swirling motions and can be mathematically described as a superposition of Fourier components. As such, the spectral content of a pressure signal defines the energy of each relevant eddy for a whole range of frequencies of interest. Power spectral curves of homogeneous and isotropic free turbulence distinguish three main zones of eddies:

1) energy extracting zone, containing large-scale eddies at low frequencies,
2) viscous dissipation range, containing the smallest eddies, that transform energy into heat,
3) inertial subrange, representing the intermediate-scaled eddies.

Kolmogoroff (1941) stated that turbulent energy dissipates as a power function of the frequency of the eddies. As such, the spectral content of homogeneous and isotropic free turbulence attains the viscous dissipation range at a slope decay of –5/3. This, however, only holds when the size of the turbulent structures (eddies) is significantly different from the size of the governing flow structures. For very small eddies (high frequencies), no vorticity interaction with the main flow occurs. In a non-dimensional (Strouhal) domain, the Strouhal numbers ($S_h = f \cdot Y/V_j$) are then generally larger than 1.

On the other hand, the intermediate and large-scale eddies can be of the same size as the flow structures and, thus, their vorticity can interact. Hence, they exhibit a milder slope decay of about –1. This value has also been found by Kraichnan (1974, 1975) for non-isotropic, two-dimensional turbulent shear flow. The corresponding Strouhal numbers are generally less than or equal to 1. Experimental evidence of the impact of developed jets shows steeper slope decays of –7/3 to –10/3 at high frequencies (Bearman, 1972; Huot et al., 1986). This is in agreement with the author's spectral measurements (Figs. III-2c & d and Chapter V).

Furthermore, the energy content of the smallest scales (at high frequencies) is influenced by the Reynolds number of the flow. Therefore, it is very difficult to correctly simulate these eddies in a laboratory scale model. Often, the energy decays faster, and thus the slope decays steeper, when one measures on small-scale models. This is typically due to the use of low velocities. For these low velocities, the turbulence that generates vortices is much less significant than in prototype models. Hence, the frequency range with a –1 slope decay is quasi inexistent and the spectrum decays almost immediately at a –5/3 slope towards the viscous dissipation range (Bollaert, 2001).

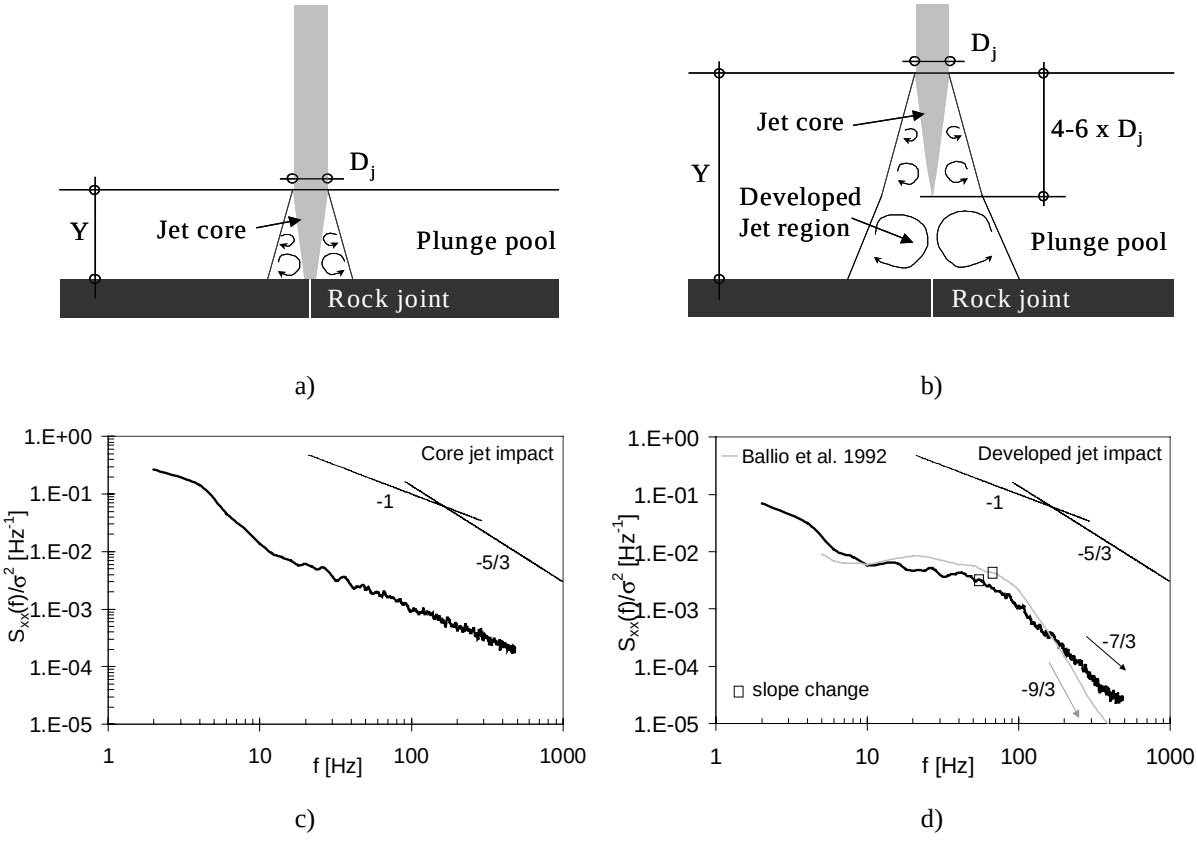

Fig. III-2 Turbulent jet impact conditions: a) core jet impact (Y/D_j < 4-6), b) developed jet impact (Y/D_j > 4-6), c) non-dimensional power spectral content $S_{xx}(f)$ for core jet impact, d) non-dimensional power spectral content $S_{xx}(f)$ for developed jet impact. Comparison with data from Ballio et al. (1992).

The only way to correctly account for the energy at high frequencies is to use near-prototype or prototype velocities. These will allow a correct vorticity of the main flow and thus of the turbulence production. The geometrical similarity of the ratio of plunge pool depth to jet diameter at impact Y/D_j generates self-preserving velocity profiles as they can be encountered in practice. In other words, throughout the whole plunge pool depth, this geometrical similarity, together with the use of prototype velocities, guarantees an appropriate vorticity of the main flow and of the turbulence. Prototype-scaled geometries are not necessary if the large-scale energy-extracting motions are of secondary importance. This is the case in the present study, assuming that these motions are not able to stimulate an underlying rock joint to resonance.

The degree of development of turbulent eddies depends on the trajectory length of the jet in the pool. For very short jets, a core region still exists and the surrounding shear layer is not fully developed, i.e. its turbulence characteristics are not fully developed and eddies are relatively small. Fully developed turbulent flow conditions are only obtained immediately after the disappearance of the core of the jet. This roughly corresponds to a pool depth of about 6 to 10 times the diameter of the jet at impact. Further increase of the jet trajectory length increases the size of the largest eddies but causes a progressive decrease of turbulent energy by diffusion.

As the turbulent eddies are directly responsible for the pressure fluctuations at the pool bottom, the ratio of the depth of the pool to the jet diameter at impact Y/D_j is of crucial importance for practice. Dynamic pressures can be the result of direct core jet impact, appearing for small plunge pool depths, or indirectly of the shear layer flow, appearing for ratios of pool depth to jet thickness (Y/D_j) higher than 4 to 6 (for impinging jets). The resulting pressure fluctuations at the water-rock interface are completely different. As stated before, terminology therefore distinguishes between **core jet impact** (Fig. III-2a) and **developed jet impact** (Fig. III-2b) (Rajaratnam, 1976).

As can be seen in Figs. III-2a & 2c, core jet impact combines a small and not fully developed shear layer with direct jet impact under the jet's centreline. The corresponding pressures have a high mean value with rather small fluctuations around this mean value (low RMS = root-mean-square value). The developing eddies are of small size and thus result in the appearance of high frequencies in the spectral content of the pressure signal.

On the other hand, developed jet impact has no core anymore and generates a large shear layer zone that is characterized by eddies of both small and intermediate size. The mean dynamic pressure decreases, while the pressure fluctuations (RMS value) increase. The spectral content of the pressure fluctuations concentrates its energy towards the intermediate-scaled eddies (Figs. III-2b & 2d). In other words, as explained later on in § 2.2.2, the excitation capacities of the jet are completely different for core respectively developed jet impact. This has a great influence on the pressure fluctuations in the underlying rock joint.

The excitation capacity of an impacting jet is directly expressed by its spectral content. This aspect has mainly been investigated in the field of vertical take-off of aircrafts and rockets. Fig. II-14 of Chapter II gave an overview of typical spectral contents of jets impacting on flat plates and of macroturbulent flow conditions as encountered in hydraulic jumps. It was concluded that the spectral range of a jet extends much further towards high frequencies than those of macroturbulent flow conditions.

2.2. Pressure waves inside rock joints

A high-velocity jet impacting into a plunge pool generates turbulent pressure fluctuations at the water-rock interface (§ 2.1). This interface is assumed to contain certain discontinuities. Examples of discontinuities are tectonic faults, cracks, joints, fissures, etc. For a detailed description of all types of discontinuities, the reader is referred to textbooks on the subject (e.g. Jaeger & Cook, 1979; Goodman, 1980). Globally, they all have one aspect in common, i.e. they represent very thin and stretched bounded media in an otherwise relatively homogeneous and isotropic structure. As most of the discontinuities of relevance for the present study are joints, this term will be used throughout the text.

Water can enter into the joints. The pressure transfer from the pool bottom into a joint is governed by a flow change from turbulent shear-layer conditions into **pressurized flow in a thin and bounded medium** (Bollaert, 2001). Therefore, pressure fluctuations and boundary conditions inside a rock joint result in an important transformation of velocity into pressure waves and, thus, transient phenomena such as water hammer and resonance can occur. Despite the scale difference between rock joints and hydraulic pipelines, it is assumed that the flow characteristics are similar. As such, the impingement of a high-velocity water jet onto a rock joint contains all the characteristic elements of a **resonator system**. The turbulent pressure fluctuations of the impacting jet represent the necessary excitation and the bounded rock joint plays the role of resonance chamber.

Many papers and textbooks have been written about the phenomena of water hammer and resonance and the reader is referred to them for basic theory. Typical engineering fields are fluid transmission lines (pipelines, cooling systems, etc.), linear acoustics, biomedical networks (arteries) and electrical transmission lines. This section starts with an overview of the physical aspects of transient flow theory to explain those extensions of the water hammer theory that are applicable to the specific case of pressure wave propagation in rock joints.

Furthermore, when also accounting for a possible transfer of air bubbles from the plunge pool into the rock joints, the flow mixture inside the joints becomes two-phase. The compressibility of the air results in possible **non-linear** transient flow. This involves dynamic and complex effects such as shock waves, frequency dependent friction, heat transfer, etc. The present chapter outlines both one-phase (linear) and two-phase (non-linear) transient flow conditions inside simply defined boundary systems. A more detailed treatment of the non-linear two-phase transient flow equations is established in Chapter VI on numerical modeling of transient pressures in rock joints.

2.2.1. Terminology and physical concept of water hammer

A description of commonly used terms can be found for example in Chaudry (1979) or Wylie & Streeter (1978). The most pertinent ones are defined in Table III-1. The term “water hammer” strictly refers to the physical process of pressure fluctuations that are induced by a sudden change in flow conditions. Such a change in flow conditions can be due to a sudden valve closure in a single pipeline system. The water hammer phenomenon will appear and cause a certain period of intermediate flow conditions, called transient flow (i.e. the conditions are changing from one steady-state to another). Damping effects will finally install some new steady-state flow condition.

However, if the valve opens and closes at a regular time interval, the change in flow conditions will be of time-infinite and regular character, giving rise to steady-oscillatory flow. If this happens such that the amplitude of oscillation grows with time, resonance conditions will occur.

In general, whenever a periodic excitation is provided to some well-defined bounded system, oscillatory flow will happen. Whether this oscillatory flow will be damped out (= free vibration or transient flow), stay constant (= steady-oscillatory flow) or grow with time (= resonance condition), strongly depends on the energy (friction) losses in the system per cycle and on the natural periods of the system.

Steady and unsteady flow	for steady flow, the flow conditions (such as velocity, pressure and discharge) do not change with time. Unsteady flow thus implies a certain change with time. However, this change has to be referred to temporal mean values, because otherwise any turbulent flow will be strictly unsteady.
Transient flow	intermediate-stage flow for which flow conditions change from one steady-state to the other.
Steady-oscillatory flow	transient flow with flow changes that are repeated continuously after some defined time interval, the period T (in seconds). The frequency of oscillations f is equal to 1/T or 2π/T and expressed in cycles/s respectively rad/s.
Free vibration flow	attenuating oscillatory flow at one of the natural periods of the involved system.
Water hammer	pressure fluctuations caused by a sudden flow change, depending upon the fluid involved. The most frequently used terminology is hydraulic transient.
Resonance flow	Oscillatory flow phenomenon for which the amplitude of the oscillations continuously grows with time until failure or until a steady-oscillatory flow of unusually large magnitude.

Table III-1 Frequently used terminology in the field of hydraulic transients

The physical background of the water hammer phenomenon can be explained by considering the control volume of fluid in Fig. III-3. At initial conditions, fluid is flowing at a velocity V_0 and the corresponding pressure is p_0. Whenever an external source implies a change of flow conditions at one end of the control volume, a certain amount of momentum $\Delta M = \rho \cdot A \cdot \Delta V^2$ is created, expressed by a sudden change in velocity from V_0 to $V_0 + \Delta V$.

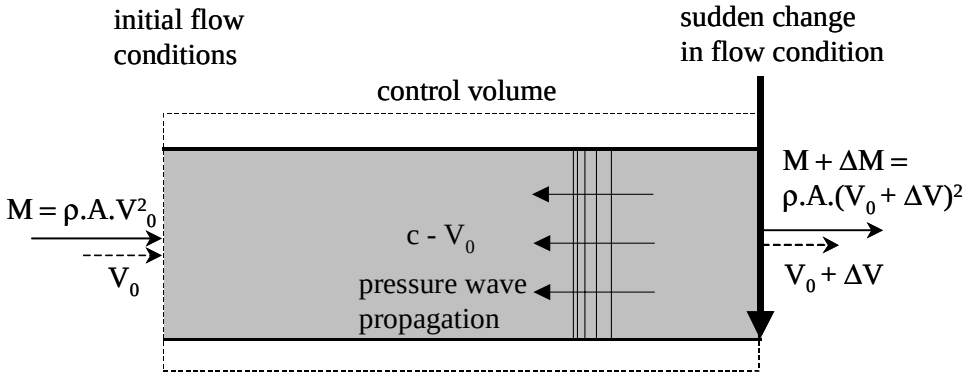

Fig. III-3 Control volume for derivation of the water hammer equation. A sudden change in flow condition is applied at the downstream end by sudden closure.

Due to the elastic character of the liquid, this change in velocity is immediately translated in a pressure change from p_0 to $p_0 + \Delta p$, and a density change from ρ_0 to $\rho_0 + \Delta\rho$. By considering the fluid as an ensemble of associated molecules, it is obvious that these sudden momentum changes will be transferred throughout the control volume, from molecule to molecule. This creates a pressure wave of magnitude Δp and speed c. This momentum transfer speed is also called the water hammer wave

velocity or **wave celerity c**. Application of the momentum equation in the x-direction builds up the basic equation of water hammer, at first introduced by Youkowski (1898) and Allievi (1903):

$$\sum \Delta H = \pm \frac{c}{g} \cdot \sum \Delta V \tag{3.1}$$

in which H stands for the pressure head [m]. This equation is valid in the absence of boundary reflections. It expresses how pressure and velocity changes are related one to the other. The negative sign is valid whenever pressure increases as a result of velocity reduction, appearing for example for a valve closure at the downstream end of a pipeline. For velocity changes at the upstream end, resulting in a downstream travelling pressure wave, the positive sign is in use. In practice, the relation between pressure and velocity strongly depends on the compressibility properties of the fluid and of the flow boundaries. In the following, appropriate relations are developed for one-phase (pure water) respectively two-phase mixtures (bubbly liquids), taking into account possible boundary effects.

2.2.2. One-phase wave celerity

Solution of the basic water hammer equation requires knowledge of the pressure wave celerity c. For a single-phase, compressible and isentropic fluid in a hydraulic system with perfectly rigid boundaries, a simple expression is obtained by application of the continuity equation to the control volume of Fig. III-3:

$$c = \sqrt{\frac{K}{\rho_0}} \tag{3.2}$$

The above expression is valid for any type of wave or medium that is responsible for the wave motion and can be given by the square-root of a simple fraction. The numerator of the fraction is always an elastic coefficient that defines the elasticity of the medium that is responsible for the wave motion. Examples are the bulk modulus of elasticity for longitudinal waves in liquids, or the Young's modulus for longitudinal waves in a rigid rod. The denominator of the fraction is always a term denoting the mass, linear or total density (i.e. mass per unit length, area or volume) of the medium transmitting the wave. For fluids, K stands for the bulk modulus of elasticity of the fluid and is given by the following formula:

$$K = \frac{\Delta p}{\Delta \rho / \rho_0} = -\frac{\Delta p}{\Delta V / V_0} \tag{3.3}$$

This modulus depends on the temperature, pressure and quantity of undissolved gases of the liquid. The latter constitutes by far the most important parameter and is discussed in § 6.1.8.

The influence of temperature and pressure depends on the structural composition of the water. Several models of water can be found in literature, as for example the one by Hall, that considers water to be a mix of an open (tridymite = icelike) structure and a more closely packed quartzlike structure. Another model is given by Eucken, which assumes the structure of water to contain a distribution of polymeric units, namely monomer, dimer, tetramer, and octamer, the last of which has the open tridymite structure.

This competition between structural redistribution and thermal expansion explains such exceptional properties of water such as the density maximum at 4° C and the speed of sound maximum at 74° C. As temperature or pressure increase, the closely packed units gain at the expense of the vanishing tridymite open structure. An expression for the sound speed in saturated water versus temperature, for atmospheric pressure is presented in Fig. III-4 and shows a celerity of 1446 m/s at 10° C and a maximum celerity of about 1550 m/s at 74° C.

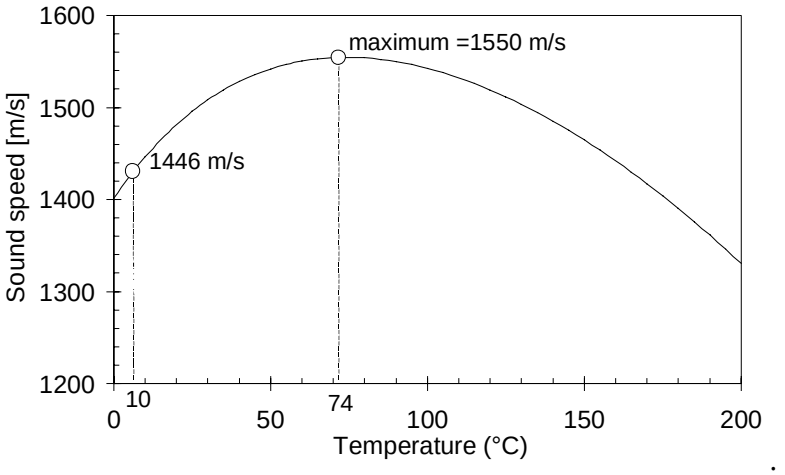

Fig. III-4 Speed of sound in saturated water versus temperature. The maximum value is obtained at 74° C. A practical value is 1'450 m/s.

In addition to the bulk modulus of elasticity K of the fluid, pressure wave celerities of hydraulic systems depend furthermore on the elastic properties of the boundaries. For hydraulic pipelines or galleries, relevant properties are the conduit size, wall thickness, wall material, type of wall support and longitudinal freedom of movement of the boundary. Halliwell (1963) presented the following expression for the wave celerity, accounting for the elastic properties of the boundary by introducing into the general equation the Young's modulus of elasticity E of the boundary material, as well as a non-dimensional parameter ψ:

$$c = \sqrt{\frac{K}{\rho \cdot [1 + (K/E) \cdot \psi]}} \tag{3.4}$$

in which ψ is a non-dimensional parameter depending on the elastic properties of the boundaries and E is the Young's modulus of elasticity of the conduit walls. Some values of modules of elasticity E, bulk modules K, Poisson's ratio ν and finally density ρ for commonly used materials are listed at Table III-2 (Chaudry, 1979):

Material	E [Gpa]	μ [-]	Liquid	K [Gpa]	ρ [kg/m^3]	c [m/s]	Temp [°C]
Granite	50	0.28	Sea Water	2.27	1025	1488	15
Limestone	55	0.21	Fresh water	2.19	999	1481	20
Quartzite	24-45	0.28	Oil	1.5	900	1291	15
Mild steel	200-212	0.27	Ethyl alcohol	1.32	790	1293	0
Concrete	14-30	0.1-0.15	Mercury	26.2	13570	1390	20

Table III-2 E and μ values for commonly used materials. Values of K, ρ and c for several liquids.

The left part of Table III-2 shows that steel is about 4 times less elastic as good quality rock (granite). Concrete is about twice as elastic as granite, and represents an elasticity close to that of quartzite. Modules of elasticity can be relevant when performing hydraulic model studies making use of other materials than rock, such as steel or concrete. The right hand side of Table III-2 reveals a theoretical wave celerity (equation (3.4)) of almost 1'500 m/s for water, whereas the other values are slightly beyond this value. These values are valid for the temperature indicated and at atmospheric pressure.

The non-dimensional coefficient ψ depends on the following parameters: the external conduit radius R_o, the internal conduit radius R_i, the conduit diameter D, the conduit wall thickness e, the Poisson's ratio ν, and the modulus of rigidity of the surrounding rock G. Typical values can be found in Chaudry (1979). Moreover, several expressions can be found in literature for non-circular conduits, such as Jenkner (1971) for thin-walled rectangular conduits, based on the steady-state bending theory, Thorley & Guymer (1976) for thick-walled squared conduits, making use of the shear force influence on the bending deflection, and Thorley & Twyman (1977) for thin–walled hexagonal conduits. Regarding equation (3.4), it is obvious that $\psi = 0$ for rigid walls. The Poisson's ratio ν can have considerable influence for both thick- and thin-walled elastic conditions. Interesting also is the case of $\psi = 1$ for unlined rock tunnels.

As a summary, the above parameters can significantly influence the celerity of pressure waves, provided that the wall boundaries are thin when compared to the lateral extent of the considered flow. For rock joints, very small flow widths ($O(10^{-3}$ m)) and very thick rock boundaries ($O(10^{0}$ m)) have to be accounted for. Furthermore, longitudinal and transversal displacement of the rock mass is strongly inhibited. Hence, the elastic properties of the flow boundaries can be neglected.

2.2.3. Pressure wave propagation in a simple hydraulic system

Pressure wave propagation is highly depending on up-and downstream boundaries that can partially or totally absorb or reflect the incoming waves. The approach adopted here is based on the simplest theoretical cases, i.e. ideally open or closed-end boundaries. This is justified because these cases have a great similarity with open or closed-end rock joints as encountered in practice. A theoretically more detailed description of boundary reflections of pressure waves, based on impedances and reflection factors, is given in § 2.2.6.

A well-known example of pressure wave propagation in a simple hydraulic system is sudden valve closure at the downstream end of a pipeline. The pipeline has a total length L and is connected to an upstream reservoir of constant level. Wave reflections at the boundaries and continuous exchange between kinetic and elastic energy result in the well-known steady-oscillatory (when neglecting any friction losses) or free vibration (with friction losses) flow conditions. Resonance conditions are impossible, because no (repeated) periodic energy input exists. For this, periodic valve open and closure is needed.

In the following, a frictionless system is considered. Frictional effects will be discussed later. A similarity between hydraulic systems and rock joints is obtained by replacing the pipeline by a one-dimensional rock joint of length L and width e. The energetic excitation, generated in a hydraulic system by the constant head reservoir and the closing valve, is provided here by an impacting jet. The wall boundaries of the pipeline are replaced by the surrounding rock mass.

Although the energy injection into a rock joint is different, the continuous exchange between kinetic and elastic energy is similar. Unlike single valve closure, jet impact onto a rock joint exhibits the characteristic elements of a resonator system: the impacting jet provides the periodic excitation source and the rock joint plays the role of resonance chamber. As such, the major difference between the rock joint and the pipeline model is the periodic nature of the excitation in the former case. Valve closure generates a single input in the hydraulic system, followed by steady-state or free vibration flow. Jet impact provides a continuous periodic excitation, defined by its spectral content. This can cause serious resonance effects whenever some part of the spectral content of the impacting jet is situated near the fundamental or higher-order natural frequencies of the joint. It is quite similar to closing and opening the valve at a time interval close or equal to the natural frequency of the pipeline. This injects energy into the pipeline during every cycle and, thus, builds up resonance conditions.

The way in which oscillatory or resonance conditions can build up inside a rock joint is presented in Fig. III-5. An intermittently jointed rock, defined by joints with an open boundary at the water-rock interface and a closed boundary at the joint end, is subjected to a sudden pressure change ΔH. This pressure change can be generated by an impacting jet and is supposed to hold for a long enough period of time to not disturb the process. The length of the rock joint is L. The sudden pressure change at the

rock joint entrance generates a pressure wave inside the joint that propagates at a certain wave propagation speed c.

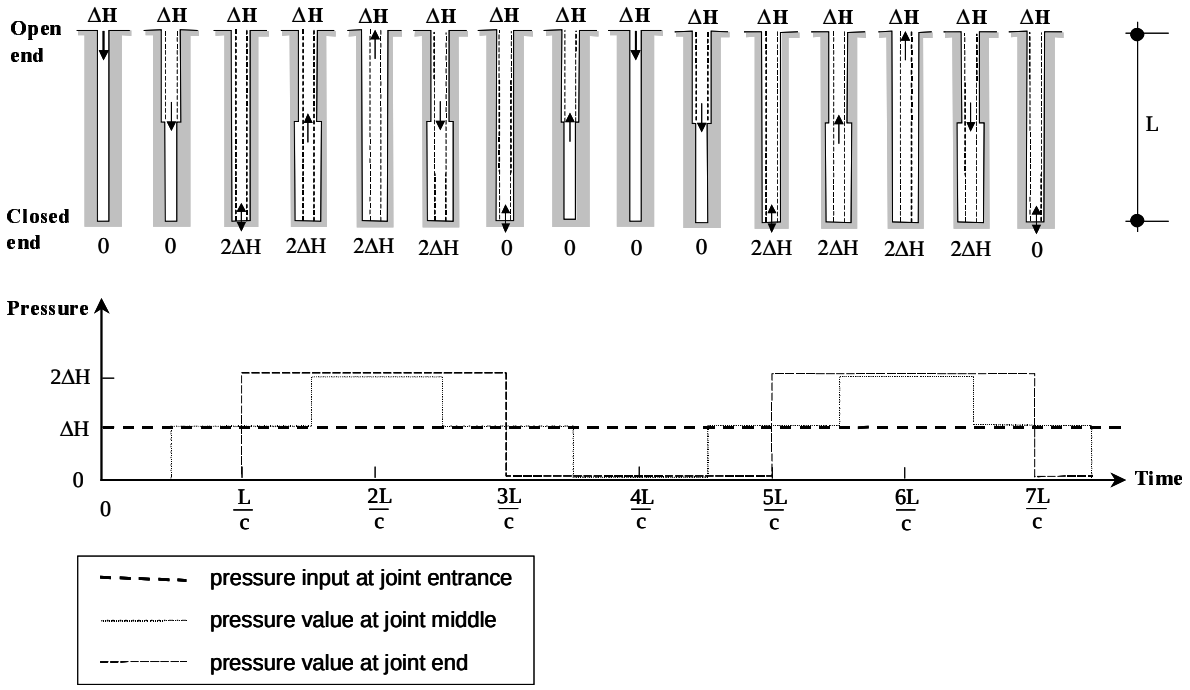

Fig. III-5 Influence of a constant excitation with amplitude ΔH on a hydraulic system with one open and one closed-end boundary. The pressure signal as a function of time is presented at the entrance (= excitation), at the middle and at the end of the rock joint. Standing waves are obtained.

Fig. III-5 visualizes the wave reflections at the boundaries. The pressure signal at the joint entrance is represented by a thick continuous line. The corresponding pressure signal at the downstream end of the joint is visualized by a dashed line, while the pressure signal in the middle of the joint corresponds to the dotted line. The incoming wave with amplitude ΔH is reflected (and doubled in amplitude) at the downstream (closed-) end of the joint. This instability then propagates upstream and creates an instantaneous pressure difference at the upstream boundary, where a pressure of ΔH still holds. This boundary is open and thus fluid starts to flow out of the joint. This creates a negative reflection, i.e. a wave with the same amplitude as the incoming wave, but with opposite sign, that travels downstream. The outwards oriented flow cannot be maintained at the closed-end of the joint (where the flow velocity is zero) and thus a negative wave propagates towards the upstream boundary. As soon as this wave reaches the upstream end, instability again occurs. This finally generates a positive wave towards the closed-end, re-installing the initial incoming pressure wave with amplitude ΔH. The theoretical period of these pressure wave reflections and propagations is equal to $1/f = T = 4L/c$ (f = frequency and T = cycle period). This characteristic is of crucial importance when considering a periodic pressure change at the joint entrance, such as for impacting jets. As outlined in § 2.1.2, turbulent flow conditions generate periodic pressure pulses at the water-rock interface. The period of these pulses is governed by the spectral content of the impacting jet. The jet generates a certain range of turbulent eddies, going from large-scale, energy containing eddies towards very small, viscous eddies. Some of these eddies, and thus some of the corresponding pressure pulses, can have the same period as the rock joint. Such a case is visualized in Fig. III-6. At each cycle $T = 4L/c$, additional energy is injected into the system and the pressure in the joint continuously increases. When this periodical energy injection is higher than the periodical energy dissipation inside the joint, catastrophic resonance conditions will occur. Although largely simplified, it shows the influence of a periodic

excitation on a well-defined boundary system. Each hydraulic system with well-defined boundaries is able to generate standing waves or resonance conditions.

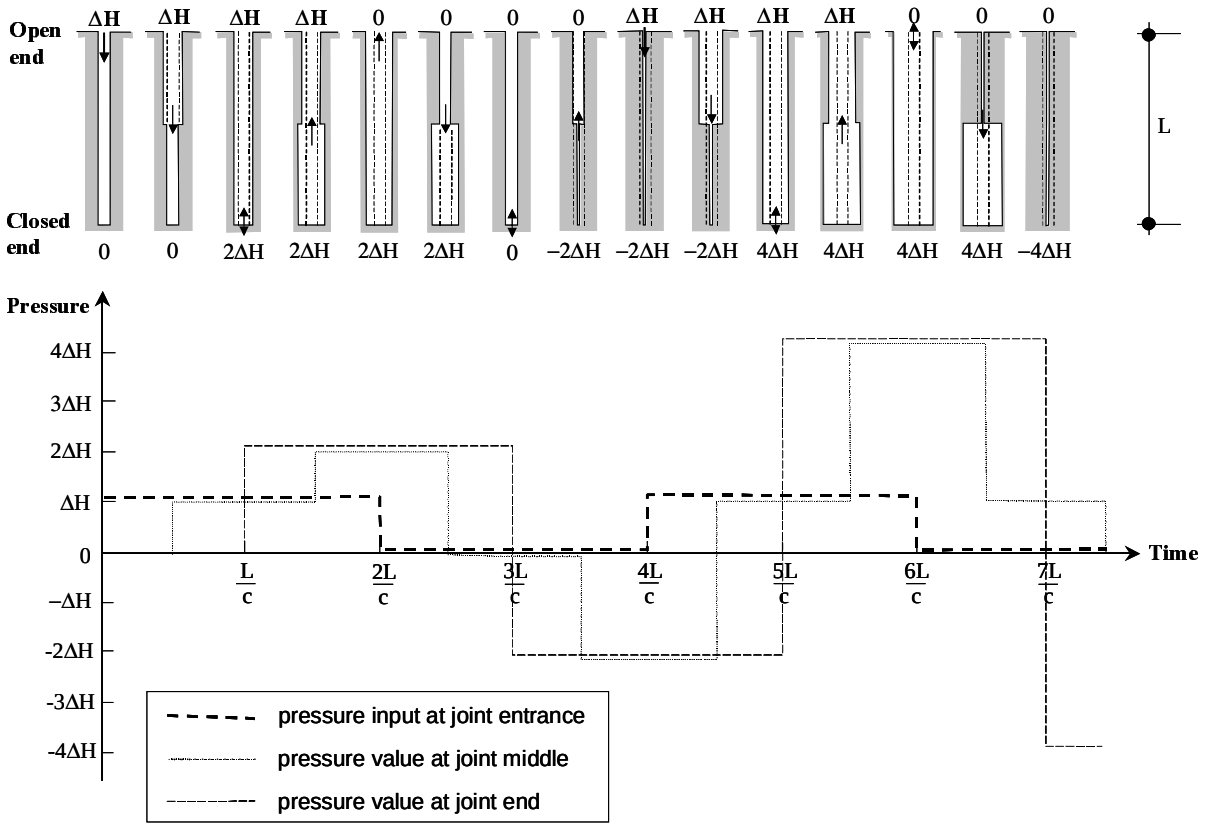

Fig. III-6 Influence of a periodic excitation with amplitude ΔH on a hydraulic system with open and closed-end boundaries. The pressure signal as a function of time is presented at the entrance (= excitation), at the middle and at the end of the rock joint. Resonance conditions build up.

These conditions occur at the **theoretical natural frequencies** or **eigenfrequencies** of the system in question. For rock joints, two main boundary systems can be distinguished:

- the open-closed boundary system (or intermittently jointed rock). This system is relevant to rock masses that are not fully broken-up. It is called the **λ/4 – resonator** and exhibits resonance frequencies at (1+2n)·(c/4L), for n = 0, 1, 2, …
- the open-open boundary system (or completely jointed rock). This system is for a completed joint pattern that forms distinct rock blocks. It is called the **λ/2 – resonator** and exhibits resonance frequencies at (n)·(c/4L), for n = 1, 2, 3…

whereas λ stands for the wavelength (=c/f). This is presented in Fig. III-7. The theoretical natural frequencies and corresponding mode shapes for these two systems correspond to theoretically perfect boundary conditions. This means that wave reflections at the boundaries happen without energy loss (perfectly weak or rigid terminations). Although radiation and other energy losses are always present in real applications, this theoretical approach is representative and justifiable when a huge difference in characteristic impedance between the fluid medium (air-water) and the wall material (rock) exists, and when no partial wave reflections due to geometrical changes occur. The influence of the characteristic impedance of the medium and of geometrical effects is discussed in § 2.2.6.

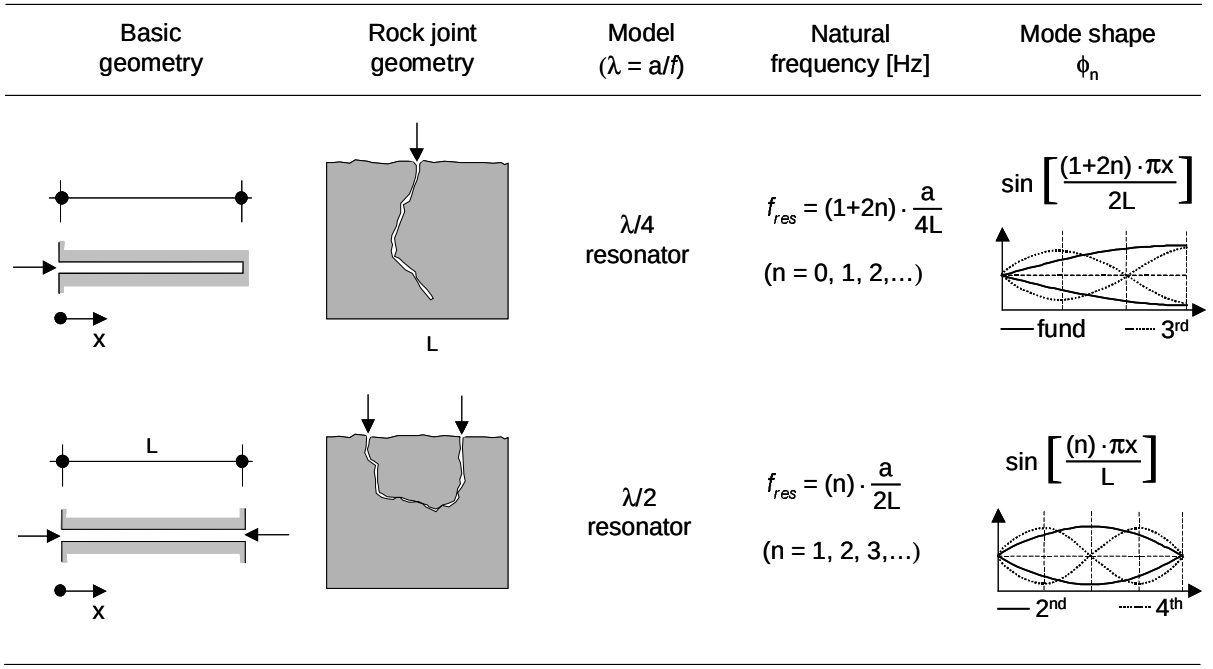

Fig. III-7 Two basic joint configurations with well-defined boundaries. The terminations are considered to be perfectly weak (open boundary) or perfectly rigid (closed boundary).

Due to the compressibility of the flow mixture inside the joint, an infinite number of modes of oscillation or degrees of freedom exist in the system, just like the vibrations of a mechanical system with an infinite number of masses and springs. The first natural mode of vibration is called the **fundamental** or **first harmonic**; the others are called **higher harmonics**. An open boundary corresponds to a pressure node; a closed boundary stands for an antinode. For the open-closed system, there is a pressure node during even harmonics (2^{nd}, 4^{th}, …) and an antinode during odd harmonics (1^{st}, 3^{rd}, …). For the open-open system, two pressure nodes always exist. The exact location of nodes and antinodes depends upon the harmonic at which the system is oscillating.

2.2.4. Linear numerical model for one-dimensional transient flow in rock joints

The periodic excitation of amplitude ΔH, used in the preceding paragraph, demonstrates the possibility of creating resonance conditions inside a bounded medium such as a rock joint. The excitation of an impacting jet physically corresponds to a series of turbulent eddies of different sizes. The mathematical homologue is described as the spectral content of the turbulent fluctuations at the water-rock interface, i.e. the sum of a range of sinusoidal pressure fluctuations. Each sinusoid represents an eddy of a certain size and thus of a certain frequency.

Therefore, the first step towards modelling of an impacting jet should be to determine the influence of a sinusoid of a certain frequency, or of just one eddy. This can be performed by means of a linear numerical model. The aim is to point out the relevance of transient flow when applied to rock joint pressure waves. Appropriate numerical modelling, accounting for the exact spectral content of the jet as well as for non-linear flow effects (free air presence, shock waves), is dealt with in Chapter VI.

A first order (linear) approach for transient flow in rock joints assumes one-phase, isentropic, one-dimensional and uniform flow conditions. The fluid density is constant and the fluid and its boundaries react in a linear elastic manner, i.e. stress is proportional to strain. Steady-state friction losses are accounted for by means of a friction factor f incorporated in the Darcy-Weisbach formula. The differential form of the conservation equations, as generally found in literature, forms a pair of hyperbolic partial differential equations that are written as follows:

$$\frac{\partial V}{\partial t} + g \cdot \frac{\partial H}{\partial x} + \frac{f \cdot V^2}{2D} = 0 \qquad \text{conservation of momentum} \qquad (3.5)$$

$$\frac{\partial H}{\partial t} + \frac{c^2}{g} \cdot \frac{\partial V}{\partial x} = 0 \qquad \text{conservation of mass} \qquad (3.6)$$

H(x,t) = piezometric head, hydraulic grade line
V(x,t) = average cross-sectional velocity
D = hydraulic diameter
f = friction factor based on Darcy-Weisbach

This linearized version of the complete conservation equations can be solved by graphical, analytical or numerical techniques. The **method of characteristics** will be adopted here. As the method of characteristics is widely used and well-known, its methodology will not be outlined. The reader is referred to available literature (e.g. Jaeger, 1977; Wylie & Streeter, 1978; Chaudry, 1979).

The method uses a linear combination of the conservation equations and converts them into a set of ordinary differential equations, which are then solved by an explicit finite-difference technique. The discretization in space *x* and time *t* is constant and small time steps have to be used to satisfy the Courant stability condition.

Despite its straightforward and simple character, boundary conditions are easily introduced. It is very similar to the linear acoustics approach, where the problem is solved by superposition of an infinite series of positive (downstream travelling) and negative (upstream travelling) pressure waves.

The first example is that of a **closed-end rock joint** as presented in Figs. III-5 & III-6. The computations are performed for a constant pressure wave celerity of c = 1'000 m/s and for different friction factors *f*. The open boundary at the joint entrance and the closed boundary at the joint end correspond to a $\lambda/4$ – resonator model, according to Fig. III-7. The pressure excitation p(x,t) for the sinusoid of amplitude *A* and cyclic frequency f is defined as follows:

$$p(x,t) = A \cdot \cos(2\pi \cdot f \cdot t) \qquad (3.7)$$

Although pressure waves can be considered as complex values, for simplicity only the real part is considered here. Table III-3 and Fig. III-8 represent the gain factor G of the resonator system at the end of the rock joint. The gain factor G is defined as the maximum pressure amplitude A_{max} encountered at the joint-end divided by the pressure amplitude A of the sinusoidal input. It gives a qualitative idea about the importance of the resonance pressure waves that are created inside the rock joint. By assuming A = 1 at the entrance, the gain factor G represents the amplification of the amplitude inside the rock joint.

Table III-3 compares gain factors G for joint lengths L of 0.80 m and 8 m and friction factors of *f* = 0, 0.5 and 5. The friction factors are chosen to point out the sensibility of the results on frictional effects. Without friction, the theoretical amplification gets infinitely high for a sinusoidal excitation equal to one of the odd harmonics of the system. This is obtained for n = 0, 1, 2, ... and results in a pressure node at the end boundary. On the other hand, between these resonance nodes, antinodes exist. They correspond to the even harmonics of the system and are obtained for n = 0.5, 1.5, ….

For a joint length of 8 m, the first and the third harmonic are visualized at Figs. III-8a & 8c. The second harmonic is presented in Fig. III-8b. Finally Fig. III-8d shows the gain factor G for a sinusoidal excitation at 25 Hz. This frequency is generally considered as the limit of the spectral content of macroturbulent flow conditions in a plunge pool (Toso & Bowers, 1988). It can be seen that, without friction effects, an amplification of up to 5 times the amplitude of the incoming sinusoid is attained.

Celerity c [m/s]	Length L [m]	Friction f [-]	Natural freq f_{nat} [Hz]	Sinusoid freq n	[Hz]	Gain factor G [-]
1'000	0.80	0.0	312.50	0	312.5	∞
1'000	0.80	0.0	312.50	0.5	625	1.78
1'000	0.80	0.0	312.50	1	937.5	∞
1'000	8.00	0.0	31.25	0	31.25	∞
1'000	8.00	0.0	31.25	0.5	62.50	1.78
1'000	8.00	0.0	31.25	1	93.75	∞
1'000	8.00	0.5	31.25	0	31.25	11.06
1'000	8.00	0.5	31.25	0.5	62.50	1.69
1'000	8.00	0.5	31.25	1	93.75	10.13
1'000	8.00	5.0	31.25	0	31.25	3.37
1'000	8.00	5.0	31.25	0.5	62.50	1.58
1'000	8.00	5.0	31.25	1	93.75	3.04

Table III-3 Gain factor G of the maximum pressure amplitude at the end of a closed-end rock joint due to a sinusoidal excitation at its entrance. The numerical computations are based on the linear method of characteristics.

The incorporation of friction damps the resonance effects. The amplitude of the oscillations grows until the energy input and energy dissipation during a cycle are equal. Since at that time there is no additional energy input per cycle, the system oscillates with finite amplitude. This is visualized in Figs. III-8a to 8d for a friction factor of f = 5. Similar to the frictionless case, Fig. III-8d presents a steady amplification of 3 times the amplitude of the incoming sinusoid for f = 5.

The fundamental and higher harmonics of these simple oscillating systems can be visualized when expressing the gain factor G as a function of frequency f instead of time. This is shown in Fig. III-9 for the cases considered at Table III-3.

When dealing with closed-end rock joints of 0.8 m of length, resonance conditions are obtained for excitation frequencies of several hundreds of Hz. This is clearly incompatible with macroturbulent flow in a plunge pool. Even in the case of high-velocity jet impact, where considerable spectral energy can still subsist at frequencies of up to 100 Hz (Ballio et al., 1992), it is not possible to put the joint into resonance.

On the other hand, closed-end rock joints of 8 m of length can exhibit resonance conditions when excitation energy exists in a frequency range of 20-30 Hz. Such values are plausible for both high-velocity jet and macroturbulent flow conditions.

The second example is that of an **open-end rock joint**. The computations are again performed for a constant pressure wave celerity c = 1'000 m/s and for different friction factors f. The open boundaries at both the joint entrance and the joint end correspond to a $\lambda/2$ – resonator model, according to Fig. III-7. The same sinusoidal excitation is now applied at each of the joint entrances. This boundary situation is relevant to a singular rock block according to Fig. III-7 and results in an additional parameter, i.e. the phase difference $\Delta\phi$ between the applied spectral excitations. Considering that a spectral excitation physically corresponds to a range of turbulent eddies that hit the joint entrance at the water-rock interface, the following cases can be distinguished:

1. The excitations are perfectly in phase (phase difference $\Delta\phi = 0°$). This situation is plausible provided that the distance between the two entrances (and thus the size of the rock block) is smaller than or equal to the size of the relevant turbulent eddies.
2. The excitations are perfectly out-of-phase (phase difference $\Delta\phi = 180°$). This situation can happen but cannot be maintained in time. It is the physically less probable situation and not very interesting

to investigate, because the corresponding pressure waves compensate one another. As a result, the theoretical pressure is zero everywhere in the joint.

3. The excitations are sometimes in-phase but are characterized by a continuously changing phase difference ($\Delta\phi$ = variable). This is plausible provided that the distance between the two entrances is bigger than the size of the relevant turbulent eddies.

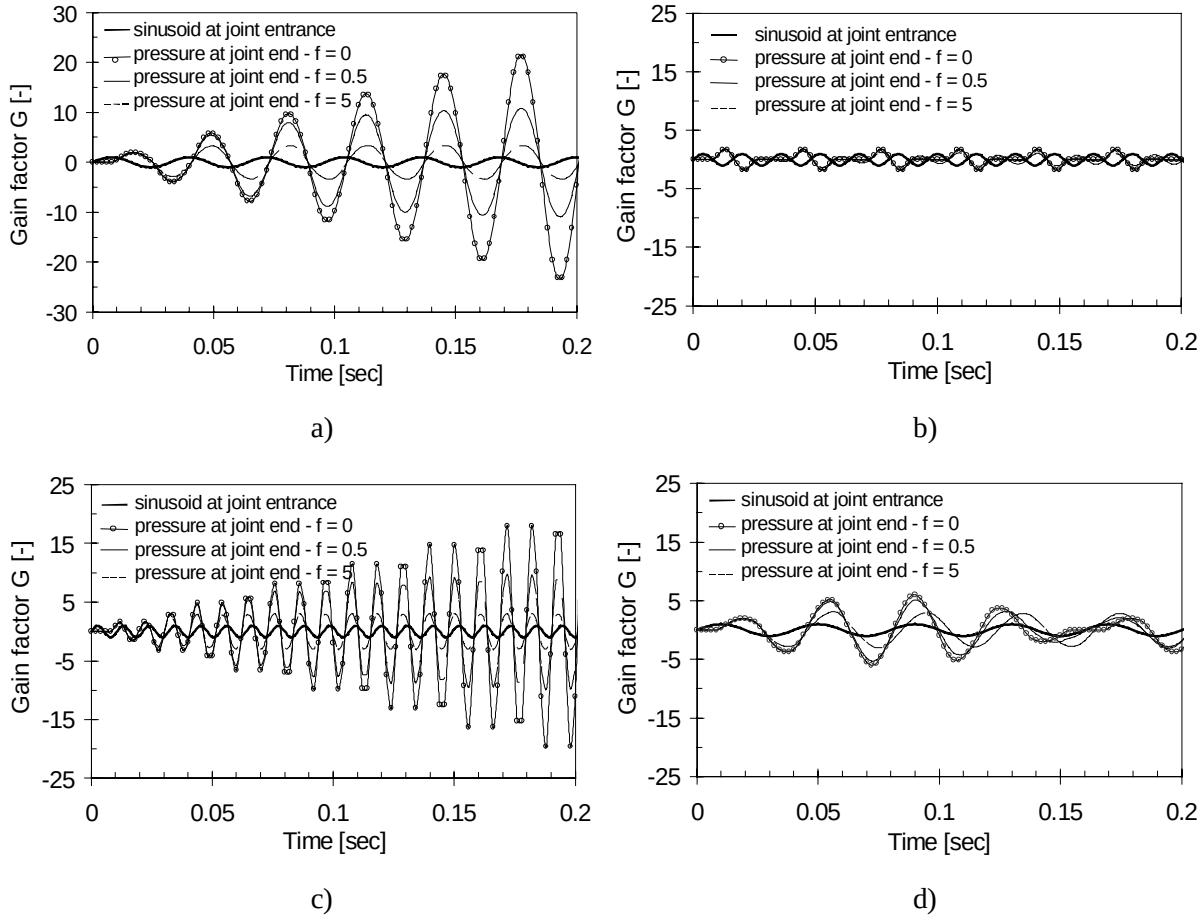

Fig. III-8 Gain factor G of the amplitude of a sinusoid applied at the entrance of a rock joint as a function of time and friction factor f: a) excitation frequency of 31.25 Hz; b) excitation frequency of 62.50 Hz; c) excitation frequency of 93.75 Hz; d) excitation frequency of 25 Hz. Resonance frequencies are clearly visible. The natural frequency of the rock joint is 31.25 Hz.

It is obvious that a precise calculation should account for the correct spectral content of the impacting pressure fluctuations. The here presented simplified approach, making use of just one sinusoidal excitation, will be applied to analyze cases 1 and 3. For case 3, phase differences of $\pi/2$ and $3\pi/4$ are used. This demonstrates the impact of phase differences on the gain factor G.

The $\lambda/2$ – resonator model involves pressure nodes at both ends and an antinode in the middle of the joint. Therefore, the presented gain factors G are applicable to the middle of the rock joint, and not to the end as in the case of an open-closed resonator model.

Similar to the open-closed end rock joints, Table III-4 compares gain factors for open-open joints of 8 m of length and for friction factors of f = 0, 0.5 and 5, as well as for phase differences of $\Delta\phi$ = 0, $\pi/2$ and $3\pi/4$.

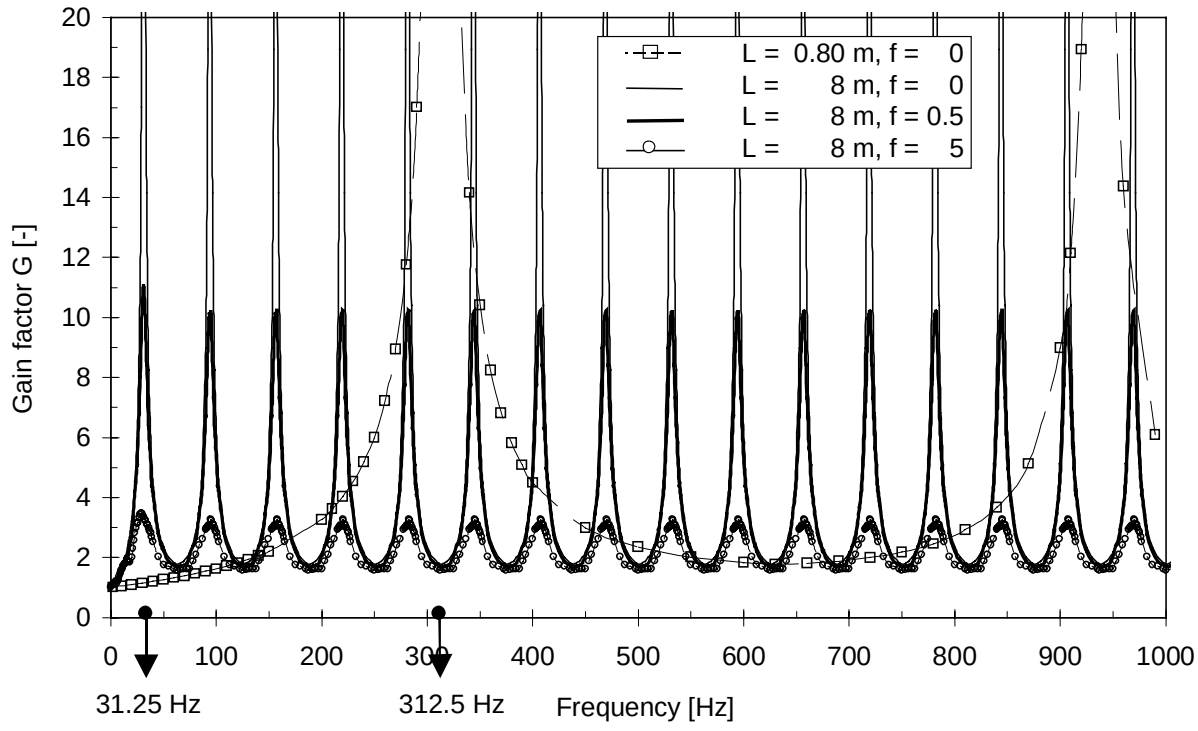

Fig. III-9 Gain factor G of the amplitude of a sinusoid applied at the joint entrance as a function of frequency. Fundamental and higher harmonics are clearly visible.

Without any friction, the theoretical amplification gets infinitely high for a sinusoidal excitation equal to one of the even harmonics of the system. This is obtained for n = 1, 2, ... and results in a pressure node at the middle of the rock joint. On the other hand, between these resonance nodes, antinodes exist. They correspond to the odd harmonics of the system and are obtained for n = 1.5, 2.5, ….

Fig. III-10 presents the corresponding pressure signals in the time domain. The first case (Fig. III-10a) corresponds to sinusoidal waves at the rock joint entrances that are perfectly in-phase. The second case (Fig. III-10b) involves a phase difference of $\pi/2$ and the third case (Fig. III-10c) a phase difference of $3\pi/4$. It can be seen that, with $\Delta\phi$ growing from 0 to π, the resonance conditions take much more time to develop. The limiting case is a phase difference of π for which the two sinusoids compensate one another.

The influence of the phase difference is much less pronounced with increasing friction factor *f*. For example, a friction factor $f = 5$ involves maximum resonance pressures between 2.84 (phase difference of $3\pi/4$) and 4.25 (in-phase conditions).

Finally Fig. III-10d shows the gain factor G in the middle of the rock joint for an excitation frequency of 25 Hz and for in-phase conditions. No significant amplification is noticed. Therefore, macro-turbulent flow cannot force an open-open rock joint of 8 m of length to resonate. The analogous case for an open-closed end rock joint of 8 m of length (Fig. III-8d) showed an amplification factor of 5.

Analogous to the closed-end rock joint case, open-end rock joints of only 0.8 m of length exhibit resonance conditions for excitation frequencies of several hundreds of Hz and are thus incompatible with macroturbulent flow in a plunge pool. The open-end rock joint of 8 m of length needs excitation frequencies around 60 Hz for resonance to develop. This is beyond the macroturbulent range but could be developed by high-velocity jet impact.

Celerity c [m/s]	Length L [m]	Friction f [-]	Natural freq. [Hz]	Phase diff. $\Delta\phi$	Freq [Hz]	Gain factor G [-]
1'000	8.00	0.0	62.5	0	62.5	∞
1'000	8.00	0.0	62.5	$\pi/2$	62.5	∞
1'000	8.00	0.0	62.5	$3\pi/4$	62.5	∞
1'000	8.00	0.5	62.5	0	62.5	14.32
1'000	8.00	0.5	62.5	$\pi/2$	62.5	12.09
1'000	8.00	0.5	62.5	$3\pi/4$	62.5	9.59
1'000	8.00	5.0	62.5	0	62.5	4.24
1'000	8.00	5.0	62.5	$\pi/2$	62.5	3.61
1'000	8.00	5.0	62.5	$3\pi/4$	62.5	2.84

Table III-4 Gain factor G of the maximum pressure amplitude at the end of an open-open rock joint due to a sinusoidal excitation at its two entrances. Numerical calculus is based on the linear method of characteristics.

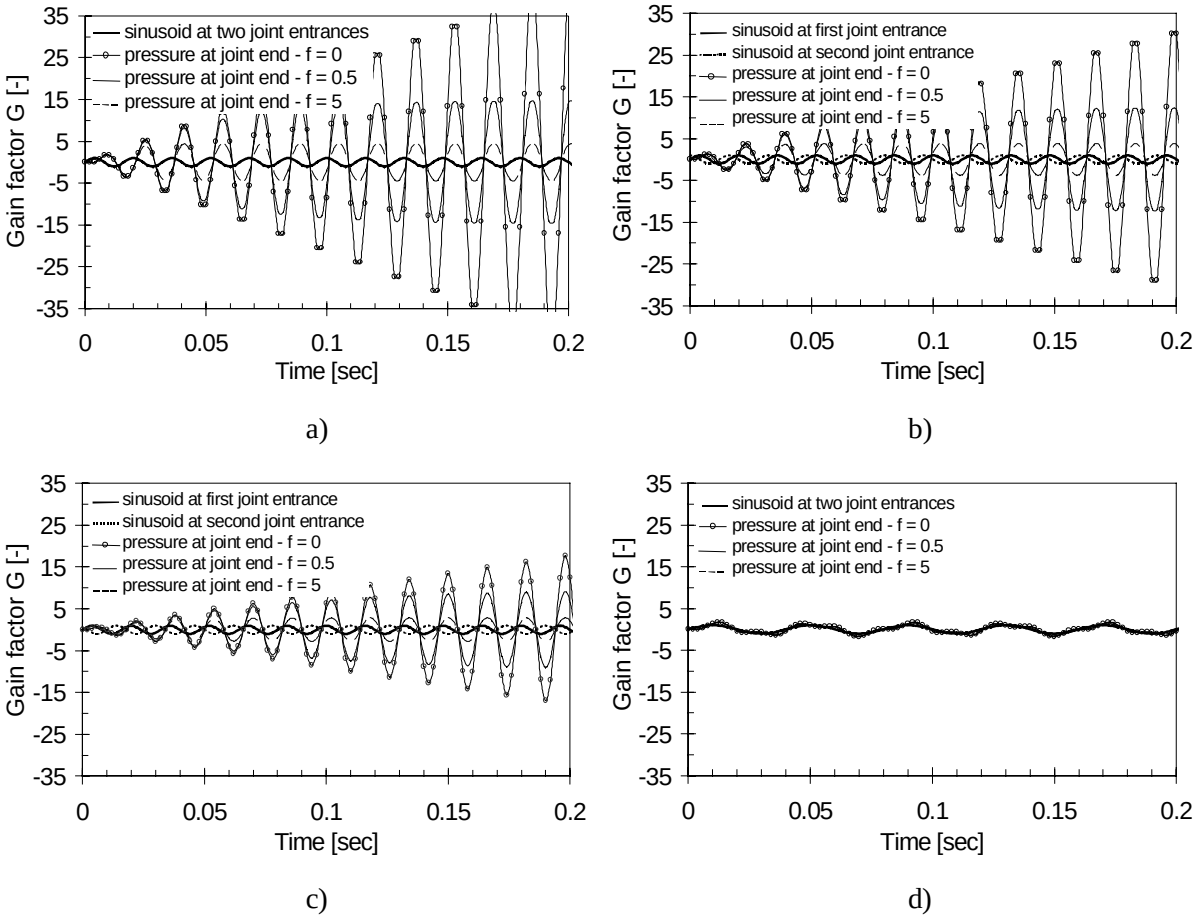

Fig. III-10 Gain factor G of the amplitude of a sinusoid applied at the entrance of an open-open rock joint in function of time and friction factor f: a) excitation frequency = 62.5 Hz and phase difference $\Delta\phi$ = 0; b) excitation frequency = 62.5 Hz and phase difference $\Delta\phi = \pi/2$; c) excitation frequency = 62.5 Hz and phase difference $\Delta\phi = 3\pi/4$; d) excitation frequency 25 Hz and phase difference $\Delta\phi$ = 0. Resonance frequencies are clearly visible. Natural frequency of the rock joint is 62.5 Hz.

2.2.5. Pressure wave propagation in real hydraulic systems and jointed rock masses.

The above theory on pressure wave propagation and reflection in simple hydraulic systems, such as one-dimensional singular rock joints, is based on simplifying physical and geometrical assumptions. The present section deals with these assumptions and aims to define their relative importance. Four simplifying assumptions are discussed:

1) only single-joint geometrical situations, with planar joint surfaces,
2) no partial pressure wave reflections at open and closed-end boundaries or at sudden geometrical changes,
3) no fluid-structure interaction effects on the hydrodynamic load,
4) no free air presence in the flow inside the joints.

The first assumption is of purely **geometrical** character. Up to now, only one-dimensional singular rock joints with an open or closed-end boundary were considered. It is obvious that real rock masses can exhibit joint patterns that are much more complicated.

Some possible geometrical situations are presented in Fig. III-11. The first geometry consists of branching closed-end rock joints. This system corresponds to a multiple $\lambda/4$ – resonator model. The theoretical resonance frequencies of the complete system can be determined by impedance or transfer matrix methods. This, however, is beyond the purpose of the present work. The frequencies and mode shapes of singular joints of the complex system are shown in Fig. III-11. Similarly, the second example corresponds to a multiple $\lambda/2$ – resonator model, and the third one to a combination of multiple $\lambda/2$ and $\lambda/4$ – resonator models. It is obvious that the resonance frequencies of a realistic joint set pattern can become quite complicated.

Basic geometry	Rock joint geometry	Model ($\lambda = c/f$)	Basic resonance frequencies [Hz]	Mode shape ϕ_n
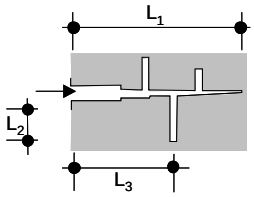	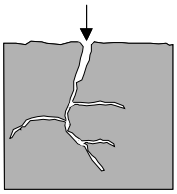	Multiple $\lambda/4$ resonator	$f_{res1} = (1+2n)\cdot \frac{c}{4L_1}$ $f_{res2} = (1+2n)\cdot \frac{c}{4(L_2+L_3)}$ $f_{res3} = \dots$	$\sin\left[\frac{(1+2n)\cdot\pi x}{2L_1}\right]$ $\sin\left[\frac{(1+2n)\cdot\pi x}{2(L_2+L_3)}\right]$ $\sin\left[\dots\right]$
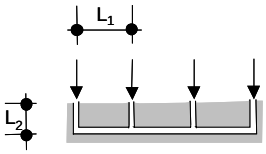	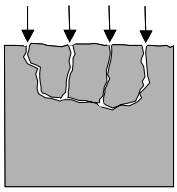	Multiple $\lambda/2$ resonator	$f_{res1} = (n)\cdot \frac{c}{2(3L_1+2L_2)}$ $f_{res2} = (n)\cdot \frac{c}{2(L_1+2L_2)}$ $f_{res3} = \dots$	$\sin\left[\frac{(n)\cdot\pi x}{3L_1+2L_2}\right]$ $\sin\left[\frac{(n)\cdot\pi x}{3L_1+2L_2}\right]$ $\sin\left[\dots\right]$
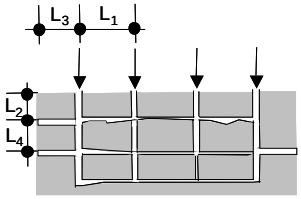	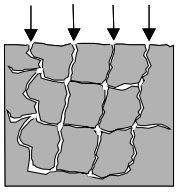	Multiple combined $\lambda/2 - \lambda/4$ resonator	$f_{res1} = (n)\cdot \frac{c}{2(L_1+2L_2)}$ $f_{res2} = (1+2n)\cdot \frac{c}{4(L_2+L_3)}$ $f_{res3} = \dots$	$\sin\left[\frac{(n)\cdot\pi x}{L_1+2L_2}\right]$ $\sin\left[\frac{(1+2n)\cdot\pi x}{2(L_2+L_3)}\right]$ $\sin\left[\dots\right]$

Fig. III-11 Examples of real rock joint systems with well-defined boundaries. The terminations are considered perfectly weak (open boundary) or perfectly rigid (closed boundary). Theoretical resonance frequencies and mode shapes of singular joints of the complex systems are added.

Beside the geometry, the question of wall boundary effects also rises. A real rock joint is characterized by a continuously changing joint thickness. At large and/or abrupt changes in joint thickness, partial wave reflections might occur and might have a profound impact on the basic mode shapes. However, knowledge of the exact form of the joint is impossible and one has to calculate by using a mean value. Moreover, sudden changes in orientation of the rock joint could exist. These changes could be considered as a sort of macroscopic geometrical changes, whether joint thickness changes stand for microscopic changes. It is assumed here that the most important geometrical influence on pressure waves and mode shapes is due to the macroscopic changes. Quantifying these effects may be possible with experimental tests on differently shaped rock joints. However, due to the complexity of the problem, it is evident that experimental and numerical investigations on transient pressure waves inside rock joints should start with an **analysis of the basic geometrical forms** shown in Fig. III-6. Once these simple cases are completely assessed and described, a further step should be to analyze a more complicated geometrical structure. This could be for example the influence of an abrupt 90° change in joint orientation, or a sudden decrease in joint thickness. The followed experimental methodology is outlined in Chapter V on the analysis of the experimental pressures measured inside rock joints of different forms.

The second simplifying assumption is related to **pressure wave reflections** at open and closed-end boundaries or at sudden geometrical changes. The presented theory only deals with compliant (negative reflection) or rigid (positive reflection) joint ends. However, in practice this is often not the case. The hereafter-adopted approach is mostly based on oscillatory or linear acoustics theory and can be found for example in Wylie & Streeter (1978).

For simplicity, consider a one-dimensional singular rock joint with an upstream boundary that is open-ended and a downstream boundary that is closed-ended. A simple periodical function excites the rock joint at its upstream boundary by means of pressure fluctuations. Due to reflections at the downstream end, the pressure signal at any time and place in the joint consists of the superposition of a downstream traveling (positive) wave f_1 (ct - x) and an upstream traveling (negative) wave f_2 (ct + x). The one-dimensional character of the joint makes it plausible to assume planar waves, i.e. the wave characteristics only vary with time t and with longitudinal coordinate x. Solution of the linearized equations (3.5) and (3.6) results in the following expression for the fluctuating part of pressure p(x,t) and discharge q(x,t):

$$p(x,t) = e^{i\omega t} \cdot \left(C_1 e^{\gamma x} + C_2 e^{-\gamma x}\right) \tag{3.8}$$

$$q(x,t) = -\frac{1}{Z_c} \cdot e^{i\omega t} \cdot \left(C_1 e^{\gamma x} + C_2 e^{-\gamma x}\right) \tag{3.9}$$

in which $C_{1,2}$ = integration constants, $\omega = 2\pi f$ = angular frequency, Z_c = characteristic impedance, $\gamma = \alpha + ik$, α = damping constant, $k = 2\pi/\lambda = \omega/c$ = wavenumber, λ = wavelength, $i = \sqrt{-1}$. The constant γ is called the propagation constant and is a complex number.

For these ideal planar waves, a constant relation between the pressure and the velocity is obtained at any place and any time. This is expressed by the characteristic impedance of the medium Z_c, which is a complex number. A detailed analysis of the complex impedance is beyond the scope of the present work. Here the real part is used to explain the physical process of pressure wave reflection:

$$Z_c = \rho_0 \cdot c \tag{3.10}$$

The characteristic impedance expresses the pressure change that is necessary to obtain a certain velocity change in the joint. In other words, it constitutes a sort of resistance that is exerted by the medium on the pressure wave.

For real pressure waves in end-bounded media with a transversal cross-sectional area S, the impedance values are not equal to the characteristic impedance Z_c. Although they are independent of time, they are influenced by the multiple reflections of the pressure waves at the end boundaries and thus become

a function of x. One speaks about hydraulic impedances and, when applied at the end boundaries, they are called the input and output impedances Z_{in} and Z_{out}. For a rock joint of length L that goes from x = -L to x = 0 these complex values are written as follows:

$$Z_{in} = \frac{p(-L,t)}{v(-L,t)\cdot S} \quad \text{and} \quad Z_{out} = \frac{p(0,t)}{v(0,t)\cdot S} \tag{3.11}$$

For example, in case of a closed-end system, the velocity at the downstream end is zero. As a result, the output impedance $Z_{out} = \infty$. Furthermore, the input impedance at the upstream end is influenced by the value of the output impedance and the characteristic impedance of the medium. The relationship between the input and the output impedances is often described by a transfer function. When considering ideal planar waves in the rock joint and making use of the hyperbolic functions, the following transfer functions are obtained for the pressure and velocity at any place and time:

$$p(x,t) = \left[(C_1 + C_2)\cdot\cosh(\gamma x) - Z_c\cdot(C_1 - C_2)\cdot\sinh(\gamma x)\right]\cdot e^{i\omega t} \tag{3.12}$$

$$q(x,t) = \left[-\frac{(C_1 + C_2)}{Z_c}\cdot\sinh(\gamma x) + (C_1 - C_2)\cdot\cosh(\gamma x)\right]\cdot e^{i\omega t} \tag{3.13}$$

The input impedance Z_{in} can now be calculated based on equations (3.11), (3.12) and (3.13):

$$Z_{in} = Z_c\cdot\frac{Z_{out}\cdot\cosh(\gamma L) + Z_c\cdot\sinh(\gamma L)}{Z_{out}\cdot\sinh(\gamma L) + Z_c\cdot\cosh(\gamma L)} \tag{3.14}$$

For a joint with a closed-end boundary the output impedance Z_{out} equals ∞, and thus the input impedance Z_{in} is equal to:

$$Z_{in} = Z_c\cdot\frac{\cosh(\gamma L)}{\sinh(\gamma L)} = Z_c\cdot\tanh(\gamma L) \tag{3.15}$$

We can now define a **reflection factor $\Lambda(x)$** that expresses the ratio of the amplitudes of the incoming pressure wave to the reflected pressure wave:

$$\Lambda(x) = \frac{B\cdot e^{+\gamma x}}{A\cdot e^{-\gamma x}} = \Lambda(0)\cdot e^{+2\gamma x} \tag{3.16}$$

The reflection factor at the joint end is thus written as:

$$\Lambda(0) = \frac{Z_{out} - Z_c}{Z_{out} + Z_c} \tag{3.17}$$

Equation (3.17) shows that the reflection coefficient at the end of the rock joint depends on the difference between the output impedance and the characteristic impedance of the medium in the joint. The extreme cases of this equation correspond to the perfectly weak or rigid end boundaries as previously assumed in the theory:

1. $Z_{out} >> Z_c$ — **$\Lambda(0) = +1$**. The end boundary is considered perfectly rigid when compared to the characteristic impedance of the medium. The reflected pressure wave has the same amplitude and sign as the incoming pressure wave. No energy is lost during this operation.

2. $Z_{out} << Z_c$ — **$\Lambda(0) = -1$**. The end boundary is considered compliant when compared to the characteristic impedance of the medium. The reflected pressure wave has

the same amplitude as the incoming pressure wave but with the opposite sign. No energy is lost during this operation.

3. $Z_{out} = Z_c$ $\Lambda(0) = 0$. The end boundary is considered free of any reflection because its impedance is equal to the characteristic impedance of the medium. It is as if the pressure waves are absorbed or that they just go on to infinity. All energy goes out of the system.

As stated before, these ideal cases rarely occur in practice. For example, the reflection at a closed-end boundary of a rock joint corresponds to a transfer of the pressure wave from water to rock. The characteristic impedances of these two media are respectively:

$$Z_{water} = (\rho \cdot c)_{water} = \left(1000 \frac{kg}{m^3} \cdot 1000 \frac{m}{s}\right) = 1 \cdot 10^6 \frac{kg}{m^2 s} \tag{3.18}$$

$$Z_{rock} = (\rho \cdot c)_{rock} = \left(2600 \frac{kg}{m^3} \cdot 5000 \frac{m}{s}\right) = 13 \cdot 10^6 \frac{kg}{m^2 s} \tag{3.19}$$

As a result, the corresponding reflection coefficient Λ becomes:

$$\Lambda = \frac{(\rho \cdot c)_{rock} - (\rho \cdot c)_{water}}{(\rho \cdot c)_{rock} + (\rho \cdot c)_{water}} = 0.857 \tag{3.20}$$

Thus only ~ 86 % of the incoming amplitude will be reflected, the other 14 % will be transmitted into the rock mass. The energy of the pressure wave is related to the square of the amplitude and therefore only ~73 % of the incoming energy is reflected, 27 % is transmitted into the rock mass. These statements hold for an infinitely thick rock mass, so that no internal reflection can occur in the rock.

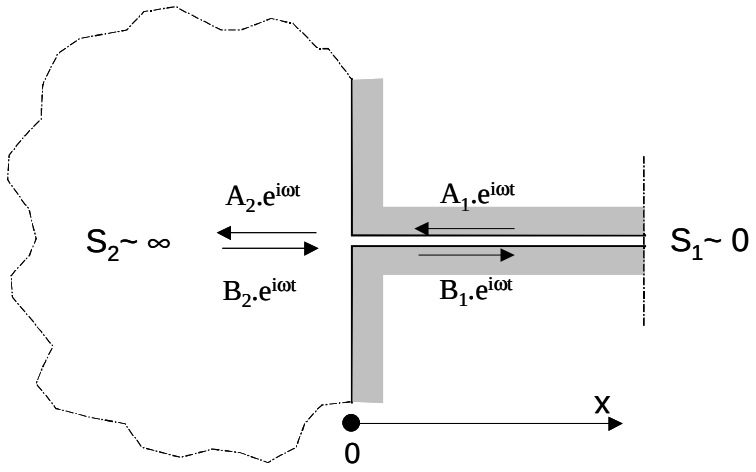

Fig. III-12 Reflection coefficient from a bounded medium into an infinitely large medium.

The upstream boundary transfers pressure from water to water and should thus correspond to a reflection coefficient = 0. However, the huge change in cross-sectional area from a tiny small rock joint into a quasi-infinite medium that represents the plunge pool drastically decreases the characteristic impedance of the plunge pool area. This is also the reason that in the plunge pool turbulent eddies develop, rather than bounded pressure wave propagation. Therefore, by expressing the equations (3.12) and (3.13) for pressure and velocity in each medium and by stating that these values should be equal at the interface, the following results are obtained (Fig. III-12):

$$\Lambda(0) = \frac{Z_{out} - \frac{Z_c}{S_1}}{Z_{out} + \frac{Z_c}{S_1}} \tag{3.21}$$

$$Z_{out} = \frac{p(0)}{v(0) \cdot S_2} \cong 0 \tag{3.22}$$

$$\Lambda(0) \cong \frac{-\frac{Z_c}{S_1}}{+\frac{Z_c}{S_1}} = -1 \tag{3.23}$$

The reflection coefficient at the water-rock interface reacts as a compliant boundary, i.e. pressure waves are reflected without energy loss but with an opposite sign. On the other hand, a pressure transfer from the plunge pool to the rock joint cannot be treated in the same way because of its physically different behavior: the pressure exerted at the water-rock interface is provided by turbulent eddies and not by traveling pressure waves. Therefore, a reflection coefficient cannot be applied.

However, the above theory is applicable in case of sudden changes in cross-sectional area in the rock joint itself. A sudden decrease in cross-section functions as a partially positive reflection, while sudden increases in cross-section give rise to a partially negative reflection. As a result, the modeling of a singular rock joint resonator system as a perfect $\lambda/4$ (closed-end joints) or $\lambda/2$ (open-end joints) resonator constitutes a reasonable first approximation of the real system, provided that large and abrupt changes in cross-section of the rock joint are absent or at least rare. Although joints can extend along a more or less plane surface, such sudden changes often exist. In that case, partial internal wave reflections could occur and eventually modify the theoretical natural frequencies of the resonator system. One then speaks about the **fundamental frequencies** of the entire system. Since the exact form of the rock joint is unknown, it gets impossible to predict the exact system response.

Fig. III-13 shows a typical side view and cross-sectional view of a closed-end rock joint. One can notice the points of contact between the wall boundaries as well as sudden changes in orientation of the joint. The points of contact are always present because they transfer the in-situ stresses of the rock mass from one wall to the other. They are usually modeled as singular islands in a network of connected free paths and constitute very important local cross-sectional changes. As a first approach, their influence on the natural frequencies of the basic resonance model of the rock joint is assumed to be negligible. Nevertheless, when several points of contact are close one to the other, they can form a rigid boundary for the pressure waves and act as a reflector. In that case, the joint is subdivided into two different simple joints. Even when changes in orientation exist in a constant cross-section, it could be expected that their particular geometry might generate internal wave reflections. Based on the linear transient flow equations (3.8) and (3.9) presented in § 2.2.4, it is clear that this phenomenon cannot be accounted for by the numerical model. Therefore, it was decided to perform experimental tests on a rock joint with a 90° sudden change in orientation rather than on rock joints with variable cross-section. The results are discussed in Chapter V.

The third simplifying assumption is related to the dynamic character of the hydrodynamic loading. It is assumed that **fluid-structure interaction is negligible**. This means that vibrations of the surrounding rock mass due to hydrodynamic action inside the joints is of no significant influence on the latter. In other words, the resonating frequencies of the rock mass itself cannot interfere with the principal mode shapes of the hydrodynamic pressure waves inside the joints.

This statement seems plausible when applied to intermittently jointed rock masses. For these, the joints are not completely interconnected and almost no potential vibrating parts exist. However, completely jointed rock masses are piecewise broken-up and consist of rock blocks that may or may not be able to vibrate in their surrounding matrix. This depends on the degree of interlocking within their matrix.

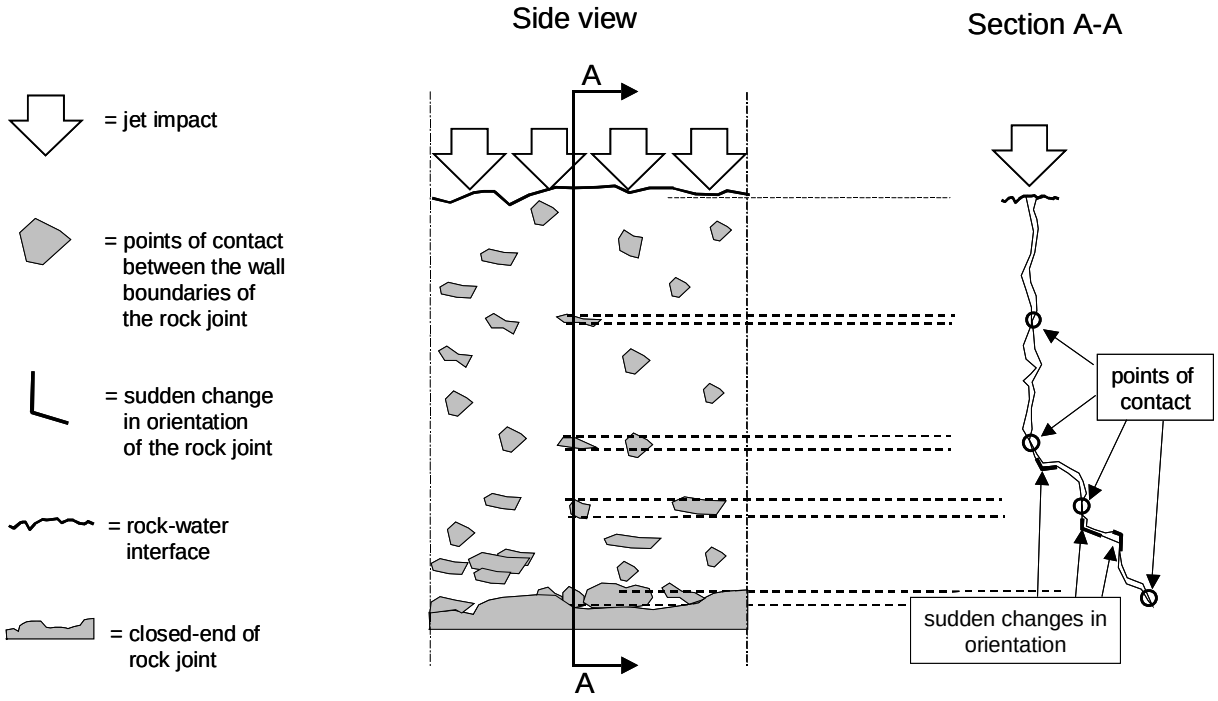

Fig. III-13 Side view and section A-A of a closed-end rock joint showing the different points of contact, the changes in cross-sectional area and the sudden changes in orientation of the joint. All geometrical discontinuities can be a source of change of the theoretical natural frequencies of the system.

Finally, the far-most significant physical assumption is the **absence of free air bubbles** inside the rock joints. The presence of a very small free air content in the flow mixture completely changes the compressibility of the system. Therefore, in case of free air presence, the here discussed resonance conditions and frequencies are not valid. A similar example of a computation with a free air content α (in [%]) is established in § 3.

2.2.6. Concluding remarks

Considering the four simplifying assumptions outlined in § 2.2.5, the generation of oscillatory and resonance flow conditions by transient pressure wave propagation inside rock joints depends on the spectral content of the hydrodynamic exciter, and on the length and the end-boundary conditions of the rock joints. For combined open and closed-end rock joints, corresponding to a $\lambda/4$ – resonator model, a high-velocity jet is capable to produce significant resonance pressure waves for joint lengths in the order of 10^0 m. For two open-end boundary conditions, corresponding to a $\lambda/2$ – resonator model, the fundamental natural frequency of the joint is twice as high. Therefore, higher frequencies are needed to excite the system. Moreover, the resonant amplification becomes less pronounced with increasing phase difference between the two open-end boundaries. For a phase difference of π, the pressure waves inside even compensate one another. High-velocity jets are able to excite such systems provided that the joint length is large (min. 5-10 m) and the phase difference is small ($< \pi$).

In the following, only single and perfectly planar joint systems are considered. The influence of contact points is assumed negligible. The influence of free air bubbles and partial reflections due to abrupt changes in orientation are investigated by experimental tests on differently shaped rock joints.

3. Air entrainment

Air entrainment aspects have already been discussed throughout the state-of-the-art review in Chapter II. However, due to its crucial importance and direct relevance with regard to this study, a separate section is justified. The aim is to outline in which way air entrainment can influence the different physical processes (Fig. I-2) that govern the scour phenomenon. According to these physical processes, three main types of air entrainment can be distinguished (Fig. III-14). The first type is **plunging jet air entrainment**. A free water jet plunging through the atmosphere entrains a certain amount of air due to its turbulent character. The second type deals with **plunge pool air entrainment**. At the point of impact of the plunging jet a considerable amount of air is entrained into the diffusing shear layer. The air bubbles in the shear layer are transferred towards the bottom, deflected sideways and finally return to the surface. The third type is **rock joint air entrainment**. It considers the effect of free air inside the rock joints. Since transient pressurized flow is assumed in the joints, the free air completely changes the oscillating and resonance conditions of the bounded system.

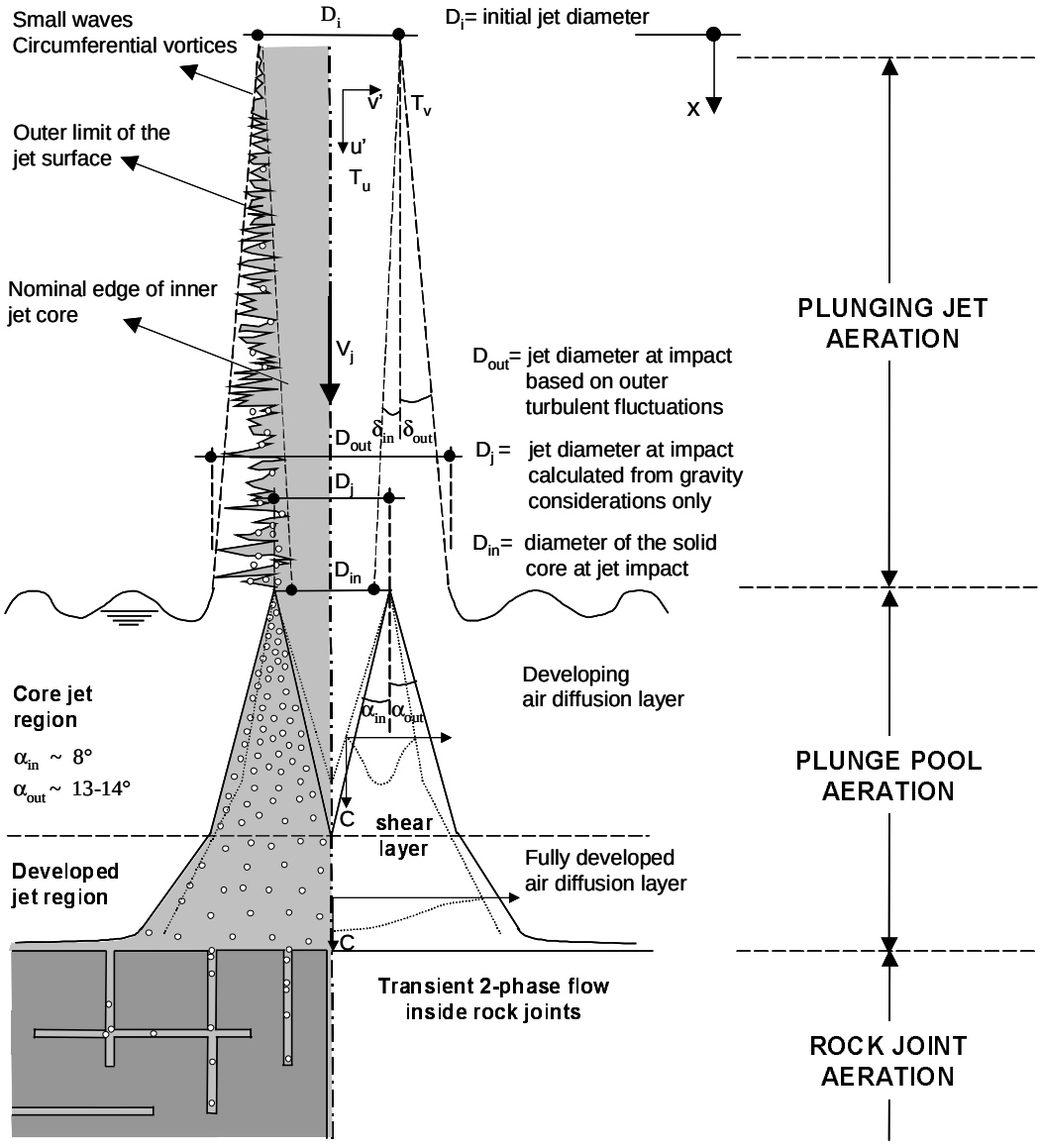

Fig. III-14 Types of air entrainment: jet, pool and rock air entrainment each of them have a significant influence on the scouring of the rock mass (Figure is partially taken from Ervine & Falvey, 1987).

3.1. Plunging jet air entrainment

Free water jets that discharge through the atmosphere can exhibit considerable air entrainment. This physical mechanism has been the subject of many studies. Some investigators advocated the falling droplet hypothesis of aeration (Sene, 1988; Volkart, 1980). This, however, is not possible at the underside of a horizontal jet, were substantial air entrainment nevertheless appears. Others accounted for spray as the dominant mechanism (Pinto & Neidert, 1982). Although spray is certainly a mechanism that is present at very high jet velocities, it doesn't account for air that is moving into the body of the jet at the underside of a horizontal jet. The actual trend is more towards recognition of turbulence as the most significant air entrainment mechanism (Ervine & Falvey, 1987; Chanson, 1996; Ervine et al., 1997; Ervine, 1998). The here outlined approach is based on Ervine & Falvey (1987) and Ervine et al. (1997).

Plunging jet behaviour is characterised by two opposite effects: stability and internal turbulence. Stability is obtained by simple gravitational contraction. Internal turbulence, which counteracts this contraction, is due to jet issuance conditions. It results in lateral spread, distortion and eventually total jet break-up. The governing parameter that accounts for turbulence effects is the **initial turbulence intensity Tu** [%]. The turbulence intensity is defined as the ratio of the root-mean-square value of the axial velocity fluctuations u' to the mean axial velocity U:

$$Tu = \frac{u'}{U} \tag{3.24}$$

For convenience of notation, the axial velocity will be notified by V instead of U. Tu can be related to the half angle of outer lateral jet spread δ_{out} and the longitudinal distance from the jet outlet X, resulting in the following experimental expression (see Fig. III-14 for significance of parameters):

$$\frac{\delta_{out}}{X} = 0.38 \cdot Tu \tag{3.25}$$

The inner core decay angle δ_{in} reacts in a similar manner. Based on measurements of the probability to encounter water at the edge of the jet, a reasonable approximation of the inner core decay angle seems to be around 15-20 % of the lateral spread angle δ_{out}. This means that, although a plunging jet may appear intensely rough and highly aerated, a substantial inner core nevertheless always is present. For turbulence intensities Tu of 5 to 8 %, corresponding to highly turbulent jets, the inner and outer decay angles can be approximated by:

$$\frac{\delta_{in}}{X} \cong 0.5-1\% \quad \text{and} \quad \frac{\delta_{out}}{X} \cong 3-4\% \tag{3.26}$$

Based on conservation of energy, Davies (1972) stated that these turbulent surface disturbances (or turbulent eddy sizes) increase linearly with the square root of the fall length L of the jet. Ervine et al. (1997) confirmed this postulate and used gravitational acceleration to derive an expression for the core diameter and the jet spread ε. For engineering purposes, the diameter of the jet at impact in the pool D_j and the minimum diameter of the solid core at impact D_{in} are defined as follows:

$$D_j = D_i \cdot \sqrt{\frac{V_i}{V_j}} \quad \text{with} \quad V_j = \sqrt{V_i^2 + 2gL} \quad \text{based on gravitational acceleration} \tag{3.27}$$

$$D_{in} = D_i - 2 \cdot (0.005 \text{ to } 0.01) \cdot L \quad \text{based on internal turbulence} \tag{3.28}$$

The maximum diameter of the outer undulating region at impact D_{out} is written:

$$D_{out} = D_i + 2 \cdot (0.03 \text{ to } 0.04) \cdot L \qquad \text{based on internal turbulence} \qquad (3.29)$$

As can be seen in Fig. III-14, small surface waves initially form at the outer surface of the jet. These waves are generated by the internal turbulence of the jet and amplify in the downstream direction. They transform into circumferential vortices and finally into turbulent surface disturbances. The air within these disturbances moves with the same speed as the falling water. The air-water interface takes a certain volume of air with it downstream. This volume increases with the fall length. The air continuity is maintained at the interface by an air flow that is perpendicular to the axis of the falling jet. The air outside the confines of the jet that flows parallel to the direction of the jet is almost negligible. This can be noticed by mist that forms around prototype falling jets. Instead of moving downwards with the jet, the mist flows slowly towards the jet.

The lateral spread of the jet thus proceeds at a rate that is proportional to the initial turbulence intensity Tu. The jet particles that move perpendicular to the flow are fed by lateral turbulent kinetic energy, and have to overcome the restraining surface tension pressure. Hence, isotropic turbulence assumptions result in the concept of an onset velocity of aeration, also called a minimum entrainment velocity V_0:

$$V_0 = \frac{0.275}{Tu} \qquad (3.30)$$

This expression is not strictly accurate because it is based on the total kinetic energy of the turbulent fluctuations. Falvey & Ervine (1988) pointed out that a correct analysis should only account for the turbulent energy that is contained in the range of air bubble sizes that are entrained by the jet. They showed that neglecting this important aspect when performing physical model studies might result in serious scale effects. A typical turbulence intensity of a real plunging jet, around 4-5 %, corresponds to an onset axial jet velocity of V_0 = 5.5-7 m/s.

Other investigations on the minimum entrainment velocity can be found in Lin & Donnelly (1966), Ervine & Elsawy (1975) and Ervine et al. (1980). A summary of available expressions can be found in Chanson (1996). For the jet velocities considered in this study, with magnitudes up to several 10^1 m/s, the air entrainment inception velocity U_0 is largely exceeded and thus of no relevance.

Furthermore, for jets that fall over a long distance, the turbulent surface disturbances may be large enough to penetrate the core of the jet. As such, disintegration into separate droplets may occur. This phenomenon can be defined by the **jet break-up length L_b**. This is an important parameter because it expresses for which fall distance the solid core of the jet completely vanishes. Table III-5 summarizes existing expressions to estimate the jet break-up length L_b for circular and planar impinging jets. We, Re and Fr notations stand respectively for Weber number, Reynolds number and Froude number of the issuing jet. Q_w corresponds to the water discharge in m^3/s and q_w is the water discharge per unit width in m^2/s. Finally, D_i and D_j are the jet diameter at issuance and the jet diameter at impact in the pool.

Based on lateral jet spread due to internal turbulence, equation (3.25), and jet contraction due to gravitational acceleration, Ervine et al. (1997) developed a theoretical expression for the jet break-up length L_b, valid for circular jets and for varying Tu:

$$C^2 = \frac{1}{\sqrt{\frac{2L_b}{D_i Fr^2} + 1} \cdot \left(\sqrt{\frac{2L_b}{D_i Fr^2} + 1} - 1 \right)^2} \qquad (3.31)$$

C is defined as the turbulence parameter in the following way:

$$C = 1.14 \cdot Tu \cdot Fr^2 \qquad (3.32)$$

Ervine et al. (1997) also established a best-fit of the available experimental data of Baron (1949), McKeogh (1978) and Withers (1991). This experimentally derived formula is mentioned in Table III-5 and is in good agreement with equation (3.31).

Jet type	L_b	Tu	Authors
rectangular nappes	$6 \cdot q_w^{0.32}$	-	Horeni (1956)
circular jets	$1.7 \cdot \frac{We}{\left(10^{-4} \cdot Re\right)^{\frac{5}{8}}}$	3 %	Baron (1949)
	$60 \cdot Q_w^{0.39}$	0.3 %	Ervine, McKeogh & Elsawy (1980)
circular jets	$17.4 \cdot Q_w^{0.31}$	3.0 %	Ervine, McKeogh & Elsawy (1980)
	$4.1 \cdot Q_w^{0.20}$	8.0 %	Ervine, McKeogh & Elsawy (1980)
circular jets	$(50\text{-}100) \cdot D_j$	3-8 %	Ervine & Falvey (1987)
circular jets	$(200\text{-}300) \cdot D_j$	0.003 %	Ervine & Falvey (1987)
circular jets	$1.05 \cdot \frac{D_i \cdot Fr^2}{1.11 \cdot Tu^{0.82} \cdot Fr^{1.64}}$	varies	Ervine, Falvey & Withers (1997)

Table III-5 Summary of expressions for the jet break-up length L_b, for rectangular and circular jets.

The preceding analysis proves that the air entrainment of a jet plunging through the atmosphere is governed by gravity, surface tension and internal turbulence effects. In other words, it is a combined Froude-Weber-Reynolds phenomenon and any scale model study should correctly simulate all these phenomena. This is clearly impossible.

However, appropriate simulation of air entrainment could be possible in Froude scale models provided that care is exercised to accurately represent the prototype turbulence intensity. In addition, the model should be large enough so that the onset velocity of air entrainment is attained and so that surface tension effects are small. While the latter aspects can rather easily be obtained in a physical model of considerable size, the power spectral content of turbulent eddies cannot be scaled (Falvey & Ervine, 1988). This problem has already been dealt with in § 2.1 and indicates that near-prototype or prototype jet velocities should be considered in order to accurately account for the spectral content of the jet. This represents a severe restriction when performing laboratory model studies.

As a conclusion, plunging jet air entrainment is of importance because it enhances plunge pool air entrainment and because it defines the particular geometry of the jet at its point of impact in the plunge pool. The diameter of the core of the jet at impact is directly influencing the extension of the jet when it develops through the plunge pool. The maximum diameter of the outer undulating and partially aerated jet region defines the zone at the plunge pool bottom that is under direct influence of jet impact. As can be seen in Fig. III-14, this zone entirely determines the region at the water-rock interface that is impacted by the two-phase shear layer of the diffusing jet and, thus, that is subjected to significant pressure fluctuations.

3.2. Plunge pool air entrainment

3.2.1. Introduction

Plunge pool air entrainment is governed by high-velocity flow impingement on an ambient or slowly recirculating flow. The supercritical flow entrains air that is caught in a spreading turbulent shear layer where it encounters deceleration and lateral diffusion.

The earliest investigations on plunge pool air entrainment were conducted to control river pollution due to a deficit of oxygen. From this point of view, outlet works of hydraulic structures were an interesting means to oxygenate rivers by aeration of the outflowing water. The studies showed the importance of the Froude number Fr (Kalinske & Robertson, 1943; Wisner, 1965; Charlton, 1970), the height of fall L of the jet (Gameson, 1957; Jarvis, 1970; Apted & Novak, 1973), the temperature T (Gameson et al., 1958) and the downstream plunge pool depth Y (Jarvis, 1970).

At present, two different types of study can be distinguished. The first one focuses on a quantification of the air entrainment at the point of impact of the jet in the plunge pool or throughout the depth of the plunge pool. Several investigators experimentally determined the quantity of air entrained in a plunge pool. Studies on circular plunging jets were performed by Lin & Donnelly (1966), Van de Sande & Smith (1973, 1976), Ervine (1976), McKeogh (1978), Ervine et al. (1980), Bin (1984) and Ervine (1998). Rectangular plunging jets have been investigated by Ervine & Elsawy (1975) and Sene (1988). A summary of existing expressions can be found in Chanson (1996).

The second type of study rather investigates the effects that air entrainment may generate on turbulent flow characteristics, and more in detail on turbulent pressure fluctuations at the water-rock interface. These studies focus on the influence of air on the scour capacity of plunging water jets. In 1967, Johnson performed laboratory experiments in order to establish this effect. Ervine & Falvey (1987) and Ervine et al. (1997) quantified the reduction of the mean dynamic pressure at the plunge pool bottom due to air bubble presence. Furthermore, May & Willoughby (1991) determined the influence of air bubbles on the root-mean-square value of the fluctuating part of the pressures at the plunge pool bottom.

Air entrainment studies did not result in a general method for prediction of aeration rates, nor did they develop appropriate scaling laws for model to prototype situations. Generally, each investigated hydraulic structure proposes its own empirical relationship. Ervine (1998) summarized the actual situation and formulated the main problems encountered at present. One of the major difficulties in aeration assessment results from the **different mechanisms of air entrainment**.

Therefore, these will be outlined firstly, followed by a summary of expressions for the quantity of air in a pool, as well as for the transfer of air bubbles from the point of jet impact down to the water-rock interface. Finally, the influence of air entrainment on the scour capacity of jets is pointed out.

3.2.2. Mechanisms of plunge point air entrainment

Several investigators (Van de Sande & Smith, 1973; Chanson, 1996; Ervine, 1998) discussed the different mechanisms of plunge point air entrainment. The approach outlined by Ervine (1998) is particularly interesting because he directly relates the mechanisms of air entrainment to an expression for the quantity of air that is entrained. He distinguishes three mechanisms, as presented in Fig. III-15. The corresponding total rate of aeration is outlined in § 3.2.3.

The first mechanism concerns **turbulent surface disturbances** of the impacting jet. These disturbances can come from a number of sources, such as turbulent eddies, instabilities or longitudinal vorticity. The size of the disturbances is assumed to be related to $V_j^2/2g$ (V_j = mean jet velocity at impact) and, hence, the aeration rate per unit jet width $q_a \sim V^3/g$. In terms of turbulent velocity, the height of the disturbances can be expressed as $(w')^2/2g$, with w' the root-mean-square value of the turbulent fluctuations. This expression is presented in Fig. III-15 and points out the sensitivity of the aeration rate to turbulence and surface disturbances.

The second mechanism of plunge point air entrainment corresponds to air that enters by means of a thin **air boundary layer** close to a smooth jet surface. A gap is formed between the jet and the recirculating flow. The thickness of this boundary layer is proportional to $V_j^{1/2}$ and thus the aeration rate per unit jet width varies with jet velocity to the power of 3/2. Evidence can be found in Van de Sande & Smith (1973, 1976). This mechanism is only significant for jet velocities above 5 m/s.

The third mechanism is called **free-surface aeration**. This can happen in the upstream jet, particularly at high jet velocities, and on the surface of the receiving plunge pool, due to violent disturbances. The latter may be the most important and is caused by intense turbulence and vorticity in the receiving pool. Its direct relation with turbulent velocities results in a linear variation with the jet velocity V_j^1.

Air entrainment as it can be encountered in practical situations often consists of a combination of these mechanisms. Each of the mechanisms has a different threshold that needs to be exceeded, and a particular relationship with the jet velocity V. The problem is that the importance of each mechanism separately is not exactly known and, thus, that a simple relationship for plunge point aeration rate is simply not possible.

Aeration mechanism	Aeration rate per unit jet width	Parameters
1. Upstream surface disturbances	$q_a = k_1\left(\frac{V_j^3}{g}\right)(Tu)^2$	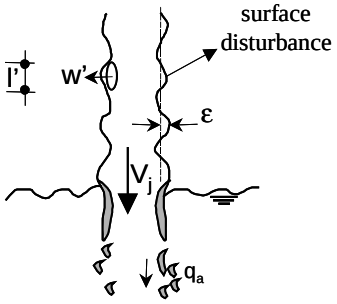
2. Air boundary layer	$q_a = 1.73\left(\frac{\nu}{2g}\right)^{1/2}(V_j)^{3/2}$	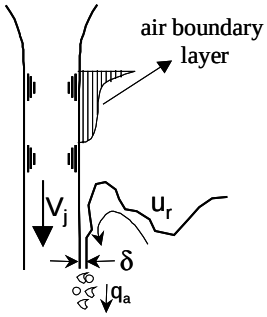
3. Free surface aeration	$q_a = k_2\left(\frac{D'}{\sin\theta}\right)V_j$	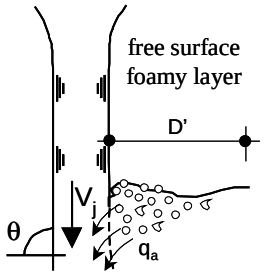

Fig. III-15 Three main mechanisms of air entrainment at point of jet impact in a plunge pool and the corresponding rate of aeration per unit width of the jet (Ervine, 1998).

The same study showed that for a jet thickness higher than 30 mm, the aeration rate becomes independent of this jet thickness. A threshold for the Reynolds number should be around 10^5.

Chanson (1996) pointed out the difference in air entrainment mechanisms between low and high jet velocities. At low velocities, the plunge pool water surface is unable to follow the undulations of the jet surface and small air pockets are entrained. The process is intermittent and pulsating. At higher jet velocities (4-12 m/s), a thin sheet of air is set into motion by the shear forces at the surface of the jet and generates the entrainment of elongated air pockets. The length of the air layer can considerably fluctuate. The latter process more or less corresponds to the second mechanism in Fig. III-15. Moreover, based on studies performed by Sene (1988) and Thomas et al. (1983), Falvey & Ervine (1988) already pointed out these two different mechanisms. They proposed a transitional jet velocity of around 10 m/s.

3.2.3. Quantity of air entrained in a plunge pool

A first approach is based on the mean velocity of the jet at impact V. Theoretically, the rate of air entrainment is dependent on the ratio of the bubble rise velocity u_b to the jet velocity at impact V. However, for most model studies and for all prototype cases, the bubble rise velocity can be assumed constant and hence the process becomes dependent on the jet velocity V. This implies that scale effects are dominated by velocity terms. As a result, many investigators proposed correlations as a function of the jet velocity V_j or of the jet Froude number at impact Fr_j (= $V/\sqrt{gD_j}$), with D_j the jet diameter at impact. The basic relationships that can be found are:

$$\beta = K_e \cdot \left(V_j - V_0\right)^{n'}$$

$$\beta = K_e \cdot Fr_j^{n'} \qquad (3.33)$$

$$\beta = K_e \cdot \left(1 - \frac{V_0}{V_j}\right)$$

where K_e is an entrainment coefficient, $\beta = Q_a/Q_w$ expresses the ratio of air discharge over water discharge and V_0 stands for the minimum inception velocity for air entrainment. Finally, n' is an exponential constant. A summary of all basic relationships can be found in Chanson (1996).

Unfortunately, considerable scatter of the entrainment coefficient K_e indicates that these functional relationships are not correct or, at least, does not incorporate all of the dominant parameters. For free falling jets impinging in a plunge pool, the Froude number is not a significant parameter because gravity does not influence the disturbances on the falling jet. Falvey & Ervine (1988) stated that the turbulence intensity Tu of the issuing jet is the dominant parameter. As a result, the magnitude of the surface disturbances is more related to the square root of the plunge length L than to gravity considerations. Such a type of relationship has been established by Ervine & Elsawy (1975) for rectangular plunging jets:

$$\beta = 0{,}26 \cdot \left(\frac{b}{p}\right) \cdot \left(\frac{L}{D_j}\right)^{0.446} \cdot \left(1 - \frac{V_0}{V_j}\right) \quad \text{approximated by} \quad \beta = 0.13 \cdot \sqrt{\frac{L}{D_j}} \qquad (3.34)$$

whereas b stands for the jet width and p for the jet perimeter. Ervine (1976) and Bin (1984) did the same for circular plunging jets:

$$\beta = \left(0.2 \text{ to } 0.4\right) \cdot \sqrt{\frac{L}{D_j}} \cdot \left(1 - \frac{1}{V_j}\right) \quad \text{Ervine (1976)} \qquad (3.35)$$

$$\beta = 0.05 \cdot Fr_j^{0.56} \cdot \left(\frac{L}{D_j} \right)^{0.4} \qquad \text{Bin (1984)} \qquad (3.36)$$

Bin (1984) also performed a correlation of the data of Van de Sande & Smith (1973) resulting in the following equation for circular plunging jets:

$$q_a = 0.015 \cdot \left(\frac{D_j^2 \cdot V_j^3 \cdot \sqrt{L}}{\sin\theta} \right)^{0.75} \qquad \text{Van de Sande \& Smith (1973)} \qquad (3.37)$$

The turbulence intensity Tu of the issuing jets is indirectly incorporated in these expressions by means of the magnitude of the proportionality coefficient.

According to the three basic mechanisms of air entrainment in Fig. III-15 and based on a vast range of independent experimental studies on different types of hydraulic structures (siphons, conduits, jets,…), Ervine (1998) plotted the maximum rate of aeration q_a as a function of the velocity of the jet V. Beside the relatively good agreement between the results, it can be noticed that the power exponent "n" in the relationship $q_a \sim V_j^n$ varies from values of 8 to 9 at jet velocities of only 2-3 m/s down to values of 1.5 to 2 for jet velocities of 10-15 m/s. This dependence demonstrates that classical relationships of $q_a \sim V_j^3$ are only valid at jet velocities in the range of 3-6 m/s because, at these velocities, the first mechanism is applicable. With increasing jet velocity, the exponent "n" decreases, indicating an increasing influence of the second and the third mechanism. As a result, the extrapolation of classical relationships from model to prototype conditions is not valid. Furthermore, the influence of the turbulence intensity Tu of the jet, considered as the most important parameter, is obvious for mechanisms one and three.

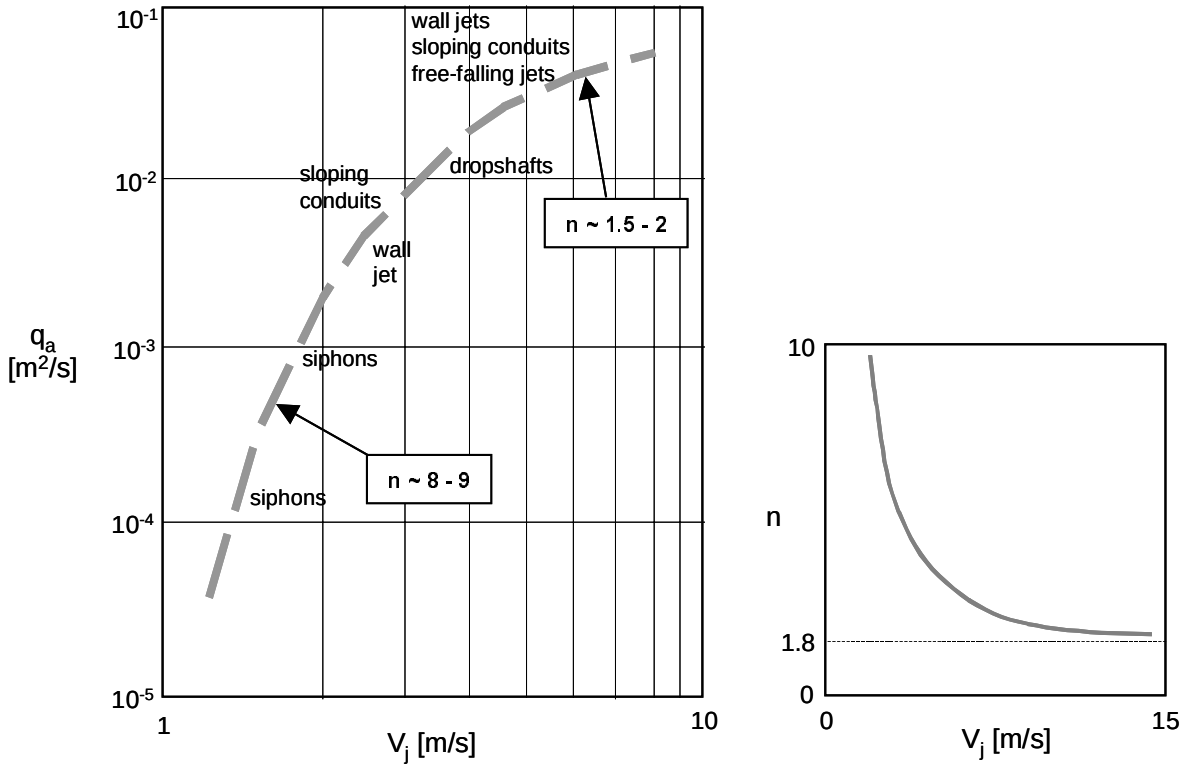

Fig. III-16 Maximum rate of air entrainment in different hydraulic structures as a function of the upstream jet velocity V_j. Corresponding variation of the exponent n with jet velocity V_j (Ervine, 1998).

Ervine (1998) performed a polynomial regression of the used data sets. The incorporation of possible scale effects by use of a minimum inception velocity of about 1 m/s resulted in expression (3.38) for the aeration rate per unit jet width q_a. This first order approach is strictly speaking only valid in a velocity range of 1.5 to 15 m/s, for any conduit slope and for a jet thickness diameter > 30 mm. However, the approach might be reasonably extended towards a higher velocity range. Its accuracy is estimated at about +/- 30 %.

$$q_a = 0.00002 \cdot (V_j - 1)^3 + 0.0003 \cdot (V_j - 1)^2 + 0.0074 \cdot (V_j - 1) - 0.0058 \quad (3.38)$$

A summary of other expressions defining the air content at the point of impact of the jet in the plunge pool is presented in Fig. III-17. Most of the expressions were developed at low jet velocities, i.e. less than 10 m/s. Some studies seem appropriate also at higher velocities, such as the polynomial regression made by Ervine (1998), or the data of Van de Sande (1973), which were obtained for jet velocities of up to 30 m/s. It is interesting to notice that both of these studies exhibit a relationship between the air concentration and the jet impact velocity that is significantly steeper than the ones established at low jet velocities. The polynomial regression curve of Ervine, however, presents much lower air contents than the curves of Van de Sande. The latter shows air contents of up to 80 % at jet velocities superior to 30 m/s. This is in contradiction with the findings of Mason (1989), who stated that the maximum physically plausible air content lies around 65 to 70 %. This physical limit corresponds to the densest possible packing of spherical-shaped air bubbles in a liquid.

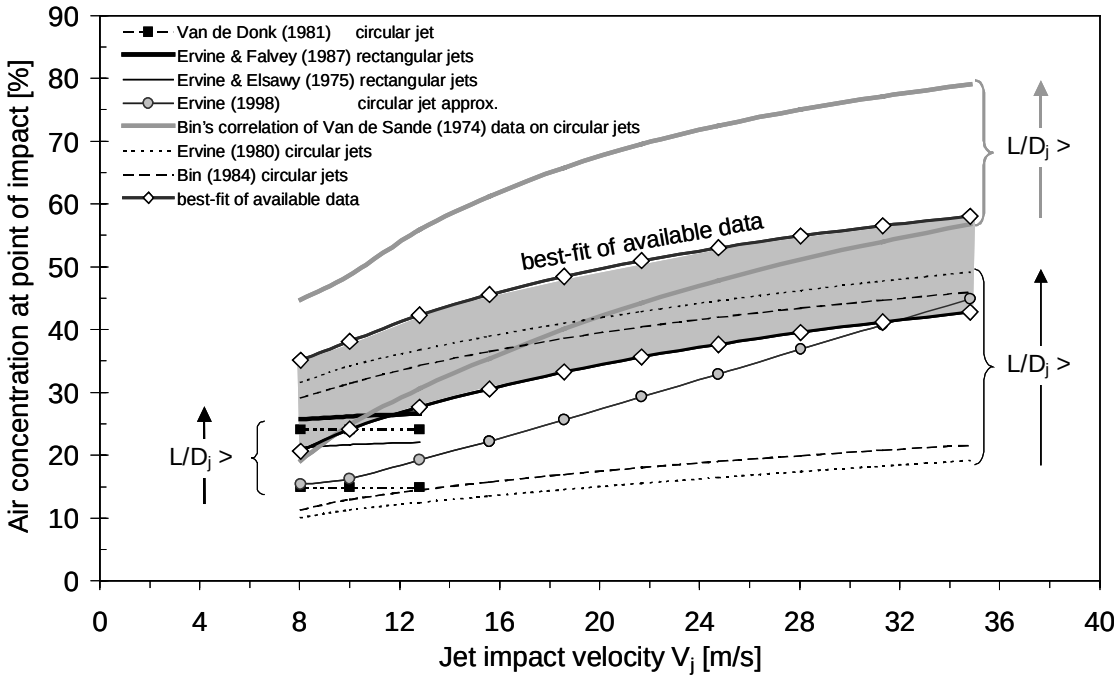

Fig. III-17 Summary of expressions for the air concentration at point of jet impact in a plunge pool. The air content is given as a function of the jet velocity at impact V_j and of the ratio of the fall length over jet diameter L/D_j, for both circular and rectangular plunging jets.

Therefore, it seems convenient to define a best-fit curve based on the expressions for circular plunging jets established by Van de Sande (1973), Bin (1984) and Ervine (1980). As the latter two procure very similar values, they are considered together. This procedure has been applied for different L/D_j values, and corresponds to air contents of 15 % to 35 % at jet velocities of 10 m/s, and air contents of 40 % to 60 % at jet velocities of 30 m/s. This means that, at near-prototype jet velocities, the physical maximum air content is approached, even under laboratory conditions.

3.2.4. Two-phase shear layer pattern

The flow pattern of a plunging jet impinging in a pool has been discussed in § 2.1 and corresponds to the two-dimensional diffusion of a water jet in a pool. For practice, however, it is important to assess how the impingement of real high-velocity jets can be different from this theoretically ideal description. It is apparent that the jet at its point of impact will not exhibit a constant diameter, or a constant air-water outer region. Jet turbulence and jet aeration can generate highly irregular flow conditions. Hence, the turbulent shear layers generated within the pool often are of intermittent nature. The zone of direct jet impact at the water-rock interface thus cannot be clearly defined.

Based on an experimental study by McKeogh (1978), Ervine & Falvey (1987) proposed values for the inner and outer angle of spread of a jet diffusing through a pool. These angles depend on the degree of turbulence and on air entrainment. For practice, the most relevant case is a roughly turbulent jet (Tu ~ 5 %) with an air entrainment on the order of 40 %. Measurements of the outer spread angle in the zone of flow establishment yielded values around 13-14°. In the fully developed flow region, this value increases up to ~ 15°. The inner angle of core decay was estimated at 8°.

The structure of the two-phase flow mixture in a plunge pool due to plunging jet impingement comprises two regions: 1) a diffusion cone with a strong downward flow of air-water, 2) an outer region with swarms of rising air bubbles. The region that is relevant to the present study is the diffusion cone. Inside this cone, a large amount of air bubbles are entrained by the mechanisms outlined in Fig. III-15. They enter the turbulent shear layer of the flow and break up into smaller bubbles. Three regions can be distinguished in the diffusion cone (Fig. III-14):

1) developing air-flow region:	the region where both the turbulent shear layer and the air diffusion layer are still developing, i.e. in the core region of the jet the air content is zero.
2) redistribution air-flow region:	the region directly downstream the point where the two (symmetrical) air diffusion layers intersect. In general, this point of intersection does not correspond to the point where the core of the jet vanishes, as one might expect, but is rather situated slightly upstream. From on this point, the air content under the jet's centreline is rapidly redistributed from zero to a maximum value.
3) fully-developed air-flow region:	the region where both the air content and the velocity profile are fully-developed. This means that the maximum value is encountered on the centreline of the jet.

Fig. III-14 also presents the typical form of the air content distribution in the developing air-flow region and the fully-developed air-flow region. Determination of the air content at a certain location in the plunge pool can now be established provided that the air content profiles are known in region 1 and 3. These, however, depend in turn on the proposed mechanism of air bubble transport from the plunge point towards the pool bottom. This is discussed in the next paragraph.

3.2.5. Air bubble transport and volume of air retained in a plunge pool

The here presented approaches for air bubble transport and air content profiles in a plunge pool are valid for infinitely high plunge pool depths, i.e. the influence of the pool bottom presence is negligibly small. The expressions for the rate of air entrainment, as discussed under § 3.2.3, constitute an upper bound for the air transport down to the pool bottom. Under certain circumstances, the quantity of air that is effectively transported downstream can be less than this maximum value. This depends on the mechanism of transport.

Two mechanisms can be distinguished. The first one is based on Thomas et al. (1983) and Sene et al. (1994) and states that air bubbles are transported by means of coherent vortex structures in a shear layer generated by two co-flowing streams at a different velocity. Vortices should be able to transport air bubbles much further downstream than expected from the mean velocity field. Both experimental

and numerical investigations showed that the main forces on an air bubble in the shear layer are inertia (pressure gradient), buoyancy, lift and drag. Two-dimensional discrete vortex modelling showed that air bubbles will not detrain for velocities above ~ 2.5 m/s. Although these developments are quite pertinent, their practical application is very limited.

Cummings & Chanson (1997) presented air bubble transport as a diffusion-advection problem, where the air bubbles get dispersed by turbulent diffusion and are advected downstream by the mean velocity field. The diffusion equation for circular jets is expressed in cylindrical coordinates:

$$\frac{V}{D_r} \cdot \frac{\partial C}{\partial x} + \frac{C}{D_r} \cdot \frac{\partial V}{\partial x} = \frac{1}{r} \cdot \frac{\partial}{\partial r}\left(\frac{r \cdot \partial C}{\partial r} \right) \tag{3.39}$$

In this equation, r corresponds to the radial direction and V is the velocity component in the longitudinal (x) direction. C stands for the air content at any point downstream of the plunge point and D_r is the turbulent diffusivity in the r-direction (= lateral direction according to Fig. III-14). Steady flow conditions are assumed, as well as a constant diffusivity D_r. Very good correlations with experimental data of air contents in shear layers (Van de Donk 1981, Bonetto & Lahey 1993) were obtained by assuming non-dimensional concentration profiles of the following form:

$$C = \frac{\beta}{\left(\frac{4D^* x}{r_0} \right)} \cdot \left[\exp\left(-\frac{1}{4D^*} \cdot \frac{\left(\frac{r}{r_0} \right)^2 + 1}{\frac{x}{r_0}} \right) \cdot I_0\left(\frac{1}{2D^*} \cdot \frac{\frac{r}{r_0}}{\frac{x}{r_0}} \right) \right] \tag{3.40}$$

These profiles are obtained by assuming superposition of point sources of air entrainment at $r = r_0$. In equation (75), x is the distance downstream from the plunge point, r_0 is the jet radius at impact, I_0 is the Bessel function of the first kind of order zero[1] and D^* is the non-dimensional turbulent diffusivity defined as:

$$D^* = \frac{D_t}{V \cdot r_0} \tag{3.41}$$

$$D_t = D_r \cdot \left(1 + \frac{1}{C} \cdot \frac{\partial C / \partial x}{\partial V / \partial x} \right) \tag{3.42}$$

D_t averages the effects of the turbulent diffusion and of the longitudinal velocity gradient. At each position the diffusivity D_t is a constant that is independent of the radial coordinate r. A suitable global value for D^* should be about 0.1–0.2 and it decreases with increasing Reynolds number of the jet. Similar values for supported or free planar plunging jets can be found in Chanson (1996).

Although equation (3.40) is valid both in the developing air-flow region and the fully-developed air-flow region, the latter region can be described more easily by Gaussian air content profiles. Based on analysis of experimental data, the radial decay of air content is expressed in function of the maximum air content C_{max} at the jet's centreline:

[1] $I_0(u) = 1 + \frac{u^2}{2^2} + \frac{u^4}{2^2 \cdot 4^2} + \frac{u^6}{2^2 \cdot 4^2 \cdot 6^2} + \ldots$

$$C = C_{max} \cdot \exp\left(-\left(1.52 \cdot \frac{y}{Y_{0.1}} \right)^2 \right) \tag{3.43}$$

$Y_{0.1}$ is the location on the lateral axis where $C = 0.1 \cdot C_{max}$. For vertical circular plunging jets, this decay can be approximated by a linear function in the following manner:

$$C_{max} = (C_{max})_0 \cdot \left(1 - \frac{(\Delta x) \cdot \sin\theta}{D_p} \right) \tag{3.44}$$

θ is the angle between the inclined jet and the plunge pool surface and D_p stands for the vertical penetration depth of the air bubbles. As a first approximation $(C_{max})_0$ can be obtained from the quantity of air entrained at the plunge point:

$$(C_{max})_0 = \frac{Q_{air}/Q_w}{1 + Q_{air}/Q_w} \tag{3.45}$$

and the air bubble penetration depth D_p is written as:

$$\frac{D_p}{D_1} = 0.04 \cdot \frac{V}{u_b} \cdot \left(\frac{\sin\theta}{\tan\theta_{out}} \right)^2 \cdot \left(1 - 12.5 \cdot \frac{u_b \cdot \tan\theta_{out}}{V \cdot \sin\theta} + \sqrt{1 - 25 \cdot \frac{u_b \cdot \tan\theta_{out}}{V \cdot \sin\theta}} \right) \tag{3.46}$$

θ is the jet impact angle with the plunge pool surface and θ_{out} is the outer spread angle of the turbulent shear layer in the fully developed flow region. According to Fig. III-14, Ervine & Falvey estimated θ_{out} at about 13-14°.

A second means to account for air entrainment in a plunge pool is to determine the volume of air that is entrained. McKeogh & Elsawy (1980) made experiments to correlate the volume of air entrained within a plunge pool having various jet parameters, such as velocity V, height of fall L, turbulence level Tu and penetration depth L_p. Although a continuous movement of air bubbles in and out of the affected plunge pool is noticed, the entrained volume of air can be considered to be nearly constant. The results showed that a maximum volume is obtained for fall heights greater than the jet break-up length L_b. The most important parameter was found to be the turbulence level. A correlation of the experimental results gives the following expressions for the entrained total volume of air $\forall_t$ for two different turbulence intensities Tu of the issuing jet:

$$\text{Tu} = 5\ \%: \quad \forall_t = 0{,}88 \cdot \forall' \cdot \left(\frac{L}{L_b} \right)^{0{,}85} + \forall_0$$

$$\text{Tu} = 1\ \%: \quad \forall_t = 0{,}9 \cdot \forall' \cdot \left(\frac{L - L_0}{L_b} \right)^{0{,}87} + \forall_0 \tag{3.47}$$

$\forall_t$	=	total volume of air entrained in the plunge pool [m^3]
$\forall'$	=	volume of air entrained when $L = L_b$ [m^3]
$\forall_0$	=	volume of air entrained when $L = 0$ [m^3]
L	=	the height of fall of the jet [m]
L_0	=	the height of fall of the jet required for minimum entrainment [m]
L_b	=	the jet breakup length [m]

These expressions are valid for jet diameters between 6 and 30 mm, and jet outlet velocities between 2 and 5 m/s. An interesting conclusion of the tests is that the pool boundaries and the pool depth affect the volume of air entrained in the pool. The previous expressions for the rate of aeration assume negligible pool depth influence. In practice some influence is always present. The volume of air that is entrained increases from a minimum of only 0.6 times the volume at free penetration (at a pool depth ~ $0.1 \cdot D_p$) to a maximum of 1,28 times this volume (at a pool depth ~ $0,6 \cdot D_p$). Beyond this value, the volume again decreases to a value of ~ $0.9 \cdot D_p$. No values on local air concentration as a function of pool depth are mentioned.

A similar result has been reported by Ervine & Elsawy (1975) and Chanson (1996). They both state that the rate of air entrainment increases with increasing pool depth until a certain pool depth Y_{crit} is reached, based on Jarvis (1970). Once the critical pool depth is reached, the rate of air entrainment stays constant.

$$Y_{crit} = 8.46 \cdot \log\left(\frac{L}{14.14}\right) \tag{3.48}$$

This critical depth can be expressed as a function of the height of fall of the jet L, as shown in equation (3.48). However, when applying a typical jet fall height of 100 m, this results in a critical pool depth of only 7-8 m.

3.2.6. Influence of air entrainment on scour capacity of plunging jets

As outlined in § 3.2.1, several studies studied the influence of the quantity of air entrained in a plunge pool on the scour capacity of plunging jets. One of the first experimental studies was made by Johnson (1967) who pointed out a substantial difference in equilibrium scour depth with and without air entrainment. The jet penetration is graphically represented as a function of the plunge pool depth for a non-aerated water jet and a 50% aerated water jet.

Mason (1989) introduced and quantified the effect of air entrainment in plunge pools as an additional parameter to calculate scour hole depths. A series of two-dimensional model tests were carried out. The expression (3.34) for rectangular jets, proposed by Ervine (1976), was used to predict the amount of air that should be injected into the model for a correct scour simulation. Mason stated that scour might in fact be dependent on the volumetric air to water ratio β instead of the drop height H. The developed formula is similar to equation (2.1), as established by Mason & Arumugam (1985). Although the physical background of the formula is questionable, it is accurate for model data and gives a reasonable upper bound for prototype data:

$$Y = 3{,}39 \cdot \frac{q^{0,60} \cdot (1+\beta)^{0,30} \cdot h^{0,16}}{g^{0,30} \cdot d^{0,06}} \tag{3.49}$$

Y = total scour depth [m]
q = unit discharge at impact point [m^2/s]
h = tailwater depth above the unscoured river bed [m]
d = characteristic particle size of the bed material [m]

Furthermore, air entrainment in model studies was found to be not significantly different from prototype conditions if the physical upper limit of β (close to 2-3) can be attained in the model. This value is feasible for model test conditions. It results from the densest packing conditions of spherical air bubbles in water.

Ervine & Falvey (1987) estimated the reduction in mean pressure at the plunge pool bottom due to air bubble presence in the pool by means of a reduced fluid density ($1-\alpha_i$), with α_i the air concentration at the plunge point, defined as $\beta_i / 1+\beta_i$. The maximum reduction appears just under the zone of flow establishment, as the inner core completely disappears from on that point. The prediction of effective

dynamic pressures needs thus the mean air concentration α as a function of depth. This can be expressed as a linear decay from a maximum value at jet impact to zero at the maximum air bubble penetration depth, according the two-dimensional jet diffusion theory. Based on the continuity equation for diffusing circular jets, the penetration depth D_p in an unconfined pool can be written as follows:

$$\frac{V_j}{V_b} = 3.12 \cdot \left[\frac{D_j}{D_p} + 4 \cdot \tan \alpha_2 + \left(4 \frac{D_p}{D_j} \right) \cdot \tan^2 \alpha_2 \right] \tag{3.50}$$

in which:

V_b = bubble rise velocity ~ 0.25 m/s [m/s]

α_2 = outer spread angle (~ 6-14) [°]

At any pool depth, the mean air concentration and corresponding mean dynamic pressure can be calculated. The volumetric air to water ratio β depends on the decay of the air concentration and on the increasing water discharge of the turbulent shear layer, the latter caused by the entrainment of surrounding water in the plunge pool. The ratio of the mean dynamic pressure with aeration to the mean dynamic pressure without aeration is then expressed as follows:

$$C_p = \frac{\bar{p}}{\frac{1}{2} \cdot \rho_w \cdot V_j^2} = \frac{1}{1 + 3.12 \cdot \beta \cdot \left(\frac{D_j}{Y} - \frac{D_j}{D_p} \right)} \tag{3.51}$$

in which $\bar{p}$ stands for the mean dynamic pressure in case of aeration [N/m^2]. The above expression is based on the hypothesis of a linear decay of the total air flow rate.

Ervine et al. (1997) later on made pressure measurements at a plunge pool bottom for jet velocities up to 25 m/s and derived the following empirical expression for C_p as a function of Y/D_j , valid for Y/D_j ratios higher than 4 to 5:

$$C_p = 38.4 \cdot (1 - \alpha_i) \cdot \left(\frac{D_j}{Y} \right)^2 \tag{3.52}$$

For ratios less than 4 to 5, a constant value of $C_p = 0.85$ is proposed by the authors.

3.3. Rock joint air entrainment

3.3.1. Introduction

The impact of a high-velocity jet into a plunge pool generates significant air entrainment. The highest air content is located at the point of impact of the jet. Due to turbulent diffusion of the shear layer through the pool depth down to the bottom, this air content decreases with increasing pool depth. Also, the buoyancy forces slow down the bubbles. At a certain depth of penetration, the air bubbles encounter a state of kinetic equilibrium and finally rise towards the water surface.

Most plunge pools are not deep enough to reach this equilibrium. They exhibit air bubbles over their whole depth, down to the water-rock interface, where the air is deflected laterally by the flow. Therefore, it seems feasible that some air might be transferred into the rock joints of the pool bottom (Bollaert, 2001). Moreover, due to the significant pressure field that exists in the impingement zone of this water-rock interface, a certain amount of air bubbles might also be dissolved in the water. The quantity of air in solution largely depends on the pressure of the water. As such, this quantity of

dissolved air is a potential source of free air when the pressure of the water suddenly drops inside the rock joint.

Two mechanisms of air bubble transfer from the plunge pool into the rock joint are plausible: 1) convective air bubble transfer, and 2) air bubble transfer by release from the water due to a pressure drop. Both mechanisms are depending on the pressure field at the water-rock interface.

In the following, three types of air presence are discussed: dispersed **free air** bubbles, **dissolved air** bubbles and localized **air bubble cavities**. Each of these types can be present in the water, and an exchange of volume can occur between them. Their physical background is pointed out in the following paragraphs. For the free and dissolved air bubbles, the two-phase mixture is considered as a pseudo-fluid. This involves homogenously distributed air bubbles, no slip velocity, momentum or energy transfer between the air and the water, and only one set of conservation equations for the air-water mixture. For the air bubble cavities, a large amount of air is present at a certain location in the water. The water pressures are defined by the characteristics of the cavity.

3.3.2. Free air bubbles

As mentioned under § 2.2.2, the most important parameter influencing the compressibility and, thus, the wave celerity of a liquid is the presence of free gases. The propagation velocity of a pressure wave is greatly reduced when a small amount of air is present in the form of free bubbles (Pearsall, 1965; Wylie & Streeter, 1978). As such, a small free air content in a liquid can produce wave speeds that are less than the speed of sound in the air alone. The free air bubbles could be imagined as springs that are compressed by a pressure pulse. The spring accelerates the liquid, which, in turn, compresses the next spring. A pressure pulse can so be transmitted at a lower velocity than in a homogenous liquid, in which the transmission is done from one molecule to the next.

According to Fig. III-3, consider a control volume $\forall$, consisting of a liquid volume $\forall_{liq}$ and an air volume $\forall_{air}$. By expressing the bulk modulus of elasticity of the individual components, K_{liq} and K_{air}, the combined bulk modulus of elasticity K yields:

$$K = \frac{K_{liq}}{1 + (\forall_{air}/\forall) \cdot (K_{liq}/K_{air} - 1)} \tag{3.53}$$

In general, there is a strong influence of interfacial heat, mass and momentum transfer between the two phases. For an idealized mixture, i.e. in the absence of temperature differentials, phase transitions, etc., the density and celerity of the mixture can be expressed as weighted combinations of those of the individual phases:

$$\rho_{mix} = \rho_{air} \cdot \frac{\forall_{air}}{\forall} + \rho_{liq} \cdot \frac{\forall_{liq}}{\forall} \tag{3.54}$$

$$\frac{1}{c_{mix}^2} = \rho_{mix} \cdot \left(\frac{\forall_{liq}/\forall}{\rho_{liq} c_{liq}^2} + \frac{\forall_{air}/\forall}{\rho_{air} c_{air}^2} \right) \tag{3.55}$$

The celerity of the mixture is always less than that of the individual phases. For small air contents, such as in a moderately bubbly liquid, the density of the mixture is essentially that of the liquid, but the compressibility is strongly dominated by the air. An increase in pressure results in an increase in celerity, with the value of the liquid as upper bound. The relationship between wave celerity and pressure is expressed by the **ideal gas law**. This law is a combination of different laws (Boyle's law, Charles's law, Avogadro's principle) and constitutes an equation of state. It relates the pressure p, the volume V and the absolute temperature T of a fixed mass of gas as follows (Atkins & Beran, 1990):

$$p \cdot \forall = n \cdot R \cdot T \tag{3.56}$$

in which R is the universal gas constant and n is the amount of molecules (= number of moles). For a constant absolute temperature T and a constant mass of air, an increase in pressure conducts to a decrease in volume:

$$\forall \propto \frac{1}{p} \tag{3.57}$$

The ideal gas law is approximately true for all gases under normal laboratory conditions (room temperature and standard atmospheric pressure) and all gases obey this law more and more closely as the pressure becomes closer to the atmospheric pressure. Real gases do not behave exactly as predicted by the ideal gas law, due to intermolecular forces, i.e. the attractions and repulsions between molecules. However, for the temperatures and pressures encountered in hydraulic systems, the ideal gas law constitutes a good approximation. Thus, the **volume of the mass of free air that is available in a liquid is inversely proportional to the pressure of the liquid**.

By accounting for the elastic properties of the wall boundaries, as defined in equation (3.4), the following expression is obtained for the **wave celerity c_{mix} [m/s] of a homogeneous mixture of free air and liquid**, in which D [m] is the hydraulic diameter, E [N/m^2] is the Young's modulus of elasticity of the boundary, e [m] is the width of the boundary, R [-] is the universal gas constant, T [K] is the absolute temperature, p [N/m^2] is the absolute pressure and m [kg/m^3] is the mass of free air per unit volume of the mixture:

$$c_{mix} = \sqrt{\frac{\frac{K_{liq}}{\rho}}{1+\frac{K_{liq}\cdot D}{E\cdot e}+\left(\frac{mRT}{p}\right)\cdot\left[\left(\frac{K_{liq}}{p}\right)-1\right]}} \tag{3.58}$$

For typical values of free air content in hydraulic systems, up to several percent, the density of the mixture may be taken equal to the density of the liquid $\rho \sim \rho_{liq}$ (Wylie & Streeter, 1978). For higher values, the influence of the mixture's density change should be checked and, if necessary, the correct mixture's density should be used. Martin & Padmanabhan (1979) numerically verified the homogeneous flow assumption for air contents of up to 30 %, and found correct wave celerities. Furthermore, the term K_{liq}/p is very large compared to the unity and the latter may be dropped.

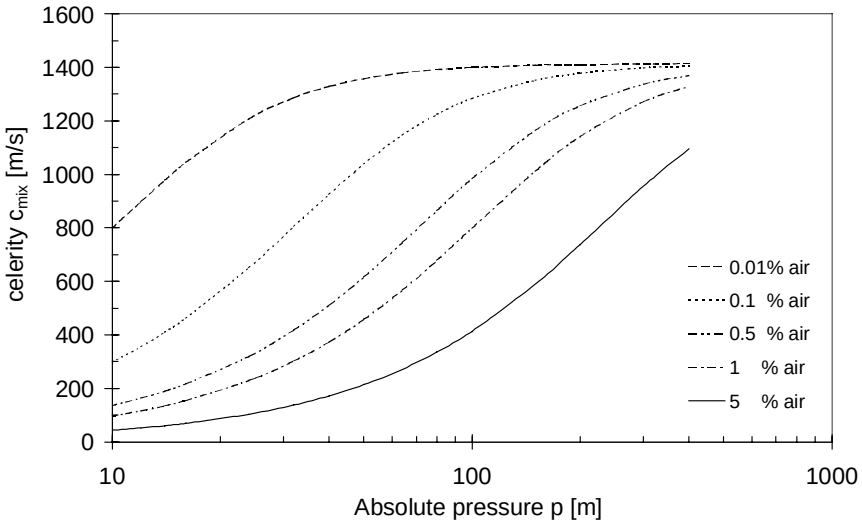

Fig. III-18 The wave celerity of an air-water mixture as a function of its absolute pressure head. The indicated air volumes are valid at atmospheric pressure. The elasticity of the boundaries is neglected.

The wave celerity as defined in equation (3.58) can be visualized as a function of the absolute pressure head for different free air contents and for different boundary characteristics. In case of rock joints, the hydraulic diameter D can be expressed as twice the joint width, and the thickness of the boundary e is considered as infinite. Therefore, the term expressing the elasticity of the boundary in equation (3.58) can be dropped.

Fig. III-18 presents the wave celerity of a homogeneous air-water mixture as a function of the absolute pressure, for different air contents. The indicated air volumes correspond to standard atmospheric pressure conditions and room temperature.

3.3.3. Dissolved air bubbles

Beside the presence of free air bubbles, most liquids also contain some air in solution. Although the dissolved air doesn't influence the compressibility of the mixture, it represents a potential free air volume whenever air release can happen. Air release is highly depending on the governing pressure, and every system subjected to severe pressure changes is sensible to it. Therefore, the dissolved air content should be quantified, as well as its potential to be released.

The mass of dissolved gas in a certain volume of liquid was determined in 1801 by the English chemist William Henry and is called **Henry's law**. This law can be found in standard chemical textbooks and states that the solubility of a gas in a liquid is proportional to the partial pressure of the gas above the liquid, provided that the temperature and molecular structure of the mixture remain constant. The partial pressure of a gas is the contribution the particular gas makes to the total pressure of the sample. In case of air bubbles, the partial pressure of the air is formed by the sum of the partial pressures of the different gases (= Dalton's law) and can be assumed equal to the pressure of the liquid. Henry's law relates the maximum concentration of dissolved air to the air saturation pressure by means of the Bunsen solubility constant S:

$$\frac{\forall'_{air}}{\forall} = m = S \cdot \frac{p_{s,air}}{p_0} \tag{3.59}$$

in which $\forall$ stands for the total volume of the mixture and the volume of dissolved air $\forall'_{air}$ is reduced to standard pressure conditions (= 1 atm) and a temperature of 25° C. The unitary mass of dissolved air m [kg/kg] is defined as the product of the Bunsen solubility constant S with the ratio of the air saturation pressure $p_{s,air}$ to the standard atmospheric pressure p_0 (= 1 atm = 1 bar ≅ 10^5 Pa). For air that is dissolved in water, S equals 0.0184. The pressures are expressed in absolute values.

The mass of dissolved air that can be released from the liquid is then defined as follows (Fig. III-19). Assume that the air-water mixture is in an undersaturated equilibrium at a pressure p_2 and a unitary mass of dissolved air m_2. A sudden decrease in pressure from p_2 to p_1 involves air release, provided that p_1 is smaller than the saturation pressure p_s of the mixture. The unitary mass of air that is released by the liquid to reinstall the dynamic equilibrium is given by (Schweitzer & Szebehely, 1950):

$$m_2 - m_1 = S \cdot \frac{(p_s - p_1)}{p_0} \tag{3.60}$$

Henry's law is a dynamic equilibrium relation between gas molecules that strike the liquid surface and dissolve, and gas molecules that escape back to the gas phase. When a perturbation is applied to the dynamic equilibrium, such as a pressure change, the dynamic equilibrium automatically adjusts the effect by increasing or decreasing the concentration of dissolved gas in the liquid (Atkins & Beran, 1990). This is called the principle of Le Chatelier, a French chemist. These dynamic equilibriums are able to response in both forward and reverse sense: a pressure increase results in a higher air content, while a pressure decrease conducts to a lower air content.

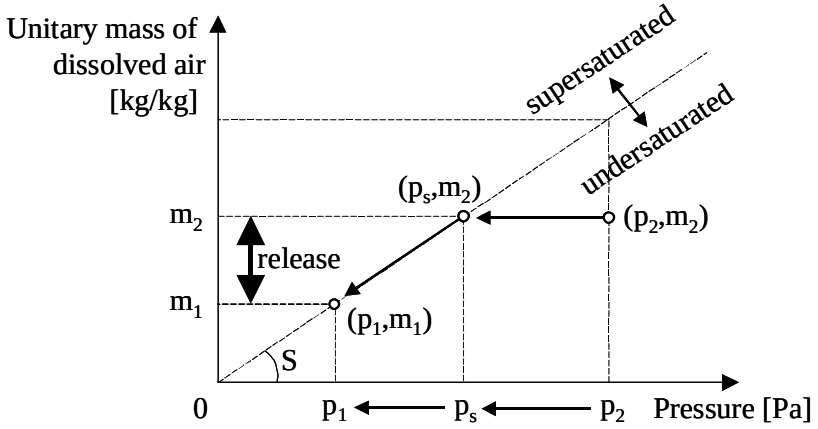

Fig. III-19 Definition sketch of Henry's law for air bubble release and re-solution. A sudden pressure drop from pressure p_2 to pressure p_1 releases a unitary mass of air defined by $m_2 - m_1$.

An application of Henry's law is the production of soft drinks and champagne. In both cases, carbon dioxide is dissolved in the liquid under pressure. When the bottle is opened, the pressure above the solution is released, the solubility of the gas is suddenly reduced, and the gas comes out of solution, pushing out the cork. Another example is the nitrogen that dissolves in the blood of deep-sea divers when they are working at great depths. When the divers return to the water surface, the dissolved nitrogen comes out of solution and forms small bubbles in the bloodstream that can block the capillaries. A hydraulic application of Henry's law can be found in systems where significant free air is entrained in the flow environment at relatively low pressures. This can happen for example at a dropshaft or a siphon spillway. A downstream rise in pressure, due to for example a closed conduit, results in a supersaturated liquid.

Gas release needs a certain time period, called the **incubation period**. For the release of air from water, the incubation period to obtain equilibrium is typically several seconds (Schweitzer & Szebehely, 1950). Moreover, the rate of evolution of the air is directly depended upon a number of parameters, such as the degree of agitation of the liquid, the void fraction of the free gas, the importance of the pressure drop (degree of supersaturation), the solubility constant S, the boundary conditions, and the size and the location of nuclei. The proportionality between the rate of evolution and the degree of supersaturation involves that it is an exponential function of time.

The inverse effects occur in case of sudden pressure increase. However, air re-solution is a much slower process than air release and, therefore, often a one-way process can be assumed. The precise expression and rate of air release in a certain flow environment is a very complex and dynamic problem. For every particular geometric and hydrodynamic situation, a different law applies. Examples of measured air release rates can be found in Schweitzer & Szebehely (1950) and Zielke & Perko (1990). A state-of-the-art relating to gas evolution and adsorption was provided by Wiggert & Sundquist (1979). However, the phenomenon is rather poorly described in literature under normal geometric conditions, i.e. in pipelines. To the author's knowledge, no studies are available on air release inside one-or two-dimensional rock joints.

Application of air release and re-solution to rock joints, due to turbulent high-velocity jet impact, clearly is a very complicated manner. The release must be a function of the drop in pressure, of the nuclei at the wall boundaries of the rock joint as well as of the turbulence level of the flow. In view of this, and pertaining to equation (3.60), the standard assumption for saturated dissolved gas conditions can be assumed as follows:

$$\frac{dm}{dt} = S' \cdot (p_s - p_1) \tag{3.61}$$

This formula makes use of a solubility constant S' that accounts for the effects related to incubation period, nuclei, turbulence, etc. The rate of mass release dm/dt is linearly proportional to the degree of under-pressurization. By neglecting the time effect, so is the unitary mass m of released air.

3.3.4. Air bubble cavity

The third type of air is present under the form of a cavity in the water. As a result, all free air is lumped at one location and no homogenous flow mixture can be accounted for. The pressure and velocity characteristics throughout the water are influenced by the properties of the cavity. A cavity can appear for example at the downstream face of a closing valve. During valve closure, a cavity forms that can be filled with vapor only or with a mixture of vapor and released air. For the latter, during the re-closing phase of the cavity, due to the reflected pressure wave, no air is allowed back into the solution. As such, the cavity may be considered as a free surface reflector (reflection coefficient of $\Lambda = -1$) for the transient pressure waves that propagate through the system. This induces secondary oscillations in the system, which is particularly visible in the middle between the cavity and the upstream end of the transient system.

The key issue is that the maximum possible pressure rise following a cavity collapse is defined by a superposition of the Youkowski pressure $\rho \cdot c \cdot V$ and twice the pressure difference between the initial line pressure and the minimum pressure in the cavity. Experimental observations have shown that the peak pressure that is generated in the trapped gas may be considerably higher than the initial supply pressure. Swaffield & Boldy (1993) presented photographic evidence of the development of the cavity at the downstream face of a closing valve using aviation kerosene as liquid. The film confirms that gas release occurs and that the released gas remains out of solution during subsequent pressure cycles. Furthermore, Fig. III-20 shows that the presence of the cavity influences the pressures and velocities throughout the whole transient system. The secondary oscillation at the midpoint (P_2) is clearly visible.

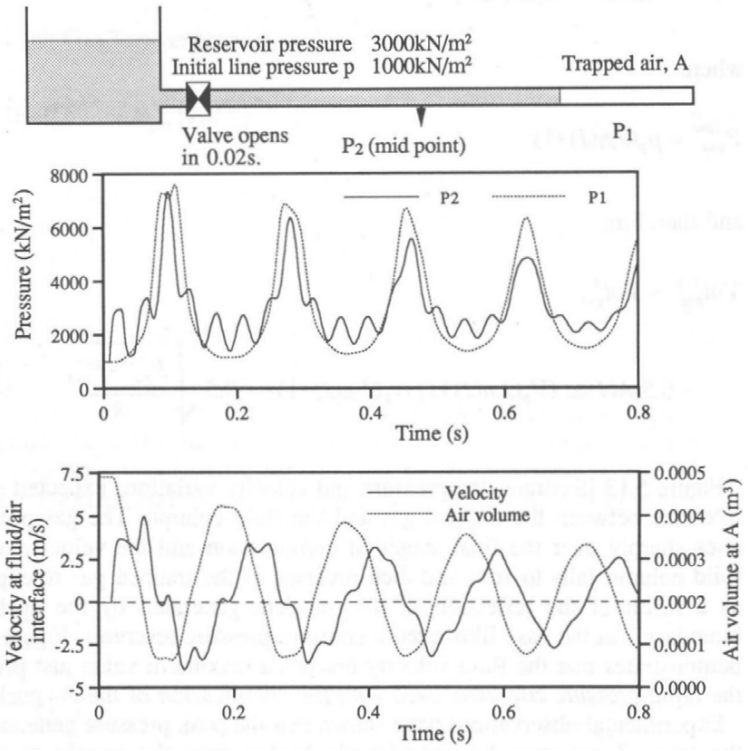

Fig. III-20 Pressure and velocity variations at the interface between the air cavity and the fluid column for a sudden valve opening. The secondary oscillation at midpoint P_2 is caused by internal reflections (Swaffield & Boldy, 1993).

3.3.5. Concluding remarks

Two mechanisms of air bubble transfer from a plunge pool into a rock joint are **convective** air bubble transfer and air bubble transfer by **release and/or resolution** from the water.

The former mechanism corresponds to free air presence in the water and depends on the ideal gas law. This equation of state relationship between temperature, volume and pressure of a gas directly expresses the volume of the available mass of free air as a function of the pressure of the water. As a result, in case of pressure fluctuations, the air bubble volume and the corresponding pressure wave celerity will continuously change. Their relationship is defined by the curves in Fig. III-18.

The latter mechanism corresponds to air that is originally dissolved in the water and that can come out of solution as a function of a sudden pressure decrease of the water. At a pressure increase, the opposite effect happens. The rate and the amount of air that can be released or re-soluted depend on a large number of parameters. For a geometrically and hydrodynamically complex situation, such as a rock joint subjected to jet impact, they are quasi impossible to predict. However, the phenomenon is linearly related to the degree of change in pressure of the liquid.

4. Geomechanical characteristics

4.1. General

Rock can be described in numerous ways. Examples are the geology, the mineralogical texture, or, more quantitatively, some important material properties. Most engineering applications are not directly concerned with the behaviour of the rock material itself, but with the complete rock mass, including the type of rock material and its major discontinuities. Application of fracture mechanics to jointed rock is one such an example. In this section, the rock mass description combines a series of intrinsic material properties, necessary to describe the resistance of the rock itself, with its most significant discontinuity characteristics, necessary to express how a destructive loading is applied to the rock mass. Based on these geomechanical characteristics, different rock mass failure criteria can then be applied. For intermittently jointed rock, for which the network of discontinuities is incomplete, only pure tensile failure will be considered, because of their dominant nature. Fully jointed rock, characterized by a fully completed network of discontinuities, is rather destroyed by means of hydrodynamic uplift of individual rock blocks.

4.2. Rock mass description

The analysis of the hydrodynamic load of a high-velocity aerated jet on a jointed rock mass needs an accurate description of the main geomechanical characteristics of the rock itself as well as of its discontinuities. In the following, only two-dimensional (in the vertical plane) rock mass representations are considered. Table III-6 (Bollaert & Schleiss, 2001b) summarizes the most important parameters that are necessary to describe how the rock will resist against tensile forces. Most of the parameters can be obtained by simple field observations and/or borehole tests. Two groups of parameters can be distinguished: 1) rock intrinsic material properties, 2) rock mass characteristics.

The first three parameters are expressed on a macroscopic scale, i.e. on the scale of tectonically induced layers of different mineralogical composition. The parameter TYPE is related to the crystallographic composition of the rock mass, whereas STRUC refers to the variation of this composition with depth. The rock mass structure STRUC subdivides the rock mass into different layers according to its mineralogical type and thickness H_l.

Group	Parameter	Symbol	Dim
Rock mass	Rock mass type	TYPE	[-]
	Rock mass structure	STRUC	[-]
	Thickness of layer	H_{layer}	[m]
	Rock Quality Designate	RQD	[%]
	Number of joint sets	N_j	[-]
	Joint set dip angle	α_j	[°]
	Joint set persistency	P_j	[%]
	Joint set typical length	L_j	[m]
	Joint set spacing	S_j	[m]
	Joint set width	e_j	[m]
	Joint set friction angle	φ_j	[°]
Intrinsic rock	Uniaxial compressive strength	σ_c	[MPa]
	Uniaxial tensile strength	T	[MPa]
	Young's modulus of elasticity	E_{rock}	[MPa]
	Material density	ρ_{rock}	[kg/m^3]

Table III-6 Main geo-mechanical parameters of: 1) the rock mass with its discontinuities; 2) the intrinsic rock material (Bollaert & Schleiss, 2001b).

For each of the layers, it is essential to know how the different parameters are correlated. This is expressed on a mesoscopic scale and can best be outlined by means of Fig. III-21 (Bollaert & Schleiss, 2001b). This illustrates in a two-dimensional way two frequently encountered layer situations. In Fig. III-21a, an intermittently jointed rock mass pattern is shown. It is characterized by two (N_j = 2) joint sets that intersect at some of their joints. In other words, the potential two-dimensional joint pattern of the rock mass is not fully established and certain joints are of the so-called "closed-end" type. These rocks have joint set persistencies P_j less than 100 %. Here, persistence is defined as the percentage of the rock mass that is already fractured. The second layer (Fig. III-21b) represents a fully accomplished stage of rock mass break-up, i.e. the two-dimensional joint pattern is completely established (P_j = 100 %) and the entire rock mass can be subdivided into a large number of similarly shaped, regularly distributed rock volumes. Despite the intersecting joint pattern, local contact surfaces between the blocks still exist and transmit in-situ stresses from block to the other.

The physical-mechanical processes described in Chapter I (Fig. I-2) that are responsible for destruction of the rock mass are hydrodynamic fracturing and uplift. It is obvious that the behavior of **intermittently jointed rock** is defined by hydrodynamic fracturing. In order to express the resistance of such a rock, it is necessary to relate the hydrodynamic forces to a failure criterion that expresses whether the joint will propagate or not. Such a criterion can be based on linear elastic tensile stresses, often used to determine in-situ horizontal stresses, or on a linear elastic fracture mechanics approach, mainly used by the oil industry to access oil reserves. A particularity of such applications to rock joints lies in the highly dynamic character of the impacting hydrodynamic forces: the loading rate modifies the static resistance of a rock mass and should be taken into account in a dynamic analysis.

In the case of **completely jointed rock**, its resistance against hydrodynamic failure can be expressed by some typical rock block characteristics, such as dimensions, shape, weight and shear and/or cohesive forces along the joints. A dynamic equilibrium of the forces acting on the rock block can then be expressed. This equilibrium depends on the instantaneous difference in pressure distribution above and underneath the rock block and, therefore, has to be formulated as a function of time (impulse). The calculated net impulse of a pressure wave on a rock block will determine whether the block will be ejected from its surrounding mass.

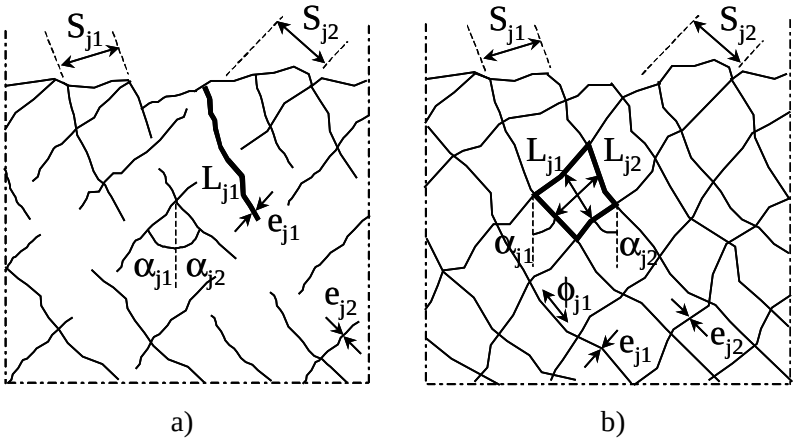

Fig. III-21 Two most encountered rock mass layer situations (N_j = 2): a) intermittently jointed rock (P_j < 100 %); b) completely jointed rock (P_j = 100 %) (Bollaert & Schleiss, 2001b).

For both of the aforementioned failure types, the end of the scour can be estimated as follows. First, maximum scour will be reached when the hydrodynamic pressures in the closed-end joints are not capable anymore to further propagate the joint. Second, for the uplift criterion, scour will come to an end when the equilibrium of forces as a function of time is insufficient to displace a rock block from the mass. In the following, each of these failure criteria will be discussed more in detail.

4.3. Failure criteria for intermittently jointed rock

4.3.1. General applicability

Failure criteria for intermittently jointed rock deal with the initiation and/or propagation of rock discontinuities. Only pure tensile failure criteria are considered. Shear stress based criteria, such as the Mohr-Coulomb or Hoek-Brown criteria, are not considered in the present analysis. Assuming that the rock is linear elastic, homogeneous, isotropic and impermeable, two main approaches to crack initiation and propagation are distinguished: the **strength-of-materials** approach and the **linear elastic fracture mechanics** approach. Both assume a continuum behavior of the rock mass. However, as can be seen at Fig. III-22, this assumption is very relative and expresses two concepts that are of crucial importance to rock mechanics: the effect of the **scale of the structure** and of the **material non-linearity**. The three elements in Fig. III-22 represent a crack length that is close to the characteristic dimension l_c of the structure itself, according to the scale at which it is viewed. This strictly means that neither of the above approaches would be applicable to crack initiation. However, rock discontinuities from a practical engineering perspective are on the scale of the Figs. III-22b & III-22c. At these scales, the crack tip might be tiny compared to the surroundings.

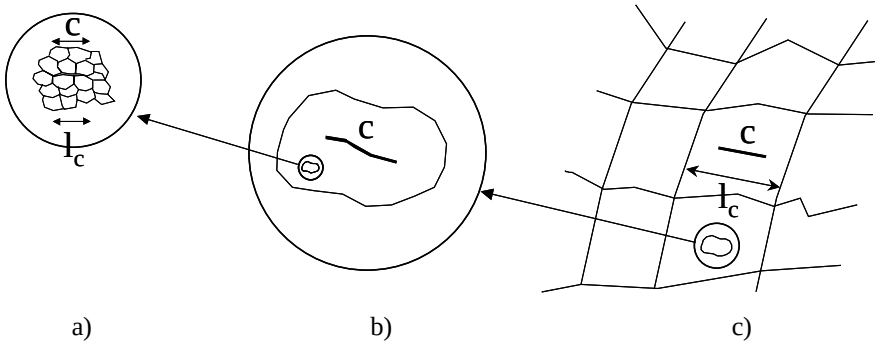

Fig. III-22 The influence of the structural scale on the concept of continuum in rock mechanics: a) microscopic view (agglomeration of grains), b) intermediate scale, c) blocky rock mass.

The question is to know what is the nature of the rock material at the crack tip. The rock will always behave as is its nature, but its response will have characteristics according to the scale of the structure that's being considered. The nature of the rock is expressed by stress-strain relationships, as indicated at Fig. III-23. Two main relationships can be outlined. The first one represents an elastic-brittle behavior and is usually assigned to rock at engineering scales. It forms the basis of the strength-of-materials approach. At the material's tensile strength T, there is an instantaneous drop in load-carrying capability. No plastic behavior or creation of a damage zone around the crack tip is considered, the rock simply withstands or fails under the loading. This of course doesn't correspond to the exact rock nature, but, at an engineering scale, sometimes constitutes a reliable response.

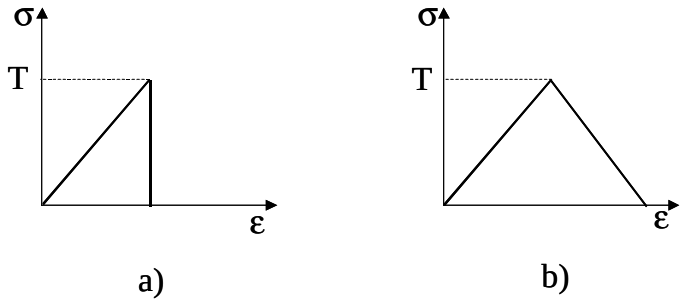

Fig. III-23 Stress-strain relationships for a rock mass (T = tensile strength): a) elastic-brittle behavior, b) elastic-plastic behavior.

The second stress-strain relationship shows strain softening after a peak stress has been reached, corresponding to an elastic-plastic behavior. A gradual damage zone develops ahead of the crack tip and material non-linearities can be simulated. This more closely corresponds to the exact nature of the rock and can be approached by a non-linear fracture mechanics approach. However, when the dimension of the plastic damage zone is rather small in comparison with typical rock volumes or crack lengths, this zone can be neglected and a linear elastic fracture mechanics approach is sufficient to describe the rock's nature. A major disadvantage of this method is that it needs a pre-existing flaw in the material. Crack initiation cannot be predicted.

A unified, comprehensive model for crack initiation and propagation should make use of the Strength-Of-Materials approach to predict crack initiation in a quasi-intact material and the Linear Elastic Fracture Mechanics approach to express crack propagation. These approaches are promising but only plausible if certain scale conditions are satisfied. Based on the standard technique for fracture toughness testing of metallic materials (ANSI/ASTM standard E399-78a), a specimen size restriction has been developed in order to assure that the size of the plastic damage zone ahead of the crack tip is small with respect to the other specimen dimensions and/or the crack size. Because rocks exhibit microcracking as main non-linearity, Schmidt (1980) suggested a similar minimum crack length criterion for rocks:

$$a > 2.5 \, (K_{Ic} / T)^2 \tag{3.62}$$

with K_{Ic} the fracture toughness (for definition, see § 4.3.3) and T the tensile strength of the rock mass. This expression yields minimum crack lengths of a few millimetres to a few centimetres for most rocks. Thus, a fracture mechanics approach seems plausible for jointed rock.

Similarly, Ingraffea (1984; in Atkinson, 1984) tested the applicability of fracture mechanics analyses to crack initiation from a circular hole in a compressively loaded plate, at two largely different scales (factor 100). He found that at small scales (tens of mm) fracture mechanics overestimates the critical load on the structure, whereas at large scales (m), accurate crack prediction was obtained. As a result, by increasing the scale of the structure under consideration, the material was made more "brittle", even if its correct brittleness remained constant. Several researchers (Hillerborg et al., 1976; Sih, 1980; Carpinteri, 1982) investigated the relation between the structural scale, the tensile strength and the fracture toughness of the material. Carpinteri (1982) proposed the following structure-material brittleness number "s":

$$s = \frac{K_{Ic}}{T \cdot a^{1/2}} \propto \sqrt{\frac{\delta_c}{a}} \tag{3.63}$$

with "a" a characteristic length of the structure and δ_c a characteristic crack opening displacement. When assuming that K_{Ic} is proportional to T and δ_c, the brittleness number "s" becomes proportional to the ratio of the characteristic material and structural (geometrical) parameters. Although this concept has not yet been developed to the point of general applicability, its analogy with the Schmidt (1980) relation (equation (3.62)), derived from metallic materials and adapted for rocks, is obvious.

Therefore, structural scale effects are of crucial importance when applying tensile failure criteria. Fig. III-24 presents the applicability of the above concepts as a function of a structural scale parameter, depending on the ratio of characteristic length to crack length. It can be seen that for jointed rock, fracture mechanics is convenient. However, with decreasing joint size, the strength based on the fracture mechanics approach becomes equal to the tensile strength of the material. For the extreme case of very small joints (mm), fracture mechanics overpredicts the material strength and the strength-of-materials approach is more appropriate. Laboratory fracture toughness tests use pre-existing cracks with a typical length of several cm to procure results that are representative for jointed rock.

In the following, each of the approaches will be outlined more in detail. It should be clear that prediction of crack initiation and propagation is not a simple matter. Both of the compared approaches have their limitations. They both oversimplify material behavior. The Strength-Of-Materials approach

is independent of the scale of the structure, while the linear elastic fracture mechanics model requires some guesswork to make it seem applicable.

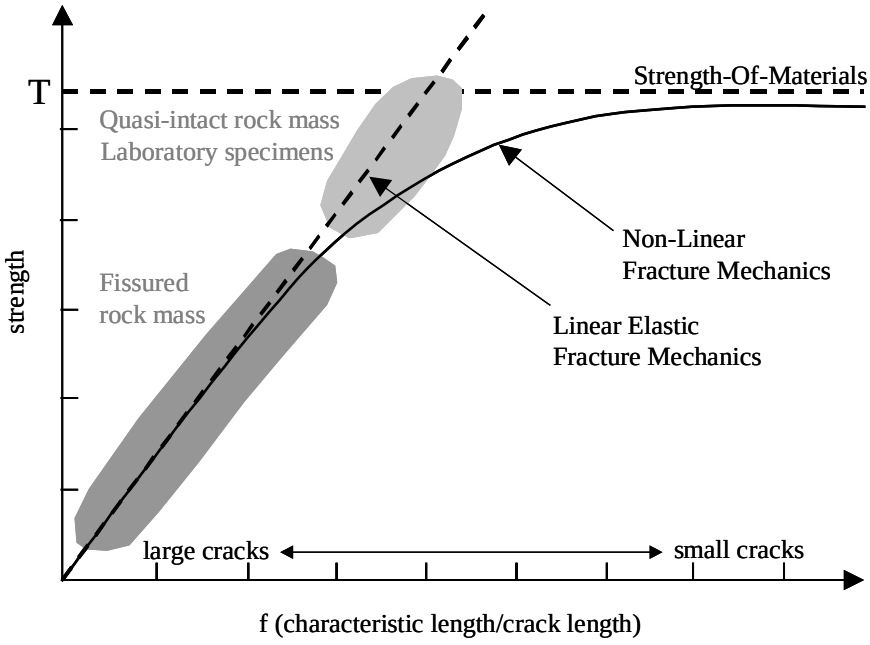

Fig. III-24 Applicability of tensile failure approaches in function of the specimen and crack dimensions.

4.3.2. Strength-of-materials approach

The strength-of-materials approach is applied in underground engineering problems, such as rock tunnels, earthquake research, and hydraulic fracturing techniques. It predicts crack initiation by comparison of a tensile stress to the tensile strength T of the rock material. Strictly speaking, the approach is only valid for a case without initial cracks. The rock is assumed elastic-brittle, no plastic yielding is considered and therefore crack initiation is instantaneous. No information regarding the crack length is available.

As shown in Fig. III-24, this approach constitutes an upper bound of the estimated material strength and is only applicable at small scales. Typical engineering scales often are larger and it is known that, as a function of the scale of the considered problem, elastic-brittle rock behavior can be a vast oversimplification of the crack initiation process. Nevertheless, this approach can be useful as an upper estimate of the ultimate rock strength, especially in the case of quasi-intact rock. It has largely been used during hydraulic fracturing tests to determine the in-situ stresses in a rock mass. This is discussed later on.

The idea of global strength of a rock mass can be used to express an equilibrium of forces on a partially jointed rock block, such as presented in Fig. III-25. A first approximation can be made by a one-dimensional approach. Assuming that a part "2a" of the total width "W" is already broken up, which defines the persistency "P" of the rock block, the following equilibrium law is obtained:

$$\sigma_{max} \cdot P = T \cdot (1 - P) \quad \text{with} \quad P = \frac{2a}{W} \tag{3.64}$$

in which T stands for the tensile strength of the material. This equation expresses the loading conditions for which the rock block will break up completely.

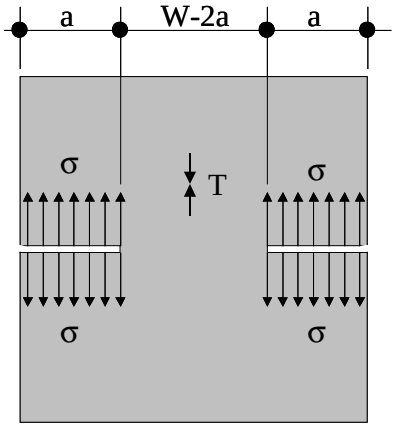

Fig. III-25 Applicability of tensile failure approaches in function of the specimen and crack dimensions.

This approach overestimates the resistance of the rock mass at typical engineering scales, such as for jointed rock blocks. Therefore, it should be applied with a lot of precaution.

4.3.3. Linear elastic fracture mechanics approach

The scientific engineering discipline of linear elastic fracture mechanics has evolved from the necessity to prevent dangerous collapse of structures such as bridges or dams. While the original framework to describe the strength of materials was already provided by Mohr (1900) and Coulomb (1773), the first successful analysis of a fracture-dominant problem was done by Griffith (1921), who considered the propagation of brittle cracks in glass. He formulated the well-known concept that an existing crack will propagate if thereby the total energy of the system is lowered, and a simple energy balance can be written. The decrease in elastic strain energy within the stressed body as the crack extends counteracts the energy needed to create new crack surfaces.

In the middle 1950's, Irwin (1957) contributed a major advance by showing that this energy approach is equivalent to a **stress intensity approach**, by which fractures only occur when a critical stress distribution ahead of the crack tip is reached. The material property governing fracture may therefore be stated as a critical stress intensity K_c, or in terms of energy as a critical strain energy release rate G_c. It is the equivalence between G and K that provided the basis for development of the discipline of linear elastic fracture mechanics. A survey of the main aspects of fracture mechanics can be found in Atkinson (1987).

Fracture mechanics was originally developed in order to avoid fractures. Presently, there are two schools of thought: one aims to provide simply definable conditions to remain on the safe side and the other one is more concerned with the physical evolution and propagation of the fracture once the loading limit has been exceeded. The majority of work in fracture mechanics correspond to the first group and effectively is very convenient to express a clearly defined limit of initiation and/or propagation. The second group however is also of great interest, especially in the field of rock mass failure by hydrodynamic jet impact, because it can account for subcritical crack growth phenomena, such as stress corrosion and fatigue.

Any description of fracture mechanics starts with an overview of the three fundamental modes of fracture of an ideal flat, perfectly sharp crack. These are termed mode I, purely tensile, mode II, in-plane shear, and finally mode III, anti-plane shear (Fig. III-26). For rock mass failure by hydrodynamic action, mode I is predominant, although mixed-mode failures sometimes can appear. In the following, only purely tensile fracturing (mode I) will be considered. Plane strain conditions are assumed throughout the analysis.

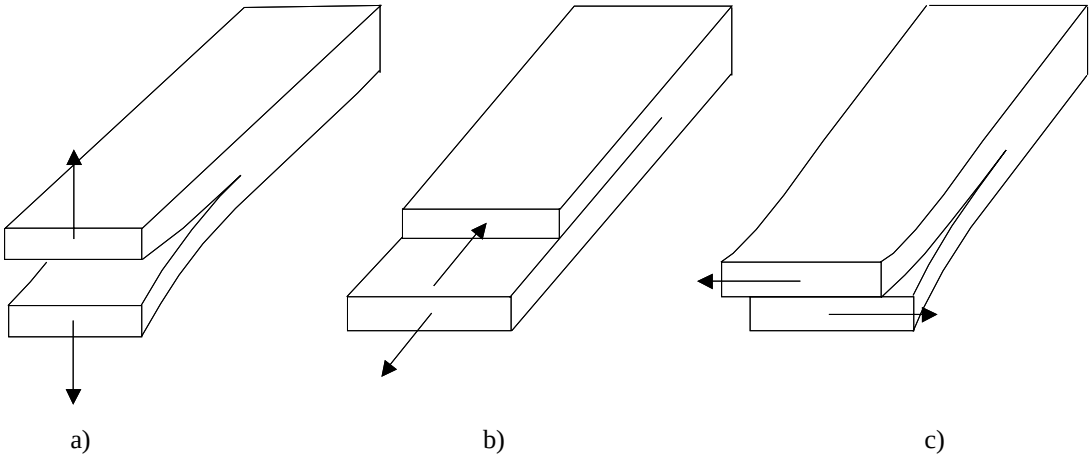

Fig. III-26 Schematic drawing illustrating the three fundamental modes of fracture: a) mode I, purely tensile or opening mode, b) mode II, in-plane shear or sliding mode, c) mode III, anti-plane shear or tearing mode (Ewalds & Wanhill, 1986).

The stress distribution around the crack tip is of crucial importance and always of similar shape. Thus, tests on suitably shaped and loaded specimens make it possible to determine what flaws are tolerable in an actual structure under given conditions. K_I is considered as a material constant that expresses the magnitude of the stress field around a crack tip. It is called the **stress intensity factor**. Assuming that the rock mass is a homogenous, linear elastic, isotropic and impermeable medium, the stresses in the vicinity of the crack tip take on the following form for mode I loading:

$$\sigma_{ij} = \frac{K_I}{\sqrt{2\pi r}} \cdot f_{ij}(\theta) \; + \; \text{higher order terms} \tag{3.65}$$

where r, θ are the cylindrical polar coordinates of a point with respect to the crack tip, as shown in Fig. III-27. This expression can be simplified and the higher order terms can be neglected provided that the region of non-linear behavior in front of the crack tip is negligibly small compared to the dimensions of the crack and the cracked body. It can be seen that the stresses are proportional to $r^{-1/2}$. The coefficient of the $r^{-1/2}$ - term is exactly the already mentioned stress intensity factor K_I.

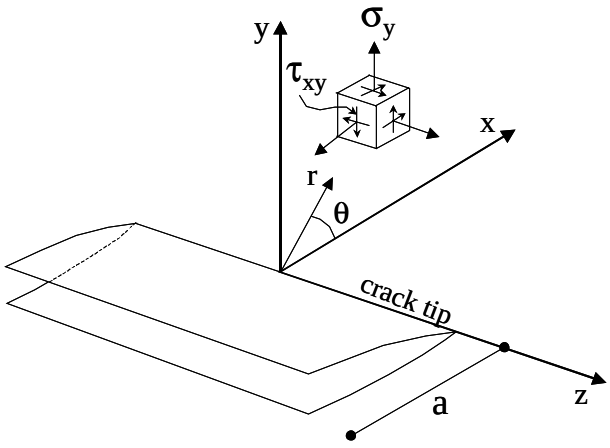

Fig. III-27 Rectangular and polar coordinate frames for linear elastic analyses of the crack tip stress field. Mode I tensile opening is shown (Ewalds & Wanhill, 1986).

The stress intensity analysis is simplified by assuming that the cracked body has a two-dimensional stress-strain field at the crack tip that does not change along the z-direction (plane strain assumption). Based on dimensional analysis and on Griffith's analysis, it can then be outlined that the general form of the stress intensity factor takes (Ewalds & Wanhill, 1986):

$$K_I = \sigma_{water} \cdot \sqrt{\pi \cdot a} \cdot f = \sigma_{water} \cdot \sqrt{\pi L_{j1}} \cdot f \tag{3.66}$$

in which σ_{water} stands for the applied stress and f for a function that accounts for the geometry of the rock block and its crack extension, the loading conditions and the edge effects. The actual length of the joint L_{j1} can be found in Fig. III-21.

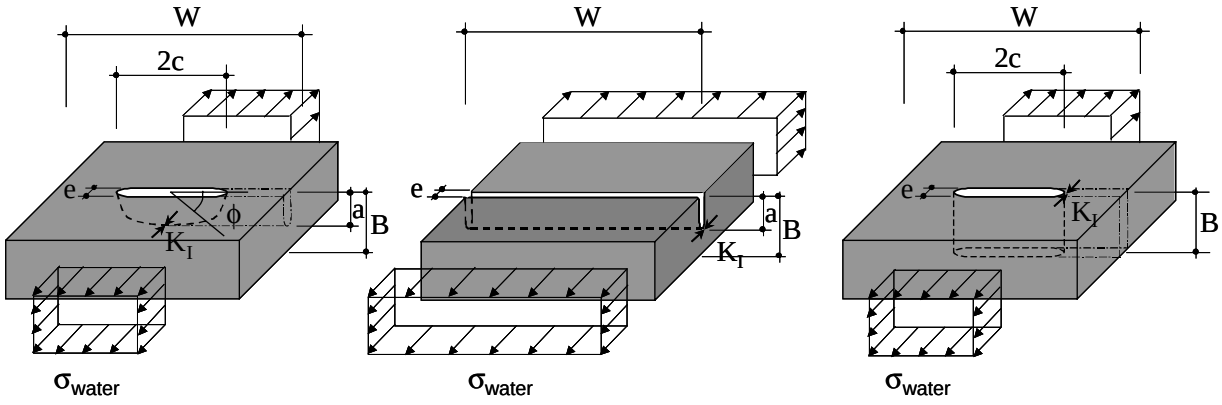

Fig. III-28 Proposed framework for the basic geometrical configurations of intermittently jointed rock: a) semi-elliptical (EL) joint; b) single edge (SE) joint; c) center-cracked (CC) joint. The water pressures are applied from outside the joints. No multiple joint configurations are considered.

For intermittently jointed rock, three relevant joint geometries are presented at Fig. III-28. They are called the **semi-elliptical** joint (EL), the **single-edge** joint (SE) and the **center-cracked** (CC) joint**.** For each of these configurations, the boundary correction factors f are defined as follows:

$$f\left(\frac{a}{B},\frac{a}{c},\phi\right) = C \cdot \frac{\left(\sin^2\phi + \frac{a^2}{c^2}\cdot\cos^2\phi\right)^{1/4}}{\frac{3\cdot\pi}{8} + \frac{\pi}{8}\cdot\frac{a^2}{c^2}} \qquad \text{semi-elliptical joint} \tag{3.67}$$

$$f\left(\frac{a}{B}\right) = \left[1.12 - 0.231\left(\frac{a}{B}\right) + 10.55\left(\frac{a}{B}\right)^2 - 21.72\left(\frac{a}{B}\right)^3 + 30.39\left(\frac{a}{B}\right)^4\right] \qquad \text{single-edge joint} \tag{3.68}$$

$$f\left(\frac{c}{W}\right) = 1 + 0.256\cdot\left(\frac{c}{W}\right) - 1.152\cdot\left(\frac{c}{W}^2\right) + 12.2\cdot\left(\frac{c}{W}\right)^3 \qquad \text{center-cracked joint} \tag{3.69}$$

The expression for the semi-elliptical joint includes the elliptical integral of the second kind and a factor C that depends on the ratios a/c, a/B, c/W and on the angle ϕ. The factor C is presented graphically in Fig. III-29 for c/W ratios of 0.1 and 0.5 and for the angles ϕ of 90° and 0°. The former angle corresponds to the midpoint, while the latter angle represents the corner points. An analytically exact expression for all parameters can be found in Newman & Raju (1981).

The expression for the single-edge joint constitutes a polynomial approximation that has an accuracy of 0.5 % for a/B < 0.6. For values of a/B superior to 0.6, the correction factor increases considerably. The expression for a center-cracked joint has an accuracy of 0.5 % for a/B < 0.35. Other expressions for single-edge and center-cracked joints can be found in Paris & Sih (1965) and Ewalds & Wanhill (1986).

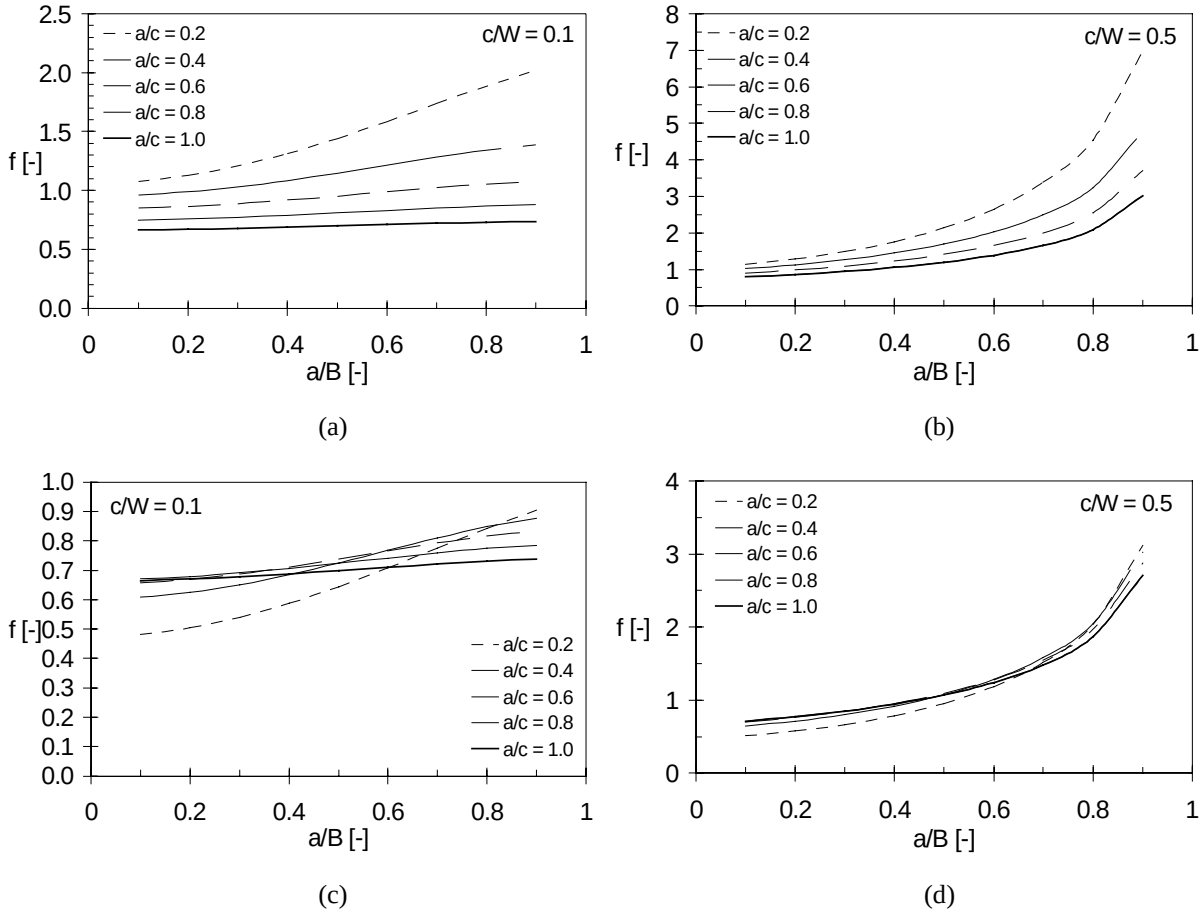

Fig. III-29 Boundary correction factors f for the semi-elliptical joint (EL):
a) for c/W = 0.1 and $\phi = 90°$; b) for c/W = 0.5 and $\phi = 90°$;
c) for c/W = 0.1 and $\phi = 0°$; d) for c/W = 0.5 and $\phi = 0°$;

The next step is to determine the critical value of the stress intensity factor, i.e. the value at which the crack propagates in an unstable manner. This is called the **fracture toughness K_{Ic}**, and is determined experimentally. In-situ investigations, by means of the hydraulic fracturing or jacking method, and laboratory specimen tests on pre-notched rock cores are the most common methods to determine the fracture toughness. They are discussed later on. The relationship between the stress intensity factor and the fracture toughness is analogous to the relationship between stress and a strength measure. For pure mode I loading, there will be no crack propagation as long as the following relation holds:

$$K_I < K_{Ic} \tag{3.70}$$

This expression is an equilibrium law and specifies that cracks extend unstably beyond some critical value of a fracture mechanics parameter. Crack extension is considered here as fast or catastrophic because the propagation speed can approach that of sound in the medium, provided that the crack is

isolated and the walls are free. For rock applications, typical maximum speeds are on the order of several thousands of m/s.

Nevertheless, crack extension also can occur at K_I values substantially less than the critical value K_{Ic}. This phenomenon is called **subcritical crack growth** and has been at first observed in glass (Grenet, 1899). Since then, experiments were conducted in order to detect the phenomenon for other brittle materials, such as ceramics, minerals and rocks (Haimson & Kim, 1971; Haimson, 1978; Scholz & Koczynski, 1979; Kim & Mubeen, 1981; Atkinson, 1982 & 1984, etc.). Subcritical crack growth relates the crack propagation speed v to the stress intensity factor K_I. A schematic diagram of the crack propagation speed versus stress intensity factor is visualized in Fig. III-30.

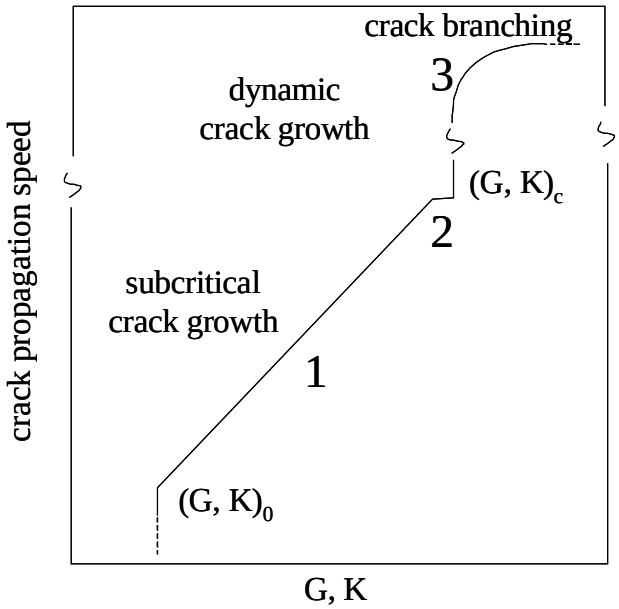

Fig. III-30 Crack propagation speed v versus stress intensity factor K_I or strain energy release rate G. Typical behavior for ceramics, glasses, rocks and minerals. Note the discontinuous velocity scale (Atkinson, 1984).

The subcritical crack growth relationship is often expressed as v = v (K,G). The specific form of this relationship depends on which mechanism is responsible for the crack growth. It is mostly derived from experimental tests. It is generally assumed that subcritical crack growth ceases beyond some small value of G or K, typically 20 to 30% of the fracture toughness (Atkinson, 1984). Above this threshold, subcritical growth can occur through a variety of different mechanisms. From the geophysical viewpoint, the most important examples are stress corrosion and cyclic fatigue.

The crack propagation speed v increases with increasing stress intensity. This holds until the critical fracture toughness value K_{Ic} is obtained. At this level, catastrophic crack growth occurs and the crack propagation rate rapidly accelerates towards a velocity close to the speed of sound in the medium. Crack branching may happen during severe dynamic loading and may generate an increase of the static fracture toughness of the material in question. This aspect can be of importance in rock fracturing due to high velocity jet impact and is discussed later on.

Subcritical crack growth that occurs in the presence of some chemically active environment, such as liquid water or water vapor, is referred to as **stress corrosion**. It is also called static fatigue. In its most elementary form, the theory of stress corrosion postulates that the presence of an environmental agent causes the progressive weakening of the material's strained bonds. The key chemical expression holds

for crystalline silicates and silicate glasses and quartz in a water environment. It represents the hydrolysis of strong Si-O bonds to weaker hydrogen bonded hydroxyl groups linking the silicon atoms. Many other, far more complex chemical reactions may occur. Many of them are not well understood. The influence of the chemical reaction on the v(K,G) relationship is very important and must be determined experimentally.

As indicated in Fig. III-30, three principal regions exist for the v(K,G) relationship. The first region is the most important because it relates a wide range of applied stress intensities to crack propagation speeds of several orders of magnitude. In the second region, the crack speed is limited by the rate of diffusion of the active species to the crack tip. This region has rarely been observed for rocks. Region 3 stands for the sudden transition to the fracture toughness value. Crack speed versus stress intensity diagrams have been obtained for a large number of rock types and are discussed in Atkinson (1987). Comparison of all these data is shown in Fig. III-31 by using a normalized stress intensity factor K_I/K_{Ic}, as well as an absolute crack propagation velocity v(K). This velocity v is often expressed as a function of K in the following manner:

$$v = v_0 \cdot K^n \tag{3.71}$$

in which v_0 and n are constants. The constant n is called the subcritical crack growth index and can be found at Table III-7 for different rock materials (Atkinson, 1984). On a logarithmic scale, it represents the slope of the K-v relationship. The presented values correspond to a water environment at 20-25 °C. The term v_0 is at present associated with a lot of uncertainty, and values have rarely been published. In the present work, its value is determined based on the fatigue exponents "m", which are also presented at Table III-7. This is outlined in Chapter VII, § 4.2.1.

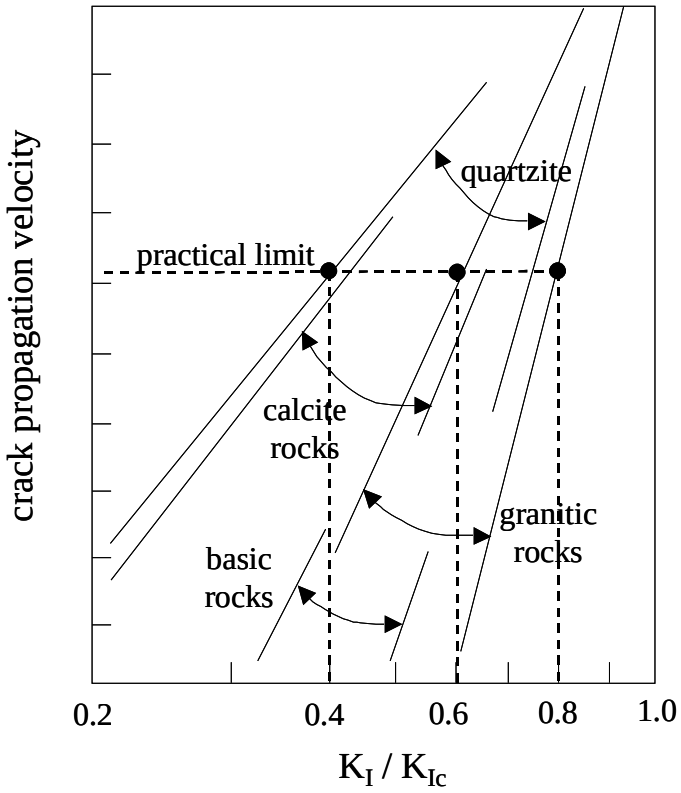

Fig. III-31 Subcritical crack propagation velocity as a function of normalized stress intensity for different geologic materials. Data obtained at room temperature in liquid water (Atkinson, 1984).

Type of rock	Subcritical index n	Fatigue exponent m	Coefficient C
Arkansas novaculite	25	8.5	1.0E-8
Mojave quartzite	30-38	10.2-12.9	3.0E-10
Ruhr sandstone	8-11	2.7-3.7	2.0E-6 - 1.0E-6
Tennessee sandstone	14	4.8	4.0E-7
Solenhofen limestone	26-28	8.8-9.5	1.1E-8
Carrara marble	15	5.1	2.5E-7
Falerans micrite	26	8.8	1.1E-8
St-Pons marble	26-29	8.8-9.9	1.1E-8 - 4.0E-9
Tennessee marble	9	3.1	2.0E-6
Merrivale granite	40-68	13.6-23.1	1.5E-10 - 4.0E-14
Westerley granite	34-36	11.8-11.9	8.0E-10
Yugawara andesite	26	8.8	1.1E-8
Black gabbro	29-36	9.9-12.2	4.0E-9 - 5.0E-10
Kinosaki basalt	33	11.2	1.2E-9
Ralston basalt	24	8.2	1.8E-8
Whin Sill dolerite	29	9.9	4.0E-9

Table III-7 Subcritical index n (Atkinson, 1984) and fatigue exponent m as a function of the type of rock. The environmental conditions correspond to water at 20-25 °C.

The second mechanism responsible for subcritical crack growth is **cyclic fatigue**. Burdine (1963) at first showed that compressive cycling of rock results in a systematic weakening of the material, which eventually results in failure. Hardy & Chugh (1970) and Haimson & Kim (1971) have performed many tests on a variety of rock types, which clearly demonstrate the progressive weakening of rock due to cyclic loading. Haimson & Kim (1971) performed a number of uniaxial compression tests, in which the stress was cycled between 50% and 80% of the uniaxial failure stress. They found that the number of cycles to failure, N, was related to the amplitude of the stress cycle S_a, with $S_a = \sigma_{max} - \sigma_{min}$. It is found that log N increases linearly with a decrease in stress amplitude, just like in the case of metallic materials.

However, some experimental results for brittle materials (Evans & Fuller, 1974) showed that the crack propagation speed under cyclic tests could be predicted by simply integrating the stress corrosion contribution, with no fatigue influence at all. Based on these results, it might be thought that fatigue could be entirely explained by stress corrosion. Scholz & Koczynski (1979) made a series of tests that show that, at small values of the cycle amplitude, stress corrosion seems to be the dominant mechanism because of the very little cycling of the stress. Nevertheless, at moderate and high values of this amplitude, the results could only be explained by cyclic fatigue.

In the 1980's, other evidence was made available of crack propagation under cyclic fatigue, regardless of stress corrosion (Dauskardt et al., 1987; Reece et al., 1989). The notion of growing crack propagation rate with increasing stress amplitude was confirmed by Kim & Mubeen (1981) who performed cyclic loading tests on three-point bend fracture specimens of Westerley granite. Their results fit an equation of the type that was originally proposed by Paris et al. (1961) to describe fatigue crack growth in metals and is written as follows:

$$\frac{da}{dN} = C \cdot (\Delta K_I)^m \tag{3.72}$$

C and m are material parameters that can be determined by the experiments and ΔK_I is the difference of maximum and minimum stress intensity factors at the crack tip. Fig. III-32 shows two experimentally derived results (Kim & Mubeen, 1981) of crack propagation rate, whereas the m value is quite constant at 11.8-11.9 and C values are between 2.10^{-10} and 8.10^{-10}, as a function of the ratio of

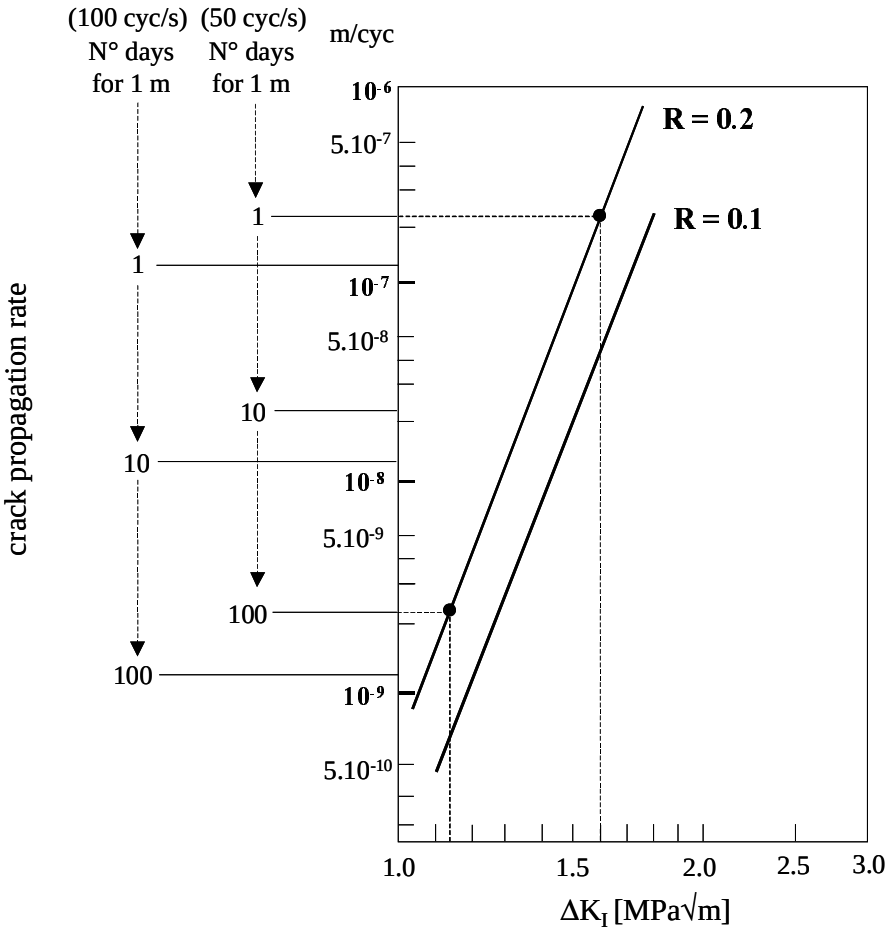

Fig. III-32 Crack propagation rate by cyclic fatigue as a function of the differential stress intensity factor ΔK_I for different minimum to maximum stress ratios R (Kim & Mubeen, 1981).

minimum to maximum applied stress $R = \sigma_{min}/\sigma_{max}$. The m values for other types of rock are presented at Table III-6. The way they have been defined is explained in Chapter VII, § 4.2.1.

Fig. III-32 has three different time scales. The first one is in m/cycles. The second and the third one indicate the number of days necessary to perform a crack advance of 1 m, given a number of cycles per second of 50 respectively 100. When, for example, one assumes that a crack advance of 1 m in 100 days of jet impingement on the rock mass signifies the practical end of scouring, it can be seen that this corresponds to a ΔK_I value of approximately 1.1 to 1.3, depending on the curve. Differential stress intensity factors beneath this value are of no influence on the scouring progression.

Stress corrosion and cyclic fatigue represent the major mechanisms of subcritical crack growth in rocks. Prediction of the dominant mechanism causing subcritical crack growth of fissured rock masses is complicated. It largely depends on the importance of the cyclic stress intensity amplitude with respect to the mean stress intensity value, as well as on the absolute value of the former. A rather small cyclic load with respect to the mean value signifies that stress corrosion is more important than cyclic fatigue, but only when the absolute value of ΔK_I is not too high. A large cyclic load with respect to the mean stress intensity value indicates that fatigue is much more important.

To circumvent this problem, Costin & Holcomb (1981) developed a method that combines the effects of both stress corrosion and cyclic fatigue. This method has originally been set up for brittle failure of rock under cyclic compressive loading, but can be easily applied to tensile stress loading cases. The main difference between compressive and tensile brittle failure of rock is that the former involves the

formation of microcrack growth, followed by coalescence of these microcracks until a macrocrack is obtained, while the latter failures at the most critical flaw, corresponding to the Griffith approach.

The method assumes that stress corrosion and cyclic fatigue act simultaneously and independently. The general equation for the rate of crack growth of a discrete crack of length *a*, where *a* is a function of the number of cycles (N) and the time is:

$$\frac{da}{dt} = \frac{\partial a}{\partial N} \cdot f + \frac{\partial a}{\partial t} \tag{3.73}$$

in which f stands for the frequency of the cyclic loading. The two terms on the right hand side represent the contributions due to cyclic fatigue respectively stress corrosion. The total change in crack length at any time, which results from a specified cyclic loading history, is given by:

$$\int_{a_1}^{a_2} da = \int_0^t \left(\frac{\partial a}{\partial N} \cdot f + \frac{\partial a}{\partial t} \right) \cdot dt \tag{3.74}$$

By assuming that the crack length *a* is entirely representative for the material strength, this equation describes the cumulative damage incurred by the material during cyclic loading. Failure will then occur when the crack length *a* attains some critical length, Δa_c:

$$\Delta a_c = \int_0^t \left(\frac{\partial a}{\partial N} \cdot f + \frac{\partial a}{\partial t} \right) \tag{3.75}$$

The time to failure for a certain cyclic loading history can now be calculated provided $\partial a/\partial N$ and $\partial a/\partial t$ are known. These two derivatives are function of the mean stress, the maximum and minimum stresses, and the environmental conditions, such as humidity and temperature. However, they basically describe two completely different phenomena.

The first derivative expresses the crack growth as a function of the number of cycles of the load. A functional relationship has been taken from work on metals, where cyclic fatigue effects have been extensively studied. Based on Paris et al. (1961), and stating that the stress intensity factor K_I is proportional to the stress S at each crack, the following expression is proposed by the authors:

$$\frac{\partial a}{\partial N} = d \cdot K_{max}^{l} \cdot K_a^{p} = C \cdot S_{max}^{m} \cdot S_a^{n} \tag{3.76}$$

where K_{max} and K_a are the maximum value and cyclic amplitude of the crack tip stress intensity factor, and S_{max} and S_a similar values but for the crack tip pressure. It is generally accepted that K_a is the dominant factor in cyclic fatigue crack growth. C, m and n are assumed to be material constants. When neglecting the influence of K_{max}, equation (3.76) corresponds to equation (3.72) that was used by Kim & Mubeen (1981) to describe fatigue crack growth for a Westerley granite.

The second derivative represents stress corrosion and is independent of stress cycling effects. If it is assumed that the mechanism of stress corrosion cracking is similar in glass than in silicate rocks such as granite, then the rate of crack growth in rock subjected to a stress S can be approximated by:

$$\frac{\partial a}{\partial t} = \upsilon \cdot e^{bS} \tag{3.77}$$

By combining the equations (3.76) and (3.77), the time to failure for a specimen subjected to a given cyclic loading program can be computed. The time to failure t_f was found to depend strongly on the mean stress value S_m and the magnitude of the stress change during each cycle S_a:

$$\Delta a_c = \int_0^{t_f} \left(f \cdot C \cdot S_{max}^m \cdot S_a^n + \upsilon \cdot e^{bS} \right) \cdot dt \tag{3.78}$$

This expression has been compared with experimental results for some simple loading histories. Scholz & Koczynski (1979) performed a series of tests in which Westerley granite was subjected to stresses at a constant confining pressure of 100 MPa and a constant stresss rate of 1 MPa/s. The applied stress cases spanned the range from pure creep tests, with f = 0 and S_a = 0, to cyclic tests in which S_{max} was kept constant (~ 82 % of the static failure strength) and S_a was nearly equal to the mean stress S_m. As a result, the influence of both stress corrosion and cyclic fatigue could be quantified independently from each other. After some mathematical manipulation of the integral describing the stress corrosion effects, the following best fit was obtained:

$$\frac{1}{t_f} = 2 \cdot 10^{-20} \cdot f \cdot S_{max} \cdot S_a^6 + 4{,}4 \cdot 10^{-25} \cdot e^{0{,}059 S_m} \cdot \left[\sinh(0{,}059 S_a) / 0{,}059 S_a \right] \tag{3.79}$$

in which all stresses are in MPa and time is in seconds. A comparison between equation (3.79) and the experimental results is visualized in Fig. III-33. It is obvious that the time to failure t_f is a double-valued function of S_a/S_m. At very low cycle amplitude S_a, near-creep test conditions prevail. As such, stress corrosion is the dominant mechanism and, with increasing S_a, the time to failure initially increases. This is logic because the material spends some of its time at a stress lower than S_m. However, with further increase of S_a, the fatigue effect becomes predominant and the time to failure starts to decrease and can even be less than the one obtained during creep. Although the theoretical curve was determined based on extreme values of S_a/S_m, a good agreement is obtained over the whole range of values. It has to be noted that the time to failure for pure stress corrosion is nearly equal to the time of failure corresponding to pure fatigue.

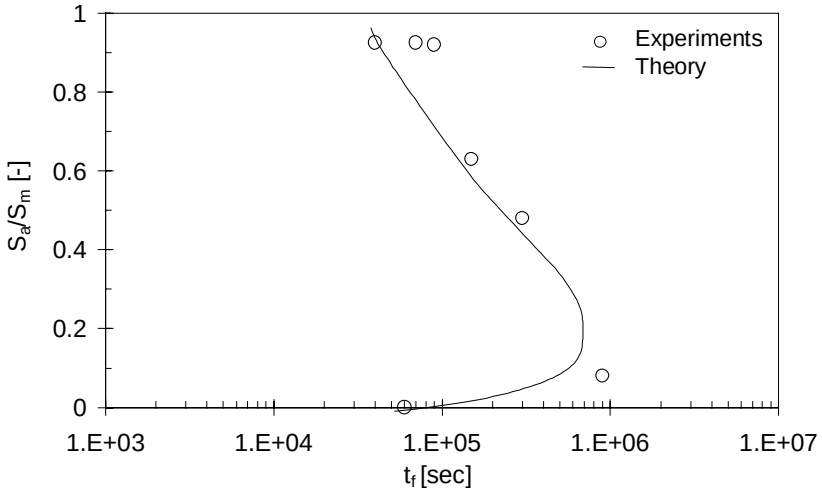

Fig. III-33 Time to failure t_f versus normalized cyclic amplitude for Westerley granite. Comparison between theory and experimental results (Scholz & Koczynski, 1979).

4.3.4. In-situ failure tests: hydraulic fracturing and hydraulic jacking

A first means to determine the fracture toughness K_{Ic} of the rock mass is to perform in-situ fracturing tests. This technique was originally developed in 1948 by the petroleum industry and since then widely applied to stimulate the production of oil-wells. Actually, it also constitutes the most commonly used method to estimate the principal in-situ horizontal stresses (σ_h and σ_H, minor and

major principal stresses in a plane perpendicular to the fracture) of a rock mass. Two major types of tests exist: 1) hydraulic **fracturing** tests, starting from an intact rock mass and creating a new fracture, 2) hydraulic **jacking** tests, that make use of existing artificial or natural rock fractures and break them open further. It is obvious that both tests are useful to experimentally derive the resistance of the rock to fracture initiation (fracturing) or to propagation (jacking). The former is closely related to the strength-of-materials approach (no initial crack), while the latter is more appropriate for the fracture mechanics model (propagation of existing crack).

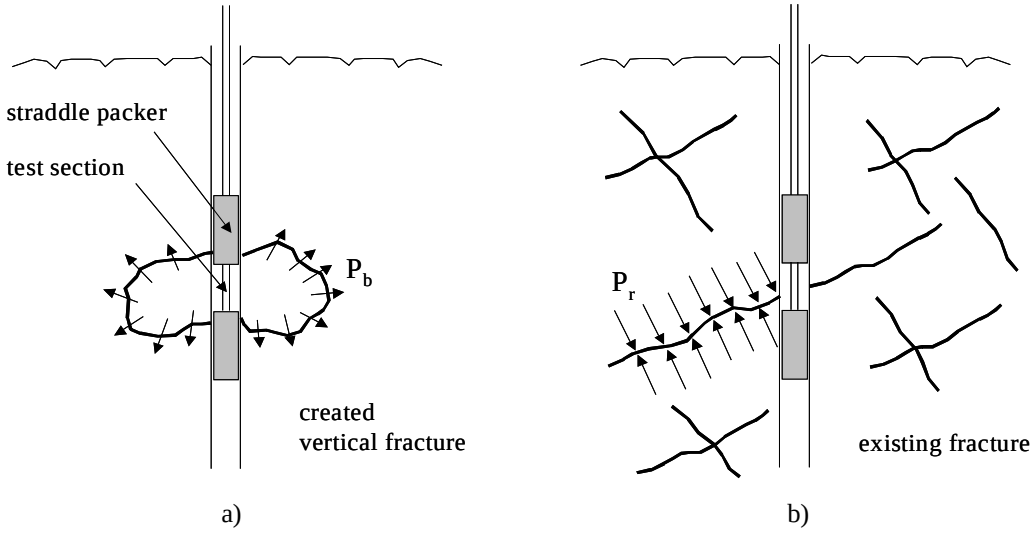

Fig. III-34 Sealed-off segment of vertical borehole during hydraulic fracturing (a) or jacking (b) tests.

The method of hydraulic fracturing is based on the progressive pressurization of a sealed-off segment of a vertical borehole until a critical value is reached at which a vertical fracture is induced, indicating rock tensile failure. This value is called the "breakdown pressure" P_b. The directions of the principal stresses are estimated from the orientation of the vertical fracture (by means of televiewer techniques or impression packers inside the sealed-off segment) that is assumed perpendicular to the minor principal stress. Further pressurization of the fractured interval followed by sudden pump shut-off results in the so-called "instantaneous shut-in pressure" P_s, obtained when the induced fracture closes back. This value is assumed approximately equal to σ_h (Fig. III-34).

Based on linear elastic assumptions, Hubbert & Willis (1957) were the first to derive a breakdown criterion relating the critical breakdown pressure P_b to the in-situ principal stresses and the tensile strength T of the rock. Their expression is based on the classical Kirsch' solution for the stress field around a circular borehole and thus corresponds to the strength-of-materials approach (Fig. III-35):

$$P_b = T + 3\sigma_h - \sigma_H - P_0 \tag{3.80}$$

with P_0 the local initial pore pressure. The "zero breakdown pressure" P_{b0}, defined as the "breakdown pressure under zero initial pore pressure and zero far-field stresses" (Haimson & Zhao, 1991) corresponds to the rock mass tensile strength T and thus represents a constant rock mechanical property. This criterion has later on been extended to permeable rock masses by Haimson & Fairhurst (1967), including the stresses induced as a result of fracturing-fluid penetration into the rock.

In general, fluid penetration due to rock permeability generates lower breakdown pressures. For intact rock, such tests are useful to determine in a direct way the rock mass breakdown pressure P_b, without knowledge of the in-situ stress field (near the surface often neglected). For cracked rock however, it overestimates the resistance of the rock mass to fracturing because of the scale effects outlined above.

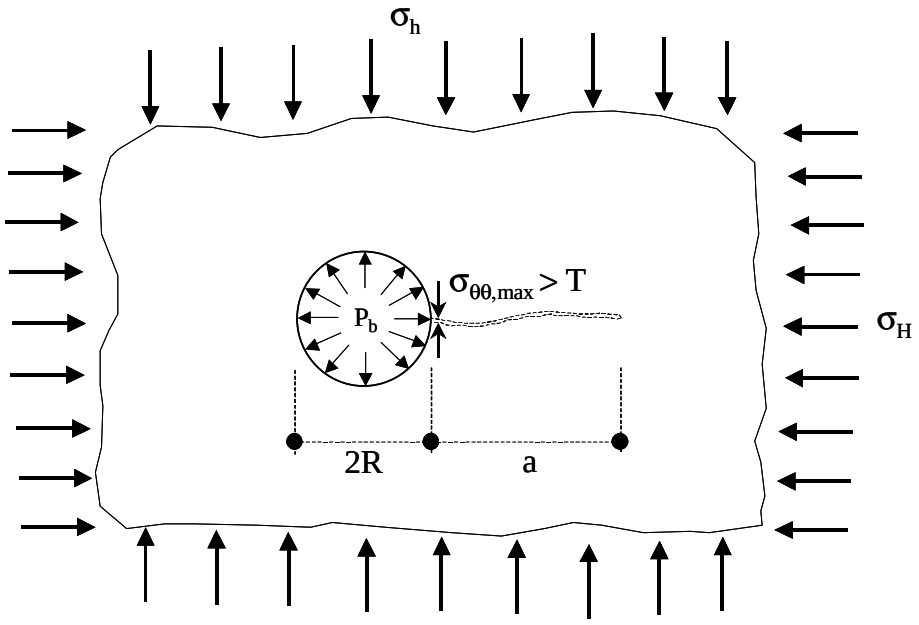

Fig. III-35 Plan view of hydraulic fracturing test showing the pressurized borehole diameter 2R, the initiated crack of length a, the location of maximum tangential tensile stress $\sigma_{\theta\theta}$, the breakdown pressure P_b and the far-field principal horizontal stresses σ_h and σ_H (Atkinson, 1984).

In a second stage of the hydraulic fracturing tests, the segment is pressurized again until the created fracture reopens. This in fact corresponds to a hydraulic jacking test and gives raise to the so-called "fracture reopening" pressure P_r. After a new pump shut-down, the process is repeated several times until stable values are obtained. It has to be noted that the P_r value generally diminishes with the number of performed reopenings. This is due to further crack propagation due to reopening and decreasing energy losses inside the crack. The P_r value principally corresponds more or less to the pressure that is necessary to further propagate an existing crack, i.e. the fracture toughness value of the crack. However, the exact crack length can only be roughly estimated, and the P_r value is not always clearly definable from the obtained pressure-time records.

Hydraulic jacking is related to the linear elastic fracture mechanics model. The major difference with the strength-of-materials approach is the assumption that the zero breakdown pressure P_{b0} is joint size-dependent and, thus, is not a constant material property. Rummel & Winter (1983) assumed the pre-existence of a symmetrical double crack of half-length a, emanating diametrically from the borehole in the direction of σ_H in an otherwise intact plate subjected to far-field compressive stresses. The model assumes that fracturing-fluid pressure is applied to both the borehole wall and the pre-existing crack. The expression for the breakdown pressure then becomes:

$$P_b = K_{Ic}/f(R,a) + k_1\sigma_h + k_2\sigma_H - P_0 \qquad (3.81)$$

whereas f(R,a) is a function of the borehole diameter 2R and the half-length a and is given in explicit form in Rummel & Winter (1983) for specific pressure distributions in the crack.

Regardless of the adopted failure criterion, hydraulic fracturing or jacking, borehole tests are an experimental means to determine at which in-situ pressure new fractures will form or pre-existing fractures will propagate. The problem however lies in the scale difference between usual borehole breakdown pressures and the pressures encountered during analysis of a rock mass. Rock scouring due to high-velocity jet impact takes place in the range of depths between 0 and 200 m. Hydraulic fracturing is typically performed at depths of several hundreds of meters. At small depths, the vertical principal stress can be approximated by the overburden stress and often is less than the horizontal

principal stresses. In other words, vertical fractures that are created at a borehole will turn towards the minimum stress orientation and continue their way in the horizontal plane, perpendicular to the vertical principal stress. This can create practical problems when performing tests at small depths and will give erroneous results for the rocks fracture toughness.

A typical pressure-time record of a hydraulic fracturing and jacking test is presented in Fig. III-36. Three pressurizing intervals can be distinguished. The first interval creates a new fracture from the borehole wall. This happens at the peak pressure P_b. The second interval reopens the existing fracture, at the reopening pressure P_r, after which a sudden pump shutdown is performed. This shutdown defines the instantaneous shut-in pressure P_s. This value is considered as the minor principal horizontal stress σ_h. The difference between the breakdown pressure P_b and the first reopening pressure P_r is often considered as an approximation of the rock's tensile strength T. The third interval is similar to the second, but a slight decrease in reopening pressure P_r can be noticed. Further reopening tests would allow to observe the same phenomenon, until a stable value is obtained, often dictated by the overall pump capacity.

The question now rises if these assumptions are valid also for the fracture mechanics analysis. The reopening pressure P_r often corresponds to the pressure that not only opens the existing fracture, but also lets it propagate. Strictly speaking, this should correspond to the in-situ horizontal stress effect plus the local fracture toughness of the rock mass. The latter however often is neglected during oil well stimulation because of the much bigger values of the in-situ stress field. For the fracture mechanics analysis, this is not the case. The slightly decreasing P_r value due to consecutive reopening probably indicates a decreasing fracture toughness with growing fracture length. The stabilized value P_f, which is situated between P_r and P_s, can be considered as the in-situ stress effect. As a result, the difference between P_r and P_f should more or less correspond to the fracture toughness of the rock mass.

Nevertheless, hydraulic jacking tests can be useful for a fracture mechanics analysis when assuming that knowledge of the fracture toughness and the in-situ stress field is not necessary. One can use the obtained reopening pressure P_r as the one that lets the fracture propagate. This could be done at different depths, depending on the rock structure STRUC and the layer thickness H_l, which would give the static fracture toughness values $K_{Ic,stat}$ for each layer.

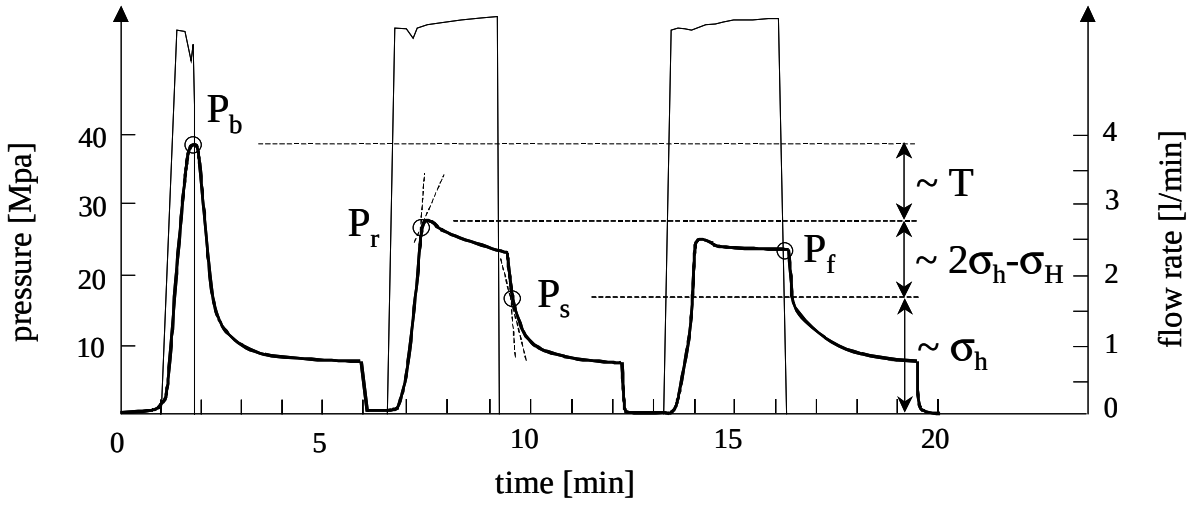

Fig. III-36 Typical pressure-time and flow rate-time record obtained during hydraulic fracturing or hydraulic jacking test.

The joint propagation is a dynamic process that modifies both the rock's modulus of elasticity E_r and its tensile strength T or fracture toughness K_{Ic}. The rate of pressure raise R_p [MPa/s] can be determined by performing laboratory dynamic fracturing tests on rock specimens (Haimson & Zhao, 1991; Zhao & Li, 2000). These tests make it possible to relate the pressure raise to the fracture toughness. As will be discussed more in detail later on, they are difficult to perform.

If these tests cannot be made, the rock failure analysis has to be based either on static laboratory tests on rock core specimen, either by using available values of similar rock formations regarding the tensile strength or fracture toughness of the rock mass, the local initial pore pressure and the in-situ principal stresses. The following two paragraphs deal with laboratory specimen failure tests and with dynamic fracture toughness values, as well as with other physical effects that influence the in-situ rock mass fracture toughness, such as temperature, moisture, chemical agents, etc.

4.3.5. Basic fracture toughness value K_{Ic} by laboratory specimen tests

Beside in-situ hydraulic fracturing or jacking tests, the fracture toughness K_{Ic} (fracture mechanics approach) or the tensile strength T (strength-of-materials approach) can also be obtained through tensile failure tests on laboratory rock specimen. These tests are always subject to possible scale effects. In any case, the minimim crack length and specimen dimensions, as expressed by equations (3.62) and (3.63), should be satisfied to avoid non-elastic effects at the crack tip. Laboratory tests have the advantage to be less expensive than hydraulic jacking tests and easier to perform and to repeat. As a result, a lot of data on the fracture toughness of different rock types is available in literature. This makes it possible to compare between them and to distinguish trends and mean values.

Two types of laboratory tests can be distinguished: 1) **pure tensile strength tests** (strength-of-materials approach), and 2) **fracture toughness tests** (linear elastic fracture mechanics approach). Both of them are shortly explained hereafter.

The strength-of-materials approach uses the direct uniaxial tensile strength T of the rock mass. Direct tensile tests are difficult to perform and are usually not made. Moreover, the tensile strength of rock is more influenced by specimen size than any other mechanical property of rock, making it necessary to conduct a large number of tests. Details can be found in Jaeger & Cook (1979) and Andreev (1995). These difficulties have led to the development of several indirect test procedures. One of them is bending of a simply supported rock beam, called the "flexural test". The flexural strength, often called the "modulus of rupture", corresponds to the maximum tensile stress on the bottom of the rock beam at peak load. It is calculated from simple beam theory, assuming elastic conditions throughout. This procedure suffers from a different Young's modulus of the rock in tension than in compression and, as a result, generally produces tensile strengths that are two to three times larger than the uniaxially determined value (e.g. Jaeger & Cook, 1979; Goodman, 1980).

A second, more popular indirect tensile test is the so-called "Brazilian test". This test consists of applying a diametrical compression to a rock cylinder, which, for convenience, is usually shorter than its diameter. Tensile strengths measured in this way are very reproducible and are in reasonable agreement with values obtained by uniaxial tension tests (e.g. Jaeger & Cook, 1979; Andreev, 1995). Therefore, most of the published tensile strength results are obtained through Brazilian tests.

The second series of tests are fracture toughness tests (linear elastic fracture mechanics approach). A wide variety of procedures exist for mode I fracturing of rock. Most of them use rock cores such as the short rod specimen (Barker, 1977), the burst cylinder specimen (Clifton et al., 1976), the semi-circular bend specimen (Chong, 1987), the modified ring specimen (Thiercelin & Roegiers, 1986) and the round bend bar specimen (Ouchterlony, 1980). The results are not always very similar, implying that the measured fracture toughness values usually do not represent a material property, like it should be. This is due to the different test procedures and crack geometries, as well as to the non-negligible influence of the plastic fracture damage zone in front of the crack tip. Furthermore, rock can be highly inhomogeneous, anisotropic and non-linear in its behavior.

Therefore, in 1988 the testing commission of the ISRM (International Society for Rock Mechanics) defined some suggested methods to provide tests that consistently yield accurate fracture toughness

values. The short rod and chevron bend specimens were recommended as standard testing methods (Ouchterlony, 1988).

The other test procedures can give rise to fracture toughness values that are not a rock material property. They can contain for example influences of the test procedure and of the shape of the crack. As such, they sometimes exhibit fracture toughness values that are too low when compared to the in-situ value. This, however, is not necessarily the case. Therefore, as a first approach, such values have also been accounted for in the present analysis. Whenever only such values are available, one should take precaution and use values obtained for the largest specimen and crack sizes used during the tests.

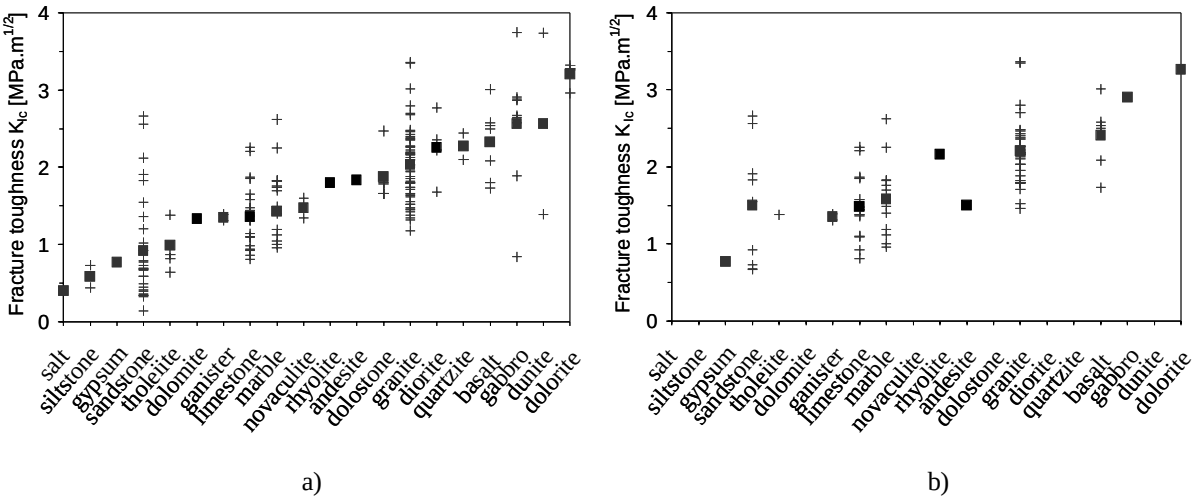

Fig. III-37 Fracture toughness values for different rock types, classified in increasing order: a) summary of available data, b) summary of data obtained through ISRM-suggested methods only. Symbols: (+) available test results, (■) mean value per rock type.

A summary is presented in Fig. III-37. Fig. III-37a classifies different rock types as a function of increasing mean fracture toughness. For this classification, both ISRM and not-ISRM suggested values have been used. Carbonate (e.g. gypsum, dolomite, limestone) and crystalline salt rocks exhibit a rather low to intermediate fracture toughness. Crystalline silicate rocks (e.g. granite, diorite, gabbro, basalt) usually have a high fracture toughness. Sedimentary rocks (e.g. sandstones, tuff) logically have a quite low strength. It can be seen that, where a large number of fracture toughness values are available for a certain rock type, also a quite large scatter occurs. The lower values often are obtained through non ISRM-suggested methods. Hence, Fig. III-37b shows the same classification, but only based on ISRM-suggested methods. A slightly better relation is obtained and the lower fracture toughness values have disappeared. However, it is difficult to obtain an accurate relationship between a rock type and its fracture toughness. When no laboratory fracture toughness values are available for the rock type in question, an estimate has to be based on the mean value of similar rock types and precaution thus should be taken.

Because of the difficulties to experimentally determine the fracture toughness of a rock mass, some more easily determinable mechanical properties of rocks are often preferred. Examples are the hardness index H, the unconfined compressive strength (UCS) or the tensile strength (T), and the Young's modulus of elasticity (E_{rock}). Previously established correlation relationships can be found in Whittaker et al. (1992) and Andreev (1995):

$K_{Ic} = 0.0044 \cdot UCS + 1.04$ (Andreev 1995) (3.82)
$K_{Ic} = 0.006 \cdot UCS + 0.708$ (Whittaker et al. 1992) (3.83)
$K_{Ic} = 0.0736 \cdot T + 0.76$ (Andreev 1995) (3.84)
$K_{Ic} = 0.107 \cdot T + 0.27$ (Whittaker et al. 1992) (3.85)
$K_{Ic} = 0.026 \cdot E_{rock} + 0.336$ (Whittaker et al. 1992) (3.86)

A correlation of available literature data has been undertaken to relate the fracture toughness value K_{Ic} to the unconfined compressive strength UCS and to the tensile strength T. It is generally assumed that the tensile strength T has been determined by a Brazilian test, i.e. an indirect method. The results are visualized in Fig. III-38. Fig. III-38a relates the fracture toughness to the tensile strength. Data is taken from Atkinson (1987), Whittaker et. al (1992) and Andreev (1995). The correlation that fits all the available data is expressed as follows:

$$K_{Ic} = 0.088 \cdot T + 0.5276 \tag{3.87}$$

Fig. III-38b shows a similar relation for the unconfined compressive strength. The obtained correlation is as follows:

$$K_{Ic} = 0.0068 \cdot UCS + 0.42 \tag{3.88}$$

Despite the reasonable correlations, it is interesting to express the fracture toughness to both the type of rock and an engineering parameter. Fig. III-38c presents the K_{Ic}-T relation as a function of the type of rock. Three types are distinguished: carbonate, silicate and quartz rocks. It can be seen that especially carbonate rocks seem to exhibit a slope that is significantly steeper than the ones for silicate and quartz rocks. The same trend was found for the K_{Ic}-UCS relationships. This is not so surprising provided that the fracture toughness highly depends on the nature of the grains of the rock mass.

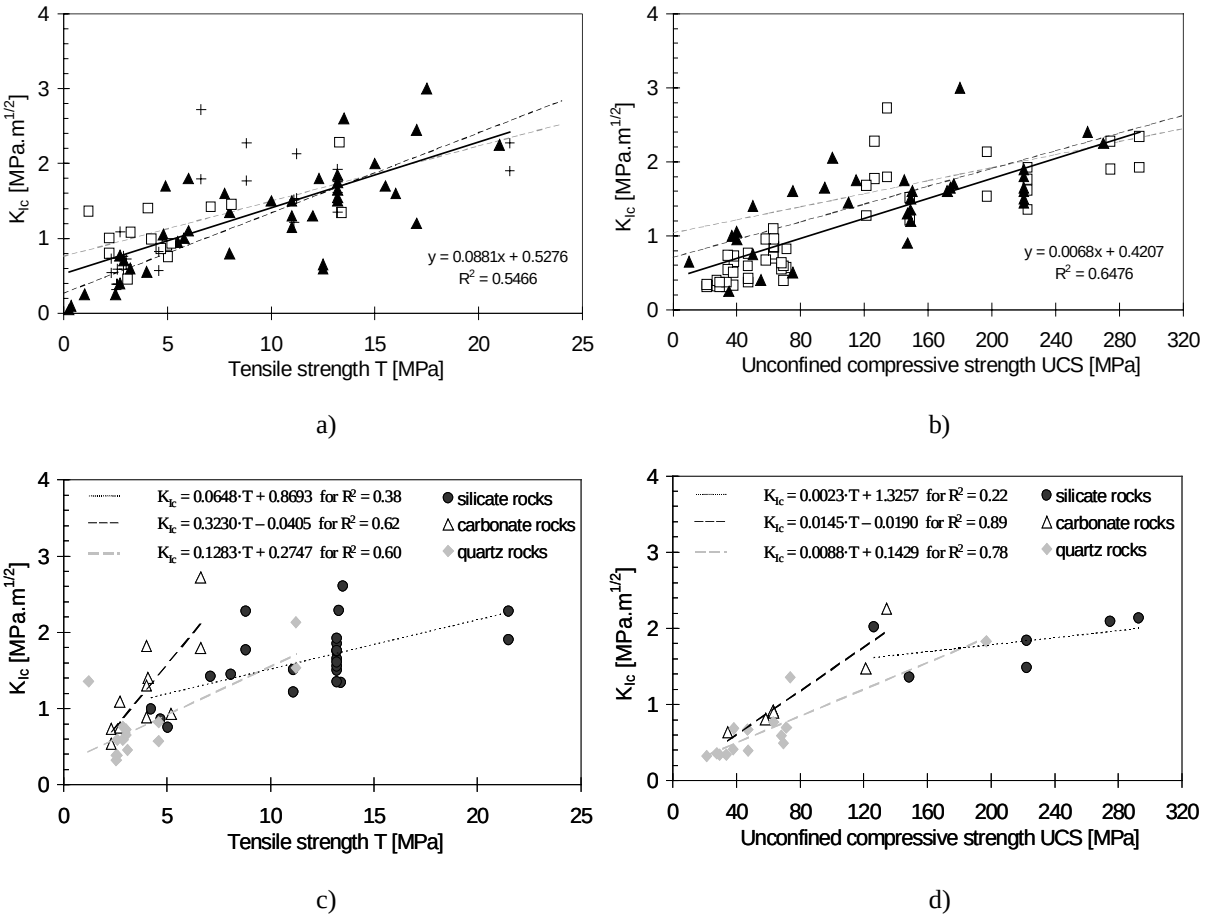

Fig. III-38 a) Fracture toughness K_{Ic} as a function of tensile strength T; b) Fracture toughness K_{Ic} as a function of unconfined compressive strength UCS; c) K_{Ic}–T relation as a function of type of rock; d) K_{Ic}–UCS relation as a function of type of rock. Data taken from: (+) Atkinson (1987); (□) Andreev (1995); (▲) Whittaker et al. (1992).

For engineering purposes, the following methodology is proposed:

- when only the type of rock is available, Fig. III-37 should be used in order to obtain a mean value,
- when also a material strength property, such as the uniaxial compressive strength or the tensile strength, is available, Fig. III-38c & d should be used.

The so obtained value represents a **basic fracture toughness value**. In practice, however, several in-situ effects can influence this basic value. The most significant influences are in-situ stresses and the rate of loading inside the cracks. These effects are quantified in the next section.

4.3.6. In-situ fracture toughness value $K_{I\,ins}$

The basic fracture toughness values K_{Ic} defined in § 4.3.5 are obtained under laboratory conditions and for static loadings. However, a lot of in-situ hydraulic fracturing tests revealed resistance values that are quite different from these laboratory obtained values. These differences are not only due to possible scale effects between the small laboratory specimen and the large, jointed rock mass. Several in-situ physical phenomena can be of influence on the fracture toughness value:

- the rate of pressurization R_p [MPa/s] of the hydrodynamic loading inside the rock joint (e.g. Grady et al., 1980; Haimson & Zhao, 1991; Zhao & Li, 2000; Zhao, 2000; Zhang et al., 2000),
- the in-situ horizontal stress field σ_h and σ_H (e.g. Schmidt & Huddle, 1977; Abou-Sayed & Brechtel, 1978; Winter, 1983; Müller & Rummel, 1986; Thiercelin, 1987; Roegiers & Zhao, 1991),
- the joint width or borehole diameter (e.g. Haimson & Fairhurst, 1969; Haimson & Zhao, 1991),
- the downhole temperature (e.g. Meredith & Atkinson, 1985; Roegiers & Zhao, 1991),
- the presence of moisture or other chemical agents (e.g. Atkinson, 1979; Akram & Karfakis, 1991),
- the presence of a non-negligible plastic yielding zone (non-linear effects) (e.g. Liu et al., 2000).
- the grain size (e.g. Meredith, 1983; Huang & Wang, 1985),
- the rock anisotropy and crack orientation (e.g. Hoagland et al., 1973)

A fracture toughness value that accounts for these effects is the **in-situ fracture toughness $K_{I\,ins}$**. This value is of great importance in the petroleum industry, where borehole tests generally are performed at great depth (several hundreds of meters). For these depths, the influences of the in-situ stress field and the downhole temperature get predominant and can completely change the order of magnitude of the laboratory obtained values.

For hydraulic fracturing of rock due to high-velocity jet impact, only the influences of the in-situ stress field and of the loading rate will be considered. The width of the joints is assumed to be of the same magnitude for in-situ and laboratory experiments. Temperature effects are negligible at moderate depths (several tens of metres). Environmental effects are discarded in the present analysis and eventual plastic effects can be neglected by considering a convenient joint and rock block scale. Grain size effects are not accounted for and rock anisotropy will be accounted for later on by considering different types of joint sets and joints.

It is known that certain rock mass properties, such as the modulus of elasticity (e.g. Eissa & Kazi, 1988; Plona & Cook, 1995), the tensile strength T (e.g. Grady et al., 1980; Zhao & Li, 2000; Zhao, 2000) and also the fracture toughness K_{Ic} (e.g. Haimson & Zhao, 1991; Zhang et al., 2000) change as a function of the applied loading (or strain) rate R_p [MPa/s]. This is of importance in assessing stability of rock structures under dynamic loads, as well as to determine rock breakage and fragmentation under explosive and percussive excavation. Typical loading rates for rock joints under high-velocity jet impact are 10^1 – 10^3 MPa/s, depending on the length of the joint and the amplitude of the pressure waves (see chapter V on experimental results).

Grady et al. (1980) developed a dynamic fracturing model to explain this rate dependence. Their study indicates that, at static loads, the largest or critical crack is responsible for failure, whether at dynamic

loads, a single crack is not sufficient to result in the failure of the rock material. Additional cracks must participate, leading to a high tensile strength T and fracture toughness K_{Ic}. However, these studies were done for very high loading rates, much higher than the loading rates of high-velocity jets.

Therefore, Zhao (2000) and Zhao & Li (2000) proposed another failure mechanism, based on the growth and nucleation of pre-existing cracks in the rock mass, to study dynamic failure of granite by means of Brazil tensile tests. They made tests at loading rates of 10^{-1} to 10^{3} MPa/s. This indicated that the tensile strength increases by approximately 10% when the loading rate increases by one order of magnitude.

A microscopic explanation for the change in fracture toughness at dynamic loading has recently been provided by Zhang et al. (2000) based on the energy required to fracture a rock mass. Their test results on rock breakage showed that the energy absorbed by a specimen in static fracture is much less than that in dynamic fracture. The main reason is that in the process of dynamic fracturing multiple crack branching occurs, much more than in static fracture, consuming thus extra energy. Haimson & Zhao (1991) made use of the strength-of-materials approach to investigate the influence of the loading rate R_p on the hydraulic fracturing breakdown pressure P_b under zero in-situ stresses. They made tests on granite and limestone for pressurization rates ranging from 0.03 to 10 MPa/s. Striking similarity was observed between the behavior of the two rocks, expressed in the form of a steady rise of the zero breakdown pressure over the tested range of loading rates.

The rise in breakdown pressure P_b was described by a linear regression of the breakdown pressure P_b as a function of the logarithm of the loading rate. This extends from 2.2 times the logarithm of R_p for granite to 2.5 times the logarithm of R_p for limestone. Similar results were obtained by Haimson & Fairhurst (1969) on Charcoal granite and hydrostone, showing a definite increase in breakdown pressure with increase in loading rate.

Assuming a quasi-static loading rate of 10^{-2} to 10^{-1} MPa/s for laboratory fracturing tests, and based on equation (3.87) and Fig. III-38a, the increase in fracture toughness can be expressed as follows, where K_{Id} stands for the dynamic fracture toughness value:

$$K_{Id} = 0.088 \cdot (1.2 \text{ to } 1.5) \cdot T + 0.5276 = (0.105 \text{ to } 0.132) \cdot T + 0.5276 \quad (3.89)$$

$$K_{Id} = 0.0068 \cdot (1.2 \text{ to } 1.5) \cdot UCS + 0.42 = (0.008 \text{ to } 0.010) \cdot UCS + 0.42 \quad (3.90)$$

The second significant in-situ influence on the fracture toughness value K_{Ic} is the in-situ (horizontal) principal stress field σ_h and σ_H. The horizontal stress field close to the surface can attain values of up to several times the vertical principal stress σ_v, expressed by the weight of the overburden. This is expressed by the ratio of horizontal to vertical stresses K_0:

$$K_0 = \frac{\sigma_h}{\sigma_v} \quad (3.91)$$

This value, however, largely depends on the existence of faults and valleys, and on the tectonic history of the rock mass. Analysis of in-situ stresses is beyond the scope of the present work. A more detailed description of expressions for K_0 can be found for example in Goodman (1980). Depending on the dip of the joint set, both vertical and horizontal principal stresses can be of importance when determining the in-situ fracture toughness.

The effect of the in-situ stresses on the fracture toughness has been studied by a large number of researchers (e.g. Schmidt & Huddle, 1977; Abou-Sayed & Brechtel, 1978; Winter, 1983; Müller & Rummel, 1986; Thiercelin, 1987; Roegiers & Zhao, 1991; Al-Shayea et al., 2000). It is accepted now that the fracture toughness increases with increasing in-situ stresses.

However, the exact reasons for this increase are still unknown. Schmidt (1980) stated that the plastic process zone ahead of the crack tip might be simply reduced by a confining pressure. Thiercelin (1987) and Roegiers & Zhao (1991) rather believe that an increase of crack closing pressure acting on a reduced process zone at its tip may cause an increase in critical loading conditions. Most researchers propose a roughly linear relationship as follows:

$K_{Ic}(\sigma_c) = (1 + 0.037 \cdot \sigma_c) \cdot K_{Ic}(0)$ (Müller & Rummel, 1986) (3.92)
$K_{Ic}(\sigma_c) \propto (T + \sigma_c)$ (Roegiers & Zhao, 1991) (3.93)
$K_{Ic}(\sigma_c) = (1 + \sigma_c/T) \cdot K_{Ic}(0)$ (Whittaker et al., 1992) (3.94)
$K_{Ic}(\sigma_c) = (0.043 \cdot \sigma_c) + K_{Ic}(0)$ (Al-Shayea et al., 2000) (3.95)

in which σ_c stands for the confining pressure value [MPa]. A summary is presented in Fig. III-39. It can be seen that, within the range of confining pressure values that can be encountered close to the surface (0-20 MPa), a linear relation holds. The best-fit correlation of all available slopes is written:

$K_{Ic}(\sigma_c) = (0.054 \cdot \sigma_c) + K_{Ic}(0)$ (3.96)

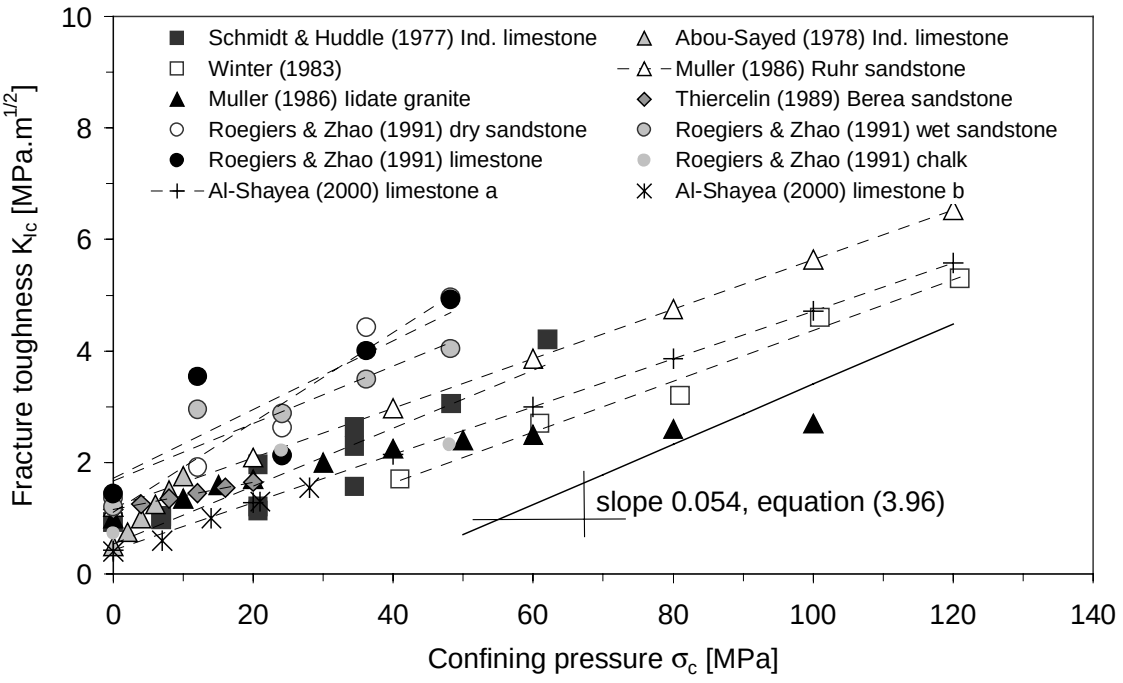

Fig. III-39 Relationship between the fracture toughness K_{Ic} and the confining pressure σ_c of a rock mass. The average slope of the linear increase is 0.054.

It is proposed to integrate the effect of the confining pressure into the dynamic fracture toughness by simply adding it to the tensile strength or the unconfined compressive strength in equations (3.89) and (3.90). This results in the following relationships:

$K_{I\,ins,\,T} = (0.105 \text{ to } 0.132) \cdot T + (0.054 \cdot \sigma_c) + 0.5276$ (3.97)
$K_{I\,ins,\,UCS} = (0.008 \text{ to } 0.010) \cdot UCS + (0.054 \cdot \sigma_c) + 0.42$ (3.98)

in which T, UCS and σ_c are in MPa. However, these relationships are general and don't account for the type of rock in question. Therefore, it is recommended to start from one of the equations as presented in Figs. III-37c & d, and then to apply a correction factor for the loading rate and for the in-situ stresses. Hence, the expression applicable for a certain type of rock is of the following form:

$K_{I\,ins,\,T} = A \cdot (1.2 \text{ to } 1.5) \cdot T + (0.054 \cdot \sigma_c) + B$ (3.99)
$K_{I\,ins,\,UCS} = C \cdot (1.2 \text{ to } 1.5) \cdot UCS + (0.054 \cdot \sigma_c) + D$ (3.100)

4.3.7. Concluding remarks

Failure criteria for intermittently jointed rock are based on the strength-of-materials approach or on the linear elastic fracture mechanics approach. The former is appropriate for crack initiation, while the latter expresses the propagation of existing cracks.

Hence, fracture mechanics seems to be the most relevant approach for intermittently jointed rock. It depends on the length of the crack, the water pressure distribution inside the crack and the shape of the surrounding rock mass. Moreover, the rate of loading and the in-situ stress field of the rock mass can be accounted for.

All these parameters will be integrated into a new scour model that relates hydrodynamic pressures in rock joints to the resistance of the rock against crack propagation. This is discussed in Chapter VII.

4.4. Failure criteria for completely jointed rock

4.4.1. Introduction

Failure of completely jointed rock is performed by ejection of a rock block that is representative for the jointed rock mass. This rock block is called the "characteristic block" (Fig. III-40) and is defined for each distinct layer of the rock mass. The geometry of the block is determined by intersection of the different joint sets in a two-dimensional space. This block is subjected to forces that change with time. Therefore, the net impulse, defined as the integral over a certain time period of the net forces on the block, is of great significance. This impulse accelerates the mass of the block up to a certain velocity. Conversion of the kinetic energy into potential energy then allows determining the height of uplift of the block.

4.4.2. Forces on a rock block

The most relevant forces that act on a characteristic rock block can be subdivided into stabilizing forces and destabilizing forces. The stabilizing forces are written:

1. the stabilizing force G_b, defined as the immerged weight of the rock block,
2. $F_o(x,t)$, which is defined as the force resulting from the time and space dependent pressure distribution acting over the block. This force results from the macroturbulent pressure pattern at the plunge pool bottom and, when reaching negative values, can become destabilizing,
3. the stabilizing force which is expressed by the shear force $F_{sh}(t,e_j)$. This force depends on several parameters, such as joint roughness, aperture, filler material, etc. It can be assumed to depend on joint width and time,

The destabilizing forces are generated by the transfer of pressures at the pool bottom into underlying rock joints. The transient two-phase flow conditions inside the joints create a pressure pattern that is completely different from the pressure pattern at the pool bottom itself. Hence, it is this different character between turbulent surface pressures and transient rock joint pressures that produces net uplift pressures on a rock block. In the following, rock joint pressures are defined as destabilizing forces, regardless of their direction of application on a rock block. Thus, the destabilizing forces are summarized as:

4. the time, space and joint width dependent pressure distribution F_u (x, t, $e_{j1}(t)$, $e_{j2}(t)$), acting along the joints between the rock blocks,

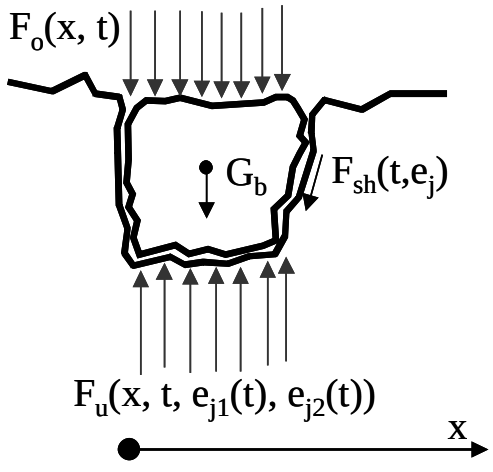

Fig. III-40 Force balance on a characteristic rock block. In the present case, the forces have to be equilibrated in each of the indicated directions separately (Bollaert & Schleiss, 2001b).

As outlined in Chapter II, several researchers have investigated dynamic pressures on rock blocks or concrete slabs of stilling basins. The first attempts focused on the time-averaged dynamic pressures in planar joints of a row of concrete elements (Montgomery, 1984; Reinius, 1986). The elements were subjected to horizontal flow impact. This study pointed out the importance of the protrusion of the blocks into the flow, as well as of the angle of the joints with respect to the flow direction. This was later on confirmed by Otto (1989), who performed dynamic pressure measurements in joints by vertical and oblique impinging jets. The location and angle of jet impact were a key issue. These studies showed that the time-averaged net forces could eject a rock block or concrete slab from its mass. This, however, is not necessarily always the case. The corresponding geometrical situation is presented in Fig. III-41a, in which p_{over} and p_{under} are the pressure fields over and under the rock block.

Cases of damage experienced on chutes and spillway basins operating under flood conditions have shown the relevance of instantaneous uplift pressures rather than time-averaged pressures (Bowers & Tsai, 1969; Toso & Bowers, 1988; Fiorotto & Rinaldo, 1992a & b; Bellin & Fiorotto, 1995). Examples are the Malpaso, Tarbela and Karnafuli dams. Although these cases involve hydraulic jumps, the physical background is identical to jet impact on completely jointed rock masses. Liu et al. (1998) made laboratory measurements of instantaneous net forces on a single rock block in a plunge pool.

In these studies, the net uplift pressures or forces are generated by assuming an instantaneous propagation of the pressure waves inside the joints. This yields a constant pressure pattern under the slab or the block. On the other hand, the upper pressure pattern, governed by turbulent flow conditions, is considered time-and space dependent. This is especially relevant when the length of the slab or the block is larger than the integral scale of the surface pressure fluctuations. A similar analysis, but also accounting for the persistence time of the pressures underneath the concrete slabs, has lastly been performed by Fiorotto & Salandin (2000). The corresponding situation for these studies is sketched in Fig. III-41b.

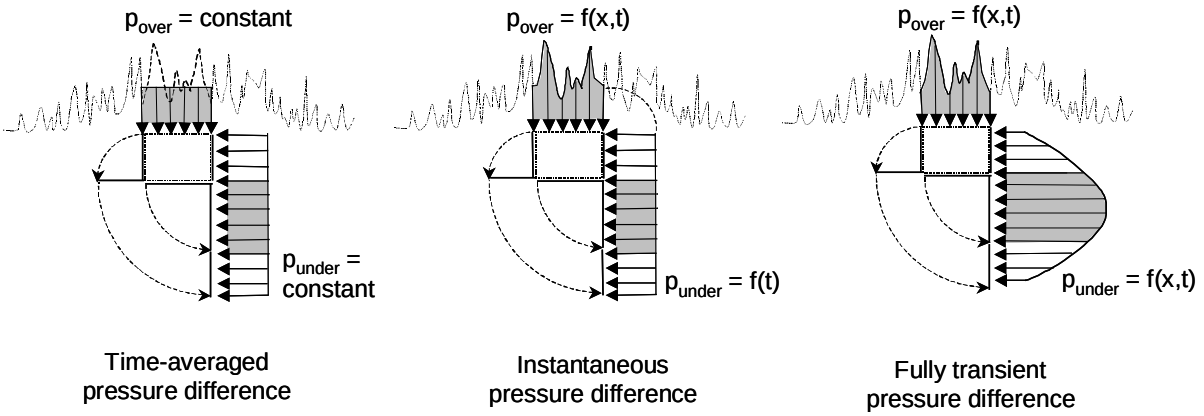

Fig. III-41 Dynamic pressure patterns measured on a rock block: a) time-averaged pressure difference, b) instantaneous pressure difference, c) fully transient pressure difference. The vertical pressures are indicated in grey.

Finally, as already outlined in § 2.2.4, pressure wave propagation inside joints cannot always be considered to happen instantaneously for the surface flow conditions. Under certain circumstances, the spectral content of the impacting flow and the celerity of the pressure waves inside the joints are strongly related. This can happen for example in case of air bubble presence inside the joints, which lowers the celerity of the pressure waves. Another example is an impacting flow with a very high frequency range. High-velocity jet impact on underlying rock joints unfortunately exhibits both phenomena. Hence, the pressure fields over and under the rock blocks are not independent anymore and have to be correlated. This is performed by accounting for a fully transient two-phase flow

analysis. Such an analysis pays the same attention to both upper and underpressures, and this at very small time scales, in the order of 10^{-3} sec. The upper pressures are able to create standing and resonance pressure waves inside the joints, generating large pressure gradients within very small time periods. As a result, not only the net instantaneous pressure values are of significance, but also the time period that these net values hold on the block. Integration over time of the net pressures determines the net impulse on the block. The corresponding situation is presented in Fig. III-41c.

4.4.3. Impulse on a rock block

The net impulse $I_{\Delta tpulse}$ on the block, corresponding to a pressure pulse of time Δt_{pulse}, is defined by integrating the net force equilibrium at every time step dt. This time step has to be chosen small enough so that no significant pressure gradients occur during each step. This procedure results in an uplift velocity $V_{\Delta tpulse}$. The net impulse is written:

$$I_{\Delta tpulse} = \int_0^{\Delta tpulse} \left(F_u - F_o - G_b - F_{sh}\right) \cdot dt = m \cdot V_{\Delta tpulse} \tag{3.101}$$

in which m stands for the mass of the block. In this equation, the pressure distributions above and underneath the block have been spatially integrated. However, due to violent transient effects, the pressure gradient with time is generally much higher than the pressure gradient with space. Therefore, as a first approach, a space-averaged value can be chosen. The kinetic energy given to the block is transformed into potential energy as a function of the mass of the block. The total uplift height of the block h_{up} is written:

$$V_{\Delta tpulse} = \sqrt{2 \cdot g \cdot h_{up}} \tag{3.102}$$

and the mass of the block:

$$m = \rho \cdot \text{Volume} = \rho \cdot \left(x \cdot y \cdot z\right) \tag{3.103}$$

in which ρ stands for the density of the rock mass and x, y and z respectively for the longitudinal, transversal and vertical dimensions of the characteristic rock block. Furthermore, the weight of the block and the pressure forces over and under the block directly depend on the horizontal surface of the block, i.e. x·y. Therefore, when neglecting the shear forces F_{sh}, which depend on the vertical length z, this product can be eliminated from both the left and right hand side of equation (3.101). As a result, the uplift velocity $V_{\Delta tpulse}$ is inversely proportional to the height of the block z. In other words, according to equation (3.102), the uplift height h_{up} of a block is inversely proportional to the square of its height z^2. This indicates that any failure criteria based on uplift of rock blocks is largely influenced by the form factor of the blocks. In the next section, a simple calculus demonstrates this dependence.

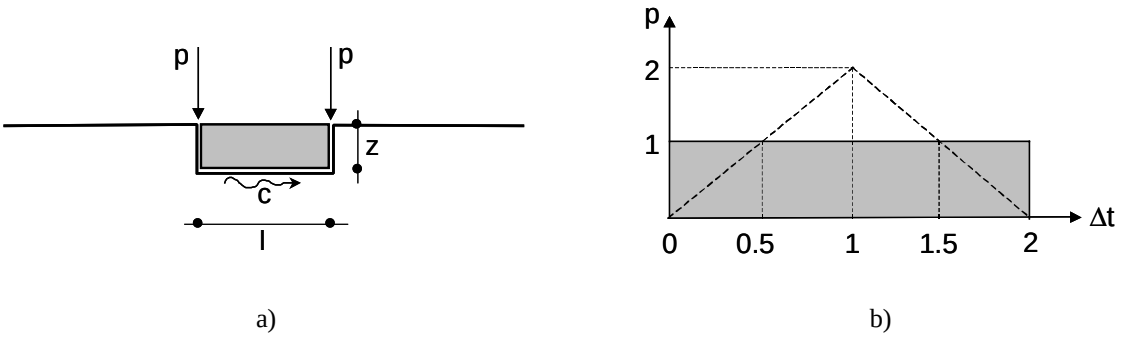

a) b)

Fig. III-42 Pressure pulses applied underneath a rock block of height z and length l: a) geometrical situation, b) triangular shape and rectangular simplification of the pressure pulse.

4.4.4. Dynamic pressure field under the block

Assuming a two-dimensional problem, the form factor of the block can be defined as the ratio of the height to the horizontal extension z/l. The abovementioned procedure has been followed for a constant net uplift pressure head of 50 and 100 m. This net pressure difference is applied underneath a rock block of height z and length l, at the joint entrances as indicated in Fig. III-42a. In other words, the pressure over the block is neglected. Furthermore, the time period of application of the underpressure is defined as in accordance with Fig. III-42b. Each of the pulses has an amplitude p and a duration $\Delta t = (l/c)$, in which c is the pressure wave celerity. Due to superposition of the pulses under the block, the total duration is considered equal to $2\Delta t$ and of triangular shape. In the following, this triangular shape has been simplified to a rectangular one with the same surface but for a constant magnitude of p.

Fig. III-43a presents the influence of the form factor z/l on the non-dimensional uplift height h_{up}/z of the block for a block length of l = 3 m. The height of the block is chosen between 0.1 and 1 times the length l. The impulse on the block has been calculated for two different wave celerities: 600 m/s and 1'000 m/s. The celerity has a significant influence on the duration of the pressure application and thus also on the velocity that can be given to the block. Fig. III-43b shows the same relationship, but for a length that is equal to only one third of the initial one, i.e. l = 1 m. The rock block is ejected more easily in this case. Again the importance of the celerity is pointed out.

For these two cases, the critical uplift height or displacement h_{cr} is assumed equal to the height of the block z. It can be concluded, first of all, that the form factor z/l is of huge importance on the ejection of the block. Secondly, the absolute dimensions of the block are also of significance. The smaller the block, the easier it will be ejected. This, of course, still under the assumption that the surface pressure field is neglected. Furthermore, the importance of the form factor seems to decrease for decreasing block dimensions.

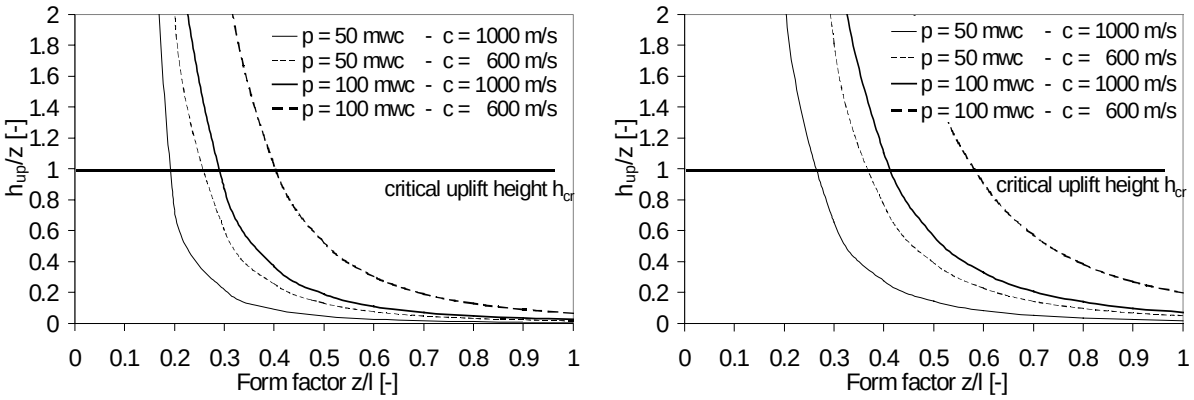

Fig. III-43 Non-dimensional displacement as a function of the form factor z/l: a) rock block of length l = 3 m, b) rock block of length l = 1 m.

4.4.5. Dynamic pressure field over the block

The above calculus represents a vast simplification of reality. Destabilization and uplift of rock blocks also depend on the pressure pattern acting at the surface of the block. This pattern is governed by turbulent flow conditions in the plunge pool. It depends on the size of the involved eddies. This means that the ratio of eddy sizes to rock block sizes is playing an important role. In other words, the macroscale, or the integral scale of the spatial correlation, of the pressure fluctuations at the rock joint entrance has to be determined. This macroscale defines the distance at which, on the average, two instantaneous values of the fluctuating pressure become uncorrelated. It determines to which extend

these pressures can be applied to the whole rock block. A mathematical description of the macroscale in the x-direction is as follows:

$$I_x = \int_0^{\infty} \rho(x,\xi,0,0,0) \cdot d\xi \tag{3.104}$$

in which ρ stands for the correlation surface, which is defined by the space-time double correlation function divided by the product of the root-mean-square values σ of the fluctuations:

$$\rho(x,\xi,y,\eta,\tau) = \frac{R(x,\xi,y,\eta,\tau)}{\sigma(x,y) \cdot \sigma(x+\xi, y+\eta)} \tag{3.105}$$

R is defined as the space-time double correlation function in the following manner:

$$R(x,\xi,y,\eta,\tau) = \lim_{T\to\infty} \frac{1}{T} \int_0^T p'(x,y,t) \cdot p'(x+\xi, y+\eta, t+\tau) \cdot dt \tag{3.106}$$

$$\text{in which } \quad p'(x,y,t) = p(x,y,t) - \bar{p} \tag{3.107}$$

Two extreme cases can be considered. They are presented in Fig. III-44. The first case (Fig. III-44b) considers eddy sizes that are equal to or larger than the rock block in question. This leads to fully correlated pressure pulses at the joint entrances and thus to a constant pressure pattern over the rock block's surface. The second case (Fig. III-44a) is relevant to eddy sizes that are much smaller than the rock block sizes, resulting in pressure pulses at the joint entrances that are partially correlated (phase difference $\phi_1 - \phi_2$) or uncorrelated. Although at first sight the second case seems to generate the highest net uplift forces, both cases are able to eject a rock block from its mass. The reason for this is that the problem is highly depending on the time duration of the pulses and on their cyclic nature. This statement becomes more significant at lower wave celerities.

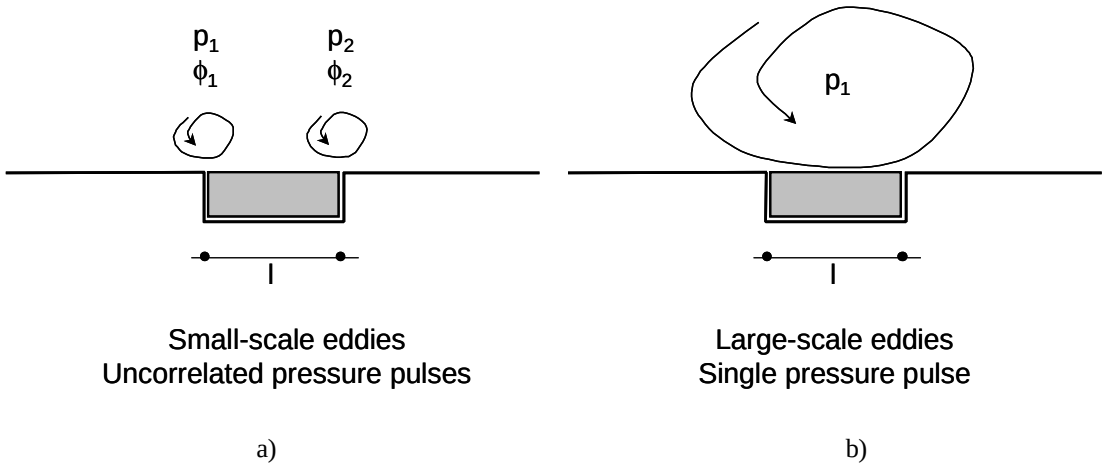

Fig. III-44 Dynamic pressure fluctuations at the pool bottom: a) small-scale eddies generate uncorrelated pressure pulses with a certain phase difference (ϕ_1-ϕ_2); b) large-scale eddies produce one single pressure pulse over the whole block.

Furthermore, the values of the underpressures change during uplift of the rock block. This is caused by the changing joint width, which decreases the governing pressure in the joint. The exact relationship is almost impossible to determine. At violent pressure pulses, its effect probably can be neglected. As a first approximation, this leads to a conservative result. In the following, the pressure that holds under the rock block is considered independent of the block movement. This will result in a safe upper limit of ultimate scour depth.

4.4.6. Concluding remarks

Failure of completely jointed rock masses is attained when the characteristic rock block is ejected from its mass or, at least, displaced within its mass such that the next pressure pulse will easily sweep the block away. Direct ejection of the block theoretically needs an uplift h_{up} of minimum the height of the block z. Displacement within the matrix could happen at displacements less than the height of the block. The lowest displacements will just cause vibrations of the block.

Hence, it is hardly possible to define the critical displacement h_{cr} of a rock block. It largely depends on the degree of interlocking of the blocks. As such, a very tightly jointed rock mass should, strictly speaking, need a displacement equal to or higher than the height of the block itself. For less tightly jointed rock masses, the critical displacement is probably somewhat lower.

As a conclusion, it is believed that the critical displacement of a rock mass is a model parameter that needs to be calibrated through model and/or prototype data. Its integration in a new scour model is described in Chapter VII.

Chapter IV. Experimental facility and equipment

1. Introduction

The objective of the experimental facility is to perform pressure fluctuation measurements at simulated plunge pool bottoms and simultaneously inside one-and two-dimensional underlying artificial rock joints, due to the impact of high-velocity plunging jets. Beside the need for a facility with near-prototype characteristics, one of the major challenges is to conceive the system such that different rock joint types and geometries can be analysed. Hence, that part of the facility that simulates the rock mass has to resist to near-prototype pressures and forces of impacting high-velocity jets and, at the same time, has to be modular.

One of the first ideas was to use real rock material, or appropriate concrete blocks, because they strongly correspond to the in-situ material. However, with regard to the particular requirements of combined rigidity and modularity, it is obvious that practical use of rock material or concrete blocks is strongly limited. Moreover, there is a risk that, with time, the rock or concrete material effectively erodes under the impact of the high-velocity jets.

Therefore, a pre-stressed steel system has finally been chosen to represent the rock mass. Such a system has the advantage of a very high rigidity that can easily be quantified and of a practically feasible modularity. Moreover, its capacity to resist to jet impact erosion is very high, and pressure sensors can easily be integrated.

In the following, a detailed description is provided of the experimental facility. Distinction is made between the structural equipment, necessary to simulate the jet, the plunge pool and the rock mass, and the measurement equipment, focusing on pressure fluctuation measurements. Also, because some parts of the installation are at near-prototype scale and other parts at a much smaller scale, the similitude laws of the system are explained.

Furthermore, a parametric analysis, based on the theory outlined in Chapter III, provides the main parameters that have been varied during the test runs. This finally conducts to a test program, which has been used as basis for the presentation of the experimental results in Chapter V.

2. Description

2.1. Structural equipment

2.1.1. General

The experimental facility is presented in Fig. IV-1 and at Photos 2a & 2b. Its structure consists of four main parts (Bollaert & Schleiss, 2001f):

a) A 300 mm diameter **water supply conduit**, with a cylindrical or convergent-shaped jet outlet system at its end, models the jet. Due to constructive limitations, the supply conduit has a 90° bend just upstream of the jet outlet system (see Photo 2a). A rigid steel frame, consisting of three I-shaped steel profiles that are welded together, guarantees the support of the supply conduit. This steel frame is not presented in Fig. IV-1, but can be observed at Photos 2 & 4. The jet outlet diameters are 57 or 72 mm.

b) A 3 m diameter **cylindrical basin in steel reinforced Lucite** simulates the plunge pool. The height of the basin is 1 m, and the steel reinforcement is provided by 10 T-shaped profiles. The bottom of the basin is made of a rigid steel frame, covered by a 10 mm opaque Lucite plate. Inside the basin, two rectangular boxes made of Lucite adjust the water level by a flat plate that is inserted. The water that flows over these plates is conducted downstream into four restitution conduits. The boxes are not visible in Fig. IV-1 but can be seen at Photo 2b.

c) A three-parts **pre-stressed steel structure** models the jointed rock mass. The rock joint is simulated by a 1 mm thin steel sheeting with a particular form. This sheeting is pre-stressed by means of 10 steel bars of 36 mm of diameter between two 100 mm thick steel plates of 1 ton each. These plates have a height and a width of 1 m and, at their top and bottom, are connected with two horizontal steel plates. The top plates form the pool bottom, while the bottom plates stabilize the structure. In the top plates, pressure sensors can be inserted.

d) A **restitution system** consisting of 4 conduits of 220 mm of diameter simulates the river downstream. These conduits are connected to the overflow boxes and conduct the water into the main reservoir of the laboratory. They are not visible in Fig. IV-1, but are presented at Photo 2b.

A fifth element of the installation is a 63 m head pump. This pump is installed in the main reservoir, from which the water is pumped into the supply conduit. After restitution through the restitution conduits, the water returns to the main reservoir. A closed water circulation system is so obtained. The maximum discharge is 250 l/s.

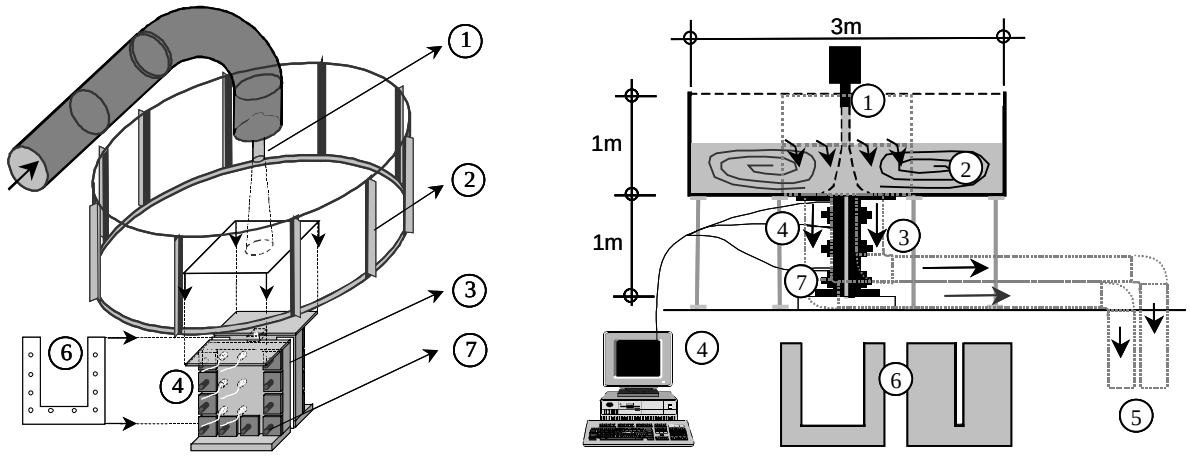

Fig. IV-1 Perspective and side view of the facility with the following elements (Bollaert & Schleiss, 2001f): 1) cylindrical jet outlet, 2) reinforced plastic cylindrical basin, 3) pre-stressed two-plate steel structure, 4) PC-DAQ and pressure sensors, 5) restitution system, 6) thin steel sheeting pre-stressed between steel structure (defining the form of artificial 1D and 2D joints), 7) pre-stressed steel bars.

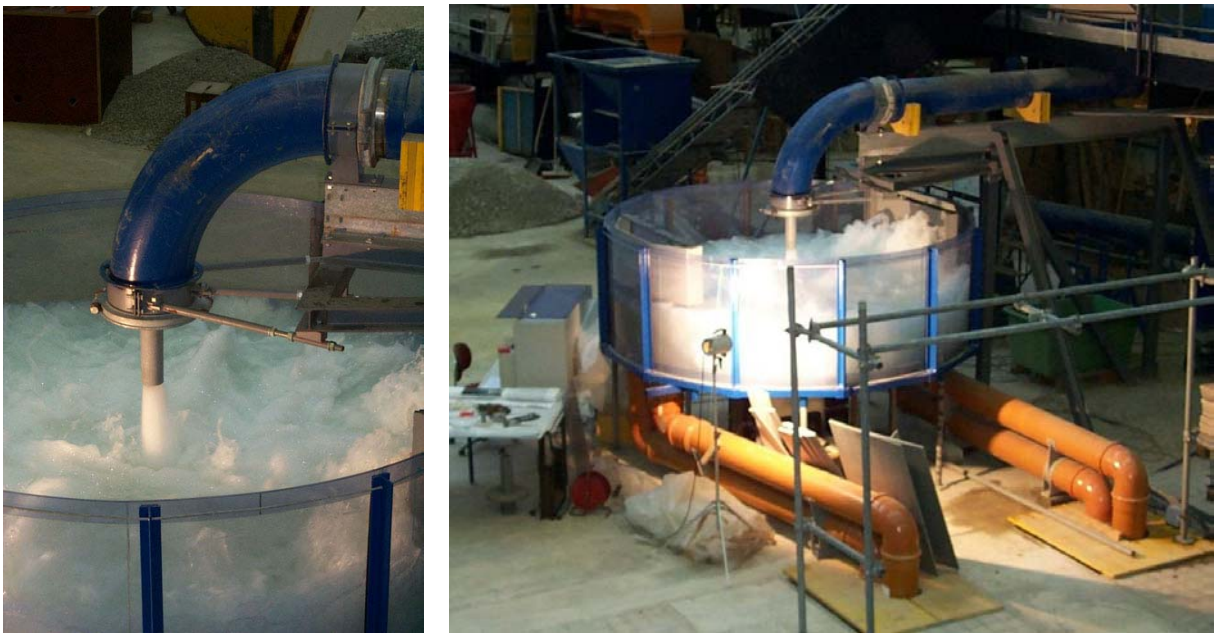

a) b)

Photo 2 a) View of the water supply conduit showing the 90° bend and a cylindrical jet outlet, b) General view of the experimental facility while running. On the foreground, the four restitution conduits are clearly visible.

Photo 2a shows the 90° bend of the water supply conduit. As will be outlined hereafter, the presence of this 90° bend is responsible for low-frequency jet turbulence. Photo 2b presents a general overview of the experimental facility while running. At the right hand side of the photo, a steel structure supporting the water supply conduit can be distinguished. At the left hand side, the PC and data acquisition system is visible.

In the following, the four main elements of the facility are presented more in detail.

2.1.2. Water supply conduit and jet outlet system

The water supply conduit has a 300 mm inner diameter and is made of stainless steel. Due to a neighboring construction that limited the maximum height of the facility, a 90° bend had to be introduced near the end of the conduit. This generated low-frequency jet turbulence that can best be described as an occasional opening and closing of the otherwise compact jet. This phenomenon is particularly visible at low jet velocities and low water depths.

The first part of the tests made use of a cylindrical-shaped jet outlet. For this outlet, no attempts were made to avoid the appearance of the low-frequency turbulence. In a second stage, a new series of tests were conducted for a convergent-shaped jet outlet, in order to compare the results with the cylindrical outlet. For this convergent jet outlet, a cross-shaped two-plate frame has been added inside the 90° bend, in order to get rid of the low-frequency turbulence. This frame is presented at Photo 3b.

The two jet outlet systems are presented in Fig. IV-2: Fig. IV-2a shows the cylindrical-shaped outlet, made of opaque Lucite, and Fig. IV-2b visualizes the convergent-shaped outlet, made of stainless steel and combined with a cross-shaped frame. The latter was at first made of Lucite. This element, however, broke down while running at high jet velocity due to the longitudinal stresses induced in the material. Both outlets have the same length.

For the cylindrical outlet, the diameters are 57 or 72 mm, while for the convergent outlet, only the 72 mm diameter has been constructed.

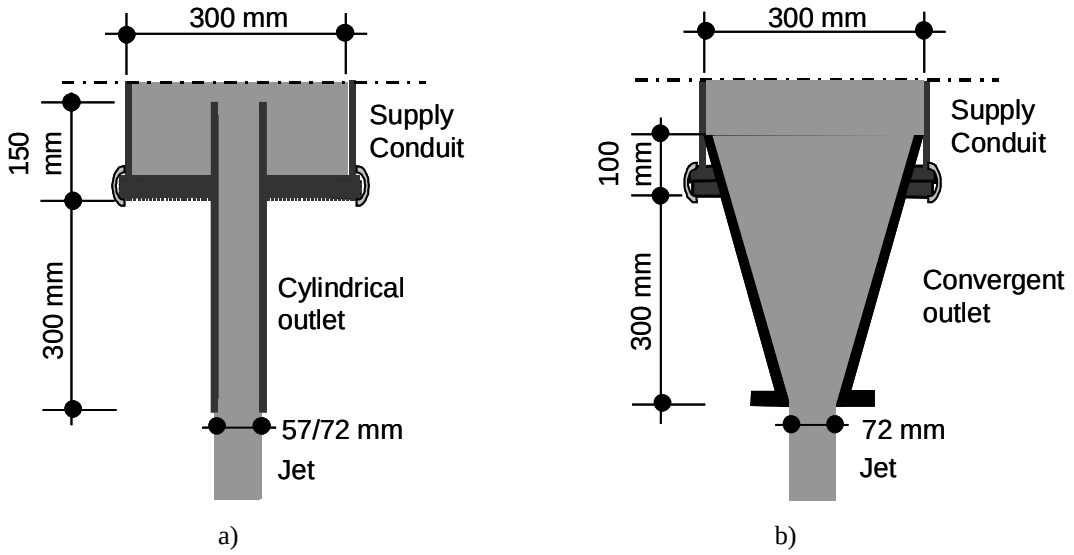

Fig. IV-2 a) View of the cylindrical-shaped jet outlet. The part of the cylindrical pipe that is outside of the supply conduit has an inner diameter of 57 or 72 mm, b) View of the convergent-shaped jet outlet. The downstream outlet diameter is 72 mm.

For the cylindrical jet outlet, the low-frequency turbulence generates two different types of jet (see Fig. IV-3): a compact form (FORM A), which is largely predominant, and a diffused form (FORM B), happening occasionally and for jet velocities less than 15-20 m/s. Fig. IV-3 also presents the corresponding pressure patterns. During a FORM B jet, a significant drop in pressure occurs. The importance of this phenomenon is outlined in Chapter V on experimental pressure measurements.

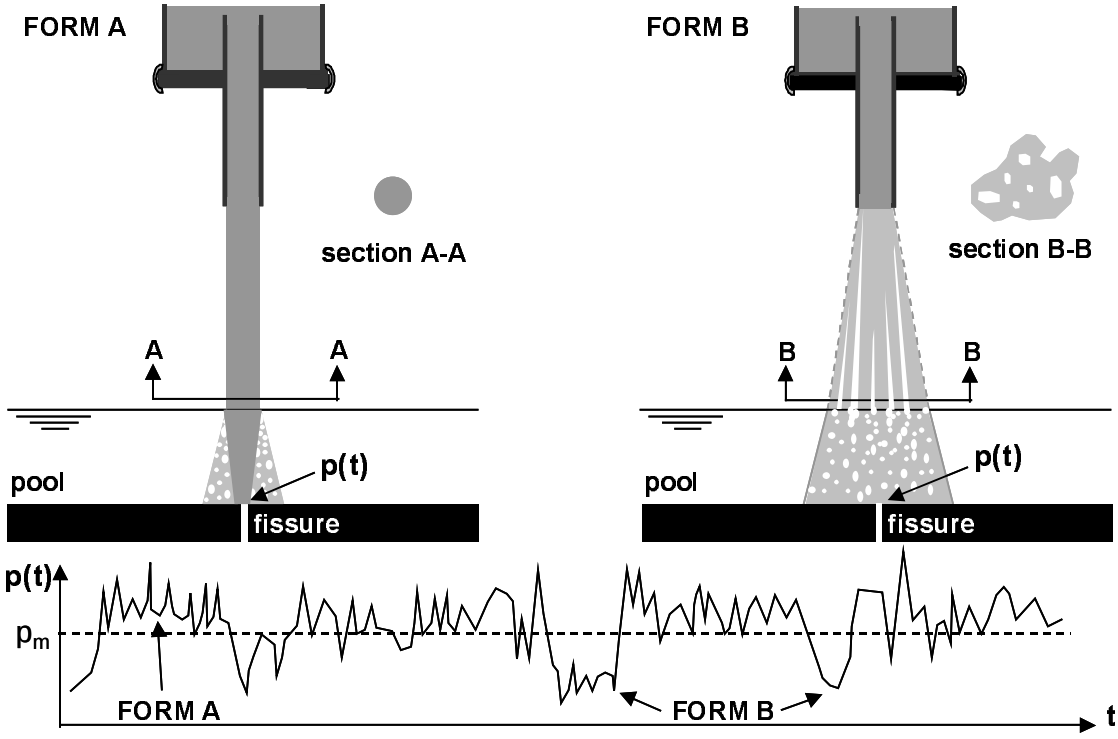

Fig. IV-3 Two different types of jet: a) FORM A, a compact jet, occurring most often, and b) FORM B, a diffused jet that can occasionally happen, especially at jet velocities less than 15-20 m/s. The importance of this diffusion increases with increasing jet fall length. The corresponding pressure patterns are also presented (Bollaert & Schleiss, 2001f).

The main jet characteristics for 72 and 57 mm diameter cylindrical-shaped outlets are summarized in Table IV-1 (Bollaert & Schleiss, 2001f). Based on pressure fluctuation measurements at the jet outlet, on the centerline of the jet, the turbulence intensity Tu (definition see Chapter III, § 3.1, equation (3.24)) of the 72 mm diameter jet has been quantified at 4 to 5 %. It can be noticed that slightly higher Tu-values are obtained at the lowest jet velocities. This is probably due to the aforementioned low-frequency turbulence. Disregarding the latter, the observed jets are rather compact because of the small fall heights (max. 0.50 m), and thus the small degree of spread (max. 0.30).

Diam.	Disch.	Mean veloc.	Froude number	Reynolds number	Weber number	Fall height	L/D_j	Pool depth	Y/D_j	Jet turb.int.	Breakup length	Degree of spread	
D_j	Q	V_j	F_j	Re_j	We_j	L		Y		T_u	L_b	$L/L_{b\,min}$	$L/L_{b\,max}$
m	l/s	m/s	-	-	-	m	-	m	-	%	m	-	-
0.072	30	7.4	8.8	4.E+05	232	0.03-0.5	0.4-6.9	0.2-0.7	2.1-9.7	5.2	1.69	0.02	0.30
	40	9.8	11.7	5.E+05	308	0.03-0.5	0.4-6.9	0.2-0.7	2.1-9.7	4.9	1.95	0.02	0.26
	50	12.3	14.6	7.E+05	386	0.03-0.5	0.4-6.9	0.2-0.7	2.1-9.7	4.6	2.22	0.01	0.23
	60	14.7	17.5	8.E+05	462	0.03-0.5	0.4-6.9	0.2-0.7	2.1-9.7	4.1	2.62	0.01	0.19
	70	17.2	20.5	1.E+06	540	0.03-0.5	0.4-6.9	0.2-0.7	2.1-9.7	4.0	2.83	0.01	0.18
	80	19.7	23.4	1.E+06	619	0.03-0.5	0.4-6.9	0.2-0.7	2.1-9.7	4.4	2.73	0.01	0.18
	90	22.1	26.3	1.E+06	694	0.03-0.5	0.4-6.9	0.2-0.7	2.1-9.7	4.2	2.95	0.01	0.17
	100	24.6	29.3	1.E+06	773	0.03-0.5	0.4-6.9	0.2-0.7	2.1-9.7	4.3	3.05	0.01	0.16
	110	27	32.1	1.E+06	848	0.03-0.5	0.4-6.9	0.2-0.7	2.1-9.7	4.1	3.23	0.01	0.15
	120	29.5	35.1	2.E+06	926	0.03-0.5	0.4-6.9	0.2-0.7	2.1-9.7	4.4	3.15	0.01	0.16
0.057	20	7.9	9.4	4.E+05	248	0.03-0.5	0.5-8.8	0.2-0.7	2.5-12.3	-	-	-	-
	30	11.8	14.0	7.E+05	371	0.03-0.5	0.5-8.8	0.2-0.7	2.5-12.3	-	-	-	-
	40	15.7	18.7	9.E+05	493	0.03-0.5	0.5-8.8	0.2-0.7	2.5-12.3	-	-	-	-
	50	19.6	23.3	1.E+06	616	0.03-0.5	0.5-8.8	0.2-0.7	2.5-12.3	-	-	-	-
	60	23.5	28.0	1.E+06	738	0.03-0.5	0.5-8.8	0.2-0.7	2.5-12.3	-	-	-	-
	70	27.4	32.6	2.E+06	861	0.03-0.5	0.5-8.8	0.2-0.7	2.5-12.3	-	-	-	-
	80	31.3	37.2	2.E+06	983	0.03-0.5	0.5-8.8	0.2-0.7	2.5-12.3	-	-	-	-

Table IV-1 Main characteristics of vertical plunging circular shaped jets (Bollaert & Schleiss, 2001f).

The convergent-shaped jet characteristics are not presented herein. They have similar Froude, Reynolds and Weber numbers and exhibit the same fall heights and pool depths. Moreover, their turbulence intensity Tu at the outlet has not been measured. Hence, no information is available regarding the jet break-up length and the degree of spread of the jet. However, based on pressure measurements made at the plunge pool bottom, directly under the centerline of the impacting jet, their turbulence intensity could be roughly estimated at 3 to 4 %. It may be assumed that the jets issuing from convergent-shaped outlets are more compact than jets issuing from a cylindrical-shaped outlet. This statement seems plausible when considering the stabilizing effect of the cross-shaped frame.

2.1.3. Plunge pool modeling

The plunge pool has been simulated by a 3 m diameter cylindrical basin made in transparent Lucite (Photo 3a). The height of the walls is 1 m and the bottom consists of a rigid steel structure covered with a 10 mm thick opaque Lucite plate. In the center of this plate, a square hole of 1 m^2 has been made in order to insert the horizontal steel plates that are connected with the underlying pre-stressed steel structure. The connection between the basin and the steel plates has been made watertight with silicone. The foundation of the Lucite basin consists of 12 steel I-beams resting on end that are linked to the rigid steel structure and that are evenly distributed over the surface of the bottom. In other words, the basin and the lower steel structure have not the same foundation. The only contact between them is the watertight.

The walls of the Lucite basin have been reinforced by means of 10 T-shaped steel profiles that are directly supported by the foundation structure of the basin. This revealed to be necessary as a result of significant low-frequency movements of the walls at high jet velocities, which put into danger the security of the structure.

The inside of the Lucite basin contains two rectangular boxes made of Lucite (Photo 3a). At the inner side of these boxes, a flat plate can be inserted in order to adjust the water level in the basin. The water level could so be varied from 0 to 1 m maximum. The jet outlet system is situated at a height of 0.70 m from the bottom of the basin and, thus, submerged jet outlet is theoretically obtained for water levels between 0.70 m and 1 m.

However, due to the appearance of surface dimples by vortices in the basin, a water height of minimum 0.85 m was necessary to avoid air from entering the pool. At water levels less than 0.40 m, the plunge pool basin had to be covered with a plastic sheet, because the impact of the jets became that strong that a considerable amount of water was occasionally ejected from the basin.

a)

b)

c)

d)

Photo 3 a) View of the 3 m-diameter, cylindrical, steel reinforced Lucite basin simulating the plunge pool, b) detailed view of the cross-shaped frame that has been inserted in the 90° bend of the supply conduit, c) side view of the foundation of the Lucite basin, d) connection between the Lucite basin and the lower, four-element steel structure.

2.1.4. Fractured rock modeling

A four-element pre-stressed steel structure simulates the fractured rock mass. The different elements are presented in Fig. IV-4.

The first element corresponds to a 1 mm thin stainless steel sheeting with a particular form. This sheeting can have any form, but for a constant thickness, and allows modeling one-and two-dimensional rock joints at prototype scale.

The second element represents two 100 mm thick steel plates, with a weight of 1 ton each, that simulate the surrounding rock mass. These plates have a height and a width of 1 m and, at their top and bottom, two small horizontal steel plates have been welded. The top plates form a 1 m^2 pool bottom and exactly correspond to the size of the hole that has been made inside the plunge pool basin (see § 2.1.3). The bottom plates stabilize the structure.

The third element constitutes a set of 20 support plates of 0.20 m x 0.20 m that are necessary to transmit the stresses of the steel bars into the steel plates in a homogenous manner.

Finally, the fourth element is formed by a series of 10 DIWYDAG steel bars of 36 mm of diameter and 430 mm of length. These bars allow pre-stressing the thin stainless steel sheeting between the two thick steel plates.

Hence, an extremely rigid and watertight system has been created, with a 1 mm small opening in the middle. The advantage of this system is its facility to modify the form and the thickness of the sheeting, as well as the stresses in the DIWYDAG steel bars.

Within this steel system, a series of holes have been made in order to introduce the pressure sensoring devices. This is discussed in § 2.1.5.

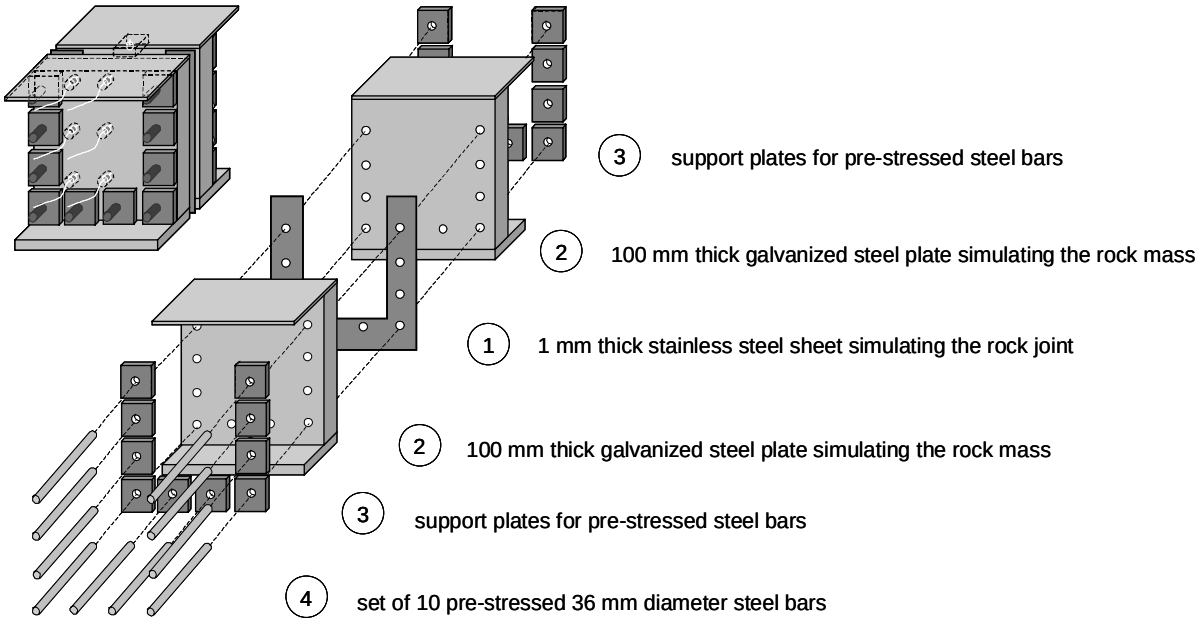

Fig. IV-4 Pre-stressed steel system showing the four main elements and their disposition: 1) thin stainless steel sheeting, 2) two thick steel plates simulating the rock mass, 3) a set of support plates, 4) a series of 10 pre-stressed DIWYDAG steel bars.

The stresses are induced in the DIWYDAG steel bars by means of a hydraulic piston, as presented at Photo 6a. With this system, forces of up to 1'000 kN can be generated. For steel bars of 36 mm of diameter, this corresponds to a stress of maximum 1018 N/mm^2. The forces induced in the steel bars during the test runs fluctuated between 150 and 300 kN, corresponding to stresses of between 152 and 305 N/mm^2. This is safely situated in the elastic range. The yield stress of the bars is 1'080 N/mm^2, and the tensile strength is 1'230 N/mm^2. The modulus of elasticity of the steel bars E_s is 205 kN/mm^2.

a)

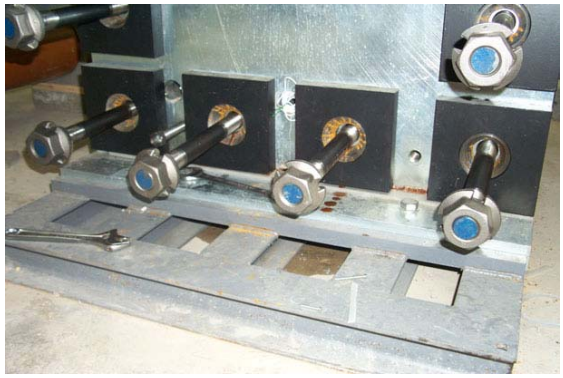

b)

c)

d)

Photo 4 a) Hydraulic piston system to pre-stress the DIWYDAG steel bars, b) detailed view of the pre-stressed system before closing, c) example of stainless steel sheeting simulating a one-dimensional closed-end rock joint, d) side view of the two thick steel plates when opened.

In order to obtain a watertight system, high-quality steel has been used. The steel has been rectified, galvanized and stress relieved. Corrosion could be prevented and the internal stresses have been reduced to a minimum. Moreover, the rectification conducted to the following precise tolerances:

- thickness: +0/+0.25 mm
- flatness: < 0.1 per 1'000 mm
- parallelism: < 0.03 mm
- length: +0.3/+0.8 mm
- width: +0.3/+0.8 mm

The particular form of the rock joint under investigation has been obtained by cutting a piece out of the 1 m^2 stainless steel sheeting. This precision work has been done by means of a high-pressure jet. The sheetings are fabricated with a tolerance of the thickness of +0/+0.1 mm. An example of a sheeting, representing a one-dimensional closed-end rock joint, is presented at Photo 4c.

2.1.5. Water restitution system

The restitution of the water is performed by means of two Lucite outlet weir structures and four connected conduits that conduct the water into the main reservoir. The weir structure defines the water level in the basin by use of a flat Lucite plate in front of the system. This plate can be easily moved in and out of the boxes. The water falls into the boxes. In the bottom of the boxes, two circular holes link

the boxes with the downstream plastic conduits. The four conduits are presented at Photos 4b & 5c. This outlet system has been designed for a maximum discharge of 250 l/s, i.e. the upper limit of the high-head pump.

2.2. Measurement equipment

2.2.1. Data acquisition hardware and software

The data acquisition equipment consists of an automated data measurement system that was particularly designed for the simultaneous acquisition and analysis of highly dynamic input signals (Photo 5a). This signal conditioning hardware has been developed at the Hydraulic Machines Laboratory (LMH) of the Swiss Federal Institute of Technology (EPFL, Lausanne, Switzerland) and uses an 8-channel platform with the following characteristics (Bollaert & Schleiss, 2001b):

1. Pre-amplification and signal conditioning card:

- *Sensor excitation*: jumper-selectable at +/-12 VDC or 4mA, tolerance +/- 0.5 V.
- *Sensor amplification*: The offset is adjustable via a potentiometer +/- 0.1 V, while the gain is jumper-selectable at 10 or 100.
- *Analog filter*: 5th order low-pass filter of the Bessel kind, jumper-selectable at 62 Hz, 125 Hz, 250 Hz, 500 Hz, 1 kHz, 2 kHz, 4 kHz or 8 kHz.
- *Output*: V_{out} filtered at +/- 10V maximum

2. Data acquisition converter ACQ4AD

- *Alimentation*: 4 simultaneously sampled channels, +/- 12VDC (160 mA), tolerance +/- 0.5V.
- *Amplification*: The offset is programmable from +5V to –5V, the gain is programmable (per channel) at 1, 2, 4 or 8.
- *A/D*: Analog-Digital conversion at 14 bits (+/-10V) = 1.22 mV/bit sensitivity.
- *Acquisition rate*: programmable from 100 Hz to 20'000 Hz per channel.
- *Acquisition time*: 0.35 µs Track/Hold
- *D/A*: adjustable offset at 12 bit (+/-5V)= 4.88 mV/bit.
- *Memory*: NVRAM 4Mb, or 65'024 values per channel.
- *Arcnet*: high-speed parallel interface at 2.5 Mbit/sec on RS485.
- *Transmission*: transmission speed 40 seconds for 1 card = 4 channels

An acquisition rate of 1 kHz has been applied during most of the tests, together with a low-pass analog filtering at 500 Hz, according to the Nyquist theorem. The maximum storage capacity of 65'024 values per channel generates 65 seconds of values for one test run. This was found to produce sufficiently reproductive and ergodic statistical values. Regular control runs were performed at acquisition rates of 5 to 20 kHz in order to check for the transient character of the measured pressure peaks.

The used software has been written by the author in the LabVIEW environment and focuses on the following statistical characteristics:

- mean, RMS, maximum and minimum pressure values,
- histogram of pressure values, 1% and 0.1% probability values,
- power spectral density of pressure values,
- auto- and cross-correlations of the different measuring points,
- phase and amplitude transfer functions between the different measuring points,
- coherence functions between the different measuring points,

a)

b)

Photo 5 View of the PC and data acquisition equipment. The high-speed simultaneous acquisition is performed by means of two A/D cards of 4 channels each. The acquisition rate is between 100 and 20 kHz per channel. The signal conditioning incorporates sensor alimentation and amplification, jumper adjustable analog filtering and simultaneous A-D conversion of the 8 channels. The PC is a 266 MHz Pentium II processor working under Windows 98.

2.2.2. Micro-pressure sensors

A series of 8 micro pressure sensors KULITE XTC-190M-17-BAR-A have been used for the pressure measurements (Photo 5b). These sensors are of the piezo-resistive type, with an absolute pressure range between 0 and 17 bar and a precision of +/- 0.1 % of the full scale output. They have been developed in order to measure highly dynamic pressure phenomena, such as shock waves. Hence, they exhibit a very high resonance frequency. Their measuring membrane has a 3 mm diameter. The sensors can be perfectly flush mounted by screwing them into the steel structure. The main sensor characteristics are summarized as follows:

- *pressure range*: 0-17 bar absolute
- *non-linearity & hysteresis*: +/- 0.1 % of full scale
- *output*: 100 mV at full scale
- *resonance frequency*: 680 kHz
- *working frequency range*: 0-15 kHz
- *temperature drift*: +/- 1% of full scale per 55°C

The integration of the sensors in the steel necessitated the installation of M5-dowels. In total, 6 dowels have been made inside one of the steel plates that simulates the rock mass, and 10 dowels into one of the horizontally welded steel plates, simulating the plunge pool bottom. The dowels without a sensor have been filled up with a screw of the same size as the sensors. In this way, a modular system of pressure measurement locations has been created. The location and the corresponding nomenclature of the different sensor positions is presented in Fig. IV-5.

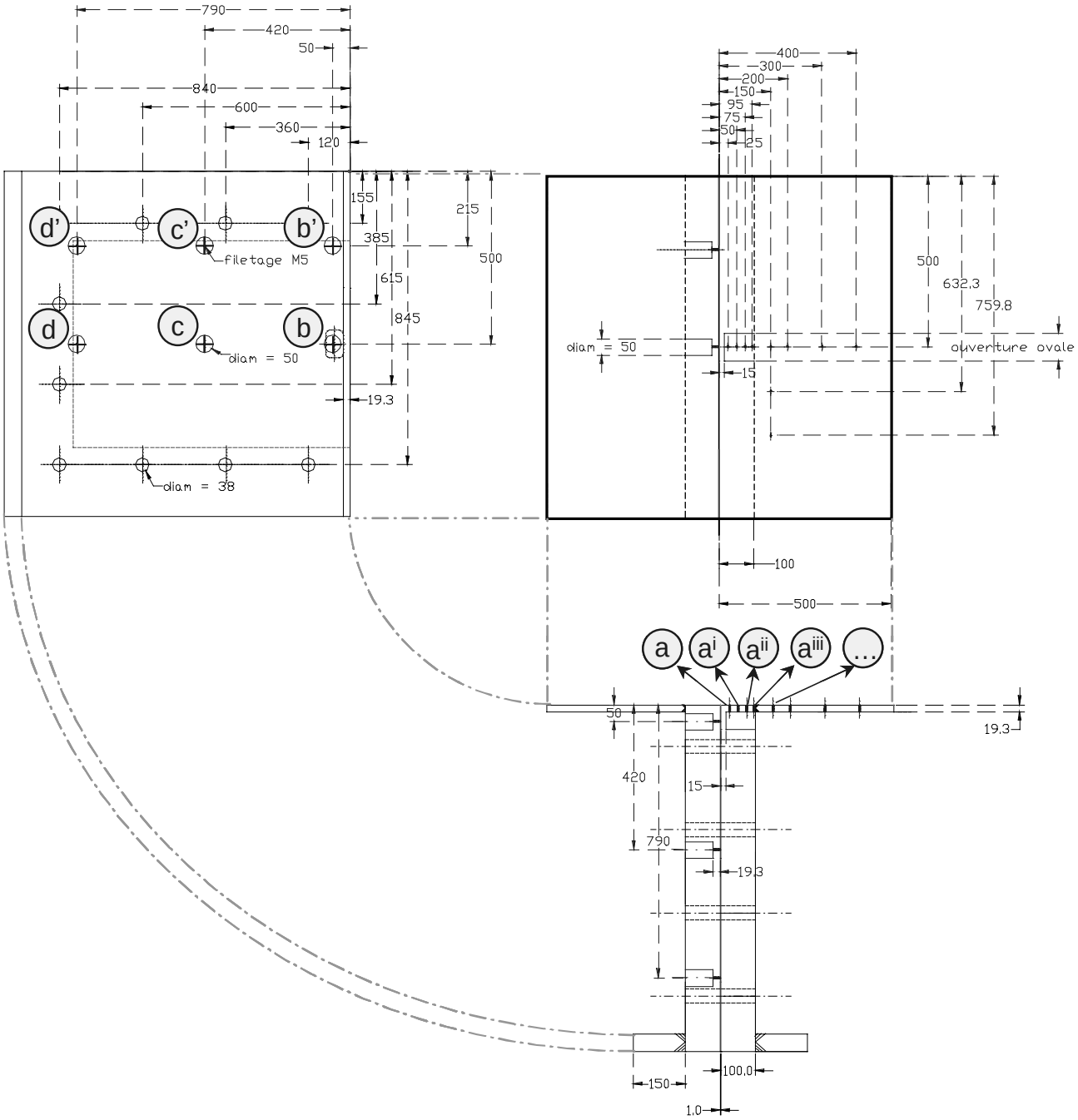

Fig. IV-5 Plan, front and side view of the lower steel structure, showing the location of the dowels necessary for the pressure sensor integration, as well as the holes made for the 10 DIWYDAG steel bars.

The nomenclature of the different dowels has been subdivided into two groups, as a function of their relative position. In the following, parentheses are used to express the sensor positions.

- *pool bottom dowels*: they are nomenclated from the center of the installation radially outwards: (a), (a^{i}), (a^{ii}), (a^{iii}), (a^{iv}), etc. 8 dowels can so be distinguished. The last two dowels, situated on another axis, have not been used during the tests and are not further discussed.
- *rock joint dowels*: they are named following the centerline vertical axis and the side vertical axis of the thick steel plates. On each of the axes, the order is from top to bottom. This gives on the centerline: dowels (b), (c) and (d); and on the outer axis, the dowels, (b'), (c'), and (d').

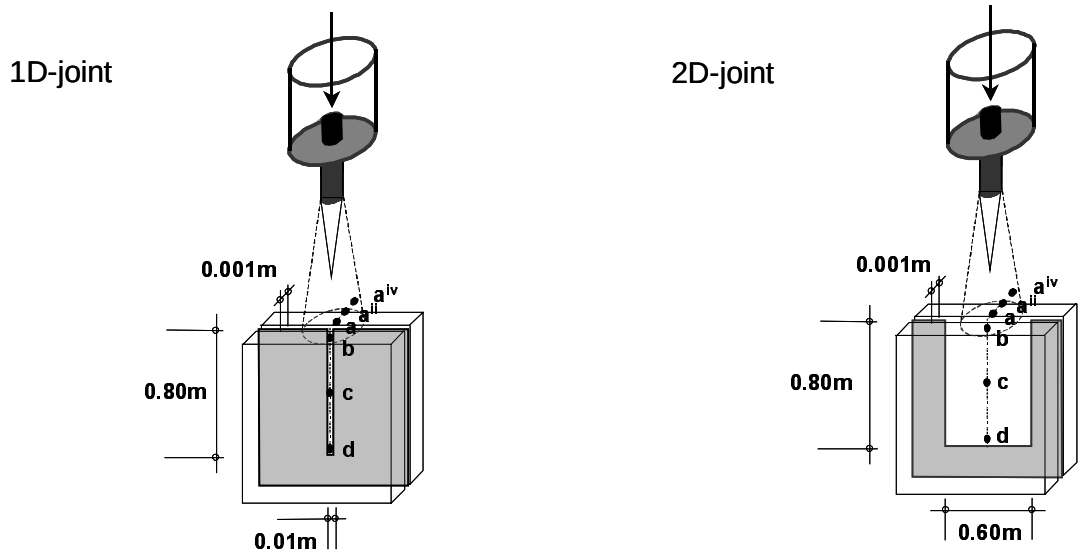

Fig. IV-6 Detailed view of the position and nomenclature of the mostly used pressure sensors: (a), (a^{ii}), (a^{iv}) at the pool bottom, and (b), (c) and (d) inside the one-or two-dimensional closed-end rock joint (Bollaert & Schleiss, 2001f).

The sensor positions that have been used most often are presented in Fig. IV-6 for a one-and two-dimensional rock joint configuration. At the pool bottom, a comparison between the sensors (a), (a^{ii}) and (a^{iv}) has been made. Inside the rock joint, the centerline sensors (b), (c) and (d) have been compared with sensor (a) at the surface.

Beside the aforementioned positions, two sensors have been used for pressure estimations at the point of issuance of the jet. This determines the initial turbulence intensities Tu (longitudinal) and Tv (transversal), which express the turbulent character of the jet. A facility has been conceived consisting of a rectangular steel frame that supports an elongated, hollow cylinder made from stainless steel. At the top of this cylinder, a pressure sensor has been integrated. The form of the cylinder at the top is conical, in order to minimize the influence of the presence of the cylinder on the turbulent flow characteristics. Secondly, a pressure sensor has been integrated in the side-wall of the cylinder, in order to measure the transversal pressure fluctuations. A side view can be seen at Photo 6.

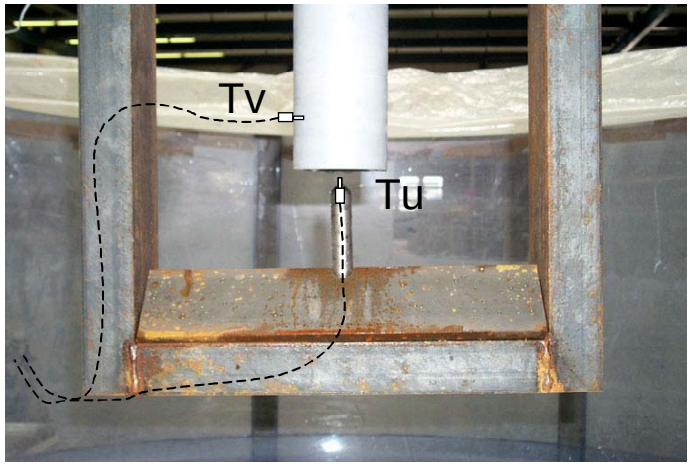

Photo 6 Side view of the facility that allows measuring the turbulence intensity level at the jet outlet. An elongated, hollow cylinder in stainless steel is supported by a steel frame. The form of the cylinder is such that flow disturbances are minimum.

3. Similitude

3.1. Introduction

As the experimental facility makes use of near-prototype jet velocities but model scaled geometries, a precise description of the similitude laws is needed. The facility simulates the three phases that govern the scouring phenomenon: the water (liquid phase), the air bubbles (gas phase) and the rock mass (solid phase).

It is obvious that each phase has different predominant laws of similitude. For example, the liquid phase often makes use of the Froude similarity, focusing on a correct modelling of the ratio of inertial over gravity forces. The diameter of the jet at impact is highly influenced by the gravitational acceleration, which results in a contraction of the jet. Air entrainment, however, is a combined Froude-Reynolds-Weber phenomenon. The aeration characteristics of a free falling jet are dictated by the influences of two opposite forces: the surface tension tends to keep the jet together and is characterized by the Weber number, while the initial turbulence intensity of the jet rather tries to disperse the jet, as described by the Reynolds number.

Moreover, the rock mass, strictly speaking, needs a similitude that accounts for dynamic fluid-structure interaction effects. These are very difficult to reproduce on a model. The pressurized flow conditions inside the fissures of the rock mass should follow a correct Strouhal similitude, because of their transient and resonating character.

3.2. Jet and plunge pool scaling

No scaled model installation is capable to satisfy all these similitude criteria together. Therefore, emphasis has been given on the construction of a prototype installation. The mean jet outlet velocities are in the range of 5 to 35 m/s, i.e. at near-prototype values. This range of velocities revealed to be sufficiently close to prototype values for a correct reproduction of the aeration of the plunge pool due to jet impact. Air contents up to the physically plausible maximum, i.e. 60-70 % at the point of jet impact in the plunge pool, could so be obtained.

The geometry of the jet and the plunge pool, however, is not at prototype scale. This is clearly impossible to perform on laboratory facilities. However, one of the major particularities of the present experimental facility is that this problem has been circumvented by the use of an appropriate ratio of the plunge pool depth over jet diameter at impact Y/D_j (for definition, see Chapter V, § 3.2). For ratios that are common in practice and for near-prototype jet velocities, the facility allows generating frequency spectra of the turbulence intensity of the jet at impact that are very close to reality. In other words, the generated turbulent excitation and prototype aeration of the jet are representative for prototype conditions and capable to stimulate a rock joint to resonance (Bollaert & Schleiss, 2001d).

These frequency spectra have some limits although. First of all, extremely low frequencies that could be present in nature due to large-eddy re-circulation in real-life plunge pools, cannot be simulated. However, these low frequencies will not excite a fissure to resonance. Therefore, the failure to simulate the extremely low frequency components of the pressures within a prototype plunge pool do not need to be replicated in the facility. Secondly, the extremely high frequency components of the spectrum do not have to be simulated because they too do not influence the transient pressures inside rock fissures.

The model-scaled water levels of the facility (ranging from 0 to 0.70 m) are sufficient to produce realistic frequency spectra at the plunge pool bottom. By adjusting the water level, different realistic turbulence levels could be created at the bottom. As such, they do not have to be considered as real water levels, but rather as a means to obtain a correct turbulence modelling at the plunge pool bottom.

The same remark is valid for the jet outlet system. As already mentioned, two types of jet outlet have been used. The cylindrical outlet generates jets with both a low-frequency component and a turbulence

intensity of 4-5 %. The convergent outlet creates more compact jets, with initial turbulence intensities of about 3 %. According to available literature data (McKeogh & Elsawy, 1980; Ervine et al., 1980; Ervine & Falvey, 1987) these values correspond to prototype jets that are moderately to roughly turbulent. Consequently, the jet and plunge pool modelling create realistic aeration and turbulence effects and, thus, can be considered at prototype scale, even with a significant geometric distortion.

3.3. Rock mass scaling

The rock mass is modelled by means of a steel structure as described in § 2.1.4. The length of the tested joints can range from 10^{-1} m to 10^{+1} m and is at prototype scale. The thickness of the joints is also realistic (10^{-3} m), while the width of the joints has been adapted to the diameter of the jet at impact in the pool and to the zone of turbulence generated by the diffusing jet at the pool bottom.

As a result of the geometric distortion of the diameter of the jet, this zone does not correspond to prototype conditions. However, as the flow conditions inside the joints are pressurized, this geometric scaling effect is not of significant importance on the pressure fluctuations inside the joints. A one-dimensional joint can be simply obtained by applying a joint width that is inferior to the zone of turbulence generated by the jet at the plunge pool bottom. Similarly, a two-dimensional rock joint is defined by a width that is superior to the latter. These zones of turbulence at the plunge pool bottom depend on the water level but typically range from 10^{-1} m to 10^{0} m. Therefore, for one-dimensional rock joints, a width of 0.01 m has been adopted, while for two-dimensional rock joints, a width of 0.60 m has been used.

Furthermore, the mass of the rock is simulated by the mass of the steel plates (1 ton each), as well as by the pre-stressed force in the steel bars. The fluid-structure interaction of the experimental facility corresponds to a simple spring-mass system and is determined by the mass of the steel plates and the stiffness of the steel bars. The latter have a module of elasticity of $E_s = 205.10^9$ N/m^2. Typical modules of elasticity of rock masses range from 10.10^9 to 50.10^9 N/m^2. As a result, the steel structure exhibits a rigidity that is superior to the one of rock masses. However, as it is very difficult to determine the exact mass of rock that is excited by a hydrodynamic action inside rock joints, as well as to take into account wave reflections at the boundaries, a prototype simulation of the dynamic stiffness of the structure is impossible. Therefore, in the following, any fluid-structure interaction effects are neglected.

4. Parametric analysis

The present parametric analysis defines the range of values of the parameters that are of importance during the several stages of scouring. Similar to the description of the experimental facility, distinction has been made between jet parameters, plunge pool parameters and finally rock mass parameters.

4.1. Jet parameters

The jet parameters are:

- cylindrical or convergent outlet,
- 57 mm or 72 mm jet diameter at outlet D_j,
- mean jet outlet velocities V_j between 5 m/s and 35 m/s.

In practice, free falling jets can issue from a lot of different outlet structures, such as for example bottom orifice outlets, ski-jumps, overflow weirs, etc. Each of these outlet structures is characterized by particular turbulence characteristics. The two different jet outlet systems that have been tested (Fig. IV-2) account for eventual influences of the turbulent quantities at the outlet.

For the cylindrical outlet, two jet diameters have been tested: 57 mm and 72 mm. For a convergent jet outlet, only the 72 mm diameter jet has been used.

For all 72 mm diameter outlets, the mean jet outlet velocity ranged from 7.4 m/s to 29.7 m/s. For the 57 mm diameter outlet, the mean jet outlet velocity was between 7.9 m/s and 31.3 m/s.

Beside the Froude, Reynolds and Weber numbers for each of these cases, as indicated in Table IV-1, the jet fall heights L range from 0.03 m to maximum 0.70 m. This implies that rather compact jets are obtained, with very small degrees of break-up. The obtained ratios of jet fall height to jet diameter at impact L/D_j were between 0.4 and 6.9 for 72 mm diameter jets, and between 0.5 and 8.8 for 57 mm diameter jets.

The theoretical ratio of plunge pool depth to jet diameter at impact Y/D_j, which is a very important parameter, ranged from 2.1 to 9.7 for 72 mm jets and from 2.5 to 12.3 for 57 mm jets, the latter value always corresponding to a submerged jet issuance condition.

4.2. Plunge pool parameters

The basic parameter of the simulated plunge pool is the governing water depth Y. Due to the fixed construction of the plunge pool basin no size or form effects of the basin are accounted for. This, however, can be of significant influence on the pool bottom pressure fluctuations and should merit more attention in future research projects.

Two different jet issuance conditions can be distinguished by changing the water level in the basin: submerged and non-submerged. For the submerged jet issuance conditions, a water level of 0.87 m has been used. With the outlet of the jet at a height of 0.70 m above the plunge pool bottom, this level was sufficient to create jet submergence at any instant, and to prevent any air from entering the water in the pool. For non-submerged jet issuance conditions, corresponding to a highly aerated plunge pool, the tested water levels were 0 m, 0.20 m, 0.30 m, 0.40 m, 0.50 m, 0.60 m and 0.67 m. The latter level corresponds to a jet outlet that is just not submerged.

The capability to create both submerged and non-submerged jet issuance conditions allows quantifying the influence of the air entrainment on the pressure fluctuations at the pool bottom and inside the rock joints.

Moreover, ten different locations of pressure measurement have been incorporated into the bottom of the simulated plunge pool. Eight of these locations have been aligned radially outwards from the

centerline of the impacting jet. The latter two are situated along an axis aside. These locations allow establishing the pattern of pressure fluctuations at the plunge pool bottom.

For most of the performed test runs, however, only three test locations have been extensively used at the bottom. According to Fig. IV-5, they correspond to the positions (a), (a^{ii}) and (a^{iv}). Moreover, for comparison between the plunge pool bottom pressures and the corresponding rock joint pressures, only the sensor (a) has been used as a reference. This sensor is situated directly near the entrance of the rock joints, and thus should be most representative for the pressures that enter these joints.

4.3. Rock mass parameters

The rock mass parameters can be subdivided into:

- one-or two-dimensional rock joints,
- total length of the rock joints,
- form of the rock joints,
- thickness of the rock joints,
- boundaries of the rock joints,
- pre-stressed forces in the steel bars,
- locations for the pressure sensors.

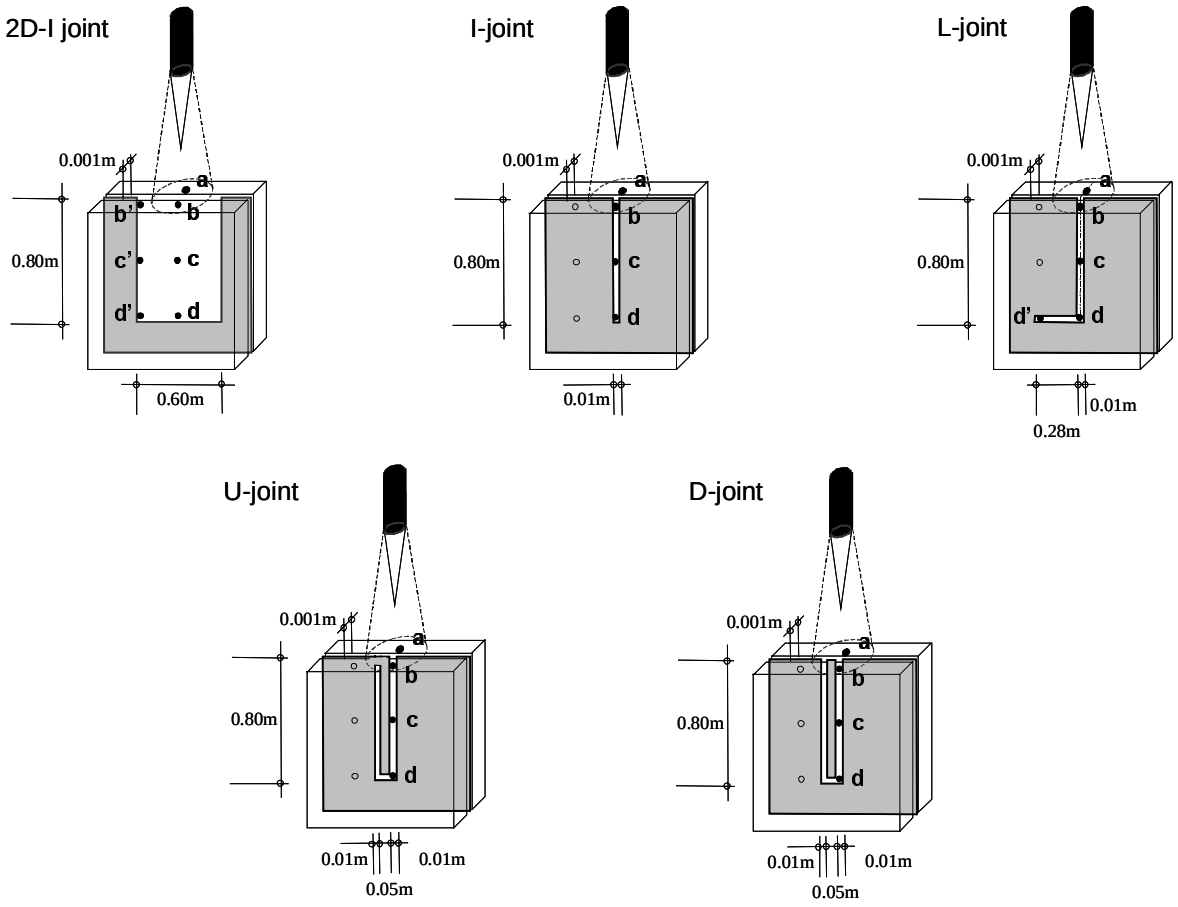

Fig. IV-7 Overview of the rock mass parameters: location of the pressure sensors and length, form and dimensions of the tested rock joints. All five rock joints are discussed in Chapter V.

For all tested rock joints, a constant thickness of 1 mm has been used. The pre-stressed forces in the steel bars varied from 150 kN to 300 kN, without any noticeable effect on the measured pressure fluctuations inside the joints. The location of the sensors, as well as the length, form and dimensions of the tested rock joints, are presented in Fig. IV-7.

One joint is two-dimensional of form (2D-joint), the others are one-dimensional. One joint is of the open-end type (D-joint), involving two open-end boundary conditions, and the other ones are closed-end, with one open boundary and one closed boundary condition.

For the two-dimensional rock joint configuration, a width of 0.60 m and a length of 0.80 m has been applied. The other five one-dimensional rock joints have a constant width of 1 cm. The simplest one-dimensional form is the I-joint, characterized by a length of 0.80 m. The second one-dimensional form is the L-joint, with a total length of 1,09 m. This form should allow qualifying and/or quantifying the influence of a 90° bend on the pressure propagation inside. Furthermore, a U-joint has been tested. This joint includes two 90° bends and has a watertight closure at the end of one of the legs. In this way, a closed-end joint configuration with a total length of 188 cm is obtained. This joint has been tested in order to account for air bubbles that could get stuck near the dead end of the joint.

Finally, the D-joint has the same form as the U-joint, but without the watertight closure. As such, an open-end joint system is obtained. This joint system corresponds to the case of a rock block that can freely move within its matrix.

The 2D-joint allowed measuring the pressures at the 6 sensor locations simultaneously. For the I, U and D-joint, only the three centreline sensors could be used. Finally, for the L-joint, four sensors have been activated.

5. Test program

5.1. Methodology

The test program has been set up in order to minimize the human interventions necessary to modify one or more of the test parameters. Due to the particular concept of the facility, and to its extreme rigidity as a result of the huge hydrodynamic forces involved, one of the interventions appeared to be time-and force consuming, namely the insertion of a new rock joint form, i.e. a thin steel sheeting.

This intervention needs a destruction of the watertight between the upper plunge pool basin and the lower steel structure, the highering of the basin, the opening of the steel bars, the opening and cleaning of the two thick steel plates, the insertion of a new steel sheeting, the closing and pre-stressing of the steel bars and finally the lowering of the basin and the re-installation of the aforementioned watertight. The total time for this intervention was two days. The other possible interventions are a displacement of the pressure sensors towards other dowels, a modification of the jet outlet system, a change in water level, and a change in jet outlet velocity.

An optimisation of all these interventions conducted to the following methodology of measurement:

1. install a rock joint form (5 forms)
2. install a jet outlet system (2 cylindrical forms, 1 convergent form)
3. install a water level (7 different levels)
4. install the pressure sensors (16 dowels in total)
5. perform test runs over the range of jet outlet velocities (about 10 different velocities)

It has to be noticed that, disregarding any displacement of the pressure sensors, or performance of control runs, this methodology already results in more than 1'000 different test runs. The basic test run period was 65 seconds. This corresponds to a 1 minute transfer and storage on the hard disk of the PC of a text file of 4 Mb per data acquisition card, i.e. per four sensors. As a result, every water level generates minimum 40 Mb of files, every jet outlet system 280 Mb of files, and every rock joint form needs about 850 Mb of storage. For the 5 rock joint forms, this corresponds to a total storage of more than 4 Gb.

5.2. Followed test program

For the mentioned range of jet velocities, the above methodology has been applied to the different rock joint forms in the order as given below. For each rock joint form, the tested jet outlets, jet diameters and water levels are given, as well as the number of used pressure sensors.

1.	2D-joint:	cylindrical outlet,	57 and 72 mm, 7 water levels, 7 sensors
2.	I-joint:	cylindrical outlet:	57 and 72 mm, 7 water levels, 4 sensors
		convergent outlet:	72 mm, 6 water levels, 4 sensors
3.	L-joint:	cylindrical outlet:	57 and 72 mm, 7 water levels, 5 sensors
		convergent outlet:	72 mm, 6 water levels, 5 sensors
4.	L-joint:*	tests performed with watertight plastic around the form of the joint	
		cylindrical outlet:	57 and 72 mm, 7 water levels, 5 sensors
		convergent outlet:	72 mm, 6 water levels, 5 sensors
5.	I-joint:*	cylindrical outlet:	57 and 72 mm, 7 water levels, 4 sensors
6.	D-joint:	cylindrical outlet:	57 and 72 mm, 7 water levels, 3 sensors
7.	U-joint:	cylindrical outlet:	57 and 72 mm, 7 water levels, 3 sensors
8.	D-joint:*	tests performed with watertight plastic around the form of the joint	
		cylindrical outlet:	57 and 72 mm, 7 water levels, 3 sensors
9.	D-joint:*	tests performed with watertight neoprene around the form of the joint	
		cylindrical outlet:	57 and 72 mm, 7 water levels, 3 sensors

The rock joint forms that are marked with the * symbol stand for test runs that were performed to control previously performed runs. This was necessary because, after insertion of the L-joint, some loss of water appeared through the steel system. At the same time, this conducted to the disappearance of pressure peaks. In order to arrange this constructive problem, several systems of watertight between the thin steel sheeting and the galvanized steel plates have been tried out. None of them were found sufficiently accurate.

It is not apparent if the loss of water is the reason for the loss of pressure peaks. As outlined in Chapter V, this might also be due to the amount of air that is freely available inside the joint.

Chapter V. Analysis of transient pressures in rock joints

1. Structure

This chapter analyses experimental pressure measurements and follows the main physical processes according to Fig. I-2 (Chapter I). These processes correspond to a jet plunging through the atmosphere, to a jet diffusing through the plunge pool, to the generation of pressure fluctuations at the bedrock by turbulence, and finally to the destruction of the rock by hydrodynamic fracturing of its joints and uplift of rock blocks.

The first section describes the turbulent characteristics of a jet at its point of issuance from a high-head dam. The parameter of significance is the initial turbulence intensity Tu. It influences the degree of air entrainment of a plunging jet. Tu has been quantified for the cylindrical jet outlet by means of pressure fluctuation measurements.

The second section deals with pressure fluctuations that are generated by the jet at the plunge pool bottom. It describes how the jet, after impacting on the plunge pool water surface, diffuses through the water cushion of the plunge pool, thereby generating a significant amount of turbulent energy. This turbulent energy is expressed by the magnitude of the pressure fluctuations at the water-rock interface.

The two previous sections define the capacity of a plunging jet to excite an underlying rock joint and to stimulate it to resonance. Hence, the turbulence of an impacting jet is characteristic for the energetic input on the underlying jointed rock. When investigating pressure fluctuations inside rock joints, it is the most important parameter to be quantified at the surface of the jointed rock.

The last and most important section of the experimental results deals with the quantification and qualification of pressure fluctuations in different one-and two-dimensional rock joints that are subjected to high-velocity jet impact. Five rock joint geometries have been tested in detail (Fig. IV-7). Distinction has been made between closed-end rock joints, corresponding to the physical process of hydrodynamic fracturing, and open-end rock joints, representative for the dynamic uplift of rock blocks. The measured pressure fluctuations have been analysed in the time domain, based on mean, root-mean-square, maximum and minimum pressure values and on probability density functions, and in the frequency domain, by means of power spectral densities, cross-correlations and amplitude and phase transfer functions.

2. Initial jet turbulence intensity Tu

The dynamic pressures measured at the plunge pool bottom highly depend on the turbulence conditions generated by the jet at its issuance from the dam. Turbulence is strongly related to the type of jet outlet (overflow crest, orifice, etc.). Hence, it is essential for the present study to verify whether the laboratory obtained issuance conditions are representative for prototype issuance conditions. The main parameter for this purpose is the initial jet turbulence intensity Tu, which describes the turbulent character of the jet. Tu is responsible for jet destabilizing phenomena, such as jet spread, jet aeration and eventual jet break-up. According to equation (3.24) of Chapter III, it is defined as follows:

$$Tu = \frac{\sqrt{\overline{u'^2}}}{U} \tag{5.1}$$

in which u' stands for the fluctuating part of the longitudinal jet velocity (root-mean-square value) and U for the mean value of the centreline jet velocity at issuance.

According to Fig. IV-2, two different types of jet outlet have been used. Most of the tests have been performed for a cylindrical jet outlet. The diameter of the cylinder was 57 or 72 mm, for a total length of 300 mm. The flow issuance characteristics can be considered quite similar to prototype orifice outflow. The validity of the results obtained with the cylindrical outlet has been verified by use of a convergent shaped outlet. Its issuance conditions are smoother than the ones for a cylindrical outlet, and could more easily be associated with crest overflow rather than orifice outflow.

Tu is often determined in an indirect manner, i.e. based on pressure fluctuation measurements at the centreline of the jet outlet. Based on a study by Arndt & Ippen (1970), it can be shown that the following relationship holds between the pressure fluctuations and the corresponding velocity fluctuations:

$$\sqrt{\overline{p'^2}} = \rho \cdot U \cdot \sqrt{\overline{u'^2}} \tag{5.2}$$

in which p' corresponds to the fluctuating part of the dynamic jet pressure. This relationship allows expressing Tu as a function of C'_p, in which C'_p stands for the non-dimensional pressure coefficient that expresses the RMS (= root-mean-square) value of the pressure fluctuations:

$$Tu = \frac{\sqrt{\overline{u'^2}}}{U} = \frac{\sqrt{\overline{p'^2}}}{\rho \cdot U^2} = \frac{1}{2} \cdot C'_p \tag{5.3}$$

Tu is simply obtained by defining the ratio of the RMS value of the pressure fluctuations over the incoming kinetic energy of the jet, and by dividing this ratio by a factor of two. This approach, however, neglects higher-order terms in its analytical developments. Arndt & Ippen (1970) stated that an error of approximately 5 % can be expected for measurements in turbulence with an intensity of up to 10 %. The jets used in the present study are rather compact at issuance and turbulence intensities less than 10 % are valid. Hence, the error in analysis is assumed to be acceptable.

Furthermore, two different turbulence intensity values are distinguished, depending on the U parameter in equation (5.1). When using the mean jet outlet velocity, determined by the total discharge and the cross section of the jet, the so-called average turbulence intensity Tu_{av} is obtained. Use of the centreline measured mean jet outlet velocity conducts to the local or central turbulence intensity Tu_{cen}. These two values can be substantially different in case of highly non-uniform velocity profiles. Unless otherwise mentioned, the here presented turbulence intensities are local values (Tu_{cen}).

The apparatus that was used for these measurements is presented at Photo 6 (§ 2.2.2, Chapter IV). Special attention has been paid to the form of the cylindrical needle in which the pressure sensor is

incorporated. The needle has an aerodynamic shape, with a diameter of only 5 mm at the sensor head, and a diameter of 15 mm elsewhere. This shape is important in order to prevent flow disturbances.

Moreover, the presence of the needle-supporting steel frame needs particular consideration, because it is situated inside the flow. Based on fluid mechanical aspects, the influence of a bluff body on the flow characteristics upstream can be significant at a distance from the body of up to 1.5 times the jet diameter. Therefore, the height of the needle has been chosen equal to twice the maximum applied jet diameter (72 mm), i.e. approximately equal to 150 mm. With this measurement system, it is believed that no significant disturbances exist.

This measurement system has only been applied to the cylindrical jet outlet. The turbulence intensity of the convergent jet outlet has been estimated based on the RMS value of the pressure fluctuations measured at the plunge pool bottom, under zero tailwater conditions. Due to the compact nature of the jet, eventual flow disturbances between the jet issuance and the plunge pool bottom could be neglected.

2.1. Cylindrical jet outlet

The cylindrical jet outlet has already been presented in Fig. IV-2a (Chapter IV). The cylinder is made of opaque Lucite and has an inner diameter of 57 or 72 mm and a total length of 450 mm. The part of the cylinder inside the water supply conduit has a length of 150 mm; the remaining part outside of the supply conduit has a length of 300 mm. The water supply conduit has an inner diameter of 300 mm. Its end position is fixed and situated at 1 m above the simulated plunge pool bottom. As a result, the jet outlet is situated at 700 mm from the plunge pool bottom. This defines the maximum water depth in the pool for impinging jet impact conditions. The cylindrical shape has been chosen for two reasons.

First of all, it constitutes an easily manufactured and reasonable approximation of pressurized outflow conditions, as they can be encountered at prototype orifice structures. Secondly, its longitudinal form allows performing test runs for submerged jet impact conditions, i.e. for a jet outlet that is located under the water level of the plunge pool. These runs are important to assess the impact of air entrainment on the dynamic pressure pattern at the pool bottom. The disadvantages of the outlet system are its fixed position and fixed angle of impact. Therefore, the fall length of the jet is neglected and only vertical falling jets are considered. This, however, is acceptable because the main topic of the study is to investigate whether or not a high-velocity jet is able to stimulate an underlying rock joint to resonance.

Photo 6 in Chapter IV presents the steel frame and the aerodynamic needle that were used for the measurement of the initial jet turbulence intensity Tu. It also shows a pressure sensor that is integrated in the side wall of the cylinder, at 50 mm from the jet outlet. This sensor accounts for horizontal pressure fluctuations. In the following, these horizontal fluctuations are expressed by Tv, the lateral initial jet turbulence intensity.

The results of the turbulence intensity measurements are presented in Fig. V-1. It can be seen that the longitudinal turbulence intensity Tu attains 3 to 4 % at jet velocities beyond 15 m/s. Based on McKeogh & Elsawy (1980), these values are typical for prototype turbulent jets. For jet velocities less than 15 m/s, the Tu values increase with decreasing jet velocity. This is due to the low-fequency turbulence (§ 2.1.2, Chapter IV), mainly generated by secondary flow currents in the upstream water supply conduit. The turbulence intensity Tu can so attain values of up to 6 %. These values are probably not fully representative for the turbulence level of the jet itself and have to be interpreted carefully. The lateral turbulence intensity Tv is situated between 1 and 2 %. Its increase at low jet velocities is less pronounced than for Tu.

The measured Tu values have been compared with the corresponding measured Tv values. A similar comparison has been made by Ervine & Falvey (1987). They related the Tu values to the half angle of jet spread, taken from high-speed photographs, and obtained the following relationship:

$$\frac{\delta_2}{X} = 0.38 \cdot \frac{u'}{U} \tag{5.4}$$

in which δ_2 stands for the lateral spread of the jet (Fig. III-14, § 3.1, Chapter III) and X is the distance from the jet outlet. They reasonably argued that δ_2/X is equal to the lateral component of turbulence intensity Tv and proposed a first estimate of the ratio Tv/Tu of 0.4. Therefore, the here measured Tv values have been divided by a factor of 0.4 in order to obtain the corresponding Tu values. The results are presented in Fig. V-1a and show exactly the same tendencies as the directly measured Tu values. This constitutes an independent confirmation of Ervine & Falvey's (1987) statement.

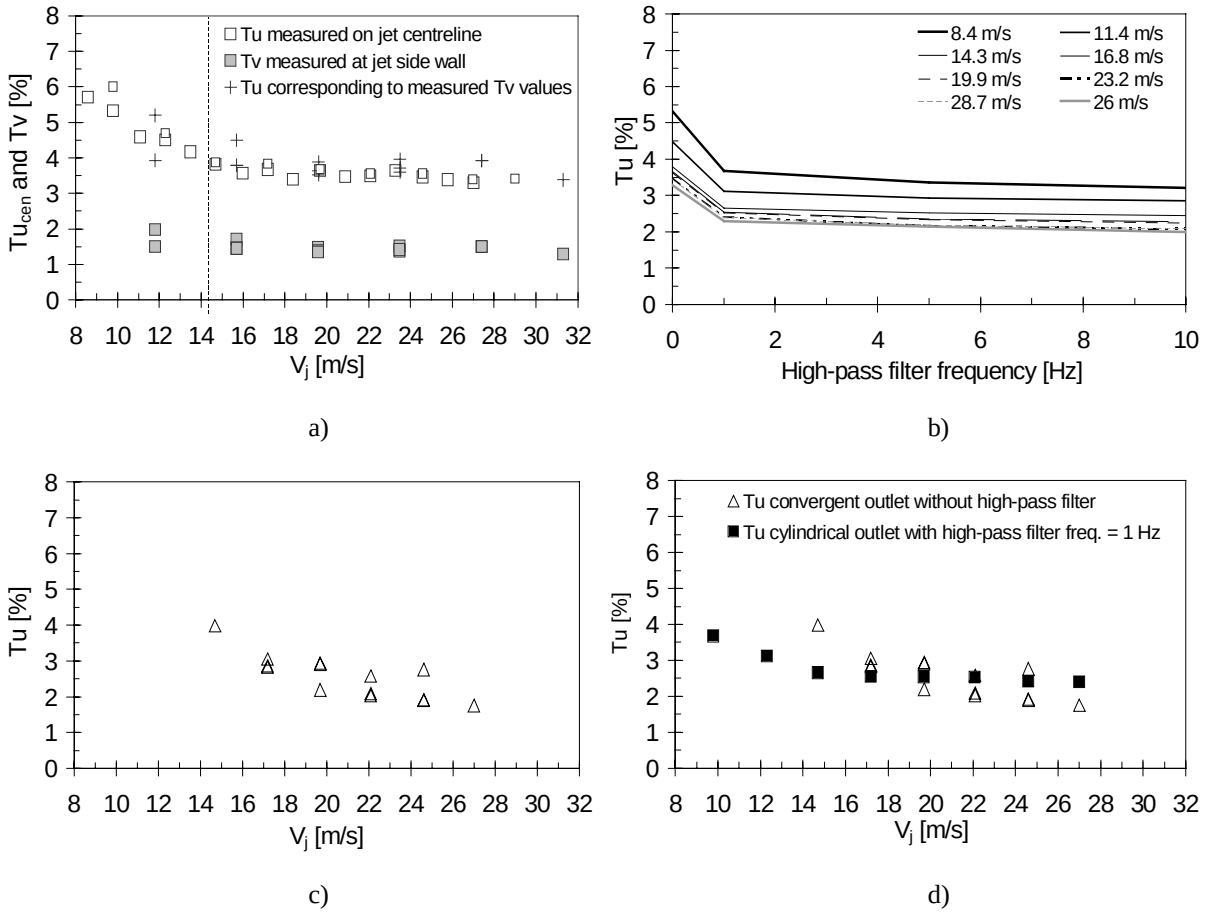

Fig. V-1 a) Longitudinal (Tu) and transversal (Tv) jet turbulence intensities of the cylindrical outlet as a function of the mean jet velocity V_j. For velocities less than 15 m/s, a gradual increase in turbulence intensity is clearly visible; b) Turbulence intensity Tu of cylindrical outlet as a function of high-pass filter frequency; c) Turbulence intensity Tu for convergent outlet as a function of mean jet velocity V_j; d) Comparison of Tu of convergent jet without high-pass filter and Tu of a cylindrical jet with a high-pass filter at 1 Hz.

In Chapter IV, distinction has been made between two jet forms that were encountered during the test runs with the cylindrical jet outlet: FORM A or COMPACT JET, which is the dominating form at jet velocities higher than 15-20 m/s, and FORM B or DIFFUSED JET, mostly appearing at low jet velocities (< 15-20 m/s). Visual observations indicated that the particular turbulence of this diffused jet appears at very low frequencies (max. 1 Hz).

The present turbulence intensity measurements allow determining more in detail the spectral character of these particular conditions. By analysing the power spectral content of the measured pressure fluctuations, the most significant frequencies of the turbulence can be roughly estimated. This has

been presented in Fig. V-1b, where the turbulence intensity Tu is represented as a function of a high-pass filter frequency. The high-pass filter frequency is the value for which all lower frequencies have been filtered out of the spectral content. In other words, a high-pass filter frequency of 10 Hz means that the spectral content of the frequency range between 0 and 10 Hz has been taken out of the calculus of the turbulence intensity. As such, it can be noticed that a substantial change in Tu values is obtained over the whole jet velocity range, whenever a high-pass filter frequency of 1 Hz is used. For higher filter frequencies, a constant slope decay is obtained. This confirms the hypothesis that particular turbulence conditions occur at frequencies less than 1 Hz. Taking out these effects from the Tu measurements results in a substantial decrease of the Tu values.

2.2. Convergent jet outlet

The convergent shaped jet outlet is presented in Fig. IV-2b (Chapter IV). It consists of a steel frame with a total length of 400 mm and is characterised by a linearly decreasing inner diameter from 300 mm at the water supply conduit down to 72 mm at the outlet of the jet. As already stated, no direct pressure fluctuation measurements have been made at the exit. The compact nature of this jet, however, made it possible to estimate the Tu values only based on pressure measurements at the bottom of the plunge pool. This has been done for most of the water depths and for high jet outlet velocities. For such velocities, the momentum of the compact jet was strong enough to completely traverse the water depth and to directly impact the pool bottom.

Fig. V-1c shows that the measured Tu values range from 1.5 to 4 %. When only considering jet outlet velocities higher than 15 m/s, the Tu values range from 1.5 to 3 %. Fig. V-2d makes a comparison between Tu values of the convergent jet outlet and measured Tu values of the cylindrical jet outlet, the latter after application of a high-pass filter frequency of 1 Hz. This points out that, for the convergent jet outlet, almost no low-frequency jet turbulence subsists anymore. Effectively, the Tu values are in good agreement with the ones for a cylindrical outlet provided that the low frequencies have been filtered from the latter.

The main reasons for the lower turbulence intensity for convergent outlets are the more progressive change in diameter from the supply conduit towards the jet outlet and the presence of a cross-shaped frame avoiding large secondary currents.

This aspect, however, revealed to be embarrassing for certain test runs. At high jet velocities and low water depths, no turbulent two-phase shear layer could be formed and thus no meaningful dynamic pressure measurements could be made at the plunge pool bottom. Such measurements would require much higher water depths, up to prototype values.

2.3. Concluding remarks

The longitudinal turbulence intensity Tu has been quantified for both cylindrical and convergent jet outlets. For the cylindrical jet outlet, values of 3 - 4 % have been found at near-prototype jet velocities (> 15 m/s), and values of up to 6 % at lower jet velocities. The latter values, however, contain some low-frequency turbulence effects. Filtering out of these effects resulted in Tu values of 2 - 2.5 % at near-prototype velocities and 3 - 4 % at lower jet velocities. For the convergent jet, no low-frequency turbulence exists at near-prototype jet velocities. Therefore, the measured Tu values ranged from 1.5 - 3 %, i.e. very close to the values obtained for the cylindrical jet. For lower jet velocities, however, some low frequencies remained and the non-filtered Tu attained values of up to 4 %.

As a consequence, the generated jets can be described as **moderately to roughly turbulent jets**. When neglecting low-frequency jet turbulence, the jets are of moderately turbulent nature. Based on Ervine & Falvey (1987), real jet issuance conditions generally exhibit turbulence intensities of 1 to 5 %. Therefore, it may be assumed that the turbulence generated by the present jets is representative for prototype jets. This statement is of importance when assessing the dynamic pressure characteristics produced by these jets at the bottom of the simulated plunge pool.

3. Dynamic pressures at plunge pool bottom

The jet turbulence intensity Tu is the major parameter that influences the turbulent fluctuations of a jet during its fall through the atmosphere (Chapter III, § 3.1). It is at the base of jet spread, jet aeration and eventual jet break-up into distinct water particles. Based on § 2.3, the jets generated by the present facility are of compact nature and have a very small fall length of max. 0.50 m. Hence, their lateral spread is poorly established.

The geometrical ratio of the plunge pool depth Y to the jet diameter at impact D_j is of great importance for the two-dimensional diffusion encountered by the jet when traversing the pool depth (Chapter III, § 2.1.1). Therefore, the jet diameter at impact has been estimated by visual observations during the test runs. The short distance between the jet outlet and the point of impact of the jet enhances the precision of the estimations. Furthermore, the plunge pool depth Y has also been estimated by visual observations. Although this parameter was prefixed for each test run, the occasional appearance of vortices at the point of jet impact made it necessary to account for practically observed values rather than theoretically calculated ones.

In the following, a brief summary is given of the location of the used pressure sensors. Furthermore, the observed jet diameters and plunge pool depths are discussed. Finally, distinction is made between the pressures that were measured directly under the centreline of the jet and the radial distributed pressure pattern. The former are directly relevant to the maximum possible damage and, thus, to the ultimate scour depth. The latter define the radial extent of possible damage and rather inform about the form and the possible extension of the scour hole.

3.1. Location of the pressure sensors

According to Fig. IV-6 (Chapter IV), two types of sensor positions are distinguished: pool bottom sensors and rock joint sensors (Fig. V-2). Conform § 2.2.2 of Chapter IV, the former are nomenclated with the letter (a) as well as with a suffix that indicates the distance from the jet's centerline. The latter are named by use of the letters (b), (c), and (d) for the sensors at the center of the rock joint, and by use of the letters (b'), (c') and (d') for the homologue sensors at the side of the rock joint. In the present section, only the measurements made with pool bottom sensors are discussed. The rock joint sensors are dealt with in § 4. Sensor (a) is located at 25 mm from the joint entrance.

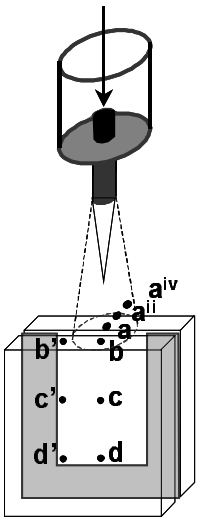

Sensor	Type	Position
a	pool bottom	25 mm from joint
a^i	pool bottom	50 mm from joint
a^{ii}	pool bottom	75 mm from joint
b	rock joint	center, 50 mm inside
c	rock joint	center, 420 mm inside
d	rock joint	center, 790 mm inside
b'	rock joint	side, 50 mm inside
c'	rock joint	side, 420 mm inside
d'	rock joint	side, 790 mm inside

Fig. V-2 Location of the pressure sensors used at the plunge pool bottom. Distinction is made between pool bottom pressure sensors and rock joint pressure sensors.

3.2. The geometrical ratio Y/D_j

Based on the theory of two-dimensional jet diffusion (Chapter II, § 2.1 & Chapter III, § 2.1.1), it is obvious that the geometrical ratio of plunge pool depth to jet diameter at impact Y/D_j is directly related to the turbulence conditions that govern in the plunge pool. Reliable assessment of this ratio has been performed based on visual observations of Y and D_j during the test runs. The maximum error of estimation has been defined at 5 cm for Y and 1 cm for D_j. At a plunge pool depth Y of 20 cm, this procures a relative error of up to +/- 45%. At a plunge pool depth Y of 67 cm, the maximum error is estimated at +/- 25 %. Hence, the obtained ratios should be handled with some precaution. They are presented in Fig. V-3 for cylindrical and convergent jets (Bollaert & Schleiss, 2001f).

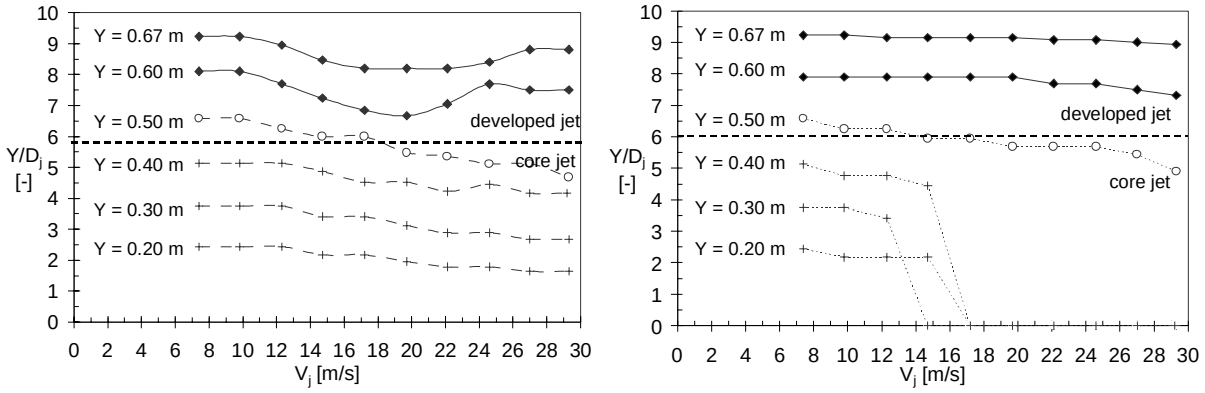

Fig. V-3 Observed Y/D_j ratios as a function of the mean jet outlet velocity V_j: a) cylindrical jet outlet, b) convergent jet outlet (Bollaert & Schleiss, 2001f).

The plunge pool depths used in the test facility are prefixed by use of two Lucite plates that are inserted into the restitution boxes and that function as linear overflow crests. As such, the theoretical Y-values range from 0 to 0.70 m for impinging jets and from 0.80 to 0.90 m for submerged jets. The values that were used during the tests with impinging jets were 0, 0.20, 0.30, 0.40, 0.50, 0.60 and 0.67 m. For submerged jet impact, a value of 0.87 m has been set.

However, for certain combinations of plunge pool depth and jet velocity, significant changes in pool depth have been observed during the test runs with cylindrical jets. These changes are caused by the appearance of vortices generated in the plunge pool basin. In some cases, the vortices entrained a pool depth decrease of almost 0.20 m. Therefore, it was decided to adapt the theoretically used geometrical ratios to the practically observed test conditions. Fig. V-3a shows that vortices are especially present at high plunge pool depths (0.60 and 0.67 m) and intermediate jet velocities (15-25 m/s). The quasi-linear decay of the Y/D_j ratio with increasing velocity, as observed at small plunge pool depths (0.20-0.50 m), is caused by the spread of the jet during its fall and not by vortices.

For the convergent jet, no vortices have been observed. However, the situation is even more particular than for the cylindrical jet. At small plunge pool depths and for jet velocities higher than 15 m/s, the jet's momentum is such that the jet directly impinges on the pool bottom. In other words, there is a clear distinction between the jet and the surrounding mass of water in the pool. For higher plunge pool depths (0.50–0.67 m), the jet cannot maintain anymore this situation, because of the strong recirculation currents in the pool. It is much like if the jet is so strong that the induced flow that hits the side walls of the pool, rebounds and is able to resist to its origin.

These direct jet impingement conditions at small plunge pool depths are very interesting for two reasons. First of all, it allows quantifying the initial jet turbulence intensity Tu for the convergent jet impact conditions. Furthermore, it generates dynamic pressures at the pool bottom and inside an

underlying rock joint that are representative for ideal core jet impact conditions, i.e. without any influence from the outer pool. It constitutes a sort of theoretically ideal case of jet impact.

It may be concluded that the geometrical ratio Y/D_j directly defines the type of jet diffusion through the pool and the type of jet impact at the pool bottom. According to § 2.1.2, Chapter III, two types of jet diffusion and impact have to be distinguished. First of all, for small pool depths, a jet core still exists and impacts on the water-rock interface. This core is characterised by a constant velocity and pressure pattern and is not influenced by the outer two-phase shear layer conditions. In other words, when a jet core is impacting on an underlying rock joint, no air from the outer pool can be of influence on the pressures inside the joint. This type of impact is called **core jet impact** and occurs for Y/D_j ratios less than 4-6 (Fig.V-4a).

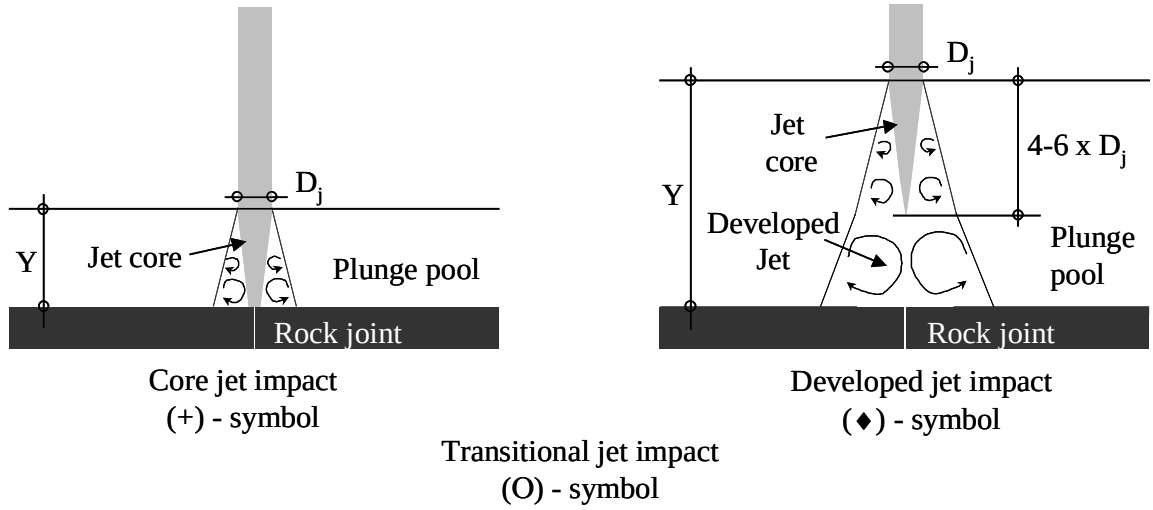

Fig. V-4 Types of jet diffusion and impact at the pool bottom: a) core jet impact (+ symbol) and b) developed jet impact (♦ symbol). Transitional jet impact (o symbol) stands for combined core-developed jet impact conditions as a function of the jet velocity (Bollaert & Schleiss, 2001a).

The pressure patterns generated by core jet impact are generally quite constant, with high values in the core and much lower values directly outside the core. The exact value of the ratio for which core jet impact transforms into developed jet impact is not clearly defined. It depends on the shape and the stability of the jet and the degree of aeration at impact. Several researchers found values between 3 and 8 (Chapter II, § 2.2.1). For practice, a value of 4 to 6 is appropriate.

Secondly, for higher pool depths, the core vanishes and a fully developed, two-phase turbulent shear layer installs. Immediately after vanishing of the core of the jet, the turbulence level generally is very high. This is called **developed jet impact** and happens at Y/D_j ratios higher than 6 (Fig. V-4b). Further increase of pool depth enhances turbulent diffusion. The angle of diffusion of the jet through the pool depends on the degree of turbulence and aeration of the jet at impact. It can be estimated at around 15° (Ervine & Falvey, 1987).

Due to the high turbulence level and the two-phase character of the shear layer, developed jet impact conditions can generate severe dynamic pressures at the pool bottom. These pressures are completely different from the pressures generated by core jet impact.

For Y/D_j ratios higher than 10-12, the diffusion of the generated turbulence becomes important, such that the dynamic pressures on the pool bottom will decrease and finally vanish at very high ratios (25-40).

The specific test conditions made it impossible in some cases to determine the Y/D_j ratio within +/- 45 % of error. Therefore, a third type of jet diffusion and impact has to be distinguished: **transitional jet**

impact. This type of impact constitutes in fact a combination of core and developed jet impact, i.e. at small jet velocities, the jet generates developed impact conditions, while above a certain velocity threshold (generally around 15 m/s) core jet impact is produced.

For the following of the present study, all of the results on dynamic pressures will be presented as a function of the type of jet impact on the pool bottom. This is summarized at Table V-1.

N°	Type	Geometrical ratio					Jet velocity	Symbol
1	core jet	0	<	Y/D_j	<	4-6	for all V_j	+
2	developed jet	4-6	<	Y/D_j	<	20-40	for all V_j	♦
3	transitional jet	0	<	Y/D_j	<	4-6	for 15 m/s < V_j	○
		4-6	<	Y/D_j	<	20-40	for V_j < 15 m/s	

Table V-1 Three different types of jet diffusion through the plunge pool, with their geometrical ratios and corresponding jet velocities. The symbols will be used throughout the present study to represent the results.

3.3. Pressures at the jet's centreline for a cylindrical jet

3.3.1. Measured pressure signal

The pressure signal in the time domain, measured under the jet's centreline at the plunge pool bottom, is presented in Fig. V-5 for core and developed jet impact conditions respectively. The corresponding jet diameter is 72 mm. The pressures are in absolute values. Fig. V-5a shows the pressure signal for core jet impact. It can be seen that a quite constant pressure pattern occurs during most of the time. However, low-frequency core turbulence is clearly visible. During this turbulence, the pressure almost drops down to the atmospheric pressure level. Fig. V-5b shows the homologue pressure signal for developed jet impact. For this case, a much more fluctuating signal is obtained. This is due to the presence of a turbulent shear-layer that impacts the pool bottom.

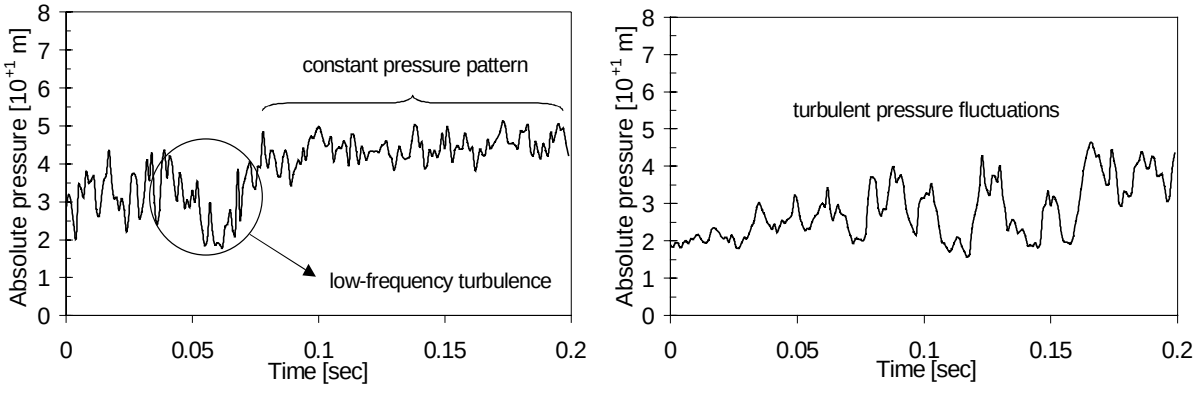

Fig. V-5 Pressure signal in the time domain, measured under the jet's centreline, at the plunge pool bottom: a) core jet impact; b) developed jet impact. Jet diameter is 72 mm.

3.3.2. Mean dynamic pressure value

The mean dynamic pressure coefficients at sensor (a) C_{pa} (= $(p_{mean}-Y)/(\phi V_j^2/2g)$) are presented in Fig. V-6a for core, transitional and developed jet impact conditions (Bollaert & Schleiss, 2001f). Jet diameters are 57 mm and 72 mm. It can be seen that, according to the best fits of available literature data on circular vertical impinging jets (Chapter II, § 3.3.2), a similar tendency is obtained. However, for core jet impact conditions, the measured values are somewhat lower than the best-fit curves. Moreover, for all possible jet impact conditions, scatter can be observed. These differences are mainly due to the low-frequency turbulence, especially at jet outlet velocities less than 15-20 m/s, and to the high aeration rate of the near-prototype facility. As will be outlined hereafter, these effects are particularly relevant at small plunge pool depths.

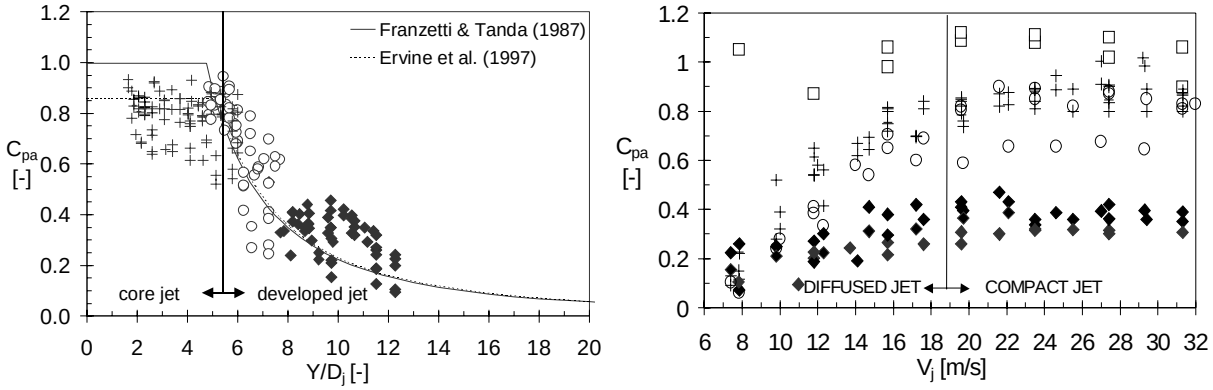

a) b)

Fig. V-6 Non-dimensional mean dynamic pressure coefficient C_{pa}: a) as a function of the geometrical ratio of plunge pool depth Y to jet diameter D_j; b) as a function of the mean jet outlet velocity V_j. Results are presented for both the 57 mm and 72 mm jet diameters (Bollaert & Schleiss, 2001f).

Fig. V-6b presents the C_{pa} values as a function of the mean jet outlet velocity V_j. For all jet impact conditions, the influence of low-frequency turbulence is clearly reflected in a decrease of C_{pa} values with decreasing velocity V_j. However, this drop is much less expressed for developed jet impact conditions, i.e. at higher plunge pool depths.

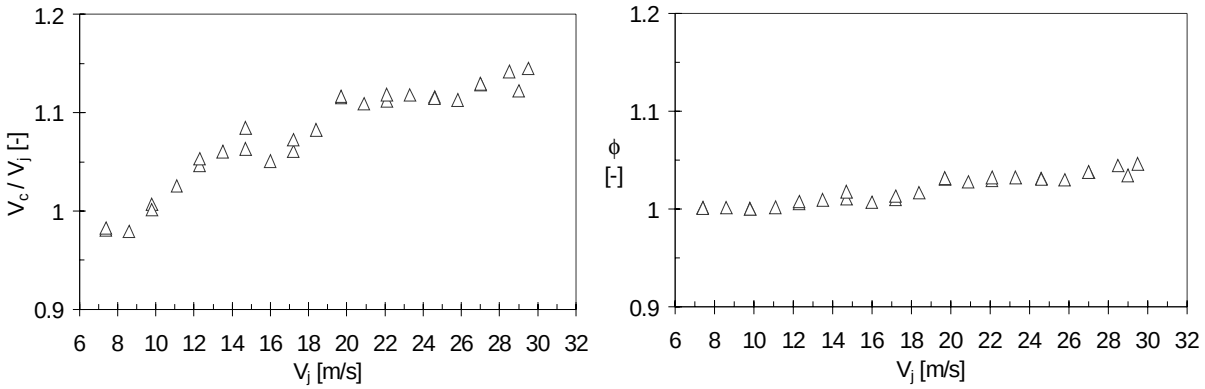

a) b)

Fig. V-7 Non-uniform velocity distribution at the jet exit for the 72 mm jet diameter: a) Ratio of centreline velocity to mean velocity V_c/V_j as a function of the mean velocity V_j. Values measured for cylindrical jet outlet; b) Correction coefficient ϕ for the kinetic energy $V_j^2/2g$ as a function of V_j.

Based on the intermittent character of the observed low-frequency turbulence, typically appearing every one to two seconds (frequencies less than 1 Hz), partial C_{pa} values were established. These values are fictitious in that they are only based on the periods of time during which the jet was compact. In other words, all pressure drops have been systematically removed from the data.

The result is presented in Fig. V-6b (symbol) for core jet impact. Although a certain drop in C_{pa} values with decreasing jet velocities might be observed, this effect is much less pronounced.

Furthermore, the high air entrainment also influences the results. Such effects have already been mentioned by May & Willoughby (1991), who made tests with rectangular slot jets and artificially generated air contents.

The velocity distribution of the jet at its exit influences the mean dynamic pressure values at the plunge pool bottom. The pressure measurements performed at the exit of the jet, as described in § 2.2.1 on the turbulence intensity Tu, allow determining the centreline outlet velocity V_c. Comparison of V_c with the mean outlet velocity V_j, derived from the pump discharge and the cross section of the jet outlet, expresses the non-uniformity of the velocity distribution. This is presented in Fig. V-7a.

The ratio V_c/V_j increases quadratically with the mean outlet velocity V_j. The minimum value is around 1.0; the maximum obtained value is about 1.15. This is in accordance with previous findings of May & Willoughby (1991) on rectangular slot jets. They found a maximum ratio of 1.16. The corresponding theoretical maximum mean pressure value C_p can thus attain values of up to $1.15^2 = 1.32$.

Fig. V-7b shows the correction coefficient ϕ for the kinetic energy $V_j^2/2g$ as a function of the mean jet outlet velocity V_j. When only using the longitudinal component v of the velocity vector, this coefficient is expressed as follows:

$$\phi = \frac{\int v^3 dA}{V_j^3 A} \tag{5.5}$$

Strictly speaking, the radial distribution of the local velocity component is needed to calculate the integral. This, however, is not available in the present study. Therefore, a simplified approach has been adopted to determine ϕ. The velocity distribution in turbulent flow is predicted theoretically by appropriate forms of the log-velocity law, but can be described by simple power-law relationships over most of the depth range:

$$v = V_c \cdot \left(\frac{y}{R}\right)^{1/n} \tag{5.6}$$

in which y stands for the radial coordinate and R for the jet's radius. The exponent n of the power law can now be expressed as a function of the measured centreline velocity V_c and the mean outlet velocity V_j in the following form:

$$n = \frac{V_j}{V_j - V_c} \tag{5.7}$$

The values obtained for n and ϕ are summarized at Table V-2. At high jet velocities, typical values are 6 to 7 for n and 1.05 for ϕ. This in accordance with findings of Cain & Wood (1981) and May & Willoughby (1991).

In the following, non-dimensional pressure parameters, such as C_p, C'_p, C_p^+ and C_p^-, will be defined as the relevant pressure head divided by a corrected kinetic energy $\phi V_j^2/2g$ (see notations at the end). Where a relationship with the jet velocity V_j is presented, the mean values are systematically used. If the centreline velocities are used instead, this will be specifically mentioned.

It can be concluded that the dependence of the mean pressure coefficient C_{pa} on the jet velocity is influenced by a combination of low-frequency jet turbulence, mainly at low jet velocities, and a non-uniform velocity distribution at the jet outlet, particularly significant at high jet velocities.

The dependence of C_{pa} values to V_j values is thereby mostly influenced by the low-frequency turbulence. However, this dependence is probably exaggerated on a laboratory-generated jet when compared to a prototype jet, due to its vulnerability to secondary flow effects induced by the supply conduit.

V_j	V_c	V_c/V_j	Tu	n	ϕ
7.40	7.26	0.98	6.33	-52.6	1.001
8.60	8.42	0.98	5.70	-48.6	1.001
9.80	9.87	1.01	5.33	142.4	1.000
11.10	11.38	1.03	4.58	39.5	1.002
12.30	12.87	1.05	4.49	21.5	1.006
13.50	14.32	1.06	4.16	16.6	1.009
14.70	15.63	1.06	3.80	15.8	1.010
16.00	16.81	1.05	3.56	19.8	1.007
17.20	18.25	1.06	3.66	16.4	1.010
18.40	19.92	1.08	3.39	12.1	1.017
19.70	21.97	1.12	3.63	8.7	1.031
20.90	23.18	1.11	3.47	9.2	1.028
22.10	24.58	1.11	3.48	8.9	1.029
23.30	26.05	1.12	3.64	8.5	1.032
24.60	27.45	1.12	3.45	8.6	1.031
25.80	28.71	1.11	3.38	8.9	1.030
27.02	30.50	1.13	3.29	7.8	1.037
28.50	32.55	1.14	3.40	7.0	1.044
29.50	33.78	1.15	3.40	6.9	1.046

Table V-2 Parameters of a non-uniform velocity distribution at the jet exit. Values obtained for a cylindrical jet outlet of 72 mm of diameter.

3.3.3. Root-mean-square (RMS) pressures

The root-mean-square value of the fluctuating part of the dynamic pressures C'_{pa} ($= \sigma/(\phi V_j^2/2g)$) is presented in Fig. V-8, for both 57 mm and 72 mm jet diameters (Bollaert & Schleiss, 2001f). When compared with the best-fit of available literature data, two remarks can be made. First of all, the general form of the relationship between the RMS values and the Y/D_j ratio is in agreement with previous findings and with the theory of turbulence. Turbulence firstly increases with increasing plunge pool depth until a certain maximum value is obtained and than decreases again with plunge pool depth, due to increasing diffusion.

Secondly, regardless of the shape of the relationship, comparison with the bandwidth of available data from Ervine et al. (1997) shows that the present measurements reveal a significant shift towards higher RMS values. The mean increase is on the order of 0.05 to 0.10. This is not surprising when accounting for the prototype character of the test facility (Bollaert & Schleiss, 2001d). The use of near-prototype jet velocities generates a turbulent shear layer with near-prototype spectral characteristics. Specifically the higher frequency part of the spectral content of an impacting jet becomes much closer to reality than on small-scale models. In other words, as the root-mean-square values are obtained by integration of the spectral curves over the frequency range of interest, significantly higher values are obtained. A similar effect is observed for extreme pressure values and for the slope decay of the power spectral densities. These will be discussed later on.

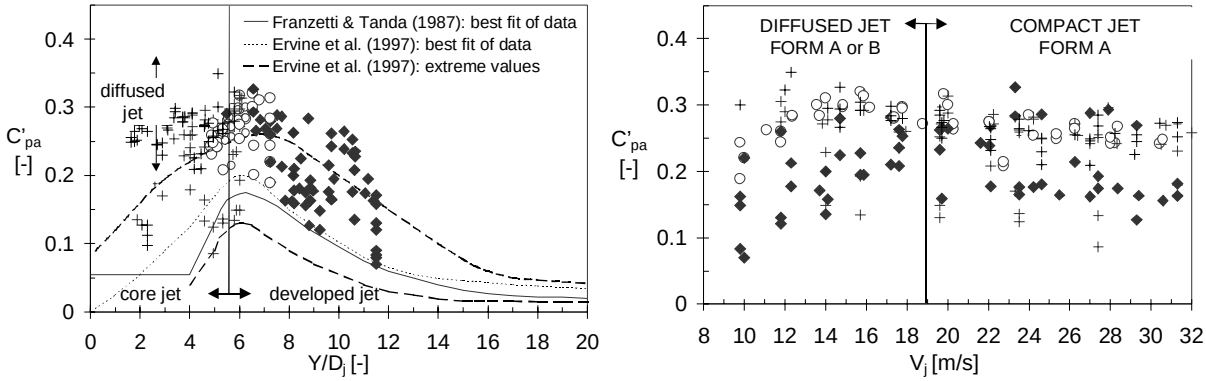

a) b)

Fig. V-8 Non-dimensional fluctuating pressure coefficient C'_{pa}: a) as a function of Y/D_j. Diffused jet conditions are particularly visible at small Y/D_j ratios; b) as a function of the mean jet outlet velocity V_j. Results are presented for core (+ sign), transitional (O sign) and developed (♦ sign) jet impact conditions, and for both 57 mm and 72 mm jet diameters (Bollaert & Schleiss, 2001f).

For core jet impact, a large scatter is obtained, with values ranging from 0.10 to 0.35. The lower values logically correspond to ideal core jet impact conditions, i.e. without any low-frequency turbulence effects. For these impact conditions and for small jet fall lengths L_j, the turbulence of the jet at the water-rock interface should be very close to the jet turbulence intensity Tu. The latter was estimated at the present facility at 0.04-0.06 (Fig. V-1). Similar results were obtained by Franzetti & Tanda (1987), who only considered perfect core jet impact conditions.

Hence, no ideal core jet impact is observed on the present facility. Apparently, even a small water depth is able to diffuse the core of the impacting jet such that its fluctuations at impact are substantially higher than the initial turbulence intensity. Such results have been obtained by most of the previous research and seem not to be that particular. For example, Ervine et al. (1997) obviously encountered the same turbulence effects. Their values for core jet impact lie between 0.03 and 0.22 and, thus, are influenced by turbulence. This phenomenon has, to the author's knowledge, never been subjected to discussions.

Furthermore, values higher than 0.20 are probably also affected by the flow conditions in the upstream supply conduit. The main reason lies in the presence of a 90° bend at a short distance from the jet outlet, producing secondary flow currents and thus additional turbulence. Such conditions generate pressures very close to developed jet impact conditions. As a matter of fact, it seems very difficult to obtain ideal core jet impact conditions with the cylindrical jet outlet. However, ideal core jet impact has been obtained with the convergent shaped jet outlet. This is discussed in § 3.4.3.

For developed jet impact, maximum values of up to 0.30-0.35 are obtained for Y/D_j ratios between 5 and 8. Although diffusion effects become predominant at higher ratios, resulting in a quasi-linear decay of the root-mean-square values, substantial high values (0.25) still persist at Y/D_j ratios of up to 10-11. The root-mean-square values can also be represented as a function of the mean jet outlet velocity V_j. This gives a better picture of the influence of low-frequency turbulence conditions at velocities V_j less than 15-20 m/s. Fig. V-8 clearly indicates quite constant RMS values at high velocities (compact jet, form A), while a lot of scatter is obtained at low velocities (diffused jet, form B). Form A and B have been defined in Fig. IV-3 of Chapter IV.

3.3.4. Extreme pressures

The extreme positive ($C^+_{pa}= (p_{max}-p_{mean})/(\phi V_j^2/2g)$) and negative ($C^-_{pa}= (p_{mean}-p_{min})/(\phi V_j^2/2g)$) pressure values are presented in Fig. V-9 for both the 57 mm and 72 mm jet diameters and result in the same analysis as for root-mean-square values. The obtained trend of data is in good agreement with available literature data, while the absolute values are far more extreme. For positive extremes, the

measured values are higher by a value of 0.10-0.50, while for negative extremes, the obtained differences range from 0.10 to 0.30. Extreme values obtained at submerged jet outlet conditions are in better agreement with previously published data. However, the negative extremes are still higher (Bollaert & Schleiss, 2001f).

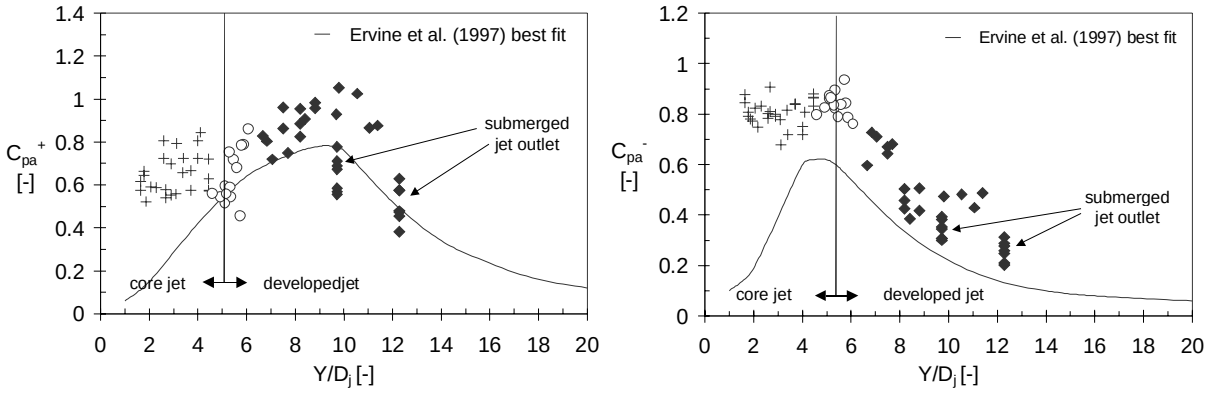

a) b)

Fig. V-9 a) Non-dimensional positive extreme dynamic pressure coefficient C_{pa}^+ as a function of the ratio Y/D_j; b) Non-dimensional negative extreme dynamic pressure coefficient C_{pa}^- as a function of the ratio Y/D_j. Results are presented for core (+ sign), transitional (O sign) and developed (♦ sign) jet impact conditions, and for both 57 mm and 72 mm jet diameters. Values obtained for submerged jet outlet conditions are specifically indicated (Bollaert & Schleis, 2001f).

3.3.5. Probability density function

Beside the mean, root-mean-square and extreme pressure values, it is interesting to discuss the probability of occurrence of the measured pressure values. This is expressed by the probability density function (PDF). The probability density function defines the probability of occurrence of pressure values as a function of their deviation from the mean pressure. In non-dimensional form, the abscissa represents the difference of each pressure from the mean value as a function of the standard deviation. It is a particularly interesting means to compare obtained curves with the Gaussian curve, valid for normally distributed values. As such, the appearance of peak pressure values for example can be easily found back in a positive skewness coefficient.

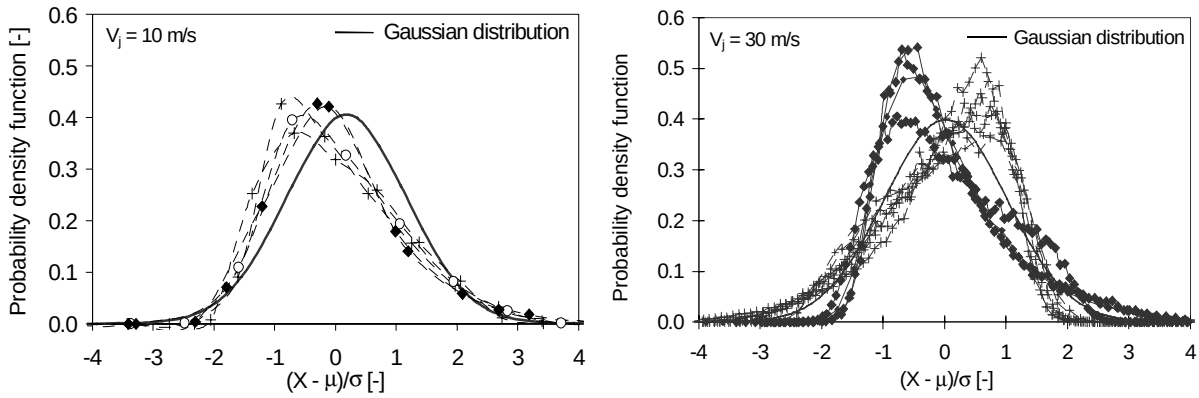

(a) (b)

Fig. V-10 Plunge pool bottom pressures: a) Probability Density Function (PDF) compared to a Gaussian distribution at a jet velocity of 10 m/s, b) Probability Density Function (PDF) compared to a Gaussian distribution at a jet velocity of 30 m/s (Bollaert & Schleiss, 2001f).

Fig. V-10b shows the probability density function normalized with regard to the mean pressure coefficient C_{pa} and the standard deviation σ, for a jet velocity of 30 m/s. Core jet impact conditions generate a negatively skewed PDF. This corresponds to the quite constant pressure pattern that is typical for core jets, alternated with occasional lower pressures, due to low-frequency turbulence. Developed jet impact conditions, on the contrary, generate a positively skewed pressure distribution, with the appearance of a significant amount of high pressures. The major part of the pressure values is below the mean pressure value, indicating a low median value. This different behaviour, however, disappears at low velocities, as indicated in Fig. V-10a. This explains the Gaussian assumptions generally adopted in physical model studies at low jet velocities (Liu et al., 1998).

3.3.6. Spectral analysis

The pressures measured at the plunge pool bottom, under the jet's centreline, can also be analysed in a frequency or Strouhal domain. These domains define the cyclic nature of the pressures and express how the energy is distributed over the range of frequencies involved. As such, they can be used to determine the capability of the impacting jet to stimulate an underlying rock joint to resonance or standing waves. Most of the frequency analyses make use of the one-sided power spectral density S_{xx} (Pa^2/Hz) as a function of frequency f (Hz). The power spectral density is defined as a decomposition with frequency of the variance σ^2 of the pressure fluctuations. Hence, the relation can be written:

$$\sigma^2 = \lim_{T\to\infty} \frac{1}{T} \int_0^T \left(p(t) - \bar{p}\right)^2 \cdot dt = \int_0^\infty S_{xx}(f) \cdot df \tag{5.8}$$

Detailed description of the characteristics of power spectral density functions and their related functions, such as autocorrelations, cross-correlations, coherence functions, etc. are beyond the scope of the present study. The reader is referred to textbooks in the field of signal data analysis, e.g. Bendat & Piersol (1980). As the integration of the power spectral density over the governing frequency range results in the variance of the fluctuating pressures, $S_{xx}(f)$ can be made non-dimensional by dividing it by σ^2. On the other hand, the frequency f can be made non-dimensional by replacing it by a plunge pool Strouhal number $S_{h,p}$ that is defined as follows:

$$S_{h,p} = \frac{f \cdot Y}{V_j} \tag{5.9}$$

The eddies of the turbulent shear layer are defined by the plunge pool depth Y and the velocity of the jet at impact V_j. Hence, dynamic pressures at the plunge pool bottom that directly result from these eddies should also be dependent on these parameters. If this is the case, the non-dimensional results in a Strouhal domain should be of self-preserving character. On the other hand, dynamic pressures that are measured outside of the turbulent shear layer do not follow this statement. They are still depending on the plunge pool depth Y, however, the governing velocity field is completely different. This different behaviour will be pointed out in § 3.6 on the radial pressure pattern.

Figs. V-11a to 11d visualize the non-dimensional power spectral density corresponding to a 72 mm jet diameter. The results are presented for core jets and developed jets, and in both the frequency and Strouhal domains. Fig. V-11a shows that the spectral curves for core jet impact are characterized by a linear slope decay with frequency of around -1, even at high frequencies (beyond 100 Hz). Moreover, it can be seen by Figs.V-11a & 11b that core jet impact cannot be correctly represented in a non-dimensional manner. The spectral curves only collapse in the frequency domain, because the core of the jet is not affected by the surrounding turbulent shear layer and related eddy sizes. On the other hand, developed jet impact produces more spectral energy at low and intermediate frequencies (Figs. V-11c and 11d), but the spectral curves suddenly decay at a quasi-linear –7/3 slope, corresponding to values available in literature (Bearman, 1972; Huot et al., 1986). The viscous dissipation range of the spectrum thus decays faster as the Von Karman form (-5/3 slope; Hinze, 1959) and starts at a frequency that clearly depends on the flow conditions (Fig. V-11d).

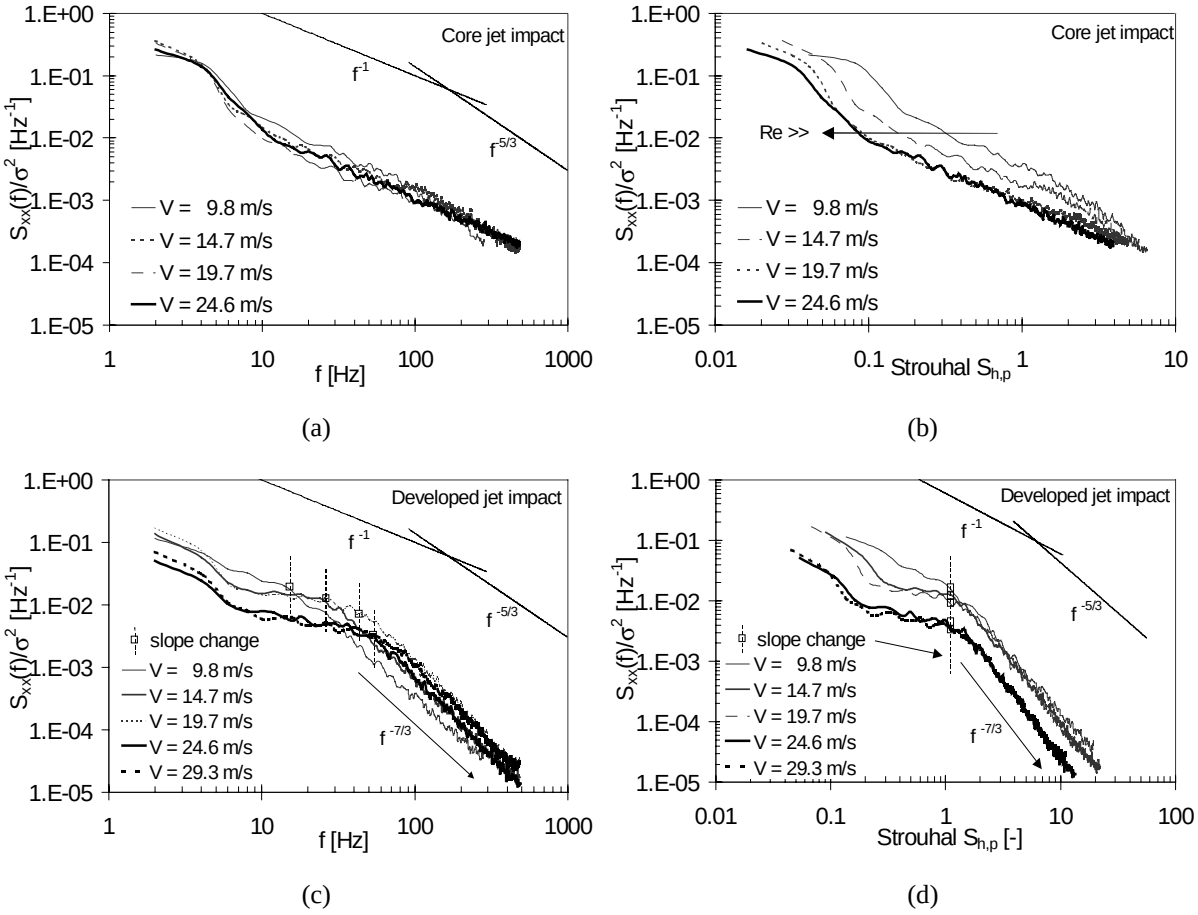

Fig. V-11 Non-dimensional power spectral density of dynamic pressures at the plunge pool bottom for a 72mm jet diameter (Bollaert & Schleiss, 2001f):
a) core jet in the frequency domain; b) core jet in the Strouhal domain;
c) developed jet in the frequency domain; d) developed jet in the Strouhal domain.

However, in the Strouhal domain, this corresponds to a constant Strouhal number $S_{h,p}$ of about 1 (Fig. V-11d). This is plausible when assuming that developed jet impact is governed by turbulent shear layer flow and therefore depends on the jet velocity V_j and the pool depth Y, which define eddy sizes. Thus, it can only be correctly presented in a non-dimensional domain. Moreover, according to the findings of Ballio et al. (1992), the –7/3 slope of the viscous dissipation range was found independent of Y/D_j for developed jet impact.

Figs. V-12a to 12d show the non-dimensional power spectral density corresponding to a 57 mm jet diameter. The results are presented for core jets and developed jets, and in the frequency and Strouhal domains. For illustration, the jet's Reynolds number is used instead of jet velocity. No significant differences pertaining to the 72 mm diameter are observed. This indicates that the spectral content of high-velocity jet impact is independent of the absolute jet diameter, but is rather governed by the jet velocity V_j and the ratio of Y/D_j.

As a conclusion, the impact of a high-velocity jet can generate excitation energy at frequencies that are much higher than those of typical macroturbulent flow conditions (max. 25 Hz; Toso & Bowers, 1988). This statement is valid for core jet as well as for developed jet impact conditions. Furthermore, core jets are characterized by a linear decay of energy with increasing frequency. Developed jets exhibit a double linear decay. At intermediate frequencies, corresponding to Strouhal numbers of less than 1, a –1 decay is valid. For higher Strouhal numbers, the –5/3 slope decay takes over and increases up to the viscous dissipation range.

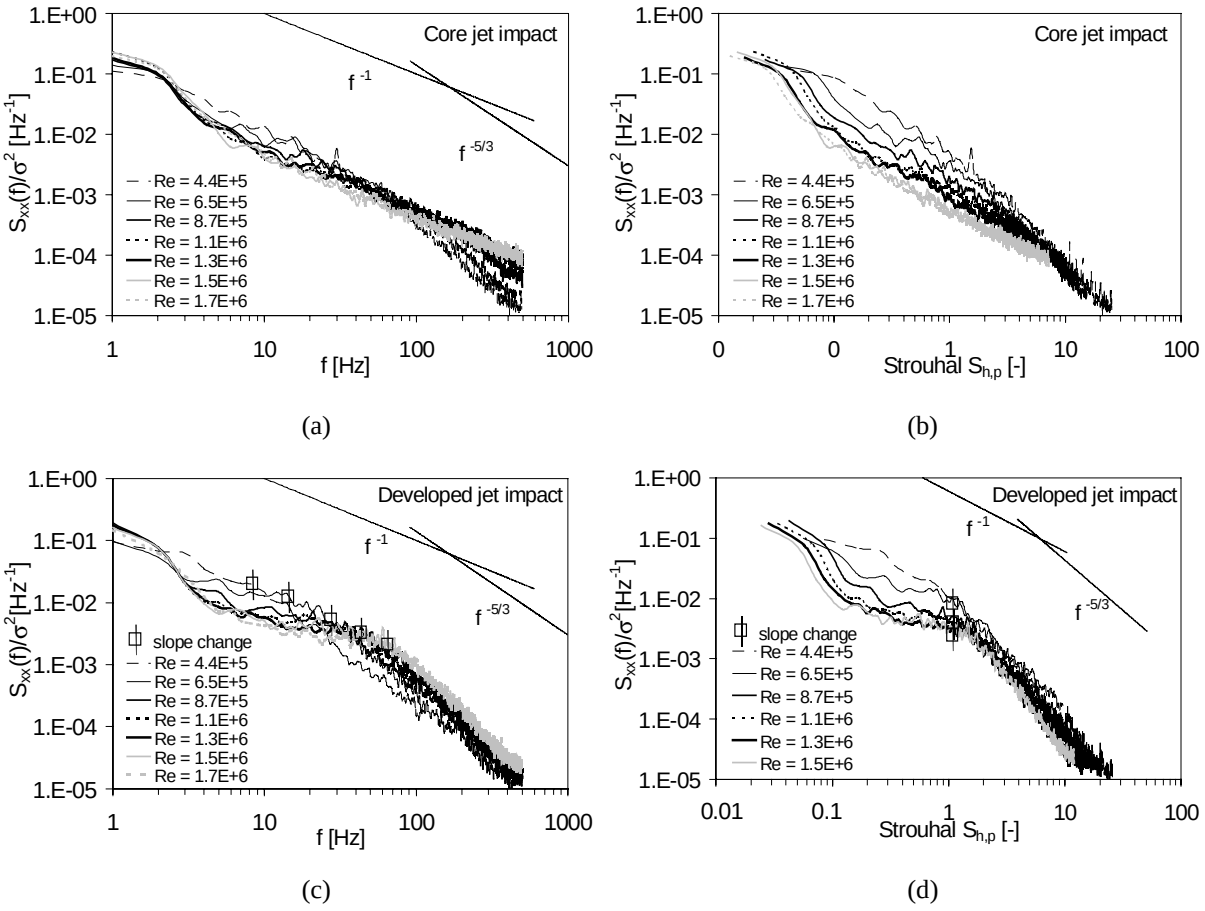

Fig. V-12 Non-dimensional power spectral density of dynamic pressures at the plunge pool bottom for a 57mm jet diameter:
a) core jet in the frequency domain; b) core jet in the Strouhal domain;
c) developed jet in the frequency domain; d) developed jet in the Strouhal domain.

3.4. Pressures at the jet's centreline for a convergent jet

The here presented pressures have only been measured for a 72 mm jet diameter.

3.4.1. Measured pressure signal

The pressure signals generated by a convergent jet outlet are presented in Fig. V-13. Fig. V-13a shows the signal for core jet impact. A very steady pressure pattern is observed. Compared with the cylindrical jet outlet, as presented in Fig. V-6a, the core of the jet is much more compact and no low-frequency turbulences occur.

This is due to the cross-shaped frame that has been inserted in the upstream water supply conduit. This frame breaks up the secondary flow currents that are induced by the 90° bend. Furthermore, the convergent shape guarantees a more gently transfer of the flow from a 300 mm conduit diameter down to a 72 mm jet outlet.

Fig. V-13b presents the pressure signal for developed jet impact conditions. As for the cylindrical jet outlet, presented in Fig. V-5b, a pattern of turbulent pressure fluctuations happens. These fluctuations are generated by eddies of the impacting turbulent shear layer.

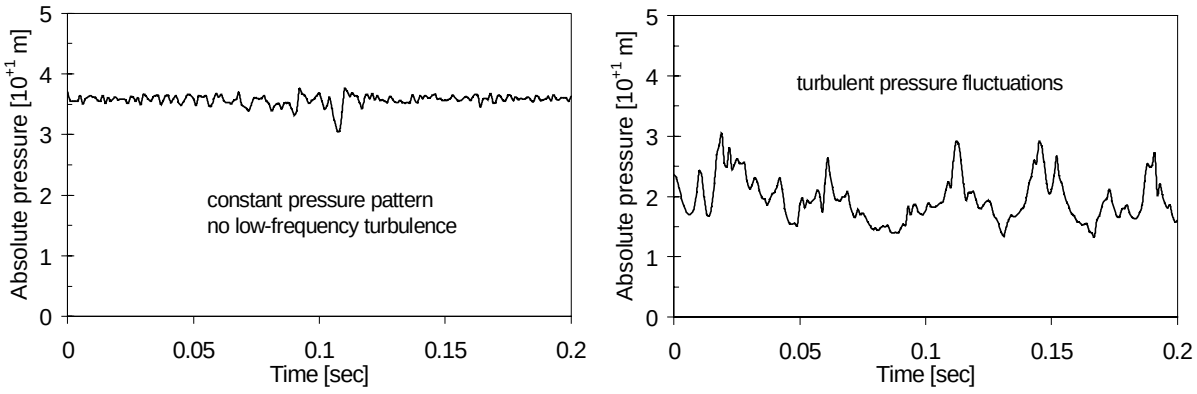

a) b)

Fig. V-13 Pressure signal in the time domain, measured under the jet's centreline, at the plunge pool bottom: a) core jet impact; b) developed jet impact.

3.4.2. Mean dynamic pressure value

The mean dynamic pressure coefficients are presented in Figs. V-14a & 14b. Part of the measured coefficients is substantially higher than the values obtained for the cylindrical outlet (according to Fig. V-6). As can be seen in Fig. V-14b, this is the case when the jet velocity is higher than roughly 12 m/s for core jets and 20 m/s for developed jets. Lower velocities generate mean values that are comparable to the ones obtained for the cylindrical outlet.

The reason for the higher values lies in the ideal character of the jet that is generated by the convergent outlet. No low-frequency turbulences exist and the jet's momentum is able to traverse the water cushion of the plunge pool. This traverse is very easy for low water depths (core jets), but becomes more difficult with increasing water depths (developed jets).

Hence, the observed jets reveal a double character. At low velocities, the jet is not able to traverse the water depth, and a typical two-dimensional shear layer installs. For higher velocities, however, the jet's momentum is able to withstand the water depth and to directly impact the pool bottom. In other words, ideal core jet impact conditions occur. Moreover, this phenomenon has been observed to be intermittent, i.e. it only occurs from time to time. This is due to the strong recirculation currents that are generated in the cylindrical basin at high jet velocities. These currents sometimes rebound and influence the jet such that its momentum is partly destroyed.

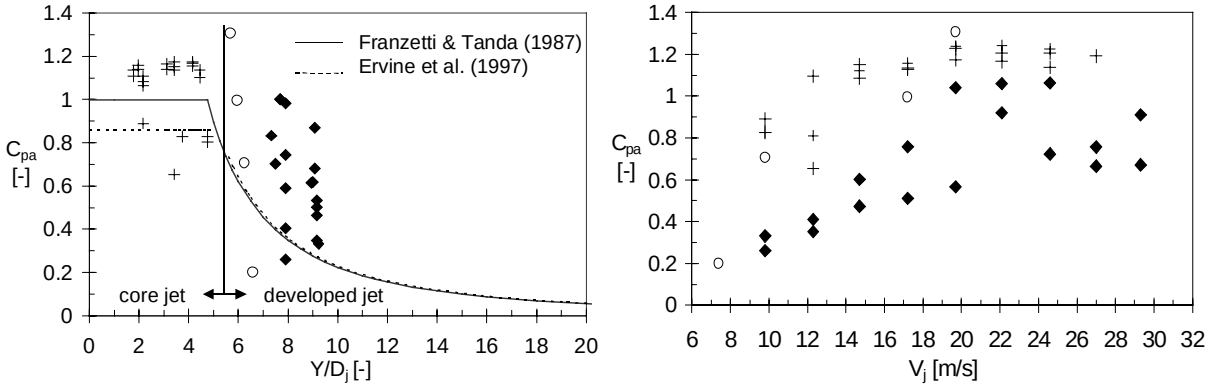

a) b)

Fig. V-14 Non-dimensional mean dynamic pressure coefficient C_{pa}: a) as a function of the geometrical ratio of plunge pool depth Y to jet diameter D_j; b) as a function of the mean jet outlet velocity V_j.

3.4.3. Root-mean-square pressures

The double character of the jets is clearly visible for core jet impact conditions in Fig. V-15. Half of the values are similar to the ones obtained for the cylindrical outlet (Fig. V-8); the other half corresponds to ideal core impact and thus close to the initial jet turbulence intensity according to Fig. V-1. This statement confirms that ideal core impact can only occur for a jet that directly impacts the pool bottom.

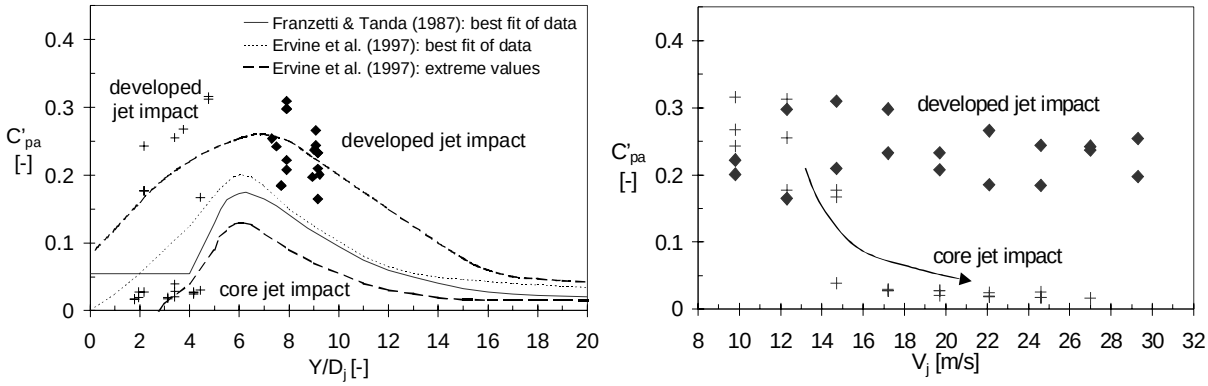

a) b)

Fig. V-15 Non-dimensional fluctuating dynamic pressure coefficient C'_{pa}: a) as a function of Y/D_j. Ideal core impact conditions are visible at small Y/D_j ratios; b) as a function of the mean jet outlet velocity V_j.

3.4.4. Extreme pressures

Similar to the abovementioned statements, part of the values corresponds to ideal core jet impact and generates pressures that are very similar to available literature data. However, when a turbulent shear layer occurs, the extreme pressures apparently can be higher than for a cylindrical jet outlet. The reason behind this is unclear.

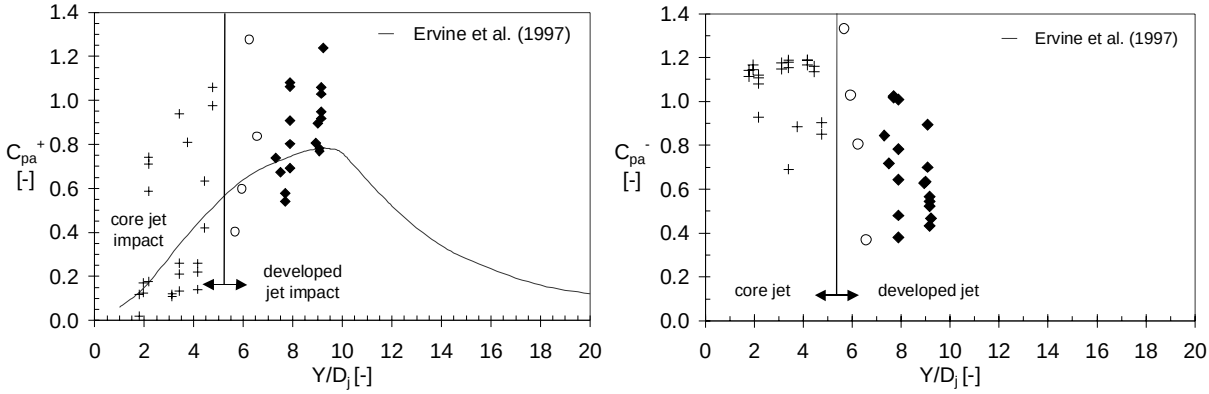

a) b)

Fig. V-16 a) Non-dimensional positive extreme pressure coefficient C_{pa}^{+} as a function of the ratio Y/D_j; b) Non-dimensional negative extreme pressure coefficient C_{pa}^{-} as a function of the ratio Y/D_j.

3.4.5. Probability density function

Fig. V-17a presents the probability density function for a low jet velocity of 10 m/s. For both core and developed jet impact conditions, comparison with the Gaussian distribution shows that a slightly positively skewed function is obtained. This is in accordance with previous studies (May & Willoughby, 1991). Fig. V-17b presents the same function for a 30 m/s jet velocity. For this velocity, developed jets can still generate a positively skewed function, whether for core jets a negatively skewed function is obtained. The probability density function for ideal core impact is not presented but corresponds to a very narrow bandwidth of data on the abscissa.

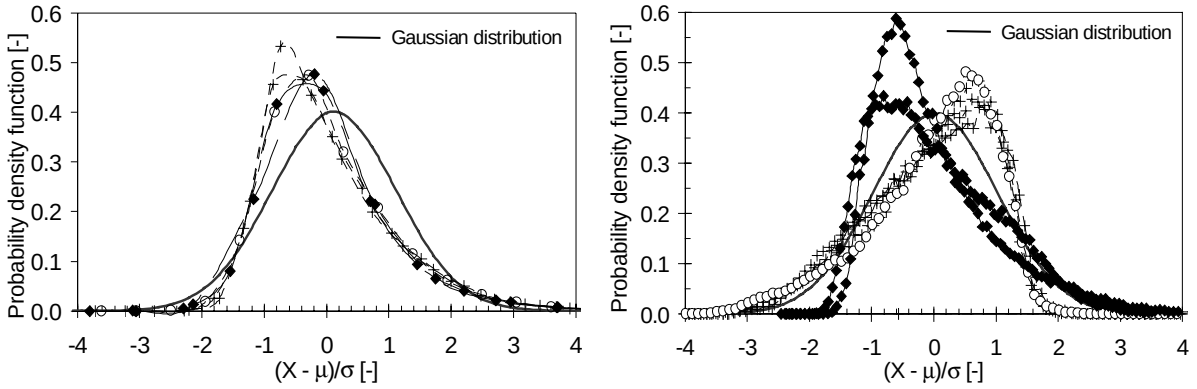

Fig. V-17 Plunge pool bottom pressures: a) Probability Density Function (PDF) compared to a Gaussian distribution at low jet velocity (10 m/s); b) PDF function for high velocities (30 m/s).

3.4.6. Spectral analysis

Figs. V-18 a to 18d present the non-dimensional power spectral density for core jets and developed jets, in the frequency domain and in the Strouhal domain. For core jet impact, low jet velocities (up to 15 m/s) generate spectra that are very similar to the ones obtained for the cylindrical jet outlet and developed impact conditions.

As such, very rapidly a –5/3 slope decay is observed. Higher jet velocities, however, produce spectral decays of –1 at high frequencies. The remarkable slope change and lack of turbulent energy at intermediate frequencies could not be explained. As this has been encountered only for the present series of test runs, it is not excluded that it is due to an error in the file generation after the tests.

Developed jet impact conditions generate power spectra that are very similar to the ones obtained for the cylindrical jet outlet (Fig. V-11). Hence, self-preserving profiles are again only obtained in a non-dimensional domain. The slope decay at high frequencies attains values of approximately –7/3. For Strouhal numbers less than 1, more turbulent energy is present and the slope decays are milder than or equal to –1.

The agreement between the power spectral densities obtained for a 57 mm diameter and a 72 mm diameter jet indicates that the jet diameter at impact is not a key issue. This confirms the aforementioned statement that the turbulence conditions at the plunge pool bottom are rather governed by the jet velocity at impact V_j and by ratio of the plunge pool depth over the jet diameter Y/D_j.

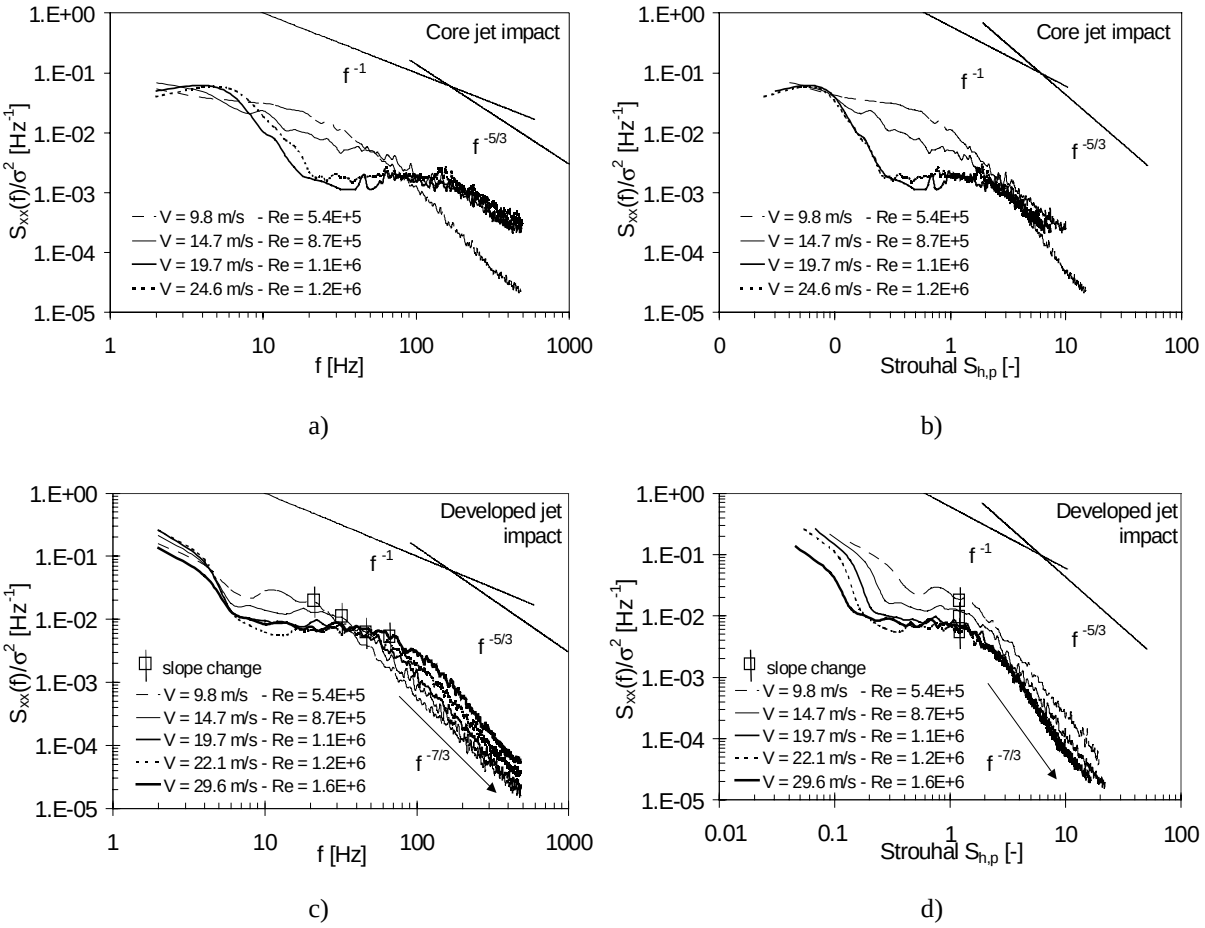

Fig. V-18 Non-dimensional power spectral density of dynamic pressures at the plunge pool bottom for a 57 mm jet diameter:
a) core jet in the frequency domain; b) core jet in the Strouhal domain;
c) developed jet in the frequency domain; d) developed jet in the Strouhal domain.

3.5. Radial pressure pattern for a cylindrical jet outlet

The pressure sensors situated at the plunge pool bottom, but outside of the jet's centreline, allow determining the radial distribution of the surface pressures. For this purpose, measurements have been performed by sensor (a^{ii}), at 75 mm from the rock joint, and by sensor (a^{iv}) situated at 150 mm from the rock joint (Fig. IV-5). Results are presented for a 72 mm diameter jet only. Similar to the centreline pressures, this section starts with an example of the pressure signal in the time domain. This is followed by the mean, root-mean-square and extreme pressure values. Where possible, the results obtained for the three pool bottom sensors (a, a^{ii} and a^{iv}) have been presented as a function of the radial coordinate. Finally, the power spectral density is compared with the one for centreline pressures.

3.5.1. Measured pressure signal

The pressure signals in the time domain, measured at sensor (a^{ii}) situated at 75 mm from the rock joint, and at sensor (a^{iv}), situated at 150 mm from the rock joint, are presented in Fig. V-19 for core and developed jet impact. Fig. V-19a shows the pressure signal for core jet impact. Unlike the quite constant pressure pattern that was obtained at the jet's centreline, a signal with high-frequency fluctuations can be observed at sensor (a^{ii}). Apparently the sensor is situated in the small shear layer close to the core of the jet. Sensor (a^{iv}), however, only exhibits very small, low-frequency pulses. This

sensor is clearly located out of the shear layer. Fig. V-19b shows the homologue pressure signal for developed jet impact. Similar to the centreline pressures, a fluctuating signal is obtained at both sensors, due to the shear-layer eddies. Sensor (a^{iv}) is probably situated at the outer limit of the shear – layer zone.

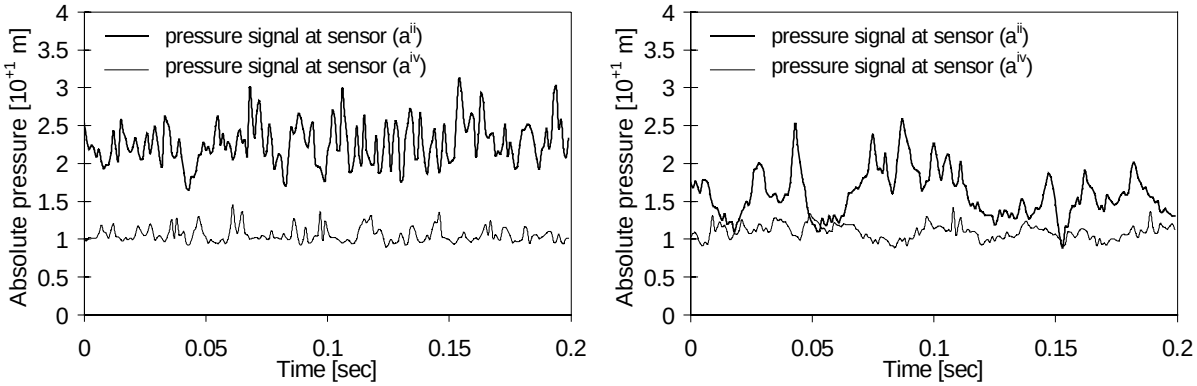

Fig. V-19 Pressure signal in the time domain, measured at sensor (a^{ii}), located at 75 mm of radial distance from the rock joint, and at sensor (a^{iv}), located at 150 mm radial distance from the rock joint; a) core jet impact; b) developed jet impact.

3.5.2. Mean dynamic pressure value

The mean dynamic pressure coefficients $C_{pa}{}^{ii}$ are presented in Fig. V-20a. It can be seen that, for core and transitional jet impact, these values are much lower than the ones measured under the jet's centerline (Fig. V-6a). For developed jet impact, this difference becomes almost negligible. The reason is that, for developed jets, the sensor (a^{ii}) is situated inside the turbulent shear layer that impacts the pool bottom. This is not the case for core jet impact, for which the turbulent shear layer is much smaller and thus closer to the rock joint. The mean values for $C_{pa}{}^{iv}$ are negligibly small and, hence, not presented.

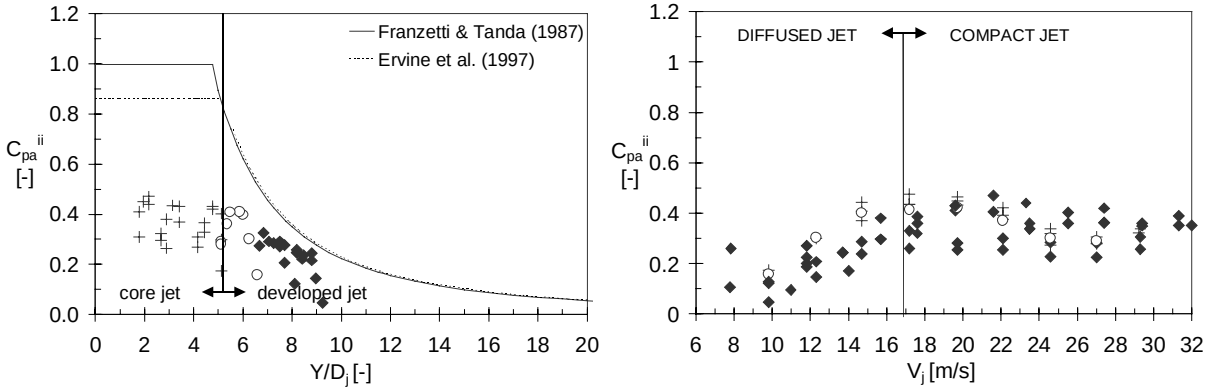

Fig. V-20 Non-dimensional mean dynamic pressure coefficient $C_{pa}ii$: a) as a function of the geometrical ratio of plunge pool depth Y to jet diameter D_j; b) as a function of the mean jet outlet velocity V_j.

Fig. V-20b presents the C_{pa}^{ii} values as a function of the mean jet outlet velocity V_j. The same trend as for the centreline values (Fig. V-6b) is observed. However, the velocity at which the values become more or less stable is lower than for the centreline values.

3.5.3. Root-mean-square pressure

The root-mean-square value of the dynamic pressures measured at sensors (a^{ii}) and (a^{iv}) is presented in Fig. V-21. The curves as a function of Y/D_j exhibit the same form as the centreline values presented in Fig. V-8a. The values are somewhat lower than most of the centreline values. However, due to the prototype character of the test facility, they are still higher than or equal to existing literature data. Fig. V-21b shows the values as a function of the mean jet velocity V_j. The same tendencies as for the centreline values can be distinguished. However, the separation between unstable and compact jets occurs at a somewhat lower jet velocity of 16 m/s instead of 20 m/s.

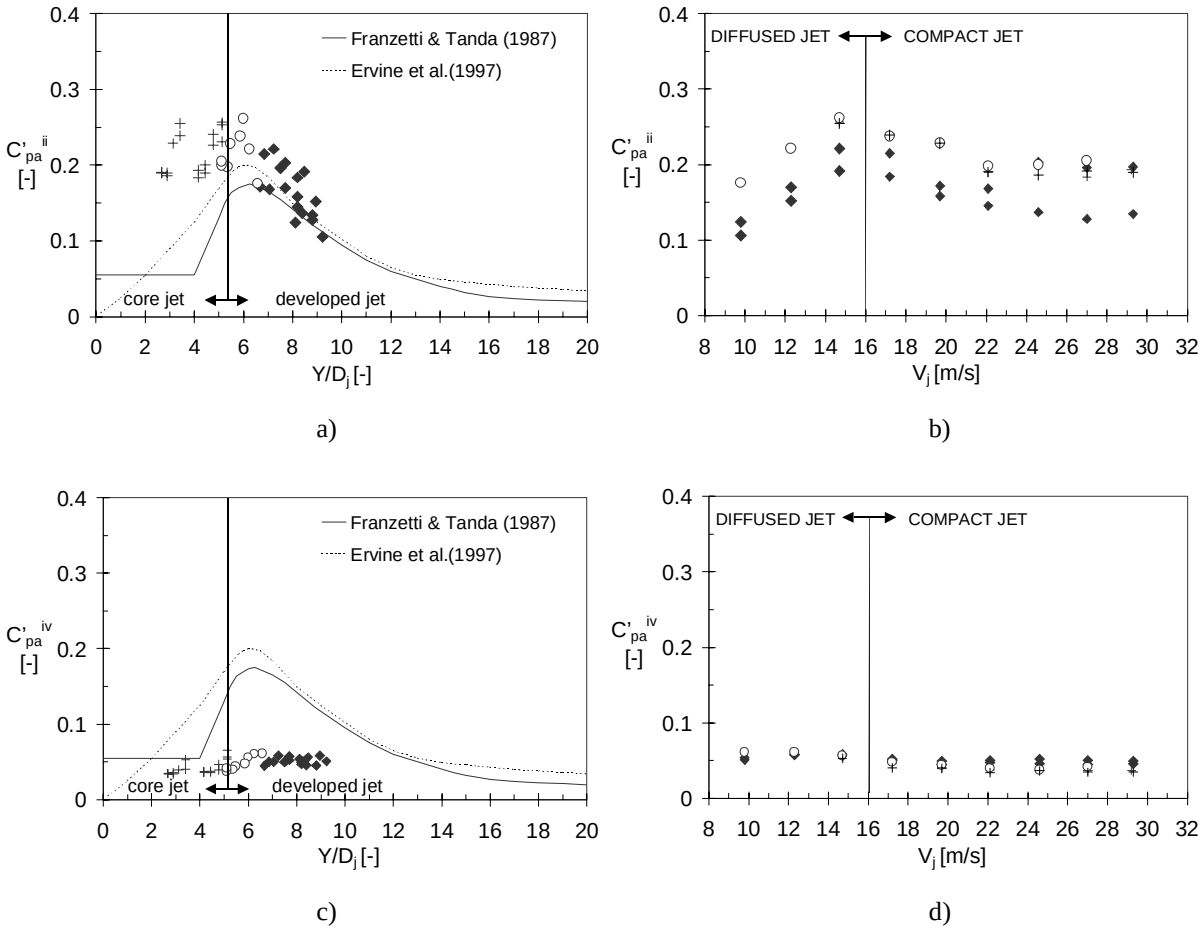

Fig. V-21 Non-dimensional fluctuating dynamic pressure coefficient C'_{pa}:
a) sensor (a^{ii}) as a function of Y/D_j; b) sensor (a^{ii}) as a function of V_j;
c) sensor (a^{iv}) as a function of Y/D_j; d) sensor (a^{iv}) as a function of V_j.

3.5.4. Extreme pressures

The extreme pressure values are presented in Fig. V-22. The positive extremes at sensor (a^{ii}) are higher than the ones observed under the jet's centreline. The negative values are much lower than the ones at the centreline. For sensor (a^{iv}), high positive extremes are visible at small Y/D_j ratios, however, with increasing ratio, the values decrease. The negative values are very low compared to the other sensors.

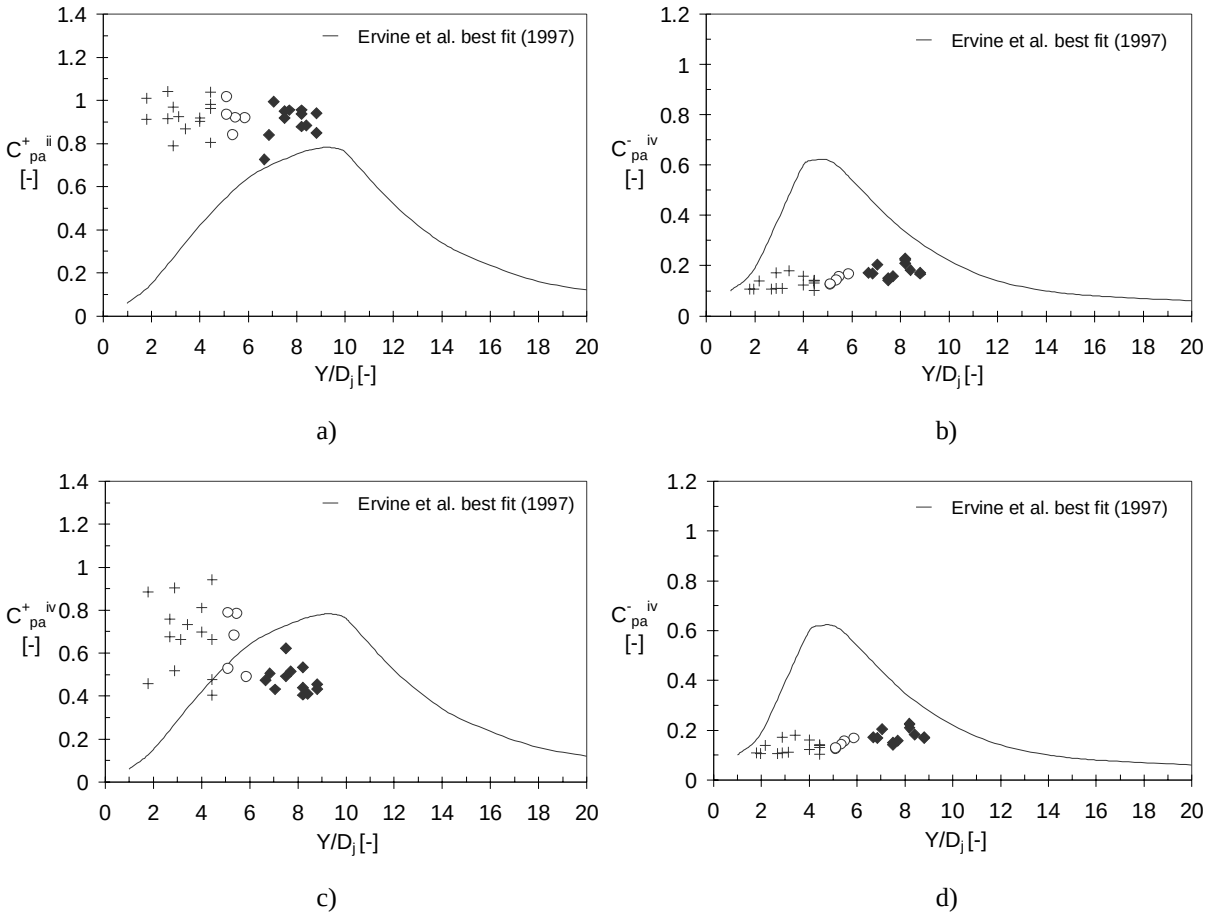

Fig. V-22 Non-dimensional positive and negative extreme pressure coefficients as a function of Y/D_j:
a) positive extremes $C^{+}_{pa}{}^{ii}$; b) negative extremes $C^{-}_{pa}{}^{ii}$;
c) positive extremes $C^{+}_{pa}{}^{iv}$; d) negative extremes $C^{-}_{pa}{}^{iv}$.

Sensor (a^{ii}) exhibits positive extremes that correspond to the values measured at the centreline for developed jet conditions (Fig. V-9a). This trend is noticed even for core jet impact. This is logic provided that, even for core jet impact conditions, this sensor is probably situated outside of the core of the jet and thus subjected to shear layer eddies.

Theoretically speaking, the core of the jet cannot generate large positive extremes because the pressure should stay quite constant. Furthermore, for sensor (a^{ii}), the combination of a decreasing mean pressure value and a still high RMS value obviously results in much lower negative pressures.

Sensor (a^{iv}) has positive extremes similar to sensor (a^{ii}) for core jet impact, but lower extremes for developed jet impact. The negative extremes become very low and are quasi insignificant.

3.5.5. Mean and root-mean-square dynamic pressures as a function of the radial coordinate

In the following, the mean and root-mean-square coefficients, measured at the pool bottom sensors (a), (a^{ii}) and (a^{iv}), are presented as a function of their radial coordinate (Bollaert, 2001). This coordinate is set at zero on the rock joint. For the mean pressure values, theoretical curves exist in literature. According to Ervine et al. (1997), the variation of the mean dynamic pressure coefficient with radial distance out from the jet's centreline is given by an exponential law as follows:

$$\frac{C_{pr}}{C_p} = \exp^{-K_2 \cdot \left(\frac{r}{y}\right)^2} \tag{5.10}$$

in which C_{pr} stands for the radial coefficient and C_p for the centreline coefficient. The parameter K_2 ranges from 30 for shallow pool depths to 50 for greater pool depths. In their study, shallow pool depths corresponded to Y/D_j values less than 4. As can be seen in Fig. V-24a, the measured values do not match the theoretical curve for core jet impact. However, for developed jet impact conditions, a very good agreement is obtained.

The RMS values persist much longer in the radial direction than the mean values. This statement has been confirmed by several research studies and is clearly visible in Fig. V-23. Even when the mean pressure value drops to almost zero, still a significant RMS value may exist. This seems particularly true for core jet impact conditions. One of the main reasons probably is the high air entrainment. Due to this phenomenon, the two-dimensional turbulent shear layer zone is not well defined anymore throughout the plunge pool depth. Air bubbles generate a continuous fluctuation of the outer limits of this shear layer zone. Hence, this effect should be accounted for when determining the region at the plunge pool bottom that is subjected to severe pressure fluctuations.

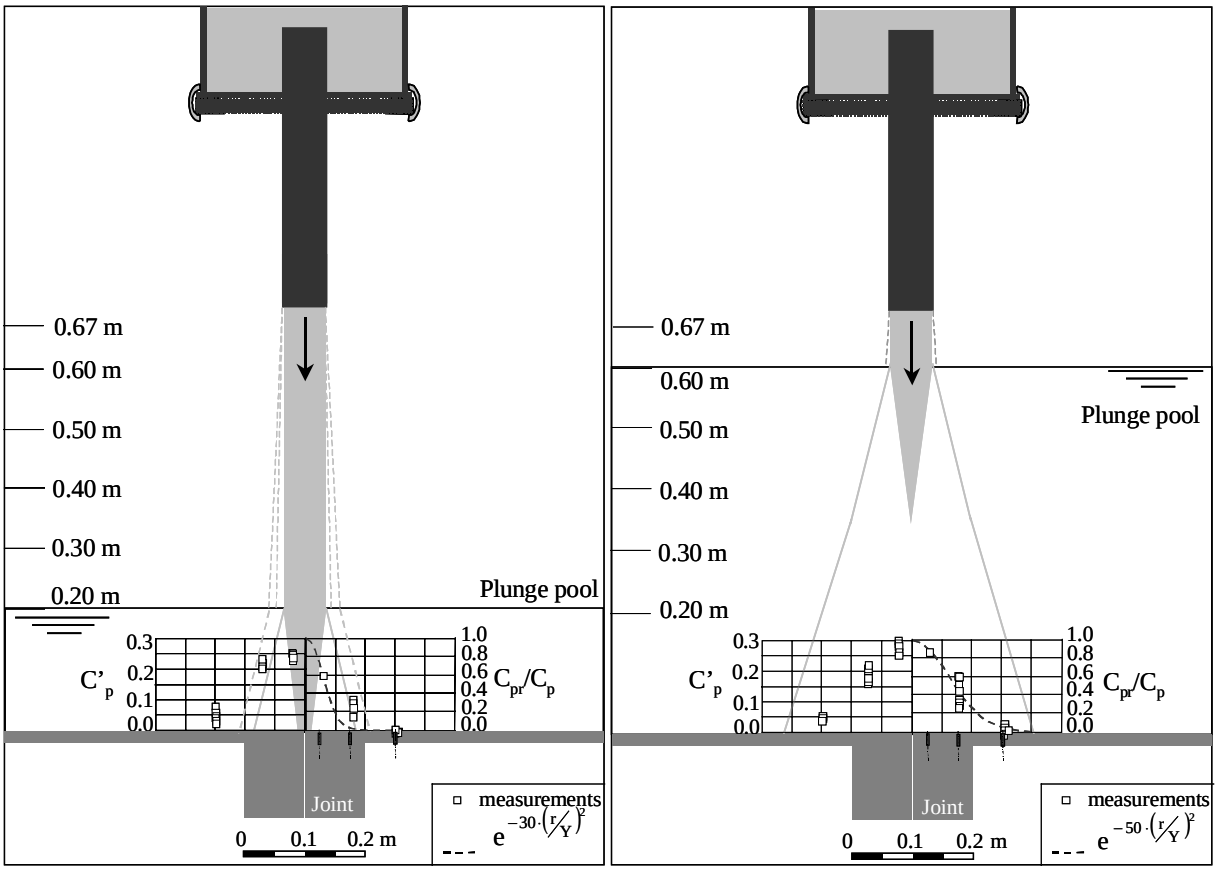

Fig. V-23 Mean and root-mean-square dynamic pressure coefficients as a function of the radial coordinate: a) for core jet impact conditions; b) for developed jet impact conditions. The jet diameter is 72 mm and the jet outlet is cylindrical (Bollaert, 2001).

3.5.6. Spectral analysis

A comparison has been made between the power spectral density of the centerline sensor (a) and the power spectral density of the sensor that is situated radially most outwards from the rock joint, i.e. sensor (a^{iv}) (Bollaert, 2001). This is particularly interesting because the latter is theoretically outside of the shear layer for core jet impact, but still inside this shear layer for developed jet impact.

The results are presented in Fig. V-24 for core and developed jet impact, in the frequency and Strouhal domains respectively. For core jet impact, almost no differences can be observed between the spectral curves of the two sensors. Even at sensor (a^{iv}), the slope decay follows a –1 law. This slope gets steeper at Strouhal numbers that are significantly larger than 1 (Fig. V-24b). Apparently, the sensor is situated just within the shear layer of the turbulent and, as a consequence, is still subjected to high-frequency jet impact. On the other hand, for developed jet impact, the difference is more evident. For Strouhal numbers larger than 1, the slope decay at the radially outside sensor is significantly greater than for the centerline sensor.

As a conclusion, it is believed that, when determining the excitation capability of high-velocity jets, the maximum possible turbulent shear layer zone at the plunge pool bottom should be taken into consideration. Although the pressure fluctuations near the outside of this zone loose in absolute value, their spectral content apparently still generates frequencies that are in the same range than the ones under the jet's centerline. As will be pointed out later on in this chapter, these frequencies are capable to stimulate a rock joint to resonance or standing waves.

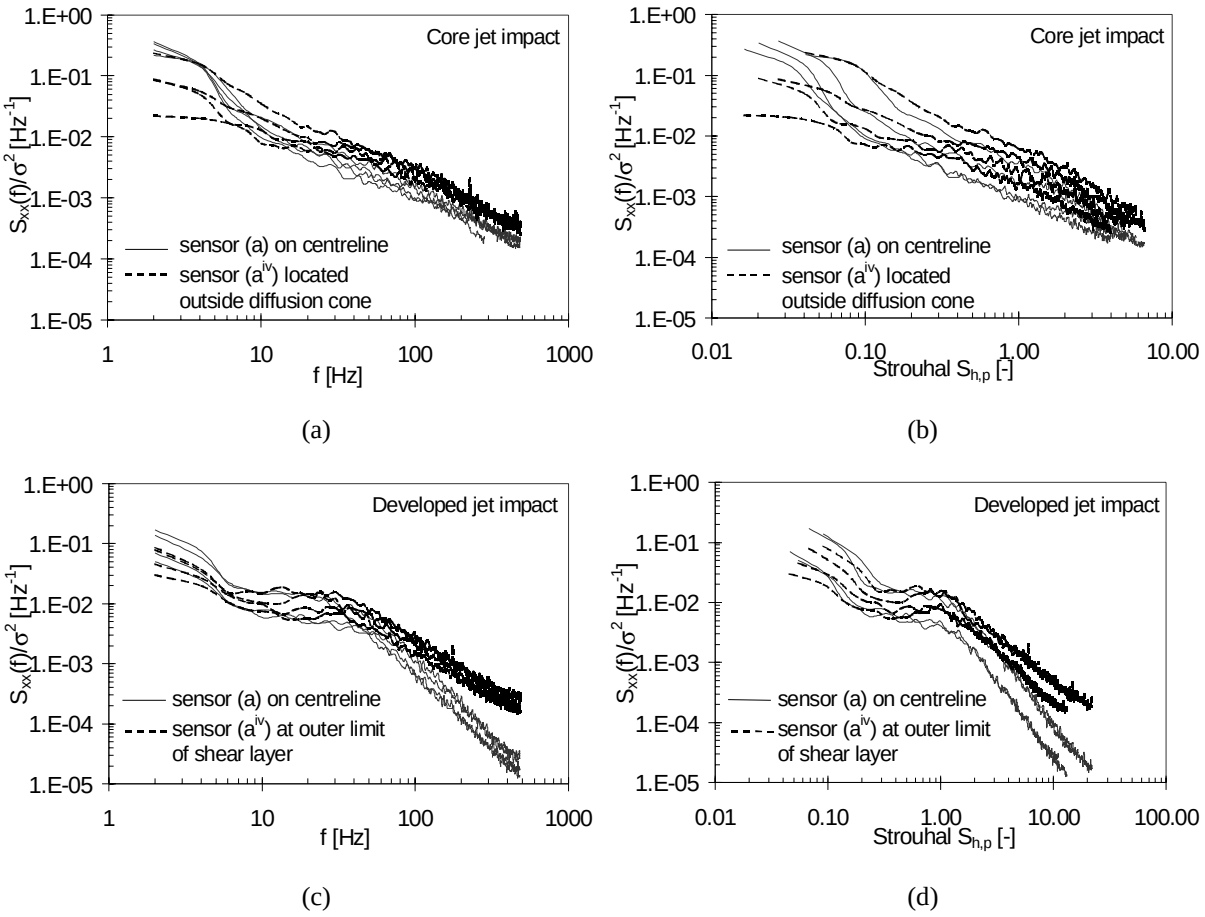

Fig. V-24 Comparison of non-dimensional power spectral density of dynamic pressures at the jet's centreline and at 150 mm away from the centreline (Bollaert, 2001):
a) core jet impact in frequency domain; b) core jet impact in Strouhal domain;
c) developed jet impact in frequency domain; d) developed jet impact in Strouhal domain.

3.6. Concluding remarks on plunge pool bottom pressures

The analysis of dynamic pressures at the plunge pool bottom has been performed by means of a cylindrical and a convergent shaped jet outlet and for jet diameters of 57 mm and 72 mm. The tested water depths in the pool ranged from 0.20 m to 0.67 m for impinging jet conditions, and were set at 0.87 m for submerged jet conditions. The mean jet velocities were situated between 5 and 35 m/s.

For these test parameters, pressure measurements have been performed under the jet's centreline, as well as at two bottom sensor locations radially outwards. The cylindrical outlet generated jets with a low-frequency component and a turbulence intensity of 4-6 %. The convergent outlet created stable jets with a turbulence intensity of only 2-3 %. Both outlet systems produced pressure patterns that highly depend on the ratio of pool depth to jet diameter at impact Y/D_j.

For ratios less than 4 to 6, core jet impact is obtained. This type of jet generates pressure patterns at the pool bottom that are quite constant, but that exhibit sudden pressure drops due to low-frequency turbulence of the core. These effects seem to be inherent to the impact of a jet core into a small water depth and cannot be avoided. Hence, the fluctuating part of the dynamic pressures can become significant. Furthermore, the spectral content of these jets extends over a wide range of frequencies and decays very slowly with increasing frequency.

For Y/D_j ratios higher than 4 to 6, developed jet impact is observed. This type of jet impact is characterized by a fully developed turbulent shear layer that impacts the pool bottom. The corresponding pressures fluctuate considerably. Hence, the RMS value is rather high and the mean value rather low. Moreover, the spectral content exhibits a significant change in slope decay at high frequencies. The slope change occurs at a Strouhal number of around 1. In other words, less turbulent energy is present in the upper part of the spectrum.

For both jet impact conditions, the root-mean-square values and the extreme pressure values were significantly higher than any previous model study. This is due to the near-prototype character of the facility. At near-prototype jet velocities, the spectral content of the modelled jet is close to the one of a real jet, even at high frequencies. This is not the case for model studies at low jet velocities. The correct simulation of the whole frequency range of the impacting jet results in higher root-mean-square and extreme values.

Modification of the jet diameter had no significant influence on the measured pressure patterns. This indicates that the governing parameter is the Y/D_j ratio rather than the jet diameter D_j. Furthermore, submerged jets were distinct from impinging jets in that they exhibited somewhat lower extreme pressures.

The presence of free air has a profound impact on the lateral extension of the shear layer zone, and, thus, on the zone at the pool bottom that is subjected to severe dynamic pressures. It is believed that significant pressure fluctuations still remain at the most outer side of this zone, and that the limits of this zone continuously change with time.

Finally, the key issue of the present section is the statement that high-velocity jets are characterized by **a spectral energy content that extends over a much wider frequency range than what is generally assumed for macroturbulent flows in plunge pools**, i.e. up to 25 Hz (Toso & Bowers, 1988). At prototype velocities and for small pool depths, substantial energy can still subsist at frequencies of several hundreds of Hz (Bollaert, 2001; Bollaert & Schleiss, 2001f).

Therefore, it is evident that such a type of flow impact could be capable to stimulate underlying rock joints to transient wave phenomena, such as standing wave or resonance waves. This is studied more in detail in the next section of this chapter for both closed-end and open-end rock joints.

4. Dynamic pressures inside closed-end rock joints

As pointed out in Chapter III on theoretical bases, the turbulent pressure fluctuations at the water-rock interface, i.e. at the plunge pool bottom, are transferred into the discontinuities of the intermittently or completely jointed rock mass. There, the free shear layer flow of the plunge pool transforms into a highly transient pressurized flow. The flow conditions inside the rock joint are governed by initial conditions and boundary conditions, and by the wave celerity of the two-phase mixture. Hence, the analysis of the pressure measurements inside the joints focuses on these aspects to better assess the flow conditions that are encountered.

The present section deals with closed-end rock joints. These joints correspond to an open-closed boundary system, in which the jet excitation is applied at the open or upstream boundary. The closed or downstream boundary reflects the incoming pressure waves and, thus, has a significant impact on the pressure pattern inside the joint. This can be the formation of water hammer in case of a single pressure pulse. However, for a continuous excitation at the upstream boundary, such as in case of high-velocity jet impact, standing waves or even resonance waves may form.

The presence of air bubbles in the liquid makes the transient system non-linear. This complicates the problem and can result in violent phenomena, such as shock waves. The air completely changes the compressibility of the fluid and its quantity inside joints has to be taken into account. This has been attempted by an analysis of the fundamental resonance frequency of the transient system. By assuming a theoretically perfect open-closed boundary system, the resonance frequency defines the mean wave celerity of the fluid. The hypothesis of a perfect system, however, can hardly be verified. Therefore, point-to-point correlations between pressure measurements at the middle and at the end of the joints were used to estimate the celerity. They have the advantage that the celerity is obtained as a function of the pressure at which they were determined. As such, “celerity-pressure” relationships are obtained. They inform about the change in air content inside the joint as a function of pressure.

In the following, dynamic pressures measured in I-shaped, L-shaped and U-shaped closed-end rock joints are presented. These joints have a width of 10 mm and a thickness of 1 mm. The width has been chosen such that the joints can be considered as one-dimensional compared to the diameter of the impacting jet. Real rock joints often exhibit this characteristic. The thickness is also characteristic for prototype joints. The pressures were mainly obtained by impact of a 72 mm diameter, cylindrical jet outlet. However, some tests have been made with a 57 mm diameter and with a convergent jet outlet, in order to assess their influence on the pressures inside the joints. Furthermore, where possible, comparison is made between impinging and submerged jet conditions. This informs about the aeration influences. Similar to the pool bottom pressures, the analysis is performed in the time domain and in the frequency or Strouhal domain. The results for the I-joint are based on Bollaert & Schleiss (2001f).

4.1. The I-shaped rock joint under the impact of a cylindrical jet

4.1.1. Geometrical configuration

The geometrical configuration of the I-shaped rock joint is presented in Fig. V-25. Four pressure sensors are of importance. Sensor (a) measures at the pool bottom, near the rock joint entrance, and defines the jet excitation. Sensors (b), (c) and (d) measure inside the joint, respectively at the beginning, at the middle and at the end. The analysis of the dynamic pressures focuses on a comparison between sensor (a) on one hand, and the sensors (c) and (d) on the other. Sensor (b) was discarded from the present analysis because of a systematic break-down of the pressure sensors at that place. Preliminary measurements indicated a weak form of cavitation. This was probably the reason that the sensors broke down. As the obtained pressure signals exhibited violent local phenomena that do not match with the present analysis, they have been treated in a separate section at the end of this chapter.

The I-form constitutes the most elementary, one-dimensional form of an open-closed transient system. Although this basic form is rarely encountered in practice, its analysis is of crucial significance for the assessment of the flow conditions that can occur inside a rock joint. The tested joint has a length of 800 mm, a width of 10 mm and a thickness of 1 mm. The length is a typical length for a real rock joint. This prototype character is important when determining the transient characteristics of the system. As such, the tests are performed on a near-prototype scale. The only parameters at model scale are the geometry of the jet, the water depth and the joint width. However, these three geometries have been chosen such that the flow characteristics they generate correspond to prototype characteristics. The small jet and water depth produce a turbulence pattern and aeration that are on prototype scale. Compared to the size of the relevant eddies of this turbulence, the simulated joints are considered as one-dimensional, just like in practice. Hence, the transient flow inside these simulated joints is representative for prototype conditions.

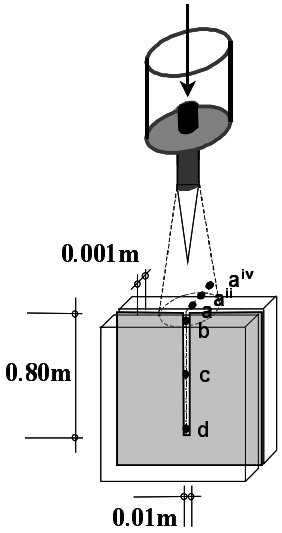

Sensor	Type	Position
a	pool bottom	25 mm from joint
b	rock joint	center, 50 mm inside
c	rock joint	center, 420 mm inside
d	rock joint	center, 790 mm inside

Fig. V-25 Geometrical configuration of the I-shaped rock joint. The analysis of the dynamic pressures focuses on a comparison between the pool bottom sensor (a) and the rock joint sensors (c) and (d).

4.1.2. Measured pressure signal

Fig. V-26 presents the measured pressure signals in the time domain, for core and developed jet impact conditions. Jet diameters are 57 or 72 mm. Pressures are expressed in absolute values. Comparison is made between sensors (a) and (d). The values for (a) correspond to the ones that are presented in Fig.V-6. The constant pressure pattern (Fig. V-26a) of core jet impact does not seem to influence the corresponding pressure at the joint end. However, a sudden core instability (= low-frequency turbulence) generates a pressure drop inside the joint, followed by a high and short pressure peak. The peak is much higher than the maximum pressures encountered at the pool bottom. After its appearance, the instability damps out quickly.

Fig. V-26b shows the pressure signals for developed jet impact. The turbulent fluctuations at the pool bottom generate a consecutive series of high peak pressures at the joint end. These peak pressures alternate with periods of low, almost atmospheric pressure (spikes). The peak pressures attain values that can be a multiple of the maximum pool bottom values. The typical time rise of a peak is on the order of only a few milliseconds, while the total duration of the peaks fluctuates from 0.01 to 0.02 seconds. The spikes seem to be twice as long as the peaks and often decrease down to the atmospheric pressure. Apparently, any pressure disturbance at the pool bottom immediately produces a highly non-linear resonating pressure flow inside the joint. For developed jet impact, this system is characterized by a resonating frequency that appears to be more or less constant. The fundamental resonance period $T = 1/f_{res}$, in which f_{res} is called the fundamental resonance frequency.

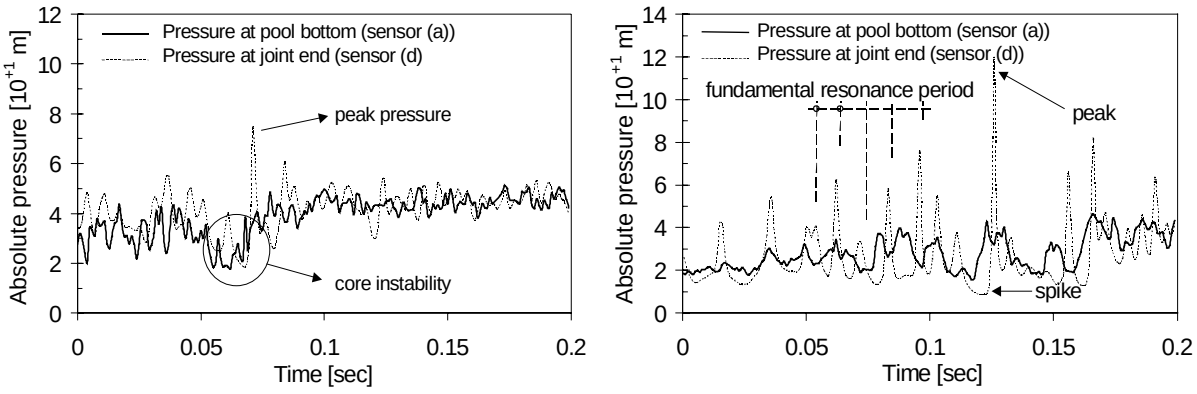

(a) (b)

Fig. V-26 Measured pressure signals in the time domain: a) core jet impact; b) developed jet impact. Comparison is made between the sensors (a) and (d). Jet diameter is 72 mm.

4.1.3. Mean dynamic pressure value

The mean dynamic pressure coefficients are presented in Fig. V-27a for sensor (c) and in Fig. V-27b for sensor (d), for core (+ sign) and developed (♦ sign) jet impact conditions. The (o) sign stands for transitional jet impact conditions. No significant differences can be observed between the two sensors. Comparison with the mean pressure coefficients that were measured at the pool bottom (C_{pa}), as presented in Fig. V-6, is performed by use of the best-fit curves of available literature data of Franzetti & Tanda (1987) and Ervine et al. (1997). Core jet impact exhibits the same values at the bottom and inside the joint. Based on the similar pressure signals according to Fig. V-26a, this is not surprising. However, for developed jet impact, the mean pressure inside the joint is slightly higher than the one at the pool bottom. The difference increases with increasing Y/D_j ratio and is probably due to the appearance of high peak pressures (Fig. V-26b). The mean values at submerged jet impact conditions show no substantial difference with the ones at impinging jet conditions.

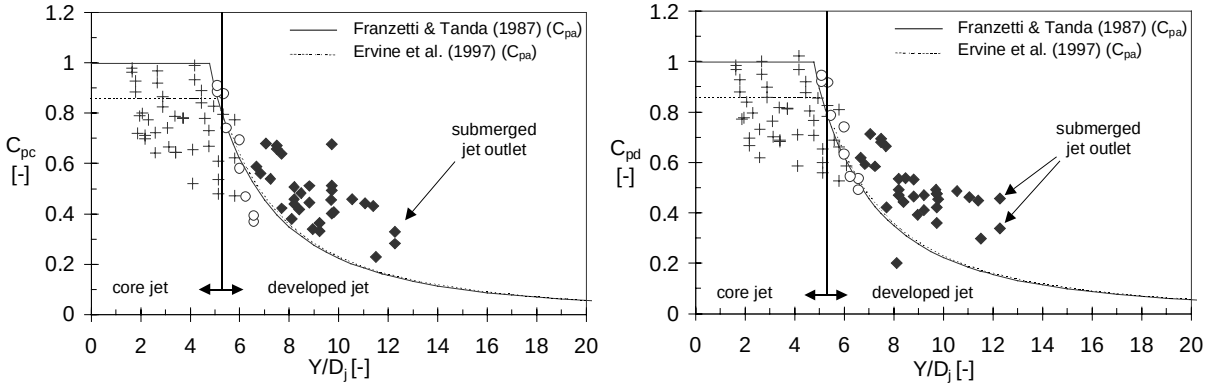

(a) (b)

Fig. V-27 Non-dimensional mean dynamic pressure coefficient C_p as a function of the Y/D_j ratio: a) sensor (c) at the middle of the joint; b) sensor (d) at the end of the joint. Comparison is made with available literature data of C_{pa} values at the pool bottom.

4.1.4. Root-mean-square pressures

The root-mean-square values at the middle (Fig. V-28a) and at the end of the joint (Fig. V-28b) define the importance of the fluctuating part of the dynamic pressures. At the middle of the joint, the obtained values are higher than the ones at the joint entrance (C'_{pa} values according to Fig. V-8a). This is particularly true for developed jet impact. The same statement holds at the end of the joint, where the

root-mean-square values are even higher than at the middle. The values inside the joint are significantly higher than the ones at the pool bottom. Moreover, the values at the end of the joint are higher than the ones at the middle. These higher values agree with the pressure signals that are presented in Fig. V-25. The pressures inside the joint show higher fluctuations, due to the excitation at the joint entrance. For core jet impact, the effect is of occasional character. For developed jet impact, the effect happens all the time. When comparing the root-mean-square values, the pressure peaks at the joint end are higher than the ones in the middle of the joint. It is interesting to notice the low root-mean-square values in case of submerged jet impact, both at the middle and at the end of the joint. These low values correspond more or less to the root-mean-square values valid that were found at the pool bottom. Hence, it becomes obvious that the presence of air bubbles in the liquid has a significant influence on the pressure pattern inside the joint.

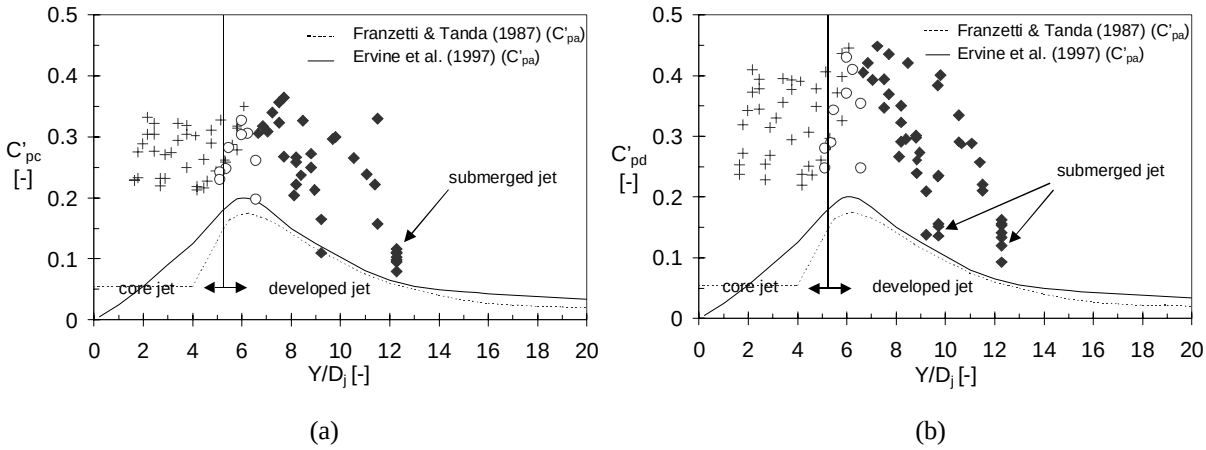

Fig. V-28 Non-dimensional fluctuating dynamic pressure coefficient C'_p as a function of the Y/D_j ratio: a) sensor (c) at the middle of the joint; b) sensor (d) at the end of the joint.

4.1.5. Extreme pressures

The positive (C^+_p) and negative (C^-_p) extreme pressure coefficients are presented in Fig. V-29. As could be expected, based on the pressure signals and the high root-mean-square values, the positive extremes inside the joint are much higher than the ones observed at the pool bottom. At the middle of the joint, coefficients of 2 to 3 are attained, while at the end of the joint, the values go even up to 4-5. In other words, throughout the whole rock joint length a significant amplification of the pool bottom pressures occurs. This amplification increases near the end of the joint. This, however, is not that surprising when assuming that the joint functions as a $\lambda/4$ – resonator. According to Fig. III-7, Chapter III, the harmonics of such a resonator system exhibit a sinusoidal mode shape. The fundamental frequency is characterised by a pressure node at the entrance of the joint and a pressure antinode at the closed-end boundary (see § 2.2.3, Chapter III). In between these boundaries, the pressure increases following a sinusoidal shape. The assumption of a $\lambda/4$ – resonator thus seems to be justified for the I-shaped joint. This assumption is used to determine the wave celerity c as a function of the fundamental resonance frequency. The negative pressure extremes in the middle of the joint are very similar to the ones at the pool bottom (Fig. V-29c). However, at the end of the joint, higher negative values are obtained (Fig. V-29d). This tendency of higher extremes at the end than at the middle of the joint is also in accordance with the sinusoidal mode shape. If the assumed transient system were linear, similar results would have been observed for negative respectively positive extremes. This is not the case. It is obvious that the system is of highly non-linear character. Moreover, it seems much easier to create peak pressures than to create high underpressures. This is characteristic for free air bubble presence, like for example in pipelines following a sudden pressure drop. The influence of free air on the pressure transient system is pointed out in § 4.1.9.

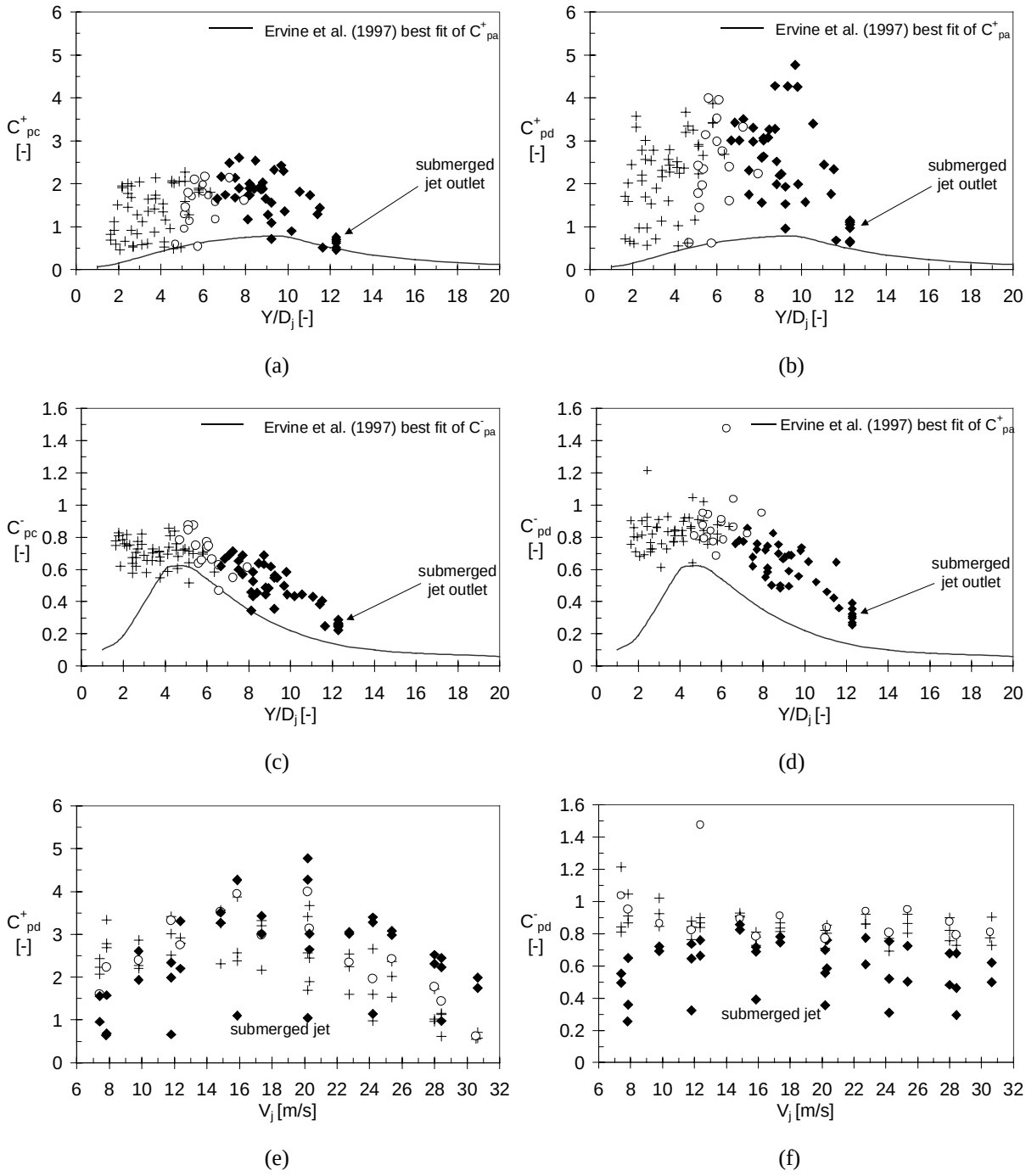

Fig. V-29 Non-dimensional extreme dynamic pressure coefficients:
a) C^{+}_{pc} at the middle of the joint; b) C^{+}_{pd} at the end of the joint;
c) C^{-}_{pc} at the middle of the joint; d) C^{-}_{pd} at the end of the joint;
e) C^{+}_{pd} as a function of V_j; d) C^{-}_{pd} as a function of V_j.

Furthermore, visualization of the positive extremes as a function of the jet velocity V_j (Fig. V-29e) reveals that the highest extremes are obtained around a velocity of 20 m/s. For higher velocities, the decrease is probably due to a corresponding decrease in pressure fluctuations at the pool bottom. Effectively, according to Fig. V-8, some significantly lower C'_{pa} values are observed at the highest velocities. At these velocities, and for certain water depths, the jet exhibits the same phenomenon as for the convergent outlet: it directly crosses the water cushion without generation of an appropriate shear layer.

4.1.6. Probability density function

The probability density function of the dynamic pressures measured at the end of the joint is presented for both core and developed jet impact in Fig. V-30. Similar to the probability density functions observed for pool bottom pressures, according to Fig. V-18, distinction has been made between low (< 15 m/s) and high (> 15 m/s) jet velocities. It is hardly possible to remark any substantial difference between the probability density functions inside the joint and the ones at the pool bottom. At low jet velocities, the pressure characteristics of core jet impact are quite similar to the ones of developed jet impact.

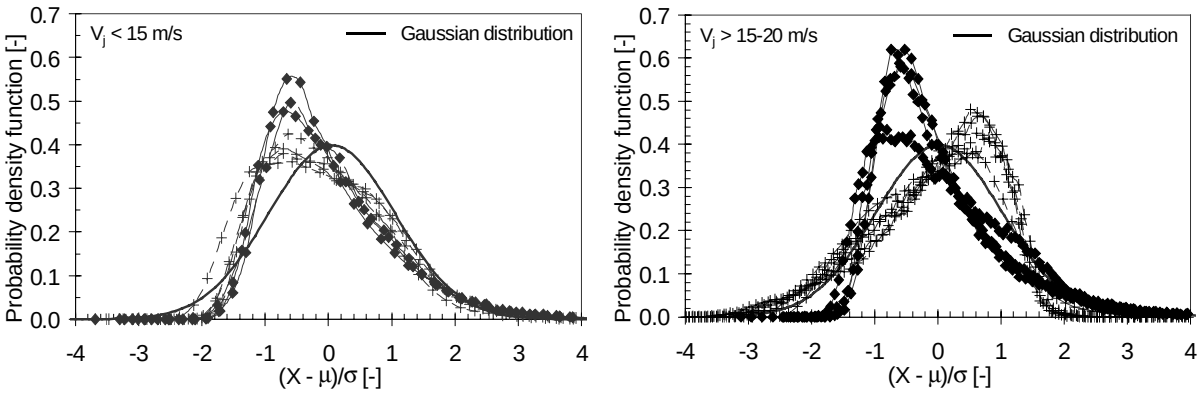

(a) (b)

Fig. V-30 Probability density function of dynamic pressures at the end of the joint, for both core and developed jet impact: a) for jet velocities V_j < 15 m/s; b) for jet velocities V_j ≥15 m/s. At low velocities, core jet impact exhibits similar characteristics as developed jet impact.

However, based on the already discussed statistical characteristics and the presented time signals, the pressures inside the joints are completely different from the ones at the pool bottom. Particularly the high peak pressures are not very visible in the probability density function. The reason is that peak pressures only happen during very short time intervals. Hence, the number of measured values that are extremely high is very small compared with the total number of values.

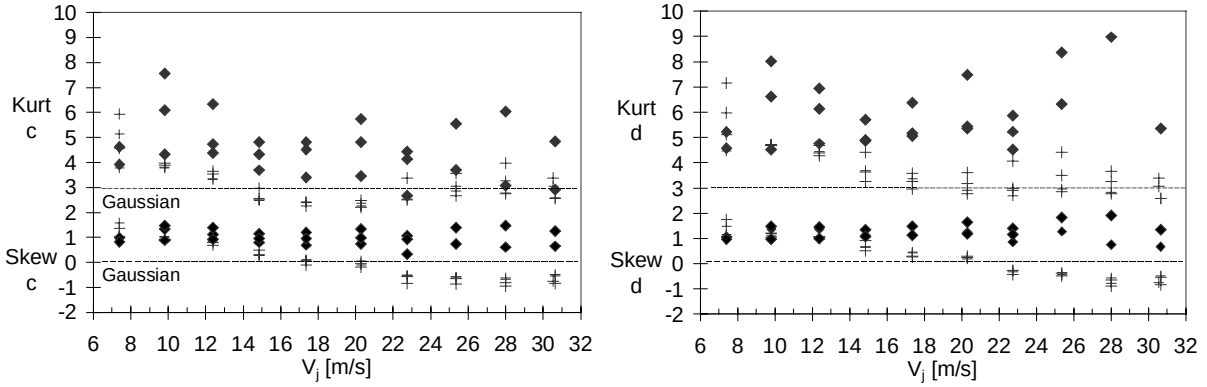

(a) (b)

Fig. V-31 Skewness and kurtosis as a function of the mean jet velocity V_j, for both core and developed jet impact: a) at the middle of the joint; b) at the end of the joint.

The statement that core jet and developed jet impact are in good agreement at low jet velocities is confirmed by analysing the skewness and kurtosis of the probability density functions. Especially at the end of the joint, it can be seen that the two types of jet impact generate similar skewness and kurtosis values. With increasing jet velocity, the values for core jet impact change towards Gaussian values.

4.1.7. Amplification factor Γ

The appearance of peak pressures inside the joint is generated by the jet excitation at the joint entrance, and is enhanced by the presence of free air inside the joint. The latter aspect will be discussed later on. The former can be analysed by means of an amplification factor Γ^+ or $\Gamma^{0.1}$. This factor is defined as the ratio of the positive extreme pressure coefficient C^+_{pd} at the joint end (or of the pressure coefficient with a 0.1 % probability $C^{0.1}_{pd}$ at the joint end) to the corresponding root-mean-square coefficient at the joint entrance C'_{pa}. The former coefficient expresses the absolute maximum value that has been measured, while the $C^{0.1}_{pd}$ coefficient stands for the pressure value in the joint that has, on the average, a 0.1 % probability of occurrence. This corresponds to peak pressures that occur from time to time. The 0.1 % probability of occurrence is a value that is often chosen for practical design criteria of dynamic pressure fluctuations (Lopardo et al., 1984).

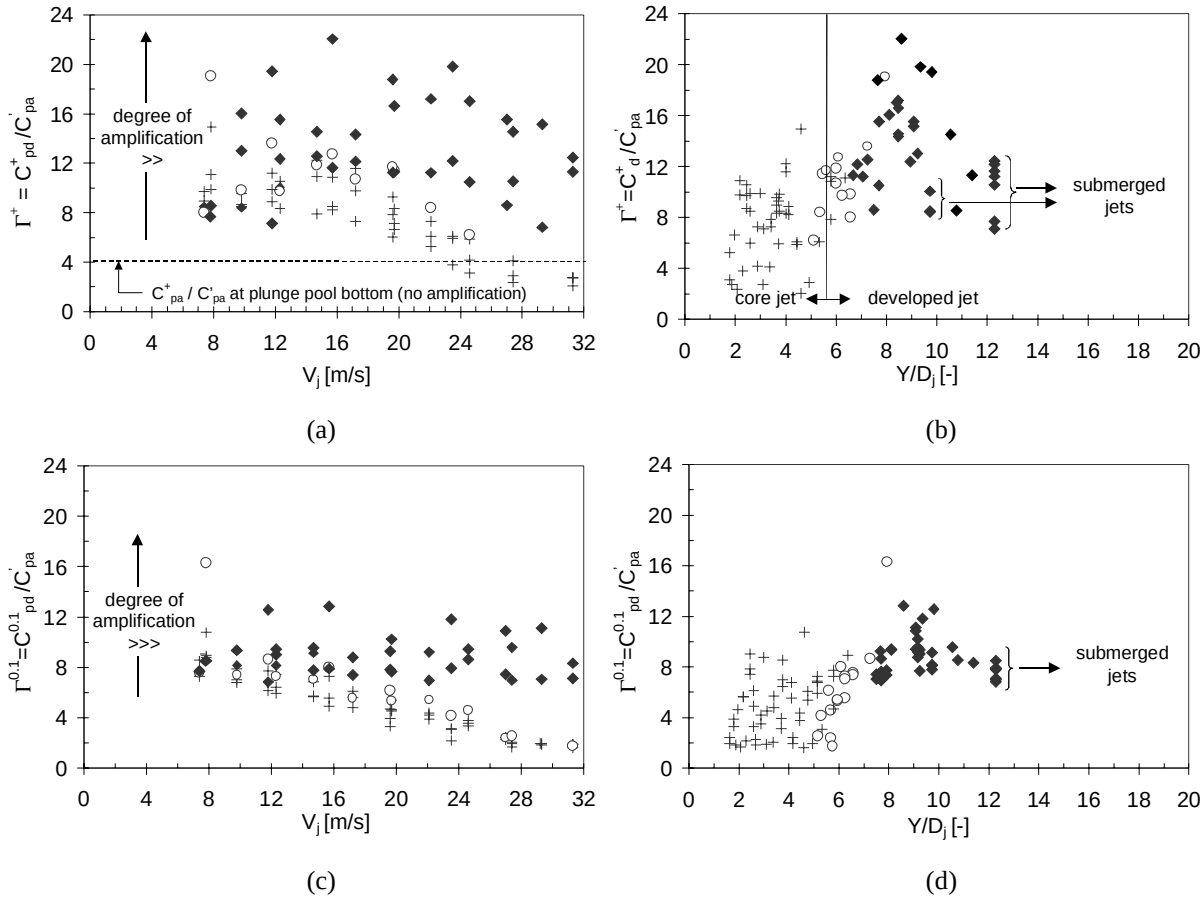

Fig. V-32 Amplification factors for dynamic pressures at the end of a joint:
a) Γ^+ as a function of jet velocity V_j; b) Γ^+ as a function of Y/D_j ratio;
c) $\Gamma^{0.1}$ as a function of jet velocity V_j; d) $\Gamma^{0.1}$ as a function of the Y/D_j ratio.

In other terms, the amplification factor Γ expresses to which extend the pressure fluctuations at the joint entrance are amplified at the joint end. As such, the factor is representative for the "resonance

sensibility" of the joint compared to the relevant jet excitation. It is clear that, for a given jet excitation and joint geometry, this sensibility can be greatly modified by the presence of free air.

For dynamic pressures impacting on a plunge pool bottom, the amplification factor is known from previous studies. Several studies pointed out the ratio between C^+ (or $C^{0.1\%}$) and C' at the bottom of a pool. May & Willoughby (1991) measured a $C^{0.1\%}$ value of roughly 4 times the C' value. Ervine et al. (1997) measured a C^+ value of roughly 3 to 4 times the root-mean-square value C'. For pool bottom pressures, the difference between C^+ and $C^{0.1\%}$ is not very significant, which explains these different results. As shown in Fig. V-33, however, inside rock joints the difference can be substantial.

Hence, an amplification factor of maximum 4 seems a plausible characteristic value for pool bottom pressures. Values higher than 4, such as encountered in Fig. V-32, indicate that the pool bottom pressures have been amplified inside the rock joint. For both the C^+ and $C^{0.1\%}$ coefficient, developed jets exhibit amplification factors that are much higher than 4. For core jets, high amplification factors are only encountered at low jet velocities. With increasing jet velocity, the amplification factor tends towards the characteristic pool bottom value of 4. The reason for this is that, at low velocities, core jets behave much like developed jets, i.e. they exhibit occasional spread due to low-frequency turbulence (diffused jet type). These effects become less significant at high jet velocities.

A striking different behaviour between core and developed jets is observed for $\Gamma^{0.1}$ in Fig. V-32c. Developed jets procure a factor from 6 to 12. Core jets start at 6, but progressively decrease down to about 2-3. The same difference is visible in Fig. V-30d, where the factor is presented as a function of the Y/D_j ratio. When changing from core jet to developed jet impact, $\Gamma^{0.1}$ factors less than 6 suddenly disappear. It can also be seen that submerged jets have lower amplification factors than impinging jets. This again proves the influence of free air bubbles on the flow characteristics inside the joints.

4.1.8. Spectral analysis

Fig. V-33 presents a comparison between the spectral content for pool bottom pressures and the corresponding spectral content inside the rock joint, as a function of frequency. This is done for pressure measurements at the middle (c) and at the end (d) of the joint, and for core and developed jet impact respectively. A significant amplitude and frequency modulation of the pool bottom spectral content is obtained inside the rock joint. This modulation is more expressed at the end of the joint than at the middle. A resonance frequency is easy to determine at low jet velocities (< 15 m/s). At higher jet velocities, the resonance frequency is not uniquely defined anymore and is more or less smeared out over a certain range of frequencies. This range of frequencies increases in width and extend with increasing jet velocity. It is typical for a highly non-linear resonating system.

Hence, at high jet velocities, a distinction has been made between the fundamental resonance frequency $f_{res}$of the transient system, and additional (higher) resonance frequencies. The latter are generated by the presence of high peak pressures of very short duration and are not representative for the time period T of the transient system. They are particularly visible for developed jet impact conditions.

The fundamental resonance frequency increases with increasing jet velocity. This means that the wave celerity increases and, thus, that the mean air content inside the joint decreases with velocity. However, for the highest velocity of 29.5 m/s, the fundamental resonance frequency shifts back towards lower values. This indicates a high air content inside the joint. This could be due to leakage of water out of the joint at high pressures or to the accumulation of an air cavity inside the joint. It is not clear at the time of writing which is the exact cause of this completely different behaviour.

The difficulty to determine the fundamental resonance frequency makes it hard to describe the spectral content in a Strouhal domain. The definition of a Strouhal number that is characteristic for the pressurized flow conditions inside the joint needs an appropriate length and velocity scale. The length scale can be chosen equal to the length of the joint. The velocity scale, however, has to include the wave celerity. This celerity depends on the pressure inside the joint and is not a constant.

However, according to Fig. V-26b, the fundamental resonance period is easier to distinguish in the time domain. The corresponding resonance frequency constitutes a sort of mean frequency, in the sense that it includes both short pressure peaks and longer pressure spikes. In other words, even if the pressure peaks and spikes make it very difficult to define the fundamental resonance frequency in the spectral content, because they cause a whole range of additional frequencies, a fundamental mode apparently subsists. As resonance conditions between two signals generally cause a 180° phase change between the incoming signal and the resulting signal, a **transfer function** between these signals should be able to detect the fundamental resonance frequency.

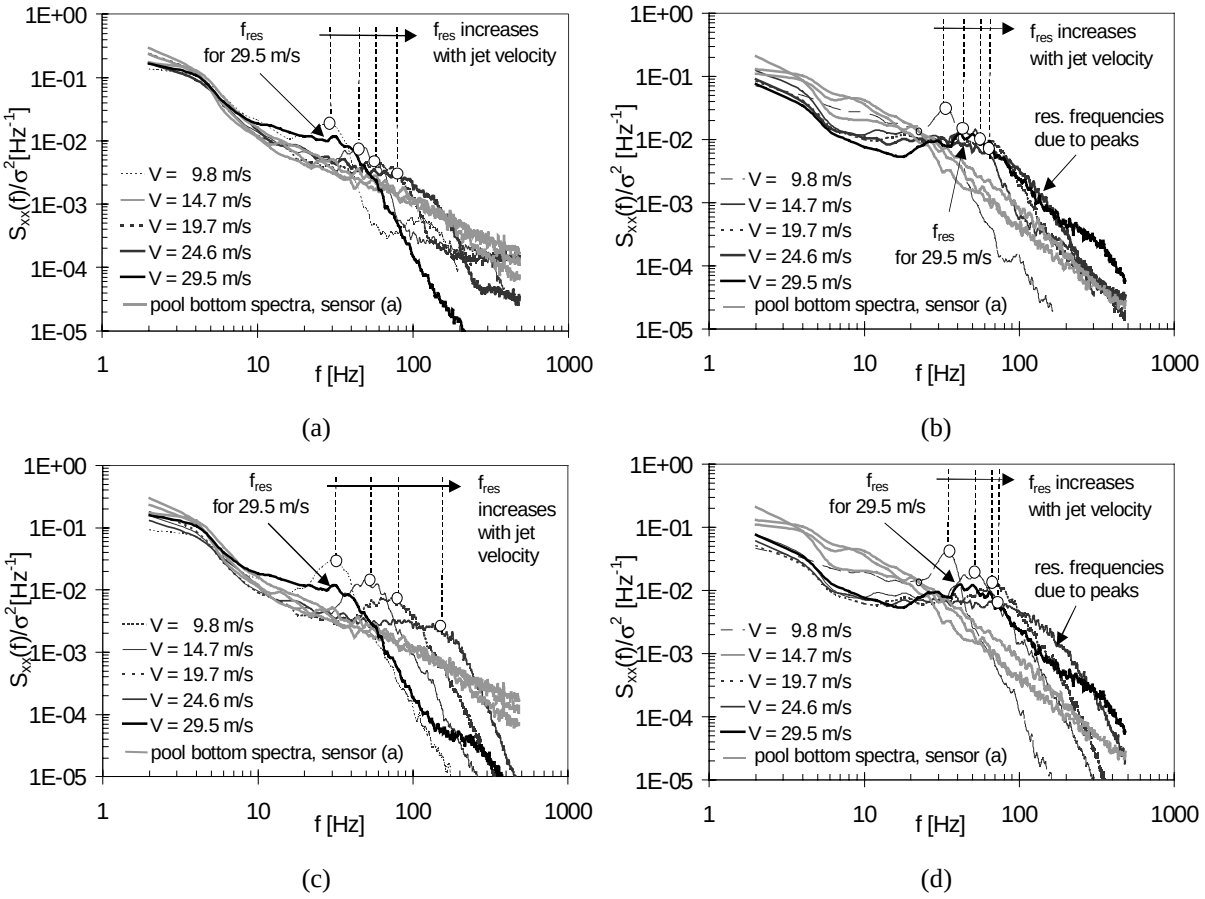

Fig. V-33 Non-dimensional spectral content of dynamic pressures at pool bottom and inside the I-joint:
a) at the middle of the joint for core jet; b) at the middle of the joint for developed jet;
c) at the end of the joint for core jet; d) at the end of the joint for developed jet.

Transfer functions distinguish between amplitude modulations and phase modulations of the response signal compared to the incoming signal. The former correspond to a decomposition of the amplification factor Γ as a function of frequency. The latter express the phase difference between the two pressure signals as a function of frequency. The phase differences between the pressures measured at the end of the joint and the ones at the pool bottom are presented in Fig. V-34, for both core and developed jet impact. When expressed as a function of frequency, it can be noticed that the curves for different velocities are of the same shape but shifted along the frequency axis.

At low jet velocities, it is possible to distinguish the fundamental resonance frequency, based on the time domain signal or on the spectral content. The resonance frequencies seem to occur at the point where the phase curve changes its slope from a negative to a positive value.

At higher jet velocities, the fundamental resonance frequency is hardly recognizable. However, the phase curves are of similar shape than the ones for low jet velocities. Hence, by similarity, these phase curves have been shifted along the frequency axis, such that they exhibit their resonance frequency at the same curve position as for low jet velocities. This defines the fundamental resonance frequency at high jet velocities. Assuming an ideal $\lambda/4$ – resonator model, the fundamental resonance frequency corresponds to a fundamental wave celerity that is written as $c_{mean} = 4 \cdot L \cdot f_{res}$. This defines a mean air content inside the joint and is presented in § 4.1.9.

The Strouhal number inside a rock joint $S_{h,j}$ can now be determined as follows:

$$S_{h,j} = \frac{f \cdot L_j}{c_{mean}} = \frac{f \cdot L_j}{4 \cdot L_j \cdot f_{res}} = \frac{f}{4 \cdot f_{res}} \tag{5.11}$$

For comprehension, it is more elegant to define the non-dimensional frequency as four times this Strouhal number, i.e. as f/f_{res}. The amplitude modulation of the transfer function can now be presented in a non-dimensional manner. This modulation is defined as the ratio of the amplitude of the resulting pressure signal (at the end of the joint) to the amplitude of the incoming pressure signal (at the entrance of the joint). This is shown on a logarithmic scale in Fig. V-35.

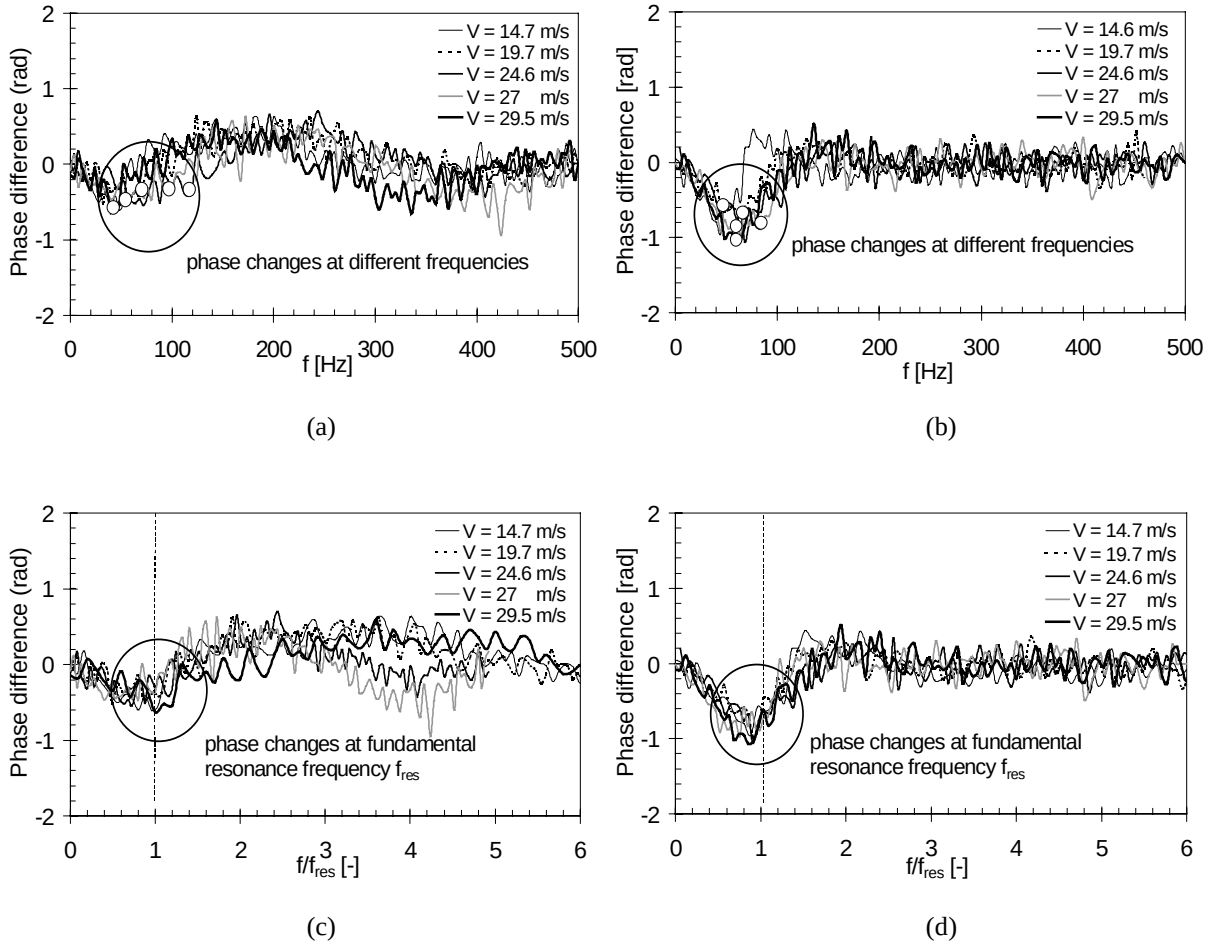

Fig. V-34 Phase modulation of the transfer function between the pressures measured at the end of the joint and the pressures at the pool bottom:
a) core jets as a function of f; b) developed jets as a function of frequency;
c) core jets as a function of a f/f_{res}; d) developed jets as a function of f/f_{res}.

At low jet velocities, core and developed jet impact exhibit almost identical amplifications. For jet velocities greater than 20 m/s, a major difference becomes apparent. Developed jets show a significant amplitude gain at frequencies that are considerably higher than the fundamental resonance frequency f_{res}. This gain at high frequencies is due to the peak pressures, which happen at very short time intervals. Such peak pressures do not occur for core jets. Thus, they do not appear in the transfer function. At a velocity of 29.5 m/s, however, the high frequency part, and thus also the peak pressures, disappear. Apparently, a high air content inside the joint takes out the peak pressures.

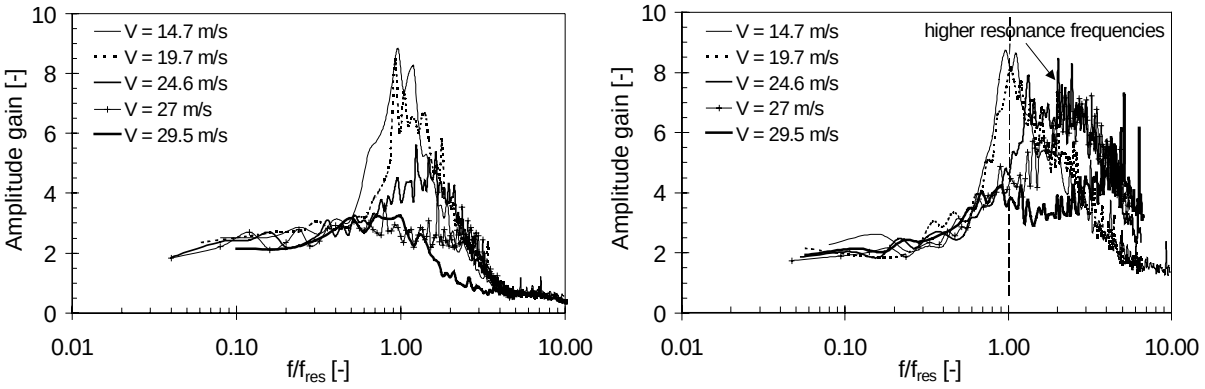

Fig. V-35 Amplitude modulation of the transfer function between the pressures at the end of the joint and the pressures at the pool bottom: a) core jets as a function of a non-dimensional resonance frequency; d) developed jets as a function of a non-dimensional resonance frequency. Scale is logarithmic.

The determination of the fundamental resonance frequency makes it possible to express the power spectral content in a non-dimensional domain. Fig. V-36 presents the comparison between the spectral content for pool bottom pressures and the corresponding spectral content inside the rock joint, as a function of this non-dimensional frequency. This is done for core and developed jet impact conditions.

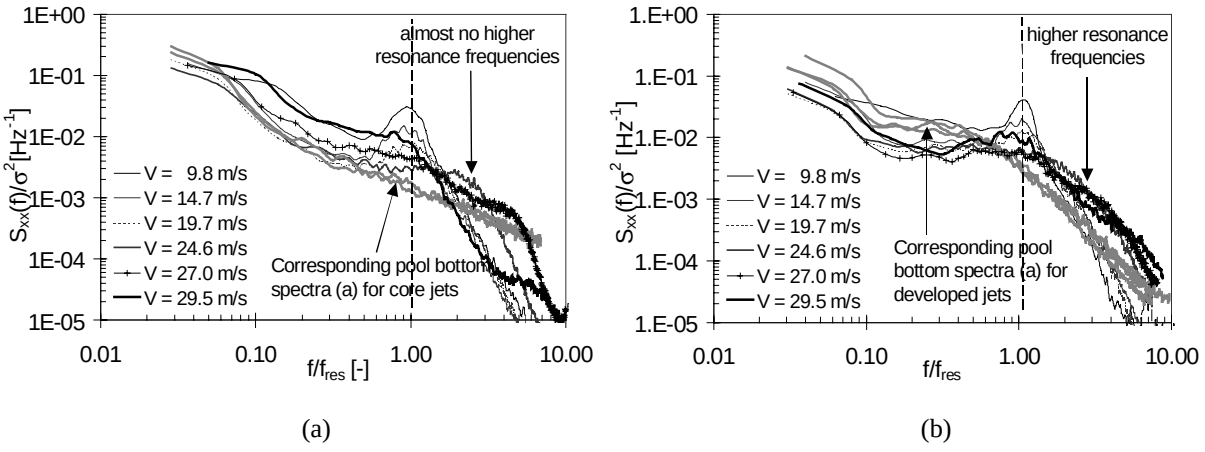

Fig. V-36 Non-dimensional power spectral density of dynamic pressures at pool bottom and at the end of the I-shaped rock joint, as a function of a non-dimensional resonance frequency f/f_{res}: a) for core jet impact; b) for developed jet impact.

4.1.9. Air content

The air content inside the joints cannot be measured in a direct manner. However, several indirect methods exist. Two methods have been applied in the present study. The first one is based on the determination of the fundamental resonance frequency f_{res} and on the assumption of an ideal $\lambda/4$ – resonator model. As outlined before, the latter defines the relation between the resonance frequency and the mean wave celerity as $c_{mean} = (1+2n)\cdot 4\cdot L\cdot f_{res}$, in which n = 0, 1, 2… For the fundamental resonance frequency, n equals zero. This method only allows to determine the **mean celerity** of the system and, thus, the mean air content.

The celerity of a pressure wave, however, is not a constant but depends on the absolute value of the governing pressure. This pressure is not a constant throughout the length of the joint and continuously changes as a function of time. Hence, only a space and time averaged, rough estimate of air content can be accounted for with this method. The mean celerities are presented in Fig. V-37 for core, developed and submerged jets. The results for convergent core jets correspond to direct jet impact onto the joint and, thus, generate so-called ideal core jets.

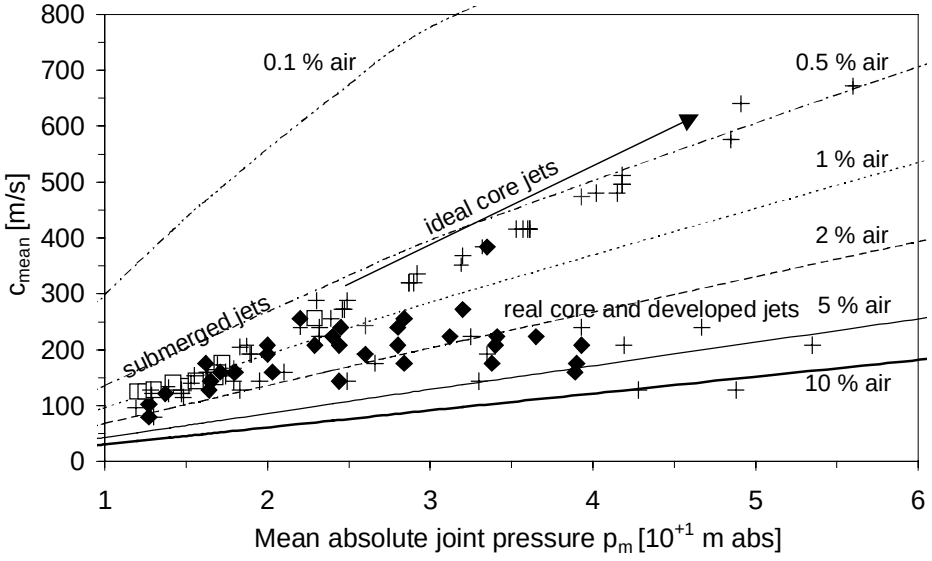

Fig. V-37 Mean wave celerity c_{mean} as a function of the mean pressure value p_m inside the joint. Results are for core (+ sign), developed (♦ sign) and submerged (□ sign) jet impact conditions, as well as for both cylindrical and convergent outlets. The indicated air volumes are at standard pressure.

Some surprising results can be noticed. First of all, the mean air content for non-ideal or real core jets and for developed jets exhibits significant scatter. There is a general tendency towards air contents that are much higher than the ones for ideal core or submerged jets. Air contents of up to 10 % have so been obtained. The data for developed jets perfectly match with the data for core jets and vice versa. This not only happens at low pressures and thus jet velocities, as could be expected based on the aforementioned statistical analysis, but also at high pressures and velocities.

At these high velocities, the mean air content inside the joint can fluctuate from 1 to 10 %, i.e. one order of magnitude. These huge differences in air content are due to the variety of flow conditions in the plunge pool: for developed jets, a turbulent shear layer containing a lot of free air bubbles impacts the joint entrance, while for core jets, air is only present during low-frequency turbulences that temporarily diffuse the jet and so entrain air into the joint.

Secondly, both submerged jets and ideal core jets generate a certain amount of free air inside the rock joints. The amount of free air changes considerably with the mean pressure. For such jets, the slope of

the "celerity-pressure" relationship is steeper than the one that corresponds to a constant quantity of free air in the liquid. The mean air content inside the joint is 1-2 % at low, almost atmospheric mean pressures, while at a mean pressure head of 50 m, the air content decreases down to 0.5 %.

This indicates that some air is inherently present in the liquid, and that this quantity is freely available inside the rock joint following jet impact. Two explanations seem plausible. The air could be present under the form of microbubbles (not visible to the eye) or could be released from the liquid during sudden pressure drops inside the joint. A thorough analysis of the change in air content as a function of the instantaneous pressure in the joint should give more insight.

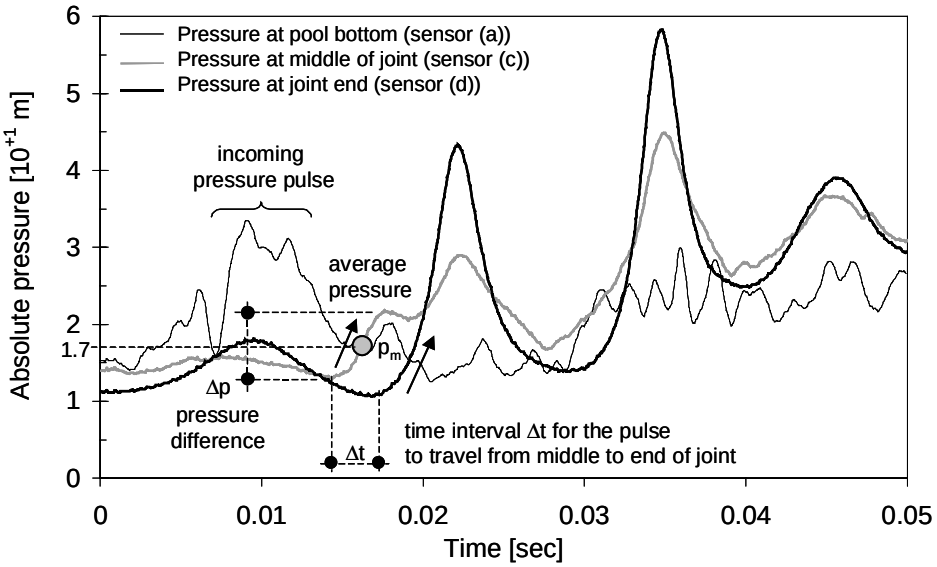

Fig. V-38 Determination of the instantaneous wave celerity c of a pressure pulse that enters the rock joint. The pool depth is 0.40 m and the jet velocity is 20 m/s. The time interval Δt between the pressure rise at the middle respectively at the end of the joint defines the propagation speed of the pressure pulse. The corresponding pressure values during this time interval define an average value p_m.

This is performed by a different method for the determination of the air content. This method is based on direct measurements of the propagation speed of the pressure waves that travel through the joint. These measurements are performed by tracking of distinct pressure pulses. Such pulses enter the rock joint and are measured successively at the middle (sensor (c)) and at the end (sensor (d)) of the joint. The distance Δl and the time difference Δt between these two points define the travel speed of the wave $c = \Delta l/\Delta t$. The pressure values during this time interval define an average value p_m.

These point-to-point correlations between different sensors can be mathematically expressed by cross-correlation functions, established over a certain time period. However, in the present application, the air content continuously changes with pressure. It was impossible to analyse the correlation functions in an appropriate manner. Hence, the only way to account for the pulse propagation speed was to **analyse separate pulses** in the time domain. The purpose is to follow a distinct pulse from the middle to the end of the joint and to estimate the time difference.

This procedure has been performed systematically for a series of test runs. For every test run, different pressure levels have been analysed. Each pressure level was checked several times on its corresponding propagation speed. It has to be noted that the degree of precision of this process increases with decreasing time step of pressure measurements, i.e. with increasing pressure acquisition rate. As the importance of free air bubbles was not evident at the beginning of the test runs, most of them have been established at an acquisition rate of only 1'000 Hz. It revealed that, at high pressures,

this rate was not sufficient to accurately predict the celerity-pressure relationship. This is because the celerity at high pressures is too high compared to this rate. Fortunately, some test runs were performed at rates of 5'000 to 20'000 Hz. These runs yielded sufficiently accurate results, even at high pressures.

An example of the followed procedure is presented in Fig. V-38. The pool depth is 0.40 m and the jet velocity is 20 m/s. As can be seen, a significant pressure pulse enters the rock joint. This is followed by a pressure rise at the middle of the joint and finally at the end of the joint. The time difference Δt between the start of the pressure rise at the middle and at the end can easily be estimated within a precision of +/- 0.00005 sec. During this time, the pressure at the middle of the joint progressively increases. By defining the pressure values at the beginning and at the end of the time interval, an average pressure value p_m can be defined. This pressure value is considered as characteristic for the pressure pulse that has travelled from one sensor to the other. It can be defined within +/- 0.5 m of pressure head. Hence, the travel speed of the pulse is determined as follows:

$$c_{pulse} = \frac{\Delta(\text{sensor(c)} - \text{sensor(d)})}{\Delta t} = \frac{0.375\text{m}}{\Delta t} \tag{5.12}$$

For the present example, the time interval Δt is estimated at 0.0025 seconds. This results in a pressure pulse propagation speed of 150 m/s. The corresponding average pulse pressure p_m equals 17 m of absolute pressure head. The obtained precision for the calculated celerity is +/- 6 m/s. This process has been repeated at different pressure levels. It has to be mentioned that a similar procedure between the entry and the middle of the rock joint is not possible because the pressure pulse that enters the joint has been measured by the sensor at the pool bottom. Hence, this sensor is located at a radial distance of 25 mm from the joint entrance. The time necessary for the pulse to travel towards the joint entrance depends on macroturbulent flow conditions and can hardly be estimated accurately.

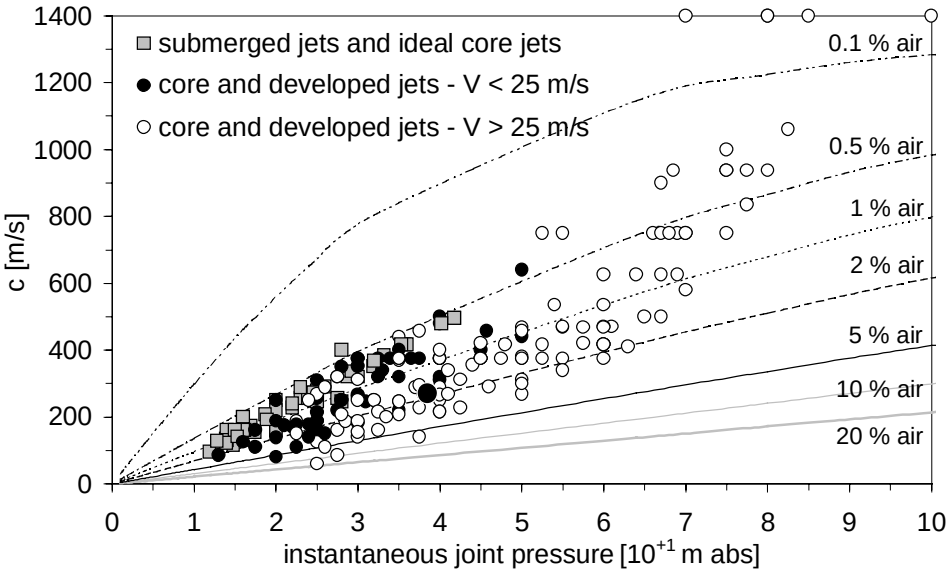

Fig. V-39 Determination of the instantaneous wave celerity c (m/s) as a function of the instantaneous pressure value p(t) inside the joint. The pressures are absolute and in 10^{+1} m of head). Results are for submerged and ideal core jets (obtained for convergent outlet), and for core or developed jets at low and high jet velocities respectively.

A summary of results is given in Fig. V-39 for core, developed and submerged jets, as a function of the instantaneous pressure inside the joint. This instantaneous pressure corresponds to the p_m value as defined in Fig. V-38. For submerged jets, the obtained relationship is very close to the one derived in Fig. V-37. For core and developed jets, some of the data points lie on this curve, other points tend towards a higher air content.

The air content increases with increasing jet velocity. Hence, just like for the mean air content, the instantaneous air content as a function of pressure is largely fluctuating. Furthermore, the quantity of free air available in the joint is clearly not a constant value. The obtained slopes of the celerity-pressure relationships are all significantly steeper than the ones for a constant mass of free air. This again implies that a certain amount of air is being generated during pressure drops.

It is believed that the present body of experimental evidence points towards air release and resolution as the phenomena that are responsible for the change in free air content. This could at the same time explain the presence of free air under submerged jet impact conditions. As has been pointed out in Chapter III, § 3.3.3, Henry's law states that a sudden pressure drop in a liquid generates air release. The inverse effect occurs in case of a sudden pressure rise. These phenomena not only modify the air volume at standard conditions but also the quantity of free air inside the joint. Therefore, they cause the measured data points in Fig. V-39 to jump from one curve of constant air volume (at standard conditions) to another.

The most surprising aspect, however, lies in the instantaneous character of the phenomena. The normal incubation period for air to be released from water is on the order of several seconds (Schweitzer & Szehebely, 1950). Following the present data, the release and resolution seem to happen quasi instantaneously. These phenomena depend on a lot of parameters, such as the degree of agitation of the liquid, the particular boundary conditions, the degree of supersaturation and the size or the location of the nuclei in the liquid. Hence, it could be reasonable argued that these results are physically relevant. To the author's knowledge, no measurements of changing air content have ever been made inside extremely bounded and turbulent media, such as rock joints under jet impact.

The statement that Henry's law is responsible for the changing air content inside the joint has been verified. For this purpose, a series of curves has been defined for which the air content changes following Henry's law. As outlined in Chapter III, § 3.3.3, a first and simplified relationship can be obtained by expressing the change in quantity of free air as a solubility constant times a relative pressure drop (equation (3.60), Chapter III). The relative pressure drop is expressed as a deviation from a certain equilibrium pressure. This pressure should be the one at which the air bubbles entered the joint. However, as only the relative pressure difference is relevant, the standard atmospheric pressure is chosen here as reference pressure. This equilibrium pressure is than related to a certain air content. As the atmospheric pressure constitutes the lowest possible pressure value inside the joint, all other pressures will exhibit less air. The rate of change in free air content with pressure is determined by the solubility constant S. No time effects are considered. This means that air release and re-solution is considered as instantaneous. Three Henry curves are compared with the core jet data in Fig. V-39. The results are shown in Fig. V-40 and at Table V-2. Although the Henry curves are more curved than the data, a quite satisfying agreement between data and curves can be observed.

Type of core impact	Jet velocity	Solubility constant S	Air conc. at 1 atm
Ideal (convergent jet)	5-35 m/s	0.009	1 %
Real (cylindrical jet)	20-25 m/s	0.012	2 %
Real (cylindrical jet)	25-35 m/s	0.020	5 %

Table V-2 Parameters of Henry-curves for different types of core jet impact. For real core jets, influenced by free air from outside the core of the jet, only the curve at maximum air content has been defined.

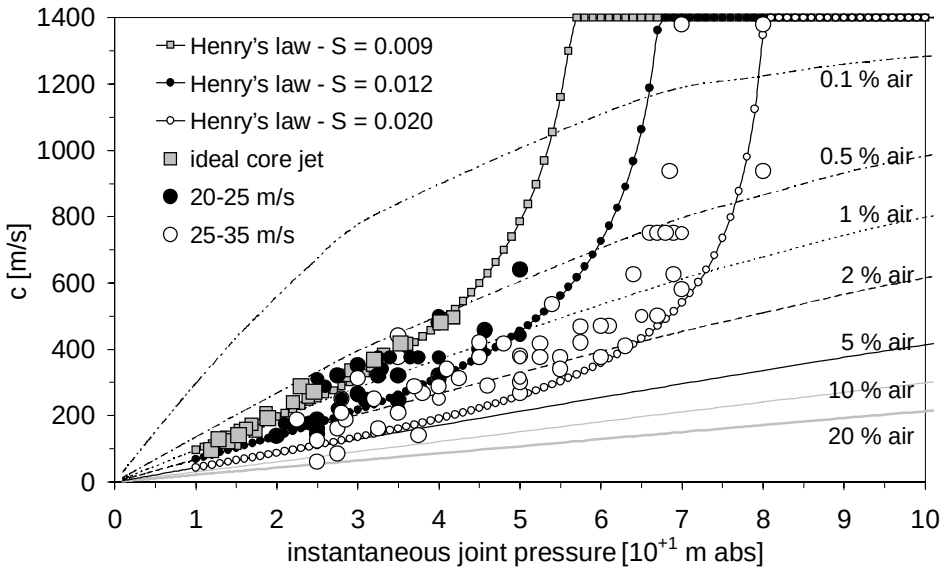

Fig. V-40 Instantaneous wave celerity c (m/s) as a function of the instantaneous joint pressure, for core jet impact conditions. The results are presented for three different core jets: ideal core impact (by convergent outlet), real core impact for a jet velocity of 20-25 m/s and finally real core impact for a jet velocity of 25-35 m/s. For each impact case, comparison is made with an appropriate Henry curve. S stands for the solubility constant as defined in Chapter III, § 3.3.3.

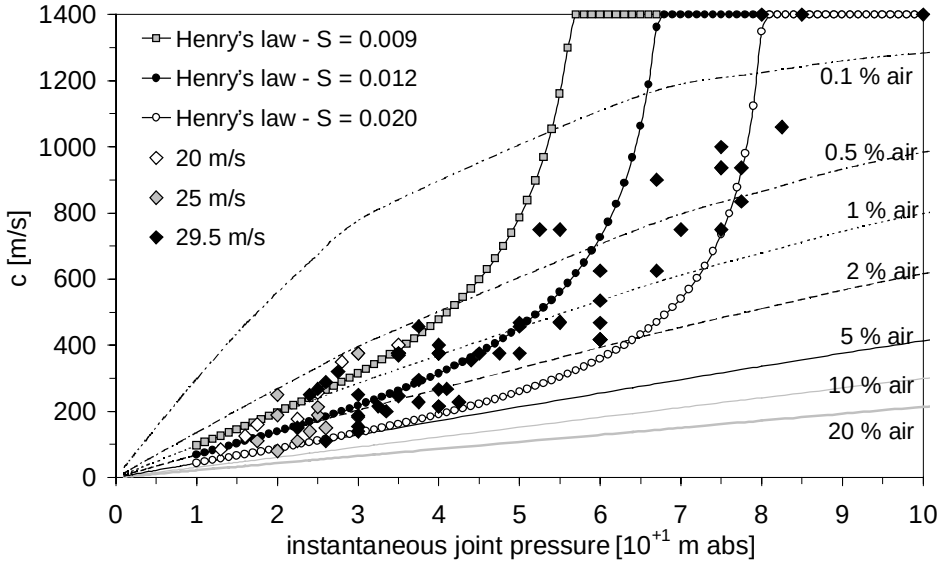

Fig. V-41 Instantaneous wave celerity c (m/s) as a function of the instantaneous joint pressure for developed jet impact conditions. The results are presented for three different jet velocities. Comparison is made with the Henry curves obtained for core jet impact.

The two different types of core jet impact are present: ideal core jet impact (obtained by convergent-shaped jet outlet) and real core jet impact (obtained by cylindrical jet outlet). The latter type is subdivided into jet velocities between 20 and 25 m/s and jet velocities between 25 and 35 m/s. Without any influence of free air that is present outside of the core of the jet, a solubility constant of

0.009 and a starting air concentration of 1 % are appropriate. For real core jets, exhibiting low-frequency core turbulence and thus free air presence from outside the core, the data points are quite dispersed. Apparently, even if a general tendency can be outlined, it is hardly possible to attribute one single curve to the test results. Therefore, only the curve for maximum air content has been determined. It is believed that the lower limiting curve is defined by the ideal core jet case. For real jets, it is obvious that the solubility constant S depends on the velocity of the jet at impact in the pool and is substantially higher than for ideal core jets. Moreover, the starting air contents are much higher and go up to 5 % and even higher. The significant influence of the jet velocity on the free air content is evident when considering that the air concentration in the plunge pool linearly increases with jet velocity (Chapter III, § 3.2.3, Fig. III-16).

The way in which the air of the pool is transferred towards the joint is hard to determine. As summarized in Chapter III, § 3.3, one possibility is a simple convective transfer (Fig. V-42). The zone of high stagnation pressure close to the water-rock interface induces a pressure increase at the pool bottom that results in a bubble volume decrease following the ideal gas law. After a drop in pressure once inside the joint, the bubble volume re-expands. Thus, the higher the pressure pulse that enters the joint, the higher can be the free air content inside. This mechanism of transfer, however, does not provide a meaningful explanation for the free air bubble presence in case of submerged and ideal core jets. A second hypothesis relies on air bubble release by the presence of the same zone of high stagnation pressure close to the joint entrance. The higher this pressure field, the more air can dissolve and thus also be released following a subsequent pressure drop inside the joint.

Knowledge of the exact transfer mechanism is perhaps not that important when stating that, regardless of the mechanism, the quantity of free air that can be transferred from the pool into the joint is directly proportional to the mean pressure at the joint entrance and thus the mean pressure inside the joint.

Furthermore, the results presented in Fig. V-40 indicate that real core jets, as encountered on the present facility, in fact behave like developed jets. They show an aeration rate inside the joint that increases with jet velocity. This is in contradiction with the previously established finding, which states that core jets only behave like developed jets at low jet velocities (< 20 m/s). This does not mean that the present analysis is wrong. The here presented air contents are only measured during single pressure pulses. For core jets at high jet velocities, these pressure pulses are extremely rare or even totally absent and, thus, are not at all representative for the whole test period.

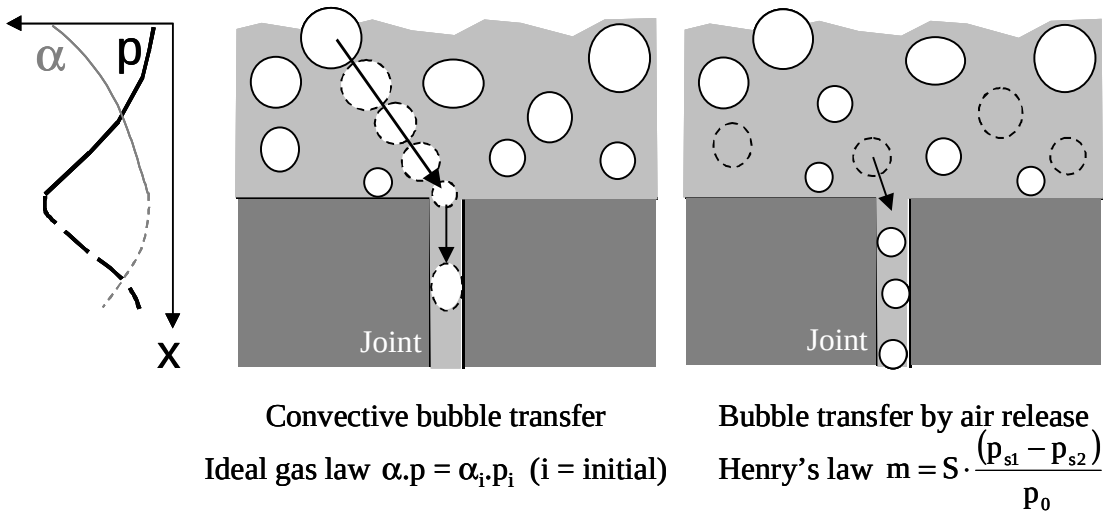

Fig. V-42 Two possible mechanisms of air bubble transfer from the plunge pool bottom into the underlying rock joint.

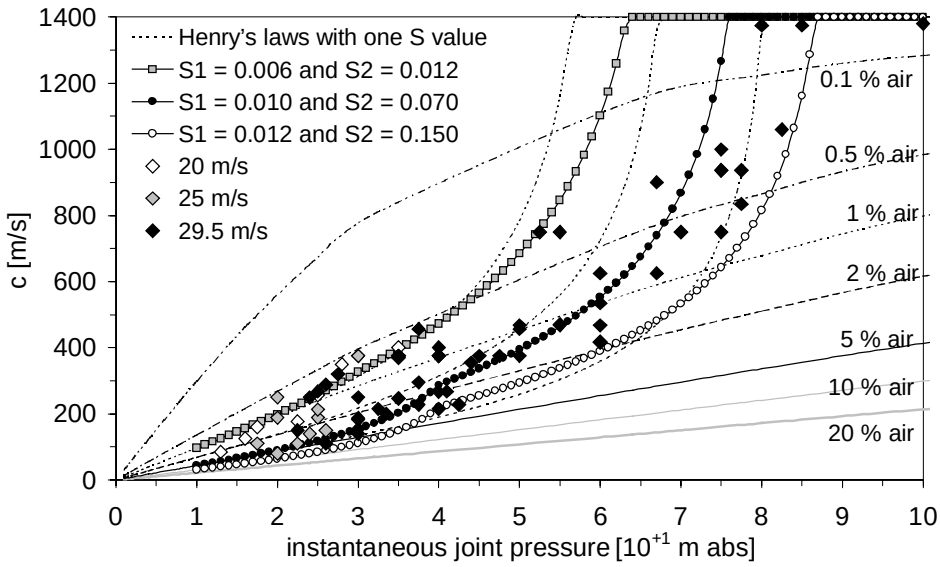

Fig. V-43 Instantaneous wave celerity c (m/s) as a function of the instantaneous joint pressure for developed jet impact conditions and two solubility constants. Comparison is made with the Henry curves with only one solubility constant.

A similar procedure has been followed for developed jets. The obtained curves are presented in Fig. V-41. Similar to core jets, the amount of air inside the joint seems to increase with the jet velocity. Furthermore, it is not clear which curve is most appropriate at high velocities. Part of the data correspond to the ideal core jet curve, part correspond to much higher air contents. A slightly different behaviour can be observed at the upper part of the pressure range. There, the changes in air content are less drastic than for core jets.

A meaningful explanation could be found in the initial assumption that time does not influence the release of air bubbles. This is a simplification of reality. Peak pressures occur during very short time intervals, much shorter than pressure spikes. It is evident that the total time period of a pressure drop from a peak pressure down to a pressure spike has an effect on the quantity of air that can be released. In fact, the air release is an exponential function of time. This means that, the lower the pressure, the more air is being released. In other words, the solubility constant S depends on the drop in pressure and continuously changes during the release process. This has been visualized in Fig. V-43 by introducing two different solubility constants. The first one is valid for pressures less than the mean pressure of the joint. The second one is only valid during peak pressures and thus is smaller than the first one. The two values can be one order of magnitude different. In reality, the solubility constant continuously changes with pressure and should be related to an exponential time function.

Moreover, it has been generally accepted that air release happens much easier and much faster than air resolution. Often a one-way process is assumed. This means that, after a certain period of time, an equilibrium celerity-pressure relationship should install inside the joint. This curve should have released all the air that was in dissolution in the liquid that originally entered the joint. It just effectuates cycles of resolution and release that are governed by the quantity of air that can be dissolved during a pressure rise.

This, however, is only true under the assumption of a constant air content in the plunge pool and, thus, again signifies a simplification of reality. Each of the pressure pulses that enter the joint can have a different air content. In other words, every rock joint exhibits a series of Henry curves. These curves are dictated by the free air content in the pool, which also continuously changes. The challenge is to find a Henry-curve that is representative for the transient peak pressures measured inside the joint.

4.2. The I-shaped rock joint under the impact of a convergent jet

4.2.1. Measured pressure signal

Fig. V-44 presents the measured pressure signal in the time domain, for core and developed jet impact. The signal measured at the pool bottom corresponds to the one presented in Fig. V-13. The left hand side corresponds to core jet impact and shows high-frequency reaction inside the joint on pressure fluctuations at the entrance. The right hand side stands for developed jet impact and is similar to the signal obtained for cylindrical developed jets.

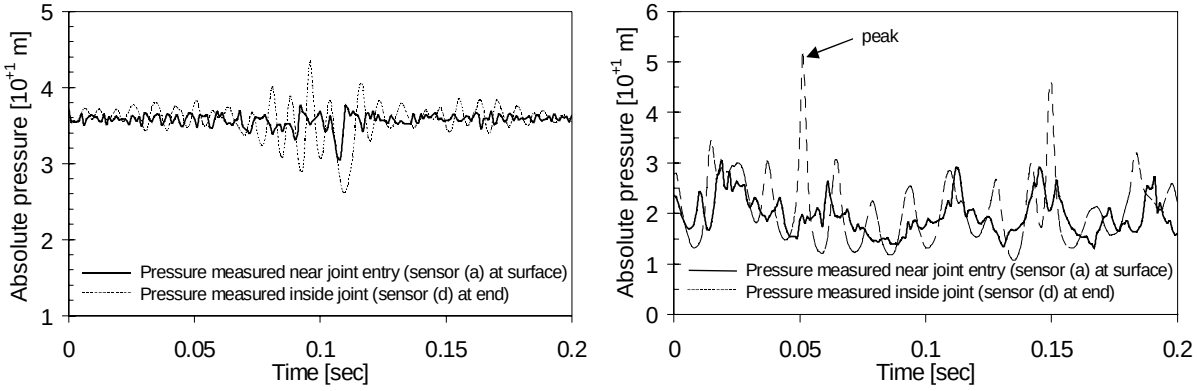

Fig. V-44 Pressure signal in the time domain, measured at the plunge pool bottom and at the end of an I-shaped rock joint: a) core jet impact; b) developed jet impact. For a convergent jet outlet and a 72 mm jet diameter.

4.2.2. Mean dynamic pressure value

According to the corresponding pool bottom values (Fig. V-14), part of the obtained coefficients are higher than the ones for the cylindrical outlet. This is logic given the ideal character of the impinging jet (almost no low-frequency turbulence effects of the core of the jet).

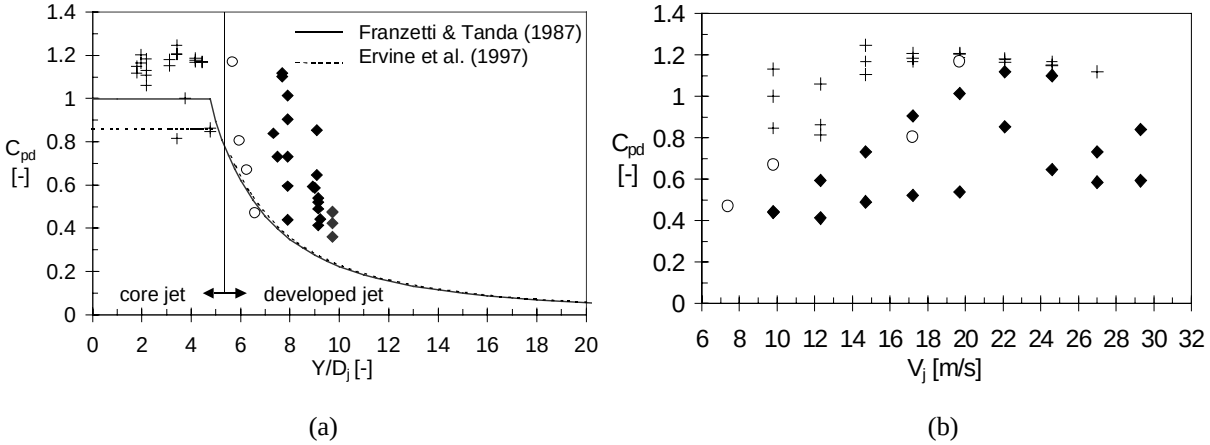

Fig. V-45 Non-dimensional mean dynamic pressure coefficient C_{pd}: a) as a function of the geometrical ratio of plunge pool depth Y to jet diameter D_j; b) as a function of the mean jet outlet velocity V_j. Results are presented for a 72 mm diameter convergent jet outlet.

4.2.3. Root-mean-square pressures

The values obtained for ideal core jet impact (direct jet impact) are equal to the corresponding values that were measured at the pool bottom. The values for developed jets are significantly higher than the ones observed at the pool bottom. This indicates that for ideal core jets, no reaction occurs inside the joint, while for developed jets an alternation of peak pressures and pressure spikes is happening.

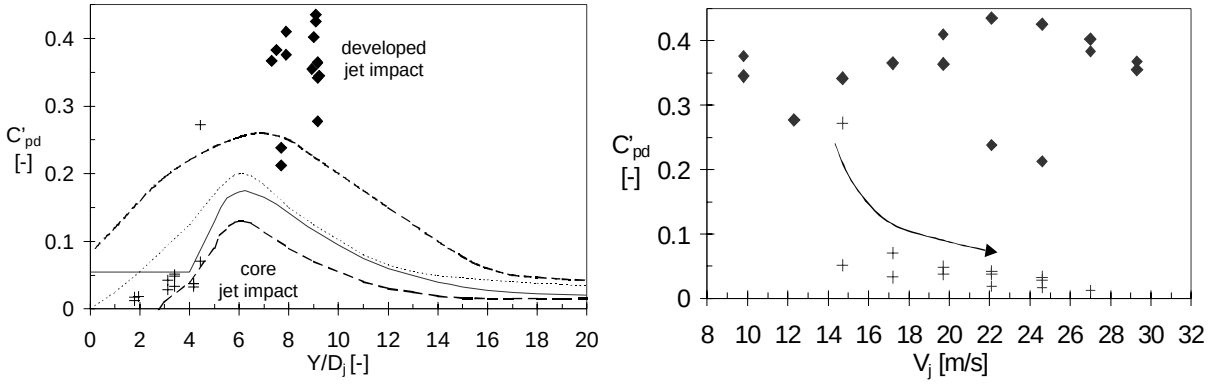

(a) (b)

Fig. V-46 Non-dimensional fluctuating dynamic pressure coefficient C'_{pd}: a) as a function of Y/D_j. Ideal core impact conditions are visible at small Y/D_j ratios; b) as a function of the mean jet outlet velocity V_j. Results are presented for a 72 mm diameter convergent jet outlet.

4.2.4. Extreme pressures

Similar to the cylindrical jet outlet, very high positive extremes are obtained. This indicates a significant amplification inside the joint of the pressures at the pool bottom. The values that correspond to ideal core jet impact, however, exhibit extremes that are equal to the ones measured at the pool bottom. For this type of impact, no amplification occurs inside the joint. The negative extremes are a little bit higher than the ones observed for cylindrical jet outlets. A reason for this could be the higher mean pressure values that were observed for convergent outlets.

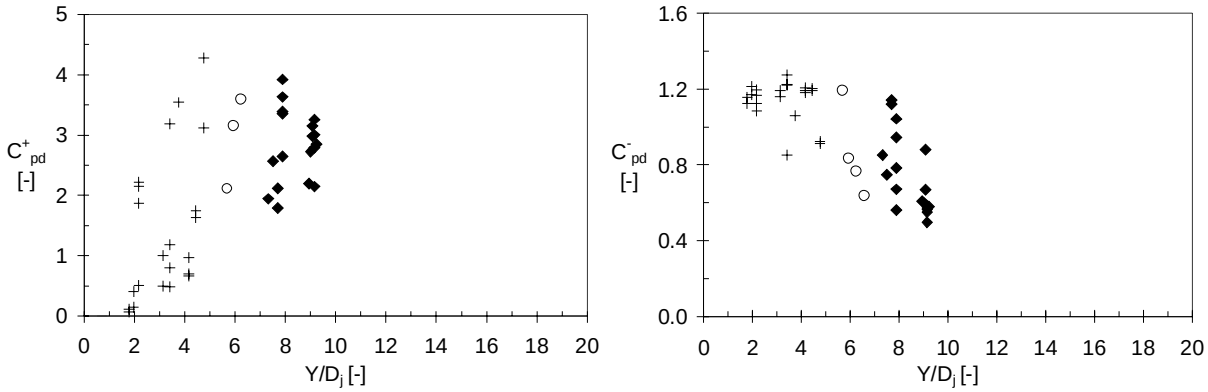

(a) (b)

Fig. V-47 a) Non-dimensional fluctuating positive extreme dynamic pressure coefficient C^+_{pd} in the time domain as a function of the ratio Y/D_j; b) Non-dimensional fluctuating negative extreme dynamic pressure coefficient C^-_{pd} in the time domain as a function of the ratio Y/D_j. Results are presented for a 72 mm diameter convergent jet outlet.

4.2.5. Amplification factor Γ

The amplification factors Γ^{+} and $\Gamma^{0.1}$ are presented in Fig. V-48. The former factor is somewhat lower than the values measured under cylindrical jet impact, especially for developed jets. This is because these jets partially or totally traversed the water cushion of the pool during the test runs. This effect causes a significant decrease of the theoretically calculated Y/D_j ratio. Hence, for developed jet impact, amplification factors typical for core jets were obtained. A second reason is the absence of low-frequency turbulences in case of convergent jets. This stabilizing effect apparently influences the maximum possible pressures.

The high amplification factors that are observed for some core jets are due to the very low C'_{pa} value they exhibit. The maximum pressures inside the joints correspond to a sudden and local low-frequency turbulence of the core of the jet. This temporary effect is not reflected in the average value of the root-mean-square coefficient. In fact, a time-local root-mean-square coefficient should be used rather than the time-averaged value. The extreme pressures with a 0.1 % probability of occurrence are also affected by the latter phenomenon. Values obtained for developed jets are in good agreement with previously observed values for cylindrical jets. Some values for core jets, however, are much too high.

This different behavior between convergent and cylindrical jet outlets indicates that, for convergent jet outlets, it is not always evident to obtain an appropriate turbulent shear layer through the water cushion of the plunge pool. This is due to the scale discrepancy between the prototype jet velocities and the geometrically scaled water depth. Hence, the amplification factors obtained for cylindrical jet outlets are more appropriate for engineering practice.

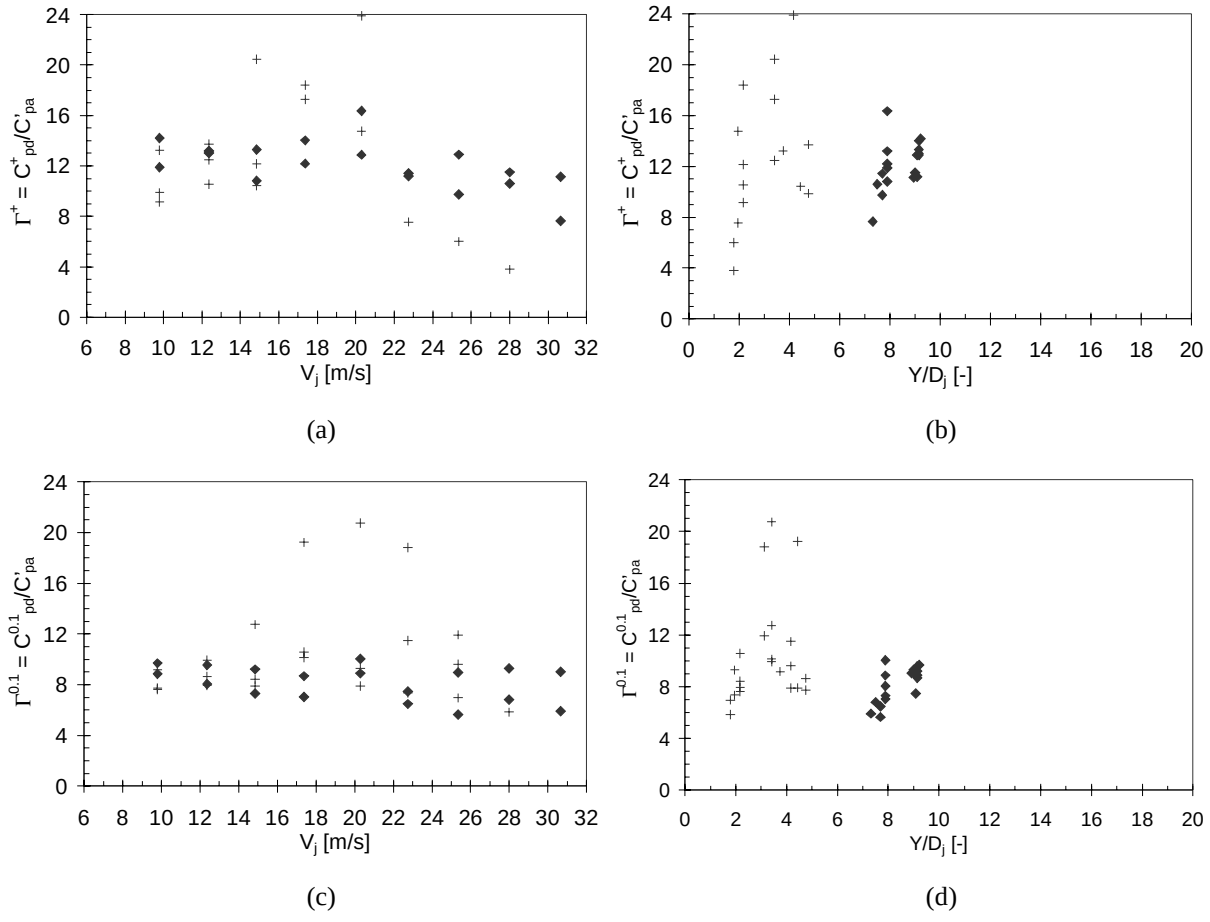

Fig. V-48 Amplification factors for dynamic pressures at the end of a joint:
a) Γ^{+} as a function of jet velocity V_j; b) Γ^{+} as a function of Y/D_j;
c) $\Gamma^{0.1}$ as a function of jet velocity V_j; d) $\Gamma^{0.1}$ as a function of Y/D_j.

4.2.6. Spectral analysis and transfer functions

The power spectral content of the pool bottom pressures is compared with the power spectral content of the corresponding pressures measured at the end of the joint. According to the cylindrical jet case, a significant amplitude and frequency modulation is observed inside the joint. This modulation is much more expressed here. Even at high jet velocities, a resonance frequency can be defined, which was hardly the case for a cylindrical jet.

This is particularly true for core jets and is due to a lower air content inside the joint. Without the presence of free air, no major changes in celerity and, thus, resonance frequency occur. It is much like if the transient system behaves more linearly.

For developed jets, the spectral curve that corresponds to a high mean jet velocity of 29.5 m/s shows a significant shift of the resonance frequency towards lower values. This effect was already observed for cylindrical jet outlets and is surprising because, based on the results for other jet velocities, a higher frequency should be expected. This shift indicates that the mean air content inside the joint is considerably higher than for the other velocities.

As already outlined for cylindrical jets, one possible explanation is leakage of water out of the joint. It is not excluded that, at very high pressures inside the joint, some of the water is able to find its way through the steel plates towards the outside.

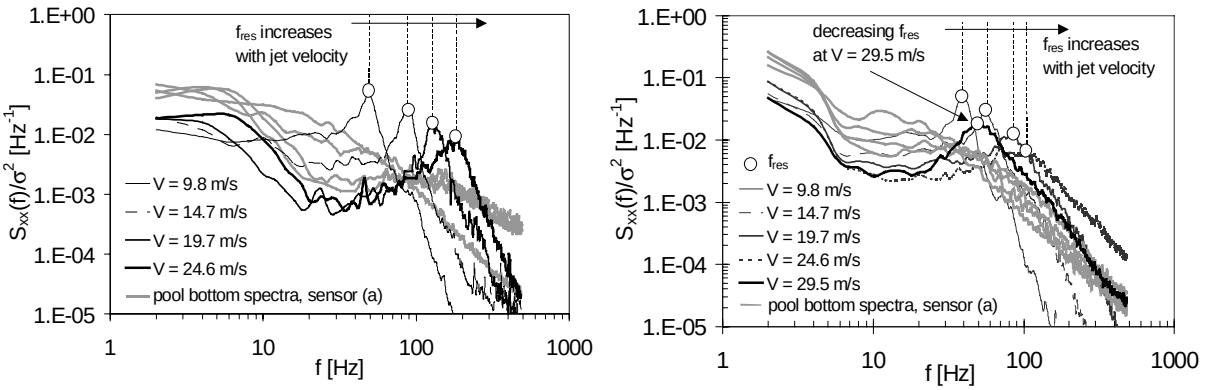

Fig. V-49 Non-dimensional power spectral density of dynamic pressures at the pool bottom and at the end of the I-shaped rock joint: a) for core jet impact; b) for developed jet impact.

The transfer functions between the pressures inside the joint and the pool bottom pressures are presented in Fig. V-50. Both the amplitude gain and the phase difference express the fundamental resonance frequency in a clear manner. This is logic because of the small free air content inside the joint. As a consequence, the amplification of the pool bottom pressures is stronger than for the cylindrical jet outlet but only happens in a narrow bandwidth of frequencies. Amplitude gains of more than one order of magnitude are observed.

For developed jets, the amplitude gain at frequencies that are higher than the fundamental resonance frequency are only visible at jet velocities of 20-25 m/s. Lower jet velocities generate peak pressures that are in the same frequency range than the fundamental resonance frequency. The highest jet velocity of 29.5 m/s has an amplitude gain and a resonating frequency that are very comparable to the ones for jet velocities less than 20 m/s. This again indicates a high air content inside the joint for this case, resulting in the disappearance of peak pressures.

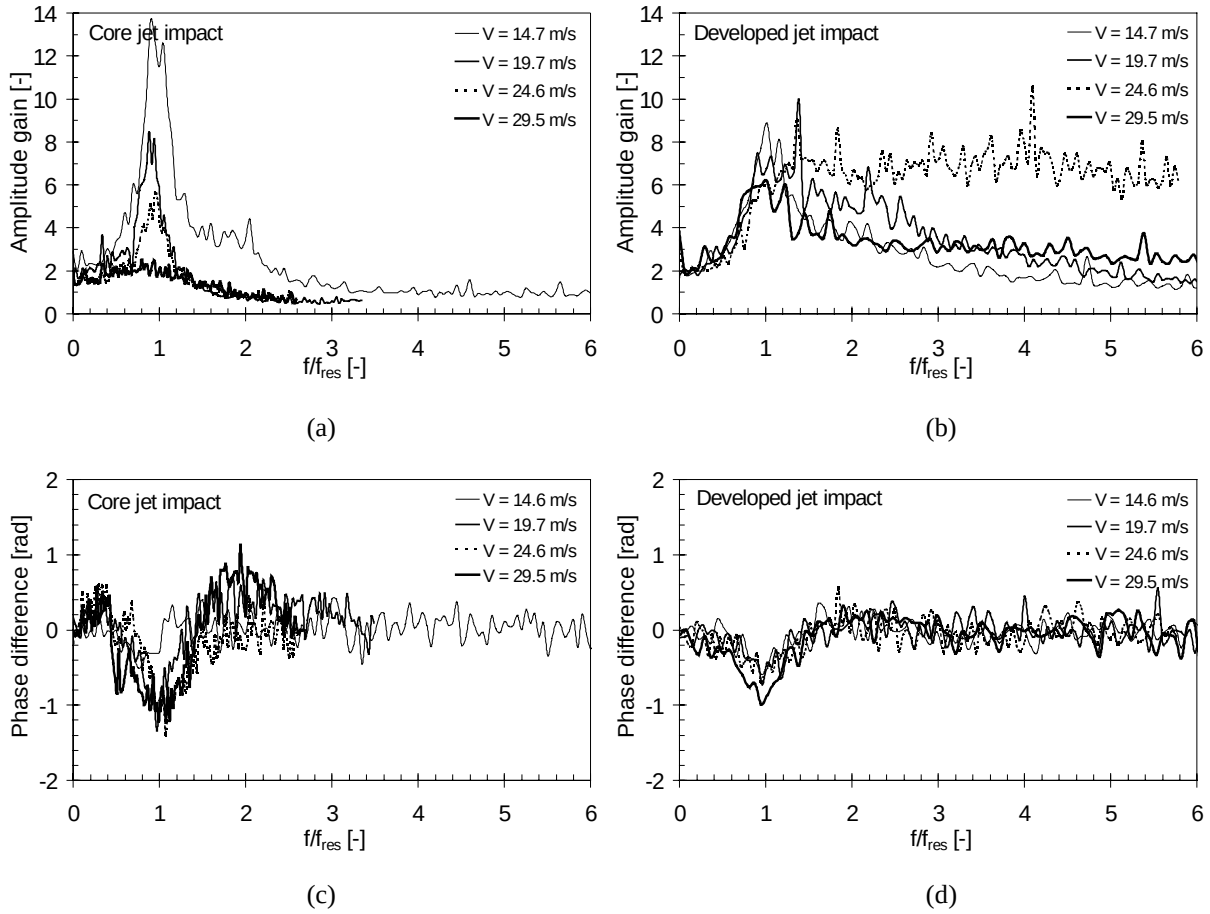

Fig. V-50 Transfer function between the pressures at the end of the I-joint and the pressures at the pool bottom:
a) amplitude gain for core jet impact; b) amplitude gain for developed jet impact;
c) phase difference for core jet impact; d) phase difference for developed jet impact.

4.2.7. Air content

The air content under convergent jet impact has already been discussed together with cylindrical jet outlets in § 4.1.9. It was found that convergent jet outlets are capable to generate ideal core jets that have an air concentration inside the joint of 0.5 – 1 %. This concentration decreases with increasing pressure in the joint. The rate of decrease is faster than the one that is due to the volume change of the bubbles based on the ideal gas law (Chapter III, § 3.3.2). This means that some air is being dissolved in the water.

The same reasoning holds for developed jets. They exhibit a higher air content, up to 10-20 % at standard atmospheric pressure conditions.

The air content measured under ideal core impact is in very good agreement with the air content that was found under submerged jet impact. For both jet types, no free air from the shear layer in the plunge pool can enter the joints. Apparently, the encountered air is inherent to the liquid. It can be present under the form of microbubbles or simply dissolved in the liquid.

The former statement involves a constant mass of free air in the liquid, which contradicts the measurements. Hence, it is believed that some part of the free air that is present inside the joint has been released from the water itself, due to sudden pressure drops.

4.2.8. Conclusions

The convergent jets have no low-frequency turbulences. Therefore, at low water depths, ideal core jet impact is obtained, with very low pressure fluctuations and low pressure amplifications inside the rock joint. The resonance frequencies of the joints are much better visible than for cylindrical core jets, especially at high jet velocities. This is because ideal core jets exhibit low air contents of 0.5 to 1 %, similar to the air contents that were measured for submerged jet conditions.

For developed jet conditions, the convergent jets have higher pressure fluctuations inside the joint, but slightly lower amplifications of the pool bottom pressures. This is because the convergent jets are stronger than their homologue cylindrical ones and, thus, partially or totally cross the water depth of the pool. They behave somewhat like core jets and it is difficult to obtain an appropriate turbulent shear layer with the low water depths of the experimental facility. The air contents are similar to the ones for cylindrical jets.

As a conclusion, it is believed that cylindrical jets create jet impact conditions that are closer to real plunge pool flow conditions than for convergent jets. The latter would need higher water depths.

4.3. The L-shaped rock joint under the impact of a cylindrical jet

The I-shaped rock joint analysed under § 4.2 constitutes the simplest possible geometrical configuration of a rock joint. It has been studied to assess the major flow characteristics in rock joints. However, as pointed out in Chapter III, § 2.2.5, real rock joints are far more complicated and irregular. Especially the influence of changes in orientations of the joint pattern could be relevant to a transient flow analysis. For this purpose, the present section investigates an L-shaped rock joint. This geometry integrates a 90° bend at 0.80 m downstream from the joint entrance, for a total joint length of 1.09 m. Hence, the influence of the sharp bend is studied more in detail.

4.3.1. Geometrical configuration

The geometrical configuration of the L-shaped rock joint is presented in Fig. V-51. It consists of a 0.29 m long prolongation of the I-shaped joint by introduction of a sharp 90° bend. As such, the total length of the joint is 1.09 m. Its width is 10 mm and the thickness is 1 mm. Beside the three sensors used for the I-joint ((a), (c) and (d)), a fourth sensor is located at the end of the joint (d').

The present analysis focuses on a comparison of the dynamic pressures of the I-joint and the L-joint. Hence, sensor (d) of the I-joint is compared with sensor (d') of the L-joint, because both sensors are situated at the end of their respective geometries. Sensor (c) of the I-joint is compared with sensor (d) of the L-joint. They are both located at more or less the same distance from their respective joint ends. This comparison allows quantifying and qualifying the influence of the joint length and the 90° bend.

In the following, all the measurements that were made inside the I-joint are presented by the symbol (■). This is done systematically, regardless of the sensor position or type of jet impact.

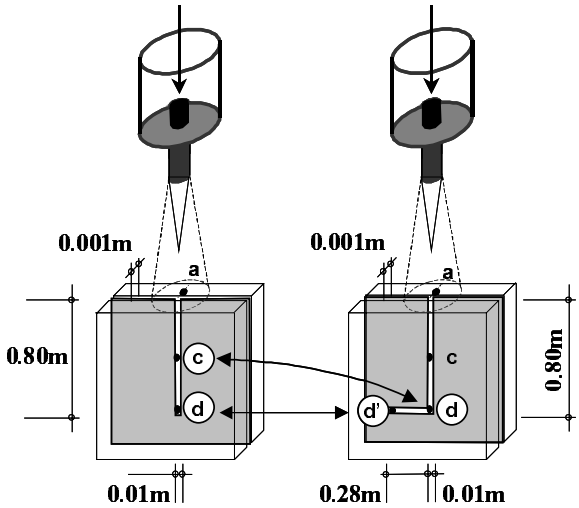

Sensor	Type	Position
a	pool bottom	25 mm from joint
c	rock joint	center, 420 mm inside
d	rock joint	center, 790 mm inside
d'	rock joint	side, 1080 mm inside

Fig. V-51 Geometrical configuration of the L-joint compared to the I-joint. The analysis focuses on a comparison between sensor (d) of the I-joint and sensor (d') of the L-joint, as well as between sensor (c) of the I-joint and sensor (d) of the L-joint.

4.3.2. Measured pressure signal

The pressure signals in the time domain are very similar to the ones measured in the I-joint. However, due to the presence of a 90° bend, a second resonance frequency is superposed on the fundamental one. This second frequency is particularly present in the part of the joint upstream of the bend. This is visible in Fig. V-52, where a comparison is made between the pool bottom pressures and the pressures measured at the middle, at the bend and at the end of the joint. The mean jet velocity is 24.6 m/s and the plunge pool depth 0.60 m. A low-frequency amplitude modulation of the fundamental resonance

frequency can be distinguished over the total presented time interval of 0.2 seconds. The signals at the end and at the bend clearly show the fundamental frequency. The signal at the middle of the joint is influenced by the fundamental frequency, but also by a second frequency. This second frequency is much higher than the fundamental one and only occurs in the part of the joint upstream of the bend.

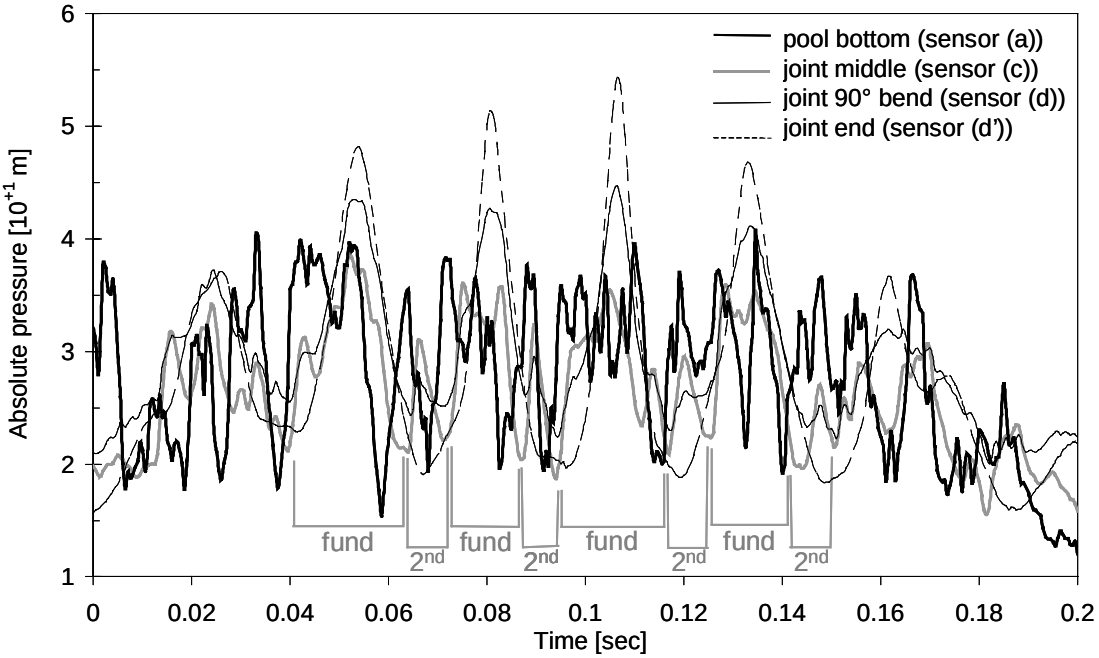

Fig. V-52 Comparison in the time domain of pressure at the pool bottom and corresponding pressures at the middle, at the bend and at the end of the L-shaped joint. Mean jet velocity is 24.6 m/s. Fundamental and higher harmonic resonance frequencies are clearly visible.

4.3.3. Mean dynamic pressures

A first comparison is between the mean pressures that were measured at the end of the L-joint and at the end of the I-joint. Figs. V-53a & 53b present the mean pressure coefficient $C_{pd'}$ as a function of the Y/D_j ratio respectively as a function of the jet velocity V_j. A good agreement between the two joints is observed. This agreement holds for all jet impact conditions. Figs. V-53c & 53d compare the bend position (sensor (d)) of the L-joint with the middle position (sensor (c)) of the I-joint. The same remarks can be made.

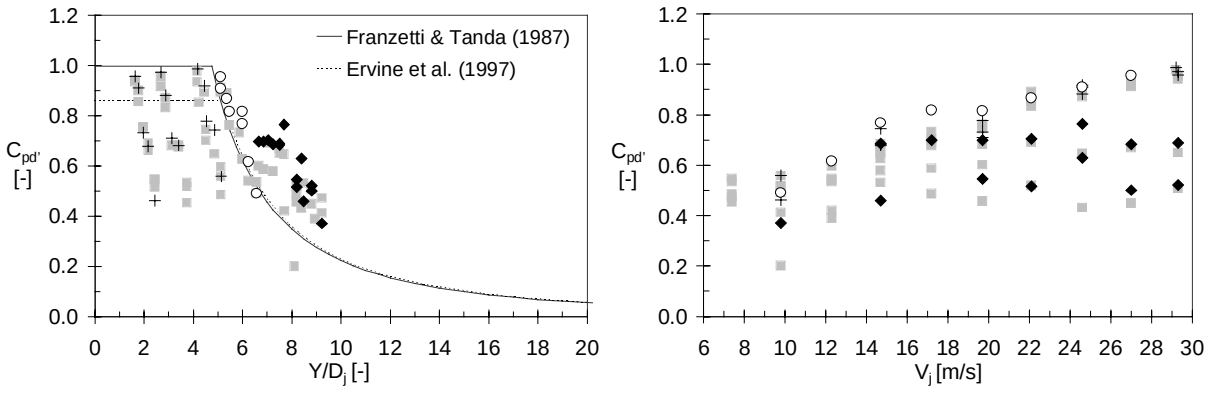

(a) (b)

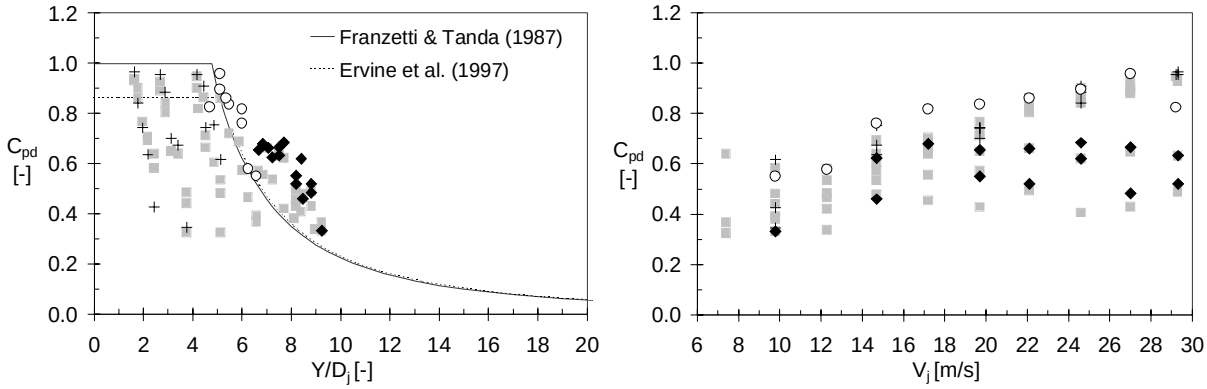

(c) (d)

Fig. V-53 Non-dimensional mean dynamic pressure coefficient of the L-joint:
a) $C_{pd'}$ as a function of the Y/D_j ratio; b) $C_{pd'}$ as a function of the mean jet velocity V_j;
c) C_{pd} as a function of the Y/D_j ratio; d) C_{pd} as a function of the mean jet velocity V_j;
The symbol (■) represents corresponding data measured inside the I-joint.

4.3.4. Root-mean-square pressures

The root-mean-square pressure coefficients have been compared in Fig. V-54. In both figures, a different behavior is observed for core and developed jets.

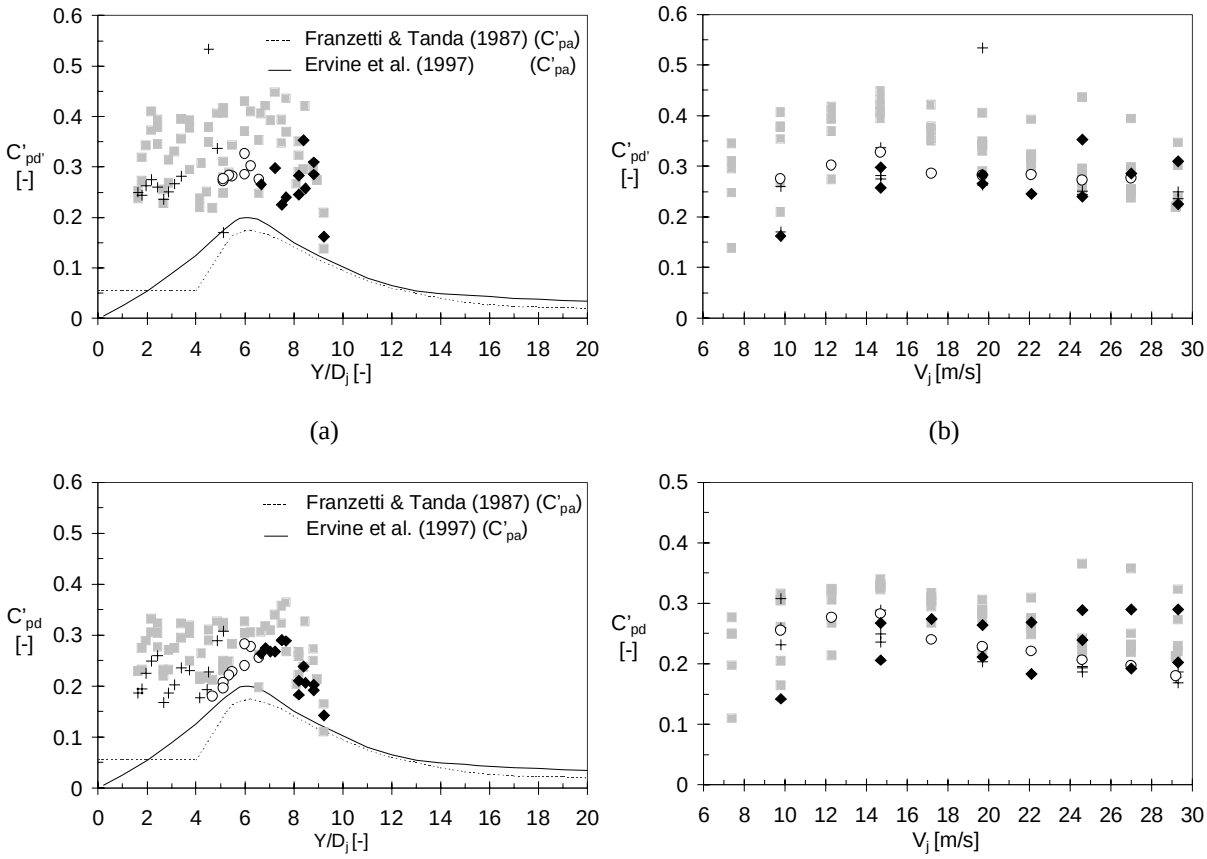

(a) (b)

(c) (d)

Fig. V-54 Non-dimensional fluctuating dynamic pressure coefficient C'_p of the L-joint:
a) $C'_{pd'}$ as a function of the Y/D_j ratio; b) $C'_{pd'}$ as a function of the mean jet velocity V_j;
c) C'_{pd} as a function of the Y/D_j ratio; d) C'_{pd} as a function of the mean jet velocity V_j;
The symbol (■) represents corresponding data measured inside the I-joint.

According to Fig. V-54a, the end of the L-joint generally has lower root-mean-square values than the end of the I-joint. However, Fig. V-54b shows that this is only true at low jet velocities. The difference becomes insignificant at jet velocities higher than 20 m/s. At low jet velocities, the end of the L-joint seems to be less excited by the impacting jet. In other terms, one can expect a lower resonance sensibility and a lower amplification factor Γ at low pressures. At the bend position of the L-joint, the obtained values are quite comparable to the ones at the middle of the I-joint. The same amplification of pressures is expected at this location.

4.3.5. Extreme pressures

The same remarks can be made for the positive extreme pressure coefficients. These are presented in Fig. V-55, both for the end position (sensor (d')) and for the bend position (sensor (d)) of the L-joint. For developed jets, a good agreement with previous data on the I-joint is observed, over the whole range of jet velocities. Core jet impact, however, shows similar values at high jet velocities only (V_j > 20 m/s). A significant decrease in extreme pressure coefficients can be observed at low jet velocities. Negative extreme pressures conduct to similar conclusions for both joint configurations and have not been presented.

The reason for the different behavior of the L-joint at low jet velocities cannot be explained by the present time domain analysis. Additional information is necessary on the spectral content and the pressure wave celerities, as well as on the air content.

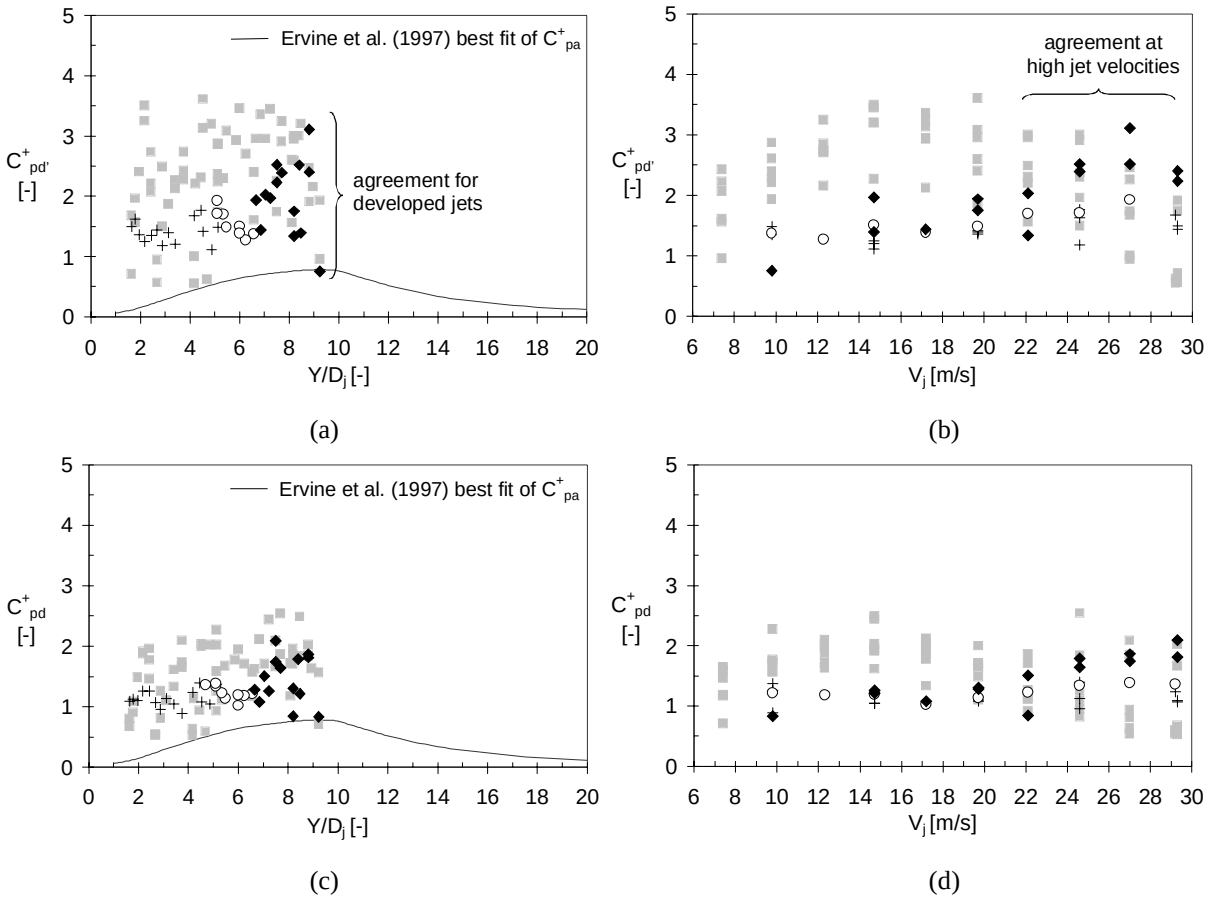

Fig. V-55 Positive extreme dynamic pressure coefficients:
a) $C^+_{pd'}$ as a function of Y/D_j; b) $C^+_{pd'}$ as a function of V_j;
c) C^+_{pd} as a function of Y/D_j; d) C^+_{pd} as a function of V_j;
The symbol (■) represents corresponding data measured inside the I-joint.

4.3.6. Amplification factor Γ

The amplification factors between the pressures measured at the end of the joint and the corresponding ones at the pool bottom are presented in Fig. V-56. Both the $\Gamma^{0.1}$ and Γ^{+} amplification factors are significantly different from the ones calculated for the I-joint. In agreement with the root-mean-square analysis, this difference becomes substantial at low jet velocities and is particularly present for core jet impact. It is obvious that the jet velocity has a profound impact on the behavior of the pressures inside the L-joint.

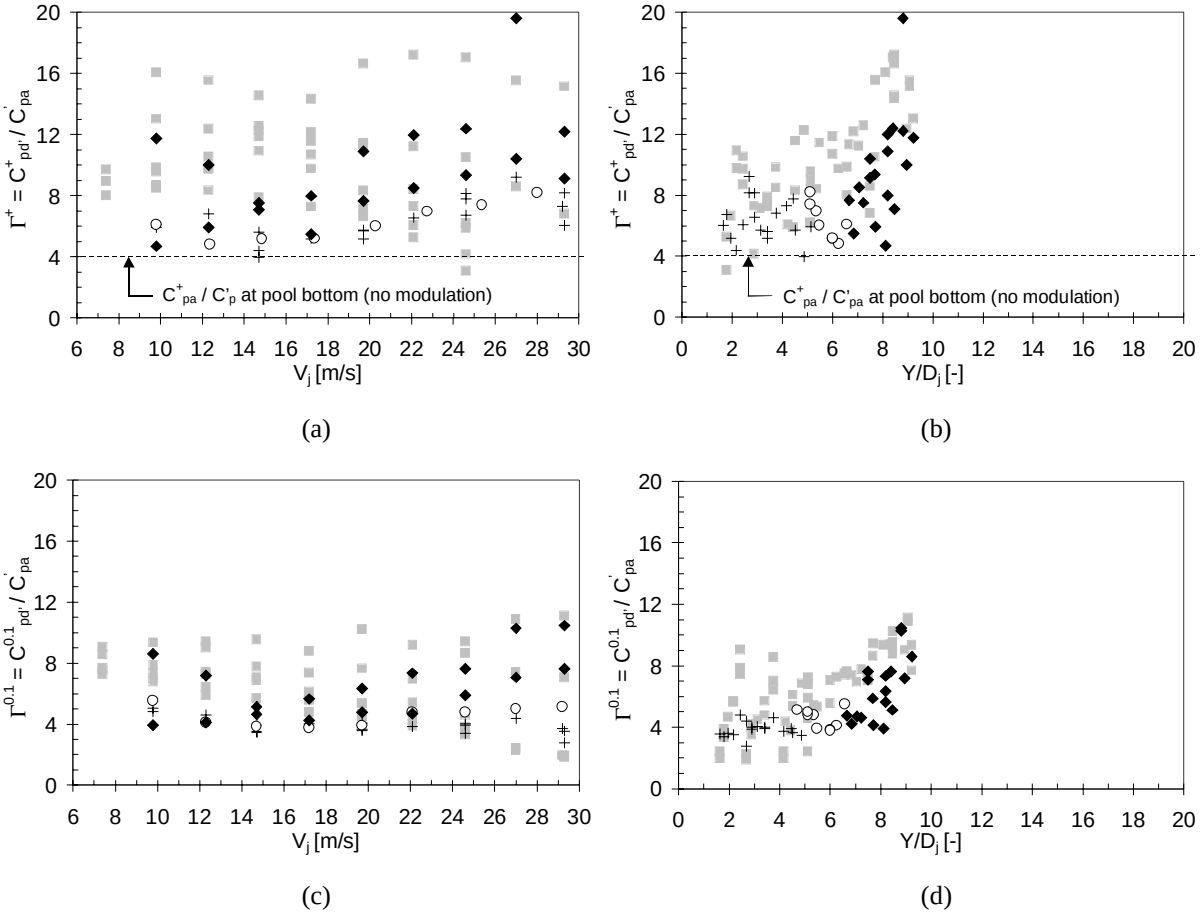

Fig. V-56 Comparison of amplification factors between the pressures measured at the end of the joint and the corresponding ones at the pool bottom:
a) Γ^{+} as a function of the mean jet velocity V_j; b) Γ^{+} as a function of the Y/D_j ratio;
c) $\Gamma^{0.1}$ as a function of the mean jet velocity V_j; d) $\Gamma^{0.1}$ as a function of the Y/D_j ratio.
The symbol (■) represents corresponding data measured inside the I-joint.

4.3.7. Spectral analysis and transfer functions

The spectral content for core and developed jets is presented at the middle, at the bend and at the end of the L-joint, as a function of the frequency f. At the middle and at the bend position, a secondary resonance frequency is clearly visible. At the end of the joint, no secondary harmonics are apparent. Furthermore, the fundamental resonance frequencies seem to be considerably lower than the ones obtained for the I-joint. This means that the air content in the L-joint is much higher, which constitutes an explanation for the basically different behavior of the L-joint when compared to the I-joint.

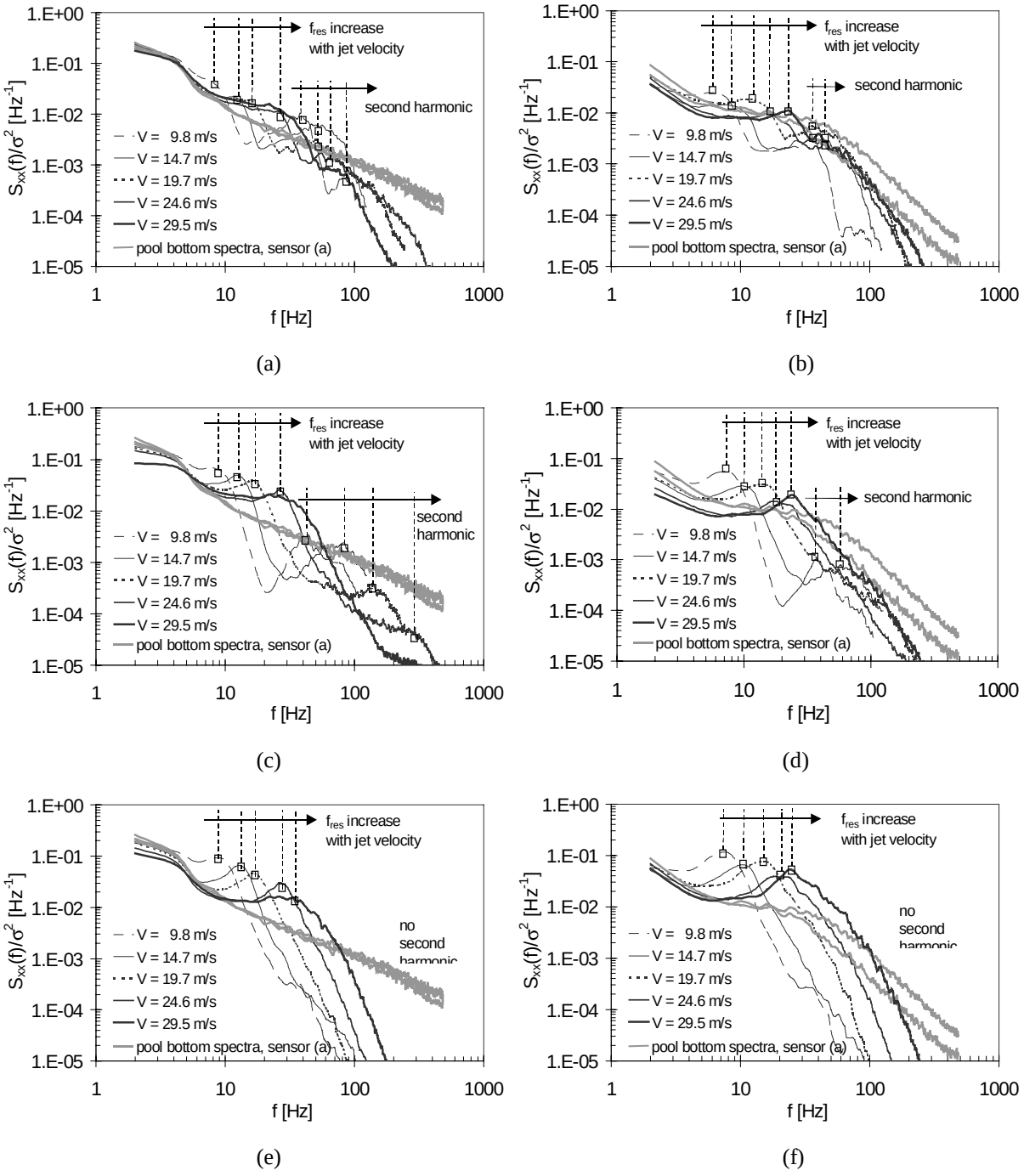

Fig. V-57 Non-dimensional spectral content of the L-shaped rock joint for core jet impact:
a) sensor (c) for core jets; b) sensor (c) for developed jets;
c) sensor (d) for core jets; d) sensor (d) for developed jets;
e) sensor (d') for core jets; f) sensor (d') for developed jets.

The 90° bend has been used to determine the influence of a sudden change in orientation of the joint pattern. It is not excluded that this particular geometrical situation generates the formation of partial reflections of the pressure waves at the bend. This could modify the transient characteristics of the whole joint system and, thus, also the pressure pattern inside the joint. More than one fundamental resonance frequency might exist, and higher harmonics might appear. On the other hand, it is also possible that the air content upstream of the bend is simply lower than the one at the end of the L-joint.

This situation seems plausible when considering that free air bubbles can get trapped and form an air cavity in the horizontal part of the joint (Chapter III, § 3.3.4). The pressure signal of Fig. V-52 is in good agreement with the one as presented in Fig. III-19 and obtained for an air cavity (Swaffield & Boldy, 1993). The analysis of the transfer function between the pressures inside the joint and the pool bottom pressures should procure more insight.

This is done twice: once for the pressures measured at the bend, and a second time for the pressures measured at the end of the joint. Fig. V-58 presents the amplitude gain and the phase difference between pressures measured at the bend (sensor (d)) and pool bottom pressures (sensor (a)). The left hand side deals with core jet impact, the right hand side is valid for developed jet impact. The former shows several consecutive phase shifts. However, beside the fundamental resonance frequency, only one secondary frequency is visible in the amplitude modulation. This harmonic is only present at low velocities and appears at frequencies 5 to 10 times higher than the fundamental one. At high velocities, no secondary harmonics can be distinguished, and the fundamental frequency seems somewhat displaced. This could be due to peak pressures. On the other hand, developed jets have only one phase shift. This shift is much more expressed than for core jets. They also show two main frequencies at low jet velocities. The higher harmonic disappears at high velocity, just like for core jets.

Apparently, different mode shapes are present at the bend. The fundamental mode shape seems to correspond to the one for the I-joint, but for a total length of 1.09 m and a higher air content. The secondary harmonics, however, cannot be directly attributed to some well-defined mode shape. They can belong to a mode shape that covers the total joint length, or to a mode shape that only occurs upstream of the 90° bend.

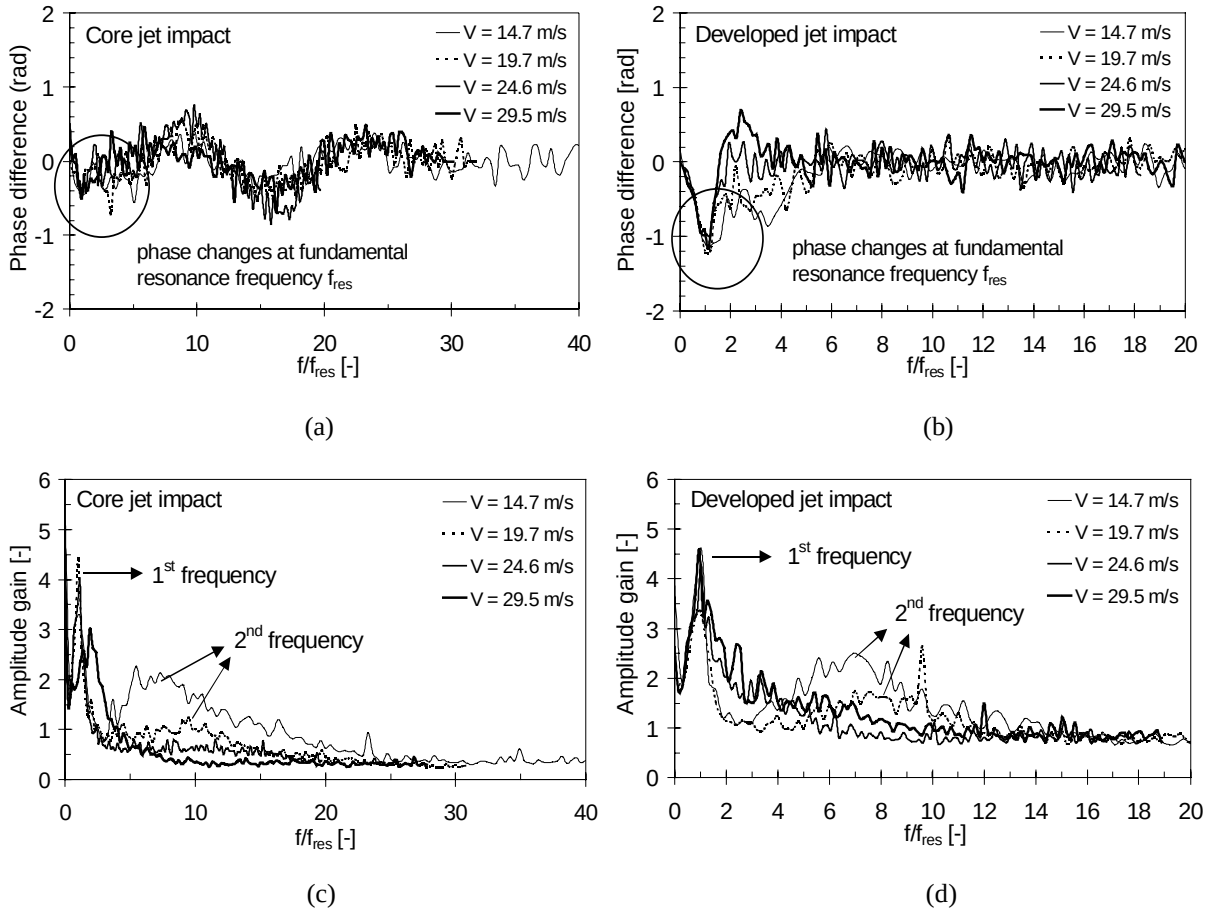

Fig. V-58 Transfer function between the pressures measured at the bend and the pressures measured at the pool bottom, as a function of the non-dimensional frequency f/f_{res}:
a) phase difference for core jets; b) phase difference for developed jets;
c) amplitude gain for core jets; d) amplitude gain for developed jets.

In the latter case, this would imply that some high-frequency reflections occur at the bend. However, the frequencies at which the secondary harmonic appears rather indicate that, upstream of the bend, probably a much lower free air content is occurring than downstream.

This is verified by analyzing the transfer function at the end of the joint, which is presented in Fig. V-59. According to the spectral analysis in Figs. V-57e & 57f, no higher harmonics are visible. For all jet velocities, the fundamental resonance frequency is well defined. At high jet velocities, the amplitude gains of the pressure peaks appear. This phenomenon is best expressed for developed jets.

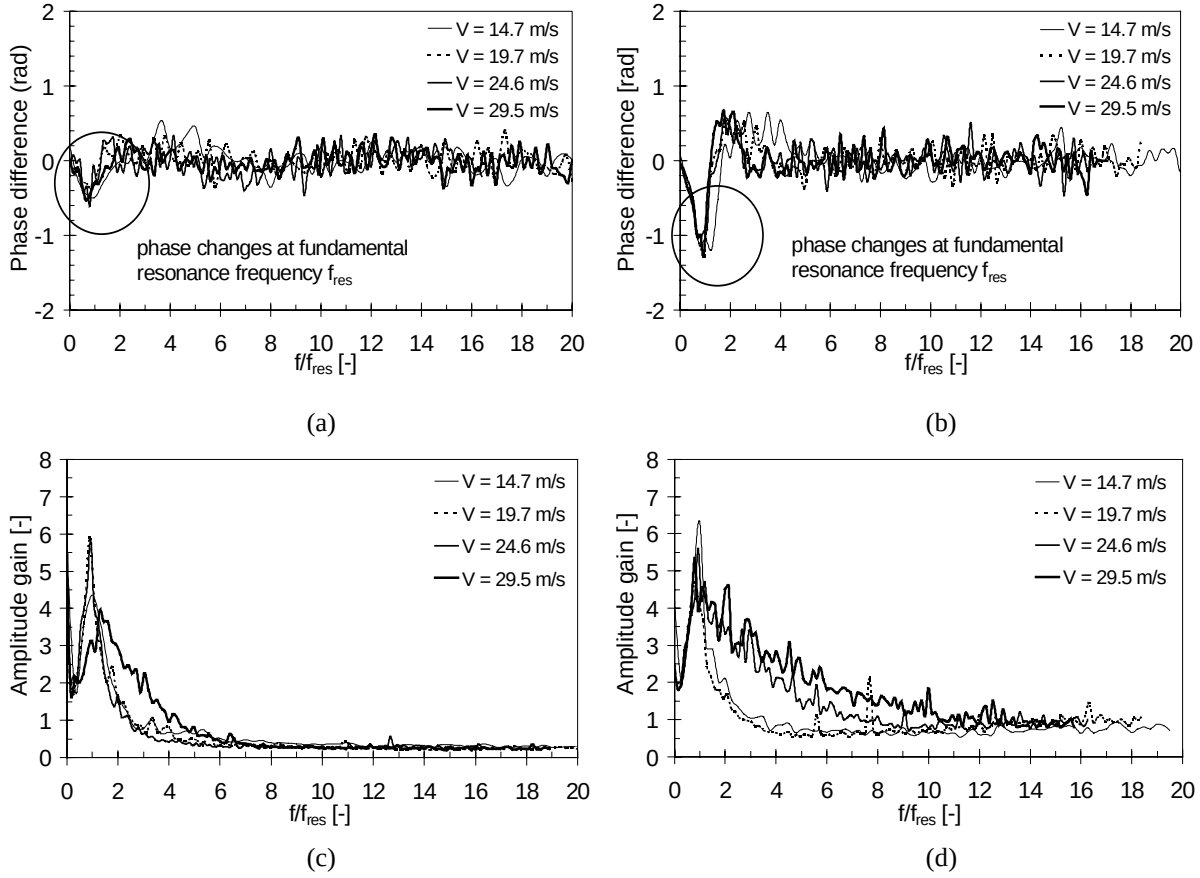

Fig. V-59 Transfer function between the pressures measured at the joint end and the pressures measured at the pool bottom, as a function of the non-dimensional frequency f/f_{res}:
a) phase difference for core jets; b) phase difference for developed jets;
c) amplitude gain for core jets; d) amplitude gain for developed jets.

Furthermore, the spectral contents that are presented in Figs. V-57a & 57b show that the middle of the joint (sensor (c)) exhibits the same secondary harmonics as the bend position. This roughly signifies that the secondary harmonic only covers the part of the L-joint between the entrance and the 90° bend. In other words, its mode shape could be generated by partial reflections of the pressures at the bend. These reflections, however, only occur at high frequencies and low jet velocities (< 20 m/s). Therefore, it is possible that the secondary harmonic also exists at the end of the joint, but that it is simply not visible because of the importance of the first (or fundamental) harmonic. As shown by the amplification factors, its influence on the pressure pattern is not so important. The fundamental resonance frequencies are considerably lower than the ones obtained for the I-joint. This can have two reasons. First of all, a frequency shift could occur due to the appearance of a second harmonic. Secondly, the frequency shift could simply correspond to a higher air content inside the joint. Pertaining to the, at first sight, quite negligible character of the higher harmonics, it is believed that the

second phenomenon is responsible. Moreover, a difference in air content up-and downstream of the bend is suspected, based on the huge difference in resonance frequencies. This is investigated in the next section.

4.3.8. Air content

Similar to the air content analysis that has been performed for the I-joint, the mean celerity is determined as a function of the mean pressure inside the L-joint. This is based on the assumptions of a $\lambda/4$ – resonator, in which the total length of the resonator depends on the considered frequency. The results are presented in Fig. V-60.

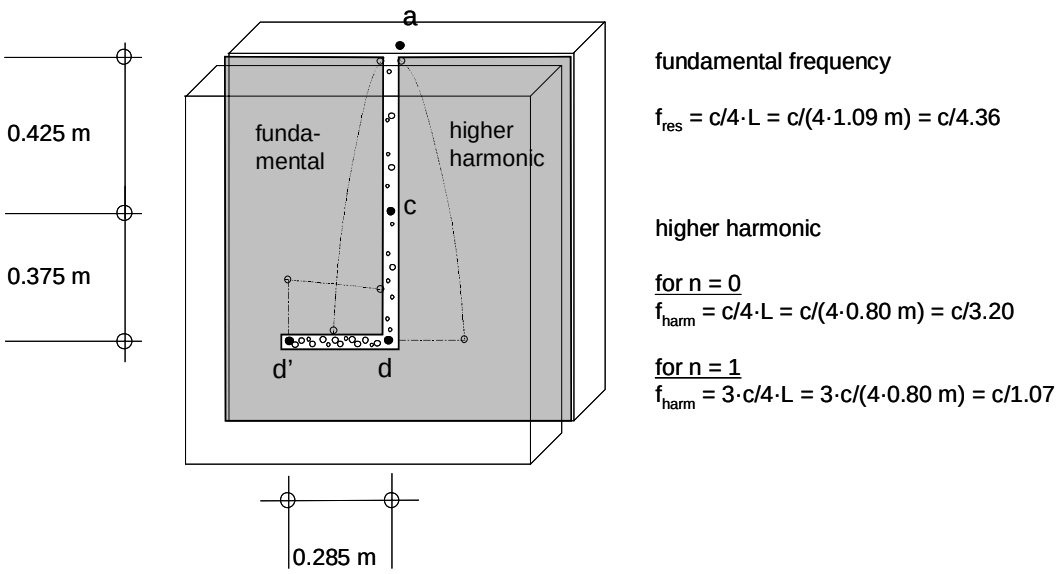

Fig. V-60 Scheme of the possible fundamental and higher harmonics of the resonance system of a L-shaped rock joint. For the fundamental frequency, the total joint length is considered. For the higher harmonic, only the part upstream of the 90° bend is used.

Based on the measured spectral densities and transfer functions, it has been found that a fundamental frequency exists over the whole joint length (measured at sensors (c), (d) and (d')). Furthermore, a higher harmonic is present only in the part of the joint that is upstream of the 90° bend, i.e. in the I-part (measured at sensors (c) and (d)). For the determination of the mean air content, an assumption has to be made concerning the "n" value of the mode shapes. For both resonating frequencies, n = 0 is assumed. This corresponds to two fundamental sinusoidal mode shapes: one for the whole joint length, and a second one for the length upstream of the bend. For simplicity, the latter will be referred to as the higher harmonic. Fig. V-61 presents the calculated mean air contents for each mode shape separately. The resonance frequencies were derived from Fig. V-58. For the higher harmonic, a difference between sensors (c) and (d) has been made. Finally, all mode shapes and sensors are presented together in Fig. V-62d.Based on the fundamental mode in Fig. V-61a, a mean air content of 5-20 % is observed. At first sight, these values are considerably higher than the ones calculated for the I-joint. However, at high jet velocities and mean pressures, the I-joint exhibits air contents that are similar. Based on the higher harmonic, two different results are obtained. The first one is based on sensor (c) situated at the middle of the joint and is presented in Fig. V-61b. This sensor gives air contents that are in perfect agreement with the ones for the I-joint, i.e. from 1-5 %. The second one is based on sensor (d) situated at the bend and is presented in Fig. V-61c. For this sensor, surprisingly high celerities have been obtained. These celerities correspond to very low air contents, even lower than the ones for submerged jet impact.

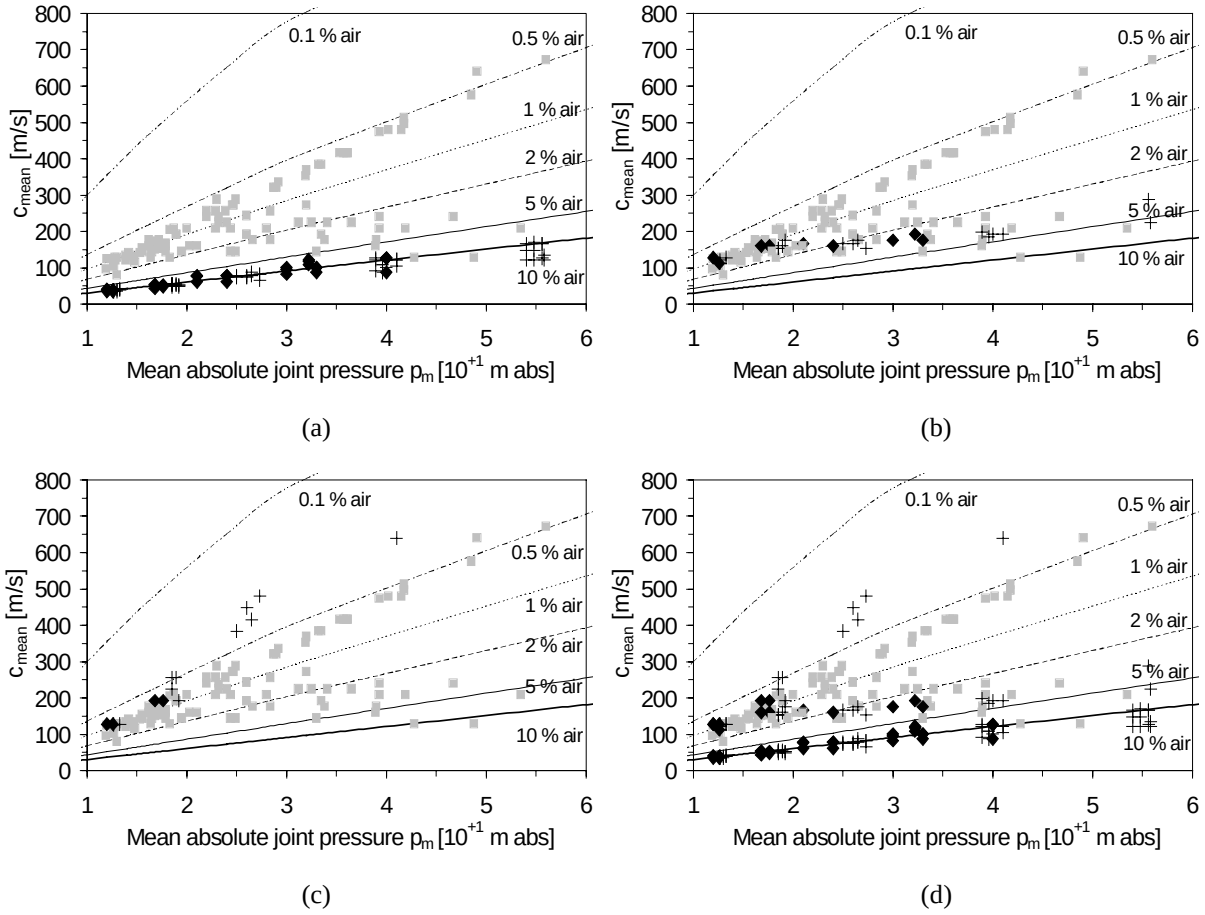

Fig. V-61 Mean wave celerity inside the L-joint as a function of the mean absolute joint pressure. The data obtained inside the I-joint are marked with a (■) symbol.
a) fundamental mode at sensors (c), (d), (d'); b) higher harmonic at sensor (c);
c) higher harmonic at sensor (d) ; d) all mode shapes and sensors together.

It is important to remark that the above analysis completely depends on the assumptions made on the governing mode shapes. At first sight, contradictory results are obtained. For the same joint, both low and very high air contents are calculated, which is clearly impossible. This problem can be handled by accounting for the relative importance of each of the mode shapes as a function of the location inside the joint. This is based on the assumption that each distinct part of the joint resonates at its own frequency. Thus, each part has its characteristic air content. For the present L-joint, two parts can be distinguished: upstream and downstream of the 90° bend. The analysis of the spectral contents as presented in Fig. V-57 shows that sensor (c) is significantly influenced by the higher harmonic and that the fundamental mode is hardly present. Sensor (d) exhibits both mode shapes, but the higher harmonic has been displaced compared to sensor (c). This could explain the different air contents at this location. Sensor (d') only shows the fundamental resonance frequency.

A more detailed analysis can be performed by consideration of the pressure signal in the time domain and by the determination of spatial correlations between the different sensors. As such, for the part situated upstream of the bend, a correlation between sensors (c) and (d) has been made. This procures the celerity-pressure relationship that is valid for this part only. Secondly, for the part downstream of the bend, the correlation between sensors (d) and (d') results in a second series of celerity-pressure relationships. The results are presented in Fig. V-62. The part of the joint between its entrance and the 90° bend is characterized by celerities that are very high, much higher as any previously measured or calculated values. However, sometimes values close to the ones for the I-joint were measured. The part downstream of the bend exhibits celerities that are similar to the I-joint values.

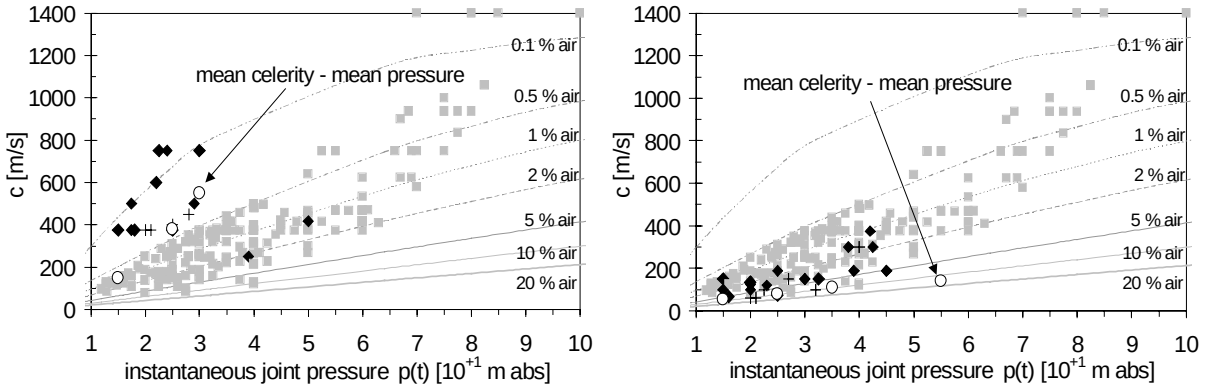

Fig. V-62 Instantaneous wave celerity inside the L-joint as a function of the instantaneous joint pressure: a) measured upstream of the bend; b) measured downstream of the bend. The data obtained inside the I-joint are marked with a (■) symbol.

It has to be accentuated here that these results have been obtained based on measurements at a 1'000 to 2'000 Hz acquisition rate. The corresponding error in wave celerity is non-negligible. Therefore, the results should only be interpreted as tendencies, and not as absolute values.

Hence, it is concluded that the L-joint is divided into **two parts with a completely different air content**. The distinction between these parts is made by the presence of the 90° bend. Compared to the I-joint, were a homogeneously distributed air content has been assumed, the present L-joint apparently transfers some of the air in the upstream part towards the horizontal, downstream part. There, the air can get stuck and thus accumulates and forms a cavity. The cushioning effect of this downstream part determines the fundamental resonance mode of the joint. The upstream part adds a second mode shape that is only present upstream of the bend. The closer to the entrance of the joint, the more this second frequency becomes important.

Furthermore, the mean air contents that were calculated based on the fundamental mode are in reasonable to good agreement with the celerity-pressure relationships obtained in Fig. V-62. With regard to the lack of precision of the used methods, the observed differences are not significant. This is also the case for the mean air contents as derived from the higher harmonic at the bend. On the other hand, the mean air contents calculated based on the higher harmonic at sensor (c) do not correspond to most of the measured celerity-pressure relationships. Although some of the measured points seem to match, it is believed that the higher harmonic at this location has been displaced and, thus, is not representative for the air content.

Finally, it is interesting to verify the above statements by analyzing the pressure signals. This can be done by taking back Fig. V-52, in which the signals of the four sensors are presented in the time domain. The signal of sensor (c) is characterized by a superposition of the fundamental frequency and the higher harmonic. The signal at the bend is dominated by the fundamental frequency, but also exhibits the higher harmonic. However, the peak pressures are completely defined by the fundamental frequency. The signal at the end of the joint only follows the fundamental frequency. These findings confirm the aforementioned assumptions and agree with Fig. III-19 valid for an air cavity.

4.3.9. Conclusions

The L-joint exhibits lower pressure amplifications than the I-joint at low jet velocities and for core jet impact conditions. The air content is not homogeneously distributed like in the I-joint; an air cavity forms downstream of the 90° bend and changes the fundamental resonance frequency. The part upstream of the bend has much less air and adds a higher resonance frequency to the fundamental one. The peak pressures at the joint end are defined by the fundamental resonance frequency and become significant at jet velocities higher than 20 m/s.

4.4. The U-shaped rock joint under the impact of a cylindrical jet

The I-joint allowed determining the main flow characteristics inside rock joints. The L-joint gave more insight into the influence of a sudden change in orientation of the joint pattern. This was accomplished by a 90° bend. At present, the U-shaped joint is investigated. This shape integrates a double 90° bend. Furthermore, its total length is 1.665 m. Hence, the joint mainly studies the influence of its length on the transient system. At the same time, it will be verified whether multiple bends are of importance on the air content distribution throughout the joint.

4.4.1. Geometrical configuration

The geometrical configuration of the U-shaped rock joint is presented in Fig. V-63. It consists of an I-shaped part with a length of 0.795 m, a 90° bend, a horizontal part of 0.075 m, a second 90° bend followed by a 0.795 m part straight upwards and closed at its end. The joint has a width of 10 mm and a thickness of 1 mm. The total length is 1.665 m.

Two sensors are used for comparison: sensor (c) at the middle of the L-joint and sensor (d) at the first bend of the U-joint. Although not exactly situated at the same distance from the end of their respective joints, it is believed that the two sensors represent quite comparable situations. Taking into account the different joint lengths, their air contents can be evaluated and compared. The measurements that were made inside the L-joint are presented by the symbol (■).

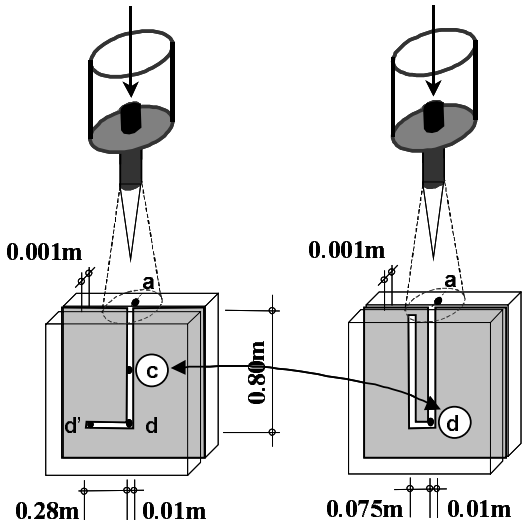

Sensor	Type	Position
a	pool bottom	25 mm from joint
c	rock joint	center, 420 mm inside
d	rock joint	center, 790 mm inside

Fig. V-63 Geometrical configuration of the L-joint and of the U-joint. The analysis of the dynamic pressures focuses on a comparison of sensor (c) of the L-joint with sensor (d) of the present U-joint. In the following, the data obtained inside the L-joint are marked with the symbol (■).

4.4.2. Mean dynamic pressures

A comparison is made with the mean pressures that were measured at the middle of the L-joint. Figs. V-64a & 64b present the mean pressure coefficient C_{pd} as a function of the Y/D_j ratio respectively the jet velocity V_j. The values of the U-joint seem to be somewhat lower than the ones for the L-joint, especially for developed jet conditions. The only plausible explanation for these lower values is the absence of peak pressures at that location of the U-joint. Thus, the mean pressures should be close to the literature values, as given by Ervine et al. (1997). It can be seen that this is effectively the case.

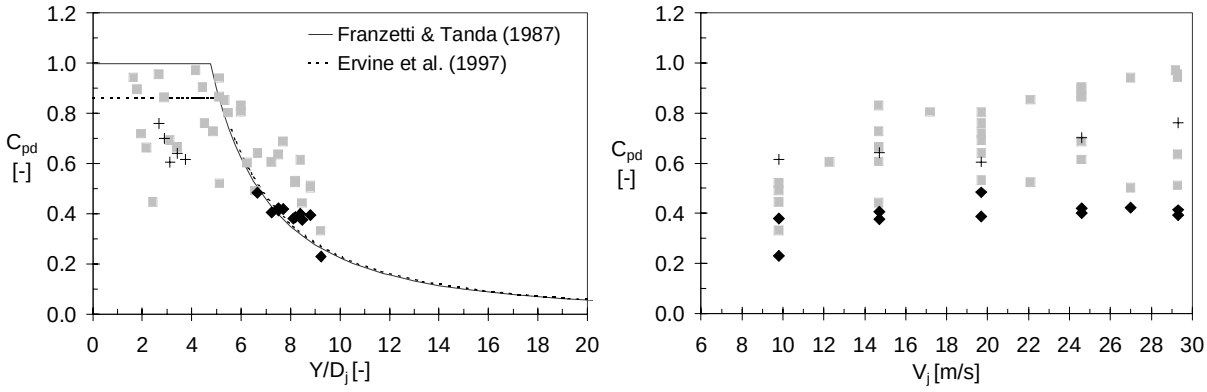

(a) (b)

Fig. V-64 Non-dimensional mean dynamic pressure coefficient C_{pd} measured at sensor (d) of the U-joint:
a) C_{pd} as a function of the Y/D_j ratio; b) C_{pd} as a function of the mean jet velocity V_j;
The symbol (■) represents corresponding data measured at sensor (c) of the L-joint.

4.4.3. Root-mean-square pressures

The root-mean-square pressures are slightly lower than the ones measured at the middle of the L-joint. Again a good agreement with the available literature values is observed. This strengthens the hypothesis that the encountered pressure pattern has to be very close to a pool bottom pattern. In other words, no significant amplification or phase modulation of the pressures occur at that location of the joint. The values for the middle of the L-joint already conducted to the same conclusion.

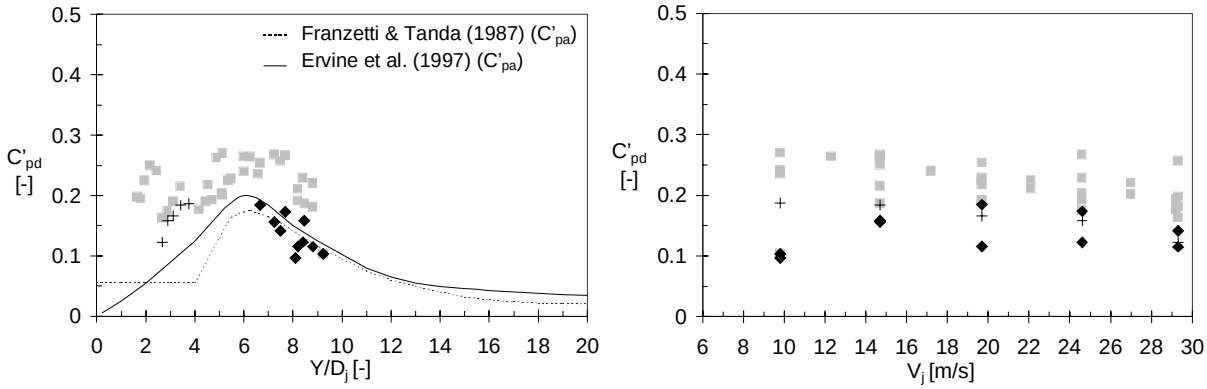

(a) (b)

Fig. V-65 Non-dimensional fluctuating dynamic pressure coefficient C'_{pd} measured at sensor (d) of the U-joint:
a) C'_{pd} as a function of the Y/D_j ratio; b) C'_{pd} as a function of the mean jet velocity V_j;
The symbol (■) represents corresponding data measured at sensor (c) of the L-joint.

4.4.4. Extreme pressures

The positive extreme coefficients are presented in Fig. V-66. They effectively correspond to extreme values that are typical for a plunge pool bottom. This again confirms the above hypothesis on the pressure pattern at sensor (d). It can be seen that the values measured inside the L-joint are also quite close to the pool bottom values, with coefficients between 0.4 and 1.3. Note that the corresponding coefficients at the end of the L-joint are typically between 2 and 4 (Fig. V-55a). Hence, no amplification effects happen at the bend position (sensor (d)) of the U-joint. The same remarks can be made for the negative extreme pressure coefficients.

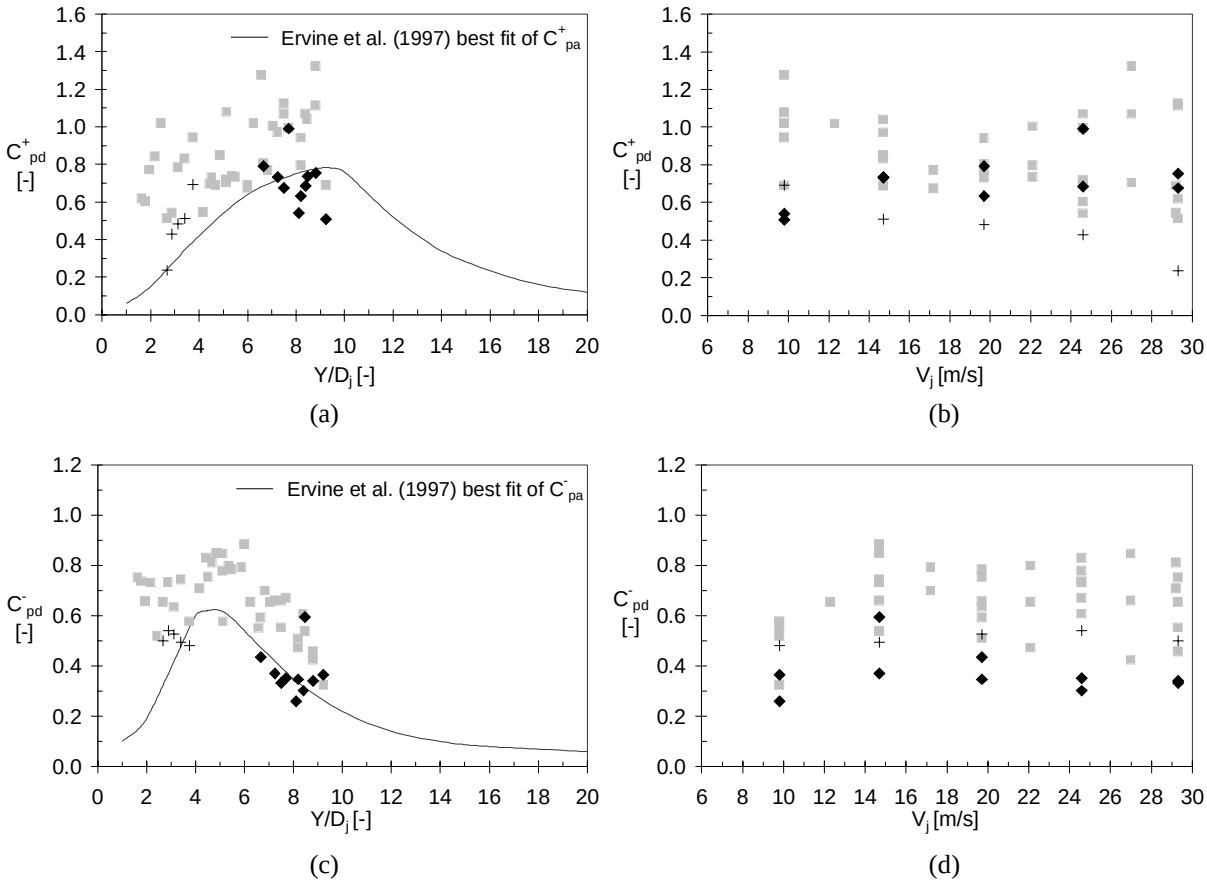

Fig. V-66 Non-dimensional extreme dynamic pressure coefficients at sensor (d) of the U-joint:
a) C^{+}_{pd} as a function of Y/D_j; b) C^{+}_{pd} as a function of V_j;
c) C^{-}_{pd} as a function of Y/D_j; d) C^{-}_{pd} as a function of V_j.
The (■) symbol represents corresponding data measured at sensor (c) of the L-joint.

4.4.5. Amplification factor Γ

The amplification factors are very close to the value of 4, which is characteristic for plunge pool bottom pressures. Occasionally, slightly higher values are encountered. This indicates that still some amplitude modulation can occur inside the joint at that location. This is visible in the spectral content.

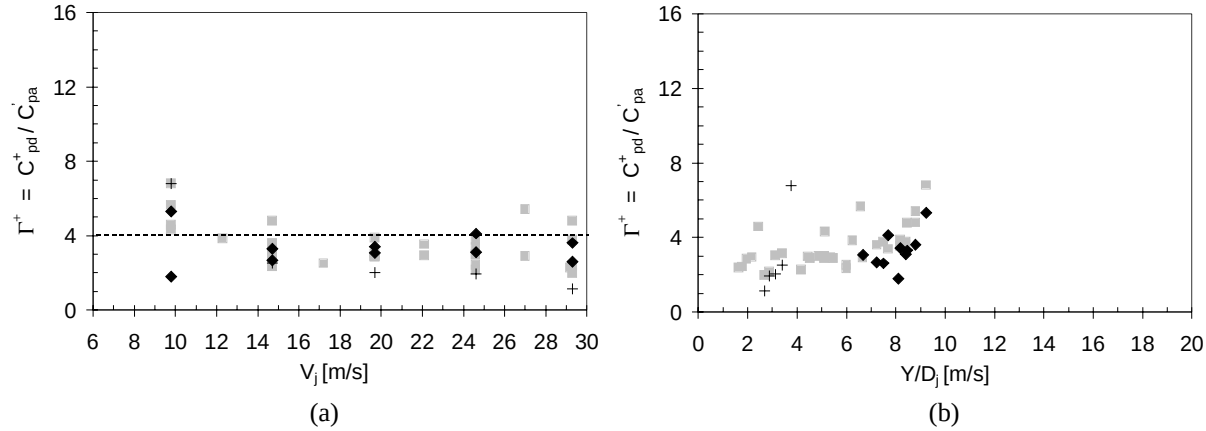

Fig. V-67 Amplification factors between pressures at sensor (d) and corresponding pool bottom pressures:
a) Γ^{+} as a function of the mean jet velocity V_j; b) Γ^{+} as a function of the Y/D_j ratio.
The (■) symbol represents corresponding data measured at sensor (c) of the L-joint.

4.4.6. Spectral analysis

The spectral content at the bend position (sensor (d)) is presented hereunder for core and developed jets respectively. For core jets, the fundamental resonance frequency is hard to define. There is a secondary harmonic, which is almost as significant as the first one. These spectra correspond more or less to the ones presented in Fig. V-57a, measured at sensor (c) of the L-joint. However, the resonance frequencies are less clear for the present U-joint. This could be expected based on the very low amplification factors and low extreme pressure coefficients for core jets.

For developed jets, the fundamental resonance frequencies are well established. The frequencies also occur at higher values than the ones for core jets. This indicates less air content. The reason for these surprising results cannot be deduced from the spectral density functions.

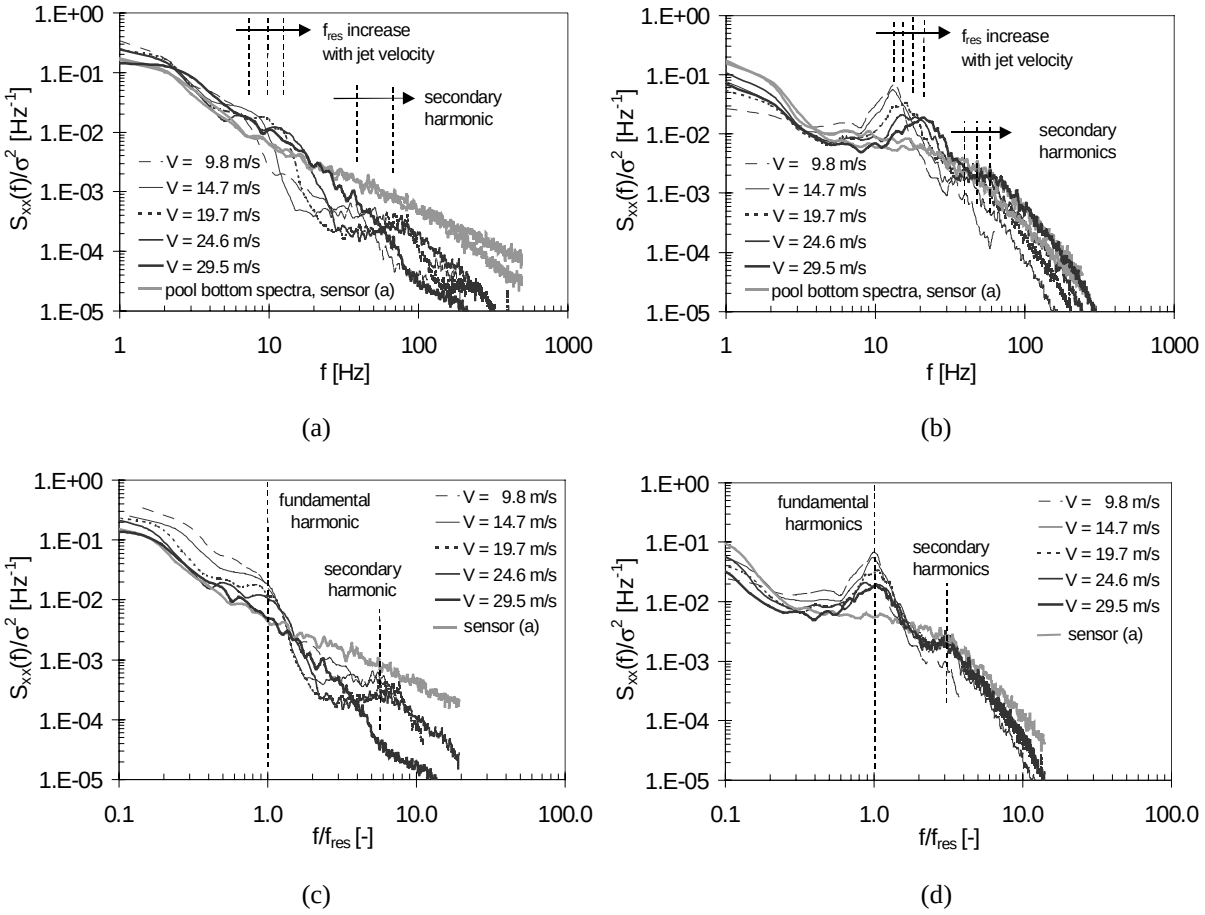

Fig. V-68 Non-dimensional spectral content of the U-shaped rock joint at the bend position (sensor (d)):
a) for core jets as a function of frequency; b) for developed jets as a function of frequency;
c) for core jets as a function of f/f_{res}; d) for developed jets as a function of f/f_{res}.

4.4.7. Air content

Just like for the other joints, the mean air content has been related to the mean pressure value inside the joint. Because only one sensor has been used inside the joint, no cross-correlation functions are available for the present L-joint. This makes it impossible to verify the derived mean air contents.

It can be seen in Fig. V-69 that core jets generate air concentrations in the U-joint that are very similar to the ones encountered in the L-joint, i.e. about 10 %. Developed jets produce air concentrations between 2 and 7 %. These values increase with increasing mean pressure, just like for the other test cases. The difference between the air volumes for core jets and developed jets is quite remarkable. An

explanation to this phenomenon could be that both test runs have been performed at different times. As such, this would imply that a certain amount of air can get stuck inside the joint and stay their during the test runs. However, all other test runs on L-shaped rock joints have been performed on different days. Nevertheless, they exhibit similar air contents.

A second explanation could be that the fundamental resonance frequency of core jets has simply been displaced by the presence of the higher harmonic. This has already been pointed out for sensor (c) of the L-joint, for which the calculated wave celerities did not match with the directly measured pressure pulse propagation speed.

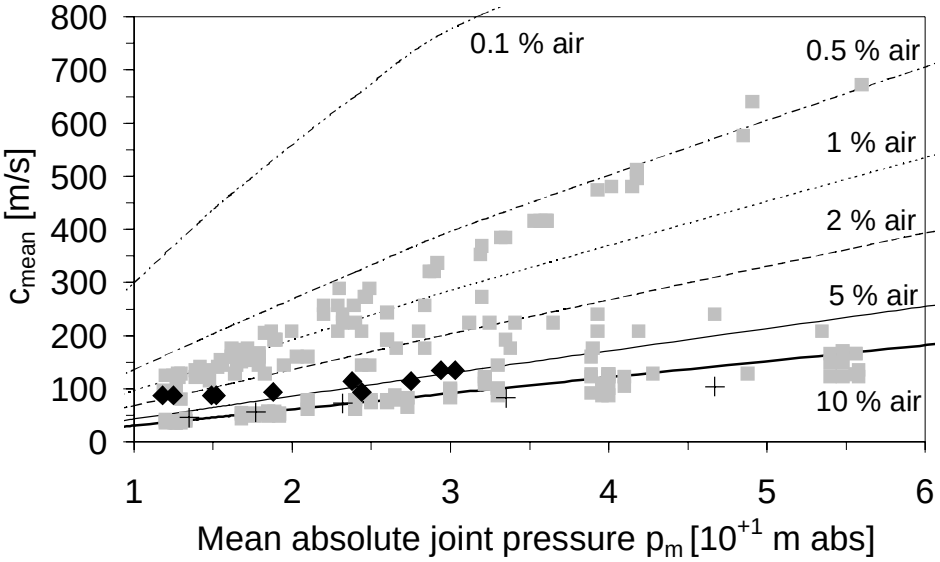

Fig. V-68 Determination of the mean wave celerity c_{mean} (m/s) as a function of the mean pressure value p_m inside the joint. Results are for core (+ sign) and developed (♦ sign) jet impact conditions. The (■) symbol represents all data previously measured in the I and the L-joints.

4.4.8. Conclusions

The U-joint has only been studied at its midpoint (sensor (d)). At that location, the pressure pattern is close the one for pool bottom pressures, i.e. almost no pressure amplification occurs. This also corresponds to the pressures measured at the middle of the L-joint. The air contents are very similar to the ones encountered in the L-joint, up to 20 %. It is assumed that the U-joint at its end behaves like the L-joint, i.e. significant pressure amplifications occur only at high jet velocities and an air cavity is formed in the downstream part of the joint.

4.5. The two-dimensional I-joint (2D-I) under the impact of a cylindrical jet

The two-dimensional I-joint is investigated to define the relevance of the width of the joint on the pressure pattern inside. The width of the joint can become important when the joint is much larger than the width of the jet at its impact at the pool bottom. Although this situation is rarely encountered in practice, its study contributes to the overall assessment of transient pressures in rock joints. Particularly the spectral contents and air concentrations are compared with the one-dimensional I-joint. The results are taken from Bollaert & Schleiss (2001f).

4.5.1. Geometrical configuration

The geometrical configuration of the two-dimensional I-shaped rock joint is presented in Fig. V-70. It has a height of 0.80 m, just like the one-dimensional case, and a width of 0.60 m instead of 0.01 m. The joint has a thickness of 1 mm and is closed at its end.

Nine sensors were used to assess the pressures: three at the pool bottom (sensor (a)) and six inside the joint. The pool bottom sensors correspond to the locations as described in § 3.5.5 on radial surface pressures. The radially most outwards sensor is situated at 150 mm from the jet's centreline. As such, a total width of 300 mm is covered, which corresponds to half of the joint width. Beyond this distance, both the root-mean-square and mean dynamic pressure coefficients were found to become negligible (§ 3.5.5, Fig. V-23). This has been visualized in Fig. V-71 for core jets and developed jets respectively.

In other words, the jet excitation covers about half of the width of the joint entrance, and the most severe loading happens near the centreline of the jet. This is particularly true for core jets. The higher the Y/D_j ratio, the wider becomes the jet excitation at the surface. For developed jets, both the mean and root-mean-square pressures cover the joint entrance much more than for core jets.

The six rock joint sensors are located on two vertical axes: one under the jet's centreline and another one near the side of the joint. As such, it is believed that the whole inside of the joint can be investigated. For comparison, the measurements that were made at the pool bottom are presented as follows: sensor (a) by the symbol (■), sensor (a^{ii}) by the symbol (▲) and sensor (a^{iv}) by the symbol (●). All three sensors are exciting the rock joint at a certain location.

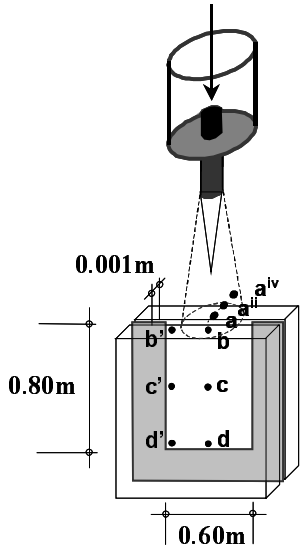

Sensor	Type	Position
a	pool bottom	25 mm from joint
a^{ii}	pool bottom	75 mm from joint
a^{iv}	pool bottom	150 mm from joint
b	rock joint	center, 50 mm inside
c	rock joint	center, 420 mm inside
d	rock joint	center, 790 mm inside
b'	rock joint	side, 50 mm inside
c'	rock joint	side, 420 mm inside
d'	rock joint	side, 790 mm inside

Fig. V-70 Geometrical configuration of the two-dimensional I-joint. In the following, the data obtained inside the one-dimensional I-joint are marked with the (■) symbol.

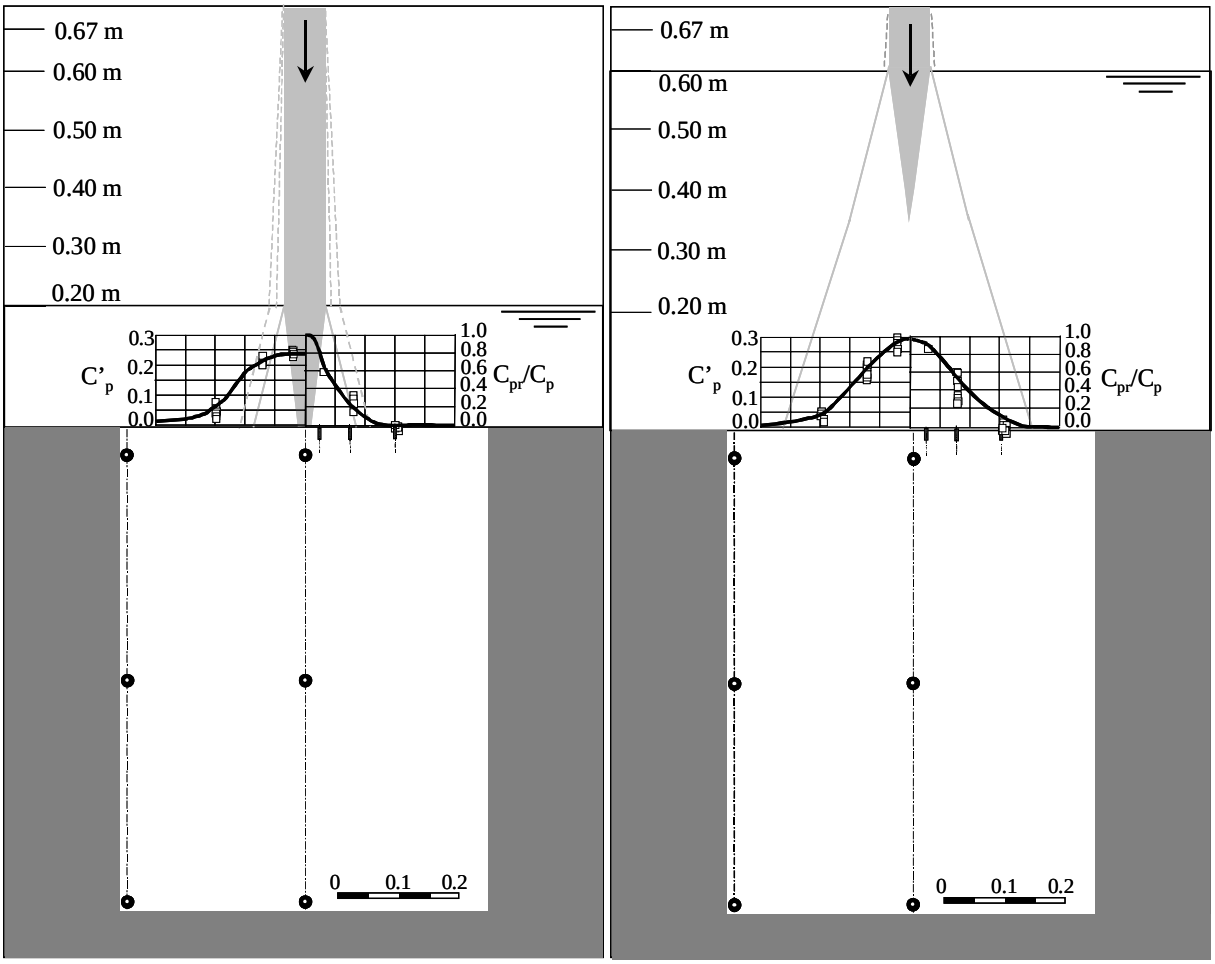

Fig. V-71 Visualization of the jet excitation at the entrance of the two-dimensional I-joint. Determination of the mean and the root-mean-square pressure coefficients as a function of the radial distance from the jet's centreline: a) for core jet impact; b) for developed jet impact.

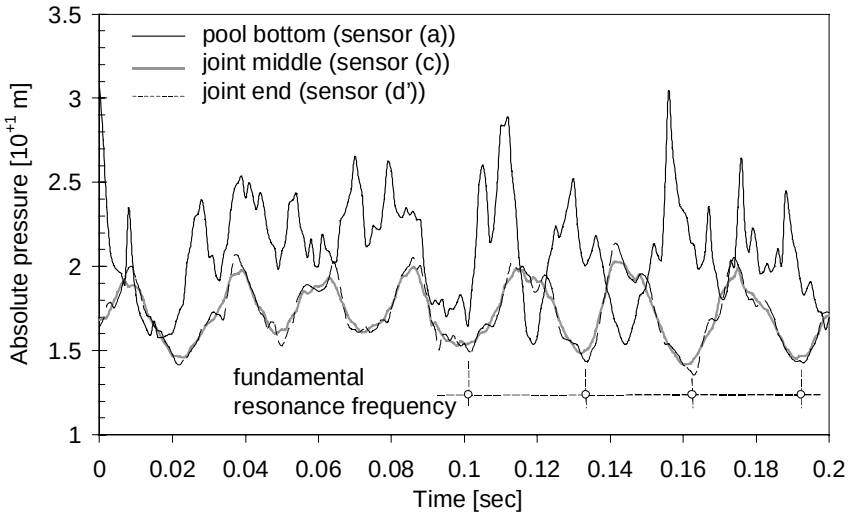

Fig. V-72 Comparison in the time domain of the pressure measured at the pool bottom and the corresponding pressures at the middle and at the end of the joint. The mean jet velocity is 19.7 m/s and the water depth 0.67 m. Fundamental and secondary frequencies of interest are clearly visible.

4.5.2. Measured pressure signal

The measured pressure signal in the time domain is presented in Fig. V-72. It can be seen that the pressures inside the joint are significantly lower than the ones at the pool bottom. This is due to the two-dimensional diffusion effect of the incoming non-uniform pressure distribution. Secondly, the pressures at the middle and at the end of the joint are characterized by a clearly outlined fundamental resonance frequency. This resonance frequency cannot be found in the pool bottom signal.

Moreover, the pressures at the end of the joint exhibit a second frequency of interest. This frequency seems to be much higher than the fundamental one. The middle of the joint does not show this second frequency.

4.5.3. Mean dynamic pressures

The mean dynamic pressure coefficients are presented for sensor (d) at the end of the joint, under the jet's centerline. Similar coefficients have been obtained for the five other sensors inside the joint and are not presented herein. Comparison with the values at the pool bottom is made for the three pool bottom sensors separately (Fig. V-73).

This allows quantifying the significance of the non-uniform pressure distribution at the entrance of the joint. Sensor (a) is presented by the symbol (■), sensor (a^{ii}) by the symbol (▲) and finally sensor (a^{iv}) by the symbol (●). All three sensors are exciting the rock joint at the location as indicated in Fig. V-71.

This shows that the values inside the rock joint represent a sort of averaged value of the ones measured at the three pool bottom sensors. It is also interesting to notice that the values inside the joint are in good agreement with the ones obtained at sensor (a^{ii}). Thus, the mean pressure coefficient of this surface sensor represents the mean pressure value that holds all throughout the joint.

The values for developed jets are relatively higher than the ones for core jets, probably due to the higher degree of covering of the joint entrance with increasing Y/D_j ratio.

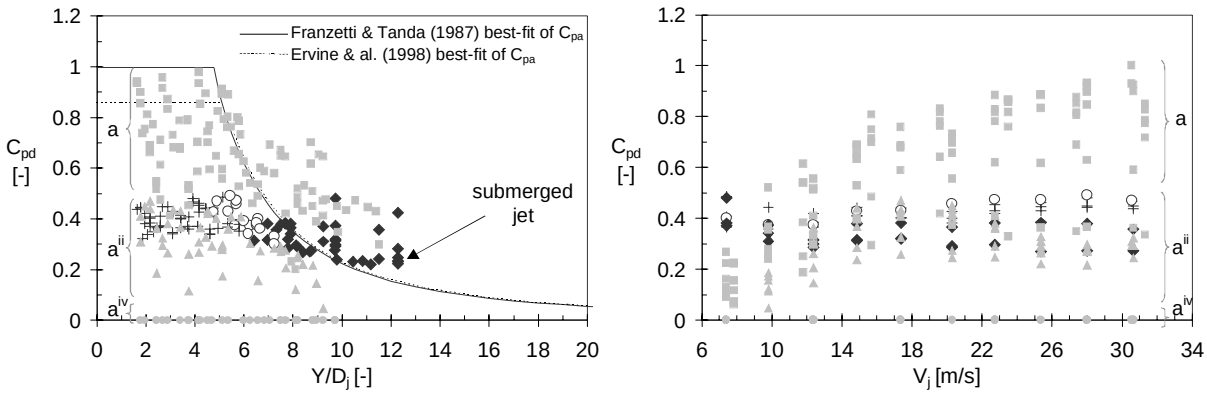

(a) (b)

Fig. V-73 Non-dimensional mean dynamic pressure coefficient C_{pd} measured at sensor (d) of the two-dimensional I-joint: a) C_{pd} as a function of the Y/D_j ratio; b) C_{pd} as a function of the mean jet velocity V_j. The data measured at the pool bottom are represented as follows: sensor (a) by symbol (■); sensor (a^{ii}) by symbol (▲) and sensor (a^{iv}) by symbol (●).

4.5.4. Root-mean-square pressures

No amplification of the pool bottom root-mean-square pressures is observed. The values inside the joint again constitute a sort of averaged value of the pool bottom root-mean-square pressures. It can be seen that the joint root-mean-square values correspond to the ones obtained at sensor (a^{iv}) (Fig. V-74).

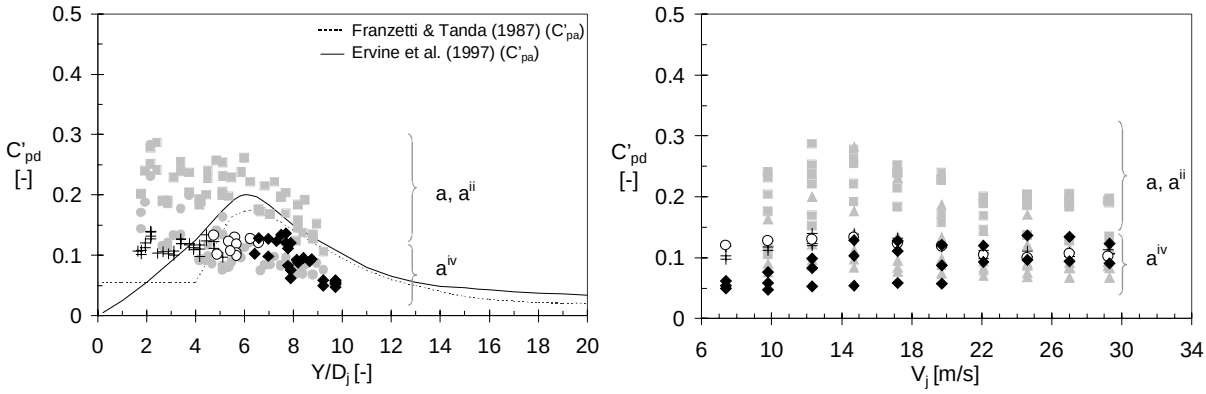

(a) (b)

Fig. V-74 Non-dimensional fluctuating dynamic pressure coefficient C'_{pd} measured at sensor (d) of the two-dimensional I-joint: a) as a function of the Y/D_j ratio; b) as a function of the mean jet velocity V_j. The data measured at the pool bottom are represented as follows: sensor (a) and (a^{ii}) by symbol (■), and sensor (a^{iv}) by symbol (●).

4.5.5. Extreme pressures

The positive extreme pressure coefficient is compared with the coefficients measured at the three pool bottom sensors (Fig. V-75). Similar to the root-mean-square pressure coefficients, the values inside the rock joint are in good agreement with the values obtained at sensor (a^{iv}). They also agree with the values at sensor (a^{ii}), but only for core jets. When looking at the second graph, it becomes obvious that the values also correspond for developed jets, but at high jet velocities. As a conclusion, the extreme pressures inside the joint are equal to the extreme pressures at the pool bottom. Nothing seems to indicate that an amplification of the surface pressures occurs inside the joint.

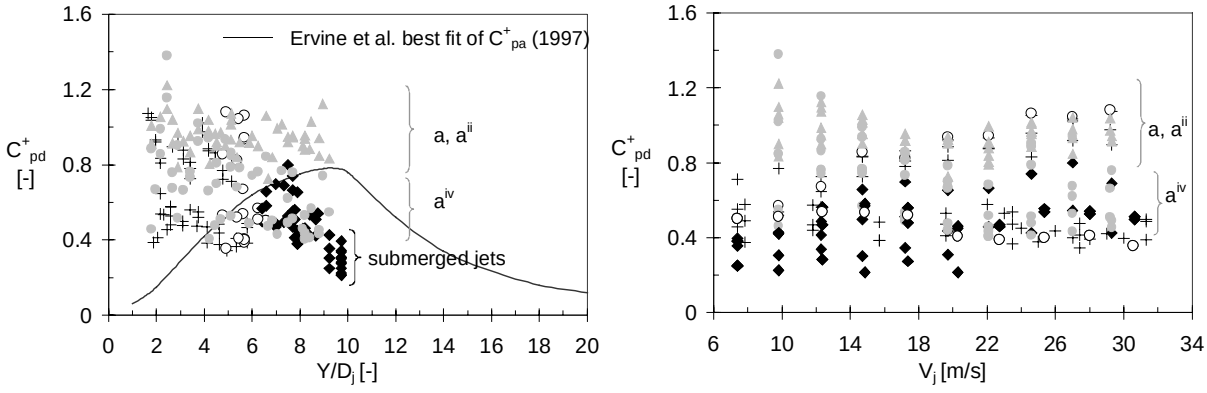

(a) (b)

Fig. V-75 Positive extreme dynamic pressure coefficient C^+_{pd} measured at sensor (d) of the two-dimensional I-joint: a) as a function of the Y/D_j ratio; b) as a function of the mean jet velocity V_j. The data measured at the pool bottom are represented as follows: sensor (a) and (a^{ii}) by symbol (■), and sensor (a^{iv}) by symbol (●).

4.5.6. Spectral analysis

The non-dimensional spectral content is presented in the frequency domain for sensor (c) and for sensor (d). The left hand side corresponds to core jet impact, the right hand side is for developed jet impact (Fig. V-76).

All the fundamental resonance frequencies are well expressed and appear at a frequency of about 35 Hz. Assuming a $\lambda/4$ – resonator model and a joint length equal to the one for the I-joint, i.e. 0.80 m, this corresponds to a wave celerity of 110-120 m/s. The fundamental frequency does not increase with increasing jet velocity. This is in contradiction with any previous observations for one-dimensional joints and is probably due to the low mean pressures that are encountered in the two-dimensional joint. Even at very high jet velocities, the absolute change in mean pressure compared to a low jet velocity is not sufficient to have a significant impact on the air content and the resonance frequency.

The second harmonic is also visible, especially at sensor (d). It occurs at a frequency of three times the fundamental frequency. As such, it could correspond to the second harmonic of the same resonance mode. This is verified in the next section on air content.

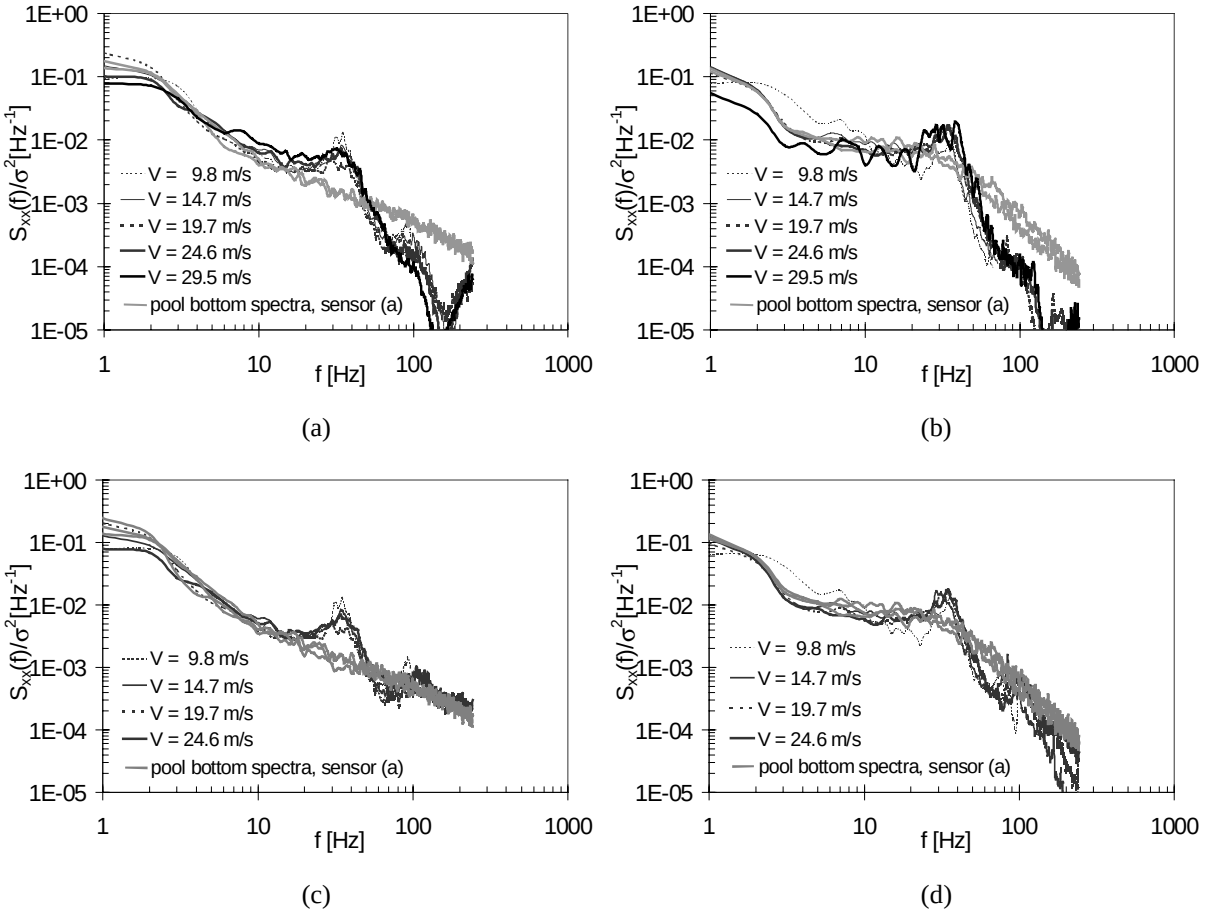

Fig. V-76 Non-dimensional spectral content of the U-shaped rock joint at the bend position (sensor (d)):
a) for core jets at sensor (c); b) for developed jets at sensor (c);
c) for core jets at sensor (d); d) for developed jets at sensor (d).

4.5.7. Air content

The mean air content and mean wave celerity are presented as a function of the mean pressure inside the joint in Fig. V-77a. For core and developed jets, it can be observed that the wave celerity exhibits a more or less constant value of 100 m/s, independent of the governing mean pressure in the joint. As such, the corresponding mean air content increases with mean pressure from 1 to 10 or even 20 %. This particular behavior is explained by an air content in the plunge pool basin that increases with increasing jet velocity.

Furthermore, the mean air contents for submerged jet impact are presented. They agree with the previous found relationships and, thus, correspond to air contents of 0.5 to 1 %.

Fig. V-77b visualizes the instantaneous celerity-pressure relationship in the two-dimensional I-joint. Comparison is made with the previous found relationships. Due to a lack of test runs at high enough acquisition rates, the found values have to be handled with precaution. They indicate, however, a similar trend as for the other tested joints.

Comparison between the mean and instantaneous wave celerities shows that, at low jet velocities, a good agreement is obtained. With increasing jet velocity, however, the mean celerity as derived from the fundamental resonance frequency progressively deviates from the measured instantaneous celerity-pressure relationships.

The instantaneous relationship could not be determined with sufficient accuracy. Hence, it cannot be concluded that the assumption of a $\lambda/4$ – resonator model is wrong or not.

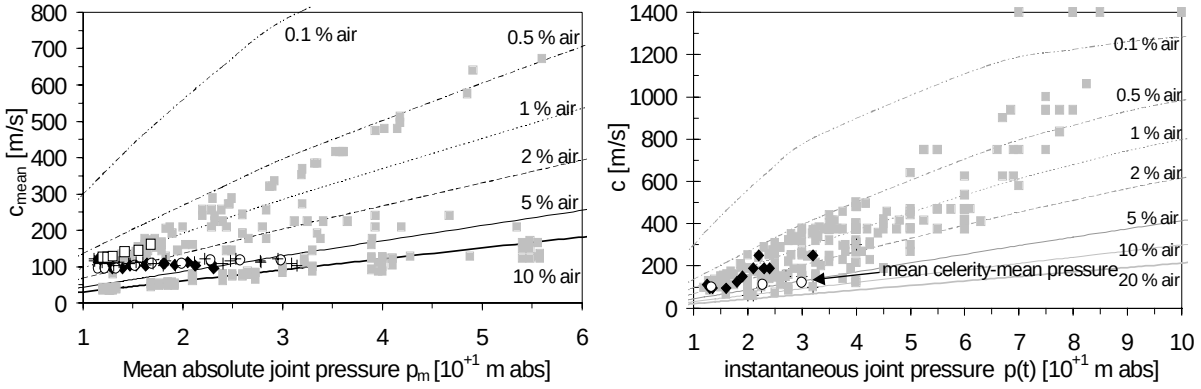

Fig. V-77 Instantaneous wave celerity inside the two-dimensional I-joint as a function of the instantaneous joint pressure: a) measured upstream of the bend; b) measured downstream of the bend. The data obtained inside the other joints are marked with a (■) symbol.

4.5.8. Conclusions

The mean and fluctuating part of the pressures inside the joint represent an average value of the ones measured at the three pool bottom sensors. The extreme pressures inside the joint correspond to the extreme pressures measured at the pool bottom, i.e. no amplification occurs inside. The air content goes up to 20 % at high jet velocities and corresponds to a more or less constant wave celerity of 100 m/s. It is believed that this high air content, as well as two-dimensional diffusion effects, is responsible for the absence of peak pressures. It has to be noted that a resonance frequency effectively occurs inside the joint for all jet impact conditions.

5. Dynamic pressures inside open-end rock joints

5.1. Introduction

The present section deals with open-end rock joints. These joints correspond to an open-open boundary system, in which the jet excitation is applied at both boundaries simultaneously. In other words, the process of dynamic uplift of rock blocks is dealt with. The joints have no downstream boundary condition. Both openings function as an entrance or upstream boundary condition.

As such, standing waves and resonance conditions inside the joints are generated by superposition of waves that enter the joint at one of the entrances and that travel forwards and backwards throughout the joint. It is assumed that wave reflections at the boundaries exhibit perfect compliance, i.e. the reflected pressure waves have the same amplitude as the incoming pressure waves but with the opposite sign. No energy is lost during this operation (Chapter III, § 2.2.5).

This corresponds to a $\lambda/2$ – resonator model. The fundamental resonance frequencies of such a model are twice as high as the ones of a $\lambda/4$ – resonator model (Chapter III, § 2.2.3). The presence of a high incoming pressure at a boundary can modify these theoretical fundamental assumptions. However, in the following, this effect is considered negligible. The mean wave celerities and air contents are defined based on the fundamental resonance frequencies. Verification is performed by means of cross-correlations between different measurement points. This leads to a celerity-pressure relationship.

The tested joint is similar to the U-joint that has been tested in section 4. The closed-end boundary of this U-joint has now been opened, so that the jet can directly excite both openings. As such, the length of the joint stays the same, but the boundary condition changes. This joint is called the D-joint, because of the outside connection between the two joint entrances. Similar to the other joints, the width is 10 mm and the thickness is 1 mm. The statistical characteristics and the air content of the D-joint will be compared with the measurements made at sensor (d) of the U-joint.

The uplift of rock blocks not only depends on the pressures inside the joints, but also on the surface pressure field (Chapter III, § 4.4.5). This pressure field has to be quantified in order to define the net instantaneous uplift pressures or forces on the block.

5.2. The D-shaped rock joint under the impact of a cylindrical jet outlet

5.2.1. Geometrical configuration

The geometrical configuration of the D-shaped rock joint is presented in Fig. V-78. It is similar to the U-joint, according to Fig. V-63, but has two openings at the pool bottom. These openings are at a distance of 0.075 m one from another. The joint thus consists of an I-shaped part with a length of 0.795 m, a 90° bend, a horizontal part of 0.075 m, a second 90° bend followed by a 0.795 m part straight upwards towards the second opening. The total length is 1.665 m.

Four pressure sensors are used for the D-joint: sensor (a) and sensor (a^i) at the pool bottom, sensor (c) at the middle and sensor (d) at the first bend. The former two sensors are used to determine the instantaneous surface pressure field over the block. As is shown in the detailed part of Fig. V-71, they are situated symmetrically in between the two joint openings.

Hence, it is believed that they constitute an accurate representation of the pressure field over the whole block surface. Therefore, when determining the net uplift pressures on the block, the value of the surface pressure is taken as the average value of these two sensors. Sensor (d) of the D-joint is compared with the measurements made at sensor (d) of the U-joint. For comparison, the measurements that were made inside the U-joint are presented by the symbol (■).

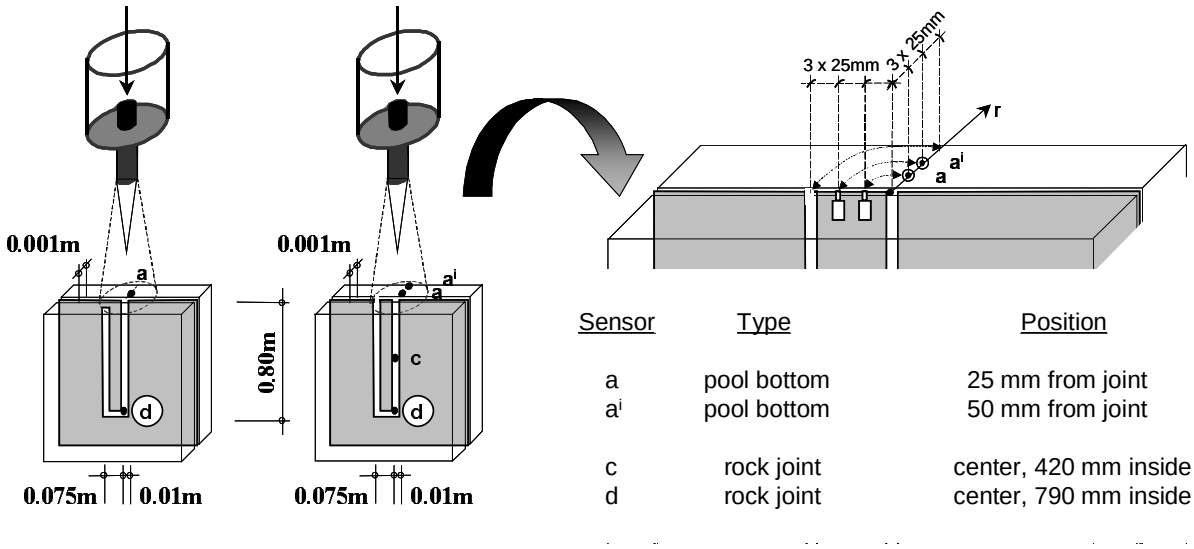

Fig. V-78 Geometrical configuration of the D-joint. The analysis of the pressures focuses on a comparison of sensor (d) of the U-joint with sensor (d) of the present D-joint. In the following, the data obtained inside the U-joint are marked with the symbol (■).

5.2.2. Mean dynamic pressures

Comparison with the mean values measured at sensor (d) of the U-joint shows that some differences are noticed (Fig. V-79). For core jets, the values are rather low, while for developed jets the values can be higher than the ones for the U-joint. These differences, however, are not significant.

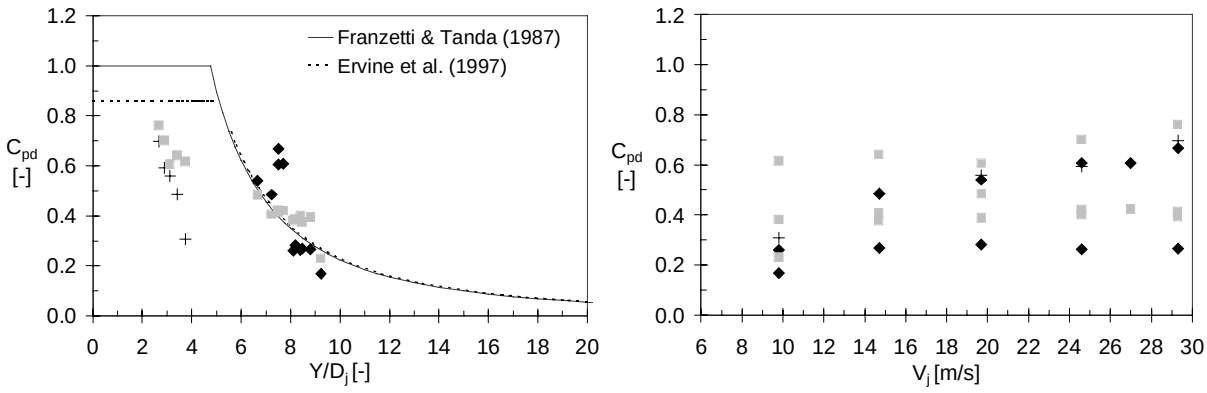

Fig. V-79 Non-dimensional mean dynamic pressure coefficient C_{pd} measured at sensor (d) of the D-joint:
a) C_{pd} as a function of the Y/D_j ratio; b) C_{pd} as a function of the mean jet velocity V_j;
The symbol (■) represents corresponding data measured at sensor (d) of the U-joint.

5.2.3. Root-mean-square pressures

The root-mean-square pressures are very similar to the ones observed inside the U-joint. This means that the consecutive peak pressures that were observed in closed-end rock joints probably do not occur in the present D-joint. This, however, does not exclude transient effects from happening. These have to be analyzed by taking the difference in pressure under and over the rock block, i.e. sensor (d) minus the average value of sensors (a) and (a^i). This is presented in Figs. V-80c & 80d. The differential root-mean-square coefficients are clearly higher than the ones at sensor (d) alone. Only for submerged jets, lower values are observed. The appearance of transient effects under the block cannot be excluded.

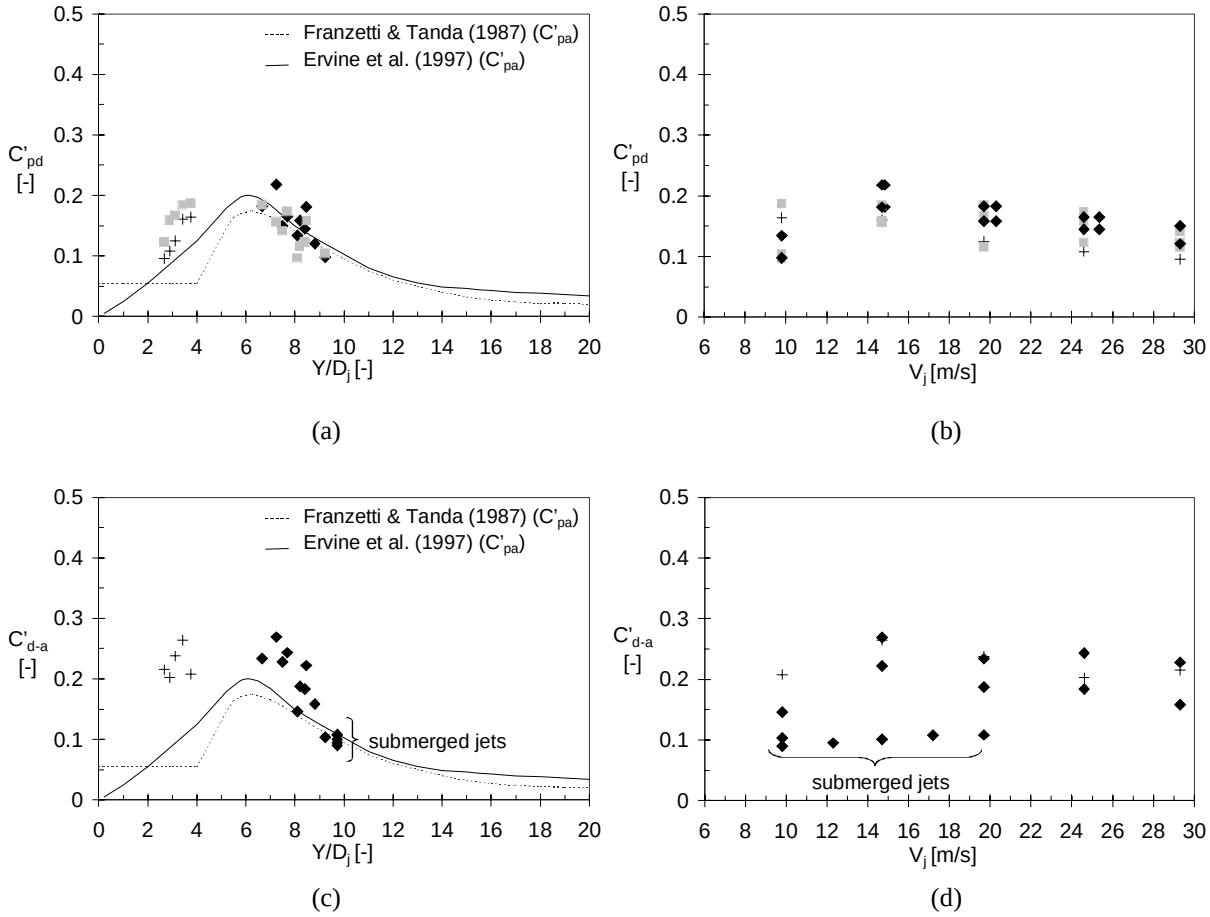

Fig. V-80 Non-dimensional fluctuating dynamic pressure coefficient C'_{pd} measured at sensor (d) of the U-joint:
a) C'_{pd} as a function of the Y/D_j ratio; b) C'_{pd} as a function of the mean jet velocity V_j;
c) C'_{d-a} as a function of the Y/D_j ratio; d) C'_{d-a} as a function of the mean jet velocity V_j.
The symbol (■) represents corresponding data measured at sensor (d) of the U-joint.

5.2.4. Extreme pressures and uplift coefficients

The positive extreme coefficients measured at sensor (d) are presented in Fig. V-81. However, it is more interesting to define the so-called net uplift coefficients C^{up}. These coefficients are defined as the maximum difference between the pressures at sensor (d) and the average value of the pressures at sensors (a) and (a^i). They correspond to the maximum net instantaneous uplift pressure that was measured on the simulated rock block.

Beside the values for submerged jets, it can be seen that most of the coefficients lie in between 0.8 and 1.6. Actual design criteria consider a C^{up} of 0.5-1.0 as the maximum possible value. Bellin & Fiorotto (1995) made measurements of net uplift forces on concrete slabs and proposed an absolute maximum value of 0.5. Liu et al. (1998) measured net uplift pressures on simulated rock blocks of 2 to 4 times the root-mean-square value, i.e. also corresponding to uplift coefficients of 0.5 to 1.0. By applying a maximum underpressure all under the rock block together with a zero pressure at the whole surface of the block, the physically maximum plausible value of 1.0 is obtained. This, however, is not possible in practice.

Hence, although the encountered pressure differentials seem to be much less violent than the ones observed in closed-end joints, it becomes obvious that transient pressure waves underneath rock blocks can play a significant role in the process of dynamic uplift.

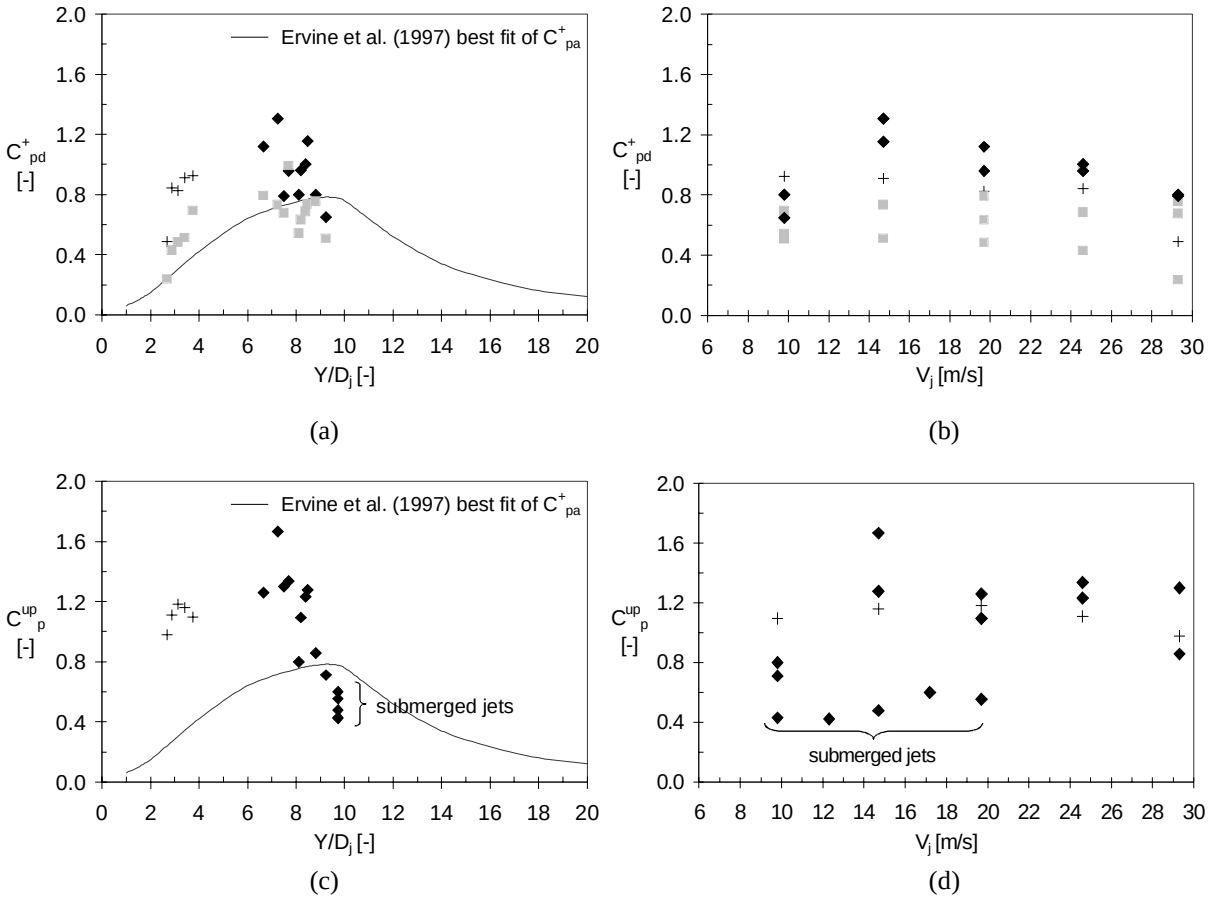

Fig. V-81 Non-dimensional positive extreme coefficients C^{+}_{pd} and net uplift pressure coefficients C^{up}_{p}:
a) C^{+}_{pd} as a function of Y/D_j; b) C^{+}_{pd} as a function of V_j.
c) C^{up}_{p} as a function of Y/D_j; d) C^{up}_{p} as a function of V_j;
The (■) symbol represents corresponding data measured at sensor (d) of the U-joint.

5.2.5. Amplification factor Γ^{up}

Most of the amplification factors are higher than 4, which is the maximum possible value that is characteristic for plunge pool bottom pressures (Fig. V-82).

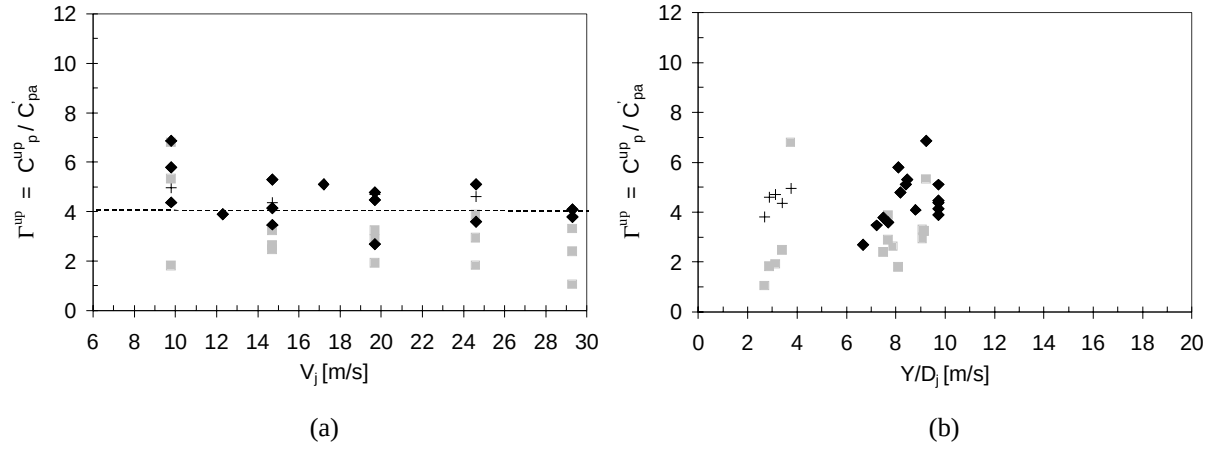

Fig. V-82 Amplification factors between pressures at sensor (d) and corresponding pool bottom pressures:
a) Γ^{up} as a function of the mean jet velocity V_j; b) Γ^{up} as a function of the Y/D_j ratio.
The (■) symbol represents corresponding data measured at sensor (d) of the U-joint.

The factors are higher than the ones calculated at the same location but for a closed-end joint. This indicates that the amplitude modulation inside the joint at that location is more significant for an open-end than for a closed-end. This finding is not so surprising given the fact that, for a $\lambda/2$ – resonator, sensor (d) is the most sensible location for transient wave effects.

Open-open resonators exhibit, for the fundamental resonance mode, a pressure node at both the open-ends, together with an antinode in the middle of the joint. Sensor (d) is located almost at the middle of the joint. It is representative for the pressure amplification inside.

5.2.6. Spectral analysis

The spectral content for core and developed jets is presented in Fig. V-83. The fundamental resonance frequencies are remarkably well distinguished, even at high jet velocities. This points, at first sight, towards low air contents inside the joint. However, when analyzing the frequencies, one can observe that the values of the fundamental ones are higher than the ones for the U-joint.

Assuming a $\lambda/2$ – resonator model, for which $c = 2 \cdot L \cdot f_{res}$, the celerity inside the present D-joint should be half of the celerity of the U-joint with the same length, provided that the same resonance frequency holds in both cases. For the U-joint, with a closed-end boundary, fundamental frequencies of 10 to 25 Hz have been noticed. For the present D-joint with the same length, frequencies of 20 to 40 Hz are obtained. In other words, the air contents in the D-joint are comparable to the ones in the U-joint.

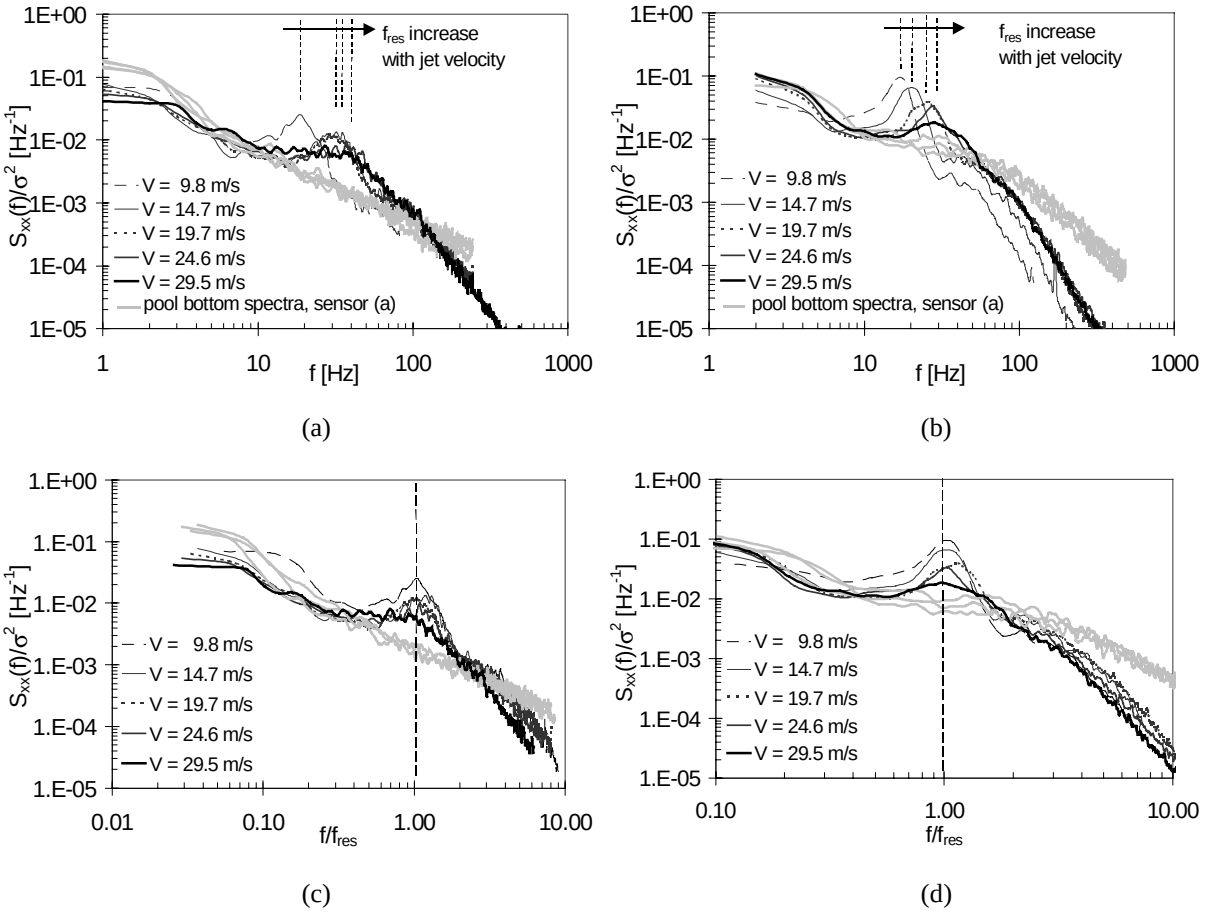

Fig. V-83 Non-dimensional spectral content of the U-shaped rock joint at the bend position (sensor (d)):
a) for core jets as a function of frequency; b) for developed jets as a function of frequency;
c) for core jets as a function of f/f_{res}; d) for developed jets as a function of f/f_{res}.

Secondly, the secondary harmonics are visible for developed jets. As they occur at twice the fundamental frequency, they could be related to reflections at the first bend. These reflections could correspond to resonance waves that travel in the first part of the D-joint only, i.e. at more or less half of the total length of the joint.

Finally, Fig. V-84 presents the spectral content measured at sensor (c). The relative importance of the secondary harmonic is much increased compared to sensor (d). This further strengthens the statement that this secondary harmonic probably occurs within the firs part of the D-joint. As the significance of the fundamental frequency is largely reduced at sensor (c), because situated too far away from the middle of the joint, the secondary harmonic becomes more visible.

The present assumptions on resonance modes and air contents are verified in the next paragraph by means of pressure wave celerity measurements. Both mean and instantaneous celerities have been determined.

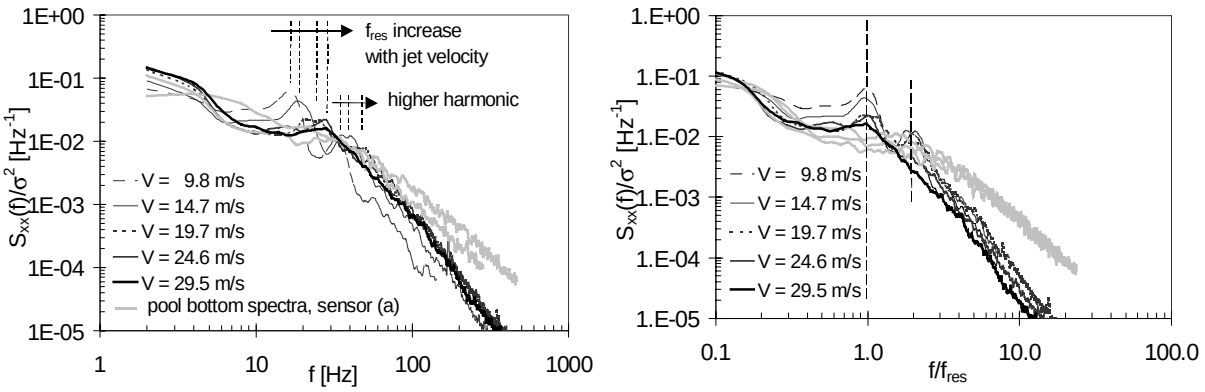

(a) (b)

Fig. V-84 Non-dimensional spectral content at the middle (sensor (c)) of the D-shaped rock joint, for developed jet impact:
a) as a function of frequency; b) as a function of f/f_{res}.

5.2.7. Air content

The mean wave celerity is easy to define because of the well-expressed fundamental resonance frequencies. Average air concentrations of 5 to 20 % have been found. These values are comparable to the ones derived for the L-joint and the U-joint. Moreover, the instantaneous wave celerity has been determined as a function of the instantaneous joint pressure. The celerity-pressure relationship is very close to previously found curves. Similar scatter in values can be observed. The assumption of a perfect $\lambda/2$ – resonator model has been verified by determining the celerity-pressure relationship for different test runs. Also, at each test run, the mean pressure has been determined and added to the curves. The so found mean celerity has to correspond to the one as given by the mean celerity-mean pressure relationship in Fig. V-80a.

A first example is given in Fig. V-85c for a jet velocity of 14.7 m/s and a plunge pool depth of 0.60 m. This corresponds to a mean pressure inside the joint of 19.4 m (absolute value). Based on the fundamental resonance frequency, a mean celerity of 75 m/s has been found in Fig. V-85a. When added in Fig. V-85c, it can be seen that a good agreement is obtained. A second example is presented in Fig. V-85d for a jet velocity of 29.5 m/s and the same plunge pool depth. The mean pressure value is now 32.8 m (absolute value). This was found to correspond to a mean celerity of 95 m/s. When added in Fig. V-85d, a value somewhat lower than the instantaneous celerities can be observed. The reason for this could be the lack of precision of the instantaneous celerity-pressure relationship. The data points have been obtained at a 1'000 Hz acquisition rate. Due to the rather high air contents and thus low celerities, this revealed to be sufficient for an appropriate determination.

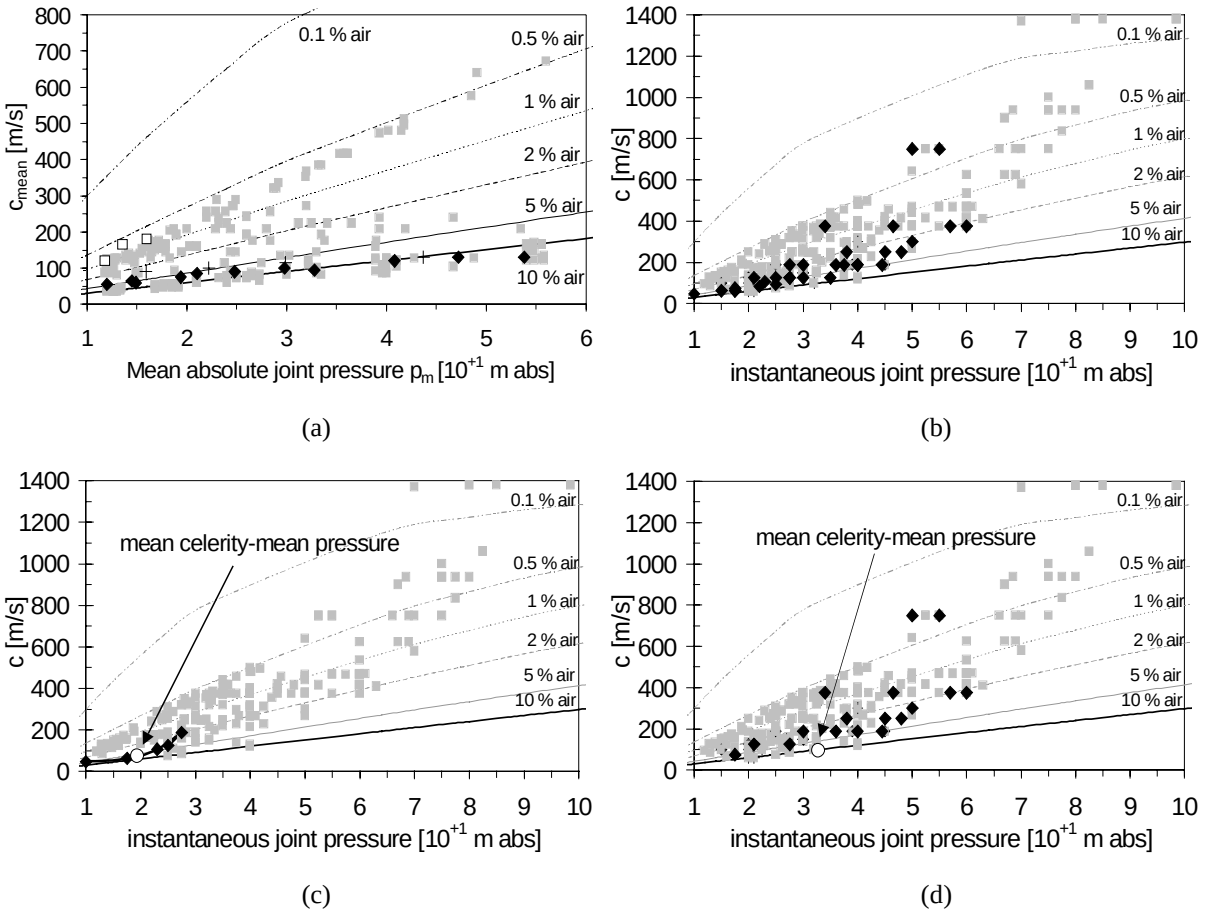

Fig. V-85 Wave celerities inside the D-joint. Data obtained for submerged jets are marked with (□). Data obtained inside other joints are marked with (■).
a) mean celerity; b) instantaneous celerity-pressure relationship;
c) comparison for a jet velocity of 14.7 m/s; d) comparison for a jet velocity of 29.5 m/s.

Thus, this cannot be the reason. Secondly, it is not excluded that the fundamental resonance frequency has been shifted towards a lower value by the presence of the secondary harmonic. This, however, is impossible to verify. Furthermore, point-to-point correlations have been performed between sensor (c) and sensor (d), i.e. in the first vertical part of the D-joint. The mean celerities are calculated based on measurements of the fundamental frequency, which is valid throughout the whole joint length. Hence, it could be argued that the first vertical part of the joint is not representative for the whole joint length. Similar to the L-joint, air could get trapped in the horizontal part. As such, somewhat more air could be expected at that location, influencing so the fundamental resonance frequency. It is believed that the latter explanation is the most plausible one. The L-joint already exhibited a higher air content in the horizontal part than in the vertical leg. The physical reason, however, is not yet clear. It could be due to buoyancy effects or leakage of fluid from the joint at high jet velocities.

5.2.8. Conclusions

The open-end joint corresponds to a $\lambda/2$ – resonator model and generates air contents that are similar to the ones for closed-end joints. The fundamental resonance frequencies are clearly distinguishable for all jet impact conditions. Net uplift coefficients of 0.8 to 1.6 times the incoming kinetic energy of the impacting jet have been measured. This is significantly higher than any previous assumptions in literature and demonstrates that transient effects have to be accounted for.

6. Conclusions on transient pressures in open-and closed-end rock joints

The present chapter presents the results of dynamic pressure measurements that have been performed at a simulated plunge pool bottom and simultaneously inside differently shaped rock joints. The rock joints are artificially created and open or closed at their end. Both one-and two-dimensional configurations have been investigated.

The one-dimensional rock joints are defined as joints for which the width at the entrance is small compared to the zone of jet impact. For such joints, it has been found that, for the closed-end cases, a **$\lambda/4$ – resonator model** can be assumed for the incoming pool bottom pressures. This means that the power spectral content of the impacting jet becomes both amplitude and frequency modulated inside the joint. Hence, significant transient pressure **amplifications** occur inside these joints, particularly at their middle and their end.

The generation of severe transient phenomena is greatly enhanced by the presence of **free air bubbles** inside the joints. These bubbles are transferred from the plunge pool into the joint or are being released from within the liquid following a sudden pressure drop. They make the air-water mixture highly compressible, resulting in a decrease of the resonance frequencies and related wave celerities. For submerged jets and ideal core jets, air contents between 0.5 and 1 % have been found. For real core jets and developed jets, the air contents fluctuated between a lower limit of 0.5-1 % and an upper limit of about 20 %. The relationship between the wave celerity and the pressure that governs inside the joint furthermore revealed that a part of the free air is released from the water following a pressure drop. The opposite effect occurs during a pressure rise. This seems to happen quasi instantaneously, which is novel to the author's knowledge.

Moreover, it has been found that for a perfectly planar I-shaped rock joint, without any branches or changes in orientation, a more or less homogenously distributed air content is present. An L-shaped rock joint with a 90° bend, on the contrary, redistributed the air towards the horizontal part downstream of the bend. As such, two fundamental resonance frequencies occurred, from which the one downstream of the bend is largely predominant. However, it could be concluded that such changes in orientation of the joint pattern are of secondary importance for the amplification of the pressures that enter the joint at the pool bottom surface.

The open-end rock joint corresponds to a **$\lambda/2$ – resonator model** and generates air contents that are similar to the ones for closed-end rock joints. Net uplift pressures of 0.8 to 1.6 times the incoming kinetic energy of the impacting jet have been measured. This is significantly higher than any previous assumptions in literature and demonstrates that transient effects have to be accounted for.

The two-dimensional rock joint diffuses the incoming pressures throughout the whole inside surface of the joint. As such, much lower pressures are obtained. However, the spectral content of the incoming pressures still becomes amplitude and frequency modulated. Air contents between 1 and 10 % have been found, for an almost constant wave celerity of 100 m/s.

As a conclusion, the pressure pattern inside closed-end rock joints can be described by a **continuous change between peak pressures and periods of near-atmospheric pressure**. This cyclic character makes it particularly interesting to apply the found hydrodynamic loading to tensile failure criteria of intermittently jointed rock. This is because these criteria are based on brittle crack propagation or progressive crack propagation by fatigue.

For practice, three parameters are of interest: the maximum possible pressure value at the joint end as a function of the incoming kinetic energy, and the amplitude and the frequency of the cycling loading. With these three parameters, both instantaneous and time-dependent propagation of rock joints can be fully assessed.

7. Pressure measurements just downstream the joint entrance

The pressure measurements at the entrance of the joints, i.e. at sensor (b), revealed a pressure pattern that was completely different from the previously discussed sensors. A typical pressure signal in the time domain is presented in Fig. V-86, for a plunge pool depth of 0.20 m and a jet velocity of 25 m/s. The measurements have been made in the two-dimensional I-joint. As a matter of fact, only very few pressure measurements could be made at this particular sensor location, due to a systematic break-down of the sensors at that place. The reason for this break-down is not very clear.

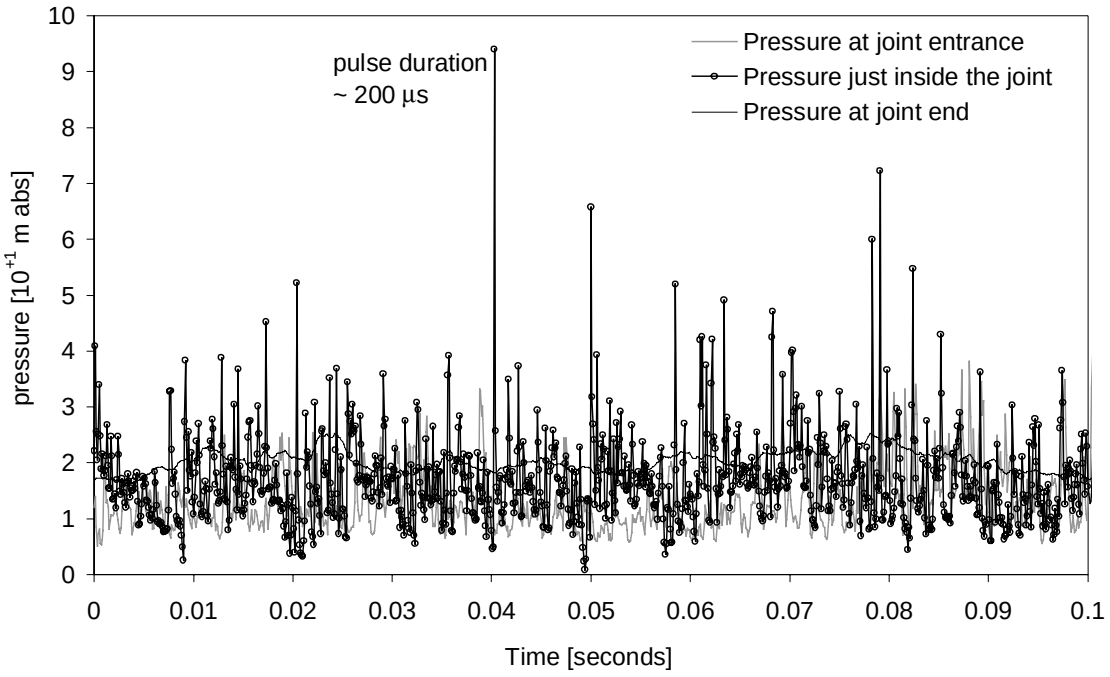

Fig. V-86 Example of pressure signal in the time domain measured at sensor (b) for a jet velocity of 25 m/s and a plunge pool depth of 0.20 m.

The obtained peak pressures are unusual for a two-dimensional rock joint. They do not correspond to the pressures found in the middle and at the end of this joint. A more detailed look reveals that the time scale of the peak pressures is completely different from what should be expected based on transient flow assumptions. Typical pulse durations are in the order of only 200 µs, i.e. two orders of a magnitude smaller than the peak pressures discussed in the previous sections.

Hence, a different physical phenomenon is happening here. The most plausible explanation that could be found up to now is that a **very weak form of cavitation** impact occurs at the entrance of the joint. Two arguments strengthen this hypothesis. First of all, during the test runs, a weak cavitation noise could be heard at the entrance of the joint. This noise is best comparable to the noise of an egg that is being cooked on a hot plate. It probably represents consecutive impacts on the steel structure.

Secondly, the measured pressure signal has been studied more in detail and might correspond to a weak form of cavitation. Fig. V-86 shows that, at multiple occasions, a pressure very close to the vapour pressure has been measured. This very low absolute pressure was systematically immediately followed by a very high pressure peak that only lasted during 1 measurement point. The test run was performed at only 10 kHz, so the exact shape of the pulse cannot be predicted. A detailed view of one pulse has been presented ion Fig. V-87.

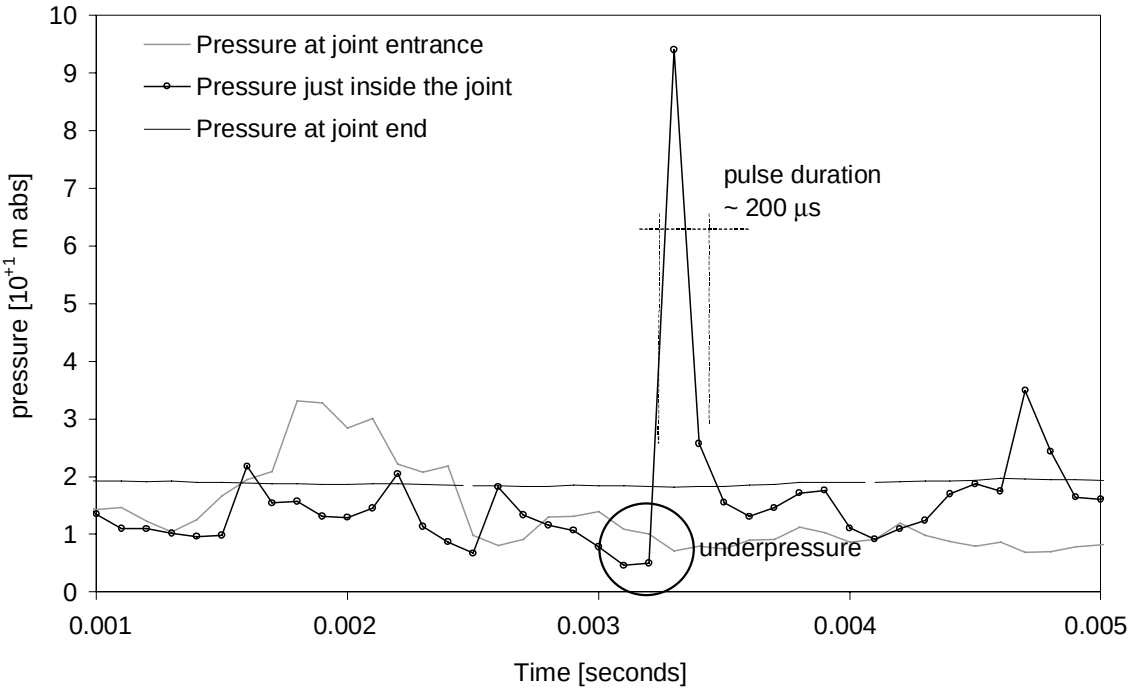

Fig. V-87 Detailed view of a pressure pulse in the time domain measured at sensor (b) for a jet velocity of 25 m/s and a plunge pool depth of 0.20 m. The acquisition rate was 10 kHz.

First of all, an absolute pressure head of 3 to 4 m has been measured. This is not low enough to reach vapour pressure. However, it can be seen that the real spike exactly happened in between two consecutive measurement points. Hence, it has not been measured. This underpressure is followed by a very high pressure peak, up to 100 m of pressure head or 1 MPa. This high pressure only lasted for one measurement point, i.e. about 200 µs in total.

It is obvious that the form of the measured pressure pattern more or less corresponds to cavitation impact. The time scale, however, seems to be too long. Cavitation impact peaks typically happen at several tens of µs, and not during hundreds of µs. This distorted time scale could be due to the particular air bubble presence in the joint. Several violent transient phenomena probably occur simultaneously, such as weak cavitation, air bubble collapse and transfer, air bubble release and resolution, shock wave propagation, etc.

It is interesting to compare the found pressure pattern with cavitation implosion pressure measurements that have been made downstream of a high-head gated outlet structure in Victoria, Australia (Lesleighter, 1988). The sensors were located at about 0.50 m downstream from the gate and the data acquisition rate was 4 kHz. “Bangs” at irregular and regular intervals were experienced, and it was common to hear a succession of bangs to simultaneously see the appearance of pressure pulses on an oscilloscope. Such pulses are presented in Fig. V-88.

Although it is very difficult to distinguish the exact duration of the pulses, they can be estimated at about a millisecond, i.e. 1000 µs. In other words, they are significantly longer than the pulses measured at the present facility. Their shape and maximum values seem particularly similar however. These pulses were experienced just upstream of a zone of severe cavitation damage due to the formation of large vapour cavities.

Hence, the similarity between these pulses and the present measurements strengthens the hypothesis of weak cavitation. These aspects merit further attention in future research.

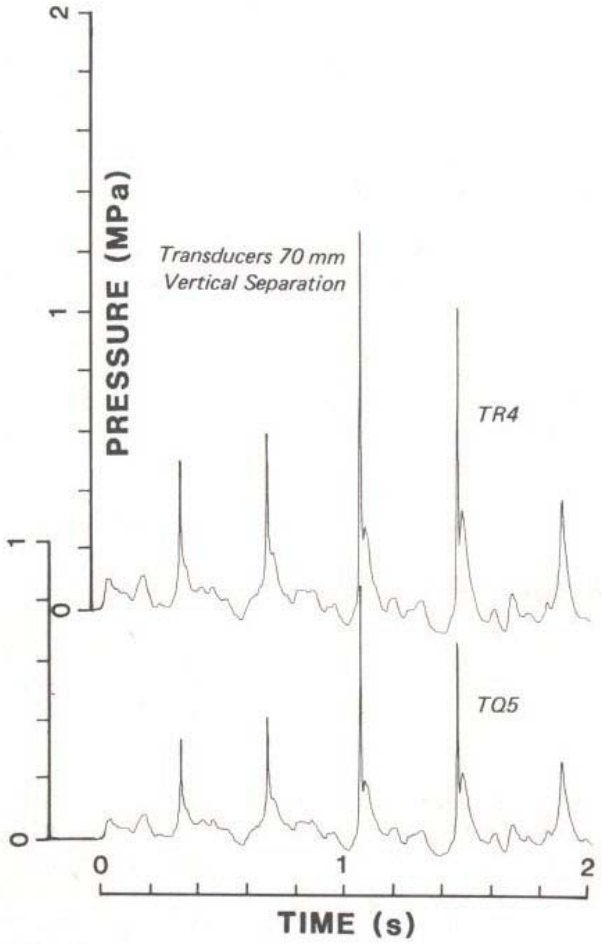

Fig. V-88 Detailed view of pressure pulses in a conduit at about 0.50 m downstream of a high-head gate. The acquisition rate was 4 kHz (Lesleighter, 1988).

Chapter VI. Numerical simulation of pressures in rock joints

1. Introduction

The theoretical framework outlined in Chapter III and the analysis of transient pressure measurements in Chapter V pointed out that dynamic pressures inside closed-and open-end rock joints are governed by a cyclic alternation of short-lived peak pressures and periods of low near-atmospheric pressures.

As will be outlined in Chapter VII, the application of this hydrodynamic loading to rock mass failure criteria needs the definition of the following four parameters:

1. maximum dynamic pressure C^{max}_{p}
2. characteristic amplitude of pressure cycles Δp_c
3. characteristic frequency of pressure cycles f_c
4. maximum dynamic impulsion C^{max}_{I}

The first parameter is relevant to brittle propagation of closed-end rock joints. The second and third parameters are necessary to express time-dependent propagation of closed-end rock joints. The fourth parameter is used to define dynamic uplift of rock blocks formed by open-end rock joints.

The definition of these parameters is performed in Chapter VII and is based on the experimental results. However, only five different rock joint configurations have been investigated during the tests. It is apparent that the corresponding pressure results do not cover the whole range of values of the geomechanical parameters of a fractured rock mass. For example, the influence of the length of a closed-end rock joint on the peak pressure at its tip has not been clearly outlined during the test runs. Furthermore, the relevance of the exact air content inside the joint on the amplification has been pointed out but merits a more detailed investigation.

Hence, the present chapter only presents a simplified numerical simulation of the transient pressures inside closed-end rock joints. This simulation assumes a homogeneous pseudo-fluid inside the joints and is based on the one-dimensional transient pressurized flow equations. Particular attention has been drawn on the relation between the celerity of the pressure waves and the mean pressure value in the joints. Furthermore, two-phase damping effects have been considered in a simplified manner.

2. Model concept

2.1. Basic equations

The numerical simulation makes use of the derivative form of the one-dimensional transient flow equations for a homogeneous two-component air-water mixture. These have already been presented in simplified form in Chapter II but are repeated here in the form they have been used for the numerical simulation (Bollaert et al., 2001c):

$$\frac{\partial p}{\partial t} + \frac{c^2}{g} \cdot \frac{\partial V}{\partial x} = 0 \qquad \text{mass conservation} \qquad (6.1)$$

$$\frac{\partial (\eta V)}{\partial t} + \frac{\partial}{\partial x}\left(\beta V^2\right) + g \cdot \frac{\partial p}{\partial x} + \frac{1}{2} \cdot \frac{\lambda}{D} \cdot V \cdot |V|^e = 0 \qquad \text{momentum conservation} \qquad (6.2)$$

in which p is the pressure head (m), V the mean velocity (m/s), c the pressure wave celerity (m/s) and D the hydraulic diameter. For a small joint, the hydraulic diameter D may be taken equal to twice the joint thickness. The terms λ, η and β account for steady, unsteady and non-uniform velocity distribution friction losses. They are three parameters to be optimized. The steady friction factor λ is calculated based on the Colebrook-White formula. The unsteady friction factor η depends on the cyclic behavior of the flow inside the joints. For a uniform velocity distribution, β equals 1 in the convective term of equation (6.2).

It is assumed that these friction terms also incorporate other possible energy losses, such as friction due to heat or momentum exchange between the air and the water phase. As such, they cannot be compared with the Darcy-Weisbach friction term that is usually applied for one-phase steady-state flow. Their values are often quite different, due to the particular damping effect generated by the two-phase transient character of the flow (Martin & Padmanabhan, 1979; Ewing, 1980). For turbulent flow conditions inside the joint, the exponent *e* has to be taken equal to 1. However, as a result of the narrow geometry, the Reynolds numbers can be very low (~ O (10^2)) and laminar flow might be more plausible under certain circumstances. The corresponding exponent *e* has then to be taken equal to 0.

The two-component air-water mixture inside the joint is simulated as a pseudo-fluid with average properties and, thus, only one set of conservation equations. The density is hardly modified by the gas and, at relatively small gas contents, may be approximated by the density of the liquid. This means that any possible mass or momentum transfer between the two components is excluded. Furthermore, no slip velocity or heat transfer between the two phases is considered, so the energy equation is omitted. According to Wylie & Streeter (1978), this simplified approach is valid for air contents of at least 2 %. Martin & Padmanabhan (1979) numerically verified the homogeneous flow assumption for air contents of up to 30 %, and found correct wave celerities. Therefore, in the here presented approach, the homogeneous flow model has been applied. No further assumption is made regarding the distribution of air throughout the joint, so the wave celerity c is dependent on both time and space.

During the experiments, the air concentration inside the joints was found to depend on the pressure. The volume of the air bubbles continuously changed as a function of the latter. Thus, significant transfer between the two phases occurs. Two physical laws dictate this transfer: the ideal gas law and Henry's law (Chapters III & V). This assumption was based on the shape of the celerity-pressure relationships, which were found to be of changing mass of free air as a function of pressure.

Hence, it has been preferred in the following to verify this basic assumption by using a constitutive relationship between the celerity c(x,t) and the pressure p(x,t). This relationship replaces any kind of transfer (heat, mass or momentum) that could occur between the air and the water and has the advantage of simplicity. It is dependent on both space and time. A quadratic form seems to match quite well with the measured data points and is written as follows:

$$c(x,t) = k_1 + k_2 \cdot p(x,t) + k_3 \cdot p^2(x,t) \tag{6.3}$$

in which k_1, k_2 and k_3 are three numerical parameters that have to be optimized. In some cases, a double quadratic form revealed to be more appropriate.

2.2. Numerical scheme

The numerical scheme that is used to solve a weak formulation of this set of three equations is a 2nd order finite-volume scheme. As the experimental pressure measurements revealed the appearance of violent transient and highly non-linear wave phenomena, it is obvious that a shock-capturing scheme, introducing a fit amount of numerical dissipation without excessive smearing of the peak pressures, is preferable.

The numerical code defines an unsteady pressure signal as weak upstream condition and imposes a zero flow velocity as weak downstream condition (at the end of the joint). The upstream pressure signal has been taken from the experimental measurements made at the entrance of the rock joint. As the transfer of this pressure signal from the pool bottom to the joint cannot be fully assessed and probably needs some length to be introduced into the joint, a weak formulation of the upstream boundary condition has been chosen. This implies that the upstream boundary condition $p_{up}(t)$ is only applied as outer condition on the upstream finite volume, and not as condition over the whole volume directly. It is believed that this smoothing of the boundary condition is most plausible for the physical situation. The boundary conditions have been presented in Fig. VI-1 together with the numerical grid.

Furthermore, an adaptive time stepping has been applied. The criterion that has been used to determine the critical time step is a classical Courant condition, in which the Courant number $C_t = (V+c)\cdot(\Delta t/\Delta x)$ is taken equal to 0.5. This condition is checked at every node of the system, and the most restrictive one is retained for the next time step. The calculations revealed numerical time steps on the order of $1\cdot10^{-5}$ to $5\cdot10^{-5}$ seconds, i.e. one to two orders of magnitude smaller than the time step of the experimental tests (= 0.001 seconds at 1'000 Hz acquisition rate).

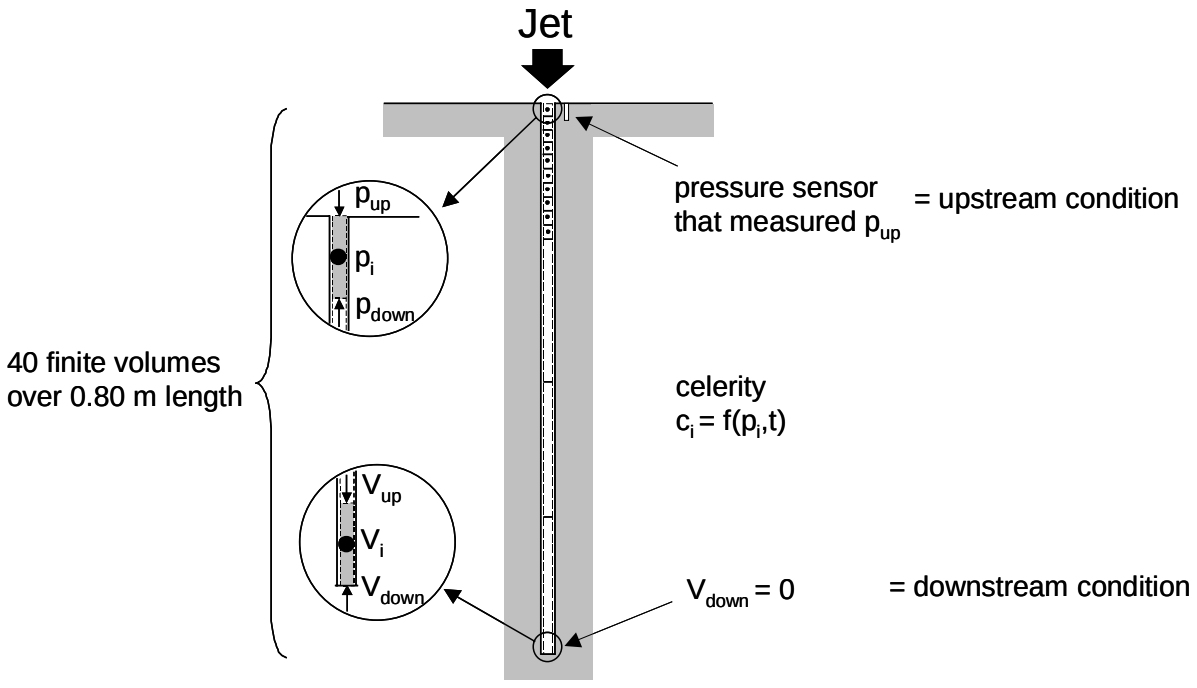

Fig. VI-1 Definition of the numerical grid and of the upstream and downstream boundary conditions.

2.3. Optimisation criteria

The adjustment of the friction losses parameters λ, η, β, and of the three k-parameters, is based on the following criteria: mean pressure value, root-mean-square value, maximum and minimum pressure values and finally the histogram and the power spectral density of the computed pressure values. The computed values are systematically compared with the corresponding measured values for different test runs.

For the histogram and the power spectral density, a least-square criterion has been applied. The application of such a criterion to the pressures in the time domain was found to be impossible due to the small time lag that can exist between the input pressure signal (measured at sensor (a)) and the output signal measured at the end of the joint (at sensor (d)). This time difference can significantly increase the sum of the least squares, even for an appropriate numerical solution. A solution to this problem has been searched by proposing a time decay parameter between the measured input pressure signal and the calculated pressures inside the joint. The calculations have shown, however, that this time decay is not a constant but continuously changes during the run. Hence, it proved unsatisfactory to solve the problem. However, when considering the histogram and power spectral density of the pressures, this time lag problem vanishes.

The optimization process has been performed for pool depths ranging from 0.20 m (core jet impact) to 0.67 m (developed jet impact), and for jet outlet velocities V_j between 10 and 30 m/s. Test run periods were of 10 seconds per optimization. This time period was found to procure an appropriate balance between correct numerical analysis and an acceptable computation time. However, for every run, the first second of calculations has been systematically omitted from the optimization process, in order to avoid influences of the initial condition. Preliminary tests with a sinusoidal input signal have shown that most of these influences die out after some tens of seconds.

The optimization is characterized by two stages. In a first stage, a trial and error process has been applied. Based on the measured data, an appropriate range of values could be found for the three k-parameters. Within this range, an optimum was then searched for by performing several consecutive numerical runs and by comparing the mean, root-mean-square, maximum and minimum pressure values, as well as the obtained histogram. Although this approach is of subjective character, it allows defining the major tendencies of the celerity-pressure relationships.

The second stage of the optimization process involves an automated process based on genetic algorithms. All of the parameters could so be optimized. This is outlined in the next section.

3. Genetic algorithms

3.1. Introduction

Genetic algorithms were formally introduced in the United States in the 1970's at the University of Michigan. They are part of Evolutionary Computing, which is a field of artificial intelligence. As such, they search for a solution to a problem based on mechanisms taken from Darwin's theory about evolution.

To use a genetic algorithm, a solution to the problem in question has to be represented by a chromosome. The algorithm then creates a population of solutions and applies genetic operators such as mutation and crossover to evolve new solutions in order to find the best ones. The performance of each solution is thereby expressed by a fitness function. The selection criteria are such that only the best individuals subsist and, thus, a sort of natural selection is occurring. Each chromosome consists of a number of genes. A gene represents a binary coded form of one of the parameters of the problem.

It is obvious that genetic algorithms are situated between classical optimisation methods, applied locally in the search space of solutions, and purely random or systematic optimisation methods, that explore all possible solutions. Genetic algorithms constitute a sort of intelligent and pseudo-random exploration of the search space of solutions. The major differences compared with other optimisation methods are (Erpicum, 2001):

1. use of a coding of the parameters and not of the parameters themselves,
2. direct use of a population of solutions instead of one solution,
3. direct use of the value of the fitness function, and not its derivative for example,
4. based on a probabilistic evolution.

The three most important aspects of genetic algorithms are: 1) implementation of the parameters of the problem, 2) implementation of the genetic operators and 3) definition of the fitness function. They are discussed hereafter in detail. For more information about genetic algorithms, the reader is referred to textbooks on the subject.

3.2. Parameters of the problem

3.2.1. Binary coding

Genetic algorithms need an encoding of the parameters of the problem in a single string of finite length. The string should represent a short and natural expression of the problem. The most used way of encoding of the parameters is a binary string. As such, each chromosome has one binary string and each bit of this string can represent some characteristic of the solution. The number of bits in a string defines the number of possible values of the parameter that is encoded by the string. For example, the string with 5 bits has $2^5 = 32$ possible values. An example is given by the string 10000, which corresponds to 1 times $2^4 = 16$.

Hence, a string with x bits covers all values between 0 and $2^x - 1$. The most appropriate value of x depends on the degree of precision wanted for each parameter. The present computations use values between 1 and 4.

3.2.2. Boundary values

The values of the binary coding of the parameters are directly used by the genetic algorithm, but do not represent real values. A systematic linear transformation between the encoded binary values and the real values is performed by defining the upper and lower bound of the parameter values. The precision of the parameter is so determined by the length of the string. For example, suppose a

parameter can take values between 10 and 40. Its binary encoding with 4 bits conducts to the following 16 possible real values:

Encoding	Binary value	Real value	Encoding	Binary value	Real value
0000	0	10	0001	1	12
1000	8	26	1001	9	28
0100	4	18	0101	5	20
1100	12	34	1101	13	36
0010	2	14	0011	3	16
1010	10	30	1011	11	32
0110	6	22	0111	7	24
1110	14	38	1111	15	40

Table VI-1 Binary encoding and real values of a parameter, based on a four bits string.

The obtained precision is equal to 1 unit. An encoding based on 6 bits procures 64 possible intervals and thus a precision of (40-10)/63/2 = 0.238, i.e. more than four times as precise as in case of 4 bits.

3.3. Genetic operators

3.3.1. Natural selection

The natural selection is the first and basic law in the evolution of the population and states that only the most appropriate chromosomes will survive. The evolution of a population is simply performed by choosing the correct amount of chromosomes from the ancient population to form a new population of the same size. The probability that a certain chromosome is chosen for the new population depends on its value of the fitness function. This value can be represented as a function of the sum of values of all chromosomes by means of a roulette wheel. The higher the fitness function of a chromosome, the bigger its part on the roulette wheel.

A random selection process is then performed on the roulette wheel to obtain the new population. Chromosomes with bigger parts will be selected more times. Their probability of selection $prob_i$ is directly defined by the part of the roulette wheel their fitness function $f_{obj,i}$ occupies:

$$prob_i = \frac{f_{obj,i}}{\sum_{j=1}^{N} f_{obj,j}} \tag{6.4}$$

Several other scaling algorithms exist, such as a simple ranking (no scaling) and the sigma truncation scaling (based on the value of the standard deviation of the population). It is important for these algorithms to not only keep the best solution, but also somewhat less good solutions, in order not to stick too quickly to just one possible best solution. On the other hand, it can be important to keep at any generation the previous best solution. This is called elitism.

3.3.2. Crossover

The crossover process is defined such that two source chromosomes are combined to obtain two new chromosomes. The basic idea of the process is to get only the most appropriate genetic material from the previous generation to the subsequent generation. A crossover point is selected somewhere in the source chromosomes and the so formed parts are interchanged between them. The best results are obtained by choosing a crossover point for each parameter string. This guarantees a good mixture of information between generations. An example is provided for two-parameter chromosomes in Fig. VI-

2. Crossover rates should generally be high, in the range of 60 % to 95 %. The present computations apply a crossover rate of 60 %. Other possible crossover processes are the single-point crossover and the uniform crossover. The former uses only one point of inversion throughout the whole chromosome, while the latter proposes to interchange any bit of the string but for a 50 % probability of occurrence. The respective exchanges of information of these two processes, however, often are too low or too high to be effective throughout the optimisation process.

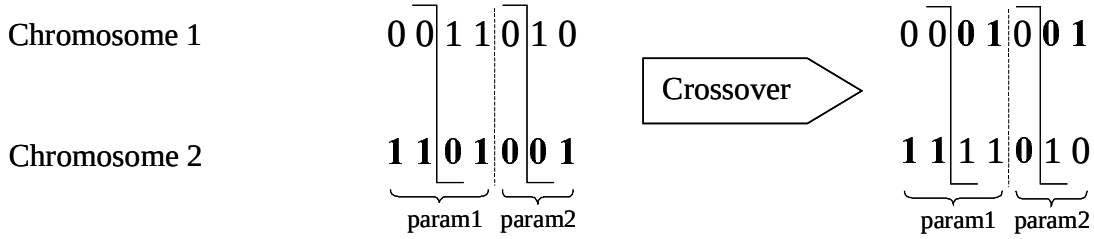

Fig. VI-2 Sketch of the process of crossover per parameter for a set of two-parameter chromosomes.

3.3.3. Mutation

The processes of natural selection and crossover reproduce new chromosomes but can result in a loss of useful genetic material (a 0 or a 1 at a precise location). Such irremediable losses can be avoided by introduction of mutation. This operation consists in a small probability of mutation of a gene (0 gets 1 or 1 gets 0) of the chromosome, during the crossover process. The probability of mutation should be kept very low in order not to loose too much source information. Typical values are in the order of a few percent. The present applications show a mutation rate of 3 %.

3.4. Fitness function

Some fitness function f_{obj} is given and the genetic algorithm tries to find the maximum of this function. This means that the fitness function has to be strictly positive and that the best-fit solution attains a maximum value. Most of the optimisation problems make use of a function e(x) that has to be minimised rather than to be maximized. The most known example is the least squares method between two given functions. In the present analysis, the fitness function f_{obj} is defined based on the least-squares function e(x) as follows:

$$f_{obj}(x) = \frac{1}{(e(x))^a} \tag{6.5}$$

in which a is a positive exponent (generally equal to 1) chosen to obtain easily distinguishable peaks in the fitness function. For the present application, a = 1. The function e(x) has to be minimised in the following way:

$$e(x) = \sum_{j=1}^{i} \left(h_{j,measured} - h_{j,calculated}\right)^b \tag{6.6}$$

in which b is a positive multiple of 2 and h stands for the measured or calculated value. This value constitutes the optimisation criterion and directly expresses to which point the calculated values correspond to the measured ones. It can be for example the mean pressure value inside the joint, the maximum pressure value inside the joint, or even the histogram or spectral content of the pressure values inside the joint.

4. Preliminary optimisation of celerity-pressure relationships

For closed-end rock joints, a first determination of the celerity-pressure relationships has been performed by assuming a linear or a quadratic dependence between the two parameters. At relatively low celerities and pressures, one quadratic curve is sufficient to describe the relationship (optimisation of parameters k_1 to k_3). At high celerities and pressures, sometimes this same curve could still be used, but sometimes it was necessary to determine a second quadratic curve (optimisation of parameters k_4 to k_6). The change from one curve to the other is determined by means of a pivot celerity c_{PIV}.

The optimisation criteria are the mean, root-mean-square and extreme pressure values, as well as the histogram of pressure values. The optimisation has been done by performing successive runs of the numerical model and by trial and error comparison of the so obtained results. As such, the followed optimisation procedure is of subjective character but nevertheless procures a good idea of the global form of the appropriate celerity-pressure relationships. Table VI-2 summarizes the results for the considered range of experimental parameters. The jet velocities that are marked with * indicate results for a convergent jet outlet. The other jet outlets are of cylindrical shape.

V_j	Y	k_1	k_2	k_3	c_{PIV}	k_4	k_5	k_6	Flow assumption	λ
m/s	m	-	-	-	m/s	-	-	-	-	-
14.7	0.60	45	12.5	0	-	-	-	-	turbulent	0.30
14.7	0.20	50	13.0	0	850	91.7	14.8	-0.04	turbulent	0.30
14.7	0.20	55	12.0	-0.024	-	-	-	-	laminar	0.20
14.7*	0.20	70	14.0	0	-	-	-	-	turbulent	0.80
14.7*	0.20	70	14.0	0	-	-	-	-	laminar	0.50
19.7	0.67	10	14.0	0	960	424	9.6	-0.024	turbulent	0.30
19.7	0.67	80	12.0	-0.024	-	-	-	-	laminar	0.50
24.6	0.67	15	12.5	0	800	37.2	14.4	-0.038	turbulent	0.50
24.6	0.67	55	11.8	-0.025	-	-	-	-	laminar	0.60
24.6	0.60	10	12.0	0	278	-15	13.8	-0.035	turbulent	0.50
24.6	0.60	20	11.0	-0.025	-	-	-	-	laminar	0.35
29.5	0.60	35	3.5	0	-	-	-	-	turbulent	0.50

Table VI-2 Parametric results of the preliminary optimisation applied to a 10 seconds test run for different jet velocities and plunge pool depths. Test runs that are marked with * are for a convergent jet outlet.

The celerity-pressure relationships are visualized in Fig. VI-3. Fig. VI-3a presents the combined linear or quadratic curves valid under turbulent flow assumptions. Fig. VI-3b presents similar results but for laminar flow assumptions. Although the curves for turbulent flow seem to indicate slightly higher wave celerities, both cases exhibit similar tendencies.

The first optimisation started with the assumption of turbulent flow conditions. The results were accurate in terms of mean, root-mean-square and extreme pressures, but the calculated histogram of pressure values could not be fully adjusted to the measured histograms. When adjusted for minimum and maximum pressures, the intermediate pressure values didn't correspond at all. Similarly, when

adjusting these intermediate values, the extreme pressures didn't match anymore. This phenomenon is probably due to a different friction at different pressure values. Moreover, the calculated flow velocities were generally very low, less than 0.2 m/s. For the narrow joint thickness of only 1 mm, this theoretically results in Reynolds numbers less than 100 and, thus, very laminar flow.

Therefore, it was decided to repeat the optimisation but for laminar flow assumptions. This resulted in a much better agreement of the calculated and measured histograms, as can be seen by comparing Fig. VI-3b with 3d.

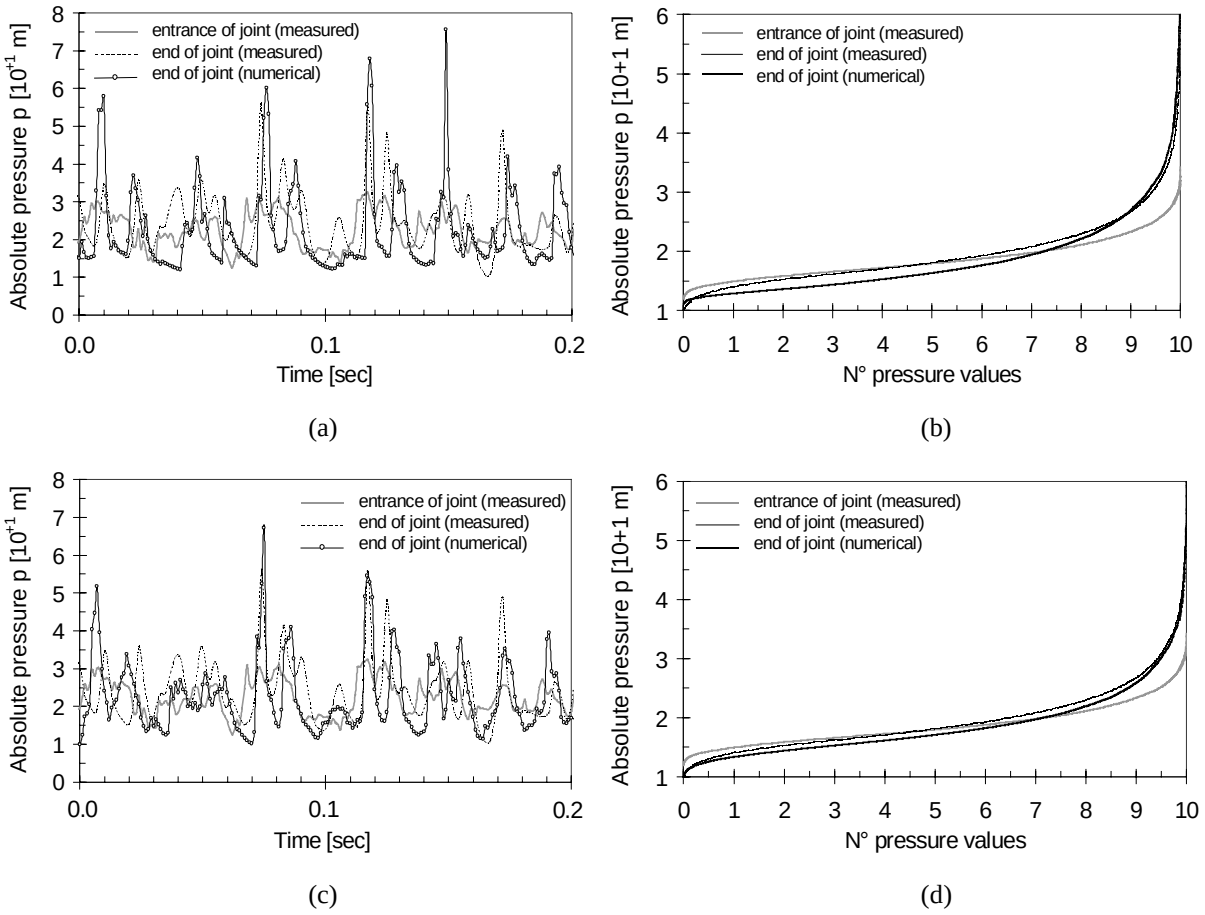

Fig. VI-3 Comparison of experimental and numerical derived pressures at end of I-joint:
a) pressure signal for turbulent flow; b) histogram for turbulent flow;
c) pressure signal for laminar flow; d) histogram for laminar flow.

The measured data points were obtained for test runs with a high acquisition rate (5'000 to 10'000 Hz) and show good agreement with the numerically obtained relationships for jet velocities less than or equal to 25 m/s (Fig. VI-4). The scatter of data at high jet velocities (> 20 m/s) is probably due to a varying air concentration in the plunge pool. This variation induces changes in free air content inside underlying rock joints. As a result, during a complete test run, different celerity-pressure relationships have to be accounted for.

This, however, cannot be taken into account by the numerical simulation. The phenomenon can be easily observed for a jet velocity of 29.5 m/s. Some of the data points match very well with the optimised celerity-pressure curve; other points exhibit a completely different air concentration.

The celerity-pressure relationships have been optimised based on test runs at only 1'000 Hz of acquisition rate. This reduces the accuracy of the results, especially at higher pressures and celerities. This can be observed by an increasing discrepancy between the measured data points and the calculated curves at higher pressures. Hence, the celerity-pressure relationships at the higher pressure range should be interpreted with a lot of precaution. It is not excluded that they are not accurate.

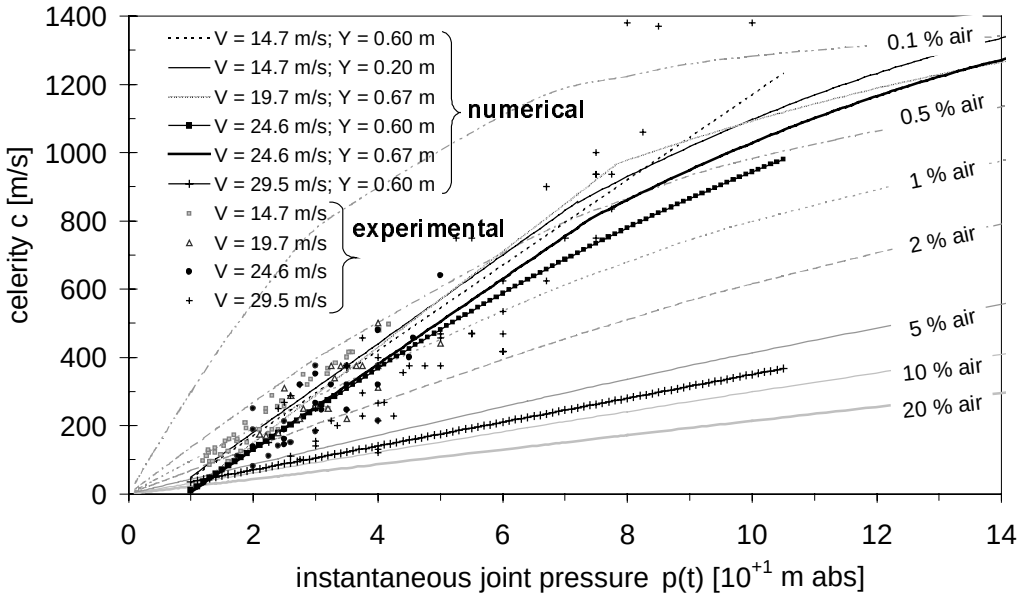

(a)

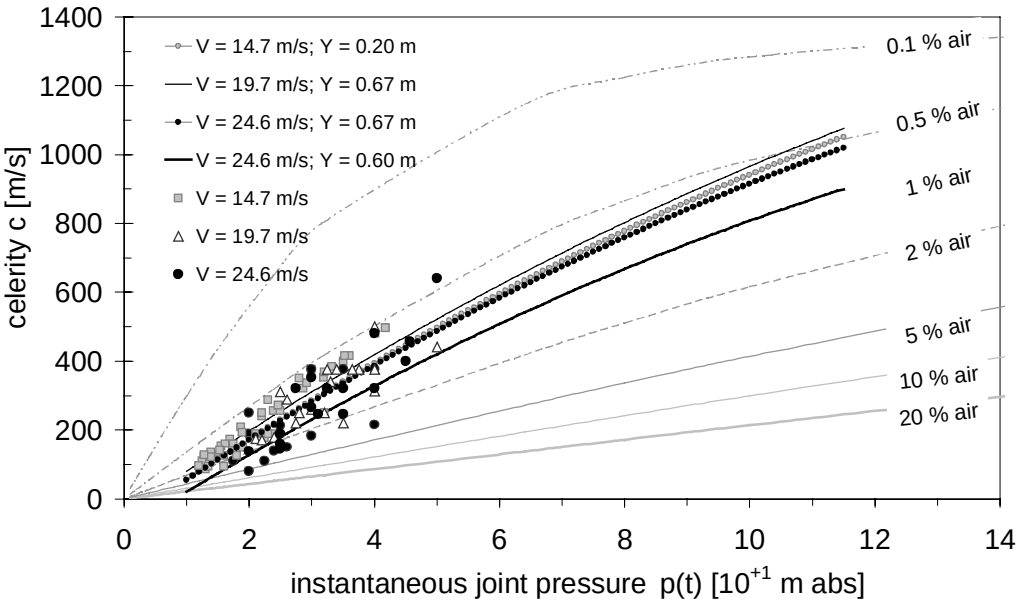

(b)

Fig. VI-4 Numerically derived celerity-pressure relationships and comparison with measured data points for different jet velocities and plunge pool depths: a) for turbulent flow assumptions; b) for laminar flow assumptions.

For a jet velocity of 29.5 m/s and for turbulent flow assumptions, a totally different celerity-pressure relationship is obtained in Fig. VI-4a. Pertaining to the completely different frequency modulation, as outlined in § 4.1.8 of Chapter V, this is not so surprising. It is the only curve that exhibits a constant mass of free air with increasing pressure. This mass corresponds to a standard air concentration of between 5 and 10 %. The other curves indicate a significant decrease of the mass of free air with increasing pressure, which can be described by Henry's law.

The phenomenon is better visualized in the lower pressure range, as presented in Fig. VI-5 for laminar flow and for absolute pressures less than 50 m of head. The curve obtained at a jet velocity of 24.6 m/s and a plunge pool depth of 0.60 m increases its air concentration from 1.5 % at 50 m of absolute pressure head up to nearly 20 % at atmospheric pressure conditions. This trend is confirmed by the measured data points.

The mean absolute pressure for these experimental conditions is situated around 30 m of absolute pressure head. Hence, it can be seen that the major part of the increase in air content occurs at pressures that are less than this mean pressure value. Furthermore, the curves seem to be displaced towards higher air contents for higher jet velocities. This phenomenon is clearly visible in Fig. VI-4, for both turbulent and laminar flow assumptions. It is in agreement with the statement that, the higher the jet velocity, the higher the air content in the plunge pool, and thus also the possible air content inside the rock joints.

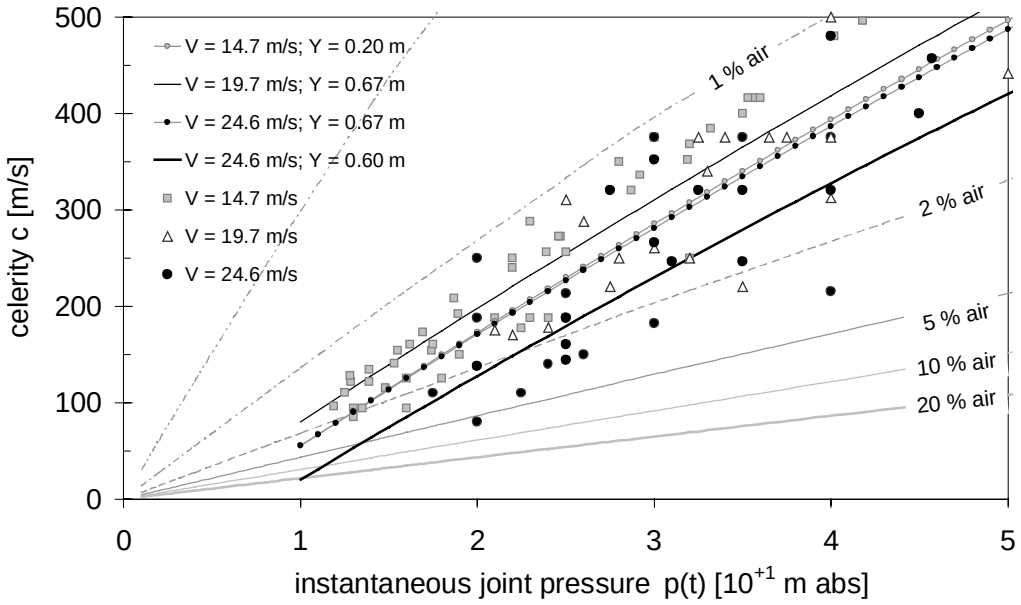

Fig. VI-5 Detail of the numerically derived celerity-pressure relationships and comparison with measured data points for laminar flow assumptions.

5. Genetic algorithm optimisation of celerity-pressure relationships

The preliminary optimisation of the celerity-pressure relationships allowed determining the general shape of the curves. Furthermore, laminar flow seemed to be most plausible. In the following, the obtained celerity-pressure relationships will be verified by means of a genetic algorithm for closed-end rock joints. Only laminar flow conditions are accounted for. Firstly, polynomial relationships will be optimised and compared with the preliminary optimisation. In a second stage, based on the ideal gas law and Henry's law, exponential celerity-pressure relationships are tested and optimised.

5.1. Experimental parameters of the modeled test cases

The numerical model is not able yet to account for internal wave reflections due to eventual geometric changes of the joint boundaries, such as a 90° bend or sudden changes in cross-sectional area. These effects will be introduced in a next phase of the project. Therefore, comparison is made with the pressure measurements made for the one-dimensional I-joint. This comparison is done at the joint end, i.e. at sensor (d). The pressure values that were measured at sensor (a) are used as upstream boundary condition for the numerical model.

The genetic algorithm optimization has been performed for the plunge pool depths and jet velocities as indicated at Table VI-3. The jet outlet was cylindrical, for a diameter of 72 mm.

Jet velocity V_j	Plunge pool depth Y		
	0.20 m	0.60 m	0.67 m
9.8 m/s	x		x
14.7 m/s	x	x	x
19.7 m/s	x		x
24.6 m/s	x	x	x
27.0 m/s			x
29.5 m/s	x	x	x

Table VI-3 Plunge pool depths and jet velocities of the test runs that were used to compare with the numerical model

The plunge pool depth of 0.20 m has been chosen to represent core jet impact conditions, while the plunge pool depth of 0.67 m represents developed jet impact conditions. Some verifying comparisons have also been made at a plunge pool depth of 0.60 m. Most of the experimental runs have been acquired at a rate of 1'000 Hz. When another acquisition rate was used, this has been explicitly mentioned.

5.2. Polynomial celerity-pressure relationships

5.2.1. Numerical optimization for a jet velocity of 19.7 m/s and a pool depth of 0.67 m

The procedure that has been followed for the range of experimental parameters as defined under § 3.1.1 is outlined here in detail for a jet velocity of 19.7 m/s and a plunge pool depth of 0.67 m. As a first approach, the following parameters have been optimised: k_1, k_2, k_3, c_{PIV}, k_5, k_6, λ and η. This means that the correction term β that accounts for an uneven velocity distribution has been omitted. The parameter k_4 is not strictly necessary when knowing the pivot celerity c_{PIV}. Furthermore, as has already been pointed out in § 2.3, the second quadratic curve, as well as the pivot celerity c_{PIV}, are

difficult to optimise when no high-pressure values are available. An attempt was made but revealed to procure unsatisfactory results.

The used optimisation criteria are the histogram of the measured pressure values and the power spectral density of the fluctuating part of the measured pressures. The results of the genetic algorithm applied to a single test run of 10 seconds are summarized at Table VI-4.

Function	Time	k_1	k_2	k_3	c_{PIV}	k_4	k_5	λ	η	criterion
-	sec	-	-	-	m/s	-	-	-	-	-
12'972	10	38	6.8	0.100	-	-	-	0.50	-	histogram
13'080	10	14.7	8.9	0.053	-	-	-	0.50	-	histogram
13'306	10	28.7	8.9	0.053	-	-	-	0.49	-	histogram
13'417	10	28.7	9.5	0.040	-	-	-	0.49	1.09	histogram
13'496	**10**	**22**	**10.2**	**0.047**	-	-	-	**0.53**	**1.14**	**histogram**
12'197	10	75.3	6.3	0.120	-	-	-	0.58	1.0	spectrum
12'236	**10**	**70**	**5.0**	**0.143**	-	-	-	**0.58**	**1.0**	**spectrum**

Table VI-4 Parametric results of the genetic algorithm optimisation applied to a 10 seconds test run with a jet velocity of 19.7 m/s and a plunge pool depth of 0.67 m. The best results for both histogram and spectrum least-squares criteria are indicated in bold.

The function value is the parameter that has to be optimised by the least-squares criterion. The better the result, the higher is this value. The optimisation of the second quadratic curve, i.e. the parameters c_{PIV}, k_4 and k_5, proved unsatisfactory and is not presented. The friction coefficient λ is very close to the preliminary optimised value of 0.50, for both histogram and spectrum optimisations. The shape of the two best-fit quadratic curves (values indicated in bold at Table VI-4) is presented in Fig. VI-6. The two curves are of similar shape and in good agreement with the previously established optimum.

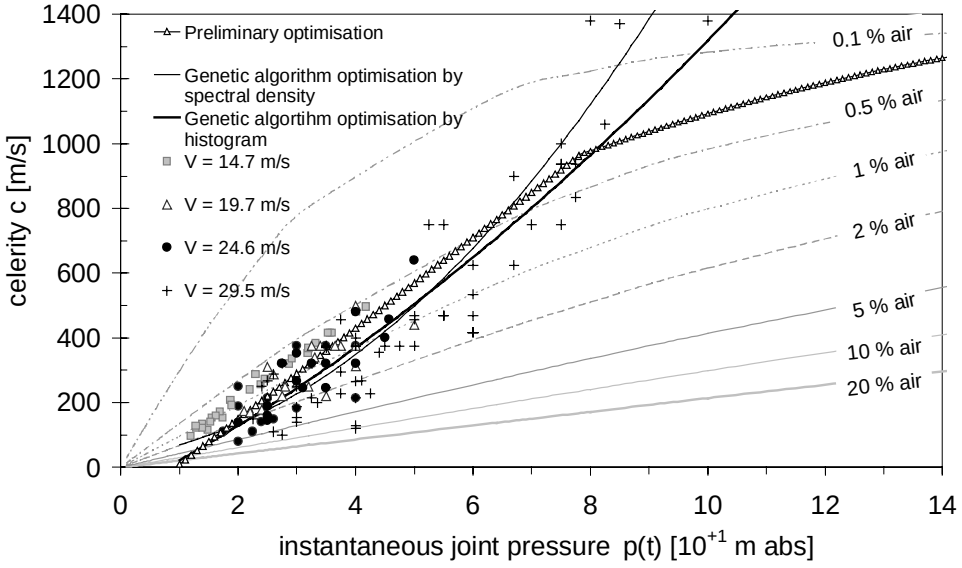

Fig. VI-6 Comparison of the celerity-pressure relationships based on both preliminary optimisation and genetic algorithm optimisation., for laminar flow assumptions.

The corresponding pressure signal in the time domain as well as the histogram and power spectral density are presented in Fig. VI-7. A good agreement with the measured pressures is apparent.

The numerically obtained power spectral content, however, overestimates the higher frequencies. This is probably due to the absence in the numerical model of significant thermal dissipation effects by high-frequency compression and expansion of air bubbles. Such effects are actually being investigated in the field of wave impact pressures on rock cliffs (by G. Muller, University of Belfast). As a result of these particular damping effects, the comparison of the spectral contents of the measured pressures and the numerically calculated pressures has only been performed for Fourier coefficients of up to 200 Hz maximum. It can be seen that the presented numerical solution is in excellent agreement with the measured power spectral content.

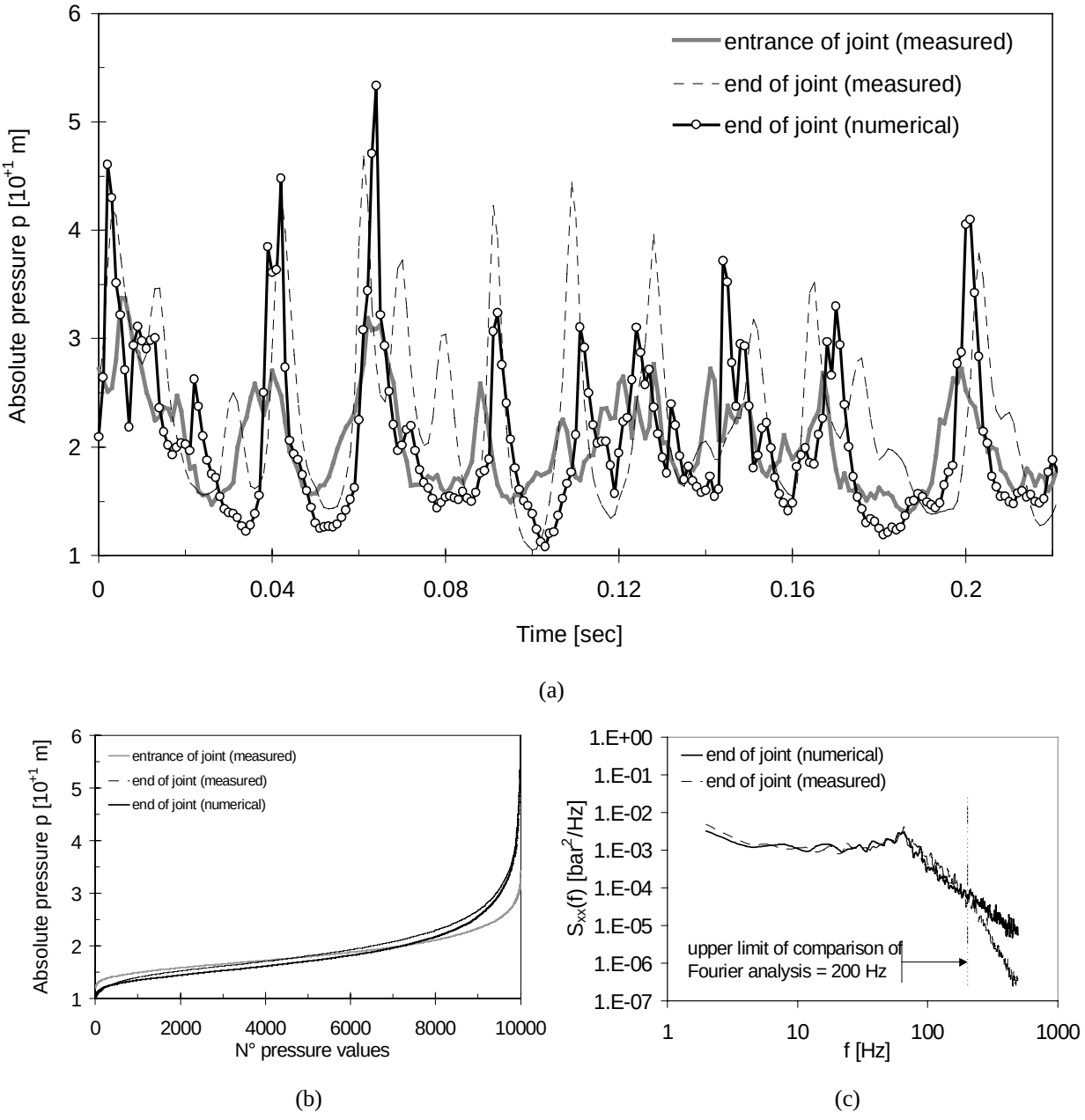

Fig. VI-7 Comparison of experimental and numerical derived pressures at end of I-joint, for a jet velocity of 19.7 m/s and a plunge pool depth of 0.67 m: a) pressure signals in the time domain; b) corresponding histograms; c) corresponding power spectral densities.

5.2.2. Summary of genetic algorithm optimisation

Similar to the preliminary optimisation, Table VI-5 summarizes the results of the genetic algorithm optimisation for different jet velocities and plunge pool depths. The experimental runs that have been used for the optimisation were for time periods of 10 seconds each.

It can be noted that the friction coefficient λ increases with increasing jet velocity and, based on the corresponding celerity-pressure relationships, also with increasing air concentration in the joint. This coefficient not only represents the classical steady-state friction but also includes all possible two-phase damping effects. It is believed, therefore, that the frictional effect due to the gas phase is by far the predominant one, which is in agreement with previous findings (Martin & Padmanabhan, 1979; Ewing, 1980).

V_j	Y	k_1	k_2	k_3	c_{PIV}	k_4	k_5	k_6	λ	η	crit
m/s	m	-	-	-	m/s	-	-	-	-	-	-
14.7	0.20	65	10.0	0.000	-	-	-	-	0.20	1.00	histo
14.7	0.67	125	9.0	0.071	-	-	-	-	0.35	1.00	histo
14.7	0.67	77.1	12.0	0.021	-	-	-	-	0.47	1.00	spec
19.7	0.67	22	10.2	0.047	-	-	-	-	0.53	1.14	histo
19.7	0.67	70	5.0	0.143	-	-	-	-	0.58	1.00	spec
24.6	0.20	-10.7	0.5	0.173	-	-	-	-	1.00	0.80	spec
24.6	0.67	55.7	11.4	0.000	-	-	-	-	0.71	1.00	histo
24.6	0.67	10.7	6.4	0.147	-	-	-	-	0.78	1.00	spec

Table VI-5 Parametric results of the genetic algorithm optimisation applied to a 10 seconds test run for different jet velocities and plunge pool depths.

Furthermore, the friction coefficient η, which accounts for unsteady friction effects (or frequency dependent friction), is close to the unity for all tested cases.

Fig. VI-8 shows that two types of relationship have been found: quadratic curves, with a slope that increases quite fast with increasing pressure, and linear curves, with a somewhat smaller but constant slope. It has to be mentioned that only the curve for a jet velocity of 24.6 m/s and a plunge pool depth of 0.67 m indicated that a linear relationship fitted better than a quadratic one. The other two linear curves were necessarily obtained because parameter k_3 was omitted from the optimisation, i.e. no possibility of curvature was possible.

Within the range of measured pressures, all the curves are in reasonable agreement one with the other. Especially for the curves that have been optimised based on the power spectrum criterion, it can be observed that they are shifted towards higher air contents (lower celerities) at higher jet velocities. Moreover, their shape shows some similarity with the celerity-pressure relationships that are governed by Henry's law, such as presented in Fig. V-42 (§ 4.1.9 of Chapter V).

Therefore, it is believed that further optimisation of celerity-pressure relationships might be performed based on Henry's law. The parameters that are needed depend on the complexity of the Henry's law. For a single solubility constant S, only two parameters are needed: the solubility constant S and the exact air concentration at standard atmospheric pressure conditions α_0. However, as pointed out in Chapter V already, it is more convenient to introduce at least two solubility constants S_1 and S_2. The underlying idea is that air release and air re-solution have two different time scales. In general, the latter takes much more time to happen and to be completed. Assuming that the flow mixture enters the rock joint at the mean dynamic pressure value, all pressures inferior to this value exhibit the first S-value. Similarly, all pressures that are higher than the mean dynamic pressure value correspond to the

second S-value. This leads to at least three parameters to optimise numerically. An example has been visualized in Fig. VI-8 of a relationship that is based on Henry's law. As can be seen, two different solubility constants S have been used.

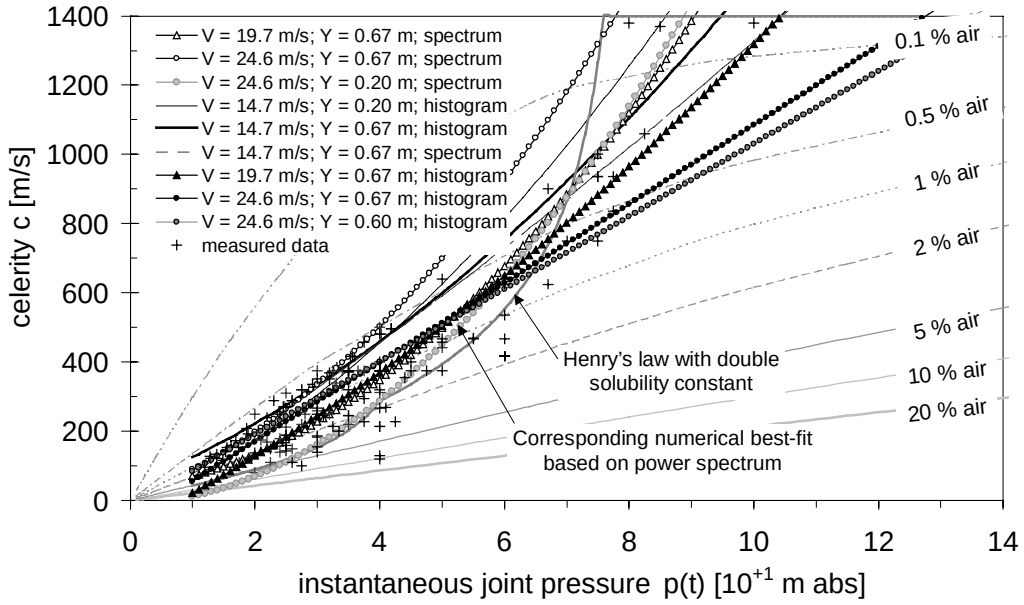

Fig. VI-8 Numerically derived celerity-pressure relationships and comparison with measured data points for different jet velocities and plunge pool depths, for laminar flow assumptions. The numerical optimisation has been performed by a genetic algorithm technique.

The physical background, however, is even more complex. Strictly speaking, the amount of air release is a function of the time period that has passed since the start of the release. An exponential relationship is plausible. As such, it seems logic that, starting with a drop in pressure from the mean dynamic pressure for example, the lowest (near-atmospheric) pressures will be reached at the longest time period. In other words, the lower the pressure, the longer the time period. If one assumes a linear relationship between the drop in pressure and the time, then S is not considered as a constant anymore but becomes an exponential function of pressure. Other phenomena that might be of influence on the change of the solubility constant S as a function of pressure, such as for example the degree of turbulence or the remaining wall nuclei, are neglected in the following analysis.

The feasibility of a solubility constant that changes exponentially with pressure has been verified by transforming the polynomial celerity-pressure relationships into solubility-pressure relationships. The followed procedure is as follows:

1. make use of relationship (3.58) of Chapter III: $$c_{exp} = \sqrt{\frac{\frac{K_{liq}}{\rho}}{1+\frac{K_{liq}\cdot D}{E\cdot e}+\left(\frac{mRT}{p}\right)\cdot\left[\left(\frac{K_{liq}}{p}\right)-1\right]}}$$

2. make use of relationship (6.3) of this Chapter: $$c_{poly} = k_1 + k_2 \cdot p + k_3 \cdot p^2$$

3. at each pressure level p: adapt m such that $$c_{exp} = c_{poly} \quad (6.7)$$

4. define the solubility constant S at each pressure p: $$m_{i+1} = m_i - S_{i+1} \cdot (p_{i+1} - p_i) \quad (6.8)$$

5. set up the $S_i - p_i$ relationship.

The results are presented in Fig. VI-9 for different jet velocities and plunge pool depths, and can be approximated very well by exponential best-fit curves. Hence, in the following an optimisation is performed based on Henry's law with exponentially changing solubility constants S.

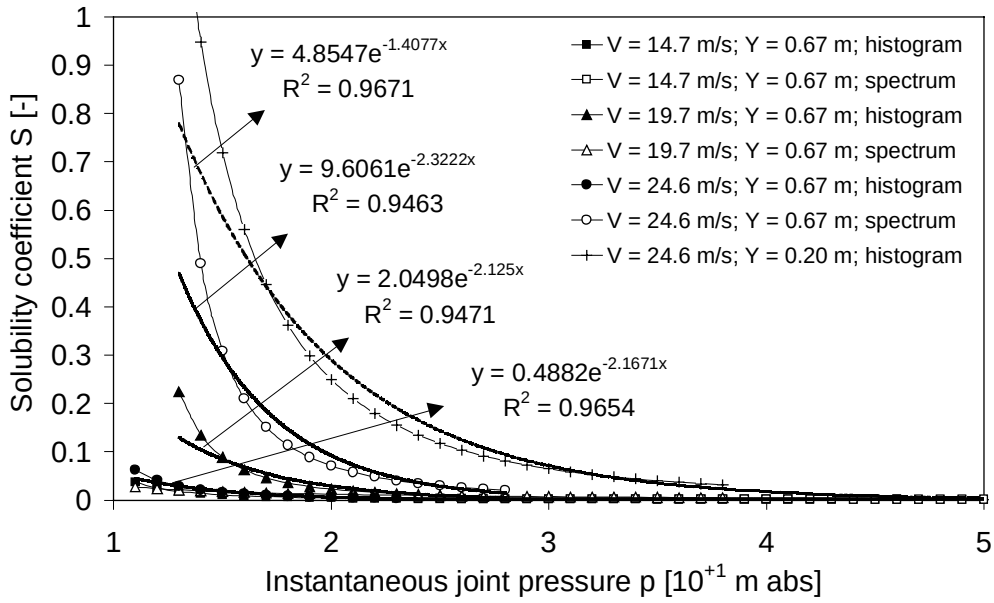

Fig. VI-9 Relationship between the solubility coefficient S and the pressure p inside the joint (absolute value), obtained for the polynomial optimisations of the celerity-pressure relationships of § 5.2. An exponential S-p relation seems relatively plausible.

5.3. Exponential celerity-pressure relationships

5.3.1. Definition of the solubility-pressure relationship

The exponential relationship between the solubility constant S and the pressure p needs the definition of a reference pressure p_{ref}. The physically most plausible choice is the mean pressure value inside the joint. However, this value changes as a function of the jet velocity at impact. Therefore, the standard atmospheric pressure p_0 seems more appropriate. The corresponding reference mass of free air in the liquid is m_0. The decay of m as a function of pressure can then be written as follows:

$$m_0 = \left[\frac{M_{air}}{\forall_{mix}}\right]_{p=1atm} = \left[\frac{\rho_{air} \cdot \forall_{air}}{\forall_{mix}}\right]_{p=1atm} = \rho_{air} \cdot \alpha_0 \tag{6.9}$$

$$m_i = m_o - \int_{p_0}^{p_i} a \cdot e^{b \cdot p} dp \tag{6.10}$$

$$m_i = m_0 - \frac{a}{b} \cdot \left[e^{bp}\right]_{p_0}^{p_i} \tag{6.11}$$

$$m_i = m_0 - \frac{a}{b} \cdot \left(e^{bp_i} - e^{bp_0}\right) \tag{6.12}$$

$$m_i = m_0 \cdot \left[1 + k_1 \cdot \left(e^{-k_2 \cdot p_i} - e^{-k_2 \cdot p_0}\right)\right] \tag{6.13}$$

in which M_{air} and $\forall_{air}$ stand for the mass and the volume of the air bubbles, and $\forall_{mix}$ for the volume of the mixture. The density of the air ρ_{air} is equal to 1.293 kg/m^3. In the last step, it is assumed that the parameter "a" of the exponential relationship for S depends on the mass of free air m_0. This results in three parameters to optimise: k_1, k_2 and m_0. As it is not clear which range of values is appropriate for k_1 and k_2, they have been investigated before starting the numerical optimisation. This is presented in Fig. VI-10.

Figs. VI-10a to c present the exponential curves for k_2 = 0.1, 0.5 and 1.0 respectively and for an air concentration of 2 %. For each of these cases, four different k_1-values (0.5 to 2.0) have been chosen. It can be seen that for k_2 = 1.0, these four different curves are quite close one to the other. On the other hand, for k_2 = 0.5, the curves are far more dispersed. For k_2 = 0.1, the situation lies in between the former two.

Comparison with the polynomial best-fits of Fig. VI-8 shows that, for k_2 values ranging from 0.1 to 1.0, appropriate k_1 values are between 1 and 2. Particularly a k_2 value of 0.5 combined with a k_1 value of 1.5 seems justified. For these values, the curves have been presented for different air concentrations in Fig. VI-10d.

Beside the three aforementioned parameters to optimise, also the friction coefficient λ is taken into account. The friction parameter β is taken equal to 1.0 and η is neglected.

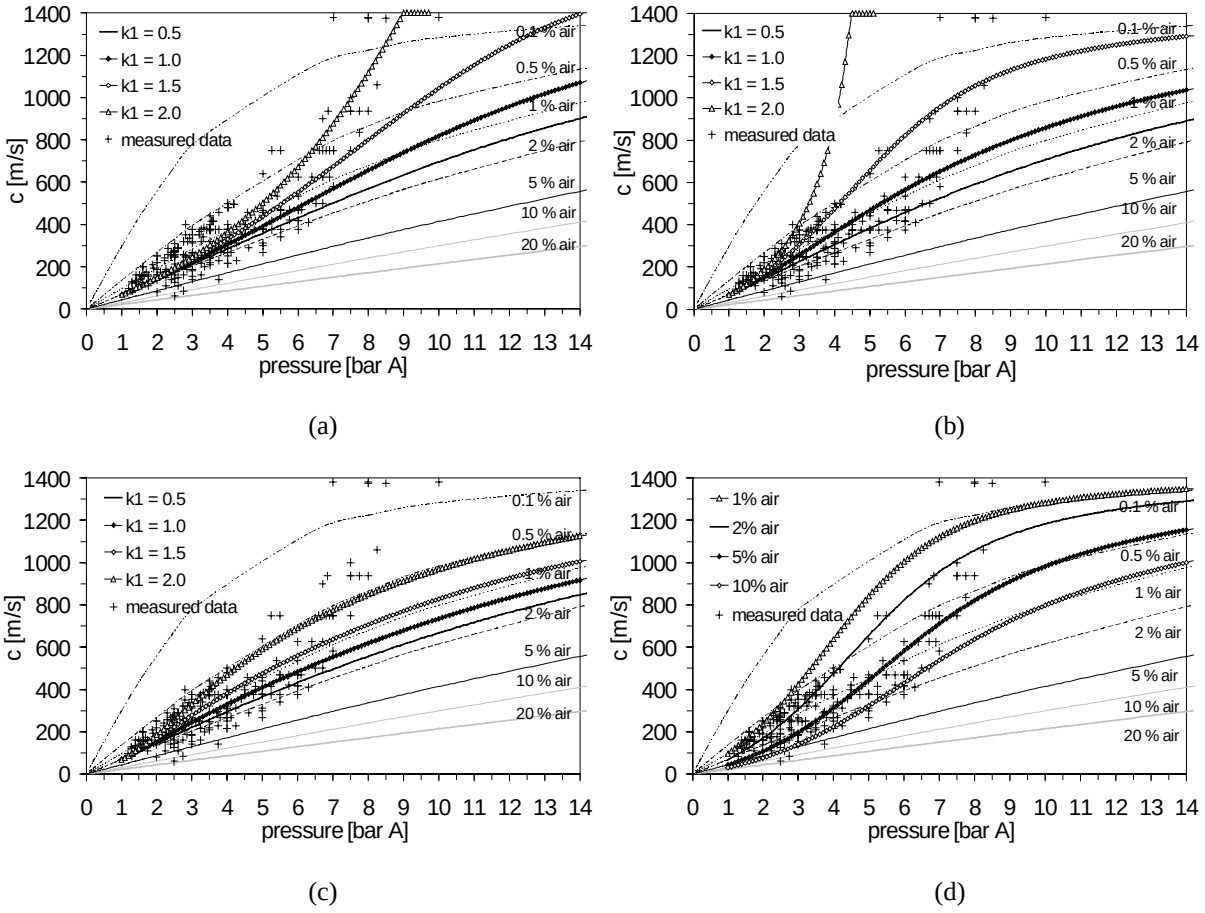

Fig. VI-10 Exponential celerity-pressure relationships for different k_1 and k_2-values:
a) $k_2 = 0.1$ and different k_1-values; b) $k_2 = 0.5$ and different k_1-values;
c) $k_2 = 1.0$ and different k_1-values; d) $k_1 = 1.5$ and $k_2 = 0.5$.

5.3.2. Definition of the optimization criteria

It could be argued that the amount of released air largely depends on the degree of supersaturation of the mixture, and much less on the other parameters. By assuming this, both the parameters k_1 and k_2 become independent of the pressure and thus of the velocity of the jet at impact. Hence, they can be optimized based on different test runs together. The only parameters that are still changing from run to run are the friction coefficient λ and the amount of free air at standard atmospheric pressure m_0. In other words, a grouped optimization of several test runs could be performed for a reduced amount of parameters. Furthermore, this approach should allow determining the physically most plausible values for the form of the celerity-pressure relationships.

5.3.3. Results for a group of test runs

The optimization of the parameters has been performed for a set of three different test runs. The test runs all have a plunge pool depth of 0.67 m. Their jet velocities are 14.7, 19.7 and 24.6 m/s respectively. The three time periods that are used are of 1 second each.

It was impossible to use longer time periods in reason of the otherwise excessive computation time. For example, one optimization with a population of 60 to 80 chromosomes and a total number of generations of only 100 took about 3 to 4 days of computation time on a Pentium III processor. This aspect can have a significant impact on the results of the optimization. The use of only one second is

questionable when using the spectral content of the pressures as optimization criterion. To obtain a smooth-like spectral curve with no white noise, up to several seconds of time period are needed.

Furthermore, even in case of the histogram criterion, the use of only one second could result in celerity-pressure relationships that are not fully representative for the test run in question. As such, the obtained relationship could indicate air contents that are significantly different from the ones that should correspond to the mean air contents of the whole test run of 1 minute. The results are presented in Fig. VI-11 for optimization criteria based on the histogram of values and on the spectral content. The latter has been obtained based on 5 seconds test runs.

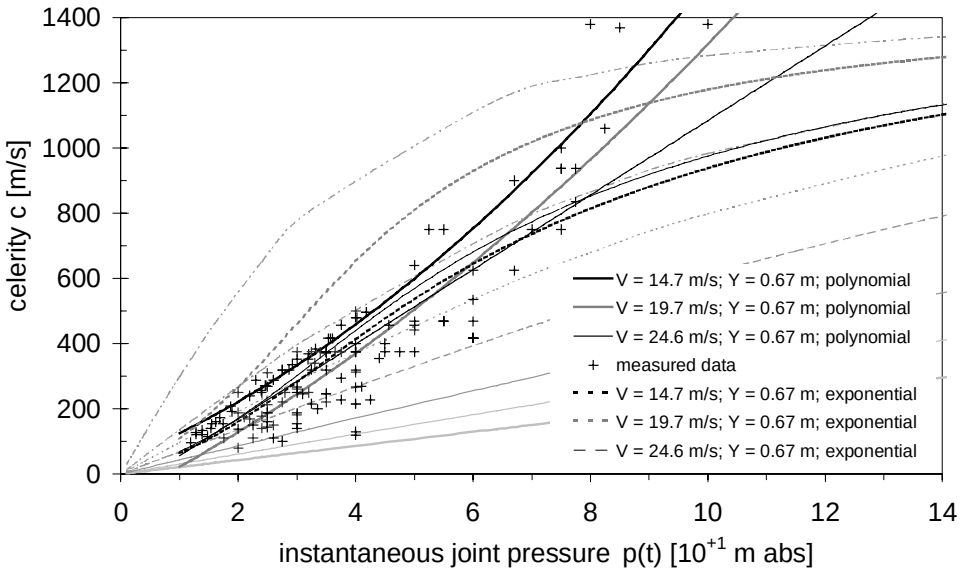

a)

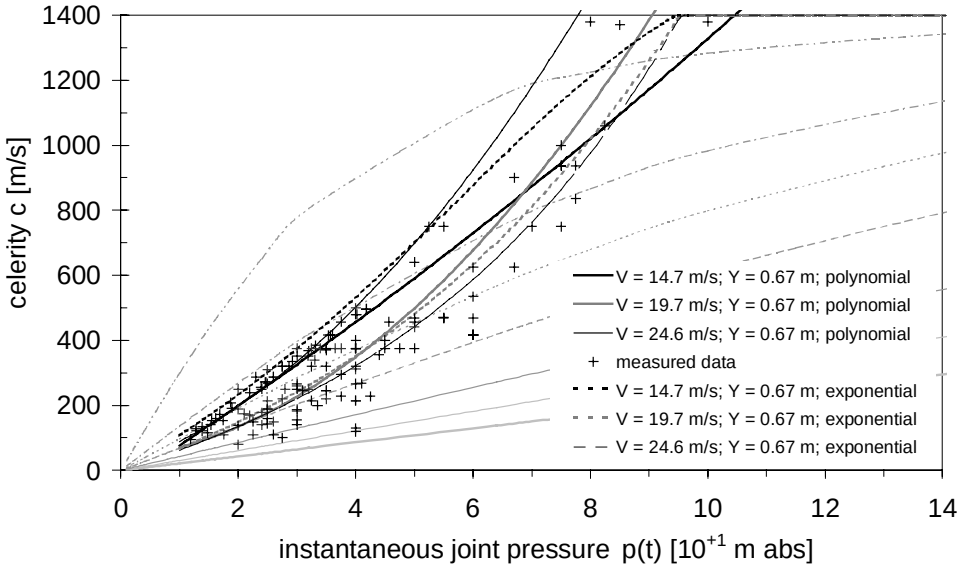

b)

Fig. VI-11 Exponential celerity-pressure relationships and comparison with measured data points for three different jet velocities and a plunge pool depth of 0.67 m, with laminar flow assumptions: a) based on histogram optimisation criterion; b) based on spectral optimisation criterion.

Table VI-6 hereunder summarizes the corresponding values of the parameters of the numerical optimisation.

V_j	Y	k_1	k_2	m_0	λ	η	criterion
m/s	m	-	-	-	-	-	-
14.7	0.67	1.50	0.70	0.030	0.16	1.00	histogram
19.7	0.67	1.50	0.70	0.009	0.41	1.00	histogram
24.6	0.67	1.50	0.70	0.026	1.20	1.00	histogram
14.7	0.67	2.18	0.08	0.010	0.43	1.00	spectrum
19.7	0.67	2.18	0.08	0.026	0.80	1.00	spectrum
24.6	0.67	2.18	0.08	0.030	1.07	1.00	spectrum

Table VI-6 Parametric results of a grouped optimisation applied to three test runs of 5 seconds each, for three different jet velocities and a plunge pool depth of 0.67 m.

For the optimisation based on the histogram of pressure values, the k_1 and k_2 parameters are quite close to the ones previously estimated as appropriate (1.50 and 0.50). However, it is surprising to notice that the amount of free air m_0 does not increase with increasing jet velocity. The curves for the jet velocities of 14.7 m/s and 24.6 m/s are in good agreement one with the other, but the curve for a jet velocity of 19.7 m/s is significantly shifted towards lower air contents. The reason for this is unclear. It might be due to the aforementioned effect of short time periods. Furthermore, the friction coefficient λ systematically increases with increasing jet velocity, as expected. In general, despite the somewhat low air content for a velocity of 19.7 m/s, a very good agreement is obtained with the polynomial curves and with the measured data points (Fig. VI-11a).

For the optimisation based on the spectral content of the pressure values, the obtained values for k_1 and k_2 are significantly different from the ones for the histogram criterion. The three free air contents and friction coefficients increase with increasing jet velocity. The three obtained curves are in good agreement with the polynomial curves and with the measured data points (Fig. VI-11b).

5.4. Conclusions on numerical modelling

The one-dimensional two-phase numerical modelling of the transient pressures that have been measured at the end of the I-shaped closed-end rock joint generates pressures that are in good agreement with the measured ones. The numerical adjustment was based on the optimisation of appropriate celerity-pressure relationships. These relationships seem to be governed by the ideal gas law and by Henry's law. However, some significant aspects need to be studied more in detail. The numerical model was unable to account for thermal dissipation effects at high frequencies. These effects are due to subsequent air bubble compression and expansion cycles and increase with frequency. Moreover, the most appropriate values for the physical parameters of the celerity-pressure relationships could not yet be defined. Therefore, the numerical computations used the pressure measured at the joint entrance as input for the model. It should be more convenient to generate a pressure signal based on a spectral distribution that is typical at the entrance of the joint. This spectral distribution depends on the Y/D_j ratio and on the jet velocity V_j. Finally, the numerical modelling should also be performed for open-end joints as well as for different geometrical configurations of the closed-end joints. It is believed that appropriate numerical calibration of the model will be greatly enhanced in the future by the continuously increasing processor speed of computers.

Chapter VII. The scour model

1. Model concept

The present chapter presents a new model for the evaluation of the evolution of the ultimate scour depth in intermittently or completely jointed rock, under the impact of high-velocity plunging jets. The model concept is based on the theoretical framework that has been outlined in Chapter III and on the transient pressure measurements as described in Chapter V. As such, the model is completely physically based and represents a comprehensive assessment of the two major physical processes that govern scour of rock: 1) hydrodynamic fracturing of closed-end rock joints, and 2) dynamic uplift of so formed rock blocks.

The model consists of three modules:

1) the **falling jet**,
2) the **plunge pool**,
3) the **rock mass**.

Each of the modules is presented hereafter in detail. Emphasis is given on the physical parameters that are necessary to accurately describe the phenomenon. These parameters are defined such that a practicing engineer can easily handle them. This guarantees the comprehensive character of the model, without neglecting basic physics behind it.

The modules for the falling jet and for the plunge pool define the hydrodynamic loading that is exerted by the jet on the fissured rock mass. The former determines the major characteristics of the jet from its point of issuance at the dam down to the point of impact onto the plunge pool. The latter describes the diffusion of the jet through the plunge pool and defines the resulting jet excitation at the water-rock interface. The module for the rock mass has a twofold objective. First of all, it transforms the hydrodynamic loading at the water-rock interface into a critical stress intensity (for closed-end joints) or a net uplift impulsion (for single rock blocks). Secondly, it defines the basic geomechanical characteristics of the rock mass, relevant for the determination of its resistance.

The scour model has finally been applied to a fictitious case study, compared with Annandale's Erodibility Index Method and tested on the well-known case of Cabora-Bassa dam in Mozambique. This points out the capabilities of the model, but also the need for appropriate calibration.

2. The falling jet

The module for the falling jet describes the jet trajectory from its point of issuance at the dam down to the impingement of the jet into the plunge pool. Emphasis is given on how the hydraulic and geometric characteristics of the jet are transformed during this trajectory. Hence, the module is based on three parameters that completely characterize the jet at its point of issuance at the dam:

1) **velocity at issuance V_i,**

2) **diameter (or width) at issuance D_i,**

3) **initial jet turbulence intensity Tu**.

The basic idea is to dispose of these initial parameters, or to derive them from the type of outlet structure and the dam reservoir level. The initial jet turbulence intensity Tu defines the spread of the jet during its fall. Furthermore, it will be used to account for low-frequency undulations of the jet. The former is based on Ervine & Falvey (1987) and defined by equation (3.25) in Chapter III:

$$\frac{\delta_{out}}{X} = 0.38 \cdot Tu \tag{7.1}$$

in which δ_{out} stands for the half angle of outer lateral jet spread as presented in Fig. III-14, and X the longitudinal distance from the point of jet issuance. Typical angles of jet spread are 3-4 % for roughly turbulent jets. Ervine et al. (1997) also estimated the jet spread ε as:

$$\varepsilon = \frac{1.14 \cdot Tu \cdot V_i^2}{g} \cdot \left[\sqrt{\frac{2 \cdot L}{D_i \cdot Fr_i^2} + 1} - 1 \right] \tag{7.2}$$

in which Fr_i stands for the Froude number of the jet at issuance. Although the turbulence intensity Tu is a parameter that reflects the whole range of frequencies of the pressure fluctuations of the jet, it is assumed herein that it also gives an idea about low-frequency fluctuations, i.e. the compactness of the jet during its fall. During the experiments of the present project, it has been found that significant scatter in root-mean-square pressure values may exist at the water–rock interface. It is believed that this scatter is also present under prototype impact conditions and that the phenomenon can be appropriately described by the initial jet turbulence intensity.

Hence, assessment of the turbulence intensity Tu defines the root-mean-square values of the pressure fluctuations at the water-rock interface. This is essential because these values are directly related to the peak pressures inside underlying rock joints. The relationship between turbulence intensity and root-mean-square pressure value is presented in Fig. VII-3. In many cases, the initial jet turbulence intensity is unknown. Under such circumstances, an estimation can be made based on the type of outlet structure. This is defined by the following Table:

TYPE OF OUTLET STRUCTURE	TURBULENCE INTENSITY Tu
1. Free overfall	0-3 %
2. Ski-jump outlet	3-5 %
3. Intermediate outlet	3-8 %
4. Bottom outlet	3-8 %

Table VII-1 Estimation of the initial jet turbulence intensity based on the type of outlet structure.

The Tu values have been estimated based on the measurements made under the impact of cylindrical and convergent jets. It is assumed that the convergent outlet is representative for free overfall jets. This outlet generated compact jets with low turbulence intensity (2-3 %). The cylindrical jet outlet is believed to be representative for both ski-jumps and intermediate or bottom outlets. This pressurized outlet system is effectively very similar to an intermediate or bottom outlet. The ski-jump is created by a free outlet, however, its particular flow pattern upstream of the point of issuance creates higher turbulence intensities than the free overfall. The cylindrical jets were generally less stable and produced a higher turbulence intensity, i.e. 4-6 %. This classification constitutes a simplification of reality. Tu can largely depend on specific geometric characteristics of the outlet, the flow pattern immediately upstream of the outlet, etc. All these aspects have to be accounted for. Although this goes beyond the scope of the present study, it is obvious that further research is necessary in this area.

The next step is to define the trajectory of the jet through the atmosphere. A summary of existing equations for different types of outlet structures (free overfall, ski-jump, bottom outlet) has been given by Whittaker & Schleiss (1984). These equations are based on ballistic aspects and drag forces encountered by the jet through the air and will not be further outlined herein. The basic output of these equations is the exact location of the jet impact, the jet trajectory length L and the jet velocity at impact V_j. Knowledge of the jet trajectory length allows determining the contraction of the jet due to gravitational acceleration. This conducts to the jet diameter at impact D_j. This diameter is essential to determine the Y/D_j ratio. Secondly, the turbulence intensity Tu defines the lateral spread of the jet in equation (7.1). Superposition of this spread to the initial jet diameter D_i results in the inner and outer limits of the jet diameter D_{in} and D_{out}. The outer diameter of the jet at impact D_{out} will be used to define the maximum zone at the water-rock interface where severe pressure damage might occur. The expressions for D_j and D_{out} have been defined in Chapter II and are repeated here for completeness:

$$D_j = D_i \cdot \sqrt{\frac{V_i}{V_j}} \tag{7.3}$$

$$D_{out} = D_i + 2 \cdot \delta_{out} \cdot L \tag{7.4}$$

in which V_i and V_j are the jet velocity at issuance and the jet velocity at impact in the pool respectively. The latter is defined by gravitational acceleration as follows:

$$V_j = \sqrt{V_i^2 + 2gZ} \tag{7.5}$$

in which Z stands for the vertical fall distance of the jet. The angle of the jet at its point of impact is neglected in the present analysis. For impingement angles that are close to the vertical (70-90°), this effect may be neglected. For smaller impingement angles, it is proposed to use the same hydrodynamic parameters as for vertical impingement, but to redefine the water depth in the pool Y as the exact trajectory length of the jet through the water cushion, and not as the vertical difference between water level and pool bottom. Table VII-2 summarizes the input and output parameters:

FALLING JET MODULE	
INPUT	OUTPUT
1. Outlet structure: type and geometry	1. Location of jet impact x_{ult}
2. Jet velocity at issuance V_i	2. Jet trajectory length L
3. Jet diameter at issuance D_i	3. Jet impact diameters D_j and D_{out}
4. Initial jet turbulence intensity Tu	4. Jet impact velocity V_j

Table VII-2 Input and output parameters of the falling jet module.

Although the falling jet process has not been extensively studied in the present work, it is of crucial importance to the downstream physical phenomena and should be determined as precisely as possible. Any inaccuracy will be transferred towards the other two modules. This can induce significant errors. Fig. VII-1 presents the main parameters.

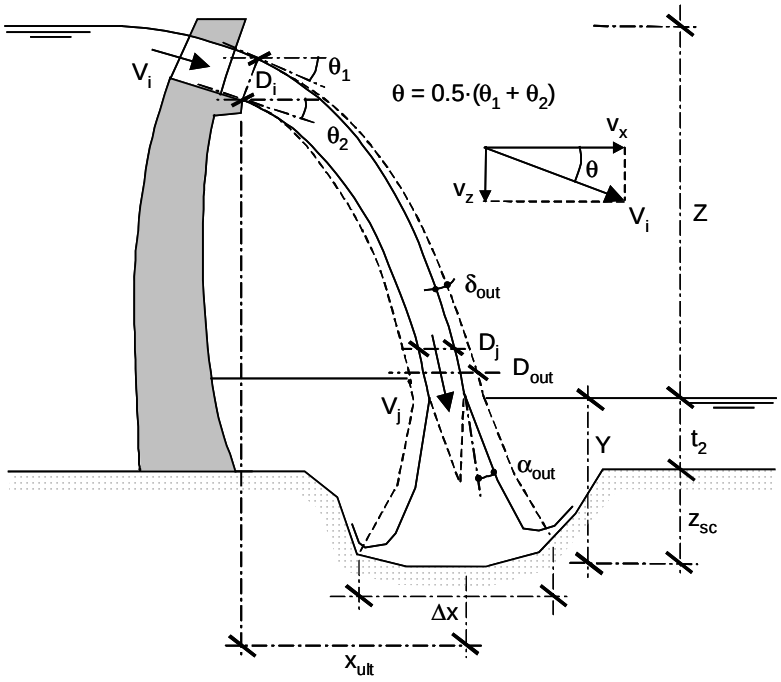

a) free overfall

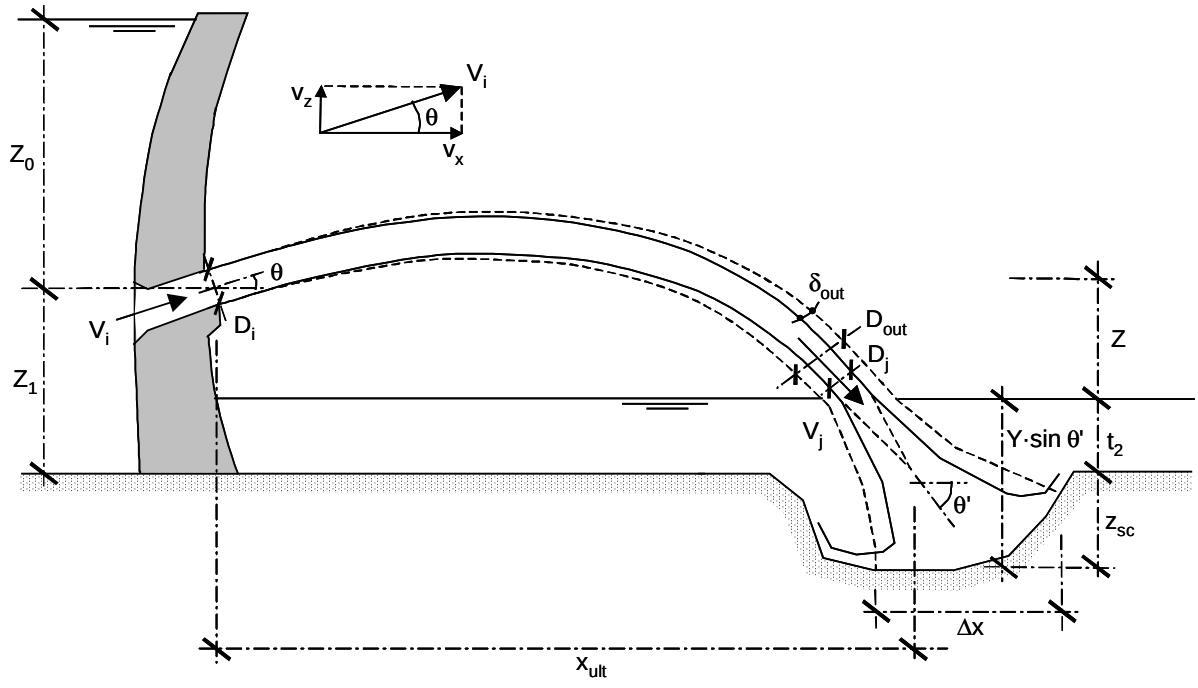

b) pressurized outlet

Fig. VII-1 Definition sketch of parameters of a falling jet: a) free overfall jet; b) pressurized outlet.

3. The plunge pool

3.1. Definition of the Y/D_j ratio

The second module refers to the hydraulic and geometric characteristics of the plunge pool basin downstream of the dam and defines the hydrodynamic loading at the water-rock interface. The basin may be natural, formed by the shape of the valley and the downstream riverbed, or artificial, by construction of a downstream structure that ensures a minimum tailwater depth at any instant. In case of natural basins, the "tailwater level Y - discharge Q" relationship is calculated in the immediate vicinity of the downstream river. For artificially created basins, it is defined by the control structure. The **water depth in the plunge pool Y** is undoubtedly one of the most important parameters of the scour model. It is defined as the vertical difference between the water level in the basin and the bedrock level. This difference increases with increasing flow discharge Q. A comparison is made here between a natural river and an overflow structure of a tailwater dam. The structure comprises a rectangular crest weir (tailpond dam) of 10 m of length, with a height of 5 m (Fig. VII-2).

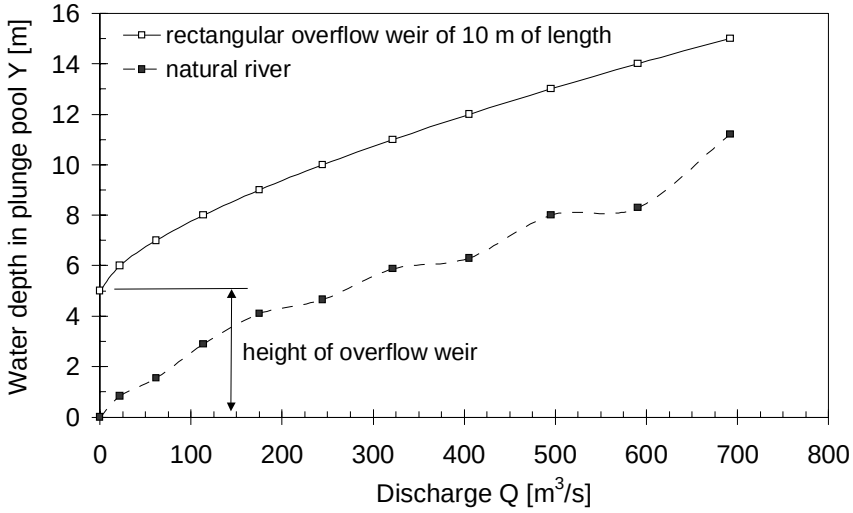

Fig. VII-2 Initial water depth in the plunge pool Y as a function of the total flow discharge from the dam Q. Comparison is made between a rectangular overflow crest and a natural river.

This defines the plunge pool water depth Y. Initially, this depth equals the tailwater depth t_2 as defined in Fig. VII-1. It is evident that, during scour progression, the water depth Y has to be increased with the depth of the already attained scour. Some prototype observations indicate possible mounding at the downstream end of the basin. This mounding results from detached rock blocks that are swept away and that deposit immediately downstream of the basin. This can cause a change of the "tailwater level Y - discharge Q" relationship, but is neglected in the present analysis.

Knowledge of the plunge pool water depth Y together with the output parameters of the jet module (Table VII-2) allows determining the ratio of water depth to jet diameter at impact Y/D_j. This ratio is directly related to the diffusion characteristics of the jet through the pool. However, its definition is purely theoretical and precaution should be taken when applying it to practice. Significant differences may exist due to the appearance of vortices or other surface disturbing effects, which can change the water depth in the pool. No model actually exist that accurately takes into account these effects. Hence, engineering judgment is required on a case-by-case basis.

The water depth Y defines the static pressure on the water-rock interface. Although this pressure is often insignificant compared to the dynamic pressures of the impacting jet, it may become relevant when the ultimate scour depth is approached. Near such depths, the diffusion of the jet becomes predominant and eliminates the dynamic action at the bedrock. However, the water depth in the pool often has increased up to several tens of metres. Such static pressures may have an impact on the calculus of crack propagation. The influence on dynamic uplift of single rock blocks is insignificant.

3.2. Definition of root-mean-square pressure fluctuations C'_{pa}

The module for the falling jet pointed out that the turbulence intensity of the jet Tu defines the degree of turbulent pressure fluctuations of the jet at its point of impact in the plunge pool. Hence, the plunge pool module assumes that the root-mean-square value of the pressure fluctuations at the water-rock interface, as expressed by the non-dimensional coefficient C'_{pa}, depends on both the Y/D_j ratio and the initial turbulence intensity of the jet Tu. This is presented in Fig. VII-3b.

The presented data points have been measured in the experimental facility, under the jet's centreline, but only for jet impact velocities higher than 20 m/s. This restriction has been introduced because Fig. V-8b (Chapter V) shows that, for such jet velocities, the root-mean-square value becomes independent of the velocity. It is believed that the presented results are exempt of scale effects and, thus, representative for prototype jets.

The measured data have been approached by a polynomial regression of third order. This polynomial form has been obtained through curve fitting of the bandwidth of upper data as given by Ervine et al. (1997) and presented in Fig. V-8a of Chapter V. The regression coefficient for this curve fitting was equal to 0.99 and yielded the following relationship (Bollaert et al., 2002):

$$C'_{pa} = 0.0022 \cdot \left(\frac{Y}{D_j}\right)^3 - 0.0079 \cdot \left(\frac{Y}{D_j}\right)^2 + 0.0716 \cdot \left(\frac{Y}{D_j}\right) + 0.0583 \qquad (7.6)$$

The first and the fourth coefficients have been modified in the way indicated at Table VII-3. This results in four similar-shaped curves but with a different offset. These curves were found to agree with the measured data and can be used up to a Y/D_j ratio of 18-20. For higher ratios, the value that corresponds to a ratio of 18-20 is proposed.

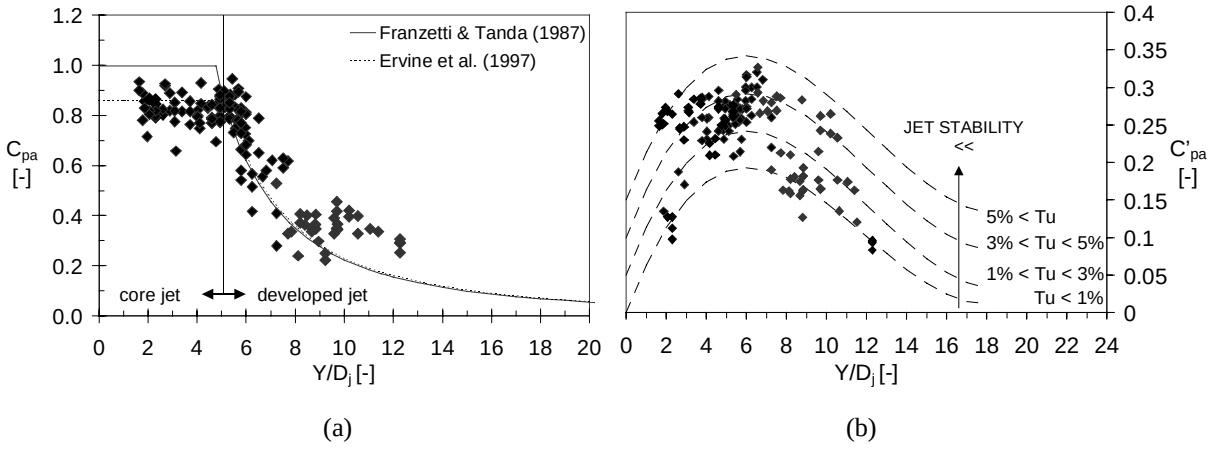

(a) (b)

Fig. VII-3 Non-dimensional dynamic pressure coefficients C_{pa} and C'_{pa} for jet velocities higher than 20 m/s: a) mean pressure coefficient. The data corresponds to the best fit curve made by Ervine et al. (1997); b) root-mean-square pressure coefficient. The data are approached by four polynomial regressions of the third order. The shape of the regressions is obtained by curve fitting of the bandwidth of upper data of Ervine et al. (1997). Data based on Bollaert et al. (2002).

It is believed that the curve with the highest root-mean-square values is valid for diffusing jets (see Fig. IV-3), i.e. jets with an undulating or low-frequency turbulent character or jets with a turbulence intensity Tu that is higher than 5 %. The curve with the lowest values is applicable to compact jets. These are jets that are smooth-like during their fall, without any possible source of low-frequency instability and with a turbulence intensity that is lower than or equal to 1 %. In between, two other curves have been defined. They are applicable to intermediate stable-unstable or unstable jets.

Tu [%]	a_1	a_2	a_3	a_4	Type of jet
< 1	0.0022	-0.0079	0.0716	0	compact
1-3	0.00215	-0.0079	0.0716	0.050	intermediate
3-5	0.00215	-0.0079	0.0716	0.100	undulating
> 5	0.00215	-0.0079	0.0716	0.150	very undulating

Table VII-3 Polynomial coefficients and regression coefficient for different turbulence intensities.

The key issue is that the turbulence intensity Tu has been directly related to low-frequency instabilities or undulations of the jet. In fact, Tu reflects the whole range of frequencies of the pressure fluctuations of the jet, and not just the ones that cause undulations and low-frequency instabilities. Nevertheless, as already outlined in § 2, it is believed that these effects have a profound impact on the Tu value. The latter can thus be used to express this phenomenon.

3.3. Definition of mean dynamic pressure coefficient C_{pa}

The non-dimensional mean dynamic pressure coefficient C_{pa} is defined by the Y/D_j ratio and by the velocity of the jet at impact in the plunge pool V_j. For high jet velocities, however, the values become independent of the jet velocity (Fig. V-6b of Chapter V). The data for jet velocities higher than 20 m/s are presented in Fig. VII-3a and are in good agreement with the best-fit of data of Ervine et al. (1997). The latter defined C_{pa} as a function of Y/D_j and of the air concentration at impact in the pool α_i:

$$C_{pa} = 38.4 \cdot (1-\alpha_i) \cdot \left(\frac{D_j}{Y}\right)^2 \qquad \text{for } Y/D_j > 4\text{-}6 \tag{7.7}$$

$$C_{pa} = 0.85 \qquad \text{for } Y/D_j < 4\text{-}6$$

The air concentration at impact α_i is defined as a function of the volumetric air-to-water ratio β:

$$\alpha_i = \frac{\beta}{1+\beta} \tag{7.8}$$

Expressions for β are summarized in § 3.2.3 of Chapter III. Following equation (7.7), the mean dynamic pressure decreases with increasing air content in the plunge pool. This, however, is without accounting for the low-frequency turbulence of the jet. This may have a significant impact on the mean pressure value. As such, on the present facility, the higher mean values were obtained at very high air concentrations, because the jet was more stable under such circumstances. Based on the experimental results, it is recommended to relate the choice of C_{pa} to the choice of C'_{pa} in the following manner: the higher the chosen curve of root-mean-square values, the lower the choice for the mean pressure value. This is logical considering that turbulent or undulating jets generate high root-mean-square values, but low mean pressures.

3.4. Definition of radial root-mean-square pressure fluctuations C'$_{pa}$

The radial distribution of the non-dimensional fluctuating dynamic pressure coefficient C'$_{pa}$ is of great significance for the radial shape and extension of the scour hole. The radial decrease of the root-mean-square values compared to the root-mean-square value under the jet's centreline is presented in Fig. VII-4b.

This has been done as a function of the non-dimensional radial distance r/r$_{max}$. The maximum radial extension of the zone that is influenced by the turbulent shear layer of the impacting jet is called r$_{max}$ and is defined as $r_{max} = 0.5 \cdot D_j + 0.25 \cdot Y$. The value of 0.25 times the plunge pool depth Y accounts for the spread of the jet through the water depth of the plunge pool. This spread is governed by an outer angle of 13-14°, i.e. a spread of one to four (McKeogh & Elsawy, 1980).

For developed jets, the decrease fits an exponential curve. At the outer boundary of the turbulent shear layer, still 10-20 % of the centreline fluctuations subsist. For core jets, no exponential law can be used at first sight. The significant spread of the jet, as well as the occurrence of jet undulations, result in a much less expressed radial decrease. A similar curve than for developed jets can be drawn but has to be shifted radially outwards with a value of about 0.5 times r$_{max}$. It is much like if the spread of the jet displaced the centreline of the jet radially outwards. This means that, at plunge pool depths less than 4-6 times the jet diameter, the radial persistence of the pressure fluctuations becomes very important. The radial distance that is subjected to the turbulent shear layer has to be increased with 0.5 times r$_{max}$. The significant radial persistence of root-mean-square pressures is in accordance with previous findings by Franzetti & Tanda (1987) and May & Willoughby (1991). For practice, the following expressions are proposed (Bollaert et al., 2002):

$$\frac{C'_{pr}}{C'_{pa}} = e^{-3\cdot\left(\frac{r}{r_{max}}\right)^2} \qquad \text{for developed jets and all r values} \qquad (7.9)$$

$$\frac{C'_{pr}}{C'_{pa}} = e^{-3\cdot\left(\frac{r}{r_{max}}-0.5\right)^2} \qquad \text{for core jets and } r > 0.5\cdot r_{max} \qquad (7.10)$$

$$\frac{C'_{pr}}{C'_{pa}} = 1 \qquad \text{for core jets and } r < 0.5\cdot r_{max} \qquad (7.11)$$

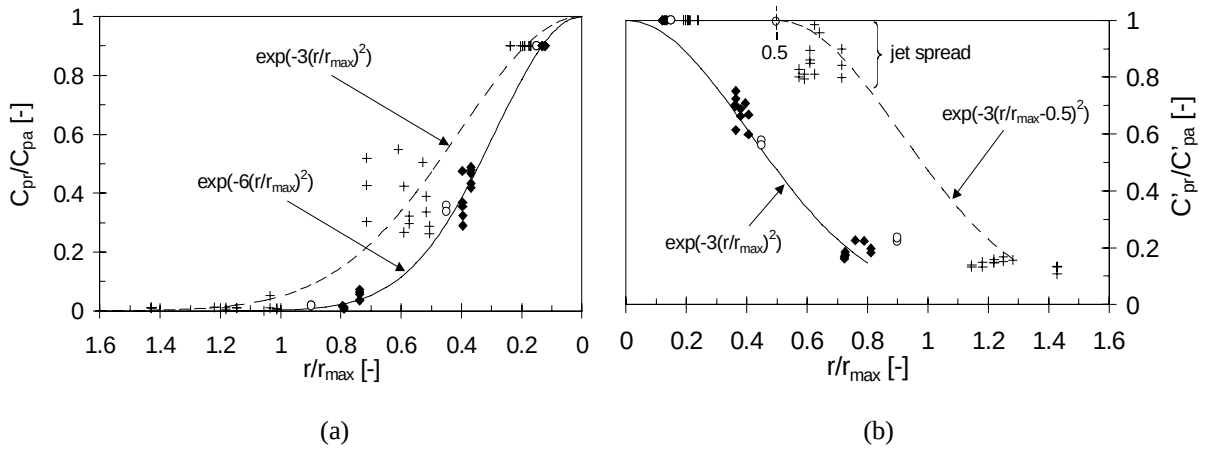

Fig. VII-4 Radial distribution of the non-dimensional dynamic pressure coefficients at the plunge pool bottom: a) mean dynamic pressure coefficients C$_p$; b) root-mean-square pressure coefficients C'$_p$. The reference distance r$_{max}$ is defined as the maximum radial extension of the zone that is subjected to the turbulent shear layer of the impacting jet $r_{max} = 0.5 \cdot D_j + 0.25 \cdot Y$ (Bollaert et al., 2002).

3.5. Definition of radial mean dynamic pressure coefficient C_{pa}

The radial persistence of the mean dynamic pressures values has been determined in Fig. VII-4a. It can be seen that both core and developed jets are described by an exponential decay. The decay curve for core jets is less expressed and the measured data show some scatter. This is due to the aforementioned low-frequency jet turbulence. For practical purposes, the following expressions are proposed (Bollaert et al., 2002):

$$\frac{C_{pr}}{C_{pa}} = e^{-3\cdot\left(\frac{r}{r_{max}}\right)^2} \quad \text{for core jets} \tag{7.12}$$

$$\frac{C_{pr}}{C_{pa}} = e^{-6\cdot\left(\frac{r}{r_{max}}\right)^2} \quad \text{for developed jets} \tag{7.13}$$

It can be concluded that the radial decay of the mean dynamic pressures is much higher than the radial decay of the corresponding root-mean-square pressures. This statement is essential for the development of the scour hole, because the root-mean-square pressures generate peak pressures inside underlying rock joints. This is dealt with in the rock mass module.

The extreme pressure values at the pool bottom have been presented in Fig. V-9 of Chapter V. According to previous studies, they can be assumed equal to 4 times the corresponding root-mean-square pressure value. Similarly, the negative extreme pressure values are equal to 3 times the root-mean-square value below the mean value.

3.6. Input and output parameters of the plunge pool module

The input and output parameters of the module for the plunge pool are presented at Table VII-4. The input parameters correspond to the output of the module for the falling jet. The output parameters will be used as input for the module for the rock mass.

PLUNGE POOL MODULE	
INPUT	OUTPUT
1. Location of jet impact x_{sc}	1. Y/Dj ratio
2. Jet trajectory length L	2. Centreline mean pressure C_{pa}
3. Jet impact diameters D_j and D_{out}	3. Centreline pressure fluctuations C'_{pa}
4. Jet impact velocity V_j	4. Radial mean pressure C_{pr}
5. Turbulence intensity Tu	5. Radial pressure fluctuations C'_{pr}

Table VII-4 Input and output parameters of the plunge pool module.

The ultimate scour depth under the jet's centerline can be defined by use of only the first three output parameters. The shape and the extension of the ultimate scour hole need use of all five output parameters. The radial pressure coefficients, however, have been determined for a flat plunge pool bottom. Significant local changes may occur in practice due to a differently shaped bottom. This aspect has never been investigated in detail and is beyond the scope of the project. It should merit some attention in further research.

4. The rock mass

The principal parameters of the hydrodynamic loading at the bottom of the plunge pool have been defined in the plunge pool module. This module is used as direct input for determination of the hydrodynamic loading inside underlying open-or closed-end rock joints. The governing parameters are defined hereafter.

4.1. Definition of hydrodynamic loading inside closed-or open-end joints

Four basic parameters describe the hydrodynamic loading inside closed-end or open-end rock joints:

1. maximum dynamic pressure C^{max}_{p}
2. characteristic amplitude of pressure cycles Δp_c
3. characteristic frequency of pressure cycles f_c
4. maximum dynamic impulsion C^{max}_{I}

The first parameter is relevant to brittle propagation of closed-end rock joints. The second and third parameters are necessary to express time-dependent propagation of closed-end rock joints. The fourth parameter is used to define dynamic uplift of rock blocks formed by open-end rock joints.

4.1.1. Maximum dynamic pressure C^{max}_{p} in a closed-end rock joint

The **maximum dynamic pressure C^{max}_{p}** is obtained through multiplication of the root-mean-square pressure value C'_{pa} by the amplification factor Γ^{+}, and by superposing this product to the mean dynamic pressure value C_{pa}. The product of C'_{pa} times Γ^{+} results in the coefficient C^{+}_{pd}. This is shown in Fig. VII-4. The superposition of C_{pa} and C^{+}_{pd} is necessary because the amplification of the root-mean-square pressures only influences the fluctuating part of the dynamic pressures. As such, the maximum pressure value is written:

$$P_{max}[Pa] = \gamma \cdot C^{max}_{pd} \cdot \frac{\phi \cdot V_j^2}{2g} = \gamma \cdot \left(C_{pa} + \Gamma^{+} \cdot C'_{pa}\right) \cdot \frac{\phi \cdot V_j^2}{2g} \qquad (7.14)$$

in which C_{pa} and C'_{pa} are defined by equations (7.6) and (7.7) and γ stands for the specific weight of the water (in N/m^3). As a first approach, the ϕ value can be chosen equal to one. The uncertainty lies in the amplification factor Γ^{+}. Similar to the root-mean-square pressure values at the bottom of the plunge pool, theoretical curves have been defined for maximum respectively minimum values of the amplification factor Γ^{+} as derived from the experiments:

$$\begin{aligned}
&\Gamma^{+} = 4 + 2 \cdot Y/D_j && \text{for } Y/D_j < 8 && \\
&\Gamma^{+} = 20 && \text{for } 8 \le Y/D_j \le 10 && \text{curve of maximum values} \\
&\Gamma^{+} = 40 - 2 \cdot Y/D_j && \text{for } 10 < Y/D_j && \\
&\Gamma^{+} = -8 + 2 \cdot Y/D_j && \text{for } Y/Dj < 8 && \\
&\Gamma^{+} = 8 && \text{for } 8 \le Y/D_j \le 10 && \text{curve of minimum values} \\
&\Gamma^{+} = 28 - 2 \cdot Y/D_j && \text{for } 10 < Y/D_j &&
\end{aligned} \qquad (7.15)$$

For jet velocities higher than 20 m/s, the measured amplification factors become more or less independent of the velocity (Fig. VII-5a). However, considerable scatter is obtained when expressing the values as a function of the Y/D_j ratio (Fig. VII-5b). For core jet impact, a value of about 4 is systematically obtained at prototype jet velocities. For developed jets, some scatter is observed.

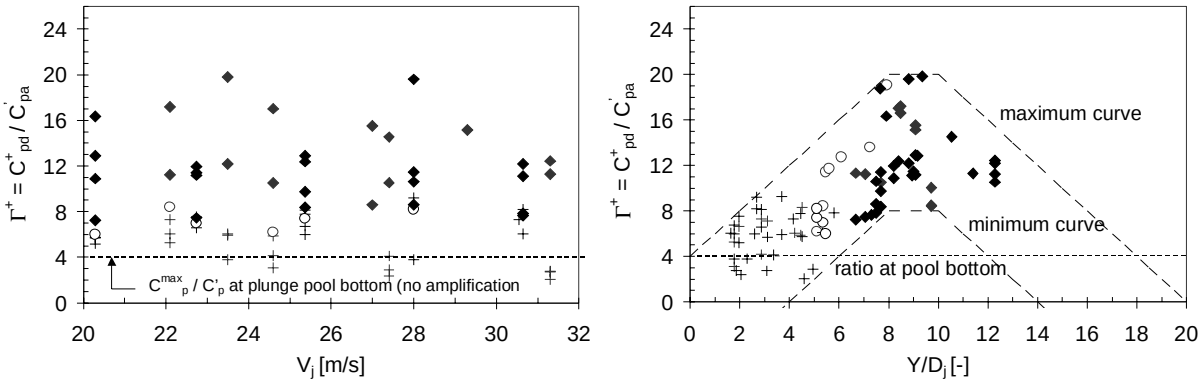

(a) (b)

Fig. VII-5 Amplification factor Γ^+ between the maximum pressures inside the joints and the root-mean-square pressures at the water-rock interface: a) as a function of jet velocity V_j; b) as a function of Y/D_j. The data are circumscribed by a maximum curve and a minimum curve.

It is also possible to directly express the C^+_p values as a function of Y/D_j. Positive extreme pressure coefficients C^+_{pd} have been measured at sensor (d). They are presented in Fig. VII-6a. The observed scatter is not higher than the one for the amplification factor and the root-mean-square values. The highest coefficients represent 5 times the incoming kinetic energy of the jet. Furthermore, the general form of the data is more or less bi-linear. A maximum, average and minimum relationship have been defined as follows:

$$
\begin{aligned}
&C^+ = 2 + 0.40 \cdot Y/D_j && \text{for } Y/D_j < 8 && \\
&C^+ = 10.54 - 0.66 \cdot Y/D_j && \text{for } 8 \le Y/D_j && \text{curve of maximum values} \\
&C^+ = 0 + 0.40 \cdot Y/D_j && \text{for } Y/D_j < 8 && \\
&C^+ = 8.54 - 0.66 \cdot Y/D_j && \text{for } 8 \le Y/D_j && \text{curve of average values} \qquad (7.16) \\
&C^+ = -2 + 0.40 \cdot Y/D_j && \text{for } Y/D_j < 8 && \\
&C^+ = 6.54 - 0.66 \cdot Y/D_j && \text{for } 8 \le Y/D_j && \text{curve of minimum values}
\end{aligned}
$$

These C^+_{pd} curves can be used to directly calculate the appropriate maximum pressure value inside the rock joints by superposition of C_{pa} and C^+_{pd}. The scatter in data might be explained by the following theory. The degree of amplification of pool bottom pressure fluctuations depends on the capability of the rock joints to generate peak pressures. This capability was found to be dependent on the air content inside the joints. The highest measured air contents, on the order of 10-20 %, seem to generate a sort of cushioning effect on the pressure waves. Under such circumstances, it is very difficult for the impacting jet to produce very high peak pressures. This has been observed in the L-joint, where a very high velocity and pressure was needed to generate significant amplifications. For this joint, it was found that the air content near the end was very high, much higher than for the I-joint. The I-joint only exhibited high air contents at the highest jet velocity that could be generated in the model. As the behaviour of the pressure pattern inside the I-joint completely changed for this particular jet velocity, it was suspected that this sudden change could be due to leakage of water from the joint towards the outside. Peak pressures were significantly lower at this high velocity.

Thus, without any further assumption on the amount of air inside the joints, it can be concluded that the scatter in maximum pressures might be caused by the exact air concentration inside. Hence, it could be argued that extremely high peak pressures can only be present when no high air content is available or no significant leakage of water occurs out of the joint. This assumption is valid in case of tightly healed rock joints. For such rock joints, the upper bound of the maximum pressure values should be used. For rock joints with several side branches, or joints that are not tightly healed, more air could be present inside. Thus, the lower bound values seem more appropriate.

Although the use of the directly measured C^+_{pd} values seems more appropriate than the determination of C^+_{pd} by means of both C'_{pa} and Γ^+, such measurements were only made for rock joints that are situated under the jet's centreline. For rock joints that are located radially outwards of the jet's centreline, the maximum pressure value has to be derived from C'_{pa} and Γ^+.

It is interesting to compare the directly measured C^+_{pd} values with the ones that can be calculated based on the theoretical curves that were defined for both C'_{pa} and Γ^+. For the root-mean-square values at the plunge pool bottom, four curves have been presented in Fig. VII-3b and have been defined at Table VII-3. The two extreme ones (for a compact and a very undulating jet) will be used in the present analysis. For the amplification factor inside the rock joints, a maximum and a minimum curve have been presented and defined in Fig. VII-5b. This procures two times two curves that have been multiplied one with another. The four resulting curves are presented in Fig. VII-6b.

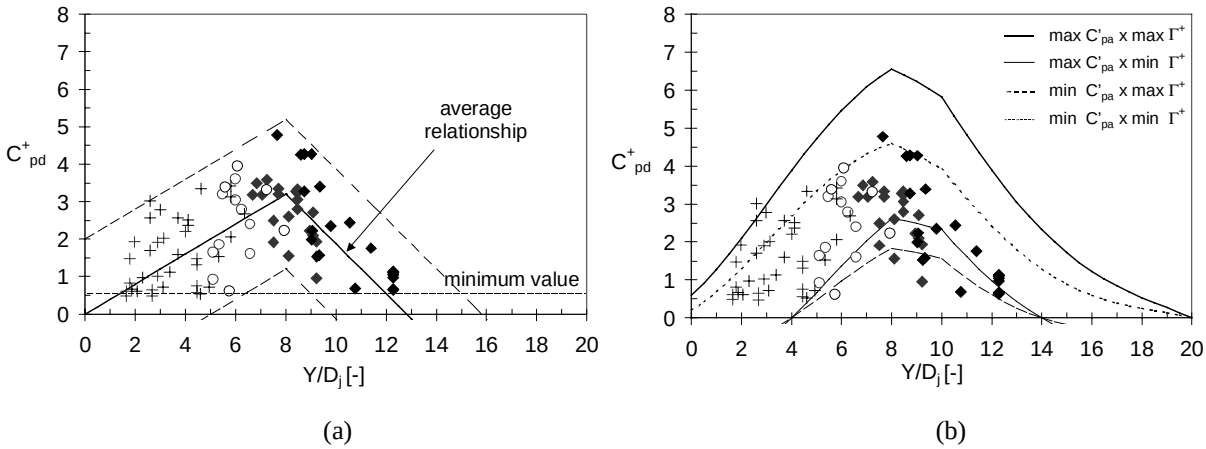

Fig. VII-6 Non-dimensional positive extreme pressure coefficient C^+_{pd} of dynamic pressure inside closed-end rock joints: a) Maximum, average and minimum curves as a function of Y/D_j; b) Comparison of data with the curves obtained by multiplication of C'_{pa}–curves and Γ^+-curves.

The combination of maximum fluctuations and maximum amplifications leads to extreme coefficients that are apparently very high. All other combinations are in better agreement with the measured data points. As a result, a very high fluctuation at the pool bottom does not necessarily result in a high amplification inside the rock joint. In fact, for this to happen, appropriate air content is needed also.

For practical purposes, the directly measured values can be used whenever possible. The appropriate theoretical curve should be chosen as a function of the tightness of the joints. For joints that are situated radially outwards, the same reasoning holds. However, in this case the maximum values have to be derived from the product of the appropriate root-mean-square curve with the appropriate amplification curve. The former can be chosen as a function of the turbulence intensity and the low-frequency turbulence of the jet. The latter is chosen as a function of the tightness of the rock joints.

4.1.2. Characteristic amplitude of pressure cycles Δp_c in a closed-end rock joint

The **characteristic amplitude of the pressure cycles Δp_c** is determined by the characteristic maximum and minimum pressures of the cycles. According to the shape of the pressure spikes, the minimum values are quite constant and always close to the standard atmospheric pressure. The maximum pressures, however, cannot be chosen equal to the C^{max}_p value. The latter is not at all representative for the pressure cycles. In fact, each cycle has a different maximum value. This value can be extremely high, in case of a maximum pressure peak, or can be rather low, for a moderate pressure peak. Hence, an average value of the maximum pressures is needed. This average value has been obtained by counting the number of peaks and by making the average of all the peak values. The number of peaks has been chosen to correspond to the fundamental resonance frequency of each

particular test run. As such, the cyclic character of the system is preserved. The results of averaged peak values are presented in Fig. VII-7.

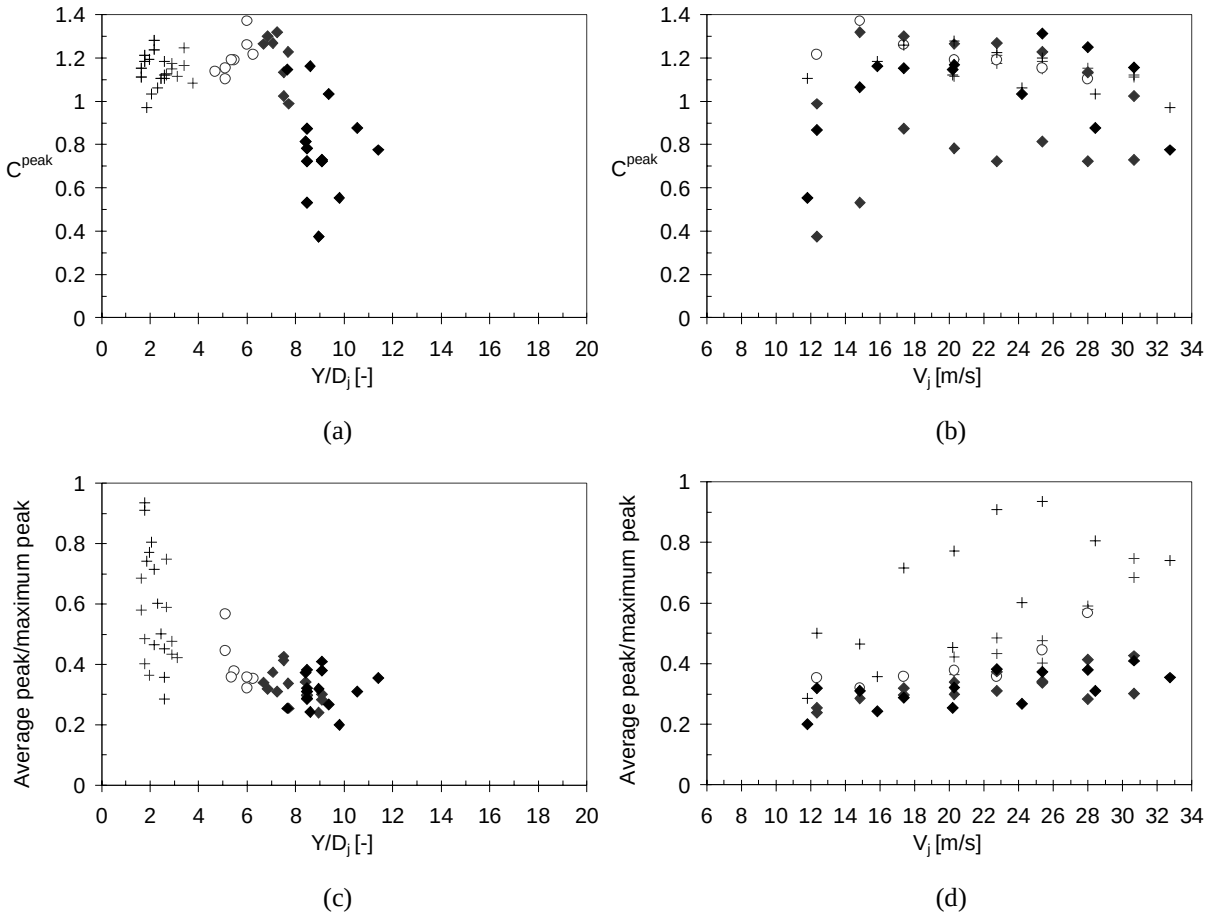

Fig. VII-7 Average values of the peak pressures C^{peak} inside closed-end rock joints:
a) average value as a function of Y/D_j; b) average value as a function of V_j;
c) average/maximum ratio as a function of Y/D_j; d) average/maximum ratio as a function of V_j.

A huge difference can be observed between core jets and developed jets. This is normal because core jets do not exhibit the same extreme peak pressures as developed jets. The lower the most extreme peak value, the higher is the average peak value when compared to the extreme one. Developed jets show somewhat lower average peak values, but nevertheless it can be seen in Figs. VII-7a & 7d that this average value corresponds to only 40 to 50 % of the most extreme peak value. Hence, the characteristic amplitude of pressure cycles inside rock joints can be defined in two ways:

	Core jets	Transitional jets	Developed jets
% of maximum peak pressure	80 %	60 %	40-50 %
N° of times the kinetic energy	1.40	1.30	1.25

Table VII-5 Definition of the characteristics amplitude of pressure cycles inside rock joints for core, transitional and developed jets.

4.1.3. Characteristic frequency of pressure cycles f_c in a closed-end rock joint

The **characteristic frequency of pressure cycles f_c** is dictated by the assumption of a $\lambda/4$ – resonator. As such, the air concentration α_i and the total length of the joint L are of significance. An assumption has to be made on the length of the joint. This depends on the interdistance between the different joints. The air content inside the joints can be related to the air content in the plunge pool as presented in Fig. VII-8. It depends on the mean dynamic pressure value C_{pa} at the bottom of the pool. However, a broad brush first hand estimation considers a mean celerity of about 100 m/s at very high mean impact pressures (50 m of water column or more), and a mean celerity of 150-200 m/s at mean impact pressures that are lower than 50 m of water column. The resonance frequency f_{res} is then defined by $f_{res} = c/4 \cdot L$, in which L stands for the total length of the joint. Typical joint lengths are on the order of 0.5 to 2 m. This results in frequencies of 12.5 to 100 Hz, depending on the mean impact pressure.

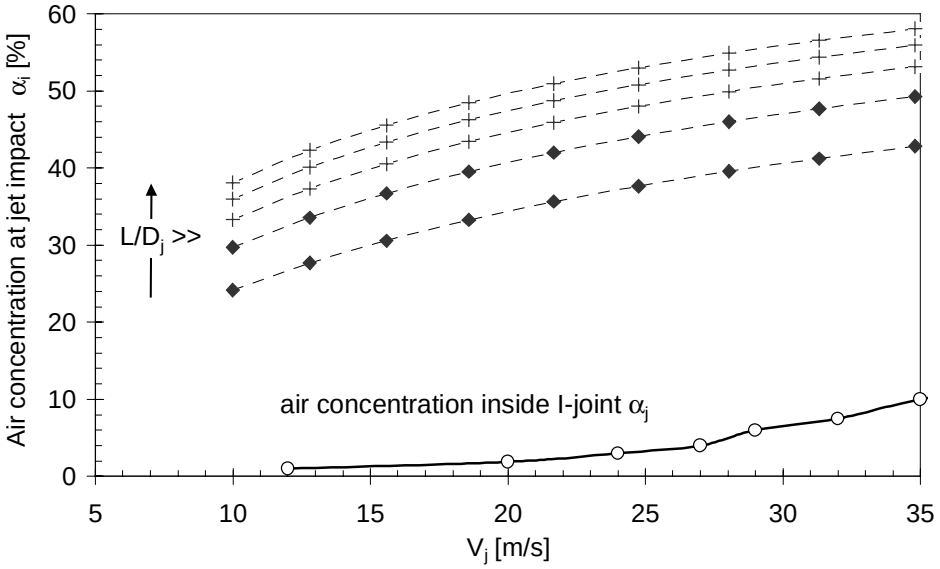

Fig. VII-8 Comparison between the air concentration at the point of jet impact in the pool α_i and the corresponding air concentration inside the I-shaped one-dimensional rock joint α_j.

4.1.4. Maximum dynamic impulsion C^{max}_I in an open-end rock joint

Finally, the **maximum dynamic impulsion C^{max}_I** in an open-end rock joint is defined based on § 4.4.3 of Chapter III. The impulse on a rock block is expressed by equation (3.101) and corresponds to a time integration of the net forces on the rock block:

$$I_{\Delta tpulse} = \int_0^{\Delta tpulse} \left(F_u - F_o - G_b - F_{sh}\right) \cdot dt = m \cdot V_{\Delta tpulse} \qquad (3.101)$$

For simplicity, a rectangular shaped rock block is assumed, with the sides directed along the horizontal and the vertical respectively. The different forces on such a rock block are defined in Fig. III-36 and consist of the upward and downward pressure forces F_u and F_o, the immerged weight of the block G_b and the shear forces along the joints F_{sh}. As a first approach, the latter can be neglected. Furthermore, the immerged weight of the block depends on the shape of the block and can be easily handled mathematically. The problem lies in the determination of the upwards and downwards directed pressure forces. These forces are generated by the pressure fields over and under the block. The pressure field over the block is governed by turbulent shear layer impact. The pressure field under the

block corresponds to the transient pressure field that is generated inside open-end rock joints as described in Chapters III and V.

The different forces are considered independent of the progressive movement of the rock block. This is a simplification of reality. For example, the shear forces can considerably increase due to a change in block position. On the other hand, the pressure forces under the block could decrease due to the cavity that is formed under the block once the latter starts moving. These effects, however, are hard to formulate. The pressure drop due to cavity formation under the block is not known. The shear forces along the joints depend on the points of contact between the blocks and on the in-situ horizontal stress field of the rock mass.

Therefore, some assumptions have to be made. First of all, the transient pressures under the block are believed to be independent of the movement of the block. This seems plausible when the net impulsion consists of a high peak pressure during a small time interval. For such an impulsion, the block has not enough time to move during the initial phase of the impulsion and, hence, cannot influence the subsequent part of the impulsion. For impulsions that consist of a low pressure during a relatively long time interval, this becomes less evident. However, it is a priori not excluded that the water can progressively fill up the formed cavity during several consecutive impulsions. These particular physical phenomena merit more attention but are beyond the scope of the present work.

Hence, the first step is to define the instantaneous differences in pressure forces over and under the block. For periods Δt during which positive differences exist, the time integral has been taken over these periods. This results in net impulsions I. A maximum net impulsion I^{max} can so be defined. This has been done systematically for the test runs with the D-joint as described in § 5.2 of Chapter V.

Similar to the pressure coefficients, the maximum net impulsion I^{max} has to be made non-dimensional. This is done by defining the impulsion as the product of a net force times a time period. The net force is firstly transformed into a pressure. This means that the problem is looked at for a unitary surface of the block ($1m^2$ according to the units). This pressure can then be made non-dimensional by dividing it by the incoming kinetic energy $\phi \cdot V^2/2g$, just like for the pressure coefficients in Chapter V. This results in a net uplift pressure coefficient C_{up}.

The time period is non-dimensionalized by the characteristic period for pressure waves inside rock joints, i.e. $T = 2L/c$, in which L stands for the total length of the joint and c is the mean wave celerity. This conducts to a time coefficient T_{up}. Hence, the non-dimensional impulsion coefficient C_I is defined by the product $C_{up} \cdot T_{up} = V^2L/gc$ [m·s] and is presented in Fig. VII-9. The net maximum impulsion I^{max} is finally obtained by multiplication of the value for C_I by V^2L/gc. Fig. VII-9a shows that, for jet velocities higher than 20 m/s, a quite constant value for C_I is observed. This is confirmed in Fig. VII-9b, where the coefficient C_I is presented as a function of the Y/D_j ratio. The observable scatter is quite low. For core jets, a value of 0.6-0.8 seems plausible. For developed jets, the values are situated between 0.2 and 0.5.

These results are valid for test runs of approximately 1 min. It can be argued that much longer time periods are needed to measure the real maximum value. This statement, however, has been derived from scale-model studies (Toso & Bowers, 1988). Its relevance to near-prototype model studies has not yet been pointed out. For practice, it is proposed to use the maximum measured values of Fig. VII-9b as C^{max}_I. This leads to the following definition:

$$C_I = 0.0035 \cdot \left(\frac{Y}{D_j}\right)^2 - 0.119 \cdot \left(\frac{Y}{D_j}\right) + 1.22 \qquad (7.17)$$

The character of the impulsions is determined by the average pressure value, by the ratio of maximum to average pressure value and by the time duration of the pulse. As such, the character cannot be deduced from the C_I coefficients alone. For example, a low pressure that holds for a long time can exhibit the same impulsion as a short-lived pressure peak. However, the character can be determined by the C_{up} and T_{up} values separately. It can be seen that, at low jet velocities, the significant increase in

C_I values is due to an increase of the time duration of the pulse rather than an increase of its average pressure value. This is valid for both core and developed jets.

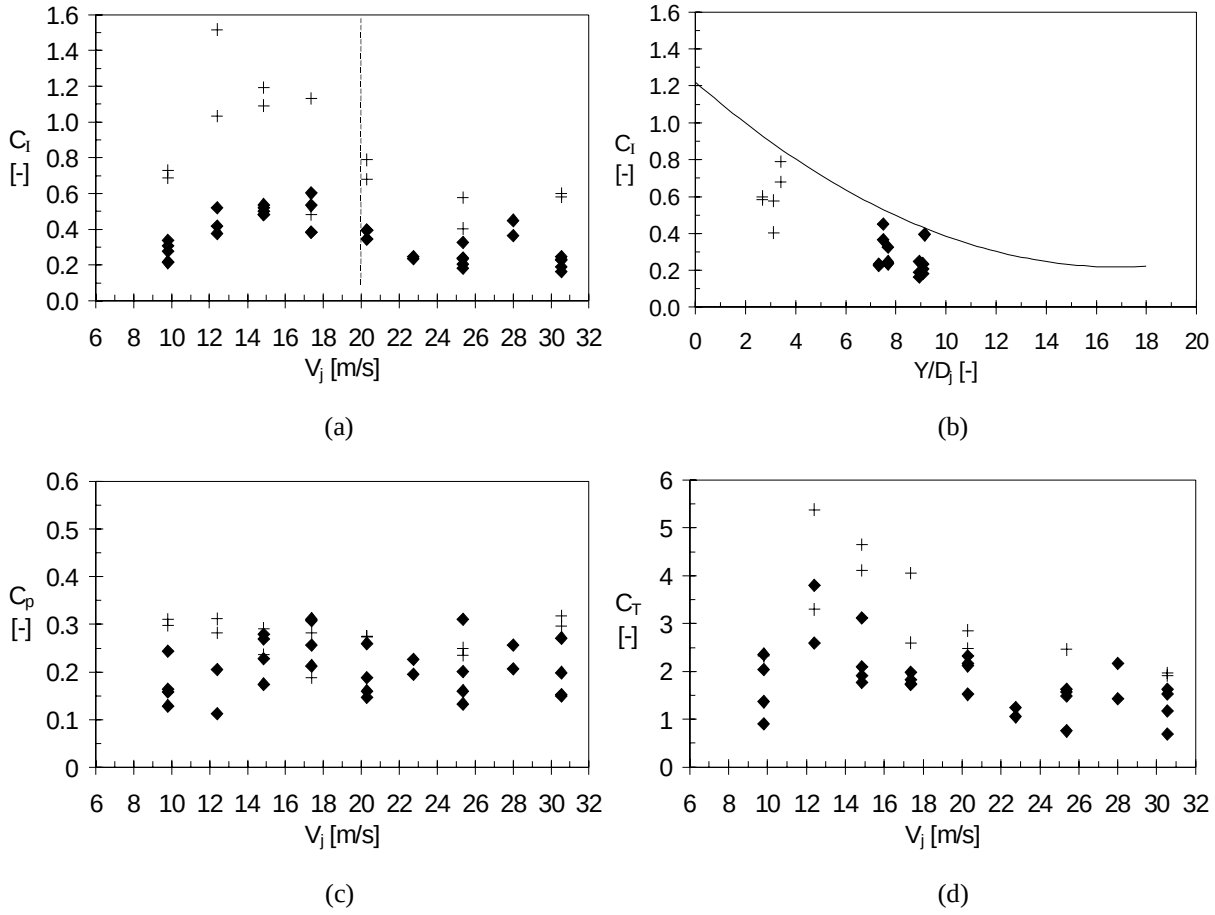

Fig. VII-9 Non-dimensional impulsion coefficients for pressures inside open-end rock joints:
a) C_I as a function of V_j; b) C_I as a function of Y/D_j;
c) C_p as a function of V_j; d) C_T as a function of V_j.

4.2. Definition of failure criteria for closed-or open-end joints

The first section of the module for the rock mass defined the characteristics of the hydrodynamic loading inside open and closed-end rock joints. The second section of the module deals with the corresponding failure criteria of the rock mass. Two criteria are presented:

1. Failure of closed-end rock joints by **progressive propagation** of the joints. This propagation can be instantaneous or time-dependent. The latter case involves failure by fatigue.
2. Failure of open-end rock joints by **dynamic uplift** or displacement of the rock blocks.

Each of these failure criteria constitutes a physical limit for development of the scour hole. Which criterion is most restrictive is not evident and depends on the geomechanical characteristics of the rock mass. For practice, it is recommended to verify each of the two criteria, because they are strongly related one to the other. Rock blocks that cannot be ejected from their mass can still be subjected to break-up into smaller pieces. These smaller pieces could be entrained by the flow more easily. On the other hand, even when no further fracturing is possible, the rock mass might already been broken up and capable to be eroded by dynamic uplift.

4.2.1. Comprehensive Fracture Mechanics (CFM) model for closed-end rock joints

The hydrodynamic loading generated by the impact of a high-velocity jet on a closed-end rock joint produces a cyclic pattern of peak pressures alternated by periods of low, near-atmospheric pressures. As such, the hydrodynamic loading is defined by the maximum peak pressure and by the mean amplitude and the frequency of the pressure cycles (§ 4.1). The maximum peak pressure value is used to check for instantaneous or brittle crack propagation. The cyclic character makes it possible to describe rock joint propagation by fatigue effects at the tip of the joint.

Linear elastic fracture mechanics (LEFM) models can handle both static and dynamic loadings and resistances assuming a perfectly linear elastic, homogeneous and isotropic material. These models become quite complicated when accounting for all the relevant parameters. Therefore, a simplified application is presented here. The application represents a practical engineering approach of the underlying theory and attempts to describe the parameters of influence such that an engineer can easily handle them. In other words, the model still accounts for the correct physical tendencies but has a comprehensive character. It is called the **Comprehensive Fracture Mechanics (CFM) model** and is applied in the present section to intermittently jointed rock.

Hydrodynamic loading in mode-I (pure tensile) is described by the stress intensity factor K_I. The corresponding resistance of the material is expressed by the fracture toughness value K_{Ic}. The problem lies in a comprehensive and physically correct implementation of the complex and dynamic situation encountered in rock joints. Crack propagation distinguishes between brittle (or instantaneous) crack propagation and time-dependent crack propagation. The former happens for a stress intensity factor that is equal to or higher than the fracture toughness of the material. It occurs for both static and dynamic loadings and the governing velocity of cracking approaches the speed of sound in the medium. The latter is valid when the applied static or dynamic loading is inferior to the material's resistance. Cracks are propagated by stress corrosion or by fatigue. Failure by fatigue depends on the number and the amplitude of the load cycles.

It has been pointed out in the previous section that the hydrodynamic loading in intermittently jointed rock can be quantified by three parameters: the maximum pressure and the amplitude and frequency of the pressure cycles. For a fracture mechanics application, these parameters have to be transformed into appropriate stress intensity factors. This is the **implementation of the stress intensity factor**. Furthermore, the resistance of the rock mass depends on the mineralogical type of rock and on its basic properties, such as the tensile strength or the unconfined compressive strength. Based on laboratory fracturing tests or on available literature data, these properties can be related to a plausible fracture toughness K_{Ic}. This is the **implementation of the fracture toughness**.

Instantaneous joint propagation: the stress intensity K_I versus in-situ fracture toughness $K_{I,\,ins}$

The fracture mechanics implementation of the hydrodynamic loading consists of a transformation of the water pressures σ_{water} into rock stresses at the crack tip. These stresses are characterized by the stress intensity factor K_I. This factor depends on the water pressure distribution along the inside of the crack, the geometry of the crack and of the surrounding rock, and on the loading rate. The implementation makes use of the following simplifying assumptions:

1) the dynamic character of the loading has no influence;
2) the pressure distribution inside the joints is constant;
3) only simple geometrical configurations of intermittently rock joints are considered;
4) the joint surfaces are planar.

According to Fig. III-25, Fig. VII-10 presents the three basic geometrical situations for intermittently jointed rock. The water pressure in the joints is applied from outside the rock elements. No geometries with multiple joints are considered. The choice of the most relevant geometry will depend on the type and the degree of jointing of the rock in question.

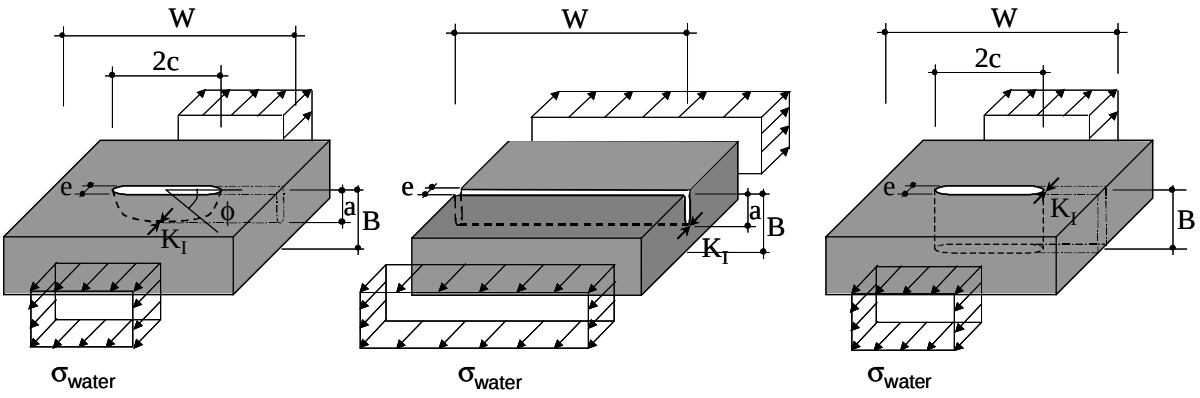

a) EL b) SE c) CC

Fig. VII-10 Proposed framework for the basic geometrical configurations of intermittently jointed rock: a) semi-elliptical (EL) joint; b) single edge (SE) joint; c) center-cracked (CC) joint. The water pressures are applied from outside the joints. No multiple joint configurations are considered.

The first crack is semi-elliptical or semi-circular in shape and, with regard to the laterally applied stress σ_{water}, partially sustained by the surrounding rock mass in two directions. As such, it is the geometry with the highest possible support of surrounding rock. Corresponding stress intensity factors should be used in case of low to moderately jointed rock. The second crack is single edge notched and of two-dimensional nature. Support from the surrounding rock mass is only exerted perpendicular to the plane of the notch and, as a result, stress intensity factors will be substantially higher than for the first case. Thus, it is more appropriate for moderately to highly jointed rock. The third geometry is center-cracked throughout the rock. Similar to the single edge notch, only one-sided rock support can be accounted for. This support, however, should be slightly higher as for the single edge notch.

It has to be noted that the second and third geometrical configurations correspond to a partial destruction of the first one. The single edge notched geometry is obtained by horizontal crack propagation of the elliptical flaw. The center-cracked geometry results from a vertical crack propagation of the elliptical flaw. As such, they both are more sensible to stresses and have to be used for moderately to highly jointed rock.

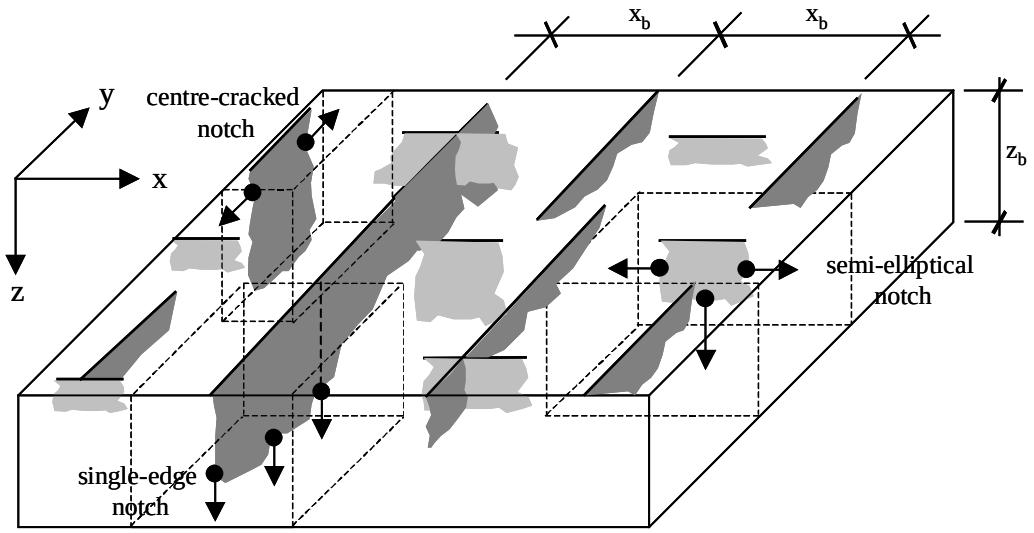

Fig. VII-11 Examples of geometrical configurations in jointed rock mass. In the vertical (z) direction, only one layer is presented.

The applicability of these geometries depends on the number and on the configuration of the joint sets and the respective joint spacings. Furthermore, combinations of geometries are most probable to be expected. The jointed rock presented in Fig. VII-11 is semi-elliptical in the x-direction and rather single-edge notched or center-cracked notched in the y-direction. For such cases, a weighted stress intensity factor has to be established. Possible weighting functions are the degree of jointing or the joint spacing.

The stress intensity factor has been defined by equation (3.66) in Chapter III. It depends on the crack length *a*, on a boundary correction factor *f* and on the water pressure at the crack tip σ_{water}:

$$K_I = \sigma_{water} \cdot f \cdot \sqrt{\pi a} \tag{7.18}$$

K_I is expressed in MPa$\sqrt{m}$ and the water pressures are in MPa. It is interesting to notice that the stress intensity factor not only grows with the square root of the crack length *a* (or the half crack length *c* for center-crack), but also increases as a function of the geometrical ratio a/B (or c/W for center-crack).

The *f* factor reflects the influence of the surrounding rock support and has been defined in Chapter III for each of the geometrical configurations presented in Fig. VII-10. It is a function of the geometrical ratio a/B (for the elliptical and single-edge notches) or c/W (for the center-cracked specimen). Fig. VII-12 presents a comparison of the *f* function for the three geometries. At small a/B ratios, all configurations are quite close one to the other. Only the values for a semi-circular joint are significantly lower. At a/B ratios higher than 0.4, the elliptical notch (EL) stays at lower values, but these values are governed by the a/c and the c/W ratios. This is due to the two-sided character of the surrounding support. The main issue is that, with a careful choice of geometrical configuration, a first tendency of fracture propagation enhancement can already be distinguished. The more the rock is already broken up, the higher the differences between the configurations.

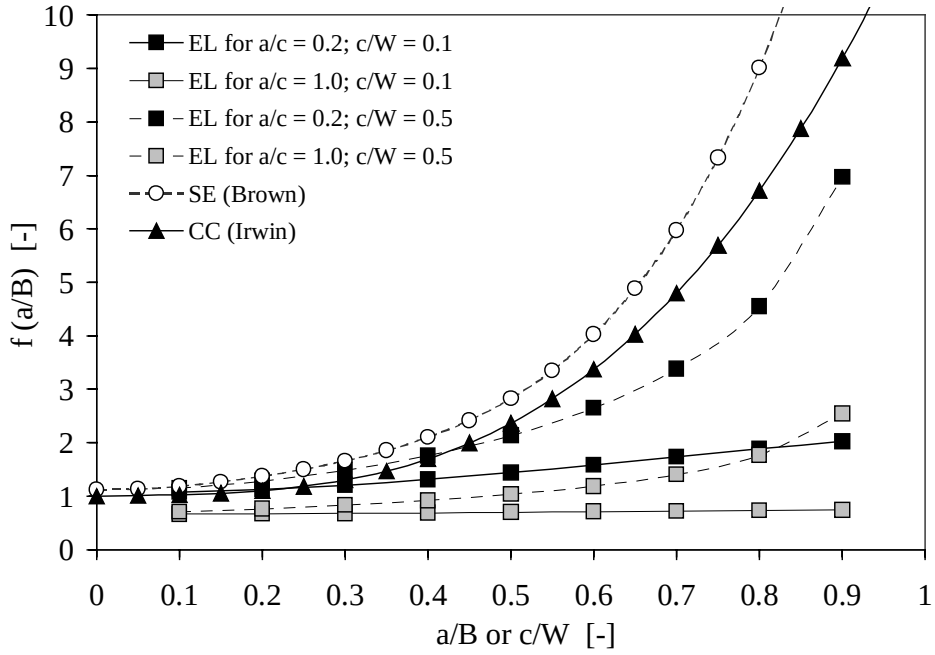

Fig. VII-12 Comparison of different geometrical situations of joints on the theoretical stress intensity factor K_I.

The water pressure σ_{water} should not be taken exactly equal to the maximum possible dynamic water pressure C^{max}_p at the tip of the joint (§ 4.1.1). The reason is that the rock mass stresses at the tip of the joint are defined by the water pressure distribution throughout the whole joint length, and not only by

the water pressure at the tip. Hence, the pressure distribution over the joint length is needed to accurately assess the stress intensity at the tip. The pressures at the boundaries are defined by the pressure signals measured at the entry (= pool bottom pressures (a) in Chapter V) and the pressure signals measured at the end of the joint (= sensor (d) pressures in Chapter V). In between, a sinusoidal mode shape is assumed, according to the λ/4 – resonator model. This results in the following definition of the pressure distribution:

$$p(x) = p_0 + (p_{max} - p_0) \cdot \sin\left(\frac{\pi \cdot x}{2 \cdot L}\right) \tag{7.19}$$

For x = L, this conducts to a maximum pressure at the tip of $(0.36)\cdot p_0 + (0.64)\cdot p_{max}$. According to § 4.1, the maximum pressure is on the order of 2 to 5 times the pressure at the entrance. This results in an average pressure value over the whole joint length that is equal to 71% - 82% of the maximum pressure p_{max}. Hence, **a value of 80% of p_{max} (or C^{max}_p) is chosen for σ_{water}** for practical applications. An exact analysis can be performed by a three-dimensional finite element simulation. This is beyond the scope of the present work.

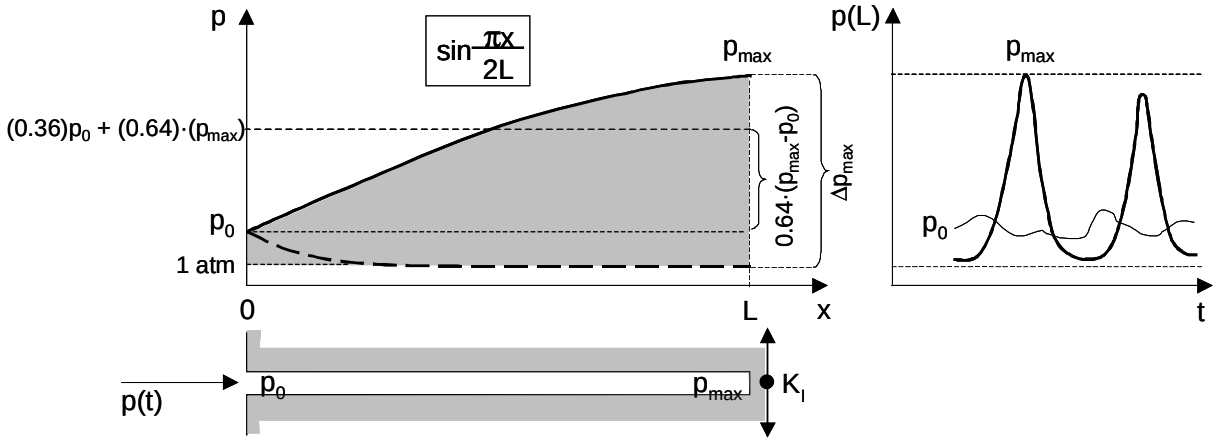

Fig. VII-13 Sinusoidal pressure distribution over the whole joint length and definition of the average maximum pressure value to be used as σ_{water}.

Similar to the stress intensity K_I, the implementation of the fracture toughness K_{Ic} of an intermittently jointed rock needs simplifying assumptions. The fracture toughness is depending on a vast range of parameters. In the following, the fracture toughness is directly related to the mineralogical type of rock and to the tensile strength T or the unconfined compressive strength UCS, according to § 4.3.5 of Chapter III. Furthermore, corrections are made to account for the effects of the loading rate and the in-situ stress field of the rock mass. The corrected fracture toughness is here called the **in-situ fracture toughness $K_{I,ins}$.** According to § 4.3.6 of Chapter III, the following general formulae are proposed for the in-situ fracture toughness value:

$$K_{I\,ins,\,T} = A \cdot (1.2 \text{ to } 1.5) \cdot T + (0.054 \cdot \sigma_c) + B \tag{3.99}$$

$$K_{I\,ins,\,UCS} = C \cdot (1.2 \text{ to } 1.5) \cdot UCS + (0.054 \cdot \sigma_c) + D \tag{3.100}$$

In which T, UCS and σ_c are expressed in MPa and $K_{I,ins}$ in MPa√m. The parameters A to D depend on the type of rock as indicated at Table VII-6:

Type of rock	A	B	C	D
Silicate rocks	0.0648	0.8693	0.0023	1.3257
Carbonate rocks	0.3230	-0.0405	0.0145	-0.0190
Quartz rocks	0.1283	0.2747	0.0088	0.1429

Table VII-6 Parameters of the expressions (3.99) and (3.100) for the in-situ fracture toughness value $K_{I,ins}$

For other types of rock, the general expressions (3.97) and (3.98) should be used. They are repeated here for completion:

$$K_{I\,ins,\,T} = (0.105 \text{ to } 0.132) \cdot T + (0.054 \cdot \sigma_c) + 0.5276 \quad (3.97)$$

$$K_{I\,ins,\,UCS} = (0.008 \text{ to } 0.010) \cdot UCS + (0.054 \cdot \sigma_c) + 0.42 \quad (3.98)$$

Finally, instantaneous or brittle crack propagation will occur if the following expression is valid:

$$K_I \geq K_{I,ins} \quad (7.20)$$

If this is not the case, crack propagation can still occur within a certain time interval. This is outlined in the next section.

Time-dependent joint propagation by fatigue or stress corrosion

The comparison of the stress intensity with the fracture toughness defines whether brittle or instantaneous rock break-up will occur. When the stress intensity is less than the fracture toughness, a second type of rock break-up can happen. It is called time-dependent or subcritical crack propagation and distinguishes between two mechanisms: stress corrosion (or static fatigue) and cyclic (or dynamic) fatigue.

Stress corrosion or static fatigue happens when a steady stress is applied in a chemically active environment. Water pressures in rock joints represent such an environment. The steady stresses exerted by the water are able to progressively weaken the strained bonds of the rock mass by chemical reactions. A qualitative relationship between subcritical crack propagation velocities v(K) and a normalized stress intensity factor (= K_I/K_{Ic}) can be found for a wide range of geologic materials in Atkinson (1984). The exact propagation velocities, however, are difficult to determine and only tendencies can be accurately determined.

Failure by dynamic fatigue of intermittently jointed rock occurs when a considerable cyclic loading is applied inside the joints. Since the 1960's, a significant body of theoretical and experimental evidence has been generated. The most interesting studies focus on a combination of stress corrosion and cyclic fatigue. At small values of the amplitude of the stress cycle Δp_c, stress corrosion is the dominant mechanism, because of the very little cycling. At moderate and high values of Δp_c, the results can only be explained by cyclic fatigue. They are fit by an equation of the type that was originally proposed by Paris et al. (1961) to describe fatigue crack growth in metals:

$$\frac{da}{dN} = C \cdot (\Delta K_I)^m \quad (7.21)$$

in which a is the crack length and N the number of cycles. C and m are rock material parameters that can be determined by experiments and ΔK_I is the difference of maximum and minimum stress intensity factors at the crack tip. Fig. VII-13b shows an experimentally derived result (Kim & Mubeen, 1981) of crack propagation rate. The obtained m value is equal to 11.9 and C is equal to 8.10^{-10}.

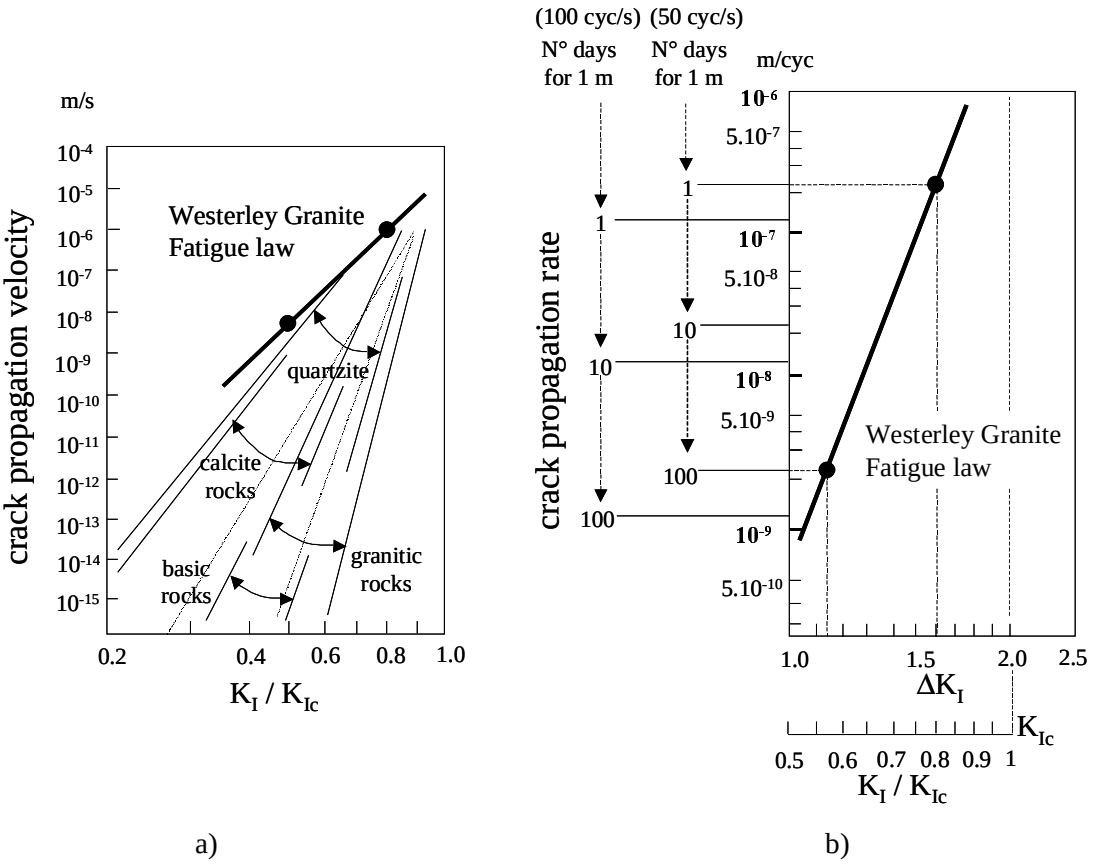

a) b)

Fig. VII-14 Time-dependent rock failure: a) crack propagation velocity by stress corrosion (Atkinson 1984); b) crack propagation rate by cyclic fatigue (Kim & Mubeen, 1981).

The fatigue law for Westerley granite is compared with the stress corrosion laws of other rock types. Based on the test results of Scholz & Koczynski (1979), as presented in Fig. III-30, it is reasonable to assume that, when the stress intensity is close to the fracture toughness value of the material, the crack propagation velocity v(K) is quite equal for both stress corrosion and cyclic fatigue. The fracture toughness for Westerley granite lies between 1.7 and 2.2 (Der et al., 1978; Atkinson & Rawlings, 1981; Swanson, 1984; Ingraffea, 1981; Costin & Mecholsky, 1983). Here it is assumed equal to 2.0 and the x-axis is made non-dimensional by dividing it by this value. This allows representing the fatigue law on the graph for stress corrosion and, thus, to relate stress corrosion to an absolute velocity scale. Apparently, the slope for cyclic fatigue of a granite is much steeper than its homologue slope for stress corrosion. In other words, jointed granite is much more sensible to cyclic loading than to steady loading, at least when the latter is not close to the critical loading.

Furthermore, Fig. VII-14a indicates that most other types of rock are more sensible to stress corrosion than a granite. This essential statement is assumed to hold for cyclic fatigue also.

To implement time-dependent crack propagation into a comprehensive engineering model, some parametric assumptions have to be made. Although Costin & Holcomb (1981) developed a model that is based on absolute pressures rather than stress intensities, the differential stress intensity of equation (7.21) will be used because of its simplicity. The parameters m and C have to be determined for each mechanism separately. Then the obtained crack growths per cycle are simply superposed.

For stress corrosion, the m-values are defined by the subcritical crack index n. This index depends on the type of rock and has been defined at Table III-7. The C-values are determined by the absolute velocity scale of the fatigue law for Westerley granite (Fig. VII-14b). For cyclic fatigue, m and C are known for granite but not for other types of rock. However, based on the different n-values for stress corrosion, it is assumed that the same qualitative differences will exist for cyclic fatigue. Thus, for rock types other than granite, somewhat milder slopes will be adopted. This means that these rocks are

more sensible to fatigue than granite. As such, both stress corrosion and cyclic fatigue laws are entirely determined as a function of the type of rock. The results for some types of rock are presented in Fig. VII-15 hereunder. The ratio of maximum to minimum stress R is assumed equal to 0.2. The corresponding values for m and C have been summarized at Table III-7 in Chapter III for a wide range of rocks.

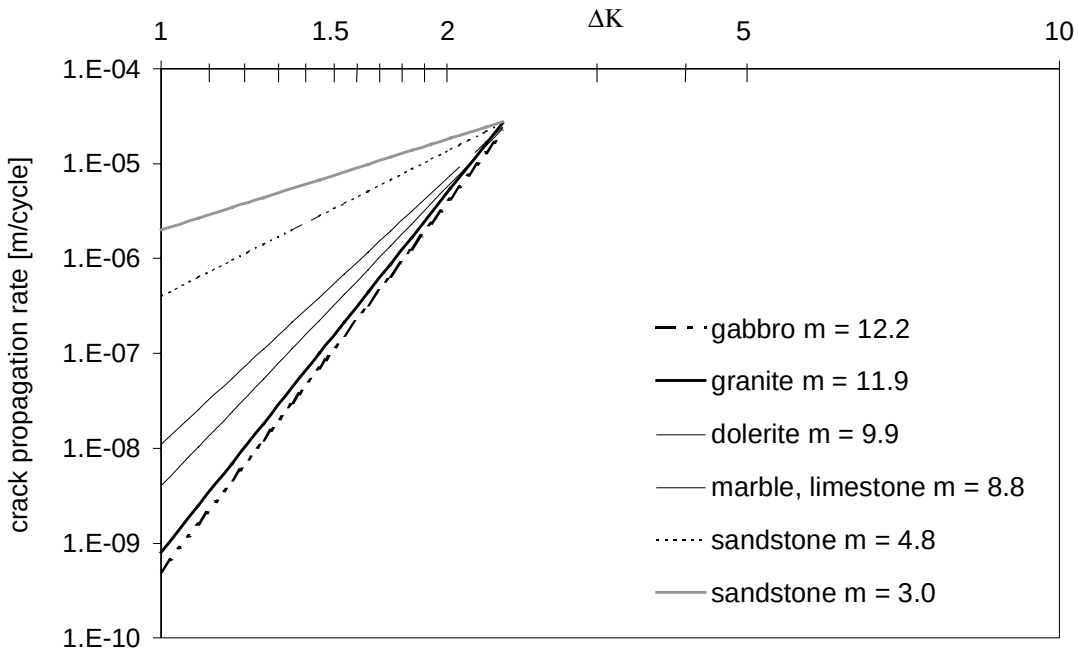

Fig. VII-15 Crack propagation rate by cyclic fatigue as a function of the differential stress intensity factor ΔK (MPa√m) for different rock types. The maximum to minimum stress ratio is assumed equal to 0.2.

Furthermore, the time scale of v(K) is transformed into a more practical scale. This scale defines the number of days of jet impact necessary to deepen the scour with 1 m. This number of days depends on the number of cycles per second or, in other words, on the frequency of occurrence of the peak pressures. Scales for typical frequencies of 50 Hz and 100 Hz are visualized. Theoretically, time-dependent cracking takes an end when the loading becomes less than 20-30 % of the fracture toughness value. For engineering purposes, it is proposed that a crack advance of 1 m in 300 days of hydraulic loading on the rock mass signifies the practical end of scouring.

As a summary, prediction of the dominant mechanism causing subcritical crack growth of jointed rock is dependent on the importance of the cyclic stress intensity amplitude ΔK_I with respect to the mean stress intensity value, as well as on the absolute value of ΔK_I. An important cyclic load with respect to the mean stress intensity value, as encountered for highly dynamic jet scouring, means that the fatigue effect is very important. A small or negligible cyclic load with respect to the mean value signifies that stress corrosion is more important, but only when the absolute value of ΔK_I is not too high. The latter is more relevant for deeply scoured plunge pools, where the dynamic effect of the impacting jet has no effect anymore on the bottom of the pool. It is evident that the here proposed methodology is no more than a broad-brush expression of reality. Knowledge of the exact fatigue and stress corrosion relationships for all types of rock is clearly impossible, but not strictly necessary. Due to the physical background of the approach, a qualitative difference in sensibility to time-dependent cracking is inherent. Careful calibration of the comprehensive engineering model, based on prototype data, should be able to transform this sensibility difference into absolute values.

4.2.2. Dynamic Impulsion (DI) model for open-end rock joints

The Dynamic Impulsion model is based on the maximum dynamic pressure impulsion C^{max}_I, as defined in § 4.1, and on the geometrical characteristics of a rock block that is representative for the rock mass. The geometrical characteristics, together with the type of rock, define the immerged weight of the block. Furthermore, the shear forces are determined by the horizontal in-situ stress field. In a first approach, these can be neglected by assuming that progressive dislodgment and opening of the joints occurred during the break-up phase of the rock mass.

The main geomechanical parameters of the rock mass have been presented at Table III-6 in Chapter III and will not be repeated herein. These parameters allow determining the shape of the rock block. For the present analysis, a definition sketch is provided in Fig. VII-16. The rock blocks are considered to be squared in the horizontal plane. This means that the analysis is two-dimensional in the x-z plane. The side length in the x-direction is called x_b, while the vertical side is of length z_b. As such, the total length of the joint that passes underneath a block is equal to $L = x_b + 2 \cdot z_b$. The thickness of the joint is neglected.

The two-dimensional character implies that the forces on the rock blocks are considered constant in the y-direction. For simplicity, the pressures will be considered equal to the forces, i.e. acting on a surface of 1 m^2. Assuming a bandwidth of 1 m in the y-direction, this means that the analysis is performed per m of length in the x-direction. Hence, the two forces that have not been considered in § 4.1 are the immerged weight of the block and the shear forces along the joints. The immerged weight of the block G_b can be defined as follows:

$$G_b = \forall \cdot (\gamma_r - \gamma_w) = x_b^2 \cdot z_b \cdot (\gamma_r - \gamma_w) \tag{7.22}$$

in which γ_r and γ_w stand for the specific weight of the rock respectively the water. For rock, typical values for γ_r are between 22'000 and 28'000 N/m^3. For a horizontal surface of 1 m^2, the weight force becomes linearly dependent on the height of the block. For a bandwidth in the y-direction of 1 m, the problem becomes dependent on the form factor z_b/x_b of the rock block. This has already been outlined in § 4.4.4 of Chapter III. Three cases of form factors can be considered: $z_b/x_b > 1$, $z_b/x_b = 1$ and $z_b/x_b < 1$. They are presented in Fig. VII-16.

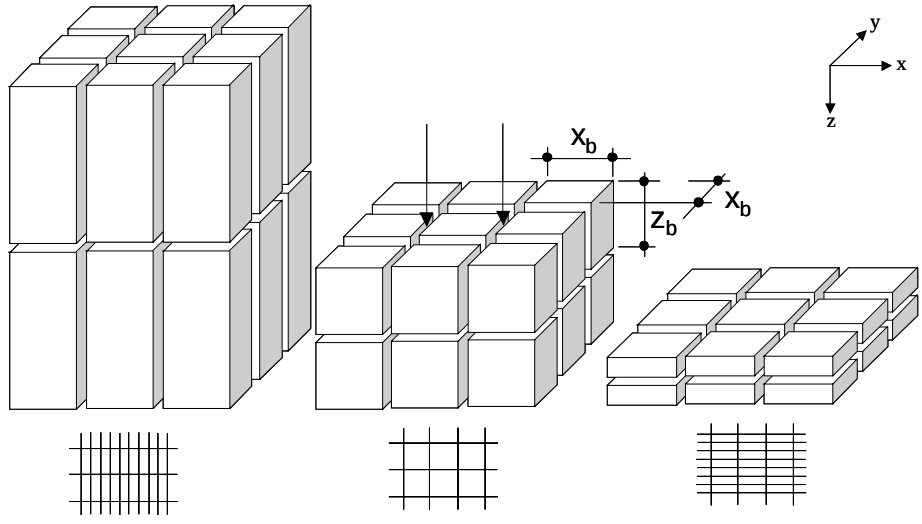

a) $z_b/x_b > 1$ b) $z_b/x_b = 1$ c) $z_b/x_b < 1$

Fig. VII-16 Three cases of form factors of a characteristic rock block. The influence of the y-direction is neglected in the present analysis.

These three cases have the same horizontal surface and, thus, the same net uplift pressure. However, their immerged weight per m^2 is completely different. It is obvious that block a) will be much more difficult to eject than block c). Moreover, the shear forces obviously will also be higher in case a) than in case c). As a result, knowledge about the joint sets and the distance between the joints is of crucial importance to define the ultimate scour depth based on dynamic uplift of rock blocks.

The weight and shear forces are considered constant in time. This means that they can be simply subtracted from the net impulsion calculated in § 4.1 by multiplying the forces by the time period of the net pressure pulse. Based on equation (3.101) in Chapter III, this net impulsion is then set equal to the product of the mass of the block times the velocity. This results in the maximum velocity that could be given to the mass of rock. This velocity or kinetic energy is transformed into potential energy by ejection of the block. Equation (3.102) expresses the displacement h_{up} of the block as a function of this velocity:

$$V_{\Delta tpulse} = \sqrt{2 \cdot g \cdot h_{up}} \tag{3.102}$$

The uplift is proportional to the square of the velocity. This again indicates the importance of the vertical height z_b of the rock block.

As already mentioned in § 4.4.6 of Chapter III, the displacement that is necessary to eject a rock block from its matrix is hard to define. It depends on the degree of interlocking of the blocks, which depends on the in-situ stress field of the rock mass.

As a first approach, a very tightly jointed rock mass will need a displacement that is equal to or higher than the height z of the block. Less tightly jointed rock will probably be uplifted more easily. The necessary displacement is a model parameter that needs to be calibrated.

5. Applications of the scour model

Firstly, the scour model is applied to a fictitious rock mass. This points out the methodology and the major parameters of interest. The first part of this fictitious case deals with the break-up phase of the closed-end joints of the rock and uses the Comprehensive Fracture Mechanics (CFM) model. The second section describes the ejection of rock blocks from their mass and uses the Dynamic Impulsion (DI) model.

Secondly, the scour model is compared with Annandale's Erodibility Index (EI) Method (Annandale, 1995). This comparison determines the sensibility of the scour model as a function of the main parameters.

Finally, the well-known case of rock scour at the Cabora-Bassa dam in Mozambique will be used as a first calibration of some of the model parameters.

5.1. Example of a good quality granite

The Comprehensive Fracture Mechanics model is applied to a fictitious case of jointed rock. The calculus has to be done on a layer per layer basis along the vertical axis. Therefore, an example is firstly outlined for one distinct layer of rock. After, the manipulations are grouped into a spreadsheet that calculates for each layer, which determines the ultimate scour depth.

The intermittently jointed rock layer presented in Fig. VII-11 is used as example. The rock is assumed to be a very good quality granite with a tensile strength T of 19 MPa and an unconfined compressive strength UCS of 296 MPa. It exhibits moderately semi-elliptical jointing in the x-direction and moderately to highly single-edge jointing in the y-direction. The rock is considered to consist of horizontal layers of 1 m of height.

5.1.1. Calculation for a rock layer of height z_b = 1 m

In the vertical direction, one layer of rock is considered. It is assumed that the jet characteristics have been calculated at the point of impact in the pool. The jet is vertically impinging with an impact velocity of V_j = 40 m/s and an estimated diameter at its point of impact of D_j = 4 m. The distance from this point of impact down to the water-rock interface is estimated to be Y = 36 m. As such, the ratio of pool depth to jet diameter Y/D_j equals 9 and developed jet impact conditions govern.

Comprehensive Fracture Mechanics model (CFM)

The jet is issuing from an intermediate outlet structure and its initial turbulence intensity Tu is estimated at 5 %. In other words, undulating jet conditions are to be considered, following Table VII-3. The corresponding coefficients are introduced in equation (7.6) to calculate the C'_{pa} coefficient of the pressure fluctuations at the entrance of the rock joints under the jet's centerline. For Y/D_j = 9, this procures a value of C'_{pa} = 0.26. According to equation (7.7), and by neglecting the air content at impact, a C_{pa}-coefficient of 0.47 is obtained.

For a uniformly distributed velocity profile at jet impact, the incoming kinetic energy $V^2_j/2g$ equals 81.5 m of pressure head. Based on the estimated non-dimensional coefficients C_{pa} and C'_{pa}, this results in a mean dynamic pressure head of 0.47·81.5 = 38.3 m and a fluctuating root-mean-square head of 0.26·81.5 = 21.2 m.

Furthermore, the extreme positive pressure head at the water-rock interface is estimated at (4·21.2 + 38.3) m = 123.1 m. The rock joints are assumed to be moderately to very tight. As a result, the curve of maximum or average C^+ coefficients has to be used, according to Fig. VII-6a. This results in a coefficient of 4.6 or 2.6, or a peak pressure head of (4.6·81.54 + 38.3) m = 413.4 m or (2.6·81.54 + 38.3) m = 250.3 m. This equals a maximum pressure at the joint tip of 4.06 MPa or 2.46 MPa.

In the following, the influence of the degree of jointing on the ultimate scour will be searched for. For this purpose, geometrical ratios a/B of 0.2, 0.4 and 0.6 (Fig. VII-13) are used. The semi-elliptical (SE) joints are assumed perfectly circular (a/c = 1). The directional stress intensities are calculated as explained in the following example, valid for the x-direction and for a/B = 0.2.

The absolute length L of the joint is 0.2 m. The function f(a/B) for a/c = 1.0 is equal to 0.8 (-). The used water pressures are taken as 80 % of the maximum pressure value at the joint tip (Fig. VII-13). The directional stress intensity factor is written in the x-direction: K_{Ix} = 0.8·(2.46 to 4.06)·√(3.14·0.2)·0.8 = 1.25 to 2.06 MPa√m. A similar expression can be written in the y-direction. The weighted stress intensity factor K_{Ixy} is then obtained as a function of the joint density in each direction. In the present example, the same importance is accorded to each of the directions x and y. As such, the following stress intensity values have been calculated:

	a/B	f(a/B)	C^+	P_{max}	K_{Ixy}
	[-]	[-]	[-]	[MPa]	[MPa√m]
x-direction	0.2	0.8	2.6-4.6	2.5-4.1	1.25-2.06
	0.4	0.8	2.6-4.6	2.5-4.1	1.77-2.91
	0.6	0.8	2.6-4.6	2.5-4.1	2.16-3.57
y-direction	0.2	1.1	2.6-4.6	2.5-4.1	1.71-2.83
	0.4	1.1	2.6-4.6	2.5-4.1	2.42-4.01
	0.6	1.1	2.6-4.6	2.5-4.1	2.97-4.90
weighted x-y	0.2	-	2.6-4.6	2.5-4.1	**1.48-2.45**
	0.4	-	2.6-4.6	2.5-4.1	**2.10-3.46**
	0.6	-	2.6-4.6	2.5-4.1	**2.57-4.24**

Table VII-7 Directional and weighted stress intensity factors K_{Ixy} as a function of the degree of jointing a/B.

The fracture toughness value of the in-situ rock mass $K_{I\ ins}$ is calculated based on equation (3.99) or equation (3.100). The horizontal in-situ stresses are considered equal to the overburden pressure, i.e. K_0 = 1. For an already scoured pool depth of 36 m, a horizontal stress of 1 MPa is obtained. As a result, the K-values are written:

$$K_{I\,ins,\,T} = 0.0648 \cdot (1.5) \cdot 19 + (0.054 \cdot 1) + 0.8693 = 2.77\ \text{MPa}\sqrt{\text{m}} \quad (3.99)$$

$$K_{I\,ins,\,UCS} = 0.0023 \cdot (1.5) \cdot 296 + (0.054 \cdot 1) + 1.3257 = 2.40\ \text{MPa}\sqrt{\text{m}} \quad (3.100)$$

The averaged value is $\mathbf{K_{I\,ins} = 2.59\ MPa\sqrt{m}}$. For a persistency of 0.6, it is obvious that even the highest possible fracture toughness is still considerably smaller than most of the calculated stress intensity factors, and thus brittle crack growth will occur. The time period involved depends on the degree of interlocking of the formed rock blocks and on the in-situ stresses of the rock mass. For engineering purposes, it may be assumed that the break-up of the 1 m rock layer takes place instantaneously.

For a persistency of 0.4, the situation is less clear. Probably instantaneous crack growth will still occur, but only for extreme peaks inside the joints. Furthermore, the break-up will start along the y-direction because much more sensible. As extreme peaks occur less often, the destruction of the rock mass will take more time than for a persistency of 0.6.

Finally, for a persistency of only 0.2, we obviously have to deal with subcritical crack growth in the x-direction and probably also in the y-direction. Assume that the fracture toughness corresponds to the lower bound of values, i.e. K_{Ic} = 2.40 MPa√m. Then, based on Table VII-3 and Fig. VII-6d, it is

assumed that the average amplitude of the peak pressures equals 40 % of the maximum possible pressure. The maximum possible pressure or stress intensity, however, continuously changes during progression of the crack. Therefore, an averaged value is taken as half in between the initial crack length of 0.2 m and the final crack length of 1.0 m. This corresponds to a persistency of 0.6. Thus, the used stress intensity values are taken equal to 40 % of the maximum pressures for a/B = 0.6, i.e. ΔK = 1.28-2.12. This corresponds to $\Delta K/K_{Ic}$ values of 0.53-0.88. Fig. VII-14b presents the fatigue law for granite. The m-value is 11.9 and the C-value is chosen equal to 8.10^{-10}. Due to the dynamic character of the loading at Y/D_j ratios of 9, stress corrosion is neglected. Equation (7.21) results in the following time periods for a crack propagation of 0.8 m:

Jointing	ΔK	da/dN	dN/dt	da/dt	t (sec)	t (days)
mod. tight	1.28	1.51E-08	100	1.51E-06	5.3E+05	6.13
very tight	2.12	6.12E-06	100	6.12E-04	1307	0.02
mod. tight	1.28	1.51E-08	50	7.55E-07	1.06E+06	12.3
very tight	2.12	6.12E-06	50	3.06E-04	2614	0.70

Table VII-8 Time-dependent crack propagation for a degree of jointing a/B = 0.2. The number of cycles per second is 100 or 50. The ΔK values correspond to moderately tight or very tight joints.

For peak pressures inside rock joints that occur at a rate dN/dt of 50 to 100 Hz, the layer will break up within 6 to 12 days for the lower bound of ΔK values, i.e. for moderately tight joints. For very tight joints, a time period of 0.02 to 0.7 days is needed, depending on the number of cycles per second.

For a wave celerity c of 100 m/s and a joint length L of 0.2 m, the theoretical resonance frequency equals 125 Hz. For a maximum joint length of 1 m, this same frequency decreases down to 25 Hz. In other words, during the first part of the joint break-up, rather high frequencies have to be expected. With increasing break-up, this frequency continuously decreases. Hence, it is concluded that the break-up of the rock layer will only take a few hours of discharge for very tight joints and 5 to 10 days for moderately tight joints.

As a summary, the present application points out some major tendencies of scour sensibility of intermittently jointed rock. The influence of the degree of jointing and the tightness of the joints on the time evolution has been outlined. It becomes obvious that the Comprehensive Fracture Mechanics model (CFM) only procures qualitative results and that calibration of its basic parameters is absolutely necessary. This calibration needs prototype data for both the hydraulic and the geomechanic in-situ parameters.

Dynamic Impulsion model (DI)

The Dynamic Impulsion model needs the geometry of a characteristic rock block. According to Fig. VII-11, the distance x_b between the joints is estimated at 2 m. This corresponds to twice the height of the vertical layer z_b and, thus, a z/x ratio of 0.5 is obtained. The total length of the joint under the rock block is equal to $L = 2 \cdot z_b + 1 \cdot x_b = 4$ m. The maximum net impulsion I^{max} is determined by the C_I coefficient as defined in Fig. VII-9. For $Y/D_j = 9$ and $V_j = 40$ m/s, a value of $C_I = 0.45$ is deduced. Furthermore, a C_p value of 0.3 and a C_T value of 1.5 can be derived. Assuming a wave celerity c of 100 m/s, the latter coefficients correspond to a net uplift pressure head of 24.5 m (= 240 kN) and a time period T of 0.12 seconds. As such, the maximum net pressure impulsion equals I^{max} = 28'800 Ns.

Secondly, the specific weight of granite is taken equal to γ_r = 26'500 N/m^3. For a horizontal block surface of 1 m^2, this corresponds to an immerged weight force of G_b = 16'500 N (= mass of 1'650 kg). Compared to the net uplift pressure of 240 kN, and by neglecting the shear forces along the joints, this

results in a total net force of 223'500 N that acts on the block during 0.12 seconds. The corresponding maximum net impulsion of all forces is I^{max} = 26'820 Ns.

This conducts to a displacement velocity of the block of 16.3 m/s. The corresponding displacement h_{up} is equal to 13.5 m or a h_{up}/z ratio of 13.5. Such an impulsion clearly is able to eject the rock block.

For displacements less than the height of the block z_b, it is difficult to state whether or not this height is able to eject the rock block from its mass. For very tight joints, a displacement of minimum the height z_b of the block is theoretically needed. For less tight joints, however, this does not hold anymore. Appropriate calibration of this parameter can solve the problem.

In the case that the block is not ejected from its mass, the impulsions that are caused by the impacting jet will cause the block to vibrate at its position. These vibrations can modify the relative position of the block compared to its surroundings. As such, a new situation is created which might be able to eject the block.

5.1.2. Calculation for the whole rock mass

The calculations of the preceding section have been grouped in a spreadsheet. As such, they can be performed for each separate layer of the rock mass. This determines both the ultimate scour hole depth and the time evolution of the phenomenon. The first spreadsheet is presented at Table VII-9 and relates to the Comprehensive Fracture Mechanics model. The fracture toughness has been calculated based on the tensile strength T. It can be seen that brittle crack propagation is to be expected until a scour depth of 40 m.

From on this depth, further scouring occurs by fatigue. The ultimate scour depth is attained when the time necessary for the depth to be reached is excessively high or when the amplitude of the pressure cycles becomes that low that no fatigue is happening anymore. The former limit is set at 1000 days, the latter at 20% of the fracture toughness value $K_{I,ins}$. Hence, the present jointed rock mass will reach its ultimate scour depth at approximately **47 m** of water depth Y.

The second spreadsheet is presented at Table VII-10 and describes the Dynamic Impulsion model. The ultimate scour depth is reached when the rock block displacement becomes less than the height of the block, i.e. for a h_{up}/z ratio of 1. This happens at a scour depth of **45 m**, which is very close to the ultimate depth obtained by the Comprehensive Fracture Mechanics model.

The Comprehensive Fracture Mechanics model indicates that the last two meters of scouring need several tens to hundreds of days of discharge. A scour depth of 46 m is reached within 23 days of discharge.

V_j	40	m/s	Persistency	0.4	-
D_j	4	m	L	1	m
T	19	Mpa	K_0	1	-

Y	H	V_j	Y/D_j	C^+	K_{Ixy}	$\sigma_{h,H}$	K_{Iins}	propagation	T	Total T
m	m	m/s	-	-	$Mpa*m^{0.5}$	Mpa	$Mpa*m^{0.5}$	-	days	days
0	81.55	40	0.0	2.0	3.02	0.00	2.72	brittle	inst	inst
1	81.55	40	0.3	2.0	3.02	0.03	2.72	brittle	inst	inst
2	81.55	40	0.5	2.0	3.02	0.05	2.72	brittle	inst	inst
3	81.55	40	0.8	2.0	3.02	0.08	2.72	brittle	inst	inst
4	81.55	40	1.0	2.0	3.02	0.11	2.72	brittle	inst	inst
5	81.55	40	1.3	2.0	3.02	0.13	2.72	brittle	inst	inst
6	81.55	40	1.5	2.0	3.02	0.16	2.72	brittle	inst	inst
7	81.55	40	1.8	2.0	3.02	0.19	2.73	brittle	inst	inst
8	81.55	40	2.0	2.0	3.02	0.21	2.73	brittle	inst	inst
9	81.55	40	2.3	2.0	3.02	0.24	2.73	brittle	inst	inst
10	81.55	40	2.5	2.0	3.02	0.27	2.73	brittle	inst	inst
11	81.55	40	2.8	2.0	3.02	0.29	2.73	brittle	inst	inst
12	81.55	40	3.0	2.0	3.02	0.32	2.73	brittle	inst	inst
13	81.55	40	3.3	2.0	3.02	0.34	2.73	brittle	inst	inst
14	81.55	40	3.5	2.0	3.02	0.37	2.74	brittle	inst	inst
15	81.55	40	3.8	2.0	3.02	0.40	2.74	brittle	inst	inst
16	81.55	40	4.0	2.0	3.02	0.42	2.74	brittle	inst	inst
17	81.55	40	4.3	2.0	3.02	0.45	2.74	brittle	inst	inst
18	81.55	40	4.5	2.0	3.02	0.48	2.74	brittle	inst	inst
19	81.55	40	4.8	2.0	3.02	0.50	2.74	brittle	inst	inst
20	81.55	40	5.0	2.0	3.02	0.53	2.74	brittle	inst	inst
21	81.55	40	5.3	2.1	3.14	0.56	2.75	brittle	inst	inst
22	81.55	40	5.5	2.2	3.32	0.58	2.75	brittle	inst	inst
23	81.55	40	5.8	2.3	3.44	0.61	2.75	brittle	inst	inst
24	81.55	40	6.0	2.4	3.62	0.64	2.75	brittle	inst	inst
25	81.55	40	6.3	2.5	3.74	0.66	2.75	brittle	inst	inst
26	81.55	40	6.5	2.6	3.92	0.69	2.75	brittle	inst	inst
27	81.55	40	6.8	2.7	4.04	0.72	2.75	brittle	inst	inst
28	81.55	40	7.0	2.8	4.23	0.74	2.76	brittle	inst	inst
29	81.55	40	7.3	2.9	4.35	0.77	2.76	brittle	inst	inst
30	81.55	40	7.5	3.0	4.53	0.80	2.76	brittle	inst	inst
31	81.55	40	7.8	3.1	4.65	0.82	2.76	brittle	inst	inst
32	81.55	40	8.0	3.2	4.83	0.85	2.76	brittle	inst	inst
33	81.55	40	8.3	3.1	4.72	0.87	2.76	brittle	inst	inst
34	81.55	40	8.5	2.9	4.42	0.90	2.76	brittle	inst	inst
35	81.55	40	8.8	2.8	4.22	0.93	2.77	brittle	inst	inst
36	81.55	40	9.0	2.6	3.92	0.95	2.77	brittle	inst	inst
37	81.55	40	9.3	2.5	3.72	0.98	2.77	brittle	inst	inst
38	81.55	40	9.5	2.3	3.43	1.007	2.77	brittle	inst	inst
39	81.55	40	9.8	2.1	3.23	1.0335	2.77	brittle	inst	inst
40	81.55	40	10.0	1.9	2.93	1.06	2.77	brittle	inst	inst
41	81.55	40	10.3	1.8	2.73	1.0865	2.77	fatigue	9.81E-03	9.81E-03
42	81.55	40	10.5	1.6	2.43	1.113	2.78	fatigue	3.90E-02	4.88E-02
43	81.55	40	10.8	1.5	2.23	1.1395	2.78	fatigue	1.08E-01	1.57E-01
44	81.55	40	11.0	1.3	1.93	1.166	2.78	fatigue	5.98E-01	7.55E-01
45	81.55	40	11.3	1.1	1.73	1.1925	2.78	fatigue	2.18E+00	2.94E+00
46	81.55	40	11.5	0.9	1.43	1.219	2.78	fatigue	2.08E+01	2.37E+01
47	81.55	40	11.8	0.8	1.23	1.2455	2.78	end	1.23E+02	1.47E+02
48	81.55	40	12.0	0.6	0.94	1.272	2.78	end	3.33E+03	3.48E+03

Table VII-9 Determination of the ultimate scour depth based on the Comprehensive Fracture Mechanics model. The fracture toughness has been calculated based on the tensile strength T.

V_j	40	m/s	γ_r	2650	kg/m^3
D_j	4	m	z	1	m
c	100	m/s	z/x	0.5	-

Y	H	V_j	Y/D_j	C_I	I^{max}	x	z	L	G_b	T	I^{net}	V_{up}	h_{up}	h_{up}/z
m	m	m/s	-	-	Ns	m	m	m	kg/m^2	s	Ns	m/s	m	-
0	81.55	40	0.0	1.00	64000	2.00	1.00	4.00	1650	0.120	62058	37.61	72.10	72.10
1	81.55	40	0.3	1.00	64000	2.00	1.00	4.00	1650	0.120	62058	37.61	72.10	72.10
2	81.55	40	0.5	1.00	64000	2.00	1.00	4.00	1650	0.120	62058	37.61	72.10	72.10
3	81.55	40	0.8	1.00	64000	2.00	1.00	4.00	1650	0.120	62058	37.61	72.10	72.10
4	81.55	40	1.0	1.00	64000	2.00	1.00	4.00	1650	0.120	62058	37.61	72.10	72.10
5	81.55	40	1.3	0.90	57600	2.00	1.00	4.00	1650	0.120	55658	33.73	57.99	57.99
6	81.55	40	1.5	0.90	57600	2.00	1.00	4.00	1650	0.120	55658	33.73	57.99	57.99
7	81.55	40	1.8	0.90	57600	2.00	1.00	4.00	1650	0.120	55658	33.73	57.99	57.99
8	81.55	40	2.0	0.85	54400	2.00	1.00	4.00	1650	0.120	52458	31.79	51.52	51.52
9	81.55	40	2.3	0.85	54400	2.00	1.00	4.00	1650	0.120	52458	31.79	51.52	51.52
10	81.55	40	2.5	0.80	51200	2.00	1.00	4.00	1650	0.120	49258	29.85	45.42	45.42
11	81.55	40	2.8	0.80	51200	2.00	1.00	4.00	1650	0.120	49258	29.85	45.42	45.42
12	81.55	40	3.0	0.80	51200	2.00	1.00	4.00	1650	0.120	49258	29.85	45.42	45.42
13	81.55	40	3.3	0.75	48000	2.00	1.00	4.00	1650	0.120	46058	27.91	39.71	39.71
14	81.55	40	3.5	0.75	48000	2.00	1.00	4.00	1650	0.120	46058	27.91	39.71	39.71
15	81.55	40	3.8	0.75	48000	2.00	1.00	4.00	1650	0.120	46058	27.91	39.71	39.71
16	81.55	40	4.0	0.70	44800	2.00	1.00	4.00	1650	0.120	42858	25.97	34.39	34.39
17	81.55	40	4.3	0.70	44800	2.00	1.00	4.00	1650	0.120	42858	25.97	34.39	34.39
18	81.55	40	4.5	0.70	44800	2.00	1.00	4.00	1650	0.120	42858	25.97	34.39	34.39
19	81.55	40	4.8	0.65	41600	2.00	1.00	4.00	1650	0.120	39658	24.03	29.44	29.44
20	81.55	40	5.0	0.65	41600	2.00	1.00	4.00	1650	0.120	39658	24.03	29.44	29.44
21	81.55	40	5.3	0.65	41600	2.00	1.00	4.00	1650	0.120	39658	24.03	29.44	29.44
22	81.55	40	5.5	0.65	41600	2.00	1.00	4.00	1650	0.120	39658	24.03	29.44	29.44
23	81.55	40	5.8	0.60	38400	2.00	1.00	4.00	1650	0.120	36458	22.10	24.88	24.88
24	81.55	40	6.0	0.60	38400	2.00	1.00	4.00	1650	0.120	36458	22.10	24.88	24.88
25	81.55	40	6.3	0.60	38400	2.00	1.00	4.00	1650	0.120	36458	22.10	24.88	24.88
26	81.55	40	6.5	0.55	35200	2.00	1.00	4.00	1650	0.120	33258	20.16	20.71	20.71
27	81.55	40	6.8	0.55	35200	2.00	1.00	4.00	1650	0.120	33258	20.16	20.71	20.71
28	81.55	40	7.0	0.55	35200	2.00	1.00	4.00	1650	0.120	33258	20.16	20.71	20.71
29	81.55	40	7.3	0.50	32000	2.00	1.00	4.00	1650	0.120	30058	18.22	16.91	16.91
30	81.55	40	7.5	0.50	32000	2.00	1.00	4.00	1650	0.120	30058	18.22	16.91	16.91
31	81.55	40	7.8	0.45	28800	2.00	1.00	4.00	1650	0.120	26858	16.28	13.50	13.50
32	81.55	40	8.0	0.45	28800	2.00	1.00	4.00	1650	0.120	26858	16.28	13.50	13.50
33	81.55	40	8.3	0.45	28800	2.00	1.00	4.00	1650	0.120	26858	16.28	13.50	13.50
34	81.55	40	8.5	0.45	28800	2.00	1.00	4.00	1650	0.120	26858	16.28	13.50	13.50
35	81.55	40	8.8	0.45	28800	2.00	1.00	4.00	1650	0.120	26858	16.28	13.50	13.50
36	81.55	40	9.0	0.45	28800	2.00	1.00	4.00	1650	0.120	26858	16.28	13.50	13.50
37	81.55	40	9.3	0.35	22400	2.00	1.00	4.00	1650	0.120	20458	12.40	7.84	7.84
38	81.55	40	9.5	0.30	19200	2.00	1.00	4.00	1650	0.120	17258	10.46	5.58	5.58
39	81.55	40	9.8	0.25	16000	2.00	1.00	4.00	1650	0.120	14058	8.52	3.70	3.70
40	81.55	40	10.0	0.25	16000	2.00	1.00	4.00	1650	0.120	14058	8.52	3.70	3.70
41	81.55	40	10.3	0.20	12800	2.00	1.00	4.00	1650	0.120	10858	6.58	2.21	2.21
42	81.55	40	10.5	0.20	12800	2.00	1.00	4.00	1650	0.120	10858	6.58	2.21	2.21
43	81.55	40	10.8	0.18	11200	2.00	1.00	4.00	1650	0.120	9258	5.61	1.60	1.60
44	81.55	40	11.0	0.15	9600	2.00	1.00	4.00	1650	0.120	7658	4.64	1.10	1.10
45	81.55	40	11.3	0.13	8000	2.00	1.00	4.00	1650	0.120	6058	3.67	0.69	0.69
46	81.55	40	11.5	0.10	6400	2.00	1.00	4.00	1650	0.120	4458	2.70	0.37	0.37
47	81.55	40	11.8	0.08	4800	2.00	1.00	4.00	1650	0.120	2858	1.73	0.15	0.15
48	81.55	40	12.0	0.05	3200	2.00	1.00	4.00	1650	0.120	1258	0.76	0.03	0.03

Table VII-10 Determination of the ultimate scour depth based on the Dynamic Uplift Impulsion model. The fracture toughness has been calculated based on the tensile strength T.

5.2. Comparison with Annandale's Erodibility Index (EI) method (, 1995)

The present section compares the scour model with Annandale's Erodibility Index Method as outlined by Annandale (1995). The basic idea is to find out whether points of similarity exist between the two models. Furthermore, this comparison highlights the tendencies and sensibilities of the ultimate scour depth as a function of the parameters of the model.

The Erodibility Index K_h has already been introduced in § 2.4 of Chapter II. Its basic characteristics will be briefly outlined herein. The index is a scalar number that is formed by the multiplication of four factors. These factors account for the main mechanical characteristics of the rock mass, such as the unconfined compressive strength UCS, the relative density, the rock block size, the discontinuity bond shear strength, the shape of the rock blocks and the orientation of the joints relative to the impacting flow. Equation (1.27) has been rewritten:

$$K_h = M_s \cdot K_b \cdot K_d \cdot J_s \tag{1.27}$$

M_s = the mass strength number

The mass strength number represents the material strength of an intact representative sample without regard to geologic heterogeneity within the mass. It equals the product of a material's uniaxial compressive strength (UCS) and its coefficient of relative density. The coefficient of relative density is the ratio of a material's bulk density over 27.0 kN/m^3. M_s can be determined by equating it to the UCS in MPa if the strength is greater than 10 MPa, and equal to $0.78 \cdot UCS^{1.5}$ when the strength is less than 10 MPa. As such, five different types of rock are distinguished, from very soft rock to extremely hard rock.

K_b = block size number

The block size number refers to the mean size of blocks of intact rock material (the cube root of the volume) as determined by the joint spacing within the rock mass. It can be calculated by dividing the RQD by the joint set number J_n. The RQD is the Rock Quality Designation, which is a standard parameter in drill core logging. The joint set number J_n is a function of the number of joint sets in a rock mass.

K_d = shear strength number

The shear strength number represents the strength of discontinuity interfaces in rock masses. It can be determined by the ratio J_r/J_a, in which J_r stands for the joint roughness number and J_a for the joint alteration number. The joint roughness number reflects the roughness condition of the facing walls of a discontinuity. It is a parameter that depends on the tightness of the joints. The joint alteration number refers to the weathering condition of the joint face material.

J_s = relative ground structure number

The relative ground structure number accounts for the structure of the ground with respect to the direction of the incoming flow. In other words, it expresses the ease with which the flow can penetrate the ground and dislodge individual blocks, and is expressed in terms of the orientation and the shape of the individual blocks determined by joint set spacings, dip angles and dip directions.

All of the aforementioned parameters can be measured in the field at low cost and are quantifiable by means of tables (Annandale, 1995). In the following, the Erodibility Index (EI) Method will be applied to different types of fissured rock. For each type of rock, the index will be determined and compared with the erosive power of an incoming flow. This incoming flow is defined by its geometrical characteristics. As such, the pressure head of the flow that is necessary to just start scour can be determined for each of the rock masses in question. This pressure head, as well as the corresponding geometrical characteristics, is then used to compare with the present new scour model.

The first example considers a rock mass with only one joint set. This corresponds to a J_n value of 1.22. The joint is vertically oriented and of the closed-end type. The distance between fissures is such that

the fissures do not interfere with each other. Hence, a very high RQD value of 95 is assumed. Together with a J_n number of 1.22, this results in a K_b number of 78. Furthermore, tightly healed joints are considered, with a discontinuous pattern, leading to a J_r number of 4 and a J_a number of 0.75 to 1.0. The dip direction of the joints is chosen in the direction of the falling jet. The dip angle is 90°, corresponding to J_s numbers ranging form 1.14 to 1.26, depending on the ratio of joint spacing. The value 1.14 is representative for equi-sided rock blocks, while the value of 1.26 rather represents rectangular strips.

The total rate of energy dissipation per unit area P [kW/m^2] is equal to the product of the unit weight of water γ [kN/m^3], the discharge Q [m^3/s] and the change in energy ΔE [m] divided by the horizontal projection of the area of the jet at impact A_i [m^2]:

$$P = \frac{\gamma \cdot Q \cdot \Delta E}{A_i} \tag{7.23}$$

The area of the jet at impact is considered almost equal to the area at the outlet and no plunge pool water depth is considered. Hence, per unit of jet width, for a critical height h_{cr} of the jet at its issuance of 1.4 m, the total jet thickness at impact is assumed to be about 2 m (= very small spread of the jet during its fall). This produces a unitary discharge of q = 5.3 [m^2/s]. From this, the pressure head H [m] that is necessary to start the scour is:

$$H = \frac{P \cdot 2}{\gamma \cdot 5.3} \tag{7.24}$$

P stands for the required stream power per unit area. It can be seen that for very soft rock, a pressure head of only 10 m is sufficient to scour the rock. For extremely hard rock, the necessary heads increase up to 200 m.

Rock type		Very Soft		Soft		Hard		Very Hard		Extremely Hard	
M_s	[-]	3.3		13		26		106		280	
RQD	[-]	95		95		95		95		95	
J_n	[-]	1.22		1.22		1.22		1.22		1.22	
K_b	[-]	78		78		78		78		78	
J_r	[-]	4		4		4		4		4	
J_a	[-]	0.75	1	0.75	1	1	1.05	1.1	1.15	1.2	1.25
K_d	[-]	5.3	4.0	5.3	4.0	4.0	3.8	3.6	3.5	3.3	3.2
J_s	[-]	1.26	1.14	1.26	1.14	1.14	1.116	1.092	1.068	1.044	1.02
Erodibility Index K_h	[-]	1727	1172	6803	4616	9232	8607	32776	30662	75875	71166
Power Required P	[kW/m^2]	268	200	749	560	942	894	2436	2317	4572	4357
Necessary Head H	[m]	10	8	29	22	37	35	94	90	177	169

Table VII-11 Erodibility Index K_h for different types of rock and stream power P required to erode the rock. Comparison with the pressure head H that is necessary to generate the required stream power.

The next step is to apply the present scour model, consisting of the Comprehensive Fracture Mechanics model and the Dynamic Impulsion model, to the same situation. This has been done at Table VII-12 for different degrees of jointing. The considered rock mass has an unconfined compressive strength of 106 MPa, corresponding to very hard rock at Table VII-11. Semi-elliptical and semi-circular surface cracks are assumed. The a/c ratio is taken equal to 0.2 and 1.0. The total joint lengths L are 1.0 m or 2.0 m and the maximum dynamic pressure value at the tip of the joint C^{max}_p is defined as 1.0, 1.5 or 2.0 times the kinetic energy of the impacting jet.

Where instantaneous or brittle crack propagation has been obtained this has been indicated by "I". For a time-dependent crack propagation of up to 200-300 days of discharge, the results are indicated in light grey. This case is considered to represent where, during the life-time of the dam structure, the rock mass will be scoured at some point in time. In other words, it is a broad-brush expression for the ultimate scour depth or, in the present case, for the pressure head or dam height that will cause scour. Finally, where time-dependent crack propagation is obtained with more than 200-300 days of discharge, the results are indicated in dark grey. The latter case is considered here to represent the end of scour.

Some very interesting tendencies and sensitivity of the scour model can be distinguished. First of all, the maximum dynamic pressure coefficient C^{max}_{p} has a profound impact on the scour limit. Secondly, the degree of jointing also significantly influences the results. As such, a C^{max}_{p} of 1.0 combined with a degree of jointing of 0.2 and an a/c ratio of 0.2 (elliptical flaw) will result in a necessary dam height of 120 m. The same C^{max}_{p} but with a degree of jointing of 0.6 will commence with scour of the rock at a lower dam height of 80 m.

It can be observed that these results do not hold in the case of a circular joint. Apparently, the semi-circular joint is much more difficult to erode than the semi-elliptical one. This corresponds to the findings in Fig. VII-12 on boundary correction factors *f*.

P_e	f(a/W)	a/c	H (EI)	H (CFM)	C_{max} = 1.0 L = 1.0 m T	C_{max} = 1.5 L = 1.0 m T	C_{max} = 2.0 L = 1.0 m T	C_{max} = 1.0 L = 2.0 m T	C_{max} = 1.5 L = 2.0 m T	C_{max} = 2.0 L = 2.0 m T
-	-	-	m	m	days	days	days	days	days	days
		0.2		80	14400	116	3.7	933	7.5	I
		0.2		90	3550	29	0.9	230	1.8	I
0.2	1.116	0.2	90-94	100	1000	8	0.26	65	I	I
		0.2		110	326	2.6	I	21	I	I
		0.2		120	116	0.9	I	7	I	I
		0.2		80	60	0.5	I	3.9	I	I
		0.2		90	15	I	I	I	I	I
0.4	1.294	0.2	90-94	100	4.2	I	I	I	I	I
		0.2		110	1.3	I	I	I	I	I
		0.2		120	0.4	I	I	I	I	I
		0.2		80	0.6	I	I	I	I	I
		0.2		90	I	I	I	I	I	I
0.6	1.642	0.2	90-94	100	I	I	I	I	I	I
		0.2		110	I	I	I	I	I	I
		0.2		120	I	I	I	I	I	I
		1.0		80	6500000	52000	1700	421000	3360	110
		1.0		90	1600000	12800	419	104000	828	27
0.2	0.668	1.0	90-94	100	457000	3650	120	29600	236	7.7
		1.0		110	147000	1170	38	9520	76	2.5
		1.0		120	52000	417	13.7	3380	27	I
		1.0		80	136000	1090	36	8800	71	2.3
		1.0		90	33600	269	8.8	2170	17	I
0.4	0.676	1.0	90-94	100	9580	77	2.5	620	5	I
		1.0		110	3080	25	0.8	199	1.6	I
		1.0		120	1090	9	I	71	I	I
		1.0		80	7400	60	2	5350	3.8	I
		1.0		90	1800	15	0.5	1320	I	I
0.6	1.107	1.0	90-94	100	521	4.2	I	376	I	I
		1.0		110	168	1.3	I	121	I	I
		1.0		120	59	0.5	I	43	I	I

Table VII-12 Sensitivity analysis of the main parameters of the Comprehensive Fracture Mechanics model by comparison with Annandale's Erodibility Index Method. The analysis makes use of semi-elliptical and semi-circular shaped single joint. The UCS of the rock mass is 106 MPa.

The interesting aspect about Table VII-12 is that comparison with Annandale's Erodibility Index Method procures different combinations of parameters that are in agreement with the former. For example, for a total joint length L of 1.0 m and a semi-elliptical shape (a/c = 0.2), a plausible combination would be a persistency a/B of 0.4 and a C^{max}_p of 1.0. This results in 10 to 15 days of discharge before the scour starts, which is a realistic value. Another possibility is obtained for a total joint length L of 1.0 m and a semi-circular shape (a/c = 1.0), which results in 5 to 9 days of discharge for a persistency a/B of 0.4 and a C^{max}_p of 2.0. For a total joint length L of 2.0 m and a semi-circular shape (a/c = 1.0), a persistency a/B of 0.4 and a C^{max}_p of 1.5 conduct to 10 to 17 days of discharge to scour the rock mass.

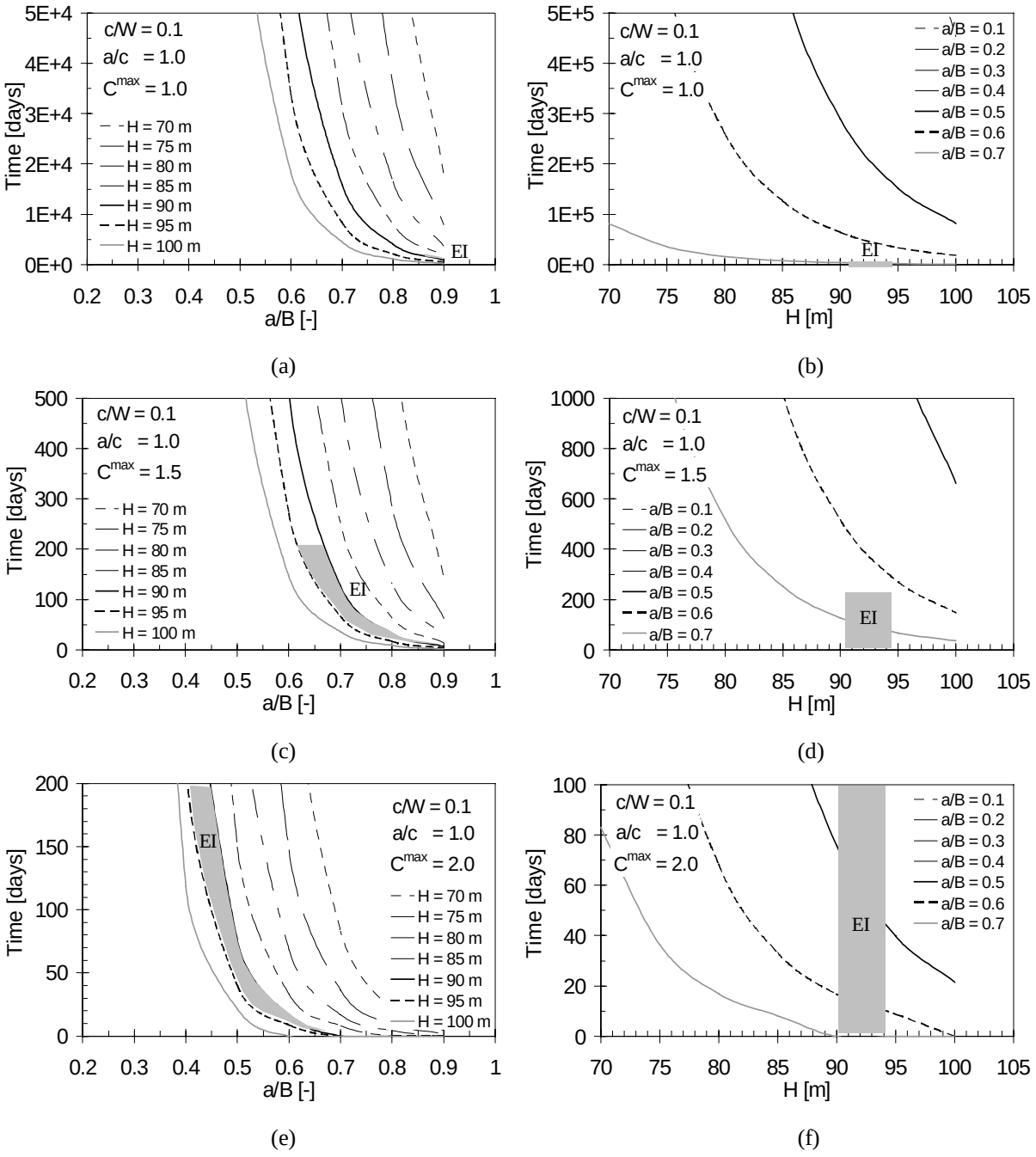

Fig. VII-17 Time necessary to scour a very hard rock mass (UCS = 106 MPa) with a single semi-circular joint:
a) as a function of a/B with C^{max} = 1.0; b) as a function of H with C^{max} = 1.0;
c) as a function of a/B with C^{max} = 1.5; d) as a function of H with C^{max} = 1.5;
e) as a function of a/B with C^{max} = 2.0; f) as a function of H with C^{max} = 2.0.

The sensibility of the a/B ratio, the a/c ratio, the c/W ratio and the C^{max} coefficient has been studied more in detail. The results are presented in Fig. VII-17 and consider the case of a **semi-circular** joint, i.e. a/c = 1.0. Furthermore, according to the singular joint assumption made in Annandale's Erodibility Index Method, the c/W ratio has to be taken very small. A value of 0.1 has been chosen, which corresponds to a longitudinal distance W between the successive rock joints of four times the joint width 2c.

The left hand side of Fig. VII-17 deals with the time necessary to completely break-up the joint as a function of the a/B ratio, i.e. the persistency of the rock mass. This has been done for three C^{max} coefficients: 1.0, 1.5 and 2.0. For the fatigue law, 80 % of this maximum pressure has been used, according to Table VII-4 for core jet impact. At each graph, the curves corresponding to pressure heads between 70 m and 100 m are compared. Assuming core jets and, thus, no significant water cushion, these heads can be considered equal to the fall height of the jet.

According to Table VII-11, a very hard rock mass with a UCS of 106 MPa and a RQD of 95 has been used. The Erodibility Index for this rock indicates that the pressure head H that is necessary to scour the rock lies **between 90 and 94 m**. It is assumed that this scour is obtained within maximum 200 days of discharge on the rock. These limits have been systematically added to the graphs for purpose of comparison. When considering the curves for 90 m and 95 m of pressure head in Fig. VII-17a, it can be derived that a C^{max} coefficient of 1.0 needs a degree of jointing of 0.9 to scour the rock within 200 days of discharge. A C^{max} coefficient of 2.0 (Fig. VII-17e) would need an initial degree of jointing of only 0.4 to 0.7, which seems much more plausible. A similar conclusion can be drawn from the Figs. VII-17b and 17f, as a function of the necessary pressure head H.

The issue is to determine which is a plausible maximum pressure coefficient. Equation (7.14) defines this coefficient as the sum of the C-coefficient (mean pressure) and the C^+-coefficient (extreme positive deviation from the mean pressure). Based on Fig. VII-6a, the curve for maximum C^{+-} coefficients indicates a value of 2.0 at Y/D_j equal to 0 (= without any water cushion). Fig. VII-3a moreover procures a C-coefficient of mean pressure that is equal to 0.85. Hence, an upper limit for the C_{max} coefficient should be around 3. The corresponding results are presented hereunder.

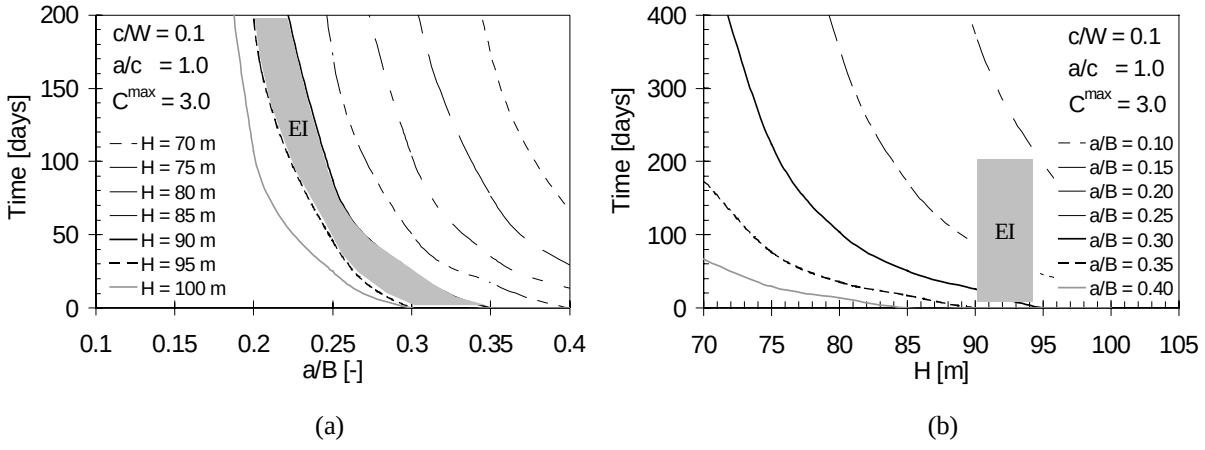

Fig. VII-18 Time necessary to scour a very hard rock mass (UCS = 106 MPa) with a single semi-circular joint: a) as a function of a/B with C^{max} = 3.0; b) as a function of H with C^{max} = 3.0.

It is concluded from Fig. VII-18 that, in order to obtain a pressure head that is similar to the Erodibility Index method, the present scour model combines a maximum pressure coefficient C^{max} of 3.0 with an initial degree of jointing of 0.25 to 0.35. This result is valid for a single semi-circular rock joint inside a very hard rock mass. The fatigue law of granite (Fig. VII-14b) has been used.

A similar sensibility analysis has been performed for a single **semi-elliptical** rock joint. The a/c ratio has been taken equal to 0.5. This means that the vertical depth of the rock joint is equal to half of the horizontal radius. All other parameters are the same as in the previous analysis. The results are presented in Fig. VII-19 and mainly indicate that the semi-elliptical rock joint is slightly more sensible to crack propagation than the semi-circular one. A C^{max} coefficient of 1.0 (Fig. VII-19a) needs a degree of jointing of only 0.65 to scour the rock within 200 days of discharge. A C^{max} coefficient of 2.0 (Fig. VII-19e) would need an initial degree of jointing of only 0.3 to 0.4.

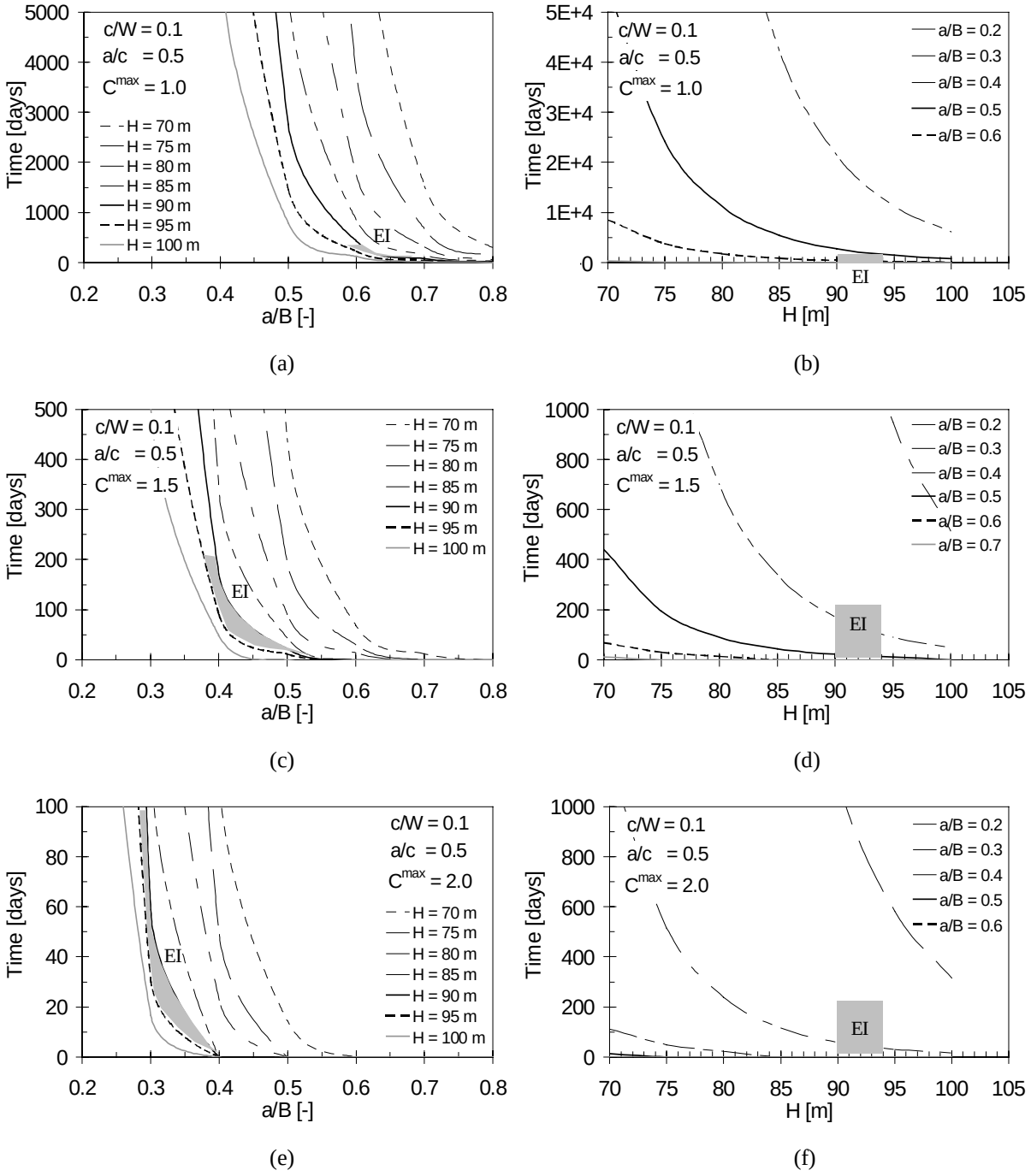

Fig. VII-19 Time necessary to scour a very hard rock mass (UCS =106 MPa) with a single semi-elliptical joint:
a) as a function of a/B with C^{max} = 1.0; b) as a function of H with C^{max} = 1.0;
c) as a function of a/B with C^{max} = 1.5; d) as a function of H with C^{max} = 1.5;
e) as a function of a/B with C^{max} = 2.0; f) as a function of H with C^{max} = 2.0.

Finally, the case of a **single-edge** rock joint has been investigated. As already pointed out before, this type of joint has much less support from the surrounding rock mass and, therefore, should be much easier to break-up. This is confirmed by the results in Fig. VII-20, where a C^{max}-coefficient of 2.0 corresponds to a degree of jointing of only 0.15 to 0.20. These values are significantly lower than for the other two types of rock joints. When introducing the critical degree of jointing that was obtained for the semi-elliptical joint, i.e. 0.3 to 0.4, brittle crack propagation is obtained, even at pressure heads of only 70 m.

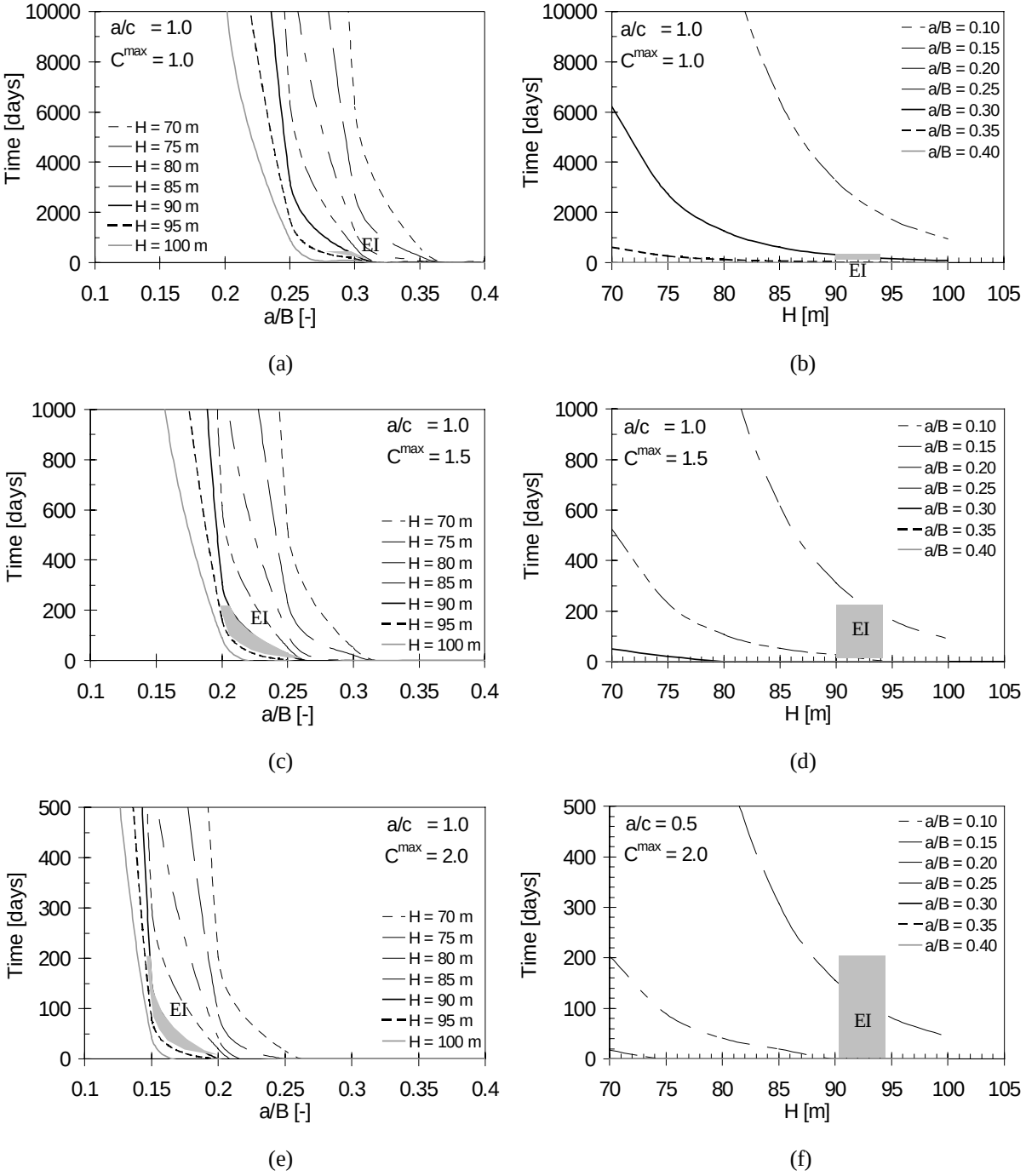

Fig. VII-20 Time necessary to scour a very hard rock mass (UCS = 106 MPa) with a single single-edge joint:
a) as a function of a/B with C^{max} = 1.0; b) as a function of H with C^{max} = 1.0;
c) as a function of a/B with C^{max} = 1.5; d) as a function of H with C^{max} = 1.5;
e) as a function of a/B with C^{max} = 2.0; f) as a function of H with C^{max} = 2.0.

The conclusions drawn from the preceding calculations are only valid for a very hard rock with a UCS = 106 MPa. A similar analysis is performed for a hard rock and a **semi-circular** joint. According to Table VII-11, this rock has a UCS = 26 MPa. The Erodibility Index for this rock indicates that the pressure head H that is necessary to scour the rock lies **between 35 and 37 m**. The results are presented in Fig. VII-21. The relationship between the C^{max} coefficient and the appropriate degree of jointing is in good agreement with the corresponding relations found for the very hard rock mass.

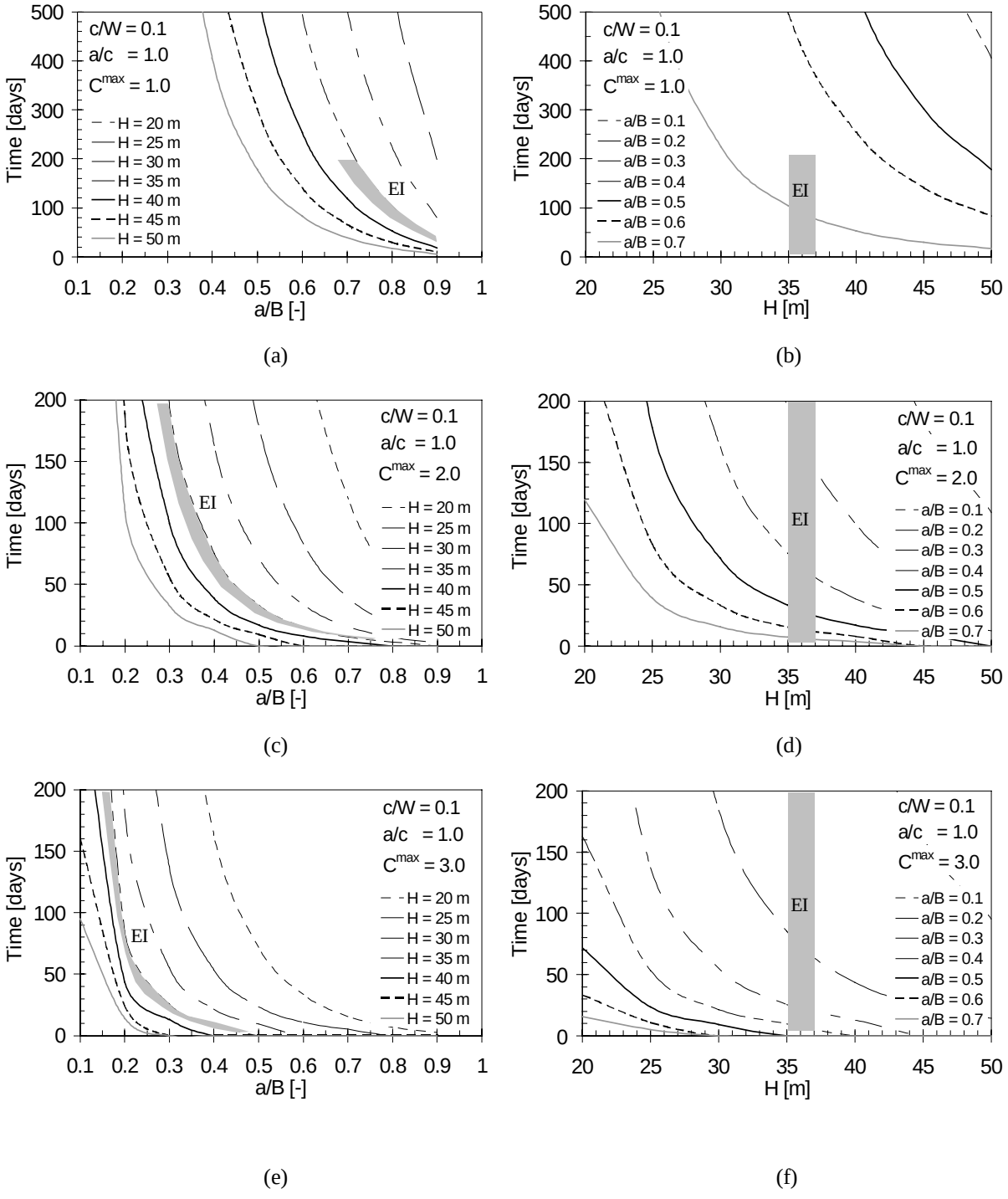

Fig. VII-21 Time necessary to scour a hard rock mass (UCS = 26 MPa) with a single semi-circular joint:
a) as a function of a/B with C^{max} = 1.0; b) as a function of H with C^{max} = 1.0;
c) as a function of a/B with C^{max} = 2.0; d) as a function of H with C^{max} = 2.0;
e) as a function of a/B with C^{max} = 3.0; f) as a function of H with C^{max} = 3.0.

Finally, comparison is made with the Erodibility Index for a very hard rock mass (UCS = 106 MPa) but with two joint sets instead of one. Analogous to Table VII-11, this conducts to a necessary pressure head **between 70 and 78 m** for the onset of scour.

The presence of the two joint sets can be integrated in the scour model by two means: 1) assume semi-elliptical joints with an a/c factor that is low and a c/W factor that is equal to 0.5; 2) assume single-edge joints. The former case considers semi-elliptical joints that touch one another at the surface and that are very long compared to their depth. As such, they are quite comparable to the single-edge joints. This is visible in Fig. VII-12, where the boundary correction factor f is presented for these two cases. Both cases become very sensible to the degree of jointing, once the a/B ratio is higher than 0.4. This is due to the lack of surrounding rock support.

Secondly, the hydrodynamic loading inside the joints is assumed minimal, i.e. without the appearance of peak pressures. This is based on the assumption of a high air content inside the joints and the possibility of leakage of water out of the joints towards connected joints. As such, a C^{max}-coefficient of only 1.0 to 1.5 is considered.

For C^{max} = 1.0, appropriate a/B values range from 0.35 to 0.40. For C^{max} = 1.5, these values decrease down to 0.25-0.30. The obtained values are close to the ones obtained for a single-edge rock joint in Fig. VII-20.

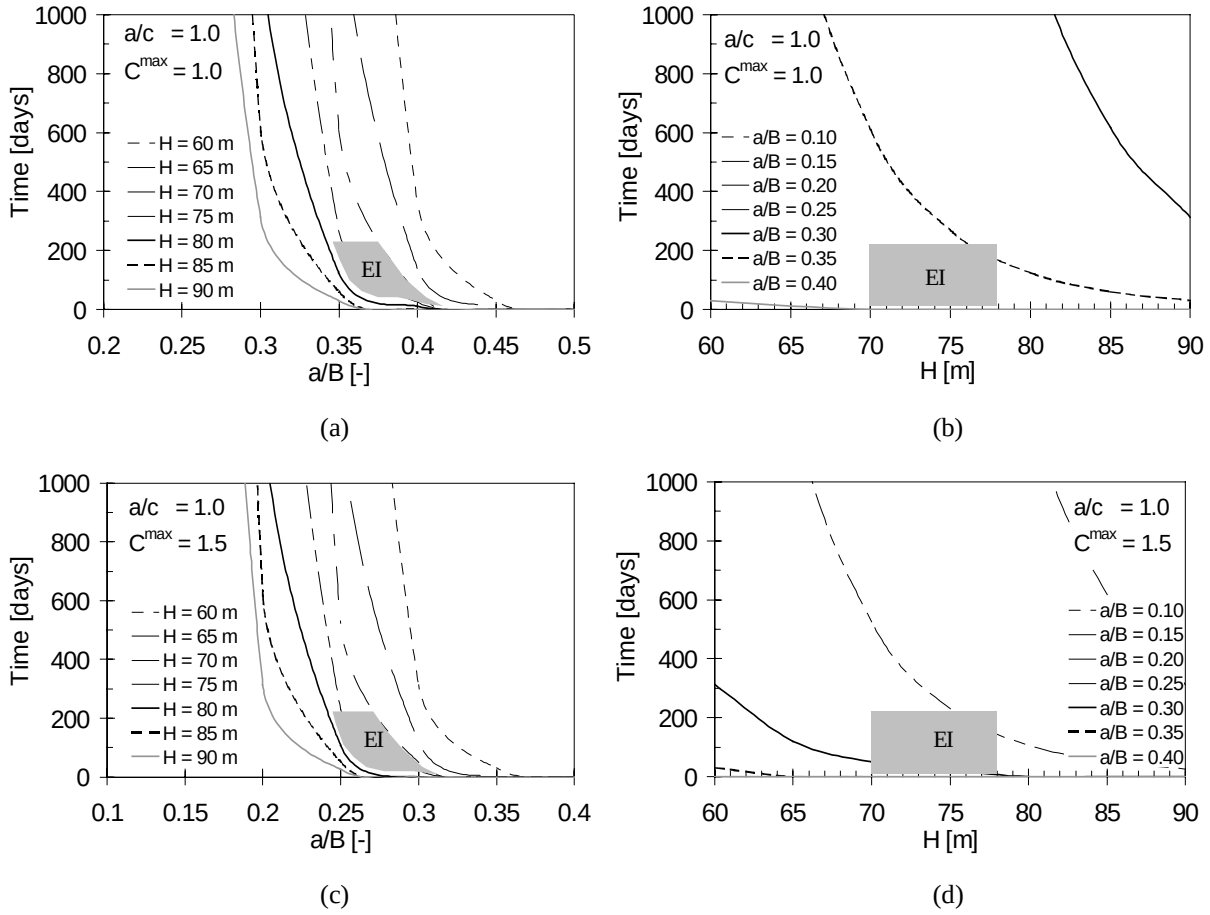

Fig. VII-22 Time necessary to scour a very hard rock mass (UCS = 106 MPa) with two interconnected joints sets of the single-edge type:
a) as a function of a/B with C^{max} = 1.0; b) as a function of H with C^{max} = 1.0;
c) as a function of a/B with C^{max} = 1.5; d) as a function of H with C^{max} = 1.5;

5.3. Case study for Cabora-Bassa dam

5.3.1. Introduction

The Cabora-Bassa dam is localized on the Zambezi River in Mozambique (Photo 7). The dam is a thin double curvature arch dam with a total spillway discharge capacity of 13'100 m^3/s, valid at a maximum reservoir level of 326 m a.s.l. The corresponding tailwater level is at 225 m a.s.l. with a depth of nearly 50 m above the natural riverbed. The spillway consists of eight identical sluice gates with a height of 6 m and a width of 7.8 m. The eight sluice gates are distributed into two groups, at each side of the dam axis. The exit lip of the gates is at elevation 244.30 m a.s.l. and makes an angle of 32.3° with the horizontal. The riverbed is very irregular and has its elevations varying from 170 to 180 a.s.l. The rock is mainly **granitoide gneiss** with exceptionally little cracking, but with a few gabbro and lamprophire dykes.

Photo 7 View from downstream to upstream of the Cabora-Bassa dam while discharging through 6 of the eight sluice gates.

Hydraulic model tests at a 1/75 scale have been conducted at LNEC, Lisbon. A moveable bed model was used, made with gravel of characteristic diameters d_{85}, d_{50} and d_{15} of respectively 35, 28 and 13 mm weakly aggregated with aluminous cement. The test results resulted in a maximum scour depth at an elevation of 150 m a.s.l. and a downstream distance from the jet outlet of 250 m. Furthermore, the trajectory length of the jet from the tailwater level to the bottom of the rock was found to be 115 m.

The prototype behavior of the dam is characterized by two important operating periods. The first one happened in 1975 during 42 days, for a discharge of 6'000 m^3/s (= 4 gates). The upstream reservoir levels ranged from 309 m a.s.l. to 313 m a.s.l. The scour depth after this gate operation was measured in-situ at about 170 m a.s.l., with a considerable extension downstream. The tailwater level corresponding to 6'000 m^3/s was about 215 m a.s.l.

The second period occurred in 1978. The spillway was being operated for four and a half consecutive months as presented at Table VII-13. The maximum reservoir level was 327.74 m a.s.l. An extensive survey of the scour pit in 1980 is summarized in Fig. VII-23. The deepest point of the scour pit was situated at 158 m a.s.l., i.e. 22 m deeper than the original riverbed. This occurred at a downstream distance from the jet outlet ranging from 240 to 260 m.

Number of gates	Discharge	Period	Duration
> 4	6'300 m^3/s	6 March – 23 July	139 days
> 5	8'200 m^3/s	13 March – 18 April	36 days
> 6	9'800 m^3/s	17 March – 12 April	26 days
> 7	11'500 m^3/s	22 March – 5 April	14 days
> 8	13'100 m^3/s	23 March – 5 April	13 days

Table VII-13 Spillway operating conditions in 1978 at Cabora-Bassa dam.

5.3.2. Falling jet characteristics

The module for the falling jet defines the geometric and hydraulic characteristics of the jet at its point of impact in the plunge pool. The diameter of the jet at issuance from the dam has been estimated as the equivalent hydraulic diameter of the 6 m x 7.8 m rectangular outlet. This results in an equivalent diameter D_i = 7.7 m. The jet trajectory has been calculated based on ballistic equations. The initial turbulence intensity of the jet has been estimated at Tu = 4 %. This resulted in a jet impact velocity of V_j = 35 m/s and an impact diameter of D_j = 8 m. The outer diameter was estimated at D_{out} = 20 m. The jet break-up length was estimated at 167 m of total trajectory length, corresponding to x_{ult} = 150 m of downstream distance from the jet outlet. This means that the jet is just broken-up at impact in the plunge pool. Therefore, the outer diameter has been chosen as representative diameter.

5.3.3. Annandale's Erodibility Index Method

For calculation of the Erodibility Index, a jet spread through the plunge pool depth of 8° has been assumed. This spread defines the velocity decay through the water depth. The rock mass has been considered to be soft rock with a UCS = 13 MPa and very little cracking, thus a RQD = 90%. When considering one set of smooth, planar and tightly healed joints, under an angle of about 67° with the horizontal, the Erodibility Index equals 384 (Table VII-13, a.s.l. = above sea level).

Rock type		Soft	Assumption
M_s	[-]	13	soft rock
RQD	[-]	90	very little cracking
J_n	[-]	1.22	one joint set
K_b	[-]	74	
J_r	[-]	1	smooth, planar tight joints
J_a	[-]	1	unaltered joint walls
K_d	[-]	1.0	
J_s	[-]	0.40	large spacing, angle of 67 °
Erodibility Index K_h	[-]	384	
Corresponding elevation pool bottom	[m a.s.l.]	160	tailwater level at 225 m a.s.l.

Table VII-13 Calculus of the Erodibility Index and comparison with the corresponding elevation of the pool bottom where the required and available stream power are equal (a.s.l. = above sea level).

The elevation where the required and available stream power intersect is at about 160 m a.s.l. Assuming an angle of jet impact of 67° with the horizontal, this corresponds to a total water trajectory length Y of 167 m, or a Y/D_j ratio of 8.3. The vertical equilibrium depth of the pool is 65 m. Hence, developed jet impact conditions govern. Fig. VII-23 presents the intersection of the required and available stream power.

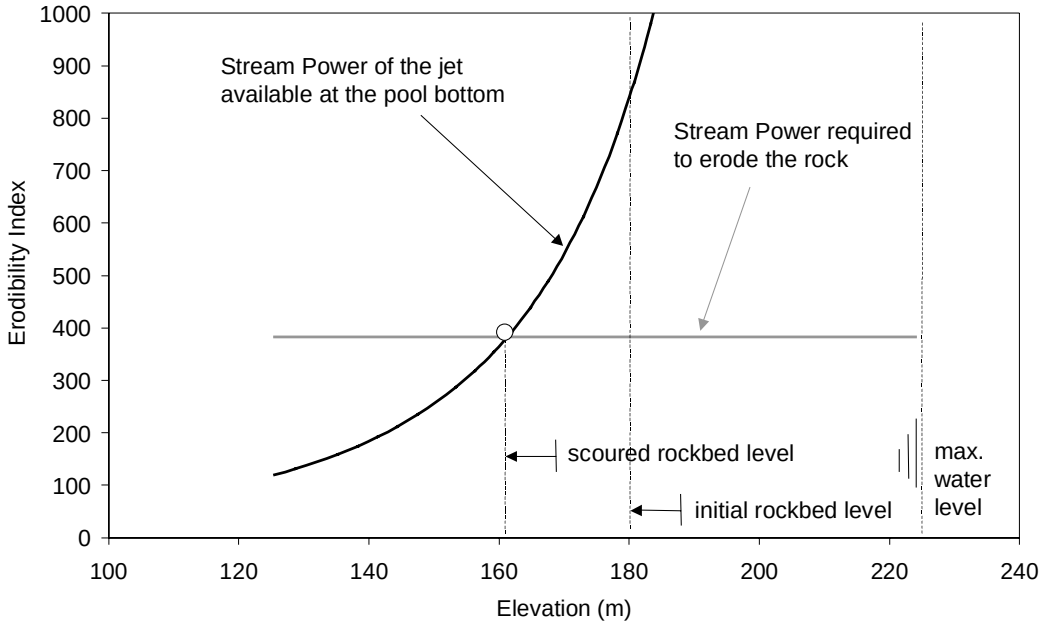

Fig. VII-23 Comparison of available stream power and required stream power as a function of the absolute elevation in m a.s.l. The equilibrium scour depth is observed at 160 m a.s.l.

5.3.4. The Comprehensive Fracture Mechanics model

The falling jet has a high degree of break-up upon impact in the plunge pool. The amount of entrained air is very high and the available excitation capacity of the jet is probably decreased due to the break-up. Therefore, it is not plausible to account for high amplification effects of the pool bottom pressures inside rock joints. Hence, the relationship between C^{max} and Y/D_j starts at a value of 2.0 and progressively decreases from on a Y/D_j value of 8, due to jet diffusion.

According to Fig. VII-21c, the model assumes semi-circular joints with a persistency a/B of 0.7 for a total possible length of 2 m. The total length is derived from the dimensions of rock blocks as found in-situ. These revealed to have a side length of about 2 m (§ 5.3.5). The persistency value a/B revealed to be in good agreement with the Erodibility Index results for a C^{max} of 2.0. As such, it is not a calibrated parameter of the model. The boundary correction factor is taken equal to 0.7, according to Fig. III-29 for semi-circular joints.

The fracture toughness has been calculated as a function of the unconfined compressive strength UCS assumed by the Erodibility Index Method (= 13 MPa) and for silicate rocks (based on Fig. VII-38d). The horizontal in-situ stress field corresponds to an overburden pressure of 100 m of rock and for K_0 = 1. The narrow shape of the surrounding valley justifies this value. The lack of amplification effects implies that no dynamic resistance effects of the rock mass are accounted for. The m and C parameters of the fatigue law have been chosen equal to 10 respectively 2.E-6. The former value is chosen stating that granitoide gneiss is probably somewhat more sensible to fatigue effects than a pure granite, which exhibits an m value of 12. The C parameter has been calibrated based on the prototype observations.

The results are presented at Table VII-14. It can be seen that brittle crack growth is obtained until an elevation of 170 m a.s.l. Hence, the elevation of 170 m a.s.l., which was attained in the prototype after 42 days, is found almost immediately in the present model. In fact, it exactly constitutes the separation between brittle crack growth and fatigue crack growth. It is obvious that brittle cracking also needs some time to happen. This is not accounted for in the present model.

Secondly, the 1978 spillway period of 139 days in total scoured the pit further down to 160 m a.s.l. The model attains this level after 137 days of additional discharge. Hence, a very good agreement is

obtained for the chosen parameters. The model allows to predict further scouring of the rock mass as a function of the time of discharge. Further scouring down to 150 m a.s.l. needs another 140 days of similar discharge conditions. After this, the phenomenon slows down due to jet diffusion effects. As such, an additional 10 m of scouring would need 800 days more of discharge. Stating that the 1978 discharges were exceptional, and accounting for the life-time of the dam, it can be argued that the elevation of 140 m a.s.l. constitutes a practical limit of ultimate scour depth.

V_j	35	m/s	Persistency	0.7	-
D_j	20	m	L	2	m
UCS	13	MPa	K_0	1	-

Y	V_j	Y/D_j	C^{max}	K_{Ixy}	$\sigma_{h,H}$	K_{Iins}	propagation	El.	T	Total T
m	m/s	-	-	$MPa*m^{0.5}$	MPa	$MPa*m^{0.5}$	-	m a.s.l.	days	days
114	35	5.7	2.0	1.54	2.65	1.50	brittle	180.5	inst	inst
116	35	5.8	2.0	1.54	2.703	1.51	brittle	179.7	inst	inst
118	35	5.9	2.0	1.54	2.756	1.51	brittle	179.0	inst	inst
120	35	6.0	2.0	1.54	2.809	1.51	brittle	178.2	inst	inst
122	35	6.1	2.0	1.54	2.862	1.51	brittle	177.4	inst	inst
124	35	6.2	2.0	1.54	2.915	1.52	brittle	176.6	inst	inst
126	35	6.3	2.0	1.54	2.968	1.52	brittle	175.8	inst	inst
128	35	6.4	2.0	1.54	3.021	1.52	brittle	175.1	inst	inst
130	35	6.5	2.0	1.54	3.074	1.53	brittle	174.3	inst	inst
132	35	6.6	2.0	1.54	3.127	1.53	brittle	173.5	inst	inst
134	35	6.7	2.0	1.54	3.18	1.53	brittle	172.7	inst	inst
136	35	6.8	2.0	1.54	3.233	1.53	brittle	171.9	inst	inst
138	35	6.9	2.0	1.54	3.286	1.54	brittle	171.2	inst	inst
140	35	7.0	2.0	1.54	3.339	1.54	brittle	170.4	inst	inst
142	35	7.1	2.0	1.54	3.392	1.54	fatigue	169.6	9.79E+00	9.79E+00
144	35	7.2	2.0	1.54	3.445	1.55	fatigue	168.8	9.79E+00	1.96E+01
146	35	7.3	2.0	1.54	3.498	1.55	fatigue	168.0	9.79E+00	2.94E+01
148	35	7.4	2.0	1.54	3.551	1.55	fatigue	167.3	9.79E+00	3.92E+01
150	35	7.5	2.0	1.54	3.604	1.55	fatigue	166.5	9.79E+00	4.90E+01
152	35	7.6	2.0	1.54	3.657	1.56	fatigue	165.7	9.79E+00	5.88E+01
154	35	7.7	2.0	1.54	3.71	1.56	fatigue	164.9	9.79E+00	6.86E+01
156	35	7.8	2.0	1.54	3.763	1.56	fatigue	164.1	9.79E+00	7.84E+01
158	35	7.9	2.0	1.54	3.816	1.57	fatigue	163.4	9.79E+00	8.82E+01
160	35	8.0	2.0	1.54	3.869	1.57	fatigue	162.6	9.79E+00	9.79E+01
162	35	8.1	2.0	1.54	3.922	1.57	fatigue	161.8	9.79E+00	1.08E+02
164	35	8.2	2.0	1.54	3.975	1.57	fatigue	161.0	9.79E+00	1.18E+02
166	35	8.3	2.0	1.54	4.028	1.58	fatigue	160.2	9.79E+00	1.27E+02
168	35	8.4	2.0	1.54	4.081	1.58	fatigue	**159.5**	9.79E+00	**1.37E+02**
170	35	8.5	2.0	1.54	4.134	1.58	fatigue	158.7	9.79E+00	1.47E+02
172	35	8.6	2.0	1.54	4.187	1.59	fatigue	157.9	9.79E+00	1.57E+02
174	35	8.7	2.0	1.54	4.24	1.59	fatigue	157.1	9.79E+00	1.67E+02
176	35	8.8	2.0	1.54	4.293	1.59	fatigue	156.3	9.79E+00	1.76E+02
178	35	8.9	2.0	1.54	4.346	1.59	fatigue	155.6	9.79E+00	1.86E+02
180	35	9.0	2.0	1.54	4.399	1.60	fatigue	154.8	9.79E+00	1.96E+02
182	35	9.1	2.0	1.54	4.452	1.60	fatigue	154.0	9.79E+00	2.06E+02
184	35	9.2	2.0	1.54	4.505	1.60	fatigue	153.2	9.79E+00	2.15E+02
186	35	9.3	2.0	1.52	4.558	1.61	fatigue	152.4	1.14E+01	2.27E+02
188	35	9.4	1.9	1.50	4.611	1.61	fatigue	151.7	1.33E+01	2.40E+02
190	35	9.5	1.9	1.47	4.664	1.61	fatigue	150.9	1.55E+01	2.56E+02
192	35	9.6	1.9	1.45	4.717	1.61	fatigue	150.1	1.82E+01	2.74E+02

Table VII-14 Determination of the ultimate scour depth based on the Comprehensive Fracture Mechanics model. The fracture toughness has been calculated based on the unconfined compressive strength UCS used in the Erodibility Index Method.

5.3.5. The Dynamic Impulse model

The calculus makes use of a maximum net impulsion C_I as defined by Fig. VII-9b. The characteristic block dimensions are based on model tests performed at LNEC, Lisbon. These tests represented in-situ blocks with a weight between 50 and 290 kN (Ramos, 1982). Assuming a cubic shape, this corresponds to side lengths ranging from 1.2 to 2.2 m. A side length of 2 m has been used. Due to the high aeration rate, a small wave celerity of 100 m/s is taken. The scour depth of 160 m a.s.l. that was attained after 1978 corresponds to a critical displacement of 2.6 times the height of the characteristic rock block (Table VII-15). In other words, the ultimate scour depth based on the dynamic uplift criterion is much deeper. The theoretical critical displacement of one times the height of the block is attained at an elevation of 133 m a.s.l. This agrees with the value of 140 found by the CFM model. Pertaining to the tightness of the joints, the theoretical critical displacement is justified.

V_j	35	m/s	γ_r	2700	kg/m^3	
D_j	20	m	z	2	m	
c	100	m/s	z/x	1	-	

Y	V_j	Y/D_j	C_I	I^{max}	x	z	L	G_b	T	I^{net}	V_{up}	h_{up}	h_{up}/z	El
m	m/s	-	-	Ns	m	m	m	kg/m^2	s	Ns	m/s	m	-	m a.s.l.
166	35	8.3	0.53	38785	2.00	2.00	6.00	3400	0.180	34783	10.23	5.33	2.67	160.2
168	35	8.4	0.52	38362	2.00	2.00	6.00	3400	0.180	34359	10.11	5.21	**2.60**	**159.5**
170	35	8.5	0.52	37941	2.00	2.00	6.00	3400	0.180	33938	9.98	5.08	2.54	158.7
172	35	8.6	0.51	37522	2.00	2.00	6.00	3400	0.180	33520	9.86	4.95	2.48	157.9
174	35	8.7	0.50	37107	2.00	2.00	6.00	3400	0.180	33104	9.74	4.83	2.42	157.1
176	35	8.8	0.50	36694	2.00	2.00	6.00	3400	0.180	32691	9.62	4.71	2.36	156.3
178	35	8.9	0.49	36283	2.00	2.00	6.00	3400	0.180	32281	9.49	4.59	2.30	155.6
180	35	9.0	0.49	35875	2.00	2.00	6.00	3400	0.180	31873	9.37	4.48	2.24	154.8
182	35	9.1	0.48	35470	2.00	2.00	6.00	3400	0.180	31468	9.26	4.37	2.18	154.0
184	35	9.2	0.48	35068	2.00	2.00	6.00	3400	0.180	31065	9.14	4.25	2.13	153.2
186	35	9.3	0.47	34668	2.00	2.00	6.00	3400	0.180	30665	9.02	4.15	2.07	152.4
188	35	9.4	0.47	34271	2.00	2.00	6.00	3400	0.180	30268	8.90	4.04	2.02	151.7
190	35	9.5	0.46	33876	2.00	2.00	6.00	3400	0.180	29874	8.79	3.93	1.97	150.9
192	35	9.6	0.46	33484	2.00	2.00	6.00	3400	0.180	29482	8.67	3.83	1.92	150.1
194	35	9.7	0.45	33095	2.00	2.00	6.00	3400	0.180	29093	8.56	3.73	1.87	149.3
196	35	9.8	0.45	32708	2.00	2.00	6.00	3400	0.180	28706	8.44	3.63	1.82	148.5
198	35	9.9	0.44	32324	2.00	2.00	6.00	3400	0.180	28322	8.33	3.54	1.77	147.7
200	35	10.0	0.43	31943	2.00	2.00	6.00	3400	0.180	27941	8.22	3.44	1.72	147.0
202	35	10.1	0.43	31564	2.00	2.00	6.00	3400	0.180	27562	8.11	3.35	1.67	146.2
204	35	10.2	0.42	31188	2.00	2.00	6.00	3400	0.180	27186	8.00	3.26	1.63	145.4
206	35	10.3	0.42	30815	2.00	2.00	6.00	3400	0.180	26813	7.89	3.17	1.58	144.6
208	35	10.4	0.41	30444	2.00	2.00	6.00	3400	0.180	26442	7.78	3.08	1.54	143.8
210	35	10.5	0.41	30076	2.00	2.00	6.00	3400	0.180	26074	7.67	3.00	1.50	143.1
212	35	10.6	0.40	29711	2.00	2.00	6.00	3400	0.180	25708	7.56	2.91	1.46	142.3
214	35	10.7	0.40	29348	2.00	2.00	6.00	3400	0.180	25345	7.45	2.83	1.42	141.5
216	35	10.8	0.39	28988	2.00	2.00	6.00	3400	0.180	24985	7.35	2.75	1.38	140.7
218	35	10.9	0.39	28630	2.00	2.00	6.00	3400	0.180	24628	7.24	2.67	1.34	139.9
220	35	11.0	0.38	28275	2.00	2.00	6.00	3400	0.180	24273	7.14	2.60	1.30	139.2
222	35	11.1	0.38	27923	2.00	2.00	6.00	3400	0.180	23921	7.04	2.52	1.26	138.4
224	35	11.2	0.38	27574	2.00	2.00	6.00	3400	0.180	23571	6.93	2.45	1.22	137.6
226	35	11.3	0.37	27227	2.00	2.00	6.00	3400	0.180	23224	6.83	2.38	1.19	136.8
228	35	11.4	0.37	26882	2.00	2.00	6.00	3400	0.180	22880	6.73	2.31	1.15	136.0
230	35	11.5	0.36	26541	2.00	2.00	6.00	3400	0.180	22538	6.63	2.24	1.12	135.3
232	35	11.6	0.36	26202	2.00	2.00	6.00	3400	0.180	22199	6.53	2.17	1.09	134.5
234	35	11.7	0.35	25866	2.00	2.00	6.00	3400	0.180	21863	6.43	2.11	1.05	133.7
236	35	11.8	0.35	25532	2.00	2.00	6.00	3400	0.180	21529	6.33	2.04	**1.02**	**132.9**
238	35	11.9	0.34	25201	2.00	2.00	6.00	3400	0.180	21198	6.23	1.98	0.99	132.1

Table VII-14 Determination of the ultimate scour depth based on the Dynamic Impulsion model.

5.3.6. Conclusion

The scour hole of the Cabora-Bassa dam has been predicted based on both Annandale's Erodibility Index Method and the Comprehensive Fracture Mechanics and Dynamic Impulsion models of the present study. These predictions have been calibrated by means of available in-situ investigations of the scour depth evolution with time.

The Erodibility Index Method has been calibrated based on the equilibrium scour depth of **160 m a.s.l.** attained on the prototype after 1978. For a tightly healed single joint set, this resulted in a rather low UCS value of 13 MPa.

The Comprehensive Fracture Mechanics model has used this value to define the fracture toughness of the rock mass. This resulted in instantaneous crack growth until an elevation of 170 m a.s.l. Further scouring down to 160 m a.s.l. needed 137 days of discharge, whether this elevation was obtained in-situ after 139 days. Further scouring down to 150 m a.s.l. will need another 140 days of similar discharge conditions. After, the phenomenon slows down due to jet diffusion effects. The elevation of **140 m a.s.l.** is considered as a practical limit of ultimate scour depth.

The Dynamic Impulsion model assumes cubic rock blocks with a side length of 2 m. The theoretical critical displacement of one times the height of the block is attained at an elevation of **133 m a.s.l.** This is quite close to the value of 140 found by the CFM model.

Hence, the CFM and DI models are in good agreement with each other and with the EI Method. The two models were calibrated based on available prototype observations of the scour depth and based on the parametric relationship with the EI Method as defined in § 5.2. This allowed to describe and explain the observed in-situ scour depth evolution, as well as to predict further scouring. Both models have determined a physical limit of the ultimate scour depth independently. The results are in good agreement, which is encouraging for future calibration.

Chapter VIII. Conclusions and recommendations

1. Conclusions

This research project investigates the influence of transient water pressures on scour of jointed rock due to high-velocity jet impact and proposes a new method for the evaluation of the development of the ultimate scour depth. The method is physically based and investigates how the water pressures inside the rock joints are capable to propagate the joints and how they eventually pull out the rock blocks from their mass.

Scour of rock is governed by both hydrodynamic and geomechanic aspects. Therefore, any physically plausible description of the phenomenon has to consider both of these aspects, as well as possible interactions between them.

1.1. Hydrodynamic aspects

1.1.1. Experimental modelling of falling jet and pool bottom pressures

An experimental facility of the impacting jet, the plunge pool and the underlying rock fissure has been built at near-prototype scale. It has been found to generate correct turbulence and aeration in the pool as well as realistic transient water pressures inside the underlying joint. The jets are simulated with two types of nozzles and by passing them through various water depths. A first nozzle is cylindrical in shape and reveals to produce jets with a moderate to high turbulence level and a low frequency component. Its turbulent characteristics correspond to prototype jets issuing from pressurized outlet systems, such as intermediate or bottom outlets. A second nozzle is of convergent form and allows generating a more compact jet with a lower turbulence level. This type of jet is representative for prototype jets coming from overflow weirs.

The water depth in the facility influences the amount of air entrained by the jet and the pressure pattern generated by the jet at the bottom of the pool. A first pressure pattern has been obtained for core jet impact. This occurs at water depths less than 4 to 6 times the diameter of the jet at impact in the pool. The pressures are constant with low fluctuations. These fluctuations, however, still have

significant spectral energy at very high frequencies, up to several hundreds of Hz. Moreover, low-frequency turbulences of the jet induce a low-frequency component in the spectrum. These turbulences are found to widen the zone of impact of the jet into the pool and, thus, also the zone at the water-rock interface that is influenced by pressure fluctuations.

A second pressure pattern occurs for developed jet impact, i.e. at water depths larger than 4 to 6 times the diameter of the jet at impact. A turbulent two-phase shear layer defines the corresponding pressures and significant fluctuations are produced. Their spectral content has been found significant at frequencies up to 100 HZ and spectral energy might subsist even at frequencies of 200 Hz.

As a summary, the water pressures that are generated at the pool bottom of the facility are representative for prototype jet impact pressures. This prototype character produces pressures with a wide spectral content, up to several hundreds of Hz.

1.1.2. Experimental modelling of rock joint pressures

The water pressures inside the rock joints are governed by the propagation, superposition and reflection of pressure waves induced at the entrance of the joints. These pressure waves reveal to have a highly transient and cyclic behaviour that is defined as a continuous change between peak pressures and periods of low, near-atmospheric pressure. Peak pressures up to several times the kinetic energy head of the impacting jet (= $V^2/2g$) have been measured, indicating the formation of standing waves and resonance conditions.

The frequency of the cycles is dictated by the presence of free air bubbles inside the joints. Wave celerities down to 60-100 m/s have been measured, corresponding to free air contents of up to 10-20 %. The amount of free air inside the joints continuously changes as a function of time, depending on the governing pressure value. It appears that the corresponding wave celerity-pressure relationships could be entirely described by the ideal gas law and Henry's law. The air is thereby released or dissolved at a quasi-instantaneous rate, which is in contradiction with experimental evidence in pipelines. It is believed that this is due to the particular geometrical and turbulent conditions that govern inside narrow rock joints. Also, the presence of free air makes the transient system highly non-linear and theoretical resonance frequencies are sometimes difficult to distinguish.

By testing differently shaped rock joints, it has been found that sudden changes in orientation of the joint geometry, such as a 90° bend for example, do not significantly alter the transient pressure characteristics or the air content inside. Although, at places in the joints where air could get stuck and form a cavity, the resonance frequencies of the system are different from the theoretical ones.

The values of the peak pressures are found to decrease at air concentrations higher than 10 %. This is probably due to the dampening effect of the air. Air bubbles dissipate a large amount of energy (heat) by subsequent compression and expansion. The more free air, the more this dissipation becomes significant. The author assumes that from on a certain amount of free air, a level of critical damping is obtained, resulting in the disappearance of peak pressures. This has been confirmed by pressure measurements inside a two-dimensional joint, in which both the amount of free air and two-dimensional diffusion effects excluded the appearance of peak pressures.

Based on the experimental tests, it is believed that transient water pressures are essential to the process of break-up of closed-end joints of a rock mass. The two-phase flow mixture inside the joints is sensible to the pressure fluctuations produced by the impacting jet and creates peak pressures that are much higher than what may be predicted based on existing methods and theories.

Furthermore, these transient flow conditions also influence the dynamic uplift forces that can be produced by a jet impacting on a rock block. Although the pressure amplifications inside the joints are less spectacular than for closed-end joints, net uplift pressures of 0.8 to 1.6 times the incoming kinetic energy have been measured. This is significantly higher than any previous assumptions in literature and clearly demonstrates that transient effects have to be accounted for when expressing dynamic uplift of rock blocks.

1.1.3. Numerical modelling of transient pressures in rock joints

A one-dimensional two-phase numerical modelling has been performed of the transient pressures that were measured at the end boundary of a closed-end rock joint. Based on the transient flow equations and on appropriate celerity-pressure relationships, the calculated pressures are in good agreement with the measured ones and thus, the model is representative for prototype water pressures in closed-end joints. However, it is unable to account for thermal dissipation effects at high frequencies and, thus, overestimates the high frequency part of the spectral content of the pressure fluctuations (> 200 Hz).

For closed-end rock joints, appropriate celerity-pressure relationships have been defined. This numerical modelling constitutes an independent confirmation of the theoretical assumptions made on the experimentally measured transient pressures inside the joints.

1.1.4. Conclusions on hydrodynamic aspects

The cyclic behaviour of the transient pressures inside closed-end rock joints makes it particularly interesting to apply them to tensile failure criteria of intermittently jointed rock. This is because these criteria are based on progressive crack propagation by fatigue. For practice, three parameters reveal to be of interest: the maximum possible pressure at the joint end and the amplitude and the frequency of the cycling loading. With these three parameters, both instantaneous and time-dependent propagation of closed-end rock joints can be completely assessed.

1.2. Geomechanic aspects

The geomechanic aspects distinguish between intermittently jointed rock (closed-end joints) and completely jointed rock (open-end joints). They have been derived from available theory.

1.2.1. Failure by progressive break-up of rock joints

For intermittently jointed rock, the resistance of the rock mass against scour has been expressed by a tensile failure criterion, such as the linear elastic fracture mechanics approach. Two types of failure have been distinguished: brittle growth and subcritical growth. The former happens when the stress intensity exceeds the fracture toughness and corresponds to an infinitely fast break-up of the rock mass. The latter occurs when the stress intensity is less than the fracture toughness of the rock mass. The cyclic character of the water pressures has been found particularly convenient for this type of crack growth. Theoretical fatigue laws have been derived from literature data for different types of rock. As such, a time evolution has been added to the scour phenomenon. The processes of brittle and subcritical break-up have been described in a **Comprehensive Fracture Mechanics** (CFM) model. They need an appropriate calibration for practical application.

1.2.2. Failure by dynamic uplift of rock blocks

For completely jointed rock, failure is obtained by dynamic uplift of a rock block that is representative for the jointed rock mass. This rock block can be defined for each vertical layer of the rock mass. The geometry of the block is determined by intersection of the different joint sets in a two-dimensional (x-z) space. This block is subjected to pressure forces that change with time. The forces have been chosen as the immerged weight of the block, the pressure forces over and under the block and the shear forces between the block and its surroundings. The net impulsion, defined as the integral over a certain time period of the net forces on the block, reveals to be of great significance and has been defined in a **Dynamic Impulsion** (DI) model.

Failure has been defined as a critical displacement of the characteristic rock block. For a tightly jointed rock mass, the critical displacement has been determined equal to the height of the characteristic block. For less tightly jointed rock masses, the critical displacement is probably

somewhat lower. It is believed that the critical displacement of a rock block is a model parameter that can be calibrated through model and/or prototype data.

1.2.3. Conclusions on geomechanic aspects

An appropriate theoretical description of a jointed rock mass has made it possible to relate the hydrodynamic loading induced by the impacting jet to the resistance of the rock against this loading. Two failure criteria express whether or not the ultimate scour depth is attained: a fracture mechanics criterion and a dynamic uplift impulsion criterion. The former criterion is able to describe the evolution of the scour formation as a function of time.

1.3. The new scour model

It is believed that the relationship between the air-water pressures and the rock mass resistance allows to express the ultimate scour depth in a physically-based manner.

Therefore, a new scour model is proposed. The model represents a comprehensive assessment of hydrodynamic fracturing of closed-end rock joints and dynamic uplift of so formed rock blocks. Emphasis is given on the physical parameters that are necessary to accurately describe the phenomenon. These parameters are defined such that a practicing engineer can easily handle them. This guarantees the comprehensive character of the model, without neglecting basic physics behind it.

The scour model has firstly been tested on a fictitious rock mass. This pointed out the methodology and the major parameters of interest. Secondly, the scour model has been compared with the Annandale's Erodibility Index (EI) method (1995). This comparison allowed determining the sensibility of the scour model as a function of the main parameters. Finally, the well-known case of rock scour at the Cabora-Bassa dam in Mozambique has been used as a first calibration of some of the model parameters. This calibration allowed the model to simulate the observed scour depth evolution with time as well as to predict future scour hole development.

Hence, these applications confirm the promising nature of the new scour model. Especially for cases where previous scour hole development has been observed and described, the model will be useful to predict future scouring. However, before any engineering use, a calibration phase is needed. This last step towards practical use has been onset during this project but should be further accomplished in the future.

2. Recommendations

The influence of transient water pressures in simplified one-and two-dimensional rock joints on the formation of scour due to high-velocity jet impact has been clearly highlighted. The problem, however, is three-dimensional and involves a complex network of irregularly shaped, partially connected joints. These aspects might have a significant impact on the nature of the pressures inside the rock joints.

Hence, further experimental pressure measurements should be conducted for differently shaped joint configurations. For example, the influence of the width of a joint and of the angle that a joint makes with the jet angle at impact could be of importance. Also, the pressures should be investigated in case of more complicated joint paths, such as small networks composed of several joints that are interconnected.

Furthermore, numerical modelling has only been performed for closed-end I-shaped rock joints, i.e. for the simplest possible geometry. Further research on more complex geometries as well as on the particular two-phase dissipation effects are proposed.

It has been found that the pressures at the joint entrance, i.e. at the water-rock interface, define the water pressures inside the joints. These pressures have been measured and described for a perfectly flat pool bottom. Real pool bottoms are highly irregular and continuously change their shape and irregularities due to scour formation. The exact form influences the turbulent characteristics of the pressures at the interface and should be accounted for. Therefore, experimental tests are proposed.

Moreover, the turbulent characteristics of these pressures are also defined by the turbulence of the jet at impact. This turbulence depends on the trajectory of the jet through the air and on the stability characteristics of the jet. Jets with low-frequency turbulences will generate higher turbulence intensities at impact and thus also higher pressure fluctuations at the water-rock interface. It is believed that low-frequency jet turbulence is an essential parameter in defining the ability of a jet to stimulate an underlying rock joint to resonating pressures.

Notations

The present list of notations is valid throughout the whole work, unless otherwise mentioned explicitly in the text.

Lower case

b_j	jet thickness at impact (rectangular jets)	[m]
c	pressure wave celerity	[m/s]
c_{mean}	mean pressure wave celerity in rock joint	[m/s]
d	rock block size (equivalent cube size)	[m]
d_m, d_{90}	grain sizes	[m]
e_j	joint width	[m]
f	frequency or boundary correction factor	[Hz]
f_{res}	resonance frequency	[Hz]
g	gravitational acceleration	[m/s^2]
h_2	tailwater depth in riverbed downstream of scour hole	[m]
j	number of a joint set	[-]
p	pressure head	[m]
p_m	mean pressure head	[m]
p_{max}	maximum instantaneous fluctuating head	[m]
p_{min}	minimum instantaneous fluctuating head	[m]
q	discharge per unit width	[m^2/s]
r	radial coordinate	[-]
t	time	[sec]
u', v'	root-mean-square value of longitudinal/transversal velocity fluctuations	[m/s]
t_j	jet width at impact (only for rectangular jets)	[m]
x	distance from dam to river downstream	[-]
x_{ult}	longitudinal distance from dam of the ultimate scour depth	[-]
y	lateral direction	[-]
z	vertical direction	[-]
z_{sc}	scour depth below initial bed level	[m]
z_{model}	modelled scour depth below initial bed level	[m]
z_{proto}	prototype scour depth below initial bed level	[m]

Pressure coefficients (s = position)

C_{ps}	$= (p_{mean} - Y)/(\phi V_j^2/2g)$	[-]
C'_{ps}	$= (\sigma)/(\phi V_j^2/2g)$	[-]
C^+_{ps}	$= (p_{max} - p_{mean})/(\phi V_j^2/2g)$	[-]
C^-_{ps}	$= (p_{mean} - p_{min})/(\phi V_j^2/2g)$	[-]
C^{max}_{ps}	$= (p_{max})/(\phi V_j^2/2g)$	[-]
C^{min}_{ps}	$= (p_{min})/($	[-]
$C^{0.1}_{ps}$	= (pressure with a 0.1% probability) / $(\phi V_j^2/2g)$	[-]

Upper case

D_i	jet diameter at issuance from the dam	[m]
D_j	jet diameter at impact in plunge pool	[m]
E_m	Young's modulus of elasticity	[MPa]
Fr	Froude number	[-]
H_j	incoming total pressure head (= $V^2_j/2g$)	[m]
L_b	jet break-up length	[m]
L_c	jet core length	[m]

H	difference between upstream and downstream water level	[m]
L_j	length of joint	[m]
N	number of joint sets	[-]
P_j	persistency of joint (= fissured length/total possible joint length)	[%]
Q_a	air discharge	[m^3/s]
Q_w	water discharge	[m^3/s]
Re	Reynolds number	[-]
RQD	Rock Quality Designate	[-]
S_j	spacing of joints	[m]
$S_{h,p}$	$= (f \cdot Y)/V_i$, plunge pool Strouhal number	[-]
$S_{h,j}$	$= (f \cdot L_j)/c_{mean}$, rock joint Strouhal number	[-]
S_{xx}	power spectral density of pressure fluctuations	[Pa^2/Hz]
T	Uniaxial tensile strength of rock	[MPa]
Tu	longitudinal jet turbulence intensity	[%]
Tv	transversal jet turbulence intensity	[%]
UCS	Uniaxial compressive strength of rock	[MPa]
V_i	mean jet velocity at issuance from the dam	[m/s]
V_j	mean jet velocity at impact in plunge pool	[m/s]
V_{air}	minimum air entrainment velocity	[m/s]
We	Weber number	[-]
Y	$= z_{sc} + h_2$, total plunge pool water depth	[m]

Greek case

α_j	dip angle of joint set	[°]
α_p	air content at point of jet impact in plunge pool	[%]
α_r	air content in rock joint	[%]
β	volumetric air-to-water ratio	[-]
ϕ	coefficient of non-uniform velocity profile	[-]
γ_s	particle or rock specific weight	[N/m^3]
φ	residual friction angle of joint set or plunge pool side wall	[°]
λ	hydraulic friction factor (Darcy-Weisbach)	[-]
θ	jet angle with horizontal at impact in plunge pool	[°]
ρ_a	density of air	[kg/m^3]
ρ_r	density of rock	[kg/m^3]
ρ_w	density of water	[kg/m^3]
σ	standard deviation of pressure fluctuations (root-mean-square)	[m]
ω	mean particle fall velocity	[m/s]
Λ	reflection factor	[-]

Bibliography

Abou-Sayed, A.S.; **Brechtel**, C.E. (1978): In Situ stress determination by hydrofracturing: a fracture mechanics approach, *Journal of Geophysical Research*, Vol. 83, N°B6, pp. 2851-2862.

Abramovich, G.N. (1963): The Theory of Turbulent Jets, *The MIT Press*, US.

Al-Shayea, N.A.; **Khan**, K.; **Abduljauwad**, S.N. (2000): Effects of confining pressure and temperature on mixed-mode (I-II) fracture toughness of a limestone rock, *International Journal of Rock Mechanics and Mining Sciences*, Vol. 37, pp. 629-643.

Akram, M.; **Karfakis**, M. (1991): Rock fracture toughness and fracture energy in aqueous chemical environments, *Proceedings of the 28th US Symposium on Rock Mechanics*, Balkema ed., Rotterdam, pp. 211-230.

Albertson, M.L.; **Dai**, Y.B.; **Jenson**, R.A.; **Rouse**, H. (1950): Diffusion of Submerged Jets, *Proceedings A.S.C.E, Vol. 74*.

Allievi, L. (1903): Teoria Generale del moto perturbato dell'acqua nei tubi in pressione, Annali della societa degli ingegneri ed architetti italiani, Milan.

Altinbilek, H.D.; **Okyay**, S. (1973): Localized scour in a horizontal sand bed under vertical jets, Proceedings of the 15th IAHR Congress, Istanbul, Turkey, pp. 99-106.

Andreev, G.E. (1995): Brittle Failure of Rock Materials, *Balkema*, Rotterdam, Brookfield.

Annandale, G. W. (1995): Erodibility, *Journal of Hydraulic Research*, IAHR, Vol. 33, N°4, pp. 471-494.

Annandale, G.W.; **Wittler**, R.J.; **Ruff**, J.; **Lewis**, T.M. (1998): Prototype validation of erodibility index for scour in fractured rock media, *Proceedings of the 1998 International Water Resources Engineering Conference*, Memphis, Tennessee, United States.

Apted, R.W.; **Novak**, P. (1973): Oxygen uptake of weirs, *Proceedings of the 15th IAHR Congress*, paper B23, Vol. 2, Istanbul, Turkey.

Armengou, J. (1991): Disipacion de energia hidraulica a pie de presa en presas boveda, *PhD thesis*, Universitat Politechnica de Catalunya, Barcelona.

Arndt, R.E.A.; **Ippen**, A.T. (1970): Turbulence measurements in liquids using an improved total pressure probe, *Journal of Hydraulic Research*, IAHR, Vol. 8, N° 2, pp. 131-157.

Atkins, P.W.; **Beran**, J.A. (1992): General chemistry, Second ed., *Scientific American Books,* New York.

Atkinson, B.K. (1979): *Pure Appl. Geophysics*, Vol. 117, pp. 1011-1024.

Atkinson, B.K. (1982): *Journal of Structural Geology*, Vol. 4, pp. 41-56.

Atkinson, B.K. (1984): Subcritical crack growth in geological materials, *Journal of Geophysical Research*, Vol. 89, N°B6, pp. 4077-4114.

Atkinson, B.K. (1987): Fracture Mechanics of Rock, *Academic Press Inc.*, London.

Atkinson, B.K.; **Rawlings**, R.D. (1981): In: *Earthquake Prediction, An International Review*, Maurice Ewing Ser., Vol. 4, Eds. D.W. Simpson and P. G. Richards, American Geophysical Union, Washington, DC, pp. 605-616.

Ballio, F.; **Franzetti**, S.; **Tanda**, M.G. (1994): Pressure fluctuations induced by turbulent circular jets impinging on a flat plate, *Excerpta*, Vol. 7.

Barker, L. M. (1977): A simplified method for measuring plane strain fracture toughness, *Engineering Fracture Mechanics*, Vol. 9, pp. 361-369.

Baron, T. (1949): *Technical Report*, University of Illinois, N° 4.

Bearman, P.W. (1972): An investigation of the forces on flat plates normal to a turbulent flow, *Journal of Fluid Mechanics*, Vol. 46, pp. 177-198.

Bellin, A.; **Fiorotto**, V. (1995): Direct dynamic force measurement on slabs in spillway stilling basins, *Journal of Hydraulic Engineering*, ASCE, Vol. 121, N° HY 10, pp. 686-693.

Beltaos, S.; **Rajaratnam**, N. (1973): Plane turbulent impinging jets, *Journal of Hydraulic Research*, IAHR, Vol. 11, N° 1, pp. 29-59.

Beltaos, S.; **Rajaratnam**, N. (1974): Impinging circular turbulent jets, *Journal of the Hydraulics Division*, ASCE, Vol. 100, N° HY10, pp. 1313-1328.

Beltaos, S. (1976): Oblique impingement of circular turbulent jets, *Journal of Hydraulic Research*, IAHR, Vol. 14, N° 1, pp. 17-36.

Bendat, J.S.; **Piersol**, A.G. (1980) : Engineering Applications of Correlation and Spectral Analysis, *J. Whiley & Sons Ltd.*, US.

Bin, A.K. (1984): Air entrainment by plunging liquid jets, *IAHR Symposium on Scale Effects in Modeling Hydraulic Structures*, Esslingen.

Bohrer, J.G. (1996): Plunge pool velocity prediction of jets formed by overtopping steep dams, MsC Thesis, *Colorado State University*, United States.

Bohrer, J.G.; **Abt**, S.R.; **Wittler**, R.J. (1998): Predicting plunge pool velocity decay of free falling, rectangular jet, *Journal of Hydraulic Engineering*, ASCE, Vol. 124, N° 10, pp. 1043-1048.

Bollaert, E. (2001): Spectral density modulation of plunge pool bottom pressures inside rock fissures, *Proceedings of the XXIXth IAHR Congress*, Student Paper Competition, Beijing.

Bollaert, E., **Schleiss**, A. (2001a): Air bubble effects on transient water pressures in rock fissures due to high velocity jet impact, *Proceedings of the XXIXth IAHR Congress*, Beijing.

Bollaert, E., **Schleiss**, A. (2001b): A new approach for better assessment of rock scouring due to high velocity jets at dam spillways, *Proceedings of the 5th ICOLD European Symposium*, Geiranger, Norway.

Bollaert, E., **Pirotton**, M, **Schleiss**, A. (2001c): Multiphase transient flow and pressures in rock joints due to high velocity jet impact: an experimental and numerical approach, *Proceedings of the 3rd International Symposium on Environmental Hydraulics*, Arizona State University, Tempe.

Bollaert, E., **Schleiss**, A. (2001d): Discussion of: Simulation of Scour process in Plunging Pool of Loose Bed-Material, Jia et al. (2001), Vol. 127, N°3, pp. 219-229. *Accepted for publication in the Journal of Hydraulic Engineering*, ASCE, United States.

Bollaert, E., **Schleiss**, A. (2001e): Scour of rock due to high velocity plunging jets: Part I: a state-of-the-art review, *submitted to the Journal of Hydraulic Research*, IAHR, Delft, The Netherlands.

Bollaert, E., **Schleiss**, A. (2001f): Scour of rock due to high velocity plunging jets: Part II: Experimental results of dynamic pressures at pool bottoms and in one-and two-dimensional closed-end rock joints, *submitted to the Journal of Hydraulic Research*, IAHR, Delft, The Netherlands.

Bollaert, E., **Falvey**, H.T., **Schleiss**, A. (2002b): Turbulent jet impingement in plunge pools: the particular characteristics of a near-prototype physical model study, *submitted to Riverflow 2002*, Louvain-la-Neuve, Belgium.

Bonetto, F.; **Lahey**, R.T. Jr. (1993): An experimental study on air carryunder due to a plunging liquid jet, International Journal of Multiphase Flow, Vol. 19, N° 2, pp. 281-294.

Bormann. E. (1988): Physical model of local scour at grade-control structures, *Proceedings of the ASCE National Conference on Hydraulic Engineering*, ASCE, pp. 1129-1134.

Bormann, E.; **Julien**, P.Y. (1991): Scour downstream of grade-control structures, *Journal of Hydraulic Engineering*, ASCE, Vol. 117, N° 5, pp. 579-594.

Bowers, C.E.; **Tsai**, F.Y. (1969): Fluctuating pressures in spillway stilling basins, *Journal of Hydraulics Division*, ASCE, Vol. 95, N° 6, pp. 2071-2079.

Breusers, H. N. C. (1963): Discussion of "Sediment transport mechanics: erosion of sediment, Journal of the Hydraulics Division, ASCE, Vol. 89, N° HY1.

Breusers, H. N. C. (1967): Time scale of two-dimensional local scour, *Proceedings of the 12th IAHR Congress*, Fort Collins.

Breusers, H. N. C.; **Raudkivi**, A. J. (1991): Scouring, *IAHR Vol. 2, Hydraulic Structures Design Manual*, Balkema, Rotterdam.

Burdine, N.T. (1963): Rock failure under dynamic loading conditions, *Soc. Petrol. Eng. J.*, pp. 1-8.

Burgi, P.H: (1988): Model-Prototype Correlation of Hydraulic Structures, *Proceedings of the International Symposium*, ASCE, New York.

Cain, P.; **Wood**, I.R. (1981): Instrumentation for aerated flow on spillways, *Journal of the Hydraulics Division*, ASCE, Vol. 107, N° HY11, pp. 1407-1424.

Carpinteri, A. (1982): *Journal of Structural Division*, ASCE, Vol. 108, ST4, pp. 833-848.

Chanson, H. (1996): Air bubble entrainment in free surface turbulent shear flows, *Academic Press*, London.

Charlton, J.A. (1970): The air control of self priming siphon spillways, PhD thesis, King's College, London.

Chaudry, M. H. (1979): Applied Hydraulic Transients, *Van Nostrand Reinhold Company*.

Chee, S.P.; **Kung**, T. (1971): Stable profiles of plunge basins, *Journal of the American Water Resources Association*, Vol. 7, N° 2, pp. 303-308.

Chee, S.P.; **Strelchuk**, D.L.; **Kung**, T. (1972): Configurations of water basin for energy dissipation, *Proceedings of the 86th Annual Congress of Engineering Institute of Canada*, Saskatoon.

Chee, S.P.; **Yuen**, E.M. (1985): Erosion of unconsolidated gravel beds, *Canadian Journal of Civil Engineering*, Vol. 12, pp. 559-566.

Chong, K.P.; **Kuruppu**, M.D.; **Kuszmaul**, J.S. (1987): Fracture toughness determination of rocks with core-based specimens, *SEM/RILEM Int. Conference on Fracture of Concrete and Rock*, Houston, Texas, S.P. Shah & S.E. Schwartz eds., pp. 9-15.

Clifton, R.J.; **Simonson**, E.R.; **Jones**, A.H.; **Green**, S.J. (1976): Determination of the critical stress intensity factor K_{Ic} in a circular ring, *Exp. Mech.*, Vol. 16, pp. 233-238.

Cola, R. (1965): Energy dissipation of a high-velocity vertical jet entering a basin, *Proceedings of the 11th Congress of the I.A.H.R.*, Leningrad.

Costin, L.S. ; **Holcomb**, D.J. (1981) : Time-dependent failure of rock under cyclic loading, *Tectonophysics*, Vol. 79, pp. 279-296.

Costin, L.S. ; **Mecholsky**, J.J. (1983) : *Proceedings of the 24th US Symp. on Rock Mechanics*, pp. 385-394.

Cummings, P.D. ; **Chanson**, H. (1997) : Air entrainment in the developing region of plunging jets ; part 1 and aprt 2, *ASME Journal of Fluids Engineering*, Vol. 119, pp. 597-608.

Cunha, L.V.; **Lencastre**, A.C. (1966): La dissipation de l'énergie dans un évacuateur en saut de ski, observation de l'érosion, *L.N.E.C. Publication N°288*, Lisboa, & *Proceedings of the 11th Congress of IAHR*, Leningrad 1965.

Dauskardt, R.H.; **Yu**, W.; **Ritchie**, R.O. (1987): Fatigue crack propagation in transformation-toughned ceramic, *Journal of Am. Ceram. Society*, Vol. 70, pp. 248-252.

Davies, J.T. (1972): Turbulence Phenomena, *Academic Press*, New York and London.

Der, V.; **Holloway**, D.C.; **Kobayashi**, T. (1978): Techniques for dynamic fracture toughness measurements, *Report to US Nat. Sc. Found. from Photomech. Lab., Mech. Eng. Dept.*, University of Maryland, College Park, Maryland.

De Vries, F.; **Volkart**, P.U. (1988): Field measurements of pressure fluctuations in a high head bottom outlet structure, Conference Proceedings, *Model-Prototype Correlation of Hydraulic Structures, P. Burgi*, pp. 199 – 209.

Doddiah, D. (1949): Comparison of scour caused by hollow and solid jets of water, *unpublished Master's thesis, Colorado A & M College*, 156 pages.

Doddiah, D.; **Albertson**, M.L.; **Thomas**, R. (1953): Scour from jets, *Proc. Minnesota International Hydraulics Conference.*

Eissa, A.; **Kazi** (1988): Relation between static and dynamic Young's moduli of rocks, *International Journal of Rock Mechanics and Mining Sciences*, Vol. 25, N°6, pp. 479-482.

Elder, R.A. (1961): Model-prototype turbulence scaling, Proceedings of the 9th IAHR Congress, Dubrovnik, pp. 24-31.

Erpicum, S. (2001): Application des algorithms génétiques aux problèmes d'optimisation en hydrodynamique de surface, HACH, *Université de Liège*, Belgique.

Ervine, D.A. (1976): The entrainment of air in water, *Water Power and Dam Construction*, 28(12), pp. 27-30.

Ervine, D.A. (1998): Air entrainment in hydraulic structures: a review, *Proceedings of the Institution of Civil Engineers Wat., Marit. & Energy*, Vol. 130, pp. 142-153.

Ervine, D.A.; **Elsawy**, E.M. (1975): The effect of a falling nappe on river aeration, *Proceedings of the 16th IAHR Congress*, Vol. 3, Paper CAS, pp. 390-398.

Ervine, D.A.; **Falvey**, H.R. (1987): Behavior of turbulent jets in the atmosphere and in plunge pools, *Proceedings of the Institution of Civil Engineers*, Part 2, Vol. 83, pp. 295-314.

Ervine, D.A.; **Falvey**, H.R. (1988): Aeration in jets and high velocity flows, Conference Proceedings, *Model-Proto Correlation of Hydraulic Structures, P. Burgi*, 1988, pp. 22-55.

Ervine, D.A.; **Falvey**, H.R.; **Withers**, W. (1997): Pressure fluctuations on plunge pool floors, *Journal of Hydraulic Research*, IAHR, Vol. 35, N°2.

Ervine, D.A.; **McKeogh**, E.; **Elsawy**, E.M. (1980): Effect of turbulence intensity on the rate of air entrainment by plunging water jets, *Proceedings of the Inst. Civ. Eng*., Part 2, pp. 425-445.

Evans, A.G.; **Fuller**, E.R. (1974): Crack propagation in ceramic materials under cyclic loading conditions, *Metall. Transactions*, Vol. 5, pp. 27-28.

Ewalds, H.L.; **Wanhill**, R.J.H. (1986): Fracture Mechanics, *Delftse Uitgevers Maatschappij*, The Netherlands.

Ewing, D.J.F. (1980): Allowing for free air in waterhammer analysis, *Proceedings of the 3rd International Conference on Pressure Surges*, Canterbury, England.

Fahlbusch, F. E. (1994): Scour in rock riverbeds downstream of large dams, *Hydropower & Dams*, pp. 30-32.

Falvey, H.T.; **Ervine**, D.A. (1988): Aeration in jets and high velocity flows, *Proceedings of Model-prototype Correlation of Hydraulic Structures,* Colorado.

Farhoudi, J.; **Narayanan**, R. (1991): Force on slab beneath hydraulic jump, *Journal of Hydraulic Engineering*, ASCE, Vol. 117, N° 1, pp. 64 – 82.

Fiorotto, V.; **Rinaldo**, A. (1992a): Fluctuating uplift and lining design in spillway stilling basins, *Journal of Hydraulic Engineering*, ASCE, Vol. 118, HY4.

Fiorotto, V.; **Rinaldo**, A. (1992b): Turbulent pressure fluctuations under hydraulic jumps, *Journal of Hydraulic Research*, IAHR, Vol. 30, N° 4.

Fiorotto, V.; **Salandin**, P. (2000): Design of anchored slabs in spillway stilling basins, *Journal of Hydraulic Engineering*, ASCE, Vol. 126, N° 7, pp. 502-512.

Franzetti, S.; **Tanda**, M.G. (1984): Getti deviati a simmetria assiale, *Report of Istituto di Idraulica e Costruzioni Idrauliche*, Politecnico di Milano.

Franzetti, S.; **Tanda**, M.G. (1987): Analysis of turbulent pressure fluctuation caused by a circular impinging jet, *International Symposium on New Technology in Model Testing in Hydraulic Research*, India, pp. 85-91.

Gameson, A.L.H. (1957): Weir and aeration of rivers, Journal I.W.E., Vol. 11, p. 447-490.

Gameson, A.L.H.; **Vandyke**, K.G.; **Ogden**, C.G. (1958): The effect of temperature on aeration at weirs, Water and mar. Engineering, Vol. 62.

Gerodetti, M. (1982): Auskolkung eines felsigen Flussbettes (Modellversuche mit bindigen Materialen zur Simulation des Felsens). Arbeitsheft N° 5, VAW, ETHZ, Zürich.

Goodman, R.E. (1980): Introduction to Rock Mechanics, *J. Wiley & Sons Ltd*., US.

Grady, D.E.; **Kipp**, M.E.; **Smith**, C.S. (1980): Explosive fracture studies on oil shale, *Soc. of Petroleum Engineers Journa*l, pp. 349-356.

Grenet, L. (1899): *Bulletin Soc. Eng. Industr. Nat. Paris*, Series 5, Vol. 4, pp. 838-848.

Griffith, A.A. (1921): The phenomenon of rupture and flow in solids, *Phil. Trans. R. Soc. London*, Series A, Vl. 221, pp. 163-198.

Gunko, F.G. (1967): Macroturbulence of flows below spillways of medium head dams and their protection against undermining, *Proceedings of the 12th Congress of the I.A.H.R.,* Fort Collins, United States.

Gunko, F.G. ; **Burkov**, A.F :; **Isachenko**, N.B. ; **Rubinstein**, G.L. ; **Soloviova**, A.G. ; **Yuditskii**, G.A. (1965): Research on the Hydraulic Regime and Local Scour of River Bed Below Spillways of High-Head Dams, *11th Congress of the I.A.H.R., Leningrad*.

Haimson, B.; **Fairhurst**, C. (1969): In-Situ Stress Determination at Great Depth by means of Hydraulic Fracturing, *Proceedings of the 11th US Symposium on Rock Mechanics*, Berkeley, California, US.

Haimson, B.C.; **Kim**, C.M. (1971): Mechanical behavior of rock under cyclic fatigue, *Proceedings of the 13th Symposium on Rock Mechanics,* pp. 845-863.

Haimson, B.C.; **Zhao**, Z. (1991): Effect of Borehole Size and Pressurization Rate on Hydraulic Fracturing Breakdown Pressure, *Proceedings of the 28th US Symposium on Rock Mechanics*, Balkema, Rotterdam, pp. 191-199.

Halliwell, A.R. (1963): Velocity of a waterhammer wave in an elastic pipe, Journal of the Hydraulics Division, ASCE, Vol. 89, N° HY4, pp. 1-21.

Hardy, H.R.; **Chugh**, Y.P. (1970): Failure of geologic materials under low cycle fatigue, *Proceedings of the 6th Canadian Symposium on Rock Mechanics*, pp. 14-25.

Hartung, F.; **Hausler**, E. (1973): Scours, stilling basins and downstream protection under free overfall jets at dams, *Proceedings of the 11th Congress on Large Dams,* Madrid, pp.39-56.

Hillerborg, A.; **Modeer**, M.; **Peterson**, P.-E. (1976): Cement and Concrete Research, Vol. 6, pp. 773-782.

Hinze, J.O. (1959): Turbulence, *McGraw-Hill Inc.*, US.

Hoagland, R.G.; **Hahn**, G.T.; **Rosenfield**, A.R. (1973): *Rock Mechanics*, Vol. 5, pp. 77-106.

Hoffmans, G.J.C.M. (1994a): Scour due to plunging jets, Report W-DWW-94-302, Ministry of Transport, Public Works and Water Management, Road and Hydraulic Engineering Division, Delft.

Hoffmans, G.J.C.M. (1994b): Scour due to submerged jets, Report W-DWW-94-302, Ministry of Transport, Public Works and Water Management, Road and Hydraulic Engineering Division, Delft.

Hoffmans, G.J.C.M. (1998): Jet scour in equilibrium phase, *Journal of Hydraulic Engineering*, ASCE, Vol. 124, N°4, pp. 430-437.

Hoffmans, G.J.C.M.; **Verheij**, H.J. (1997): Scour Manual, *Balkema ed.*, Rotterdam.

Homma, M. (1953): An experimental study on water fall. *Proceedings of the Minnesota International Hydraulics Conference,* United States.

Horeni, P. (1956): Disintegration of a free jet of water in air, Byzkumny ustav vodohospodarsky prace a studie, Sesit 93, Praha.

Huang, Jian-An; **Wang**, S. (1985): An experimental investigation concerning the comprehensive fracture toughness of some brittle rocks, *International Journal of Rock Mechanics and Mining Sciences*, Vol. 22, N°2, pp. 99-104.

Hubbert, M.K.; **Willis**, D.G. (1957): Mechanics of hydraulic fracturing, *Transactions AIME*, Vol. 210, pp. 153-162.

Huot, J.P.; **Rey**, C.; **Arbey**, H. (1986): Experimental analysis of the pressure field induced on a square cylinder by a turbulent flow, *Journal of Fluid Mechanics*, Vol. 162, pp. 283-298.

Ingraffea, A.R. (1981): *Proceedings of the 22nd US Symp. On Rock Mechanics*, Cambridge, pp. 186-191.

Irwin, G.R. (1957): Analysis of stresses and strains near the end of a crack traversing a plate, *ASME Applied Mechanics Division*, N° 57, pp. 361-364.

Jaeger, C. (1977): Fluid Transients, *Blackie & Son Limited*, Glasgow.

Jaeger, J.C.; **Cook**, N.G.W.W. (1979): Fundamentals of Rock Mechanics, *Chapman and Hall*, London.

Jarvis, P.J. (1970): A study in the mechanics of aeration at weirs, MSc thesis, University of Newcastle upon Tyne, England.

Jenkner, W.R. (1971): Über die Druckstossgeschwindigkeit in Rohrleitungen mit quadratischen und rechteckigen Querschnitten, *Schweizerische Bauzeitung*, Vol. 89, pp. 99-103.

Jia, Y.; **Kitamura**, T.; **Wang**, S. (2001): Simulation of scour process in plunging pool of loose bed-mateial, *Journal of Hydraulic Engineering*, ASCE, Vol. 127, N°3, pp. 219-229.

Johnson, G. (1967): The effect of entrained air in the scouring capacity of water jets, *Proceedings of the 12th Congress of the I.A.H.R.,* Vol. 3, Fort Collins.

Johnson, G. (1977): Use of a weakly cohesive material for scale model scour tests in flood spillway design, *Proceedings of the 17th Congress of the I.A.H.R.,* Vol. 4, Baden-Baden.

Kalinske, A.A.; **Robertson**, J.M. (1943): Closed-conduit flow entrainment of air in flowing water, Transactions of the ASCE, Vol. 108, pp. 1435-1516.

Kim, K.; **Mubeen**, A. (1980): Relationship between differential stress intensity factor and crack growth rate in cyclic tension in Westerley granite, *Proceedings of the ASTM Symposium on Fracture Mechanics Methods in Ceramics, Rocks and Concrete*, Chicago.

King, D.L. (1967): Analysis of random pressure fluctuations in stilling basins, *Proceedings of the 12th IAHR Congress*, Fort Collins, United States.

Kirschke, D. (1974): Druckstossvorgänge in wassergefüllten Felsklüften, Veröffentlichungen des Inst. Für Boden und Felsmechanik, *Univ. Karlsruhe*, Heft 61.

Kobus, H.; **Leister**, P.; **Westrich**, B. (1979): Flowfield and scouring effects of steady and pulsating jets impinging on a moveable bed, *Journal of Hydraulic Research, Vol. 17, N° 3*, pp. 175-192.

Kolmogorov, A.N. (1941): C.R. Aced. Sciences, USSR, Vol. 30, p. 301.

Kraichnan, R.H. (1974): On Kolmogorov's inertial-range theories, Journal of Fluid Mechanics, Vol. 62, Part 2, pp. 305-330.

Kraichnan, R.H. (1975): Statistical dynamics of two-dimensional flow, Journal of Fluid Mechanics, Vol. 67, Part 1, pp. 155-175.

Lelliavsky, S. (1955): An introduction to fluvial hydraulics, *Constable & Co. Ltd.*, London, England.

Lencastre, A. (1961): Descarregadores de lamina livre: bases para o seu estudo e dimensionamento, *Laboratorio Nacional de Engenharia Civil*, Memoria N° 174, Lisboa.

Lesleighter, E.J. (1988) : Cavitation in hydraulic structures, *Proceedings of the International Symposium on Model-Prototype Correlation of Hydraulic Structures*, edited by P. Burgi, Colorado, United States.

Levy, J.J. (1961): Effet dynamique d'un courant à haute turbulence sur les ouvrages hydrauliques et sur le lit des rivières, *Proceedings of the 9th IAHR Congress, Dubrovnik*, pp. 133-140.

Lewis, T.M. (1996): Prediction of velocities within jets formed by overtopping steep dams, MsC Thesis, *Colorado State University*, United States.

Lin, T.J.; **Donnelly**, H.G. (1966): Gas bubble entrainment by plunging laminar liquid jets, *Associate Institute of Chemical Engineers Journal*, Vol. 12, N° 3.

Liu, P.Q. (1999): Mechanism of energy dissipation and hydraulic design for plunge pools downstream of large dams, *China Institute of Water Resources and Hydropower Research*, Beijing, China.

Liu, Da'an; **Wang**, S.; **Li**, L. (2000): Investigation of fracture behavior during rock mass failure, *International Journal of Rock Mechanics and Mining Sciences*, Vol. 37, pp. 489-497.

Liu, P.Q.; **Dong**, J.R.; **Yu**, C. (1998): Experimental investigation of fluctuating uplift on rock blocks at the bottom of the scour pool downstream of Three-Gorges spillway, *Journal of Hydraulic Research*, IAHR, Vol. 36, N°1, pp. 55-68.

Lopardo, R.A. (1988): Stilling basin pressure fluctuations, Conference Proceedings, *Model-Prototype Correlation of Hydraulic Structures,* P. Burgi, pp. 56 – 73.

Lopardo, R.A. ; **Lio**, F.C. ; **Vernet**, G.F. (1984) : Model-prototype comparisons on pressure fluctuations in hydraulic jump energy dissipators, *Proceedings of the Symp. On Scale Effects in Modelling of Hydraulic Structures*, IAHR, Esslingen, Germany, paper 5.7.

Lopardo, R.A. et al. (1988): Prototype Instrumentation for Pressure Fluctuations, Conference Proceedings, *Model-Prototype Correlation of Hydraulic Structures,* P. Burgi, pp. 267–275.

Machado, L.I. (1982): O Sistema de Dissipacao de Energia Proposto para a Barragem de Xingo, *Transactions of the International Symposium on the Layout of Dams in Narrow Gorges*, ICOLD, Brazil.

Martin, C.S.; **Padmanabhan**, M. (1979): Pressure pulse propagation in two-component slug flow, *Journal of Fluids Engineering*, Vol. 101, pp. 44-52.

Martins, R. (1973): Contribution to the knowledge on the scour action of free jets on rocky river beds, *Proceedings of the 11th Congress on Large Dams,* Madrid, pp. 799-814.

Mason, P. J. (1989): Effects of air entrainment on plunge pool scour. *Journal of Hydraulic Engineering*, ASCE, Vol. 115, N° 3, pp. 385-399.

Mason, P. J.; **Arumugam**, K. (1985): Free jet scour below dams and flip buckets, *Journal of Hydraulic Engineering*, ASCE, Vol. 111, N° 2, pp. 220-235.

Mason, P.J. (1983): Energy dissipating crest splitters for concrete dams, *Water Power and Dam Construction*, pp. 37-40.

May, R.W.P.; **Willoughby**, I.R. (1991): Impact pressures in plunge pool basins due to vertical falling jets, *Report SR 242*, HR Wallingford, UK.

McKeogh, E. (1978): A study of air entrainment using plunging water jets, PhD Thesis, *Queens University Belfast*, Ireland.

McKeogh, E.J.; **Elsawy**, E.M. (1980): Air retained in pool by plunging water jet, *Journal of the Hydraulics Division*, Vol. 106, N°10, pp. 1577 – 1593.

Meredith, P.G. (1983): PhD thesis, University of London.

Meredith, P.G.; **Atkinson**, B.K. (1985): *Phys. Earth Planet. Int*., Vol. 39, pp. 33-51.

Mih, W.C.; **Kabir**, J. (1983): Impingement of water jets on nonuniform streambed, Journal of Hydraulic Engineering, ASCE, Vol. 109, N° 4, pp. 536-548.

Mirtskhulava, T.E.; **Dolidze**, I.V.; **Magomeda**, A.V. (1967): Mechanism and computation of local and general scour in non cohesive, cohesive soils and rock beds, *Proceedings of the 12th IAHR Congress*, Vol. 3, Fort Collins, pp. 169-176.

Montgomery, R.A. (1984): Investigations into rock erosion by high velocity water flows, *Hydraulics Laboratory Stockholm*.

Müller, W.; **Rummel**, F. (1986): Fracture toughness of granites, special issue: the Falkenberg geothermal project, *BGR*, Hannover.

Otto, B. (1989): Scour potential of highly stressed sheet-jointed rocks under obliquely impinging plane jets, PhD thesis, James Cook University of North Queensland, Townsville.

Ouchterlony, F. (1980): A new core specimen for the fracture toughness testing of rocks, *Swedish Detonic Research Foundation Rep.,* DS, P10, Stockholm, Sweden.

Ouchterlony, F. (1988): Suggested methods for determining the fracture toughness of rock, *ISRM: Fracture Toughness Suggested Methods*, pp. 73-96.

Pan, S.; **Shao**, Y. (1984): Scale effects in modeling air demand by a ramp slot, IAHR Symposium on scale effects in modeling hydraulic structures, Esslingen Germany, Paper 4.7.

Paris, P.C.; **Gomez**, M.P.; **Anderson**, W.E. (1961): *Trend Engineering*, Vol. 13, pp. 9-14.

Paris, P.C.; **Sih**, G.C. (1965): Stress analysis of cracks, *Fracture toughness Testing and its Applications*, ASTM STP 381, Philadelphia, pp. 63-77.

Pearsall, I.S. (1966): The velocity of waterhammer waves, *Proceedings of the Symposium on surges in pipelines*, Inst. Mech. Eng. 180, 3E, pp. 12-20.

Pinto, N.; **Neidert**, S.H. (1982): Model-prototype conformity in aerated spillway flow, BHRA, International Conference on Hydraulic Modelling, Coventry, England, Paper E6, pp. 273-284.

Plona, T.J.; **Cook**, J.M. (1995): Effects of stress cycles on static and dynamic Young's moduli in Castlegate Sandstone, *Proceedings of the 31st US Symposium on Rock Mechanics*, Balkema ed., Rotterdam.

Poreh, M.; **Hefez**, E. (1967): Initial scour and sediment motion due to an impinging submerged jet, *Proceedings of the 12th IAHR Congress*, Fort Collins.

Puertas, J.; **Dolz**, J. (1994): Criterios hidraulicos para el diseno de cuencos de disipacion de energia en presas boveda con vertido libre por coronacion, *PhD thesis*, University of Catalunya, Barcelona, Spain.

Quintela, A.C.; **Da Cruz**, A.A. (1982): Cabora-Bassa dam spillway, conception, hydraulic model studies and prototype behaviour, *Transactions of the International Symposium on the Layout of Dams in Narrow Gorges*, ICOLD, Brazil.

Rajaratnam, N. (1976): Turbulent Jets, *Elsevier*, New York.

Rajaratnam, N. (1981): Erosion by plane water jets, *Journal of Hydraulic Research*, Vol. 19, N° 4, pp. 339-358.

Ramos, C.M. (1979): Statistical characteristics of the pressure field of crossed flows in energy dissipation structures, *Proceedings of the 11th ICOLD Congress*, Q.41, R.3, Madrid, pp. 39-56.

Ramos, C.M. (1982): Energy dissipation on free jet spillways. Bases for its study in hydraulic models, *Transactions of the International Symposium on the Layout of Dams in Narrow Gorges,* ICOLD, Rio de Janeiro, Brazil, Vol. 1, pp. 263-268.

Reece, M.J.; **Guiu**, F.; **Sammur**, M.F.R. (1989): Cyclic fatigue crack propagation in alumina under direct tension-compression loading, *J. Am. Ceram. Society*, Vol. 72, pp. 348-352.

Reeve, L. N. (1932): Erosion below Conowingo Dam proves value of model tests, *Engineering News-Record vol. 108*, pp. 127-130.

Reichardt, H. (1941): Zum angew. Mathematik Und Mechanik, Vol. 21, p. 257.

Reinius, E. (1986): Rock erosion, *Water Power and Dam Construction 38(6),* pp.43-48.

Reynolds, A.J. (1974): Turbulent Flows in Engineering, *J. Wiley & Sons Limited*, London.

Resch, F.J.; **Leutheusser**, H.J. (1971): Mesures de turbulence dans le ressaut hydraulique, *La Houille Blanche, 4*, pp. 17-31.

Ribeiro, A.A. (1975): The macroturbulence downstream a stilling basin. Erosion (Scouring), *Proceedings of the 16th Congress of the I.A.H.R.* Vol. 5, Sao Paulo, Brazil.

Roegiers, J.; **Zhao**, X.L. (1991): Rock fracture tests in simulated downhole conditions, *Proceedings of the 28th US Symposium on Rock Mechanics,* Balkema, Rotterdam.

Rotta, J.C. (1972): Turbulente Strömungen, B.G. Teubner: Stuttgart.

Rouse, H. (1940): Criteria for similarity in the transportation of sediment, *Proceedings of the First Hydraulic Conference*, University of Iowa, Iowa City, IA, Bulletin 20, pp. 33-49.

Rouse, H.; **Sio**, T.T.; **Nagaratnam**, S. (1959): Turbulence characteristics of the hydraulic jump, *Translation ASCE*, 124, pp. 926-950.

Rubinstein, G.L. (1963): Laboratory investigation of local erosion on channel beds below high overflow dams, *Transactions of Coordination Conferences on Hydraulic Engineering. Iss. VII*, Conference on Hydraulics of High Head Water Discharge Structures. Gosenergoizdat M.L.

Rummel, F.; **Winter**, R.B. (1983): *Journal of Earthquake Prediction Research*, Vol. 2, pp. 33-45.

Schmidt, R.A. (1980): *Proceedings of the 21st US Nat. Symp. Rock. Mech.*, University of Missouri, pp. 581-590.

Schmidt, R.A.; **Huddle**, C.W. (1977): Effect of confining pressure on fracture toughness of Indiana Limestone, *International Journal of Rock Mechanics and Mining Sciences,* Vol. 14, pp. 289-293.

Schoklitsch, A. (1932): Kolkbildung unter Ueberfallstrahlen. *Wasserwirtschaft.*

Schoklitsch, A. (1951): Berechnung der Kolktiefen flussabwärts eines Stauwerkes., *Wasser-und Energiewirtschaft N°2.*

Scholz, C.H.; **Koczynski**, T.A. (1979): Dilatancy Anisotropy and the Response of Rock to Large Cyclic Loads, *Journal of Geophysical Research*, N°B10, pp. 5525-5534.

Schweitzer, P.H.; **Szebehely**, V.G. (1950): Gas evolution in liquids and cavitation, *Journal of Applied Physics*, Vol. 21, pp. 1218-1224.

Sene, K.J. (1988): Air entrainment by plunging jets, *Chemical Engineering Science*, Vol. 43, N° 10, pp. 2615-2623.

Sene, K.J.; **Hunt**, J.C.R.; **Thomas**, N.H. (1994): The role of coherent structures in bubble transport by turbulent shear flows, *Journal of Fluid Mechanics*, Vol. 259, pp. 219-240.

Sih, G.C. (1980) : Naval Research Review, Vol. 32, 3.

Simons, D.B. ; **Stevens**, M.A. (1971) : Scour control in rock basins at culvert outlets, *in River Mechanics*, Vol. II, edited by H.W. Shen, P.O.Box 606, Fort Collins, CO, chapter 7.

Spurr, K. J. W. (1985): Energy approach to estimating scour downstream of a large dam, *Water Power & Dam Construction,* Vol. 37, N°11, pp. 81-89.

Stein, O.R. ; **Julien**, P.Y. and **Alonso**, C.V. (1993): Mechanics of Jet Scour downstream of a Headcut, *Journal of Hydraulic Research*, Vol. 31, N° 6, pp. 723-738.

Swaffield, J.A.; **Boldy**, A.P. (1993): Pressure surge in pipe and duct systems, *Avebury Technical*, Hampshire, England.

Swanson, P.L. (1984): Subcritical Crack Growth and Other Time-and Environment-Dependent Behavior in Crustal Rocks, *Journal of Geophysical Research*, Vol. 89, N°B6, pp. 4137-4152.

Tao, C.G.; **JiYong**, L.; **Xingrong**, L. (1985): Translation from Chinese by **de Campos**, J.A.P.: Efeito do impacto, no leito do rio, da lamina descarregada sobre uma barragem-abobada, Laboratorio Nacional de Engenharia Civil, Lisboa.

Taraimovich, I.I. (1978): Deformations of Channels below High Head Spillways on rock Foundations, *Hydrotechnical Construction N°9, pp. 917 - 923*, September 1978.

Taraimovich, I.I. (1980): Calculation of local scour in rock foundations by high velocity flows, *Hydrotechnical Construction N°8.*

Tennekes, H.; **Lumley**, J.L. (1972): A First Course in Turbulence, *The MIT Press*, US.

Thiercelin, M. (1987): Fracture toughness under confining pressure using the modified ring test, *Proceedings of the 28th US Symp. on Rock Mechanics*, pp. 149-156.

Thiercelin, M.; **Roegiers**, J.C. (1986): Fracture toughness determination with the modified ring test, *Proceedings of the 27th US Symp. On Rock Mechanics*, Alabama, pp. 284-290.

Thomas, N.H. et al. (1983): Entrapment and transport of bubbles by transient large eddies in multi-phase turbulent shear flows, *International Conference on Physical Modelling of Multi-phase Flow*, Coventry, pp. 169-184.

Thorley, A.R.D.; **Guymer**, G. (1976): Pressure surge propagation in thick-walled conduits of rectangular cross section, Journal of Fluids Engineering, ASCE, Vol. 98, pp. 455-460.

Thorley, A.R.D.; **Twyman**, J. W.R. (1977): Propagation of transient pressure waves in a sodium-cooled fast reactor, *Proceedings of the 2nd Conference on Pressure Surges*, London, published by British Hydromechanic Research Association.

Tollmien, W. (1926): Zum angew. Mathematik Und Mechanik, Vol. 6, p. 468.

Toso, J.; **Bowers**, E.C. (1988): Extreme pressures in hydraulic jump stilling basin, *Journal of Hydraulic Engineering*, ASCE, Vol. 114, N° HY8, pp. 829-843.

Van de Donk, J.A.C. (1981): Water aeration with plunging jets, PhD thesis, Technische Hogeschool Delft.

Van de Sande, E.; **Smith**, J.M. (1973): Surface entrainment of air by high velocity water jets, *Chem. Engrg. Sci.*, 28, pp. 1161-1168.

Van de Sande, E.; **Smith**, J.M. (1976): Mass transfer from plunging water jets, *Chem. Engrg. J.*, 10, pp. 225-233.

Vasiliev, O.F.; **Bukreyev**, V.I. (1967): Statistical characteristics of pressure fluctuations in the region of hydraulic jump, *Proceedings 12th IAHR Congress*, Vol. 2, pp. 1-8.

Veronese, A. (1937): Erosion of a bed downstream from an outlet, *Colorado A & M College*, Fort Collins, United States.

Viscaino, A.C.; **Bribiesca**, S. (1973): Turbulent effects on the lining of stilling basin, Proceedigns of the 11th ICOLD Congress, Madrid, Q.41

Vischer, D.L.; **Hager**, W.H. (1995): Energy Dissipators, IAHR Hydraulic Structures Design Manual, AA Balkema, Rotterdam.

Volkart, P.U. (1980): The mechanism of air bubble entrainment in self-aerated flow, International Journal of Multiphase Flow, Vol. 6, pp. 411-423.

Volkart, P.U.; **Speerli**, J. (1994): Prototype investigation of the high velocity flow in the high head tunnel outlet of the Panix Dam, Proceedings of the 18th ICOLD Congress, Durban, Q. 71, R.6.

Whittaker, J.; **Schleiss**, A. (1984): Scour related to energy dissipators for high head structures, Zürich.

Whittaker, B.N.; **Singh**, R.N.; **Sun**, G. (1992): Rock Fracture Mechanics, *Elsevier Science Publishers BV*, Amsterdam The Netherlands.

Wiggert, D.C. ; **Sundquist**, M.J. (1979) : The effect of gaseous cavitation on fluid transients, *Journal of Fluids Engineering*, Vol. 101, pp. 79-86.

Winter, R.B. (1983) : Bruchmechanische Gesteinsuntersuchungen mit dem Bezug zu hydraulischen Frac-Versuchen in Tiefbohrungen, *Ber. Inst. F. Geophysik, Ruhr-Universität Bochum*, Reihe A, N° 13.

Wisner, P. (1965) : Role of the Froude number in the study of air entrainment, Proceedings of the 11th IAHR congress, Leningrad, USSR, Paper 1.15.

Wisner, P.; **Radu**, M.; **Armences**, G. (1967): Note sur les méthodes d'étude sur modèle réduit des affouillements locaux des lits rocheux, *Proceedings of the 12th Congress of the I.A.H.R,* Vol. 3, Fort Collins.

Withers, W. (1991): Pressure fluctuations in the plunge pool of an impinging jet spillway, PhD Thesis, *University of Glasgow*.

Wylie, E.B.; **Streeter**, V.L. (1978): Fluid Transients, *Mc Graw-Hill Int. Book Company*, US.

Xu-Duo-Ming (1983): Pressao no fundo de um canal devido ao choque de um jacto plano, e suas caracteristicas de fluctuacao, Translation from chinese by J.A. Pinto de Campos, Lisboa.

Youkowski, N. E. (1898): Mem. Imperial Academy Soc. Of Petersburg, Vol. 9, N° 5, *Translated by O. Simin, Proceedings of the Amer. Water Works Association*, Vol. 24, 1904, pp. 341-424.

Yuditski, G.A. (1963): Actual pressure on the channel bottom below ski-jump spillways, *Izvestiya Vsesoyuznogo Nauchno – Issledovatel – Skogo Instituta Gidrotekhiki*, Vol. 67, pp. 231-240.

Yuditskii, G.A. (1971): Experimental Prediction of Rock Bed Scour below a Ski-Jump Spillway Dam. (Translated from Russian by the IPST, Jerusalem, 1971).

Yuen, E.M. (1984): Clear water scour by high-velocity jets, Master's thesis, Department of Civil Engineering, University of Windsor, Ontario.

Zhang, Z.X.; **Kou**, S.Q.; **Jiang**, L.G.; **Lindqvist**, P.A. (2000): Effects of loading rate on rock fracture: fracture characteristics and energy partitioning, *International Journal of Rock Mechanics and Mining Sciences*, Vol. 37, pp. 745-762.

Zhao, J. (2000): Applicability of Mohr-Coulomb and Hoek-Brown strength criteria to the dynamic strength of brittle rock, *International Journal of Rock Mechanics & Mining Sciences*, Vol.37, pp. 1115-1121.

Zhao, J.; **Li**, H.B. (2000): Experimental determination of dynamic tensile properties of a granite, *International Journal of Rock Mechanics and Mining Sciences*, Vol. 37, pp. 861-866.

Zielke, W.; **Perko**, H-D (1990): Gas release in transient pipe flow, *Proceedings of the 6th International Conference on Pressure Surges*, BHRA, Cranfield, UK.

Acknowledgments

My thesis adventure began in May 1998. At that time, Prof. Dr. Anton Schleiss had just arrived as new Director of the Laboratory of Hydraulic Constructions, and so had also his ideas in hydraulic research. One of these ideas was to perform an experimental study on water pressures in artificial rock fissures under the impact of falling jets. He proposed to build an experimental facility that makes use of prototype jet velocities. The proposal looked much like a challenge, and I decided to pick up the gauntlet.

I would first of all like to thank Prof. Dr. Anton Schleiss for helping me and for giving me the opportunity to perform this research work. Furthermore, I am very grateful for the possibilities he gave me to make the best out of this work: during four years, I had the chance to collaborate with several researchers and practical engineers that are specialized in the subject, and I was able to present my results at several occasions at international conferences throughout the world. At the same time, I kept a significant degree of freedom to orientate my research like I wanted to. All of these conditions give the impression to be of secondary importance when performing a thesis, but they aren't. Appropriate research needs motivated students, and motivation is directly enhanced by every day working conditions and by particular opportunities, such as international collaboration and conferences.

Thanks are also addressed to those with whom I had the chance to directly collaborate. Starting in Europe, and more precisely in Belgium, special thanks go to Prof. Dr. Michel Pirotton and Sébastien Erpicum, from the Université de Liège, for their significant contributions in the field of numerical modeling. Michel taught me how to search for air bubbles without pressure sensors, and our multiple collaborations were not only very fruitful, but also full of sympathy. Under the same circumstances, I would like to thank Prof. Dr. Hank Falvey, from Colorado State University, for his significant support and guidance he provided me during the last two years in any field of my thesis. Hank likes to "scramble the boat" and to "hit the ground running", and his particular insight and experience largely contributed to the readability and to the scientific level of the work. Furthermore, I'd like to thank Prof. Dr. Alan Ervine, from the University of Glasgow, for his very useful advice on turbulence and aeration of jets and plunge pools. Alan and Hank have the particular capability to make the best out of any work, and to transmit this feeling towards the people they work with. I also appreciated the practical advice I received from Dr. George Annandale, from Engineering & Hydrosystems Inc. George has a nose for practical engineering applications of basic research, which is as important as the research itself. The last person I'd like to mention is Dr. Michael Benesch from ETHZ, who introduced me into the world of pressure sensors and data acquisition techniques.

In addition to the aforementioned people, I am also grateful to Prof. Dr. François Avellan, Director of the Laboratory of Hydraulic Machines at EPFL, and Daniel Rouiller, from the same Laboratory, for their help and advice in preparing the pressure sensors and data acquisition equipment. Also, I address my thanks to the Swiss Committee on Dams (CSB), the engineering company Stucky Ingénieurs Conseils and the Commission on Technology and Innovation (CTI) for their financial aid to the project. Their recognition of my work constitutes an additional stimulant and aid for the future.

No experimental modeling is possible without the professional and friendly help of the people that know better than any hydraulic engineer how flowing water looks like: I'd like to thank René Fontanellaz and Eric Pantillon for their mechanical support and help during the construction of the facility, and also for their patience when helping me to solve practical problems. Eric and René largely contributed to the success of the test runs. I also want to thank Louis Schneiter for his help and advice during the conception phase of the facility.

Last but not least, I thank my parents for have given me the opportunity to study and to stand where I am today, and of course also my wife Marianne, for her continuous support during this sometimes difficult period. I don't even dare to count the number of evenings and weekends I spent working at university or simply reading an "interesting" textbook at home.

The accomplishment of this thesis is not only an enlightenment for both of us, but also the fruit for that part of our time in common that we gratefully sacrificed to this work during the last few years.

Communications du Laboratoire de constructions hydrauliques
Ecole Polytechnique Fédérale de Lausanne
Editeur: Prof. Dr A. Schleiss

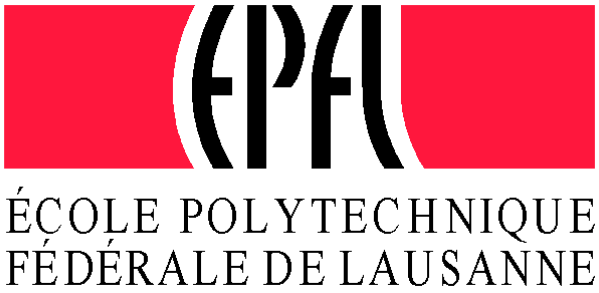

Prof. Dr A. Schleiss
Laboratoire de constructions hydrauliques - LCH
EPFL, CH-1015 Lausanne
http://lchwww.epfl.ch
e-mail: secretariat.lch@epfl.ch